SAPIENZA
UNIVERSITÀ DI ROMA

Final dissertation submitted in satisfaction of the requirements for the degree of Doctor of Philosophy

Department of Structural and Geotechnical Engineering

XXXI cycle

Soil-structure interaction for bridge abutments: two complementary macro-elements

Supervisor
Prof. Luigi Callisto

Candidate
Davide Noè Gorini

Academic year 2017-2018

Contents

Introduction **6**

1 Soil-abutment-superstructure interaction **11**

1.1 Existing approaches 12

1.2 Towards the plastic response of the abutment 16

1.2.1 Full-scale testing of abutments 18

1.2.2 Numerical simulations of the mobilisation of the passive resistance of bridge abutments 20

1.2.3 Empirical relationships for lateral pressure and displacement . 21

1.3 Direct approach and substructuring in soil-structure interaction . . . 28

1.4 Macro-element representations in geotechnical engineering 29

2 A complementary macro-element approach **38**

2.1 A step forward: two complementary macro-elements 38

2.2 The analysis framework OpenSees 39

3 The case study of the Pantano viaduct **43**

3.1 Description of the case study 43

3.2 The Pantano subsoil 46

3.2.1 Geotechnical model of the subsoil 46

3.3 Constitutive models for soil 63

3.3.1 The SANISAND model 63
3.3.2 The PDMY model 79
3.3.3 Calibration procedure 86
3.4 Seismic demand 105
3.5 Deconvolution of the seismic records 107
3.6 From the real case study to a simplified structural model 116
3.6.1 Bridge structure 118
3.6.2 Foundation soils 120
3.6.3 Embankment 121
3.6.4 Soil-structure contact 127
3.6.5 Solution procedure 127
3.6.6 Modal analysis of the bridge 131

4 Dominant responses of the soil-abutment system 136
4.1 Analytical evaluation of the dominant responses 137
4.1.1 Transverse response 138
4.1.2 Longitudinal response 145
4.1.3 Vertical response 155
4.1.4 Generic direction of motion 160
4.2 Numerical evaluation of the nonlinear dominant responses of the soil-abutment system 162
4.3 Comparison between analytical predictions and numerical evaluations 175

5 A macro-element for bridge abutments 182
5.1 Conceptual framework 182
5.2 The thermodynamic approach 184
5.3 One-dimensional formulation 193
5.3.1 Balance and compatibility 197

5.4 Energy function . . . 199
5.4.1 Gibbs free energy . . . 202
5.4.2 Helmholtz free energy . . . 205
5.5 Dissipative response . . . 207
5.5.1 Yield functions . . . 207
5.5.2 Dissipation function . . . 208
5.6 Incremental response . . . 210
5.7 Multi-axial formulation . . . 224
5.7.1 Balance and compatibility . . . 225
5.8 Energy function . . . 226
5.8.1 Gibbs free energy . . . 229
5.8.2 Helmholtz free energy . . . 230
5.9 Yield functions . . . 231
5.9.1 Ultimate conditions of the soil-abutment system . . . 232
5.9.1.1 Limit analysis and numerical modelling . . . 232
5.9.1.2 Non-dimensional formulation . . . 234
5.9.1.3 Bi-axial load . . . 236
5.9.1.4 Moment transmission at the deck-abutment contact . 238
5.9.1.5 Inertial effects . . . 242
5.9.1.6 General formulation of the ultimate surface . . . 245
5.9.1.7 Normalised representation and calibration . . . 250
5.9.2 Identification of the elastic domain . . . 254
5.9.3 Generalised hardening rule . . . 259
5.10 Dissipation function . . . 265
5.11 Incremental response . . . 266
5.12 Implementation . . . 281
5.12.1 Numerical integration of the equations of motion . . . 282

5.12.2 A new material in OpenSees: one-dimensional macro-element . 290
5.12.3 A new finite element in OpenSees: multi-axial formulation . . 290
5.13 Application in numerical analysis 294
5.14 Calibration 297
5.14.1 Static parameters 299
5.14.2 Mass of the macro-element 306
5.15 An energetically compatible macro-element for shallow foundations . 315
5.15.1 Mathematical formulation 317
5.15.2 Application to the case study 328

6 A macro-element of the bridge structure 332
6.1 Conceptual framework 332
6.2 Calibration of the elastic transfer tensor 335
6.3 Validation 337
6.3.1 Uni-axial elastic macro-element 337
6.3.2 Bi-axial elastic macro-element 350
6.4 Effect of the dynamic response of the embankment 358
6.5 Effect of the elastic-plastic behaviour of the foundation soil 362
6.5.1 Soil plasticity curves of the transfer tensor 364
6.5.2 Relevance in engineering applications 368
6.6 Different seismic scenarios 371
6.7 Effect of pore water pressure 376
6.8 Nonlinear structural behaviour 378
6.8.1 Nonlinear macro-element 381
6.8.2 Bi-linear representation 384
6.8.3 Validation 384
6.9 Macro-element for the reference multi-span girder bridge 389

7 Seismic performance of the soil-bridge system 393

7.1 Site response analysis 393

7.1.1 One-dimensional site response 394

7.2 Different representations of the soil-abutment interaction 399

7.2.1 Structural model with dynamic impedance functions 400

7.2.2 Structural model with macro-elements 402

7.3 Seismic performance of the structure 403

7.3.1 Foundation input motion 403

7.3.2 Seismic performance of the bridge 408

7.3.3 Local performance of the abutment 420

Conclusions 424

Bibliography 429

8 Appendix 1: dissipative abutments 441

9 Appendix 2: incremental response of the macro-element for bridge abutments 462

10 Appendix 3: three-dimensional site response analysis 494

Introduction

In recent years, the designers of long girder bridges in seismic areas have frequently opted for a continuous structural scheme, in which the abutments are called to carry large seismic forces engaging the dynamic response of the soil-abutment system. In view of this, the abutment response assumes a central role in evaluating the seismic performance of a bridge as an effect of its strong interaction with both the soil and the superstructure. This consideration introduces the cardinal question pursued in the present research: how and to what extent can the dynamic response of the abutments alter the global behaviour of a bridge and vice versa?

The dynamic soil-abutment-superstructure interaction is a complex problem involving expertise in different fields, with a challenging physical and numerical modelling. From a numerical point of view, a direct approach to account for the soil-abutment-superstructure interaction would require the implementation of coupled soil-bridge models, including the structural model, the abutment and the foundation soils down to the bedrock. Dynamic simulations of such large models imply a hardly manageable computation and a not immediate interpretation of the results, that confine their use only to an advanced verification stage of the design process. Hence, there is the need to limit the computational demand of the numerical models, without however renouncing to a clear representation of the salient aspects of the soil-abutment-superstructure interaction. This usually constitutes a limitation either in evaluating the performance of the structure or in studying the

local dynamic response of the abutments because of the difficulties associated with the identification of suited mechanical systems able to represent the global effects of the missing part of the domain. The global structural model should include a reasonable representation of the abutment structure and also of the volume of soil interacting with the latter, while the geotechnical analysis of the abutment should incorporate a simplified description of the dynamic response of the bridge into a finite-element model of the soil-abutment system.

The present research proposes a method of analysis based on macro-elements, whose main objective is to incorporate the salient aspects of the soil-structure interaction occurring at the abutment locations in the structural and geotechnical analyses of the bridge, preserving a manageable computational demand and creating a link between the response of the two sub-systems identified. A macro-element is a generalised force-displacement relationship that simulates the mechanical response of a sub-domain. Therefore the whole soil-bridge domain is divided into two problems through the introduction of two macro-elements, conceived to reproduce, in a complementary manner, the soil-abutment-superstructure interaction effects: a macro-element of the soil-abutment system, developed as a useful tool for the structural analysis, and a macro-element of the superstructure to be included in the local model of the abutment instead.

This study starts with a literature review of the existing methods usually used to represent the interaction between the abutments and the superstructure of the bridge, trying to give a complementary overview of the problem. In Chapter 1, the main features of the soil-structure interaction for bridge abutments are described, giving evidence of the current analysis methods.

The proposed methodology is presented in its essential characteristics in Chapter 2, with description of the integrated approach with macro-elements. Then, the numerical platform employed to carry out the nonlinear dynamic analyses on the

soil-structure interaction models is introduced.

A fully coupled soil-bridge model was developed, inspired by a real case study in Italy, as the reference system for validating the macro-element method. It constituted an interesting case study for the problem under examination, in virtue of the high seismicity of the site of the bridge and for the numerous experimental data available for the foundation soils. Chapter 3 is therefore devoted to the description of the case study, from the geotechnical characterisation and the structural identification to the numerical modelling. In this regard, two advanced constitutive models are employed to get an accurate description of the soil behaviour under cyclic loading conditions. The sub-systems identified by the macro-element method are also illustrated, showing the solution procedure adopted in the numerical analyses and giving some insight into the computational demand associated with the different numerical representations implemented.

In Chapter 4, a study on the nonlinear dominant responses of the soil-abutment system is presented with the aim to evaluate the inertial effects arising from the dynamic excitation of the embankment, considering the multi-directionality of the ground motion and the nonlinear behaviour of soil. This study is developed following two approaches: a numerical investigation of the dynamic response of soil-abutment interaction models and an analytical evaluation of the modal characteristics of the system. The former is accomplished through the implementation of numerical models in the analysis framework OpenSees, using non-linear advanced constitutive models to describe the soil behaviour. In this way, the dominant responses of the soil-abutment system are identified, framing them in a conceptual scheme useful to interpret the dynamic response of the abutments. Taking the numerical results as an element of comparison, the analytical procedure is aimed to provide a rigorous method for an immediate evaluation of the vibration modes of bridge abutments at small strain levels. As a result, closed-form solutions for the

modal characteristics are provided.

Focusing on the dynamic response of the whole structure, in Chapter 5 the formulation of the macro-element of the soil-abutment system is exposed in detail. The force-displacement relationship for the model is elastic-plastic and is derived from a rigorous thermodynamic approach. In the model, the ultimate capacity of bridge abutments under multi-axial loading conditions is described by a limit surface in the force space. The surface of ultimate loads is determined with the aid of numerically-evaluated limit analysis solutions and verified a posteriori through advanced elasto-plastic analyses. As a result, a general formulation is proposed to describe the ultimate conditions of bridge abutments, applicable in the case of abutments with both shallow and deep foundations. The formulation takes also explicitly into account the inertial effects developing in the soil interacting with the abutment, which are simulated by introducing appropriate participating masses in the model formulation. A straightforward calibration procedure of the macro-model is devised, making use of a limited number of constitutive parameters. The mathematical formulation was coded in the OpenSees library for a prompt use in engineering applications.

In Chapter 6, the focus moves towards the local behaviour of the soil-abutment system. In this regard, the macro-element of the bridge structure represents a novel approach to the study of the seismic behaviour of bridge abutments. The proposed method incorporates a simplified description of the dynamic response of the bridge into a finite-element model of the soil-abutment system. Specifically, the dynamic behaviour of the bridge structure is described by an expressly conceived elastic-plastic macro-element, that simulates the complex loading pattern transferred to the abutment during the seismic event. The general, nonlinear version of the macro-element presents a simple formulation, easily identifiable by a few constitutive parameters. This approach allows to take into account both the seismic sources perturbing an abutment: the propagation of seismic waves through the foundation soils and the

inertial forces coming from the superstructure. The response of the macro-element is tested against the results of nonlinear dynamic analyses on idealised soil-bridge systems. As a result, a general calibration procedure is delineated, providing useful information about the use of the macro-element in finite element codes.

In Chapter 7, the entire methodology is implemented in nonlinear dynamic analyses carried out in the analysis framework OpenSees and it is validated against the response of fully coupled dynamic analyses of the reference soil-bridge model. The results of a preliminary study of the site response highlight some interesting characteristics of the multi-directional dynamic response of the two advanced constitutive models used for soil. From the full soil-bridge model, several insight into the soil-abutment-superstructure interaction are given with particular focus on the relationship between the responses of the two complementary macro-elements. It is this relationship that defines a link between the soil-abutment system and the superstructure, representing a step forward to a semi-direct approach of the dynamic soil-structure interaction, in which the response of the missing part of the domain is explicitly included in the computation for a more reliable sub-structuring, leading to an unique overview of the problem.

Chapter 1

Soil-abutment-superstructure interaction

The abutment is a crucial component of a bridge for its significant mass and because it is characterised by a strong interaction with the soil. The dynamic behaviour of an abutment depends on its interaction with a large volume of soil involved in the dynamic response of the bridge and, moreover, it is influenced by its interaction with the superstructure, producing a reciprocal time-dependent exchange of inertial forces at the deck-abutment contact under seismic conditions. Accordingly, the local dynamic response of the abutment might alter significantly the global response of the bridge and vice versa.

An accurate evaluation of the seismic performance of a bridge cannot neglect the inertial forces and the effective behaviour of the deck-abutment contact resulting from the dynamic response of the abutments, which instead are often modelled as fixed or deformable constraints subjected to the free field ground motion. Similarly, the geotechnical analysis of an abutment usually neglects completely the deck-abutment interaction, or at most includes a very rough representation of the dynamic response of the remaining structure of the bridge. The objective of the

present research is to provide a macro-element approach to account for the soil-abutment-superstructure interaction effects in both the structural and geotechnical analyses. A literature review of the most classical approaches used in this field is provided in the following, that constituted the starting point for the present study.

1.1 Existing approaches

The main features associated with the soil-abutment-superstructure interaction under dynamic conditions may be summarised as follows: a frequency-dependent response, the arise of considerable inertial forces and a marked nonlinear behaviour. The several models developed in time have aimed to reproduce these features following different approaches that are recounted in the following.

Probably the most basic model to account for the soil-abutment interaction in the structural analysis consists in the insertion of a simple linear spring element at the end of the deck, usually along the longitudinal and transverse directions of the bridge. This model neglects all the fundamental features reported above, in favour of an extreme simplicity. Its excessive essentiality, in fact, leads to a difficult identification of the elastic properties of the springs, that instead depend on the level of strain attained in the soil and varies with the frequency of the external perturbation. On the geotechnical side, this translates in applying a linear elastic spring to the top of the abutment wall in the local model of the abutment. Also in this case, the model does not take into account the inertial effects induced by the oscillations of the bridge, as well as the possibility to admit a nonlinear structural response.

The first linear frequency-dependent model for soil-structure interaction is represented by the dynamic impedance functions, initially proposed by Luco and Westman (1971) and Veletsos and Wei (1971) in the early seventies. There is a bound-

less literature concerning frequency-dependent solutions for the dynamic impedance functions and their applications in soil-foundation interaction problems. The use of an impedance function in seismic engineering has the aim to represent the frequency-dependent stiffness and damping characteristics of soil-foundation interaction. Classical solutions for the complex-valued impedance function k_j^* can be written as

$$k_j^*(\omega) = k_j + i \cdot \omega \cdot c_j \tag{1.1}$$

where j is an index denoting modes of translational displacement or rotation, k_j and c_j denote the frequency-dependent foundation stiffness and damping coefficient, respectively, and ω is the circular frequency (rad/s). Many solutions are available for rigid circular or rectangular foundations located on the surface of, or embedded within, a uniform elastic, or visco-elastic half-space. In the case of a rigid rectangular foundation, Pais and Kausel (1988), Gazetas (1991), and Mylonakis et al. (2006) reviewed impedance solutions in the literature and presented equations for computing the stiffness and damping of the soil-foundation system. The generic term k_j of the dynamic stiffness matrix is obtained as follows

$$k_j = K_j \cdot \alpha_j \cdot \eta_j \tag{1.2}$$

in which K_j is the static elastic stiffness of the soil-foundation system, function of the geometry of the foundation and of the elastic properties of the soil; α_j is denoted as the dynamic stiffness modifier including the frequency-dependence, and η_j is the embedment correction factor that applies in the case of embedded foundations. Eq. 1.1 represents the properties of a Kelvin-Voight rheological system, composed of the parallel connection of an elastic spring and a viscous dashpot. In principle, the concept of dynamic impedance could be extended to the soil-abutment interaction in order to reproduce the desired frequency-dependent features, but the main issue

is associated with a proper identification of the relative stiffness and damping. In first approximation, the solutions for shallow foundations might be used, regarding the abutment as an equivalent embedded foundation. This is a strong assumption that leads to a very rough approximation of the abutment response, not verified neither experimentally nor numerically, and a more appropriate characterisation of the soil-abutment system would be necessary when using this method. The definition of an equivalent damping representing the dissipative mechanisms occurring in the soil interacting with the abutment is still an open question, while some steps forward have been made in the identification of the frequency-dependent stiffness of the soil-abutment system at small strains. Kotsoglou and Pantazopoulou (2007) provided closed-form solutions for the modal characteristics of bridge embankments oscillating in the transverse direction of the bridge, evaluating not only the modal stiffness but also the mass participation factors of the embankment according to a rigorous analytical development, under the assumption of elastic behaviour of the soil. Hence, in this study a more complete characterisation of the embankment-abutment system is provided, in which the importance of the inertial effects developing in the large volume of soil interacting with the abutment is highlighted. The solutions proposed by Kotsoglou and Pantazopoulou (2007) were employed in the integrated approach proposed by Stefanidou et al. (2017) to include the soil-structure interaction effects in the seismic response of the superstructure. In this approach, every element of the model was assumed as a linear elastic body and soil-structure interaction at the pier foundation and at the abutment locations was reproduced through a dynamic impedance function placed in the transverse direction of the bridge. The impedance function at the deck-abutment contact was also provided with a mass representing the first vibration mode of the embankment.

In a specular manner, Price and Eberhard (2005) used two single degree of freedom systems with visco-elastic behaviour, placed on the abutment top in the longi-

tudinal and vertical direction of the bridge, to reproduce the inertial effects coming from the superstructure in the soil-abutment model. The oscillators are calibrated to yield the same force transfer function as the first global mode of the structure. The stiffness k_{eq}, damping ξ_{eq} and mass m_{eq} of the idealised structure are given by

$$k_{eq} = (-\mathbf{e}_j \cdot \mathbf{K}_{sf} \cdot \phi_1) \cdot (\phi_1 \cdot \mathbf{K}_{ss} \cdot 1) \tag{1.3}$$

$$\xi_{eq} = \xi_1 \tag{1.4}$$

$$m_{eq} = \frac{k_{eq}}{\omega_1^2} \tag{1.5}$$

where ϕ_1, ω_1 and ξ_1 are the mass-normalised mode shape, circular frequency and damping ratio for the fundamental structural mode, respectively; $\mathbf{e}_j$ is the row of the identity matrix corresponding to the support degree of freedom considered and $\mathbf{1}$ is the vector whose entries are equal to 1. This procedure allows to determine the dynamic characteristics of the simplified equivalent system of the superstructure based on the assumption that the first global mode of the bridge represents the main contribution to the transmission of the inertial forces at the deck-abutment contact.

Hence, the use of dynamic impedance functions has been partially extended to the case of bridge abutments with a more appropriate identification of the equivalent mechanical systems. Nonetheless, although its remarkable computational efficiency, the impedance-based approach presents two intrinsic limitations: it is a linear representation of the soil-structure interaction and it does not present any form of directional coupling of the response yet. The equivalent Kelvin-Voight model imposes, in fact, a linear force-displacement law and therefore it is not able to reproduce the marked nonlinear behaviour of soil, nor the eventual attainment of the structural strength,

likewise situation for abutments with deep foundations under severe seismic conditions for instance. This implies that the method might be applied only to reproduce in an equivalent linear manner material nonlinearities, with all the uncertainties associated with the calibration of the equivalent elastic parameters. A significant directional coupling of the displacement field might be instead caused by the peculiar geometry and the partially or totally embedded structure of the abutment so that a generic perturbation applied to the abutment, intended as seismic excitation coming from the soil or the static and dynamic loads transmitted by the deck, may produce the development of a displacement field in a different direction with respect to the direction of loading. This would translate in introducing off-diagonal terms of the impedance functions in the dynamic stiffness matrix, as already proposed for shallow foundations (Pais and Kausel 1988, Gazetas 1991, Mylonakis et al. 2006).

The two limitations above associated with linear frequency-dependent models opened the way to a more recent conception of bridge abutments, in which the highly nonlinear behaviour of soil becomes an integral part of the abutment response for a better understanding and control of the seismic response of the whole structure.

1.2 Towards the plastic response of the abutment

In 1934, Terzaghi performed the well-known experiment on a retaining wall supporting a sandy backfill, schematically illustrated in Figure 1.1. The equilibrium of the system at rest is guaranteed by a longitudinal force $Q_{1,0}$ applied on top of the wall pushing the latter towards the backfill. From this condition, an increase of the force provokes a rotation of the wall towards the backfill but not in a proportional manner. In fact, starting from very low horizontal displacements of the wall top, the response becomes nonlinear with a stiffness Q_1/q_1 that reduces progressively until the attainment of the maximum force $Q_{1,p}$ that can be transferred to the backfill,

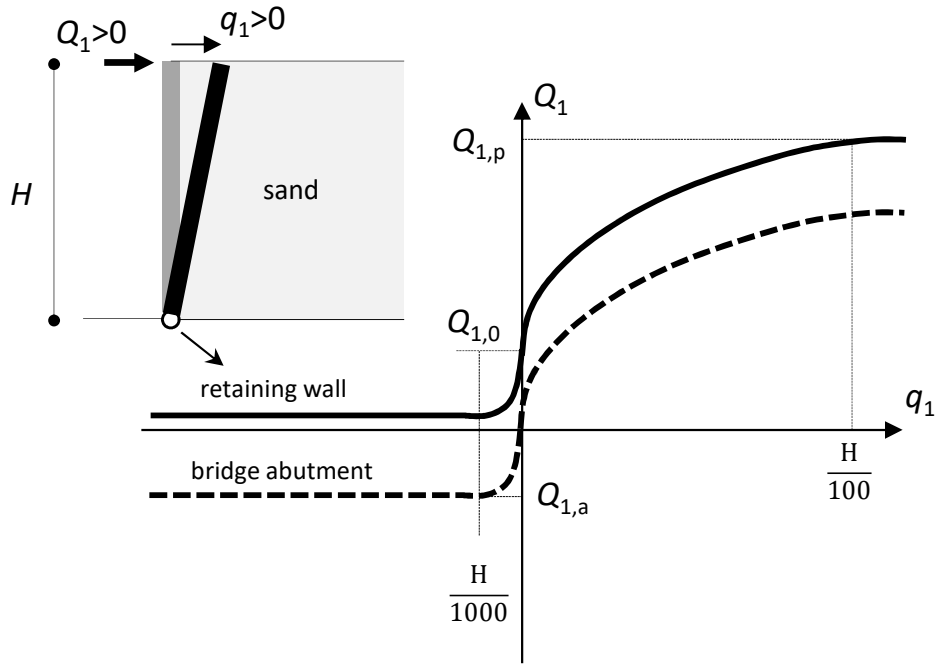

Figure 1.1: Qualitative representation of the force-displacement relationship for a retaining wall.

associated with the mobilisation of the passive resistance in the latter. When the force $Q_{1,0}$ reduces, the wall displaces downstream showing again a marked nonlinear behaviour, with stiffness that decreases more than linearly until becoming null in correspondence of the limit force $Q_{1,a}$ that mobilises the active resistance in the backfill. Hence, $Q_{1,a}$ and $Q_{1,p}$ identify the domain of the admissible states for a retaining wall. This experiment demonstrated that the nonlinear response of the wall, in terms of force-displacement relationship at the wall top, is highly nonlinear also far from the attainment of the ultimate conditions. These considerations are still valid in the case of a bridge abutment, for which a homothetic force-displacement relationship can be assumed (dashed line in Figure 1.1), this time passing through the axes origin since the stability of the system must be verified also without any force applied to the top.

In recent years, the nonlinear behaviour of the soil-abutment system was analysed in some experimental load tests (Maroney et al. 1990, Fang et al. 1994, Romstad et

al. 1995, Gadre and Dobry 1998, Stewart et al. 2007) and by some analytical studies (Martin et al. 1996, Siddharthan et al. 1997, Shamsabadi et al. 2005, Shamsabadi et al. 2007), as discussed in the following section.

1.2.1 Full-scale testing of abutments

The main scope of the experimental investigations was to study the progressive mobilisation of the passive resistance in the backfill induced by a purely longitudinal force impressed to the top of the abutment. In particular, two tests performed on full scale specimens are reviewed in the following. Conducted at UC-Davis (Romstad et al. 1995) and at UCLA (Stewart et al. 2007), these two tests were aimed to quantify passive response of cohesive (UCD test) and granular backfills (UCLA test). One of the first large-scale tests of passive earth pressures was the aforementioned cyclic tests of abutments by Romstad et al. (1995), that involed a 3.05 m (width) by 1.67 m (height) wall specimen that was displaced both into the backfill and along the backfill, simulating longitudinal and transverse deck excitation, respectively. The failure surface was observed to plunge down into the backfill from the base of the wall and then rise towards the surface at increasing distance from the wall. The ultimate passive pressure of the abutment was measured to be approximately 265 kPa, which was reached at a lateral displacement of 16.8 cm (10 % of the abutment height). The failure was two-dimensional in geometry because of a rigid connection of concrete wingwalls to the backwall. Those tests form the basis of current Caltrans seismic design criteria.

Stewart et al. (2007) tested a 4.6 m wide, 1.67 m m tall seat-type abutment wall with a silty sand backfill under one-way cyclic loading. The backfill was compacted to over 95 % Modified Proctor relative compaction. The backwall was pushed horizontally without any vertical movement. The one-way cyclic loading involved pushing the wall into the backfill by prescribed amounts, followed by unloading and

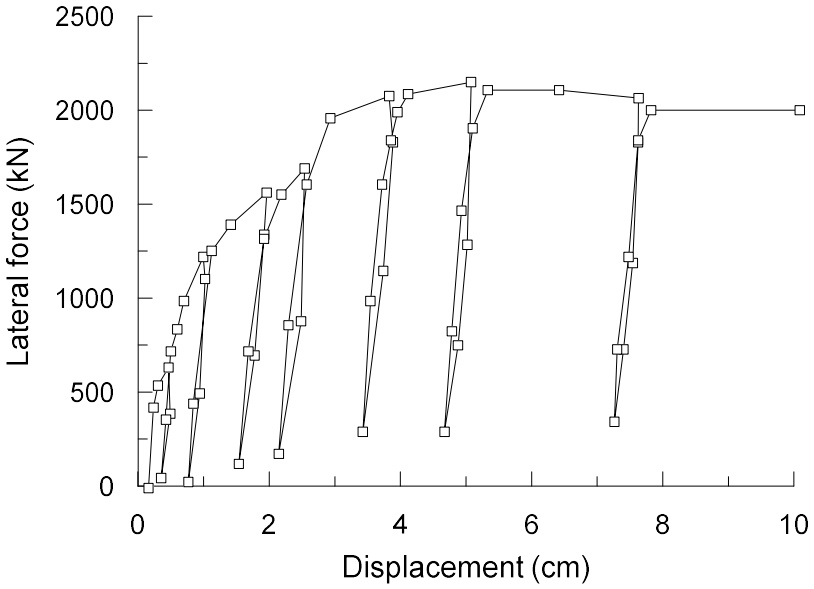

Figure 1.2: Measured longitudinal backbone curves of the cyclic tests conducted by Stewart et al. (2007).

further pushing. The wingwalls were constructed using smooth plywood with plastic sheeting on the interior face to minimise friction and, therefore, to impose plane strain conditions. The resulting force-displacement relationship at the abutment top is illustrated in Figure 1.2. The capacity of the abutment, intended as the maximum value of the lateral force, was measured to be approximately 2150 kN reached at a lateral displacement of about 5 cm, that is 3 % of the abutment height. After the maximum value, the lateral force shows a slight softening up to the residual capacity of approximately 2000 kN, which was mobilised for a displacement of about 8.5 cm (5 % of the abutment height). The initial tangent stiffness of the backbone curve resulted equal to $1.58 \cdot 10^5$ kN/m. These tests provided also information about the surface cracking patterns, showing systematically a log-spiral-shaped sliding surface developing in the backfill when the horizontal abutment capacity is attained, as depicted in Figure 1.3.

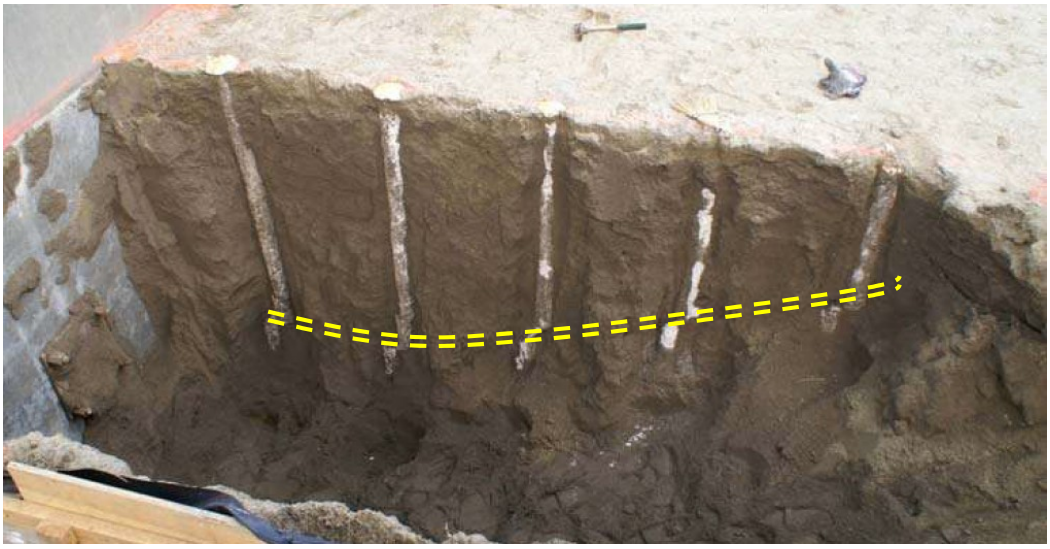

Figure 1.3: Log-spiral-shaped sliding surface associated with the backfill failure, obtained from the UCLA tests (reproduced from Stewart et al. 2007).

1.2.2 Numerical simulations of the mobilisation of the passive resistance of bridge abutments

After the experimental tests illustrated in the previous paragraph, several numerical simulations have been carried out to reproduce the observed progressive mobilisation of the passive resistance in the backfill. Shamsabadi et al. (2010) carried out two- and three-dimensional finite element simulations on soil-abutment models of the UCLA and the UCD tests, using the software package PLAXIS (Vermeer and Brinkgreve 1998). The hardening soil model (Schanz et al. 1999) was used to reproduce the behaviour of the backfill soil. Each simulation comprised two analysis steps: a first stage in witch gravity was applied and a subsequent step in which the wall was pushed into the backfill with prescribed displacements until passive failure occurred. The backfill failure obtained by the three-dimensional plane strain analyses is displayed in Figure 1.4, revealing the formation of a passive wedge within the abutment backfill. The shape of the ultimate band of localized shear strain is consistent with that of a logarithmic spiral curve and the cracking patterns observed

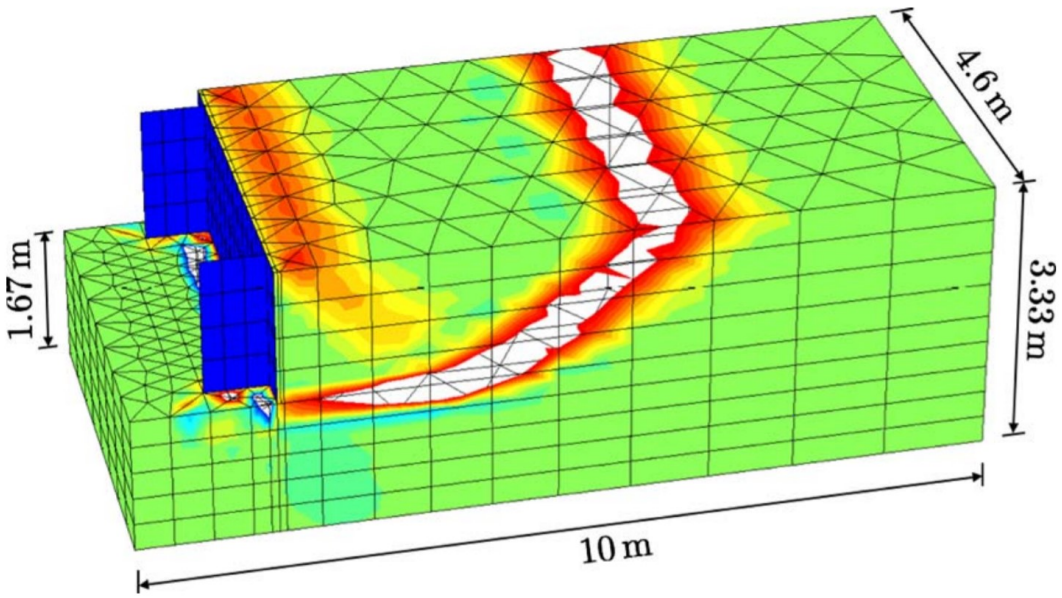

Figure 1.4: Three-dimensional plain-strain backfill failure obtained in finite element simulations of the UCLA tests (reproduced from Shamsabadi et al. 2010).

by Stewart et al. (2007). The resulting lateral force-displacement backbone curves are shown in Figure 1.5, which are in quite a good agreement with the experimental data from the UCLA test. The upper bound and lower bound curves refer to a different calibration of the strength parameters of the soil model. Similarly, numerical simulations of the UCD tests, represented in Figure 1.6, gave a good comparison between the experimental data and the numerical evaluations (Shamsabadi et al. 2010).

The two validated numerical models described above were then used to carry out a parametric study on the effect of the backwall height that finally led to the definition of empirical models to predict systematically the progressive mobilisation of the passive resistance in the backfill.

1.2.3 Empirical relationships for lateral pressure and displacement

Shamsabadi et al. (2005, 2007) proposed a model to predict the longitudinal re-

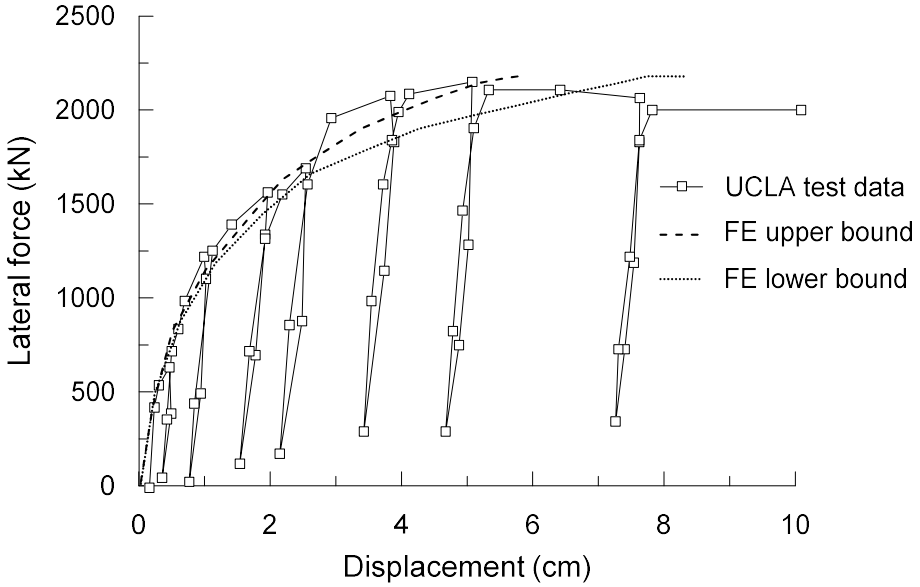

Figure 1.5: Lateral force-displacement backbone curves from three-dimensional FE simulations versus data from the UCLA test (reproduced from Shamsabadi et al. 2010).

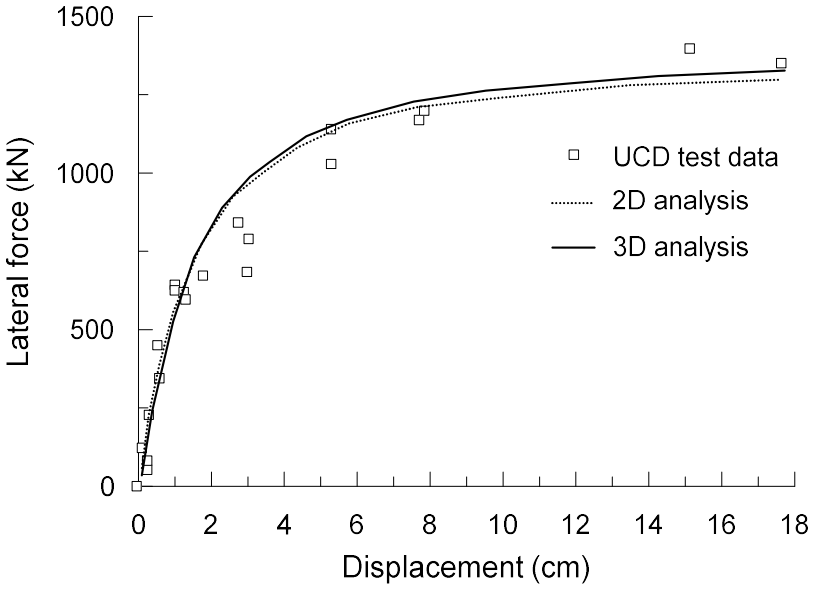

Figure 1.6: Lateral force-displacement backbone curves from two- and three-dimensional FE simulations versus backbone data from the UCD abutment test. (reproduced from Shamsabadi et al. 2010).

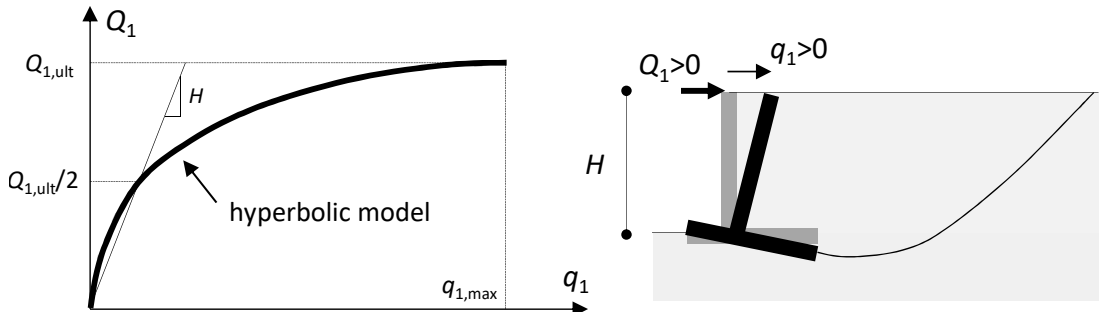

Figure 1.7: Hyperbolic force-displacement formulation proposed by Shamsabadi et al. (2005).

sponse of seat-type bridge abutments, from small strain levels up to the mobilisation of the passive resistance in the backfill, considering a longitudinal external force pushing the backwall into the backfill. They employed limit-equilibrium methods using logarithmic-spiral failure surfaces coupled with a modified hyperbolic law to estimate the nonlinear force-displacement relationship at the abutment top, shown in Figure 1.7. The model was initially validated against the experimental data from the UCD and UCLA tests, compared in Figures 1.8 and 1.9 respectively, and against the data measured by Fang et al. (1994) obtained from a small-scale laboratory test, in Figure 1.10.

The hyperbolic model was generalised to the case of a generic height of the backwall by introducing some height adjustment factors in the expression of the backbone curve, which therefore assumes the following form

$$F(y) = \frac{a_r \cdot y}{\overline{H} + b_r \cdot y} \cdot \overline{H}^n \tag{1.6}$$

$$\overline{H} = H/H_r \tag{1.7}$$

in which H_r is the reference abutment height and H is the effective abutment height of the problem under examination; a_r and b_r are instead empirical coefficients that specialise according to the specific mechanical properties of the backfill.

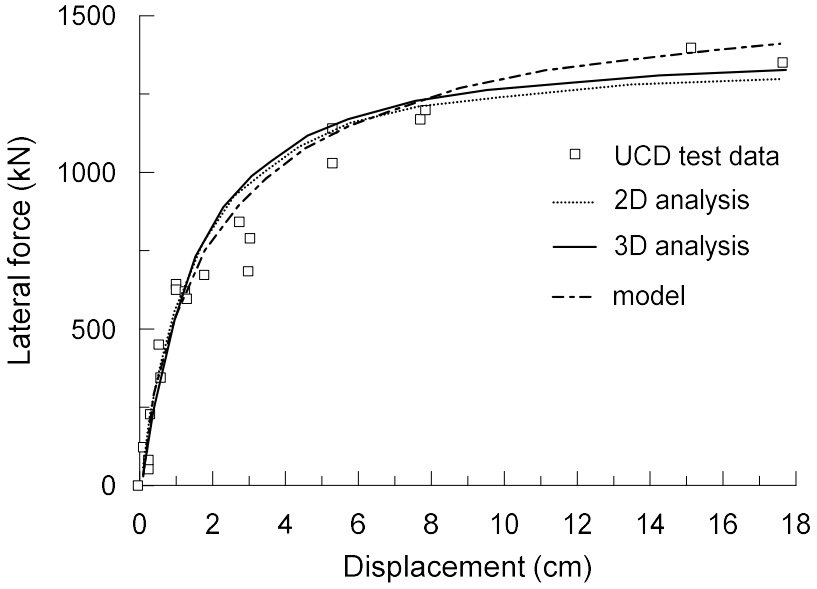

Figure 1.8: Comparison between the model proposed by Shamsabadi et al. (2005) and the data from the UCD abutment tests (reproduced from Shamsabadhi et al. 2007).

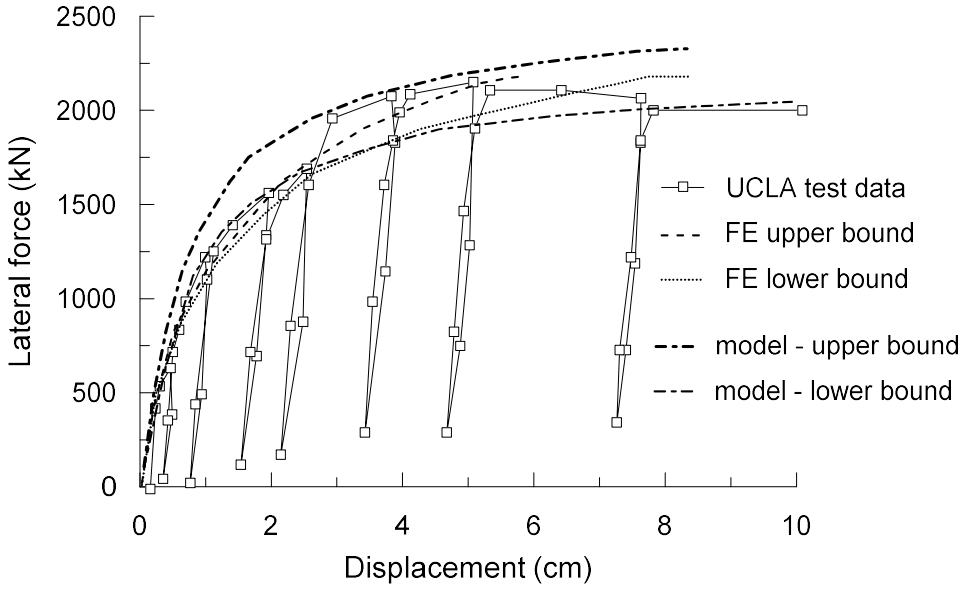

Figure 1.9: Comparison between the model proposed by Shamsabadi et al. (2005) and the data from the UCLA abutment tests (reproduced from Shamsabadhi et al. 2007).

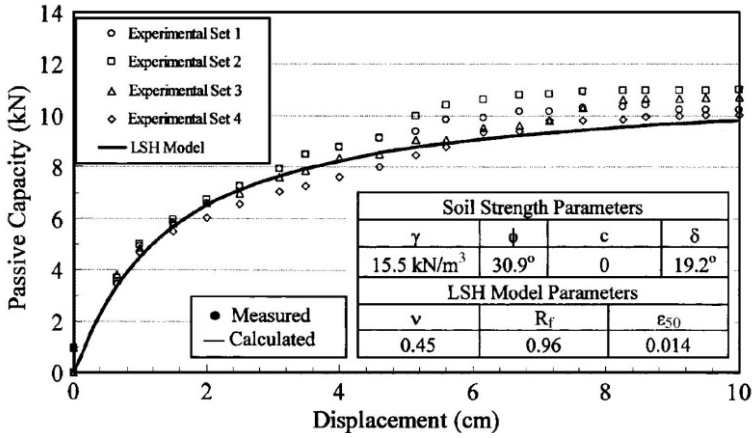

Figure 1.10: Comparison between the model proposed by Shamsabadi et al. (2005) and the experimental results on the passive capacity of Fang's wall in loose sand (Fang et al. 1994) (reproduced from Shamsabadhi et al. 2007).

From a numerical point of view, the authors introduced the hyperbolic formulation in the seismic analysis of the bridge structure as a nonlinear spring element connected to the end of the deck. This model provides a unilateral deformable constraint for the deck that is activated only when the deck moves towards the backfill, under the assumption that the deck-abutment interaction is only due to the pounding of the deck against the backwall. This behaviour was reproduced in the numerical model of the structure through a gap element connected in series with the nonlinear spring.

The model above represented a relevant step forward in accounting for soil-abutment-superstructure interaction in the structural analysis, for its pronounced nonlinear behaviour and its simple application in numerical simulations. Its employment in dynamic simulations is however limited to the longitudinal response of bridge abutments towards the attainment of the passive resistance in the backfill and therefore it does not take into account the different plastic mechanisms that can occur for different load directions. It does not have a loading-unloading law nor a frequency-dependent response, that are essential features to simulate the behaviour under dynamic conditions.

Nowadays, this displacement-performance philosophy is beginning to be accepted also in engineering practice, for example in the current criteria for seismic design of bridges in the US (Caltrans 2010) the complete horizontal load-displacement backbone curve of the abutment backwall is required. A better understanding of the nonlinear behaviour of the soil-abutment system has also led to explore the dissipative capabilities of bridge abutments under earthquake loading as a means for a higher anti-seismic control of the bridge. The solutions proposed in this regard can be grouped into studies on local dissipative mechanisms, usually localised in the structural members of the abutment, and on global mechanisms, that instead intervene on the mechanical properties of the backfill.

The studies of the local dissipative mechanisms aim to dissipate seismic energy through the local yielding in the backwall (Mitoulis and Tegos 2005, Mitoulis and Tegos 2010, Wang and Brennan 2015) or through the sliding of the deck on the shear keys placed on the abutment top (Vasseghi 2008). Looking at the global mechanisms, instead, in 2005 Ling et al. presented an experimental study of the earthquake performance of modular-block reinforced soil retaining walls, based on large-scale shaking table tests. The reinforcement in the backfill consisted of geogrids frictionally connected to the facing blocks of the wall. It was shown that the geogrids can improve the performance of the abutment, in terms of displacement field and stress concentration in the backfill induced by the earthquake. In a subsequent research (Ling et al. 2005), the optimal reinforcement length and spacing were analysed through a parametric study on finite element models of the soil-abutment system.

A relevant source of energy dissipation for an abutment can be represented by the full-strength mobilisation in the soil and in the foundation piles during the earthquake (Callisto and Rampello 2013). Foundation piles are usually employed to carry large vertical loads, minimising the settlements of the abutment structure

and, consequently, of the approaching slab. However, under severe ground shaking, the flexural behaviour of the piles comes into play and the foundation tends to exhibit a limited capacity. Flexural yielding is a favourable mechanism for an abutment because of its ductility and can result in reasonable internal forces in the superstructure. A typical plastic mechanism activated when the full strength of the system is mobilised is illustrated in Figure 1.11. The piles attain their strength according to a long pile mechanism, with depth of the second plastic hinge depending on the row considered because the yielding moment is a function of the axial load acting in the pile. The sum of the horizontal forces carried by each pile when the plastic mechanism is activated provides an upper bound of the seismic forces that can be transmitted to the superstructure. Hence, an appropriate design of a piled foundation may constitute a valid base isolation technique for the abutment. This methodology imposes a performance-based design of the abutment in which the adequacy of the foundation is related to the predicted seismic displacements and the corresponding damage undergone by the energy-dissipating structural elements, which in turn can be expressed by the curvature ductility demand.

The above discussion demonstrated that the three central points of the dynamic soil-abutment-superstructure interaction (frequency-dependence, inertial effects and nonlinear behaviour) are often analysed for different purposes. The frequency-dependent response of the soil-abutment system and the relative inertial effects are of primary interest in the structural analysis. Accordingly, their evaluation is based on simplified representations of the soil-abutment system, under the assumption of visco-elastic behaviour of soil. On the other hand, the investigations of the local abutment behaviour provide an advanced description of the mechanical behaviour of soil but a very rough, and often absent, representation of the abutment-deck interaction. Returning to the central point of the matter, in order to have manageable numerical models with a limited computational demand, the local response of the

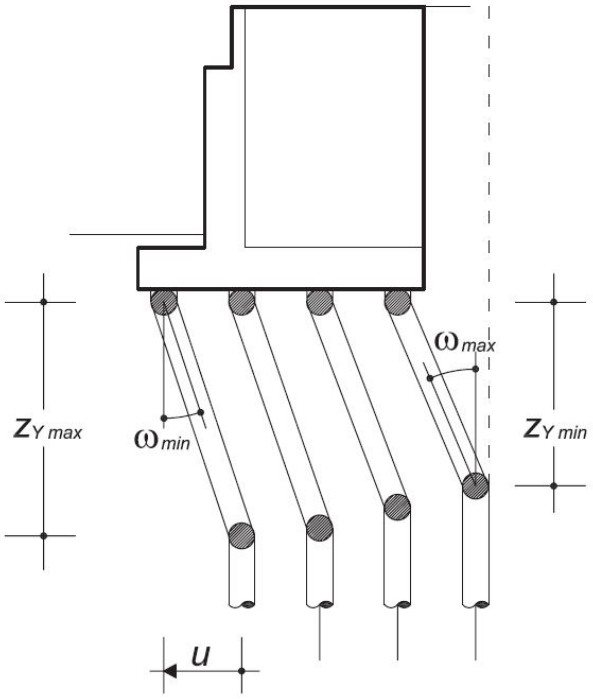

Figure 1.11: Plastic mechanism activated when the full strength of the system is mobilized (reproduced from Callisto and Rampello 2013).

abutment is usually disconnected to the behaviour of the entire bridge structure, without the possibility to quantify these effects on the global seismic performance of the bridge. In the following, a brief review of the two main analysis approaches that can be employed to analyse soil-structure interaction is presented, as an introductory stage to the semi-direct methodology proposed in the present research.

1.3 Direct approach and substructuring in soil-structure interaction

In principle, either the direct method or the substructure approaches may be used to analyse soil-structure interaction (Kramer 1996). The direct approach entails the use of coupled analyses on a numerical model of the entire soil-bridge system, simulating the propagation of seismic waves from the bedrock up into the structural members. Hence, the soil-structure interaction effects are implicitly taken into

account in a direct approach. Even though this approach allows to explore the dynamics with high nonlinear features in the geometry or in the mechanical behaviour, it requires extremely large computational efforts, becoming practically unfeasible for large structures such as bridges, especially at the design stage. Moreover, a full numerical model, including a global representation of the structure and the soil domain from the foundation level down to the bedrock, is hardly manageable either in its implementation or in the interpretation of the results.

Following a substructure approach, instead, the propagation of seismic waves through the foundation soils is studied separately from the dynamic response of the structure and the seismic actions obtained at the foundation level are then applied to a modified global model of the structure to account for soil-structure interaction. Hence, this approach would appear as a useful tool to limit the computational effort but, as commented in the previous paragraph, the challenging point for a proper use of the method consists in finding an adequate representation of the interacting behaviour of the abutment with the soil. To this end, an attracting method to account for the multiaxial, nonlinear interaction between soil and structure in the structural analysis consists in defining a macro-element representation of the geotechnical system able to describe its response from small strain levels up to failure (Roscoe and Schofield 1956, Roscoe and Schofield 1957, Nova and Montrasio 1991).

1.4 Macro-element representations in geotechnical engineering

A macro-element is a constitutive model in which the stress and deformation tensors are replaced by the resultant vectors of forces and corresponding displacements, with respect to which a suitable chosen elastic-plastic law is formulated. In this view, several formulations are available to describe the multi-axial response of shallow foundations (Paolucci 1997, Crémer et al. 2001, di Prisco et al. 2003, di Prisco et

al. 2006, Rha and Taciroglu 2007, Salciarini and Tamagnini 2009, Chatzigogos et al. 2011, Venanzi et al. 2014, Li et al. 2015) and some studies have been proposed for deep foundations (Gerolymos and Gazetas 2005, Rha and Taciroglu 2007, Correia 2011, Correia et al. 2012, Gerolymos et al. 2015, Houslby et al. 2017, Di Laora et al. 2018).

The nonlinear response of a macro-element can be regarded as a transition phase towards the limit conditions of the soil-structure system, which can be represented by a failure surface in the space of the generalised forces exchanged between the structure and the soil (Nova and Montrasio 1991, Butterfield and Gottardi 1994). The bearing capacity of shallow foundations under combined loads has been widely studied (Gottardi and Butterfield 1995, Houslby et al. 1993, Gottardi et al. 1999, Martin 1994, Martin and Houlsby 2000, Martin and Houlsby 2001, Houlsby and Cassidy 2002, Cassidy et al. 2004, Bienen et al. 2006, Chatzigogos et al. 2011) and, for a three degrees of freedom rigid foundation, it can be represented by the well-known rugby ball-shaped surface of ultimate loads illustrated in Figure 1.12. The ultimate locus is conveniently represented in a normalised space of the generalised forces, in which Q_N and Q_V are the normalised vertical and horizontal forces, respectively, and Q_M is the normalised moment. The surface is symmetric with respect to the planes $\{Q_N, Q_V\}$ and $\{Q_N, Q_M\}$, reflecting the symmetry of the problem, and it is entirely contained in the half-space of the positive values of the vertical force Q_N. A zero vertical force, in fact, is associated with the uplift of the foundation with respect to the underlying soil. The ellipsoidal shape of the ultimate surface is the result of several non-linear mechanisms representing the ultimate conditions of the foundation. An interesting modelling of these mechanisms was presented by Chatzigogos et al. (2011), who modelled the surface of ultimate loads as the combined result of all active mechanisms, as shown in Figure 1.13. The external ellipsoidal bounding surface $f_{BS}(\underline{Q}) = 0$ represents the ultimate conditions of a foundation

corresponding to the global mobilisation of the soil strength, when the foundation is not allowed to slide. As observed experimentally, however, this condition can be reached only when the vertical force is much greater than both the moment and the horizontal force. If a rough soil-foundation interface is considered in fact, with a friction angle ϕ_{int}, the admissible domain in the $\{Q_N, Q_V\}$ plane reduces, because it is further bounded by the surface $f_{int}(\underline{Q}) = 0$ associated with the attainment of the shear strength along the soil-foundation interface. The moment can cause the uplift of the foundation, identifying a region of the admissible domain, starting from the uplift initiation up to the toppling limit, in which the behaviour of the soil-foundation system is strongly nonlinear because of the partial contact between soil and foundation.

The irreversible displacements of a shallow foundation follow the normality rule only when the bearing capacity of the foundation is reached, thus for high values of the vertical force compared to the other components, as demonstrated by Gottardi and Butterfield (1995) through an experimental study of the nonlinear behaviour of shallow foundations. In this regard, Figure 1.14 shows the trajectories of the displacements in the plane of the forces acting on the foundation, obtained along different loading paths. Along radial loading paths it can be observed that, when the horizontal force V and the equivalent force M/B are comparable with the vertical force N, the increment of the horizontal displacement is limited compared to that in the vertical direction, resulting in a plastic flow mainly oriented towards the vertical direction. Along "right-angled" loading paths (Figure 1.14(b)), instead, the displacement increment can be reasonably assumed purely horizontal when the horizontal force is greater than the vertical one.

The behaviour at failure described above was also extended to the case of a six degrees of freedom foundation by several authors (Martin 1994, Martin and Houlsby 2000, Martin and Houlsby 2001, Houlsby and Cassidy 2002, Cassidy et al. 2006,

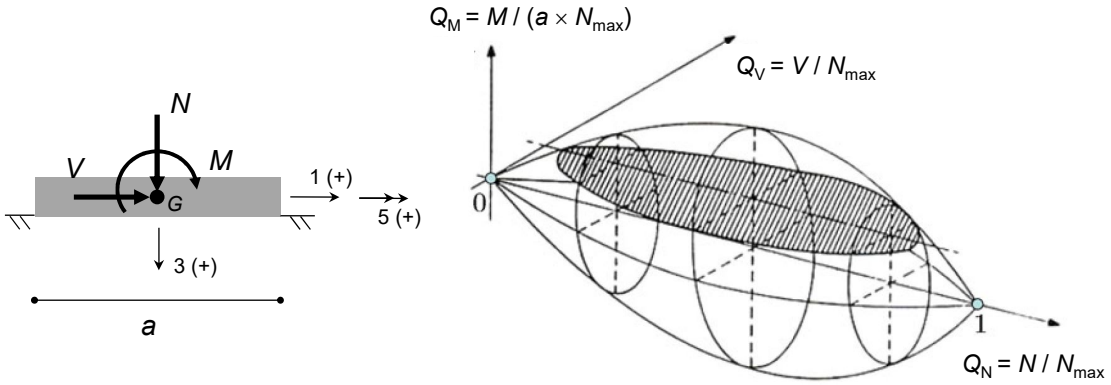

Figure 1.12: Ultimate surface for a 3 degrees of freedom shallow foundation on sand. Reproduced from Gottardi and Butterfield (1995).

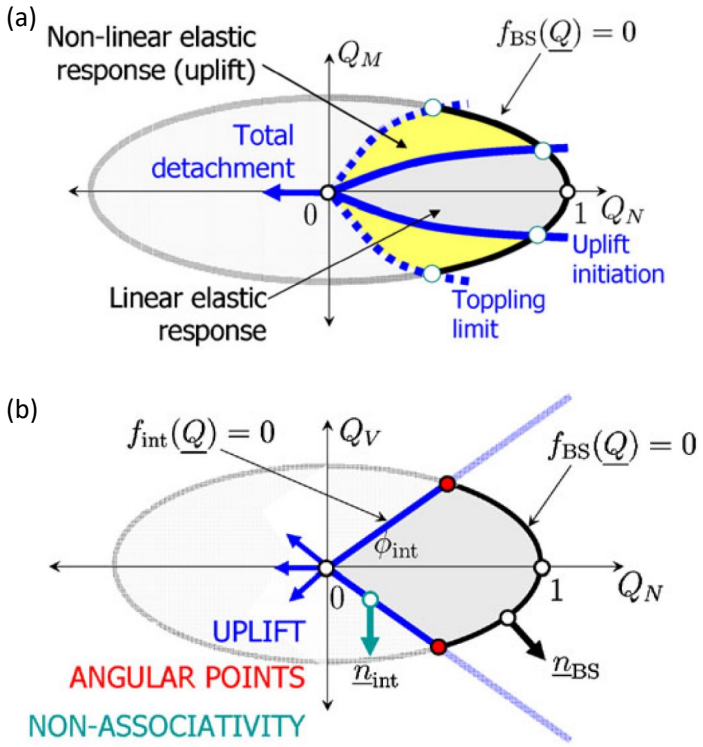

Figure 1.13: Modelling of the failure mechanisms of shallow foundations on cohesive soil in the $Q_N - Q_M$ plane (a) and $Q_N - Q_V$ plane (b) (reproduced from Chatzigogos et al. 2011).

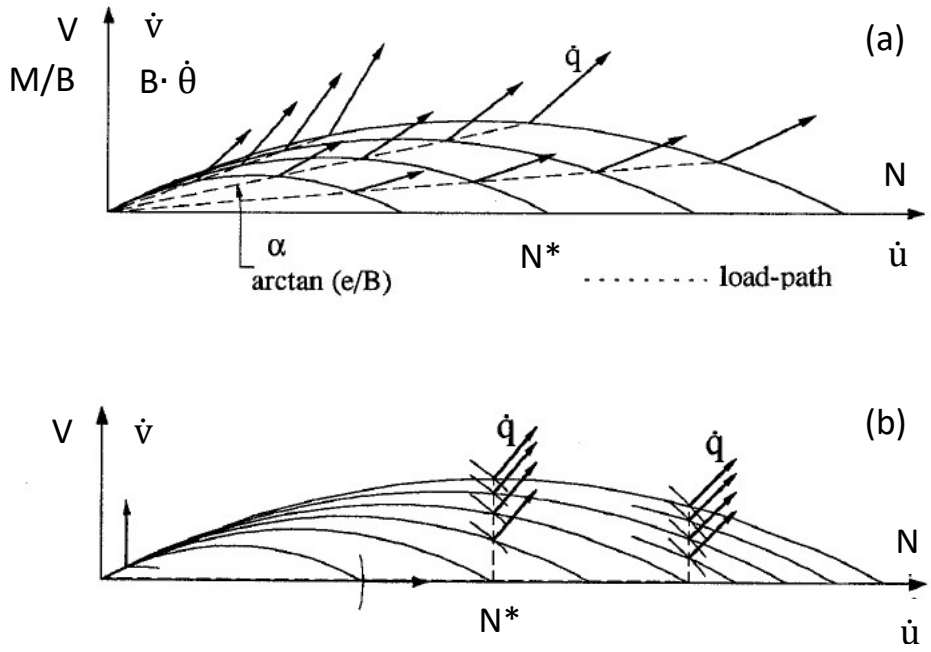

Figure 1.14: Hardening yield surfaces and displacement increment vectors along radial (a) and "right-angled" (b) loading paths (dotted lines) (reproduced from Gottardi and Butterfield 1995).

Grange et al. 2009). In his PhD thesis, Martin (1994) proposed a general expression to model failure of shallow foundations according to the following empirical equation

$$y^{(ult)} = \left(\frac{V_1}{h_0}\right)^2 + \left(\frac{V_2}{h_0}\right)^2 + \left(\frac{M_{r1}}{l_0}\right)^2 + \left(\frac{M_{r2}}{l_0}\right)^2 + \left(\frac{M_{r3}}{x_0}\right)^2 -$$

$$-\frac{2 \cdot a}{h_0 \cdot l_0} \cdot (V_2 \cdot M_{r1} - V_1 \cdot M_{r2}) -$$

$$-N^{2 \cdot \beta_1} \cdot \left(1 - \frac{N}{N^{max}}\right)^{2 \cdot \beta_2} \cdot N^{max(2-2 \cdot \beta_1)} = 0 \tag{1.8}$$

where h_0, l_0, x_0, a, β_1 and β_2 are model constants; the reader can refer to Martin (1994) for explanation on their physical meaning. Eq. 1.8 degenerates in the ellipsoidal ultimate surface illustrated in Figure 1.12 in the case of a bi-dimensional problem.

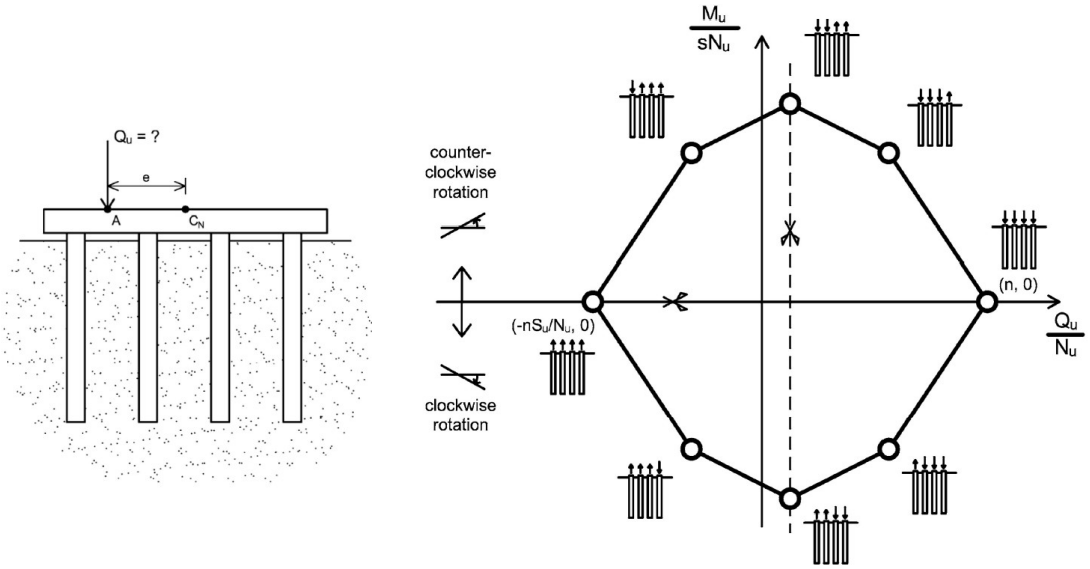

Figure 1.15: Interaction diagram for a row of 4 identical, equally spaced piles loaded by an eccentric vertical force. Reproduced from Di Laora et al. (2018).

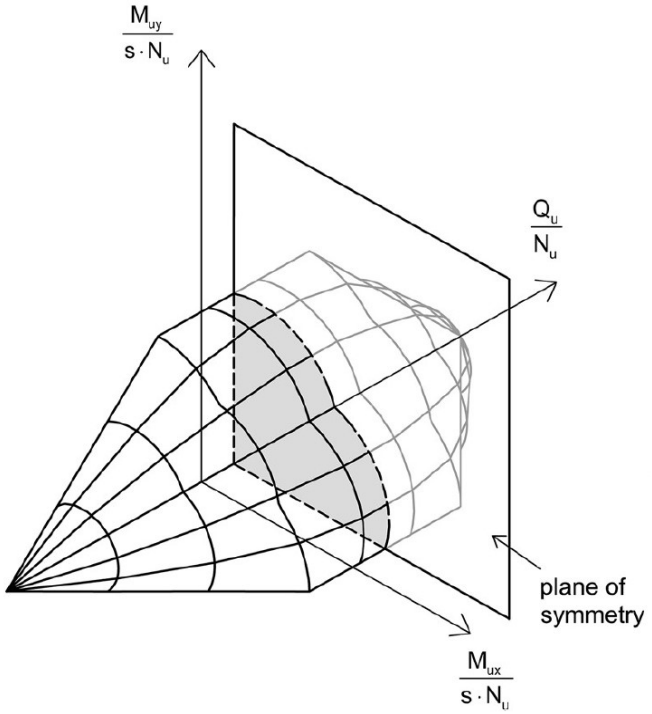

Figure 1.16: Interaction diagram in the $\{Q_u, M_{ux}, M_{uy}\}$ space. Reproduced from Di Laora et al. (2018).

Some formulations of the ultimate surface are also available for deep foundations (Gerolymos and Gazetas 2005, Correia 2011, Correia et al. 2012, Gerolymos et al. 2015, Di Laora et al. 2018). Di Laora et al. (2018) proposed interaction diagrams representing the bearing capacity of pile groups under vertical eccentric loads, obtained through the application of the theorems of limit analysis. The two-dimensional vertical force-moment diagram for a row of 4 identical, equally spaced piles is shown in Figure 1.15, in which the pile group fails by a cap rotation about the head of the pile with a full attainment of their ultimate axial strength, with except of the pile corresponding to the center of rotation. A more general representation of the ultimate locus is provided by the same authors in Figure 1.16, considering both moments in the horizontal plane. Under horizontal loads, Gerolymos and Gazetas (2005) and Gerolymos et al. (2015) provided a further version of the ultimate surface for a pile group, shown in Figure 1.17, that testifies again the important role played by the inelastic response of the piles. In fact, the main difference between the surfaces of shallow and deep foundations is that failure of a shallow foundation is essentially due to the activation of a global plastic mechanism in which the soil strength is mobilised, along the soil-foundation contact or in the volume of soil interacting with the footing, but the structural elements behave essentially as a rigid body with infinite strength; for a group of piles, instead, a global plastic mechanism generally involves the attainment of the bending or shear strength in the piles. This leads to a different shape of the surface and a different normalization scheme: the surface for shallow foundations is commonly normalised with respect to the vertical limit load while the ultimate loads for a soil-piles system are more conveniently divided by the yield threshold of the pile.

The elastic-plastic response of a macro-element is conceptually able to reproduce the essential features of the dynamic behaviour of a soil-structure system, such as a marked nonlinear response, with a relevant dynamic amplification due to the

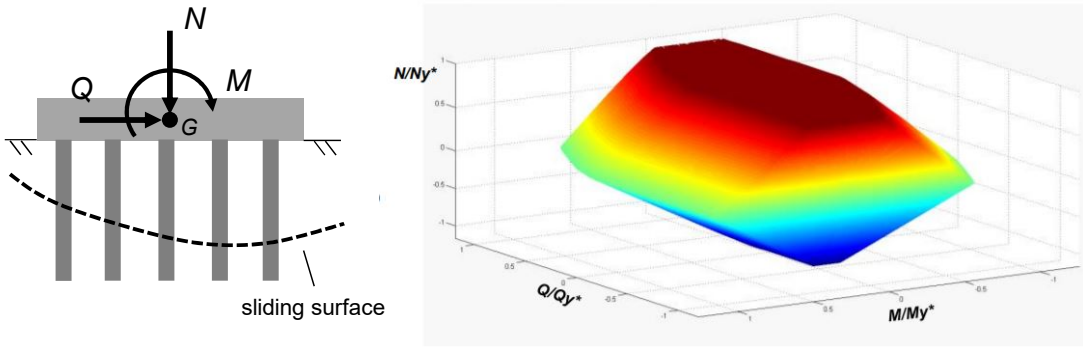

Figure 1.17: Ultimate surface for deep foundations. Reproduced from Gerolymos et al. (2015).

frequency-dependent effects, and the more or less pronounced directional properties of the system, according to its geometry. In this regard, several approaches have been employed to reproduce the dynamic characteristics of shallow foundations, developed according to different frameworks. The central point in defining the internal constitutive law of a macro-element consists in defining the tangent stiffness matrix of the global system. Without going into the details of the various models proposed in the past, some formulations used empirical relations for the terms of the stiffness matrix (Cremer et al. 2001, Chatzigogos et al. 2009, Chatzigogos et al. 2011), easily implemented in dynamic simulations, while some others were developed following rigorous analytical approaches, such as the hypoplastic models proposed by Salciarini and Tamagnini (2009), Buscarnera et al. (2010) and Venanzi et al. (2014). Also a thermodynamic model was developed for shallow foundations by Le Pape and Sieffert (2001), that represents the first attempt to derive a macro-element consistent with the dictates of Thermodynamics. The model was formulated considering a parabolic surface to represent the ultimate conditions of shallow foundations with an associative plastic flow.

For deep foundations, the model proposed by Correia (2011) represents a first formulation aimed to describe the nonlinear behaviour of a soil-pile system far from

failure. This is a bounding surface plasticity model for the pile-head resultant generalised forces and corresponding displacements, coupled with initial elastic impedance functions, that reproduces the elastic-plastic behaviour from small strains up to the ultimate conditions of the system.

For bridge abutments, only some models have been proposed (Shamsabadi et al. 2005, Shamsabadi et al. 2007), already discussed in Section 1.2.3, which focus on the one-dimensional mobilisation of the passive resistance in the backfill. A more recent study proposed by Nojoumi (2016) represents the first model simulating the combined translational and rotational behaviour of bridge abutments, particularly relevant for skew bridges. The method accounts for the nonlinear contact-gapping between the backwall and the backfill responses along three degrees of freedom of the deck-abutment contact, the transverse and the longitudinal translations and the skew moment along the vertical axis, according to a purely phenomenological formulation.

The literature review has briefly recalled the main advancements in the study of the soil-abutment-superstructure interaction, mentioning the results and methods that have been fundamental for developing the complementary macro-element methodology proposed in the present thesis.

Capitolo 2

A complementary macro-element approach

2.1 A step forward: two complementary macro-elements

A step forward is proposed in this thesis to link the abutment response and the bridge response in a semi-direct manner, to confer a high computational efficiency to the analysis method. The term semi-direct indicates that the methodology presents the essential characters of a sub-structure approach, in which the entire soil-bridge domain is divided into two sub-systems but with the introduction in the latter of two macro-elements that incorporate the response of the missing part of the model. This is a macro-element method that accounts for the salient aspects of the soil-abutment-superstructure interaction in a complementary way, in order to have a structural analysis and a geotechnical analysis that communicate by means of the internal responses of the macro-elements. The two models consist of a macro-element of the soil-abutment system, conceived as a part of the global structural model of the bridge to simulate the salient aspects of the soil-abutment interaction, and a macro-element of the bridge structure, included in the local soil-abutment model,

that simulates the global effects of the multi-directional dynamic response of the superstructure. The methodology has been coded in Matlab and in the analysis framework OpenSees (McKenna 1997, McKenna et al. 2000) and validated in non-linear dynamic analyses, taking as reference a full soil-bridge model inspired by a real case study in Italy.

2.2 The analysis framework OpenSees

The system modelling and response computations was performed by using the open source finite element analysis framework OpenSees (McKenna 1997, McKenna et al. 2000) (Open System for Earthquake Engineering Simulation) while the mesh of the models was generated and visualised through the pre/postprocessor software GID (Diaz and Amat 1999). OpenSees is a software framework for developing sequential, parallel and grid-enabled finite element applications in the field of civil engineering and it offers a high potentiality to reach an accurate modelling of the behaviour of both soil and structures. The continuous development of OpenSees is due to the participation to this project of a wide international scientific community that works to develop the code according to the new challenges in computational engineering. Though it was created for structural analysis, several constitutive models and finite elements have been added during the last decade to carry out dynamic simulations of geotechnical systems. Nowadays, OpenSees represents a powerful numerical tool to investigate the dynamic behaviour of soil-structure systems, considering a variety of natural hazards. Several methods of analysis can be used to solve the governing equations according to the specific problem examined.

OpenSees is an object-oriented framework for finite element analysis. The Tcl scripting language has been chosen to support the OpenSees commands, which are used to define the problem and its solution. Each of these commands is associated

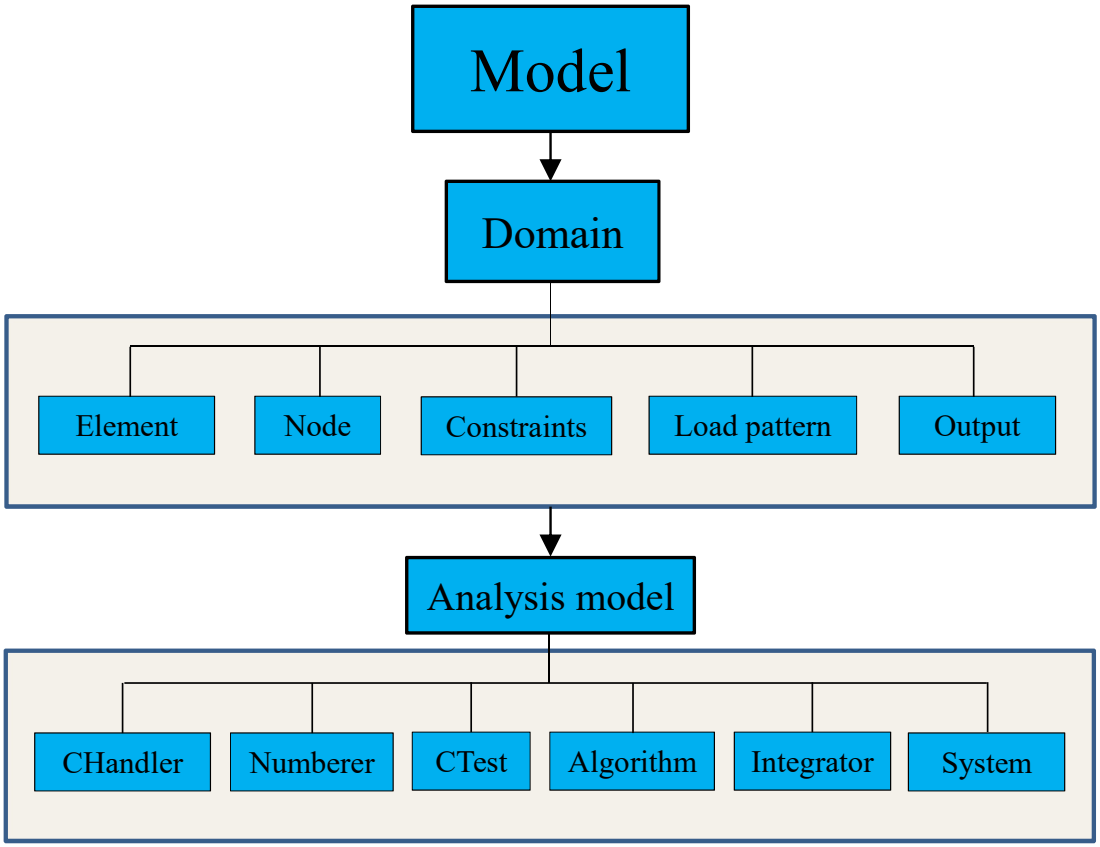

Figure 2.1: Flow chart illustrating the common structure of an OpenSees input file.

with a C++ procedure that is provided by a source code included in the OpenSees library. The common structure of an input script in OpenSees can be represented by the flow chart in Figure 2.1. As mentioned above, the scripts of very large models, such as those involved in the present research, require the use of a pre/post processor software to generate the mesh. The nodal and element information is then imported in the main Tcl script. After defining the boundary conditions, the appropriate typologies of finite elements for the problem at hand are assigned to the mesh and the relative output is set up. As a conclusive step, a model of analysis is assembled by setting the most appropriate features needed to optimise the computation.

Parallel computing can be obtained through the OpenSeesSP (Single Parallel Interpreter application) and OpenSeesMP (Multi Parallel Interpreter application)

applications (McKenna and Fenves 2008) that can be built from the OpenSees source code distribution. This was an essential feature to optimize the computation time for the non-linear time domain analyses of this research. The OpenSeesSP interpreter is conceived for the analysis of very large models with input files that take too long to run on a sequential machine (single processor). The interpreter will process the same script that the OpenSees interpreter running on a sequential machine will process, except for some additional options when it comes to choosing solvers. When running on a parallel machine, a single processor $P0$, called master processor, is running the main interpreter and processing commands from the main input script. The other processors are running ActorSubdomain objects (McKenna 1997). On the first issuance of the analyze() command in the script the model is partitioned, that is the elements are split and distributed by the master processor to the other machines. After this, the state and solving of the system of equations is done in parallel, depending on the choice of equation solver. When running as a job on a parallel computer with this interpreter, each process is running a slightly modified version of the basic OpenSees interpreter. This interpreter is particularly suitable for wide parametric studies, composed of numerous analyses running together, because able to partition the number of analyses to be run and the number of processors to be assigned to each analysis. Hence the OpenSeesSP interpreter solves a system of equations following a highly hierarchical structure: the master processor executes the commands of the main input script and partitions automatically the solving process among the other processors, for then reassembling the whole solution. The Multi Parallel interpreter, instead, allows to prescribe a specific partition of the processors and to run simultaneously many simulations among different machines. The latter interpreter results to be more efficient than OpenSeesSP but requires a more substantial modification of the main input script.

In the present research, time domain nonlinear dynamic analyses were carried out

implementing large soil-structure interaction models. The use of parallel computing was therefore needed, obtained through the OpenSeesSP interpreter, in order to optimise the computation time of the analyses. The efficiency of parallel computing on the two workstations used to carry out the dynamic simulations (see Section 3.6.5), intended as the ratio of the execution time using all the processors of the machine to that associated with the use of a sole processor, was of $80 - 85$ %.

One of the main advantages in using OpenSees consists in the possibility to integrate continuously the existing library with the new features needed to solve the specific problem under examination. In this regard, the mathematical formulation of the macro-element of bridge abutment was coded in OpenSees, generating two new source codes, written in C++, for the OpenSees library according to the procedure described in Section 5.12. The one-dimensional model was formulated as a new Uniaxial material class while the complete multi-axial formulation was included in OpenSees as a new ZeroLength finite element class.

Capitolo 3

The case study of the Pantano viaduct

3.1 Description of the case study

The Pantano viaduct was designed as the approaching structure to the Messina Strait suspension bridge, in Italy (Brancaleoni et al. 2010). As shown in Figure 3.1, the Pantano viaduct starts at the terminal structure of the suspension bridge and ends on a massive abutment situated on the Messina side.

The site of the bridge is characterized by a high seismicity due to the presence of several segmentations of active faults. The bridge was designed to transmit most of the longitudinal seismic forces to the abutment, that consequently would be loaded by large seismic actions. Figure 3.2 shows a global structural model of the viaduct implemented in SAP2000 and OpenSees in a preliminary stage of this study. The viaduct is a girder bridge composed of three curved decks, a central railway and two lateral roadways, which are supported by five piers, by the terminal structure of the suspension bridge and by the abutment.

The abutment, whose detailed representation is shown in Figure 3.3, is a massive

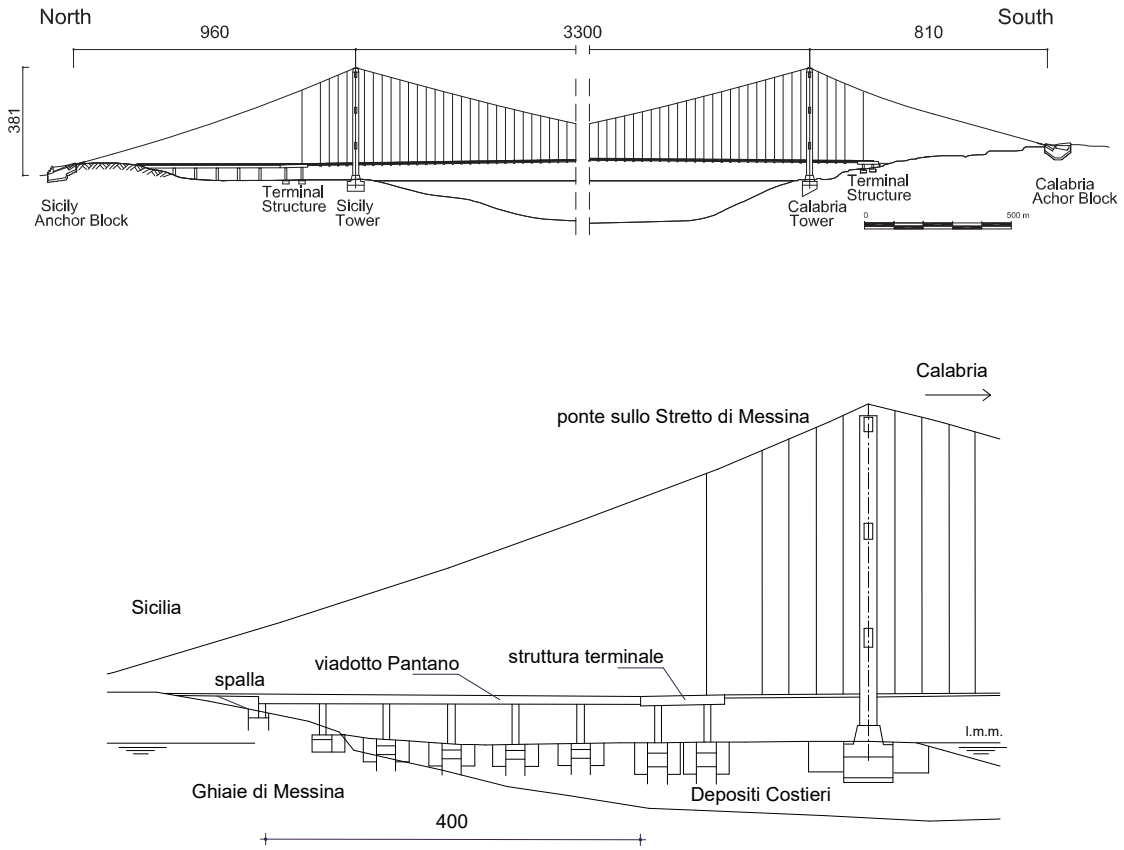

Figure 3.1: View of the Messina Strait suspension bridge, reproduced from Callisto and Rampello (2013) (upper figure), and zoomed-in view of the Pantano viaduct (lower figure).

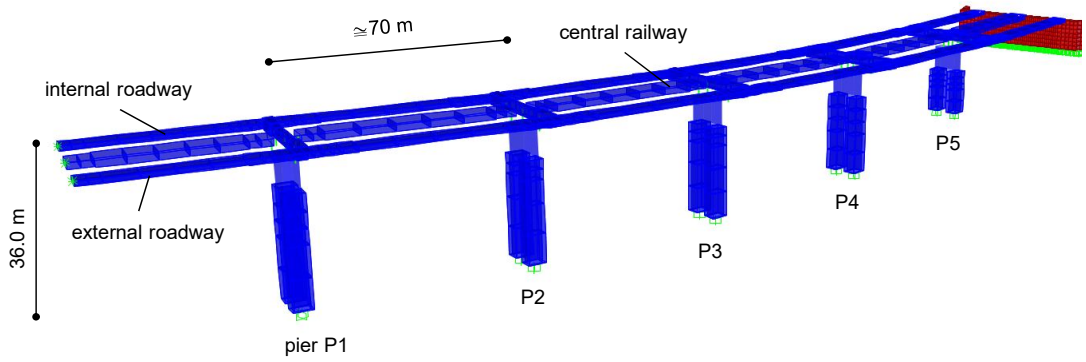

Figure 3.2: Global structural model of the Pantano viaduct implemented in SAP2000.

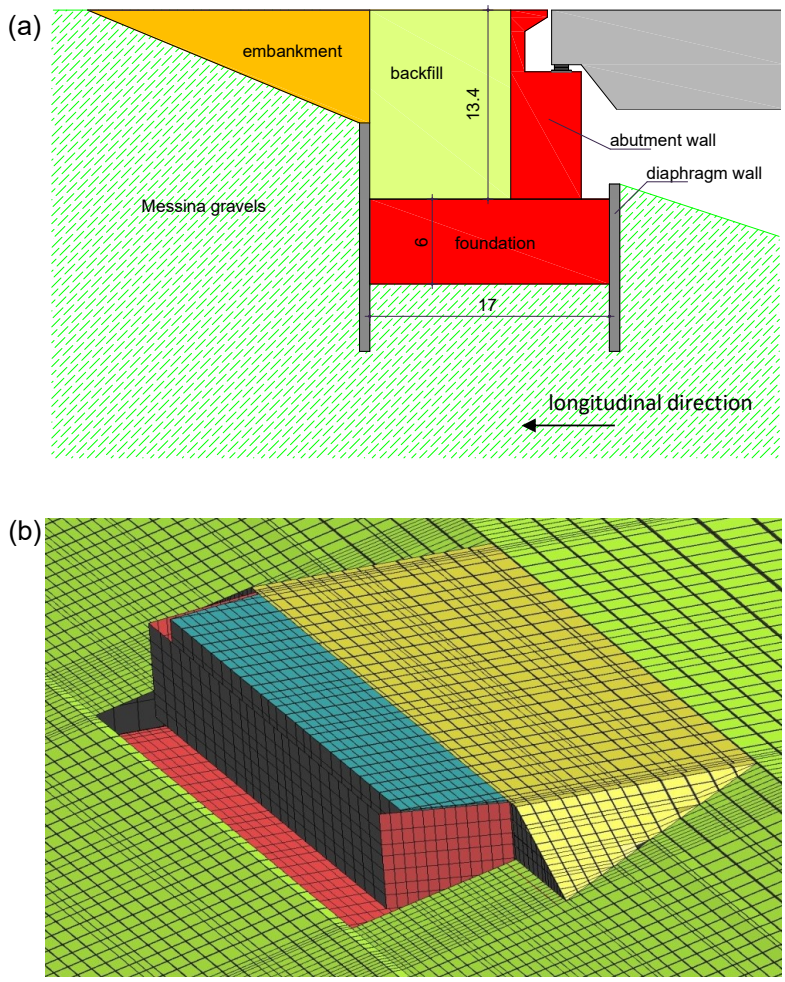

Figure 3.3: Geometry of the abutment of the Pantano viaduct (a) and its three-dimensional modelling in OpenSees (b).

reinforced concrete structure resting on a foundation slab in contact with the Messina Gravels. The central wall has a height of 13.5 m and a thickness of 5 m, while the dimensions of the foundation are 17 m and 65 m in the longitudinal and transverse direction, respectively. Because of its large strength compared to the superstructure and the soil, it is reasonable to assume that the abutment exhibits an elastic response under seismic conditions.

From the case study of the Pantano viaduct, a simplified soil-structure system was conceived, reflecting the main mechanical properties of the Pantano subsoil

and including an idealised representation of the structure, which constituted the reference model for the validation of the macro-elements of the bridge structure and of the soil-abutment system.

3.2 The Pantano subsoil

In earlier years, an extensive geotechnical program was carried out along the entire development of the Messina Strait suspension bridge, with laboratory testing and in situ investigation (Crova et al. 1993, Jamiolkowski and Lo Presti 2002, Brancaleoni et al. 2010, Fioravante et al. 2012). Most of the samples were retrieved in correspondence of the foundations of the bridge, thus the locations of the two towers, the two anchor blocks and along the Pantano viaduct. The geotechnical characterization and the subsoil model underlying the main structure of the suspension bridge were largely discussed in some earlier works by Callisto and Rampello (2013) and Rampello et al. (2014), while the subsoil of the Pantano viaduct, which basically constituted the soil domain for the soil-structure interaction models developed in this study, is described in detail in the following.

3.2.1 Geotechnical model of the subsoil

Based on the geotechnical characterization, a subsoil model of the entire Pantano viaduct was realised, whose stratigraphy is illustrated in Figure 3.4. The abutment is located on top of a slope that starts in correspondence of the foundation of the pier P3 and goes up with an average inclination of 17°. Approaching the coastline, that is close to the terminal structure, the ground level becomes flat and can be assumed at the same altitude as the sea level. The ground water table coincides with the sea level in all the area of the viaduct. This implies that from the abutment foundation down to a depth of 30 m the soil is essentially dry for then becoming completely saturated.

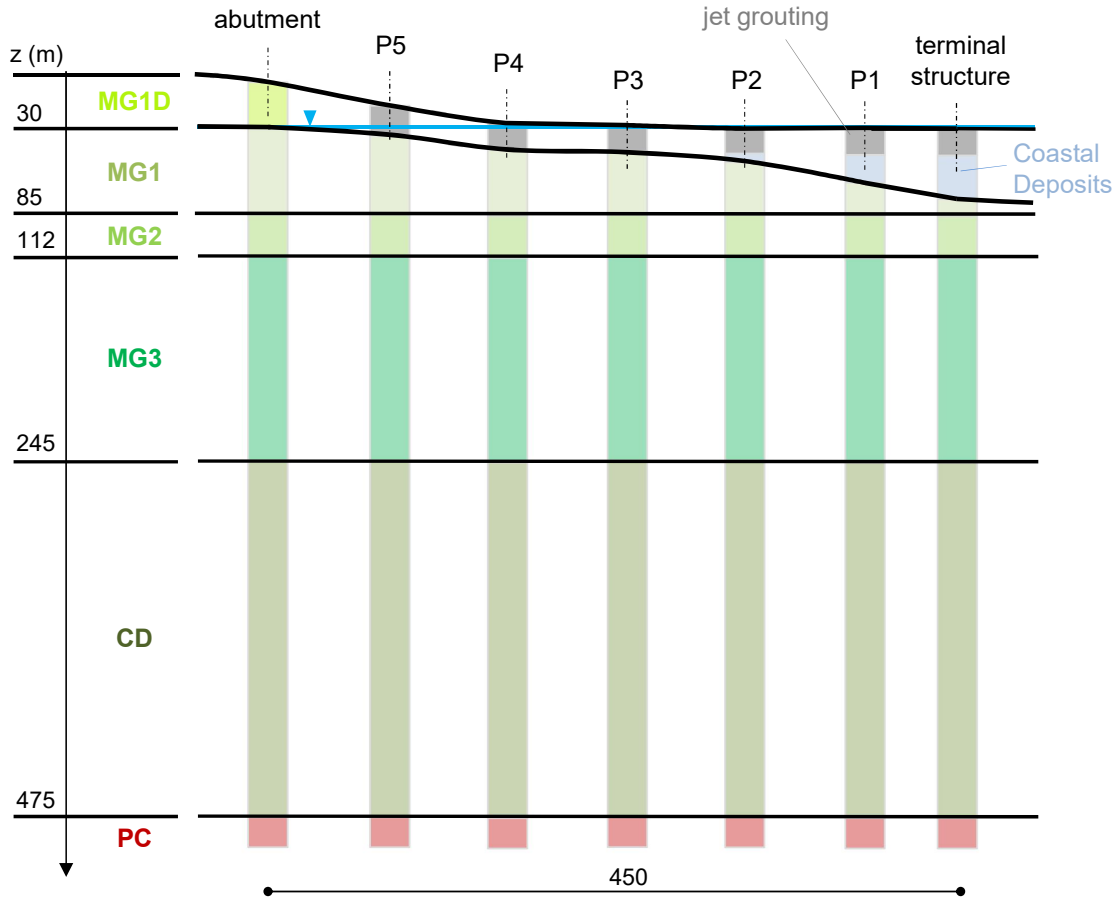

Figure 3.4: Subsoil profile for the Pantano viaduct.

In the area of the abutment, the subsoil is composed of a series of horizontal layers: a first thick layer of Messina Gravels extends down to a depth of 245 m from the abutment foundation, followed by the Continental Deposits extending down to the bedrock, the latter located at a depth of 445 m.

The Messina Gravels (MG) are made of gravel and sand with occasional silty levels. Three sub-layers can be identified characterised by the same granulometry but presenting different stiffness properties, named $MG1$, $MG2$ and $MG3$. The superficial layer $MG1D$ is identical to the underlying layer $MG1$ but the former is located over the ground water table and therefore presents a reduced unit weight. The Continental Deposits (CD) are a clayey-sandy deposit, consisting of layers of

silt or silt and sand, with significant gravel content/Bio-calcarenite and fossiliferous calcarenite, with thin silty layers. The Pezzo Conglomerate (PC) is instead a soft rock, consisting of clasts of different dimensions in a silty-sandy matrix and sandstone. This layer was regarded as a deformable bedrock for the site of the bridge.

The general features of the subsoil profile keep almost unaltered in correspondence of the pier foundations and the terminal structure. The major difference is that, starting from the pier P2 and moving towards the sea, a superficial layer of Coastal Deposits (SD) is encountered. The thickness of this formation increases progressively moving inwards the sea from the coastline, following an inclination that is approximately equal to that of the sloping ground underneath the viaduct, varying from about 45 m at the terminal structure to about 80 m at the Sicily tower location. The SD layer is composed of sand and gravel with little or no fine content. This layer has essentially the same mineralogy as the Messina Gravels, except for some levels of cementation bonds, due to the modest presence of fine content, that provides a higher stiffness compared to the MG layer. In fact, in Figure 3.5 it is evident the similarity between the Grain Size Distribution curve (GSD) of the Messina Gravels and the curve associated with the Coastal Deposits. The statistical parameters, mean trend and standard deviation, were determined on a number of GSD curves deriving from reconstituted samples of MG and SD. In virtue of this result, the experimental results obtained from a large number of tests carried out on the Coastal Deposits were also used as additional information to characterise the MG layer. From the GSD, an average value of 2.7 mm can be assumed for the diameter D_{50}, that can be used for evaluating the maximum variability of the void ratio $e_{max} - e_{min} = 0.23 + \frac{0.06}{D_{50}} = 0.252$ (Cubrinovsky and Ishihara, 1999) used in the design of the embankment. The latter, in fact, was initially assumed made of the in situ soil, since the good mechanical properties of the Messina Gravels.

The main physical-mechanical properties of the soil layers in the area of the

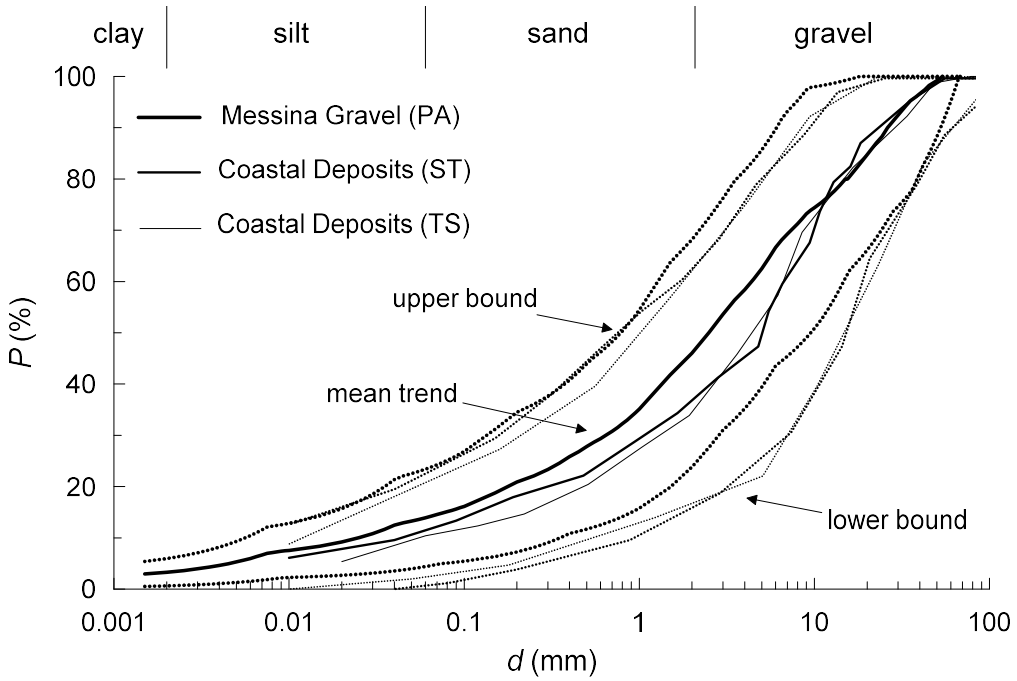

Figure 3.5: Grain size distribution of the Messina Gravels and of the Coastal Deposits.

Layer	Symbol	γ (kN/m^3)	e (-)	D_R (%)	k (m/s)	K_0 (-)	ν (-)
Messina Gravels 1D	$MG1D$	19.8	0.35	45	10^{-4}	0.65	0.2
Messina Gravels 1	$MG1$	22.0	0.35	45	10^{-4}	0.65	0.2
Messina Gravels 2	$MG2$	22.0	0.35	45	10^{-4}	0.65	0.2
Messina Gravels 3	$MG3$	22.0	0.35	45	10^{-4}	0.65	0.2
Continental Deposits	CD	22.0	0.30	50	-	0.50	0.2
Pezzo Conglomerate	PC	23.5	0.20	-	-	0.70	–

Tabella 3.1: Physical properties of the soil layers in the area of the Pantano abutment.

Pantano abutment are reported in Table 3.1. The symbol z_l denotes the lower boundary of the layer. The unit weight γ and in-situ void ratio e were evaluated from cross-hole tests and laboratory tests on frozen undisturbed samples. The relative density D_R was obtained from the results of in-situ penetration tests, employing the procedures proposed by Skempton (1986) and by Cubrinovsky and Ishihara (1999). The permeability of the granular layers was evaluated using site measurements, such as well pumping tests and Lefranc tests, and the empirical correlations proposed by Breyer (ref. Odong. 2007) and by Terzaghi and Peck (1964). For normally consolidated soils, the coefficient of earth pressure at rest K_0 was estimated from the relative density D_R referring to Baldi et al. (1985) and from the angle of shearing resistance φ' (Jaky 1948). In the area of the abutment, erosion phenomena of the Messina Gravels are less important than on the site of Sicily tower so that deviation of K_0 from its normally consolidated value is mainly due to aging effects. Therefore, in this case the empirical relationship proposed by Mesri and Castro (1989) was used to estimate the relative K_0.

The Poisson's ratio ν and the strength of the Messina Gravels were evaluated through the numerous laboratory tests carried out on reconstituted samples of Coastal Deposits and on 3 frozen undisturbed samples of Messina Gravels (Jamiolkowski and Lo Presti 2002, Fioravante et al. 2012), the latter retrieved by using the freezing technique. The results of 22 monotonic, isotropically consolidated triaxial tests under drained conditions (TRIAX-CID) are depicted in Figure 3.6. The reconstituted samples of Coastal Deposits were prepared at relative densities of 40 %, 60 % and 80 %. The samples exhibit different behaviours, from a purely contractant response to a pronounced dilation, due to the different initial state of the samples. Figure 3.7 instead shows the behaviour exhibited by the undisturbed frozen samples of Messina Gravels in three monotonic undrained triaxial tests (TRIAX-CIU), with a decided tendency to dilate in all the three tests. The strength envelope in the

Symbol	c (kPa)	φ'_{cv} (°)	φ'_p (°)
$MG1D$	0	38	40
$MG1$	0	38	40
$MG2$	0	38	40
$MG3$	0	38	39
CD	0	39	39
PC	160	42	42

Tabella 3.2: Stength parameters of the soil layers in the area of the Pantano abutment.

$q - p'$ plane is shown in Figure 3.8 and the strength parameters are summarised in Table 3.2. As expected, the effective cohesion is null for all layers above the bedrock because the subsoil is composed by coarse-grained soils. The angle of peak shearing resistance φ'_p was evaluated from the relative density D_R, the in-situ stress state and the angle of shearing resistance at constant volume φ'_{cv} according to the empirical correlation proposed by Bolton (1984).

The Li and Wang curve (Li and Wang, 1998) was adopted to describe the Critical State Line (CSL) in the $e - p'$ plane, that reads

$$e_c = e_0 - \lambda_c \cdot \left(\frac{p'_c}{p_{atm}}\right)^{\xi} \tag{3.1}$$

in which the exponent ξ is taken equal to 0.7, as suggested by the authors. The void ratio e_0 at $p' = 0$ and the coefficient λ_c were instead evaluated by determining the exponential trendline of the points at Critical State plotted in the plane $e - (p'/p'_{atm})$, shown in Figure 3.9. Although the scatter of the experimental data is significant, a Critical State Line CSL for the Messina Gravels may be expressed as

$$e_c = 0.448 - 0.0219 \cdot \left(\frac{p'_c}{p_{atm}}\right)^{0.7}. \tag{3.2}$$

The relative position between the CSL found above and the initial states of the samples is represented in Figure 3.10, together with the in-situ evaluation of the void ratio (thin continuous line). The two shadow zones refer to the significant intervals

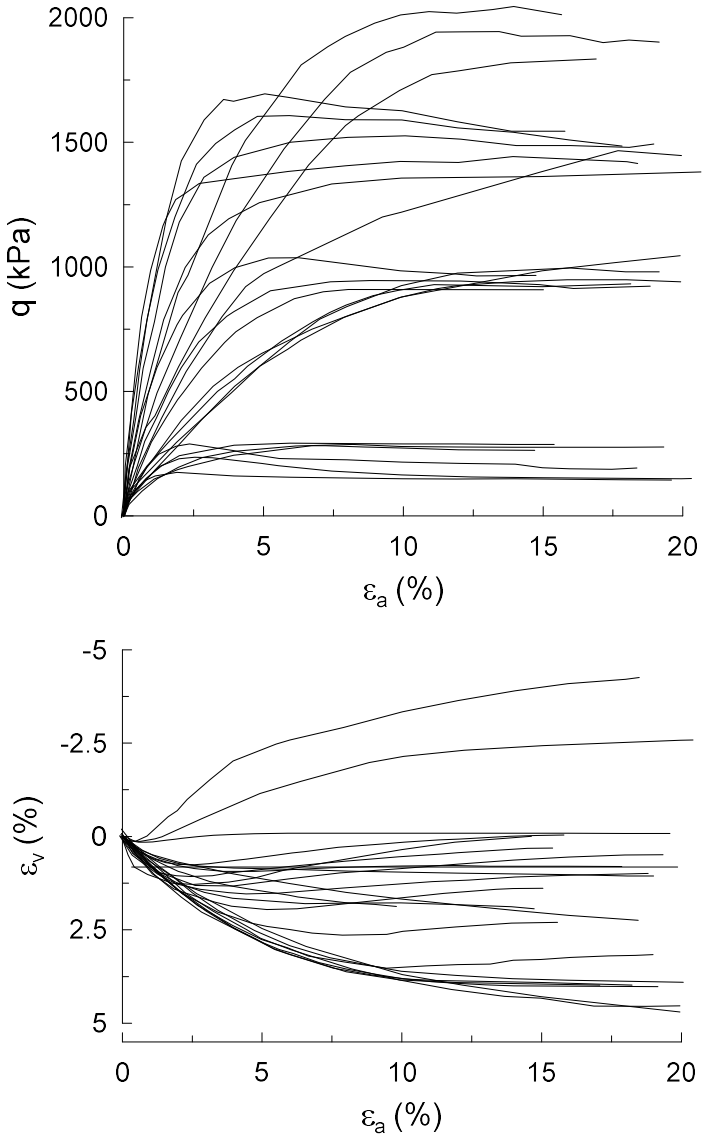

Figure 3.6: Stress-strain relationships for Coastal Deposits reconstituted samples for three values of the relative densityD_R of 40%, 60% and 80%.

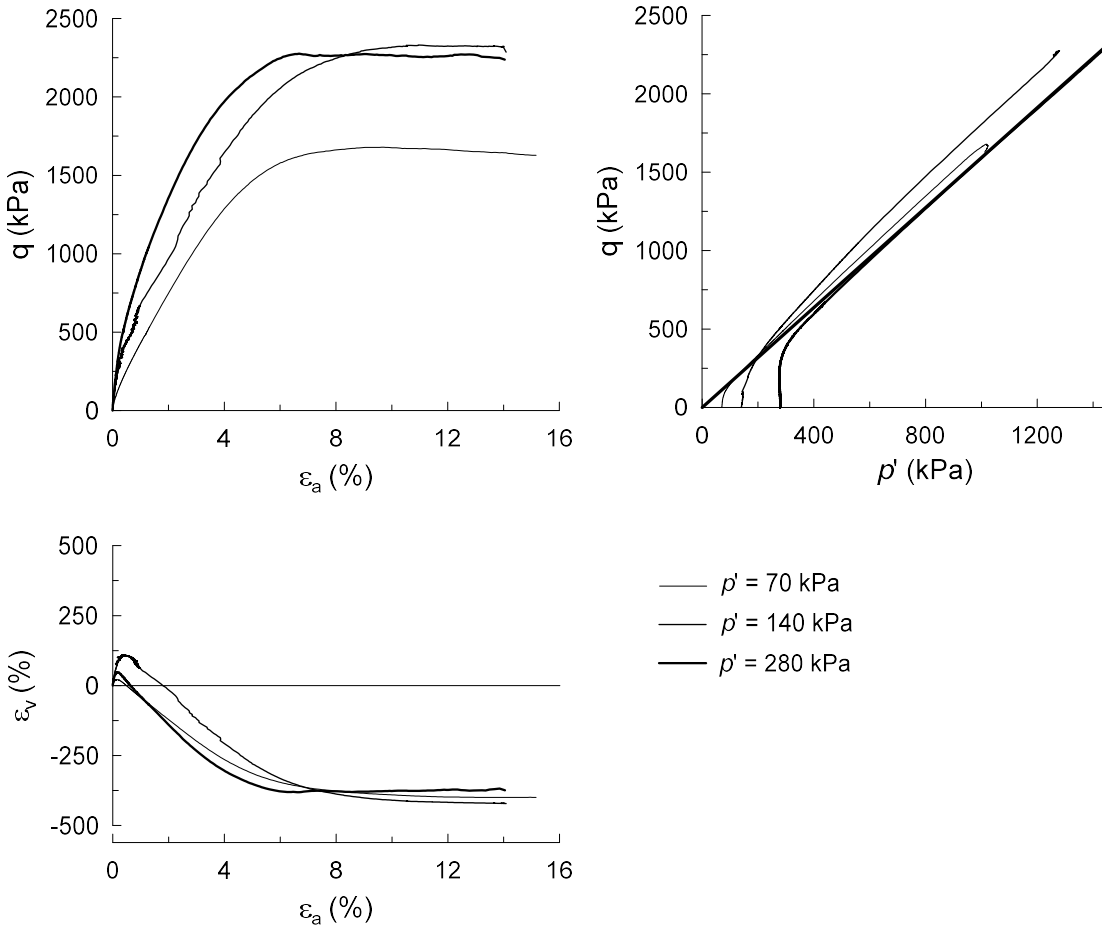

Figure 3.7: Behaviour exhibited by undisturbed frozen samples of Messina Gravels in TRIAX-CIU tests.

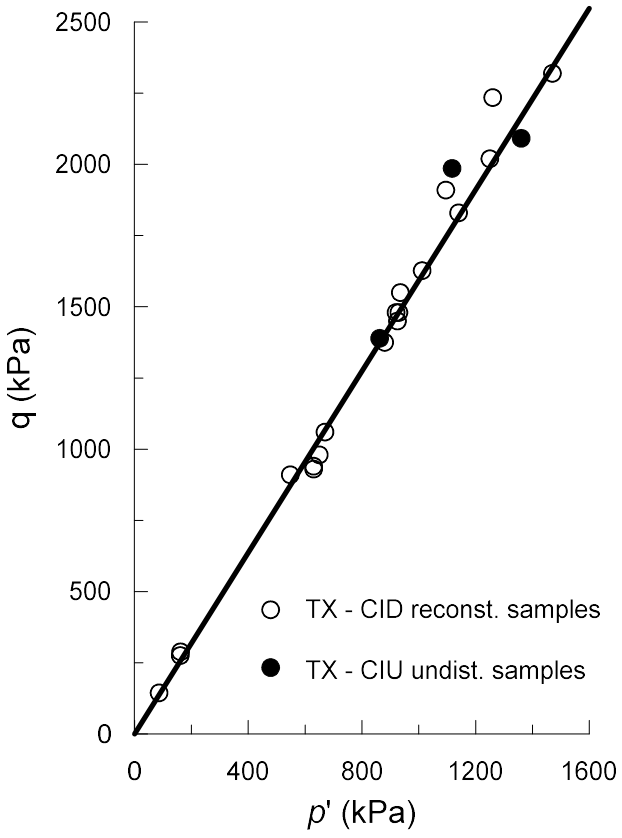

Figure 3.8: Strength envelope for Coastal Deposits reconstituted samples and Messina Gravels undisturbed frozen samples.

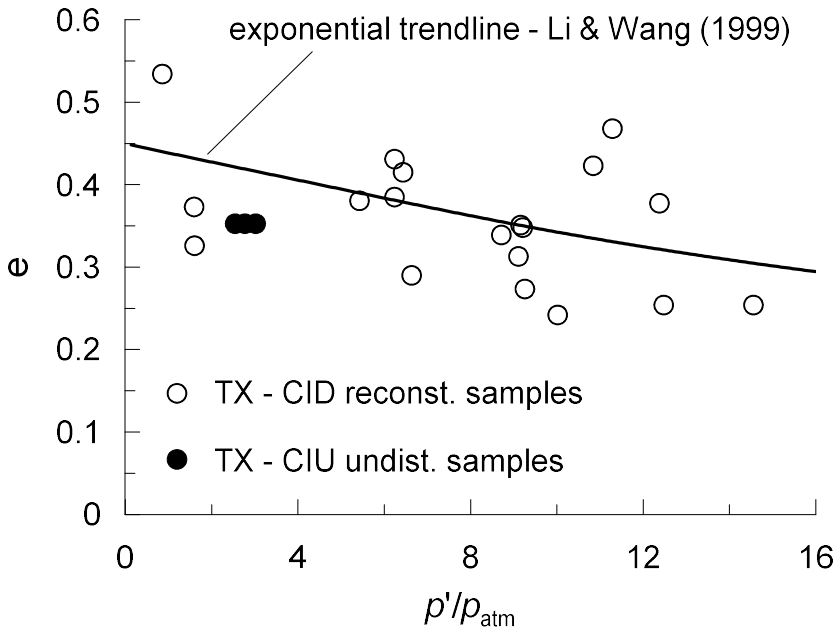

Figure 3.9: Determination of the parameter λ_c of the CSL proposed by Li and Wang (1998).

of the mean effective stress for the two upper layers $MG1D$ and $MG1$. It can be observed that the void ratio of the three undisturbed samples is equal to the value estimated through the in-situ tests. Down to a depth of about 47 m, corresponding to $p' = 800$ kPa, the soil has a negative state parameter $\psi = e - e_c < 0$ (Been and Jefferies, 1985), that is in agreement with the behaviour exhibited by the undisturbed samples in the TRIAX-CIU tests. For greater depths, the soil response is expected to become progressively more contractant. It is worth noticing that, although either reconstituted or undisturbed samples can be considered to identify the CSL, only the undisturbed frozen samples can be used for a reliable determination of the initial state of the in-situ soil.

In-situ measurements of shear wave velocity V_S, carried out in cross-hole tests in the area of the Sicily anchor block close to the Pantano abutment, together with the corresponding evaluation of the small strain shear modulus $G_0 = \rho \cdot V_S^2$ are illustrated in Figure 3.11. Different lines are used to identify different cross-hole

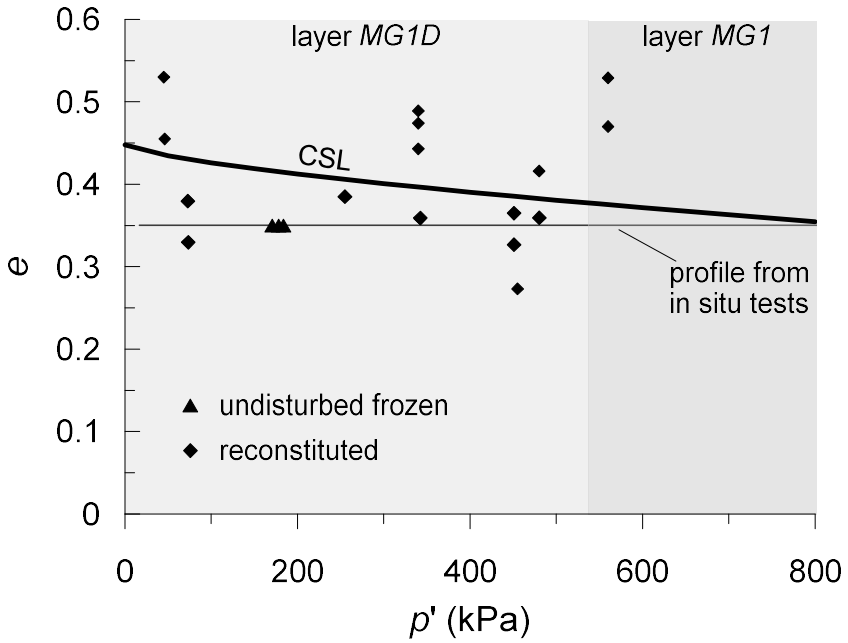

Figure 3.10: Comparison between the state of the Messina Gravels in the $e - p'$ plane determined through laboratory triaxial tests and in-situ cross-hole tests.

tests, performed at a depth of about 100 m, therefore extending throughout the Messina Gravels. A stiffer superficial stratum is encountered in the first 20 m-depth, starting from which the stiffness increases quasi-linearly down to about 80 m. In this interval, the small strain shear modulus ranges between $150 \div 500$ MPa. At higher depths, the shear modulus G_0 assumes a constant value of about 1000 MPa. Callisto and Rampello (2013) provided the values of V_S for the Continental Deposits and the Pezzo Conglomerate, equal to 750 m/s and 1700 m/s, respectively. These values can be considered as representative of the whole formation.

On the basis of the above results, the profile of the shear wave velocity used in the numerical simulations is represented in Figure 3.12. Above the ground water table, the shear wave velocity is kept constant equal to 300 m/s. In the layer $MG1$, a power law is used to approximate the trend shown experimentally, whose equation reads

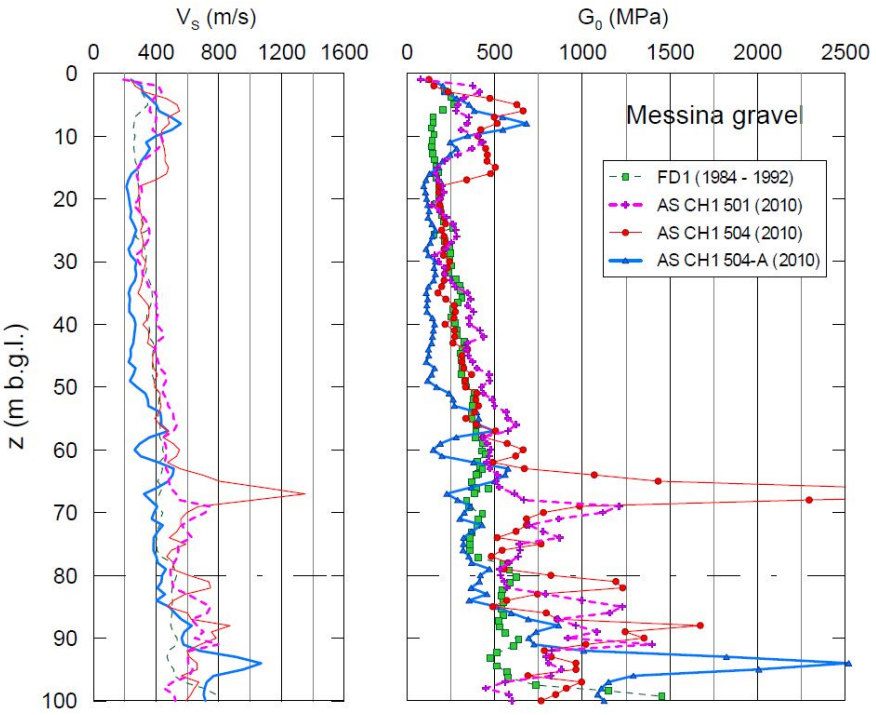

Figure 3.11: Sicily anchor block: profile of the small strain shear modulus G_0 from in-situ tests.

Symbol	$V_{S,m}$ (m/s)	$V_{P,m}$ (m/s)	$G_{0,m}$ (kPa)
$MG1D$	305	500	$1.9 \cdot 10^5$
$MG1$	400	2600	$3.6 \cdot 10^5$
$MG2$	505	2600	$5.7 \cdot 10^5$
$MG3$	1039	2600	$2.4 \cdot 10^6$
CD	750	2600	$1.3 \cdot 10^6$
PC	1700	2700	$6.9 \cdot 10^6$

Tabella 3.3: Mean stiffness parameters of the soil layers in the area of the Pantano abutment.

$$V_S = A \cdot p'^n \tag{3.3}$$

in which A and n assume the values of 21.82 and 0.44, evaluated through a list squares fitting procedure. At greater depths, a constant value of the shear wave velocity was assumed for each stratum, with average values summarised in Table 3.3.

The modulus decay of the superficial layers of Messina Gravels $MG1D$ and $MG1$ was described by the curve proposed by Seed and Idriss (1970) for coarse-grained

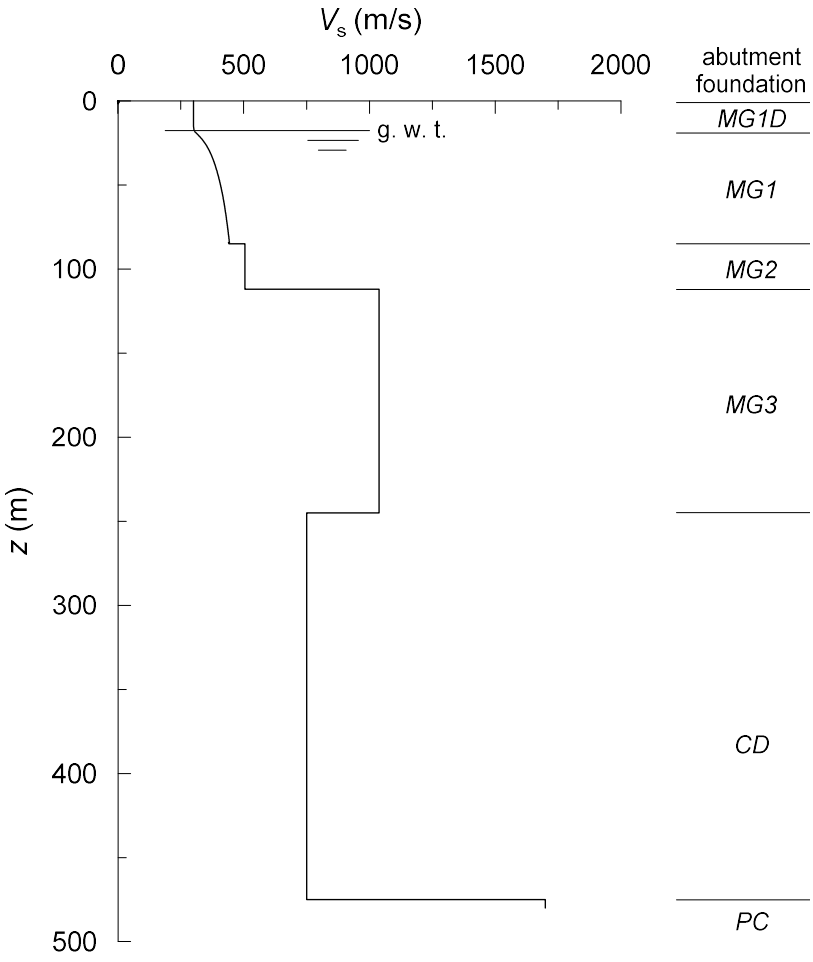

Figure 3.12: Profile of the shear wave velocity V_S adopted in the subsoil model.

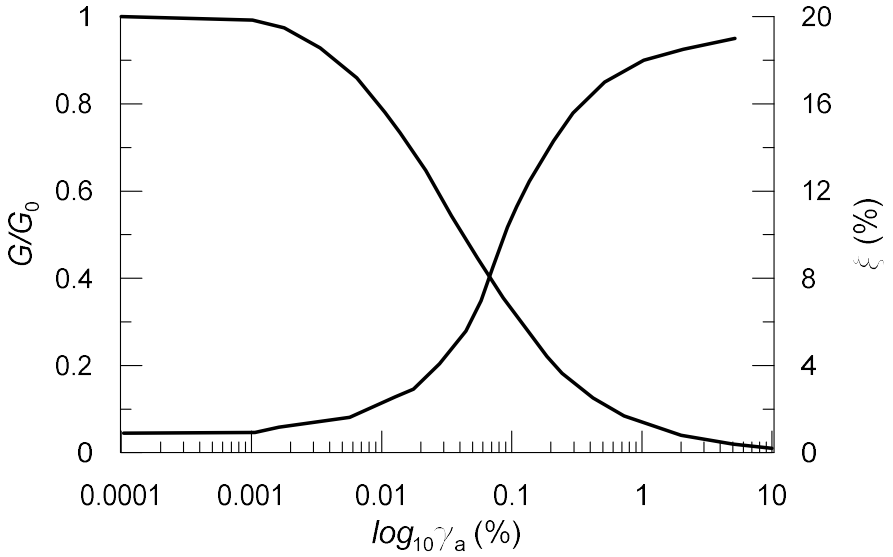

Figure 3.13: Modulus decay curve (Seed and Idriss, 1970) and damping curve adopted for the layers $MG1$ and $MG1D$ of Messina Gravels.

soils, in virtue of the similarity of this curve with the experimental results obtained by Tanaka et al. (1987) for reconstituted gravelly soils. A more gradual modulus decay was instead assumed for the deeper layers $MG2$, $MG3$ and for the Continental Deposits (Callisto and Rampello 2013). These curves, together with the corresponding equivalent damping ratio ξ, are plotted in Figs. 3.13 and 3.14 as a function of the shear strain amplitude γ_a, and they will come into play only in the preliminary site response analysis with linear visco-elastic medium.

On the three undisturbed frozen samples retrieved in the area of the Sicily tower of the suspension bridge, 11 cyclic triaxial tests were carried out under undrained conditions, with 5 tests performed on anisotropically consolidated specimens. In virtue of the same mineralogy and very similar mechanical properties, the behaviour of the frozen samples associated with the Sicily tower can be reasonably deemed to be representative of the behaviour expected at the location of the Pantano abutment. The set of the undisturbed frozen specimens with their initial properties are reported in Table 3.4. All the unfrozen specimens have a diameter and a height of 290 mm

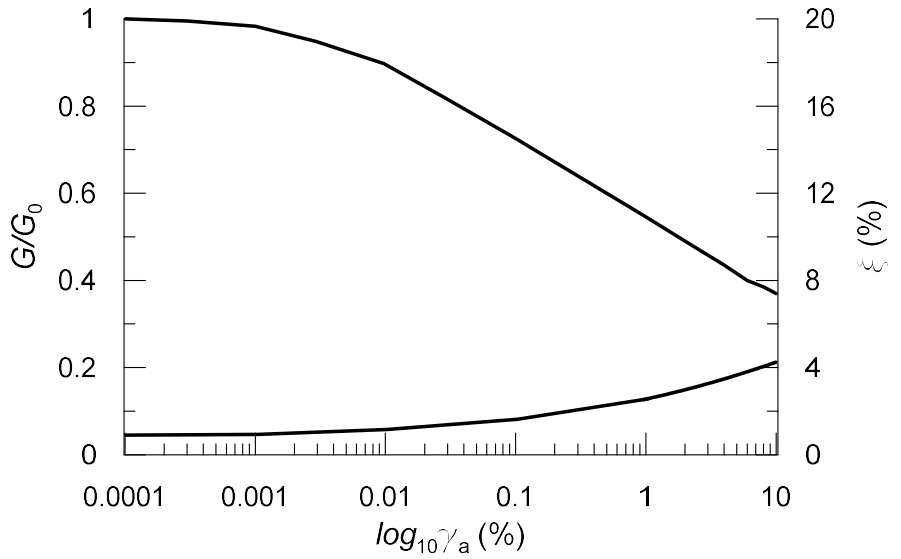

Figure 3.14: Modulus decay curve (Seed and Idriss, 1970) and damping curve adopted for the layers $MG2$, $MG3$ and CD.

and 600 mm, respectively. The sampling depth z_s ranges from 15.15 m to 22.00 m with respect to the sea bed in correspondence of the Sicily Tower ($S1 - S11$).

A detailed description of the specimen preparation and of the test mode was provided by Fioravante et al. (2012). All the undisturbed specimens were reconsolidated to best reproduce the in-situ mean effective stress at the middle of the depth interval where the undisturbed samples were retrieved. The state of the specimens after consolidation is described in Table 3.5, in terms of axial effective stress σ'_a,

Specimen	Soil	Area	Test	z_s (m)	e (-)
$S1$	Messina Gravels	Sicily Tower	TRIAX CIU	15.15 – 15.75	0.232
$S2$	Messina Gravels	Sicily Tower	TRIAX CIU	16.05 – 16.75	0.271
$S3$	Messina Gravels	Sicily Tower	TRIAX CIU	17.15 – 17.90	0.230
$S4$	Messina Gravels	Sicily Tower	TRIAX CIU	18.20 – 19.00	0.303
$S5$	Messina Gravels	Sicily Tower	TRIAX CIU	19.00 – 19.65	0.312
$S6$	Messina Gravels	Sicily Tower	TRIAX CIU	21.30 – 22.20	0.299
$S7$	Messina Gravels	Sicily Tower	TRIAX CIU	15.37 – 16.05	–
$S8$	Messina Gravels	Sicily Tower	TRIAX CIU	16.60 – 17.28	–
$S9$	Messina Gravels	Sicily Tower	TRIAX CIU	17.60 – 18.35	–
$S10$	Messina Gravels	Sicily Tower	TRIAX CIU	19.05 – 19.70	–
$S11$	Messina Gravels	Sicily Tower	TRIAX CIU	20.10 – 20.80	–

Tabella 3.4: Initial data of the undisturbed frozen specimens.

Specimen	σ'_a (kPa)	σ'_r (kPa)	ε_a (%)	ε_v (%)	e (-)
$S1$	180.0	180.0	0.40	0.50	0.196
$S2$	180.0	180.0	0.30	0.60	0.233
$S3$	177.5	177.0	0.23	0.54	0.194
$S4$	179.7	178.2	0.42	0.65	0.263
$S5$	179.3	178.2	0.30	0.68	0.271
$S6$	179.9	178.7	0.23	0.46	0.283
$S7$	181.1	84.2	0.17	0.25	–
$S8$	180.9	85.2	0.21	0.22	–
$S9$	181.9	85.1	0.17	0.58	–
$S10$	179.9	85.1	0.16	0.23	–
$S11$	182.3	85.0	0.18	0.34	–

Tabella 3.5: State of the frozen specimens after consolidation.

radial effective stress σ'_r, axial strain ε_a, volumetric strain ε_v and void ratio e. Note that for all the specimens the state parameter ψ (Been and Jefferies, 1985) is negative, therefore a dilatant behaviour is expected during the cyclic undrained triaxial tests described in the following, that is consistent with the monotonic behaviour previously shown in Figure 3.7.

After the consolidation stage, the specimen is subjected to a cyclic perturbation under undrained conditions, that is applied as a harmonic variation of the axial stress that varies in time with a frequency of 0.25 Hz, keeping constant the radial stress. The relative results are illustrated in Figures 3.15 to 3.25 (Fioravante et al. 2012), looking at the state of the material in the $q - p'$ plane and in the $q - \varepsilon_a$ plane, together with the time evolution of the axial stress in the deviatoric stage $\Delta\sigma_a$, of the excess pore water pressure Δu and of the pore pressure coefficient $r_u = u/\sigma'_r$.

Looking at the response of the isotropically consolidated specimens ($S1 - S6$), during the test the specimen undergoes a typical response known as cyclic mobility: as loading proceeds, the pore water pressure increases build up progressively and, consequently, the effective stress reduces. Liquefaction condition is attained when the pore water coefficient approaches 1 and hence the effective stress tends to zero, leading to a drastic increase of the axial strains developed in each cycle. At very low stress levels, the stress path reaches the Critical State Line and describes the

well-known butterfly orbit in the $q - p'$ plane: the stress path starts going back and forth, following the two branches of the CSL characterised by an inclination M^+ and M^- in compression and in extension, respectively. The resulting axial strains start developing in a prominent manner and with a more pronounced effect in extension loading conditions. This probably occurs for the dependence of the Critical State parameter M on the Lode's angle. In fact, the asymmetry ratio M^+/M^- ranges between 0.87 and 0.92, while the corresponding friction angle varies from 40° to 43° for the specimens under examination. The number of cycles needed to reach liquefaction decreases with the amplitude of the deviatoric stress q. The greater q the more rapid the development of positive excess pore water pressure. Since the application of the first cycle, an alternating dilative (p' increases) and contractant behaviour (p' reduces) is observed. The boundary between these two opposite tendencies is represented by the Phase Transformation Line (PTL) (Ishihara et al. 1975), which is characterised by an inclination M^d in the $q - p'$ plane estimated equal to 26° for the Messina Gravels.

The cyclic response shown by the anisotropically consolidated specimens ($S7 - S11$) is qualitatively similar to that described above under isotropic consolidation. In this case, however, the mean effective stress does not tend to zero since the parameter r_u assumes values not greater than 0.65, attained in test $S10$ and $S11$. The corresponding butterfly orbits are highly asymmetric and the resulting axial strains accumulate progressively on the compression side of the $q - p'$ plane, due to the non-zero deviatoric stress at the end of the consolidation stage. In the other tests, the pore pressure coefficient does not exceed 0.4 and therefore the cyclic response essentially depends on the level of anisotropy of the initial stress state, with a not symmetric alternation between dilative and contractant behaviour since the shorter distance of the initial stress state from the PTL in compression.

The experimental data shown above were used to calibrate the two advanced con-

stitutive models chosen to reproduce the dynamic response of the Messina Gravels in the soil-structure interaction analyses carried out in OpenSees. Even though the pore water pressures were neglected in the full soil-bridge model (see Section 3.6.2), the undrained response of the Messina Gravels shown above is however important, because it allowed to calibrate the cyclic behaviour of the two constitutive models.

3.3 Constitutive models for soil

The mechanical behaviour of soil was described through two different advanced constitutive models, the SANISAND model proposed by Dafalias and Manzari (2004) and the Pressure Dependent Multi-Yield model (PDMY) developed by Yang et al. (2003). The choice of these two models was aimed to get an accurate response of the soil under cyclic loading conditions.

3.3.1 The SANISAND model

The Dafalias and Manzari model is formulated within the Bounding Surface Plasticity framework (Dafalias, 1986) with the aim to simulate an elastic-plastic behaviour with a mixed kinematic and isotropic hardening rule. Looking at its triaxial representation in Figure 3.26, a cone-shaped yield surface surrounds the current stress state, the latter characterised by a back stress ratio α, starting from which plastic strains develop as a function of the relative distance of the current stress state from an external surface, named bounding surface, that controls the hardening of the material, and from a so-called dilatancy surface that instead influences the plastic flow. These two external surfaces evolve during plastic loading, depending on the state of the material identified through the state parameter ψ (Been and Jefferies, 1985), until becoming coincident with the Critical State locus when the ultimate conditions of the material are attained.

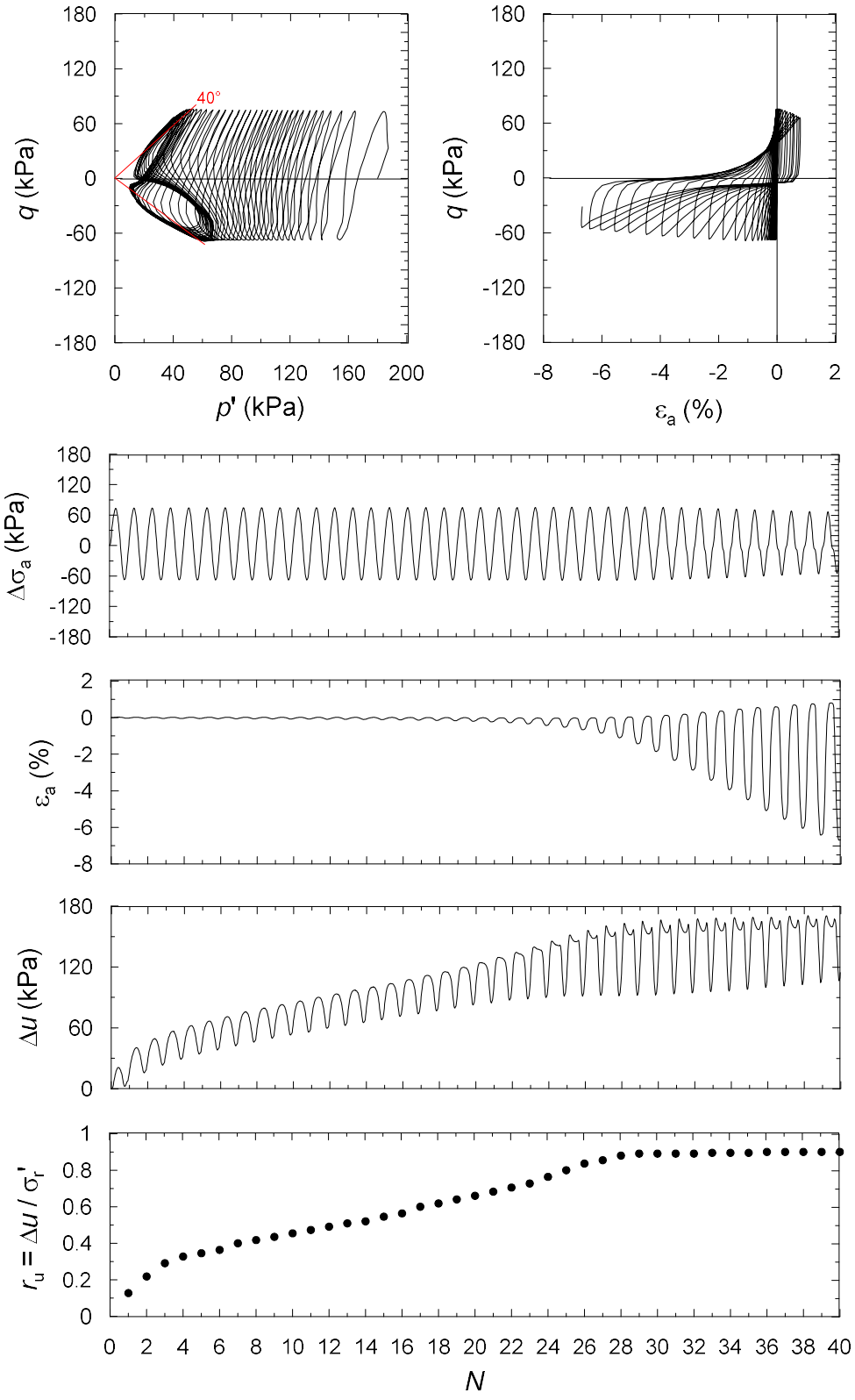

Figure 3.15: Undrained cyclic triaxial test on the isotropically consolidated undisturbed specimen $S1$.

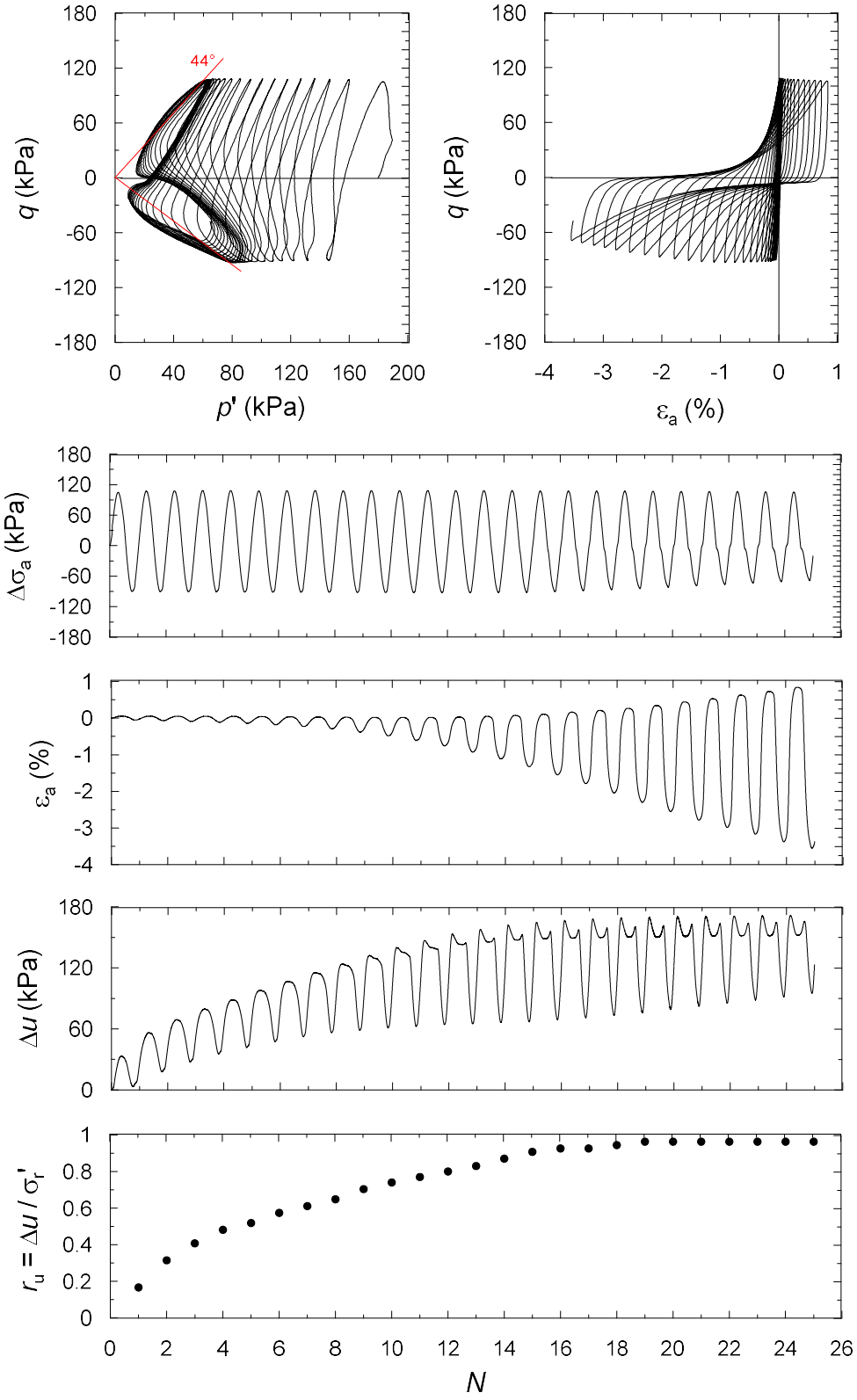

Figure 3.16: Undrained cyclic triaxial test on the isotropically consolidated undisturbed specimen *S*2.

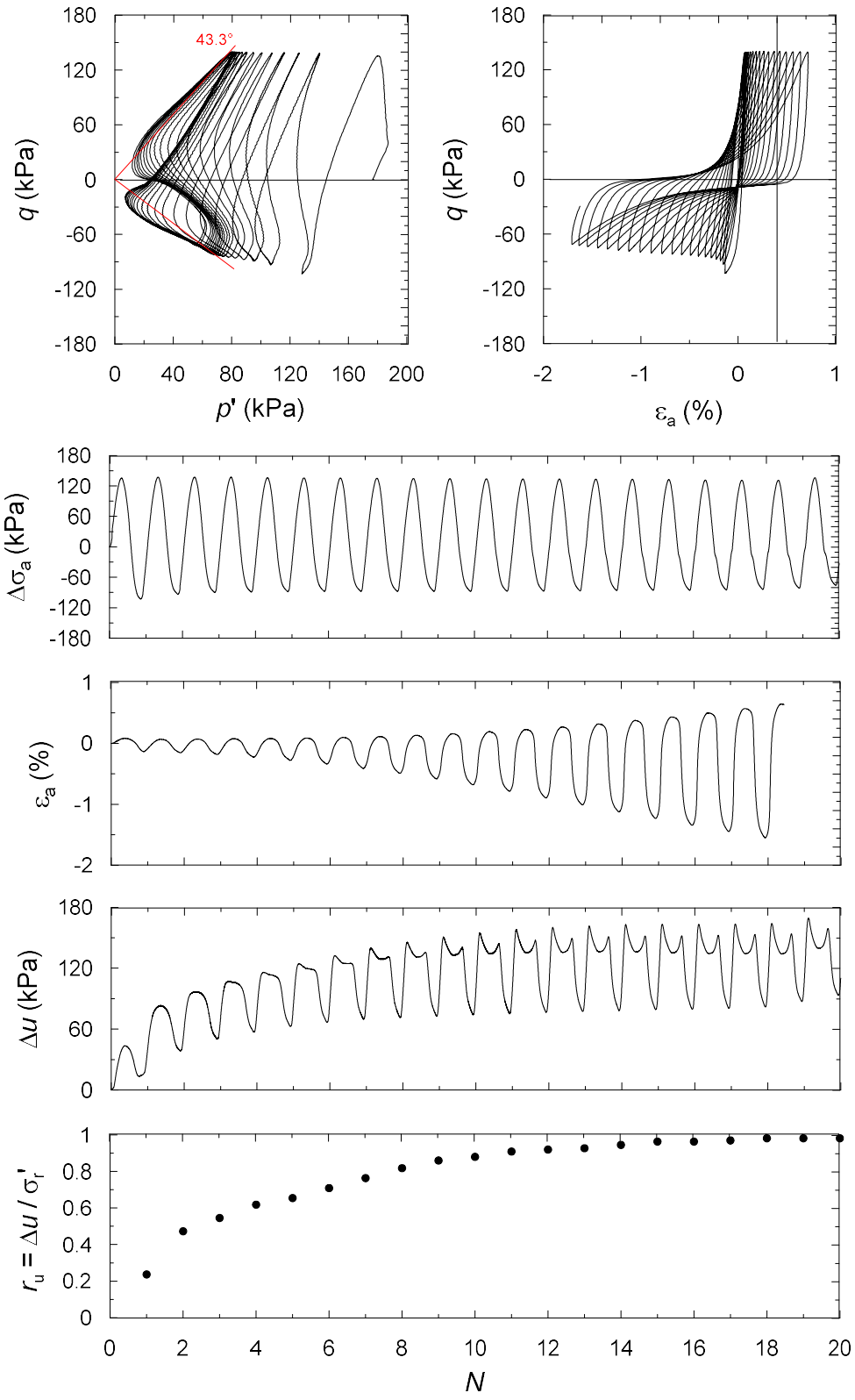

Figure 3.17: Undrained cyclic triaxial test on the isotropically consolidated undisturbed specimen *S*3.

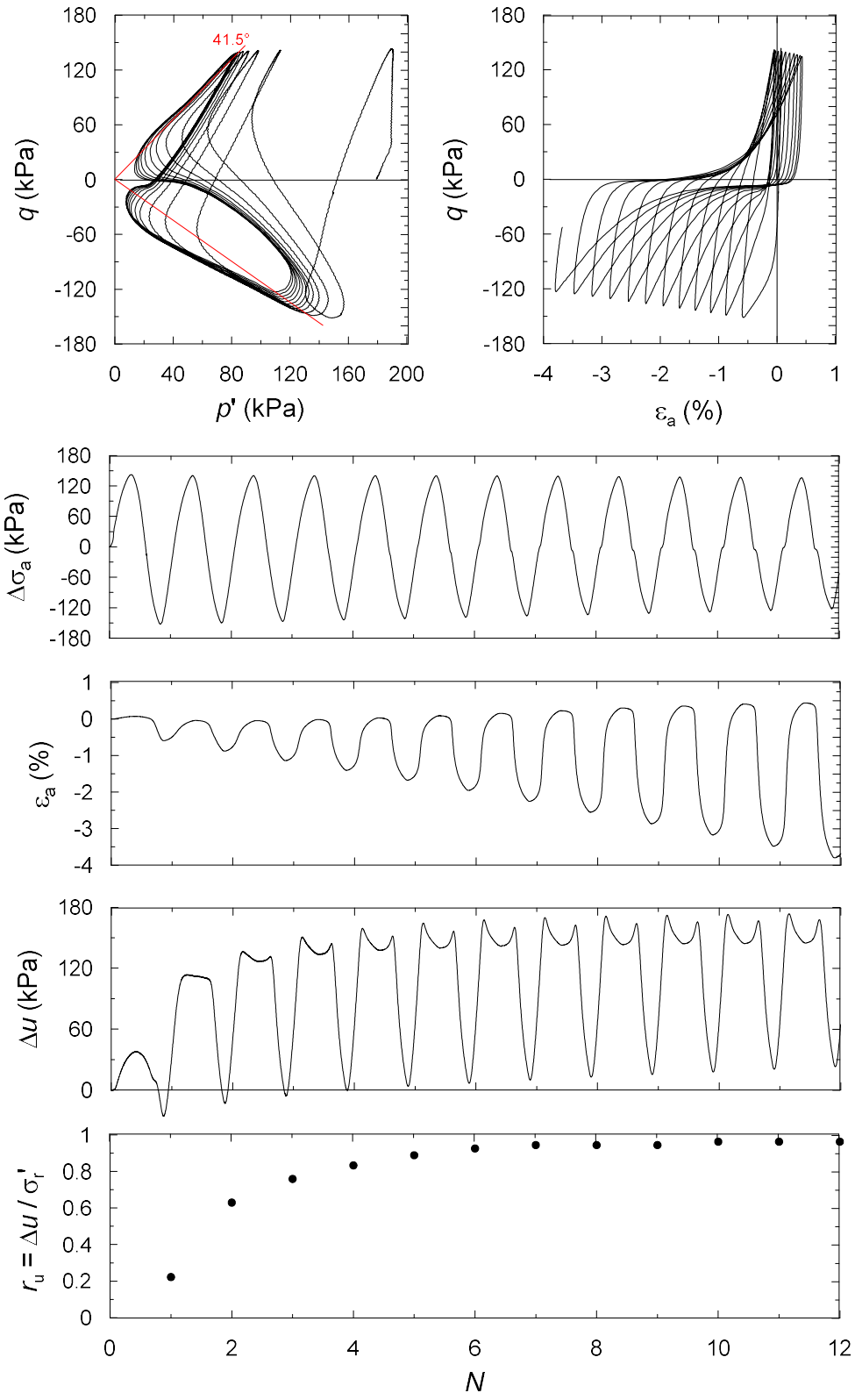

Figure 3.18: Undrained cyclic triaxial test on the isotropically consolidated undisturbed specimen *S4*.

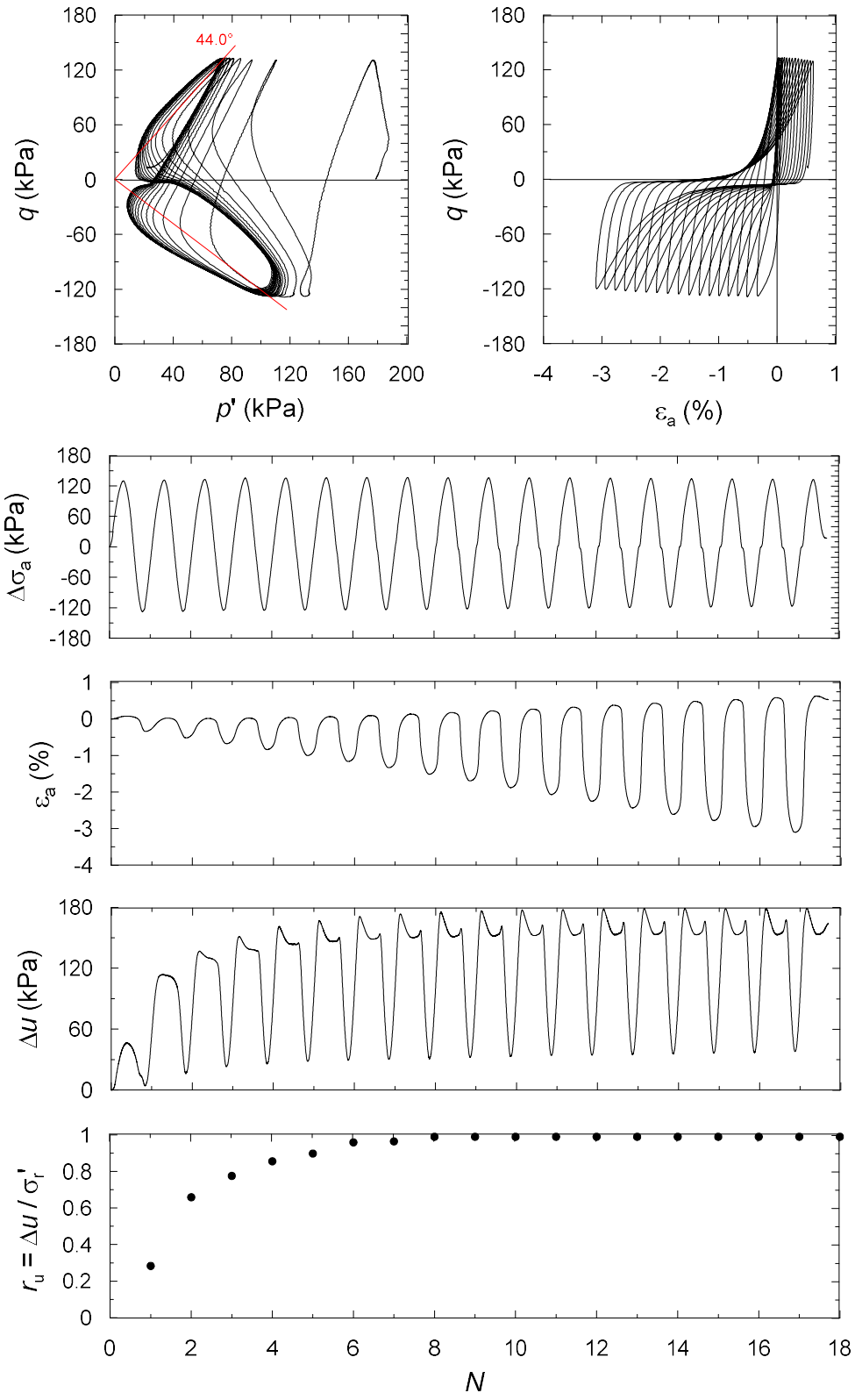

Figure 3.19: Undrained cyclic triaxial test on the isotropically consolidated undisturbed specimen $S5$.

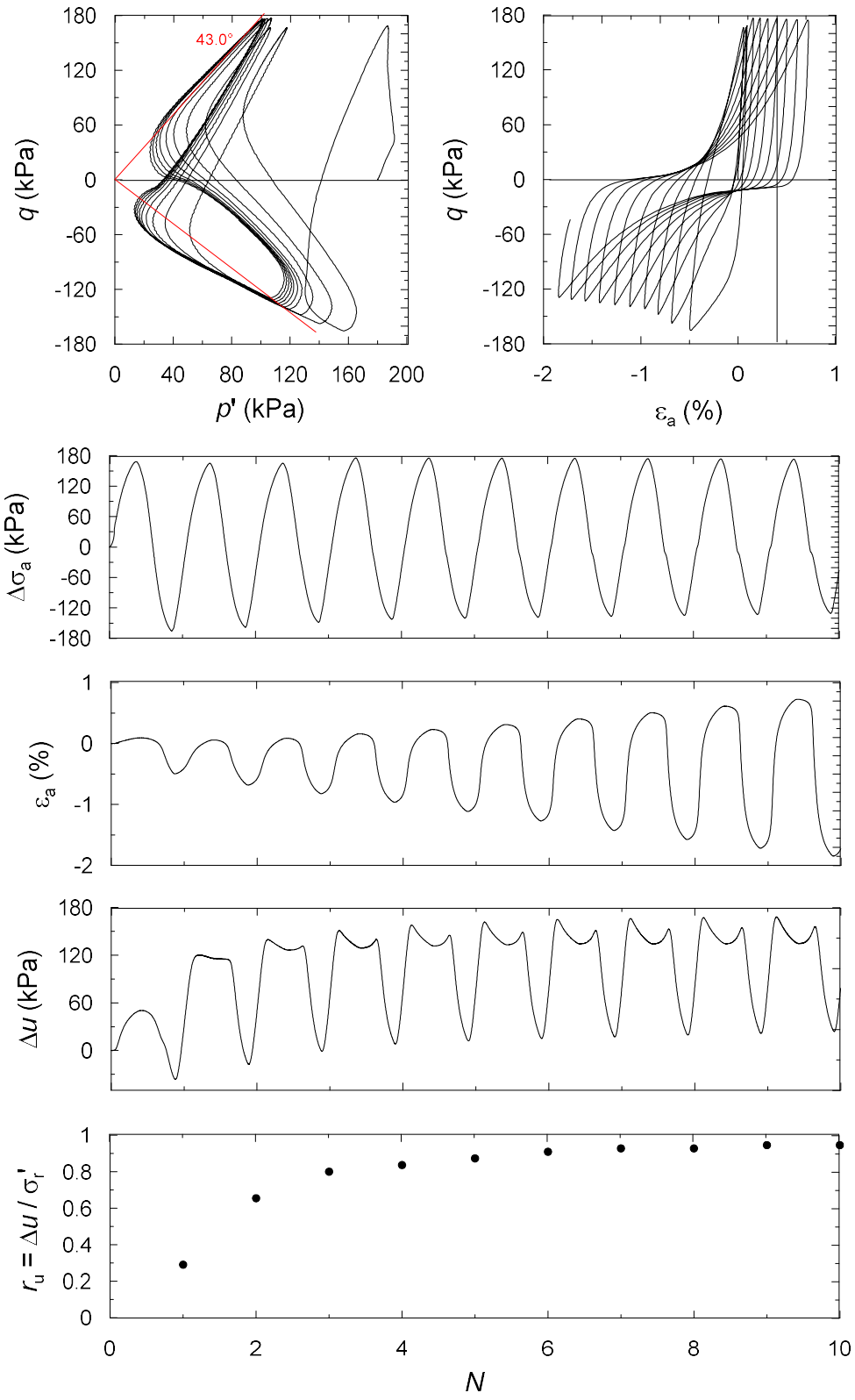

Figure 3.20: Undrained cyclic triaxial test on the isotropically consolidated undisturbed specimen *S*6.

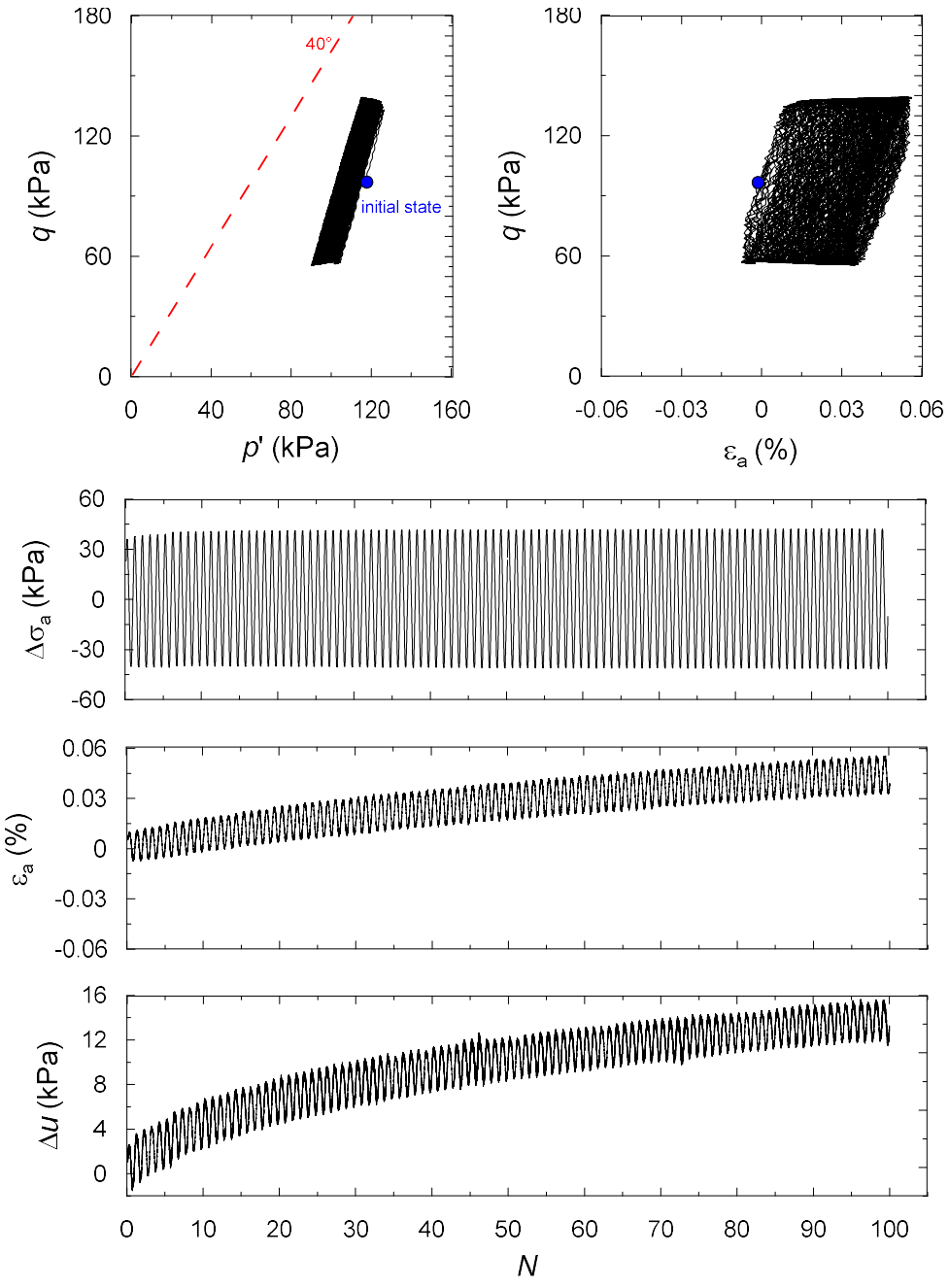

Figure 3.21: Undrained cyclic triaxial test on the anisotropically consolidated undisturbed specimen *S7*.

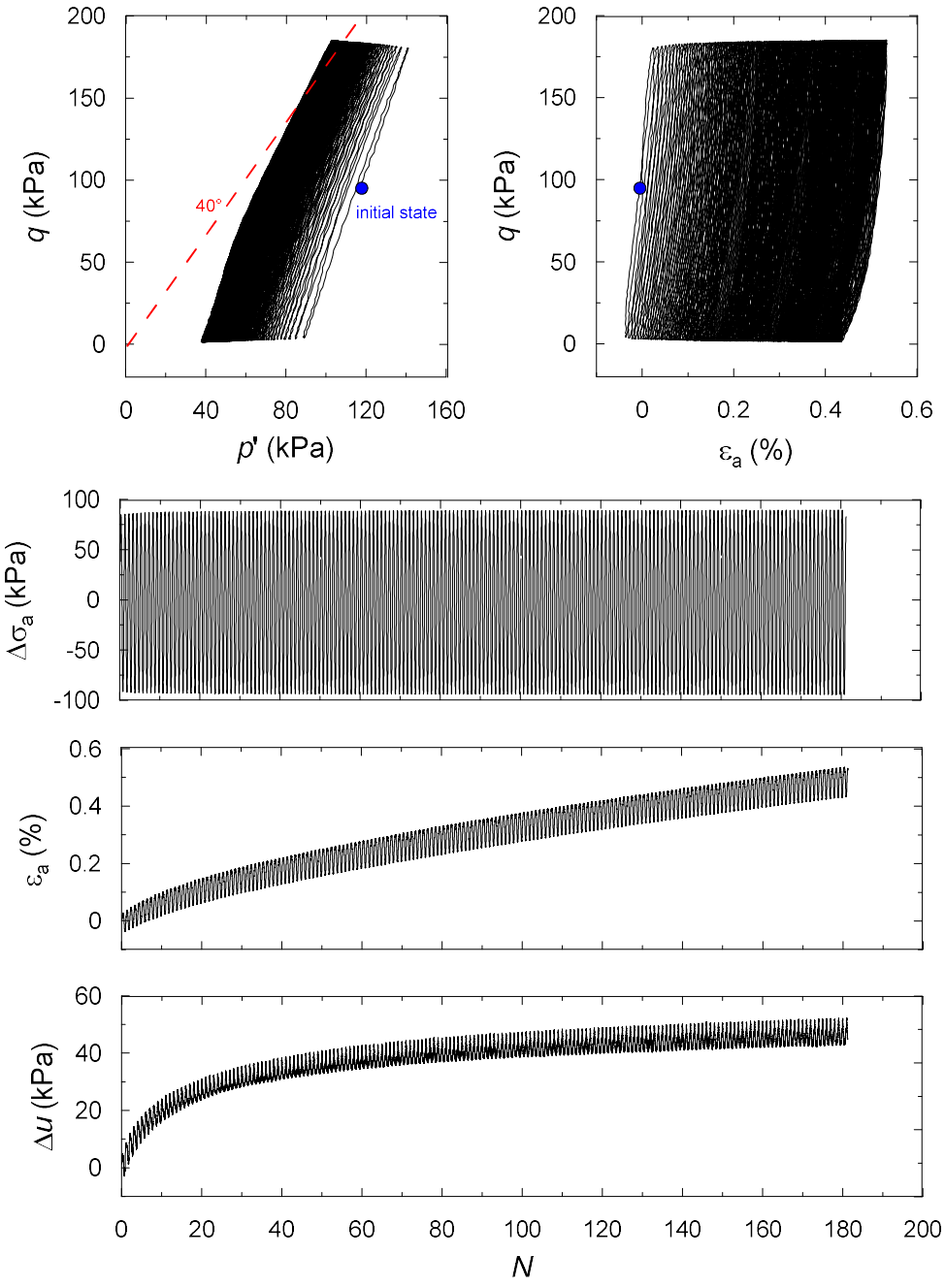

Figure 3.22: Undrained cyclic triaxial test on the anisotropically consolidated undisturbed specimen *S*8.

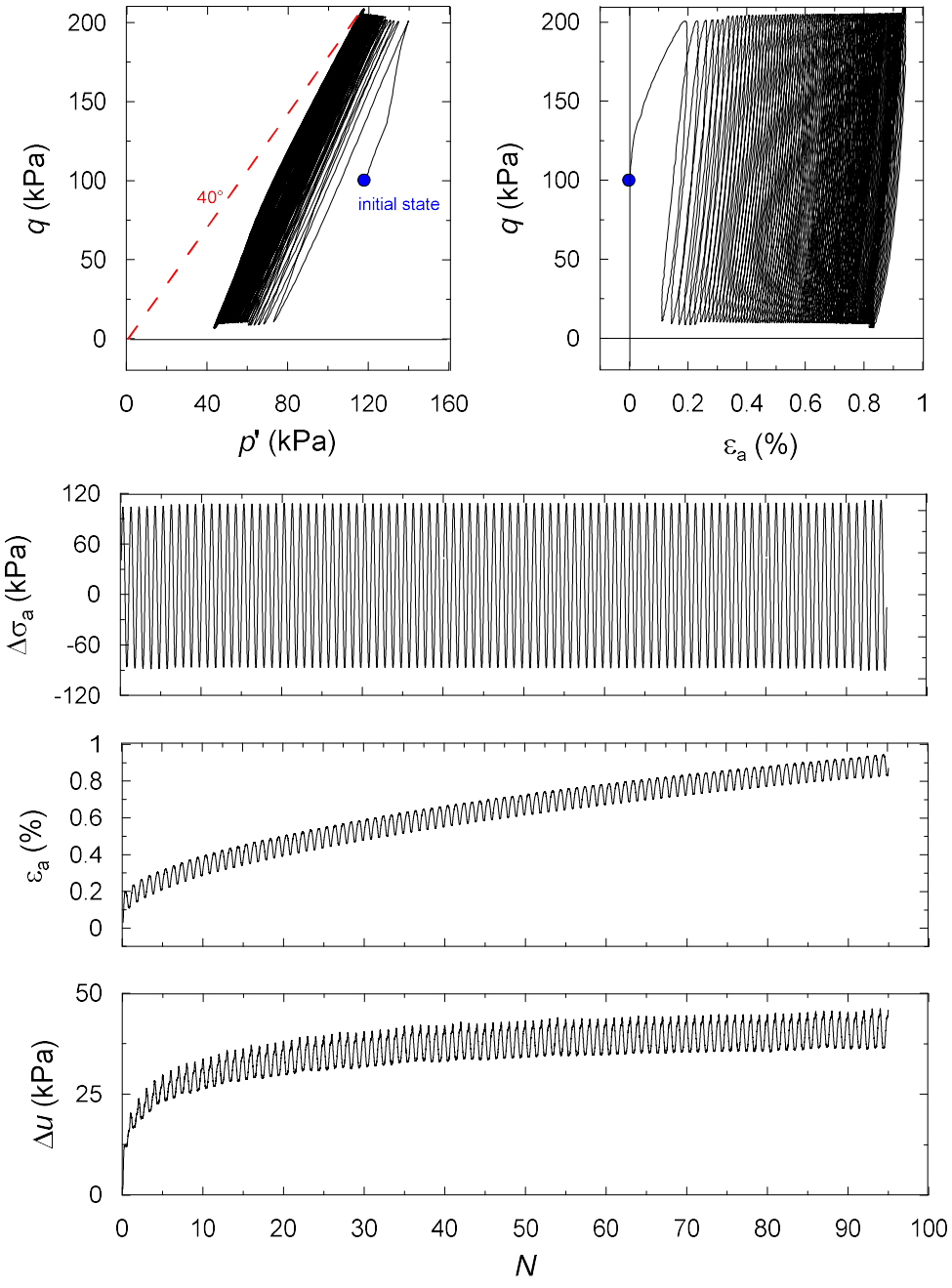

Figure 3.23: Undrained cyclic triaxial test on anisotropically consolidated undisturbed specimen *S*9.

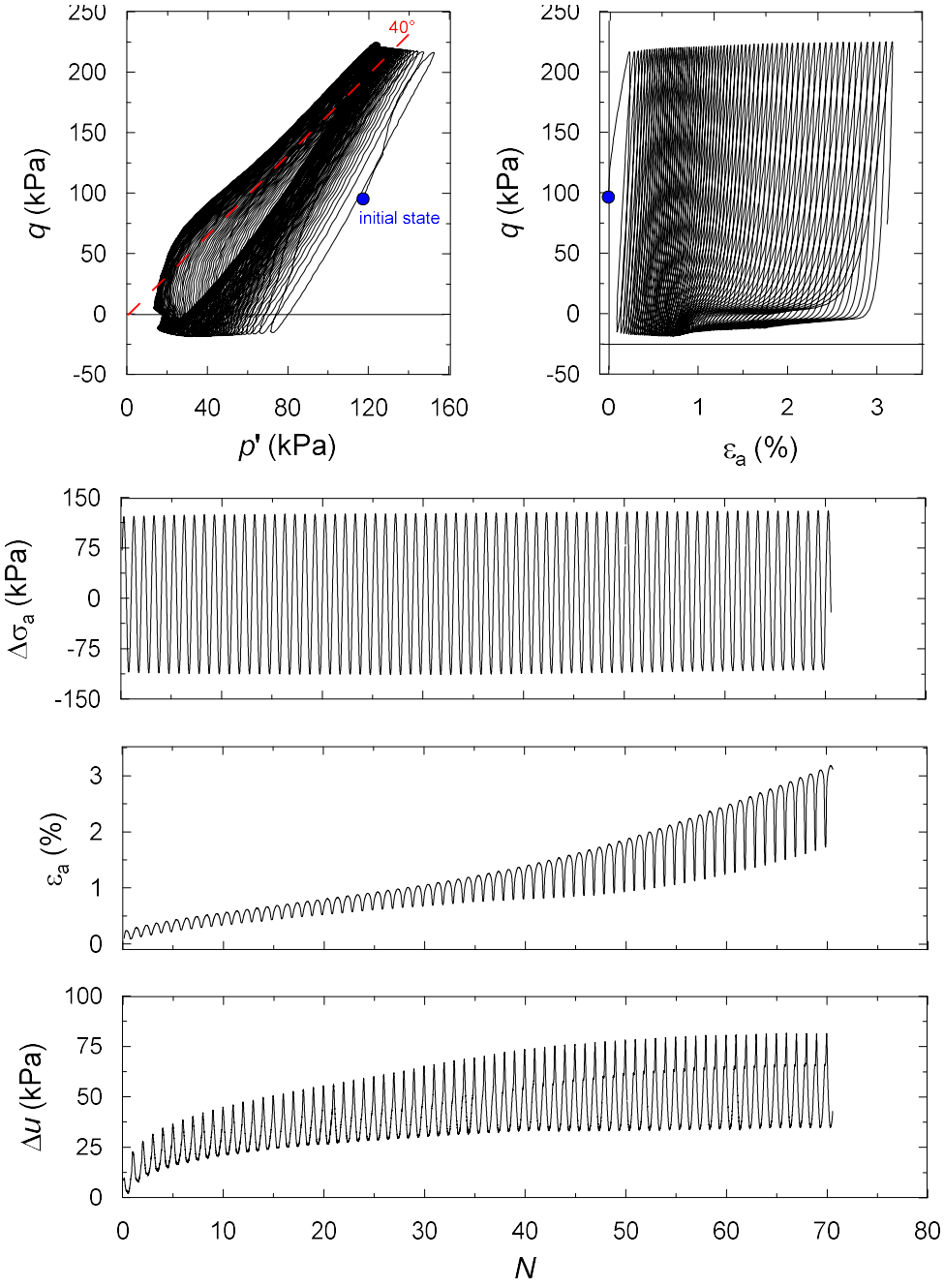

Figure 3.24: Undrained cyclic triaxial test on the anisotropically consolidated undisturbed specimen $S10$.

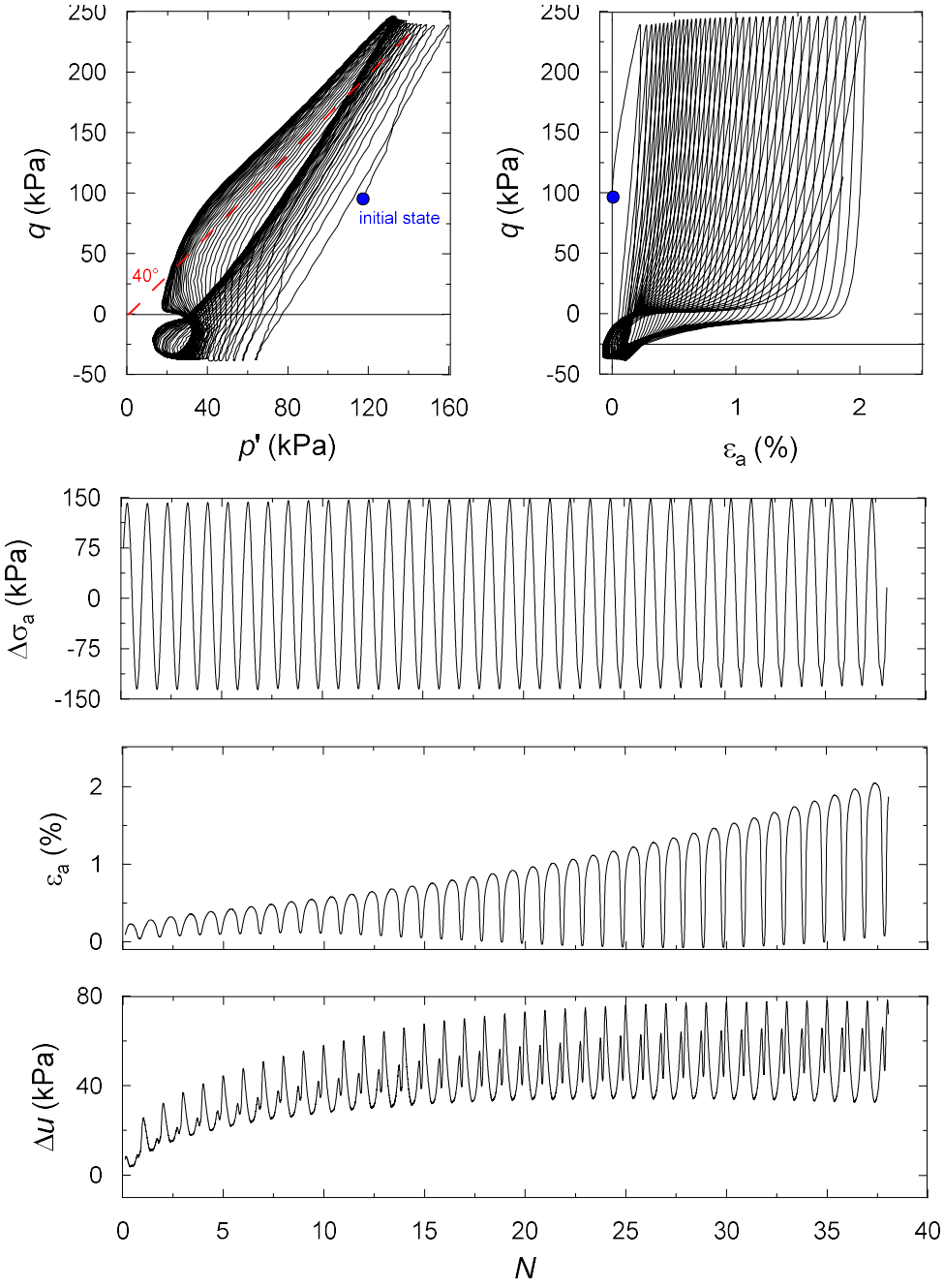

Figure 3.25: Undrained cyclic triaxial test on the anisotropically consolidated undisturbed specimen $S11$.

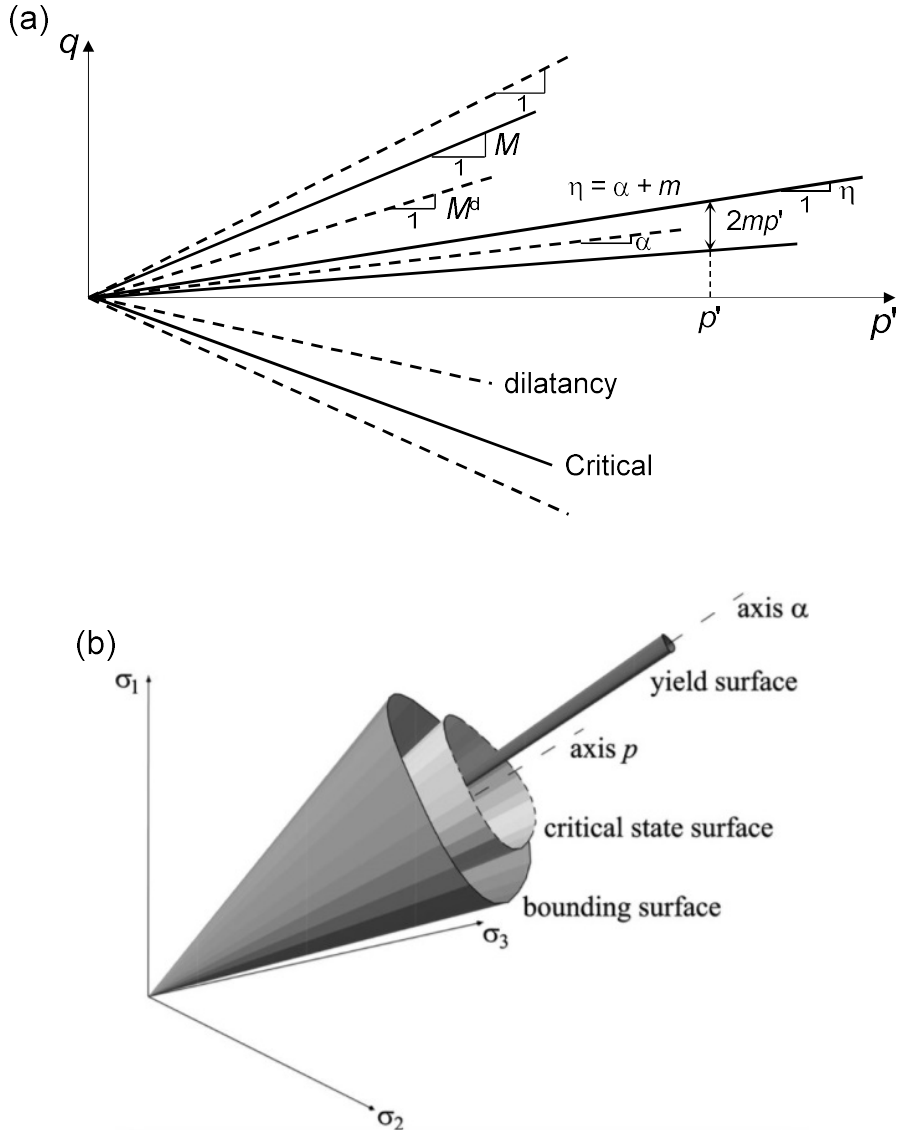

Figure 3.26: Schematic of the yield, critical, dilatancy and bounding lines in the $q - p'$ space (a) and of the respective surfaces in the three-dimensional principal stress space. Reproduced from Dafalias and Manzari (2004).

In the following, the key aspects of the formulation are described considering for simplicity the triaxial stress space, while the the reader can refer to the original paper for the multi-axial generalization. The incremental stress-strain relations are given by

$$d\varepsilon_q^e = \frac{dq}{3 \cdot G}; \quad d\varepsilon_v^e = \frac{dp'}{K} \tag{3.4}$$

$$d\varepsilon_q^p = \frac{d\eta}{H}; \quad d\varepsilon_v^p = d \cdot \left| d\varepsilon_q^e \right| \tag{3.5}$$

in which the superscripts e and p denote the elastic and plastic parts of strain, respectively, G and K are the shear and bulk moduli of soil, respectively, and d is the dilatancy parameter. The moduli G and K are considered functions of the mean effective stress p' and the current void ratio e, according to the expressions proposed by Richart et al. (1970) and Li and Dafalias (2000)

$$G = G_a \cdot p_{atm} \cdot \frac{(2.97 - e)^2}{1 + e} \cdot \left(\frac{p}{p_{atm}} \right)^{0.5}; \quad K = \frac{2 \cdot (1 + \nu)}{3 \cdot (1 - 2 \cdot \nu)} \cdot G \tag{3.6}$$

denoting as p_{atm} the atmospheric pressure and ν the Poisson's ratio. The positive constant G_a is determined by trial and error. From Eqs. 3.4 and 3.5, it is evident that only changes of the stress ratio $\eta = q/p'$ can cause plastic shear and volumetric strains. Therefore a stress-ratio defined yield surface f is assumed

$$f = |\eta - \alpha| - m = 0 \tag{3.7}$$

where α is the back-stress ratio and m defines the size of the surface. The conical shape of f confines the elastic region of the model, starting from which plastic strains develop modifying the orientation α and the size m of the yield surface. The stress ratio η can increase up to the bounding stress ratio M^b that varies with the material

state according to Li and Dafalias (2000), that is

$$M^b = M \cdot exp(-n^b \cdot \psi) \tag{3.8}$$

with n^b a positive material constant. Accordingly, M^b evolves in the process of loading and becomes equal to the stress ratio M at Critical State when the state reaches the CSL in the $e - p'$ space. The latter is described by the Li and Wang curve (1998) already introduced in Section 3.2.1. In the context of Bounding Surface Plasticity, the hardening modulus H in Eq. 3.5 depends on the difference between the current value of η and M^b, such that

$$H = h \cdot (M^b - \eta) \tag{3.9}$$

where h is a positive function of the state variables $\{\eta, e, p'\}$

$$h = \frac{b_0}{|\eta - \eta_{in}|}; \quad b_0 = G_0 \cdot h_0 \cdot (1 - c_h \cdot e) \cdot \left(\frac{p'}{p_{atm}}\right)^{-0.5} \tag{3.10}$$

with h_0 and c_h scalar parameters and η_{in} the stress ratio at initiation of a loading process. Dilatancy is controlled by the parameter d, whose expression is conceptually identical to that used for the plastic modulus H

$$d = A_d \cdot (M^d - \eta) \tag{3.11}$$

$$M^d = M \cdot exp(n^d \cdot \psi). \tag{3.12}$$

As a result, when $\psi < 0$ and $M^d < M < M^b$ a dilatant behaviour $d < 0$ occurs for $\eta \geq M^d$. Vice versa, when $\psi > 0$ and $M^b < M < M^d$ the behaviour is purely contractant. The parameters M^b and M^d varies as a function of the current state and

becomes equal to M when $\psi = 0$. The parameter A_d is a function of the state and incorporates micro-mechanical observations on the change in sand particle normal orientation distribution (fabric) upon monotonic shearing during the dilation phase of deformation, key aspect to reproduce the cyclic behaviour of coarse-grained soils at low stress levels. Hence, the dilatancy parameter d changes during dilation as a function of a fabric-dilatancy internal variable z as follows

$$A_d = A_0 \cdot (1 + \langle s \cdot z \rangle) \tag{3.13}$$

where the MacCauley brackets operate such that $\langle s \cdot z \rangle = s \cdot z$ if $s \cdot z > 0$ and $\langle s \cdot z \rangle = 0$ if $s \cdot z \leq 0$. The parameter A_0 can be taken as a constant value, $s = \pm 1$ according to the direction of the stress path $\eta = \alpha \pm m$, and the evolution law for the fabric parameter is defined as

$$dz = -c_z \cdot \langle -d\varepsilon_v^p \rangle \cdot (s \cdot z_{max} + z) \tag{3.14}$$

whose variability is controlled by the parameters c_z and z_{max}.

The conceptual framework described above is kept in the general multi-axial formulation and the input parameters of the model are listed in Table 3.6. The initial void ratio e_{ini} and the initial back-stress ratio α_{ini} play the role of internal variables of the model: the initial void ratio is needed to determine the initial value of the state parameter ψ, while α_{ini} defines the initial configuration of the yield surface. In OpenSees, the latter is initially assumed coincident with the initial stress ratio of the material. The constant c is defined as the ratio between the critical state stress ratio in extension M^- and in compression M^+ and it is introduced in the formulation in order to reproduce the dependence of the plastic deviatoric strain rate direction on the Lode angle in the multi-axial generalization. More in detail, the rate of the volumetric plastic strain is determined in terms of the dilatancy parameter d

Constant	Variable
Initial void ratio	e_{ini}
Elasticity	G_0
	ν
Critical State	M
	c
	λ_c
	e_0
	ξ
Yield surface	m
Plastic modulus	h_0
	c_h
	n^b
Dilatancy	A_0
	n^d
Fabric-dilatancy tensor	z_{max}
	c_z

Tabella 3.6: Input parameters of the SANISAND model.

while the deviatoric non-associativity applies as a function of the constant c: if $c = 1$ associated plastic flow holds, while $c < 1$ implies a non-associated flow whose evolution depends on the Lode angle.

The model is available in the OpenSees library and can be combined to three-dimensional finite elements with fully coupled hydro-mechanical behaviour.

3.3.2 The PDMY model

The PDMY model is mainly conceived to reproduce the cyclic response of coarse-grained soils. It is formulated within the framework of Multi-Surface Plasticity (Iwan 1967, Mroz 1967, Prevost 1985): the model is composed of a series of conical yield surfaces with circular directrix (Prevost 1985, Lacy 1986), depicted in Figure 3.27, that evolve in the three-dimensional principal stress space with kinematic hardening. The expression of the generic yield surface reads

$$f = \frac{3}{2}\left[\mathbf{s} - (p' + p'_0) \cdot \alpha\right] : \left[\mathbf{s} - (p' + p'_0) \cdot \alpha\right] - m^2 \cdot (p' + p'_0)^2 = 0 \tag{3.15}$$

where the symbol : denotes a doubly contracted tensor product. The quantity $\mathbf{s}$ is the deviatoric stress tensor whereas α is a second-order deviatoric stress tensor that defines the center of the yield surface in the deviatoric stress subspace (back stress ratio); m defines the size of the yield surface and p'_0 represents the distance of the apex of the yield surface from the origin along the hydrostatic axis p' such that the yield size remains finite at $p' = 0$. A tensile cut-off is provided in order to confine the admissible states of the material for $p' \geq 0$. Although sandy and gravelly materials do not have an effective cohesion, a small value of p'_0 can be particularly useful for the stability of numerical computations and because it avoids the ambiguity in defining the normal to the yield surface at its apex. The yield surfaces have a common apex along the p' axis and the innermost surface represents the boundary of the elastic region while the outermost yield surface is designated as the ultimate surface, locus of points of attainment of the ultimate conditions of the material. Differently from the SANISAND model, the PDMY model does not account for the dependence of the deviatoric plastic flow on the Lode angle since Eq. 3.15 does not include the third stress invariant. This limitation of the model can be partially overcome considering a nonzero back stress ratio α of the yield surfaces, providing a different strength in compression and extension.

A typical response in the shear stress-strain space is shown in Figure 3.27. The piecewise-linear curve of the model is aimed to reproduce the nonlinear shear behaviour of soil (Kramer 1996). More in detail, the backbone curve proposed by Duncan and Chang (1970) is taken as reference and, for a given reference confinement p'_r, it reads

$$\tau = G_r \cdot \frac{\gamma}{1 + \gamma/\gamma_r} \tag{3.16}$$

where τ and γ are the octahedral shear stress and strain, respectively, and γ_r is

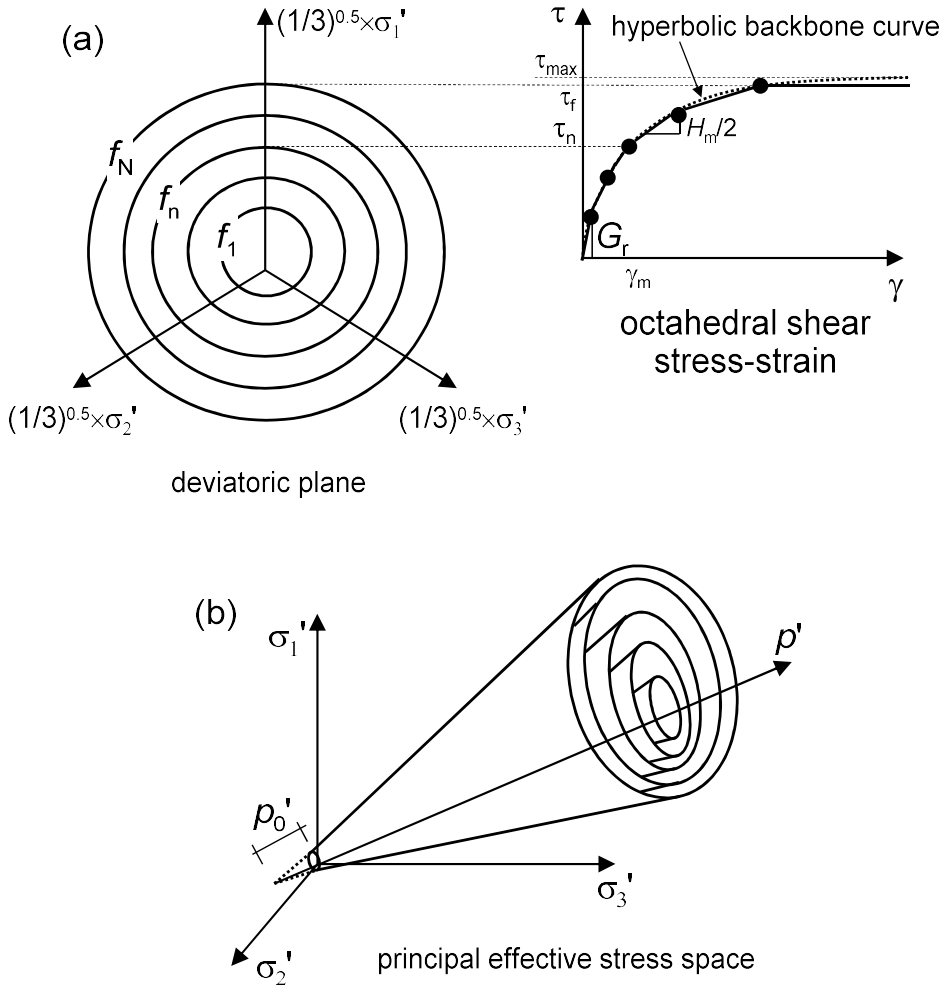

Figure 3.27: (a) Piecewise-linear approximation of the hyperbolic backbone curve used to describe the nonlinear shear stress-strain response and (b) representation of the conical yield surfaces in the principal stress space. Reproduced from Yang et al. (2003).

the shear strain associated with a purely elastic behaviour, defined as τ_{max}/G_0. The analytical curve is reproduced through a progressive decay of the plastic modulus H_n: starting from the shear modulus at small strains G_r related to the elastic response, the plastic modulus reduces towards the ultimate surface according to the evolution of the stress ratio between the surfaces. Each linear segment of the backbone curve (continuous line in Figure 3.27) constitutes the domain of a yield surface f_n, characterised by a size M_n and by an elastic-plastic shear modulus H_n, for n from 1 to the number N of the surfaces. The size of the surfaces increases progressively according to the following expression for the n-th back stress M_n

$$M_n = \frac{3 \cdot \tau_n}{\sqrt{2} \cdot (p'_r + p'_0)} \tag{3.17}$$

up to the ultimate surface in correspondence of which it reads $M_N = 6 \cdot sin\varphi' / (3 - -sin\varphi')$, consistent with Critical State conditions. The CSL is described by the Li and Wang curve (1998) also used in the SANISAND model. The plastic modulus associated with the n-th surface varies according to the following relations

$$H_n = 2 \cdot (\tau_{n+1} - \tau_n) / (\gamma_{n+1} - \gamma_n) \tag{3.18}$$

and it is bounded between the initial value $H_1 = G_0$ and the final value $H_N = 0$. Finally, the small strain shear modulus G_r, as well as all the tangent moduli H_m, is assumed to vary with the level of confinement as proposed by Prevost (1985)

$$G_0 (p') = G_r \cdot \left[\frac{p' + p'_0}{p'_r + p'_0} \right]^d \tag{3.19}$$

with the exponent d commonly taken equal to 0.5. Finally, the generic bulk modulus K_n of the soil skeleton is computed as $K_n = G_n \cdot [2 \cdot (1 + \nu)] / [3 \cdot (1 - 2 \cdot \nu)]$. The accuracy in reproducing the hyperbolic backbone curve increases with the num-

ber of yield surfaces employed in the computation. In the numerical analyses carried out in this study, 40 surfaces were used reaching a high level of approximation of the nonlinear behaviour.

As an important feature under dynamic conditions, a purely deviatoric kinematic hardening rule is employed, in which the yield surface translation rule proposed by Parra (1996) is developed to enhance computational efficiency. This is actually the primary aim of the model: describing with a sufficient level of accuracy the salient aspects of the soil behaviour under cyclic conditions supported by a highly stable formulation in numerical computing. Nonassociativity of the plastic flow is restricted to its volumetric component.

The state of the material is simply defined by the stress ratio η in the principal stress space

$$\eta = \frac{\sqrt{3 \cdot (\mathbf{s} : \mathbf{s})/2}}{p' + p'_0} \tag{3.20}$$

and the contractive and dilative tendency of soil depends on the position of the stress state with respect to the Phase Transformation Line (Ishihara et al. 1975), the latter characterised by a stress ratio η_{PTL}: when the stress state is inside the PTL ($\eta < \eta_{PTL}$) the material exhibits a contractive behaviour and vice versa. For coarse-grained soils, it is well known that a complete description of the material state requires the combined information on the stress and the strain levels in the $e - p'$ space, concisely expressed by the state parameter ψ (Been and Jefferies 1985). In the PDMY model, instead, only the information on the stress level η is considered to define the tendency of the behaviour, leading to a less accurate evaluation on the development of strains. Therefore, the ratio η_{PTL} of the PTL represents the only internal variable of the model.

Let $\mathbf{P}$ be the outer normal to the potential surface, respectively. This tensor can

be conveniently decomposed into its volumetric $P'' \cdot \mathbf{I}$ and deviatoric $\mathbf{P'}$ part, where $\mathbf{I}$ a second-order identity matrix, such that $\mathbf{P} = P'' \cdot \mathbf{I} + \mathbf{P'}$. Different expressions for the scalar quantity P'' are used to differentiate the behaviour during contraction, dilation and neutral phase when the stress state reaches the PTL.

Shear-induced contraction occurs inside the PTL when $\eta < \eta_{PTL}$, as well as when $\eta > \eta_{PTL}$ and $\dot{\eta} < 0$. Experimental observations and micro-mechanical investigations demonstrated that the rate of contraction is significantly influenced by preceding dilation phases (Ishihara et al. 1975, Ladd et al. 1977, Nemat-Nasser and Tobita 1982, Papadimitriou et al. 2001). In order to reproduce this effect, the parameter P'' is considered to be a function of the plastic volumetric strain ε_v^p accumulated during dilation (Papadimitriou et al. 2001)

$$P'' = \left[1 - \frac{sgn\left(\dot{\eta}\right) \cdot \eta}{\eta_{PTL}}\right] \cdot \left(c_1 + c_2 \cdot \varepsilon_c\right) \tag{3.21}$$

where c_1 and c_2 are positive calibration constants defining the rate of contraction or, under undrained conditions, the increment of positive excess pore water pressure. The non-negative scalar quantity ε_c is defined by the following rate equation

$$\dot{\varepsilon}_c = \begin{cases} -\dot{\varepsilon}_v^p, & \varepsilon_c > 0, -\varepsilon_v^p > 0 \\ 0, & \text{otherwise} \end{cases} . \tag{3.22}$$

Conversely, dilatant behaviour occurs when $\eta > \eta_{PTL}$ and $\dot{\eta} > 0$ and it is defined by

$$P'' = \left[1 - \frac{\eta}{\eta_{PTL}}\right] \cdot d_1 \cdot \gamma_d^{d_2}. \tag{3.23}$$

with d_1 and d_2 positive calibration constants and γ_d the octahedral shear strain accumulated during the current dilation phase. Finally, neutral phase occurs in

Constant	Variable
Elasticity	G_0
	ν
Reference mean pressure	p'_r
Pressure dependence coefficient	d
Peak shear strain	$\gamma_{d,max}$
Phase Transformation Line	ϕ_{PTL}
Contraction	c_1
	c_2
Dilatancy	d_1
	d_2
Critical State	M
	λ_c
	e_0
	ξ
Number of yield surfaces	N

Tabella 3.7: Input parameters of the PDMY model.

correspondence of the PTL, hence when the behaviour changes from contractant to dilative. In this condition P'' is kept equal to zero ($\dot{\varepsilon}_v^p = 0$) until the closest yield surface is reached.

The input parameters of the model are reported in Table 3.7. The parameter d defines the exponent in Eq. 3.19 and therefore the dependence of the tangent moduli H_n on the effective confinement. The peak shear strain $\gamma_{d,max}$ is the octahedral shear strain at which the maximum shear strength is reached, needed to describe completely the hyperbolic backbone curve. Finally, the stress ratio of the PTL is computed as $\eta_{PTL} = 6 \cdot sin\phi_{PTL} / (3 - sin\phi_{PTL})$.

In comparison with the SANISAND model, the PDMY model presents a less rigorous mathematical formulation in which some peculiar aspects of the soil behaviour, such as dilation and Critical State, are encapsulated into the formulation through some empirical expedients. By contrast, in virtue of its simpler formulation, the PDMY model is more manageable and stable in numerical simulations, especially under dynamic conditions. Therefore, as a result of an extended comparison with the response of the SANISAND model, the PDMY model constituted the reference

material in the most demanding dynamic analyses of the full soil-bridge system.

3.3.3 Calibration procedure

The parameters of the SANISAND and the PDMY models were calibrated against the experimental data shown in Section 3.2.1, relative to monotonic and cyclic tests. It was observed that both models can reproduce with sufficient accuracy the mechanical behaviour of the soil only in a specific range of strain. More in detail, it was found that a calibration based only on monotonic laboratory tests leads to a considerable overestimation of the excess pore water pressure under cyclic conditions and, as a result, an inaccurate prediction of the mechanical response in undrained conditions. To overcome this issue, the calibration was aimed to obtain a good match with the experimental trends under cyclic conditions and, at the same time, to have a reasonable static response in the range of strain of interest for the problem under examination. The procedure used to identify the optimum values of the constitutive parameters is entirely presented for the SANISAND model while only the optimised response is presented for the PDMY model.

In light of the above, two different optimum configurations of the SANISAND model were determined under monotonic and cyclic loading conditions, listed in Table 3.8. The soil mass density ρ_{soil} and the initial void ratio e_{ini} were chosen in accordance with the experimental data in Table 3.1. The Critical State parameters of the Li and Wang's curve have already been evaluated in Eq. 3.2. The size m of the elastic core is taken equal to 0.01, as a very small fraction of the external bounding surface. The elastic region represents the behaviour of soil at small strains, characterised by the shear modulus G_0 and the Poisson's ratio ν. A value of 0.2 was assumed for the elastic Poisson's ratio, that is considerably smaller than the value of 0.35 obtained by triaxial tests, because the latter is referred to a much higher range of strains in which the response is markedly elastic-plastic. The remaining

		Cyclic conditions	
Variable	Monotonic cond.	"Dilatancy"	"Hardening"
ρ_{soil} (Mg/m^3)	2.243	2.243	2.243
e_{ini}	0.35	0.35	0.35
G_a	90	170	170
ν	0.2	0.2	0.2
M	1.55	1.55	1.55
c	0.875	0.875	0.875
λ_c	0.0219	0.0219	0.0219
e_0	0.4478	0.4478	0.4478
ξ	0.7	0.7	0.7
m	0.01	0.01	0.01
h_0	4.75	4.5	16.25
c_h	1.1	1.1	1.1
n^b	1.0	9.0	3.0
A_0	1.0	0.25	0.1
n^d	2.0	15.0	1.0
z_{max}	-	12.5	8.0
c_z	-	1100	1000

Tabella 3.8: Different calibration strategies of the SANISAND model, based on monotonic TRIAX-CID and TRIAX-CIU tests ("monotonic" solution) and cyclic TRIAX-CIU tests ("dilatancy" and "hardening" solution) of the saturated layers of Messina Gravels.

parameters are the effective target of the calibration since they depend on loading conditions. The calibration based on monotonic triaxial tests, named "monotonic" solution, follows the procedure traced by Loukidis and Salgado (2009) and Taiebat et al. (2010) used to calibrate the Toyoura, Nevada and Sacramento sand, whereas the two solutions based on cyclic tests, called "dilatancy" and "hardening" solutions, were obtained by a fitting procedure.

Consider the monotonic triaxial tests illustrated in Figures 3.6 and 3.7. The constant G_a modifies the stiffness of the material and can be evaluated through the shear modulus G_0 at small strains (Eq. 3.6). The latter was computed by determining the initial tangent of the experimental trends in the $q - \varepsilon_a$ plane. The resulting values of G_a are plotted in Figure 3.28 as a function of the mean effective stress p', providing a mean value of G_a equal to 90.

The parameters n^b and n^d that control the evolution of the bounding and dilatancy surfaces, respectively, can be estimated representing the results of the TRIAX-

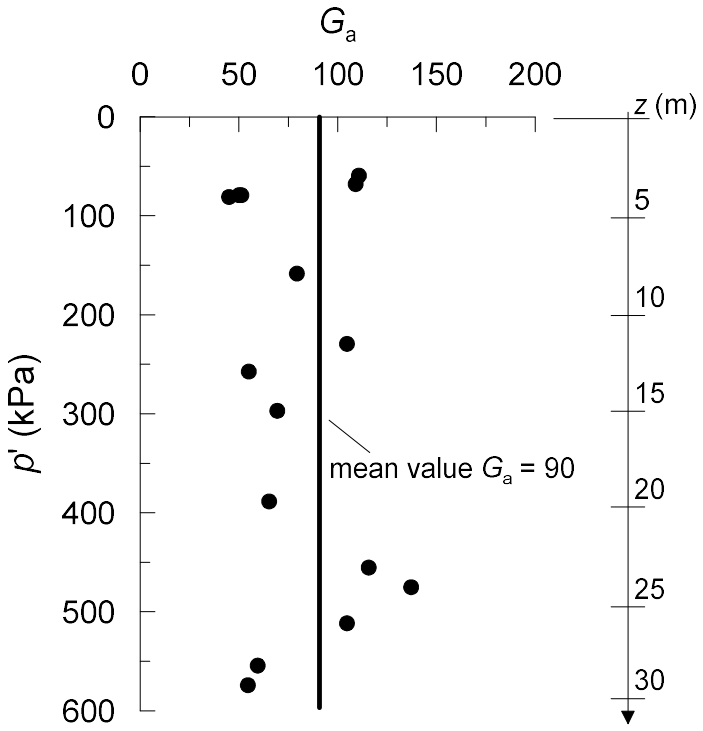

Figure 3.28: Values of G_a computed by drained and undrained triaxial tests.

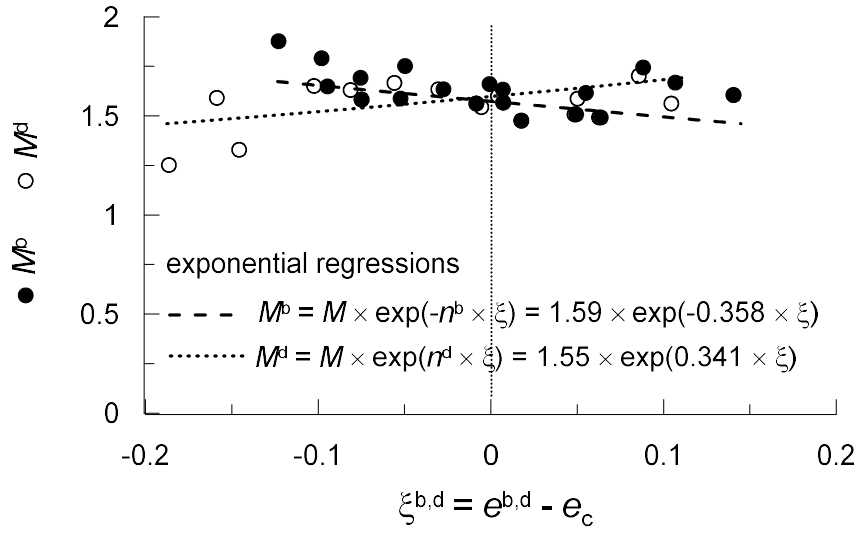

Figure 3.29: Evaluation of the parameters n_b and n_d in the plane $M^{b,d} - \psi$.

CID and TRIAX-CIU in the non-dimensional plane shown in Figure 3.29. The exponential regressions of the experimental data read

$$M^b = 1.59 \cdot exp(-0.358 \cdot \psi), \quad R^2 = 0.195 \tag{3.24}$$

$$M^d = 1.55 \cdot exp(0.341 \cdot \psi), \quad R^2 = 0.189 \tag{3.25}$$

in which the Critical stress ratio M, equal to 1.59 and 1.55 in the equations above, is consistent to the value obtained experimentally of 1.55. The parameters n^b and n^d result to be equal to 0.358 and 0.341, respectively. However, the scatter in the results is somewhat pronounced, as testified by the low values of the coefficient of determination R^2. In order to improve the evaluation of these parameters, in Figure 3.30 it can be observed that just some samples are representative of the in-situ stress-strain state and therefore the calibration of the models was restricted to those tests only. The nonlinear regressions for these data are shown in Figure 3.31 with a considerably higher correlations of the results, R^2 equal to 0.73 and 0.51 for n^b and n^d, respectively. In this significant range of the state parameter ψ, n^b and n^d were assumed equal to 1.0 and 2.0.

The parameters h_0 and c_h control the hardening of the material and were evaluated by trial and error in order to have a good fitting with the experimental behaviour in the $q - \varepsilon_a$ plane. The values chosen in the TRIAX-CID tests are represented in Figure 3.32, in which the composed parameter $h_0 \cdot (1 - c_h \cdot e)$ is conveniently plotted as a function of the void ratio. In this plane, the numerical results can be interpolated by a linear function $y = -m \cdot e + b$ from which the operative values of h_0 and c_h, representative of the entire deposit of Messina Gravels, can be derived as follows

$$h_0 = b = 4.75 \tag{3.26}$$

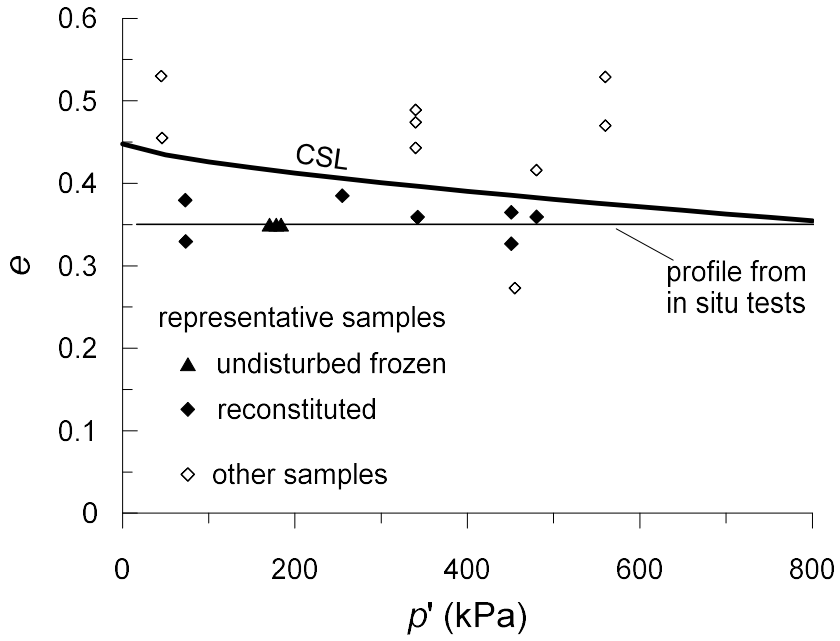

Figure 3.30: Identification of the reference samples of the Messina Gravels in the $e - p'$ plane.

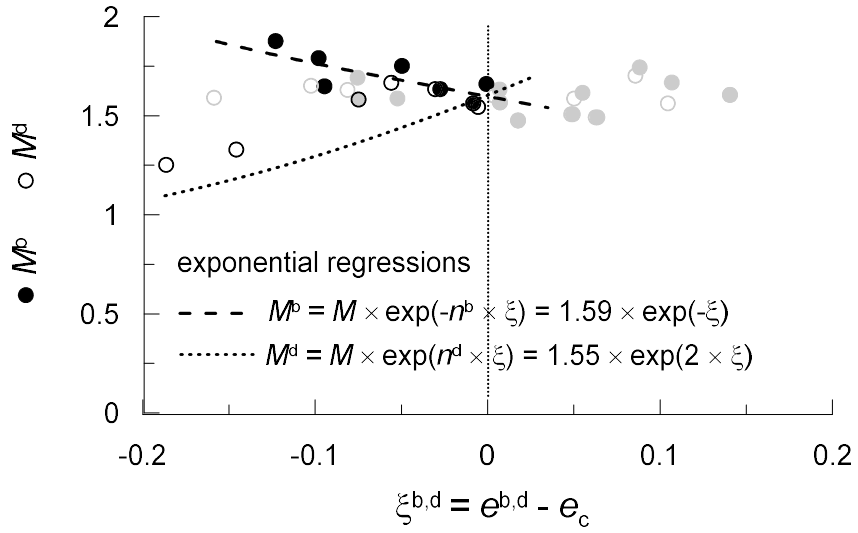

Figure 3.31: Evaluation of the parameters n_b and n_d in the plane $\psi - M^{b,d}$, considering only the experimental data representative of the in-situ soil conditions.

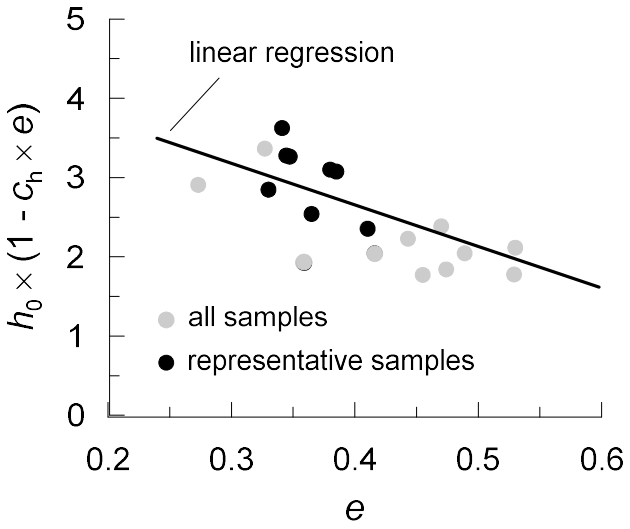

Figure 3.32: Determination of the operative values for h_0 and c_h.

$$c_h = \frac{m}{b} = 1.1. \tag{3.27}$$

The entity of the negative volumetric strains (dilation) in drained conditions, or equivalently of the excess pore water pressure in undrained conditions, is strongly controlled by the dilatancy parameter A_0. Also this parameter was evaluated by trial and error with the aim to reproduce the progressive evolution of the volumetric response with the increase of the deviatoric component of strain. The optimum values of A_0 are shown in 3.33: in the significant range of the state parameter (black dots), A_0 can be reasonably assumed equal to 1.

The monotonic response of the model is represented in Figure 3.34 for the reference TRIAX-CID tests and in Figure 3.35 for the TRIAX-CIU tests on the undisturbed frozen samples.

The cyclic response of the SANISAND model calibrated on the optimum parameters selected for monotonic loading conditions is shown in Figures 3.36, 3.37 and 3.38, only for the test $S1$ for brevity. It is evident that the excess pore water pressure

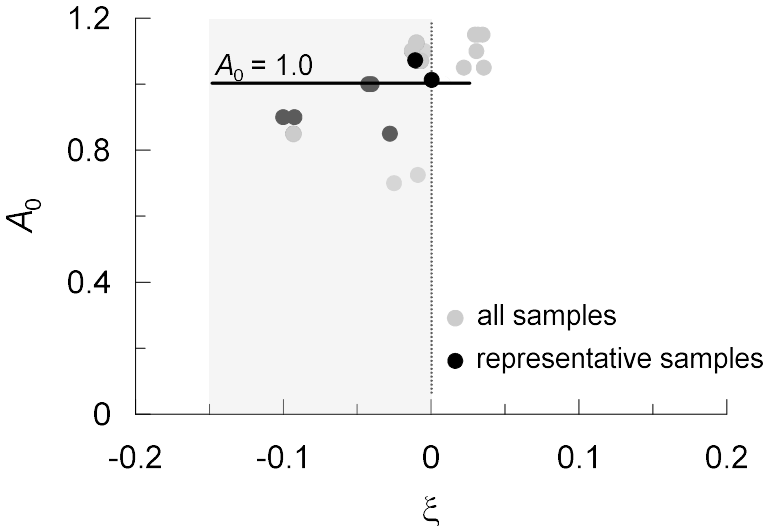

Figure 3.33: Evaluation of the parameter A_0.

builds up too rapidly compared to the experimental behaviour and, consequently, the stress path reaches the CSL after only one cycle of loading. It follows that a unique combination of the constitutive parameters is able to reproduce the experimental behaviour of soil only in the specific deformation mode considered for their calibration.

In light of the above, the parameters were newly calibrated to reproduce the undrained cyclic behaviour shown experimentally, leading to the two optimum solutions reported in Table 3.8. The "dilatancy" solution entails a relevant increase of the parameter n_d controlling the position and the evolution of the dilatancy surface, with a consequent decrease of the stress ratio M^d associated with the latter. This implies that the dilatancy surface is much more contracted with respect to the configuration defined under monotonic loading. As a result, dilation begins much earlier in a cyclic loading and the development of excess pore water pressure is strongly limited by the low value of A_0. The "hardening" solution, instead, follows a different strategy to control the development of excess pore water pressure: the hardening parameter h_0 is an order of magnitude higher than that adopted in the monotonic

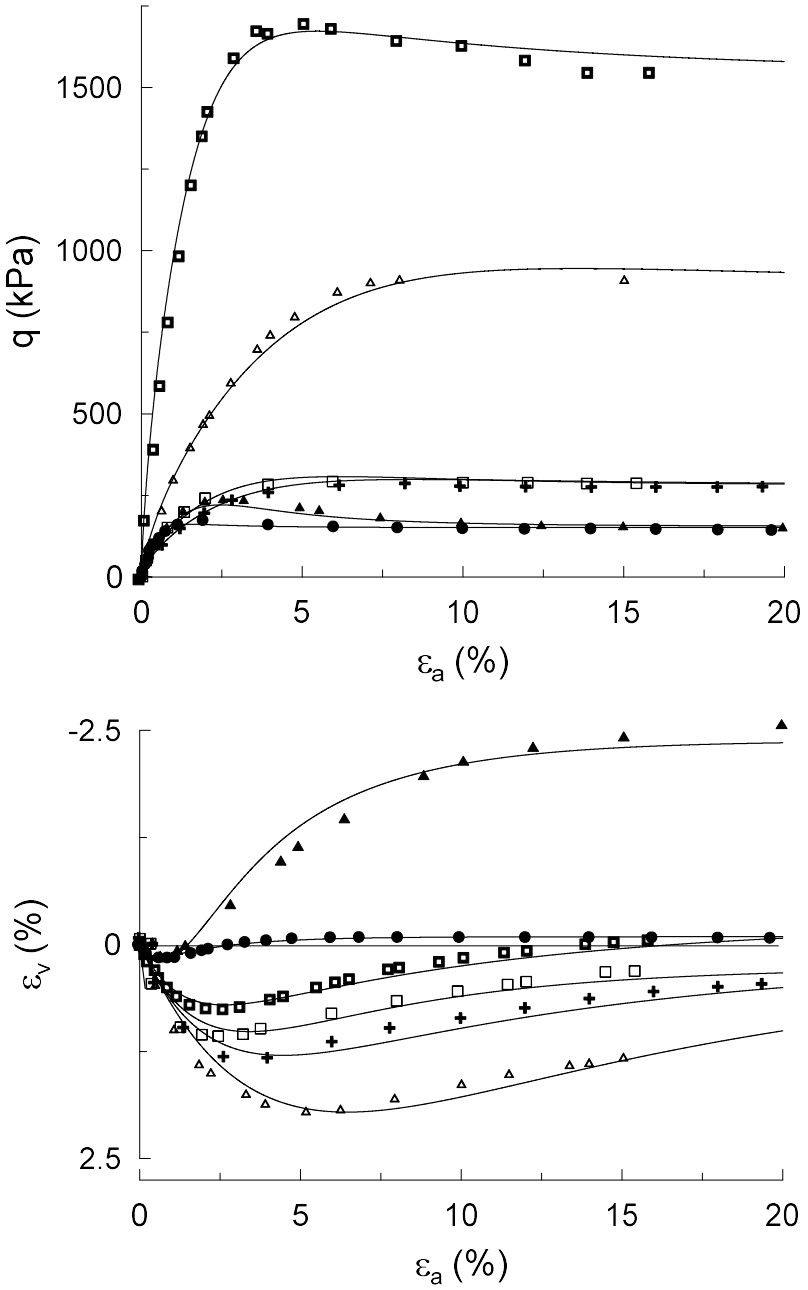

Figure 3.34: Response of the SANISAND model (continuous lines) in the TRIAX CID tests of the reference samples: (a) stress-strain behaviour in the $q - \varepsilon_a$ plane and (b) volumetric response in the $\varepsilon_v - \varepsilon_a$ plane.

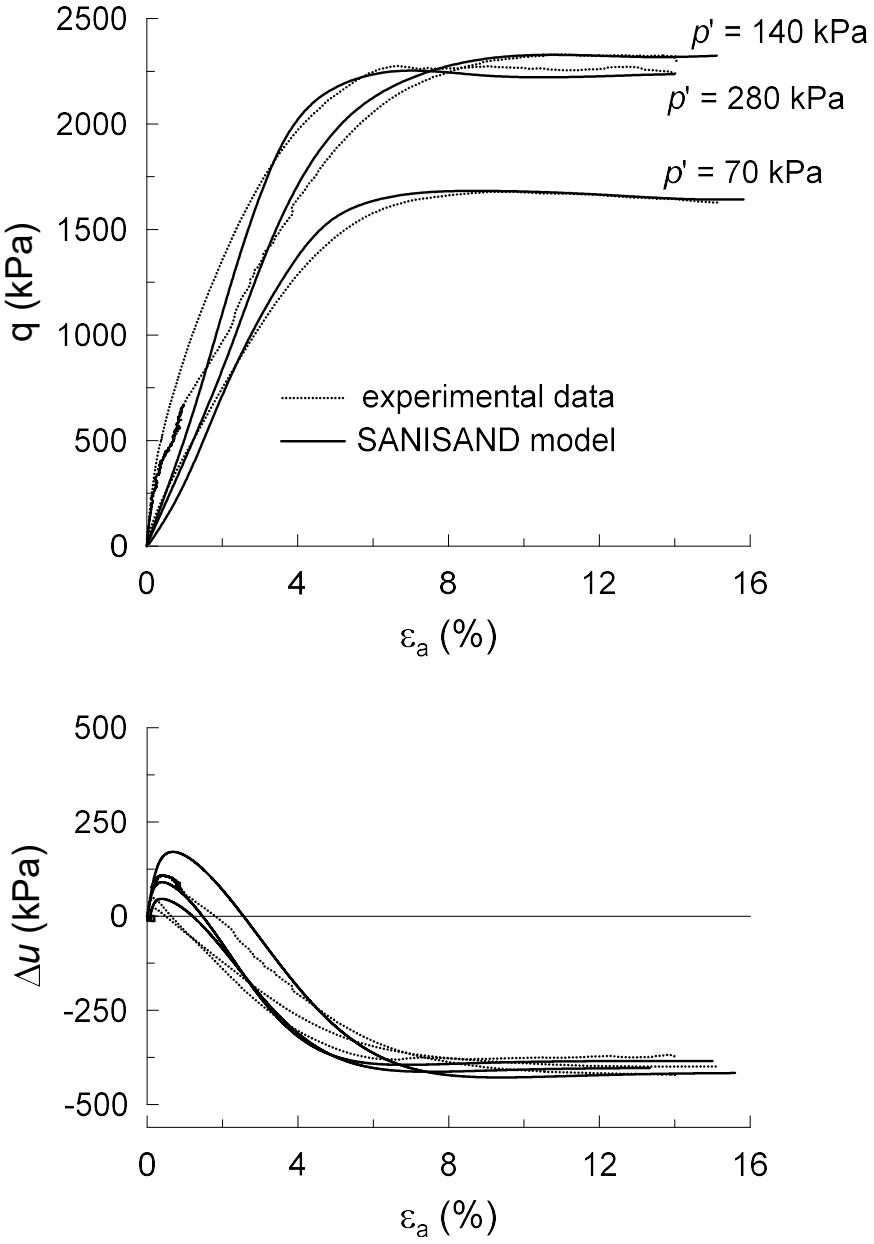

Figure 3.35: TRIAX CIU on the undisturbed frozen samples: (a) stress-strain behaviour in the $q - \varepsilon_a$ plane and (b) response in the $\Delta u - \varepsilon_a$ plane.

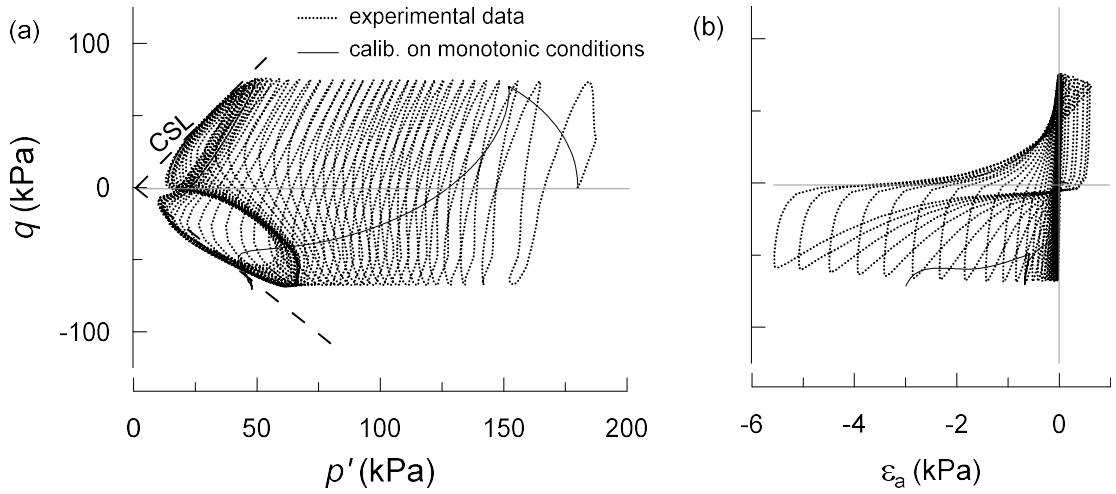

Figure 3.36: Response of the SANISAND model in $q - p'$ space (a) and $q - \varepsilon_a$ space (b) for the test $S1$.

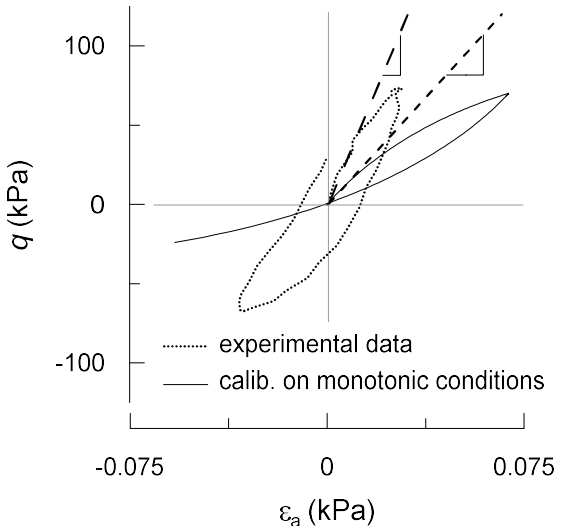

Figure 3.37: Comparison between the initial tangent evaluated experimentally and that computed by the SANISAND model, for the test $S1$.

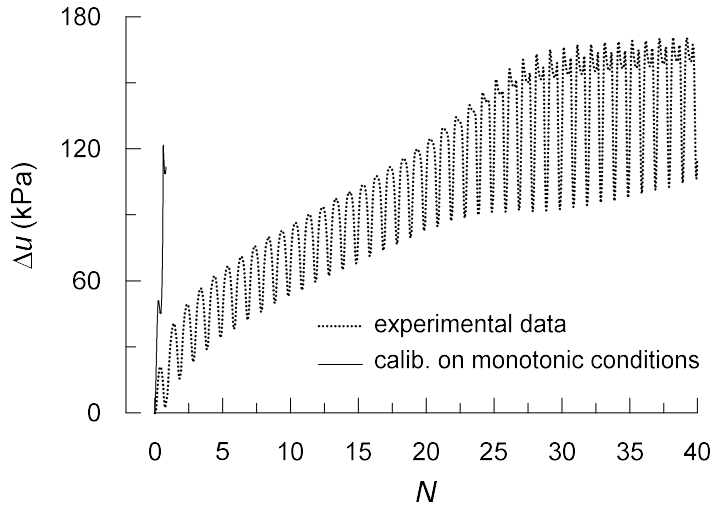

Figure 3.38: Evolution of the excess pore water pressure Δu for the test $S1$.

solution while the dilatancy factor A_0 is drastically reduced. It follows that the bounding surface expands significantly, characterised by a very high stress ratio M^b, while the configuration of the dilatancy surface does not essentially change between monotonic and cyclic conditions. Finally, the fabric-dilatancy constants z_{max} and c_h, that control mainly the response in loading-unloading reverse after a dilatant phase, were evaluated through trial and error: higher values are required for the dilatancy solution in order to have a good fitting at large strains.

The response of the two configurations is shown in Figures 3.39 to 3.42, only for the tests $S1$ and $S2$ for brevity. In the dilatancy solution, the stress-strain path follows much more closely the experimental trend since the excess pore water pressure accumulates more gradually as the axial strain rises. As expected, the dilation phase begins for a much lower deviatoric stress since the low stress ratio M^d of the dilatancy surface, giving a more accurate response from medium to large strains. In the $q - \varepsilon_a$ plane, the "hardening" response, after the first cycles in which the behaviour is somewhat stiffer than the experimental one, returns too large axial strains and an excessive ratcheting.

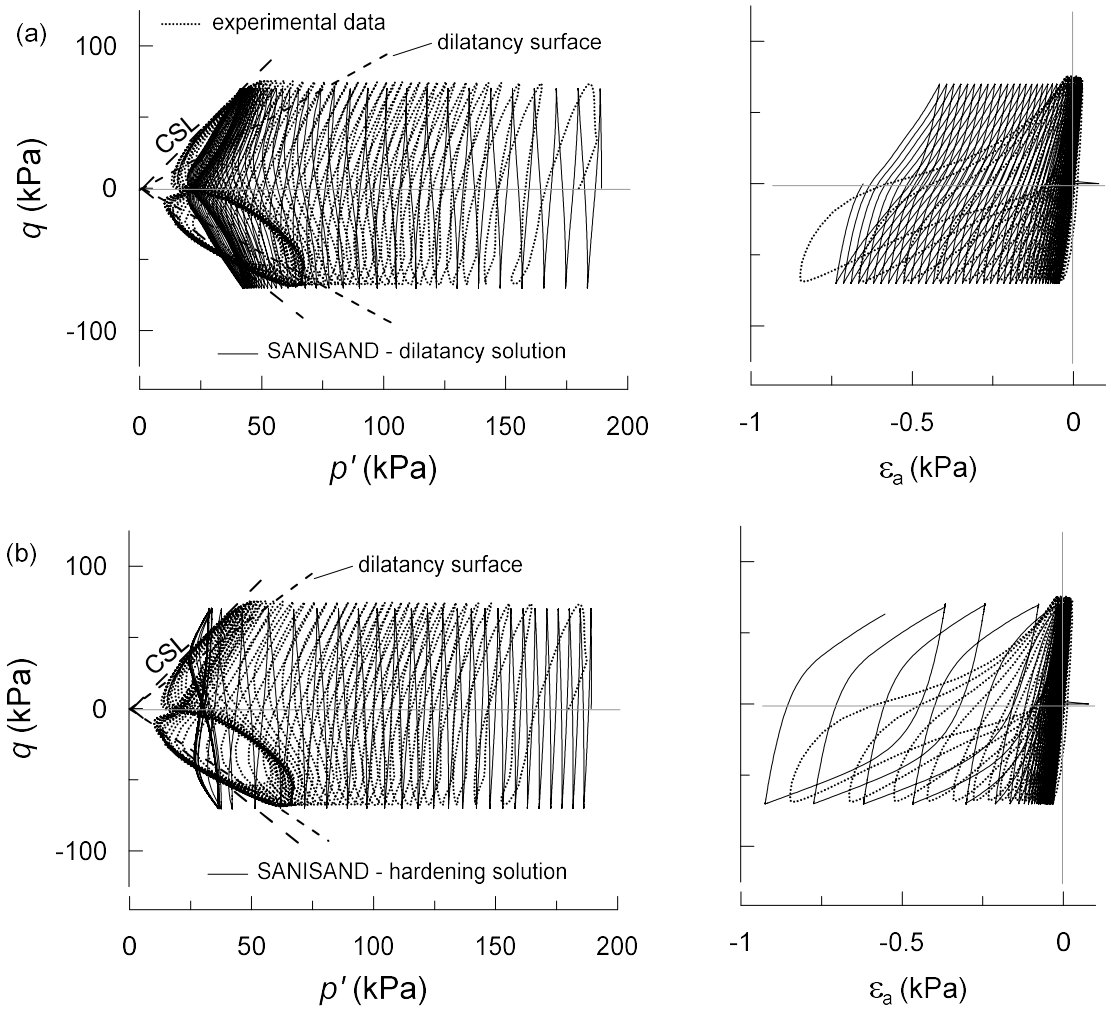

Figure 3.39: Stress paths and stress-strain response obtained with the "dilatancy" solution (a) and the "hardening" solution (b) for the cyclic test $S1$.

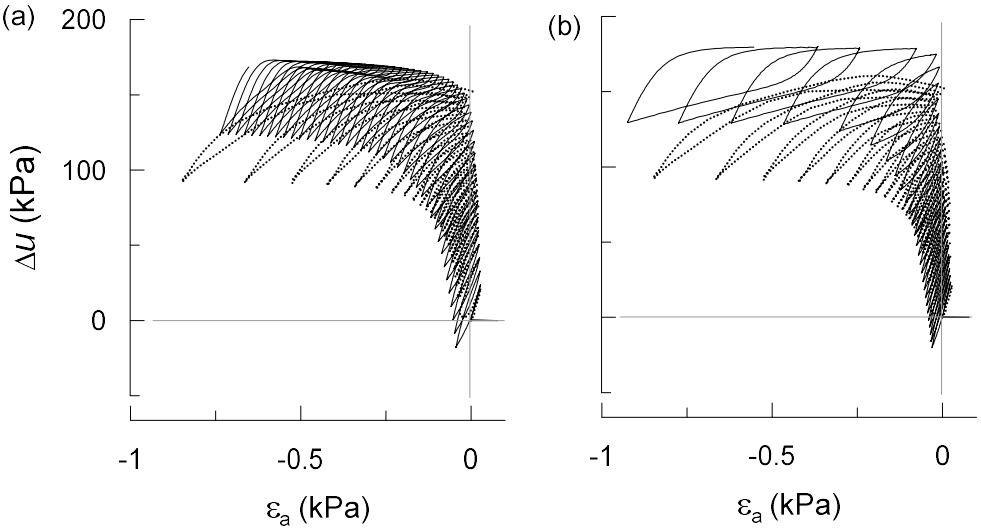

Figure 3.40: Development of the excess pore water pressure as a function the axial strain in the simulation of the test $S1$, obtained with the "dilatancy" solution (a) and the "hardening" solution (b).

In the first cycle, the initial stiffness is well captured in both cases because controlled by the parameter G_a, but when the deviatoric stress increases, activating the plastic response of the model, the hardening solution becomes too stiff because of the high hardening parameter h_0.

The modulus decay curves were obtained by carrying out a cyclic analysis in which the amplitudes of the deviatoric stress increases linearly during cycles, from small to large deviatoric strains, and the corresponding stress paths are shown in Figure 3.43, for the dilatancy and hardening solutions. The resulting trends of the normalised shear modulus G/G_0 are compared with the Seed and Idriss's curve taken as reference for the Messina Gravels in Figure 3.44. It is evident that the curve relative to the dilatancy solution follows more closely the reference curve, especially in the transition zone where the gradient of G/G_0 is maximum ($\gamma = 3{\cdot}10^{-5} \div 1{\cdot}10^{-3}$). The cyclic tests were carried out considering an initial mean effective stress of about 180 kPa, representative of the superficial layer $MGD1$. The corresponding small strain modulus G_0 is equal to $1.9 \cdot 10^5$ kPa (see Table 3.3) while the numerical

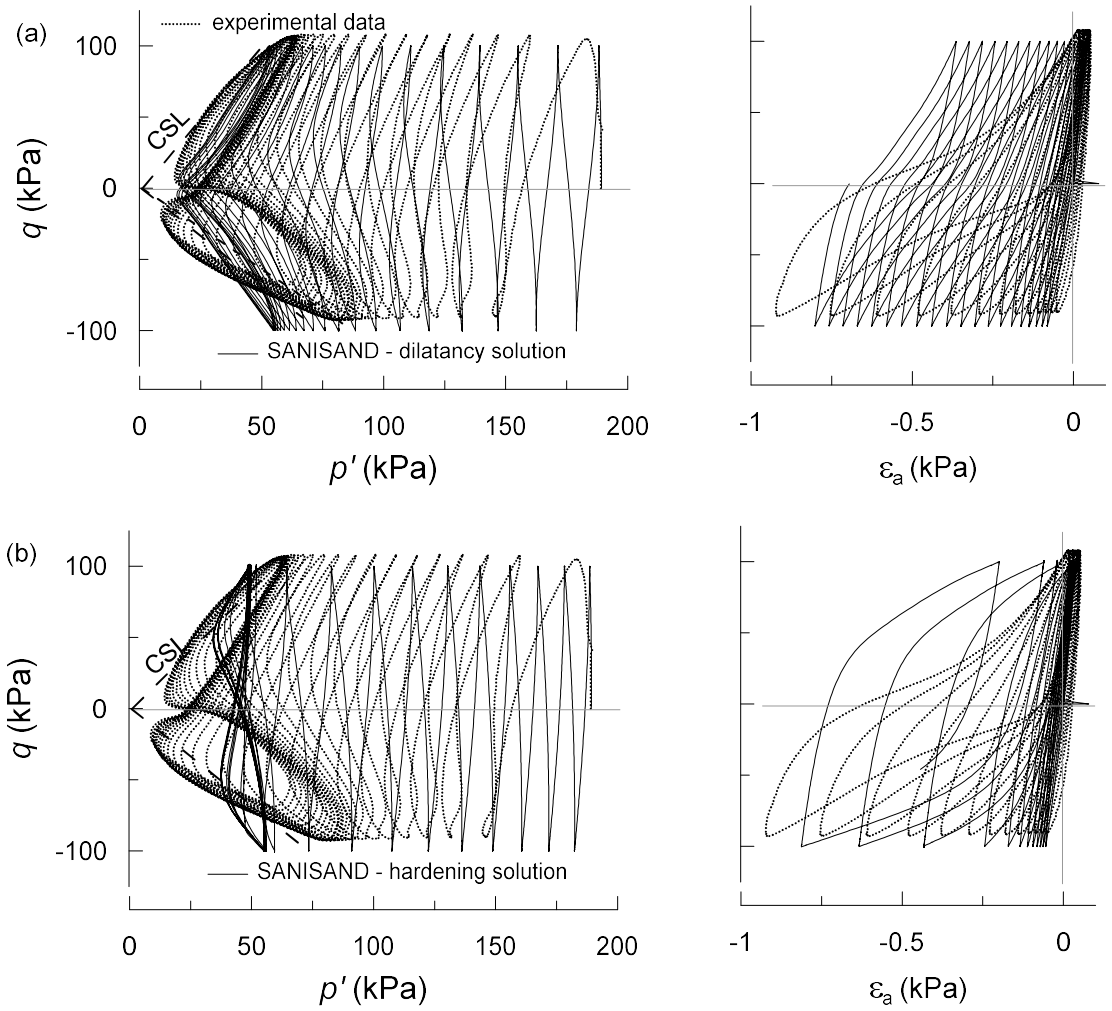

Figure 3.41: Stress paths and stress-strain response obtained with the "dilatancy" solution (a) and the "hardening" solution (b) for the cyclic test $S2$.

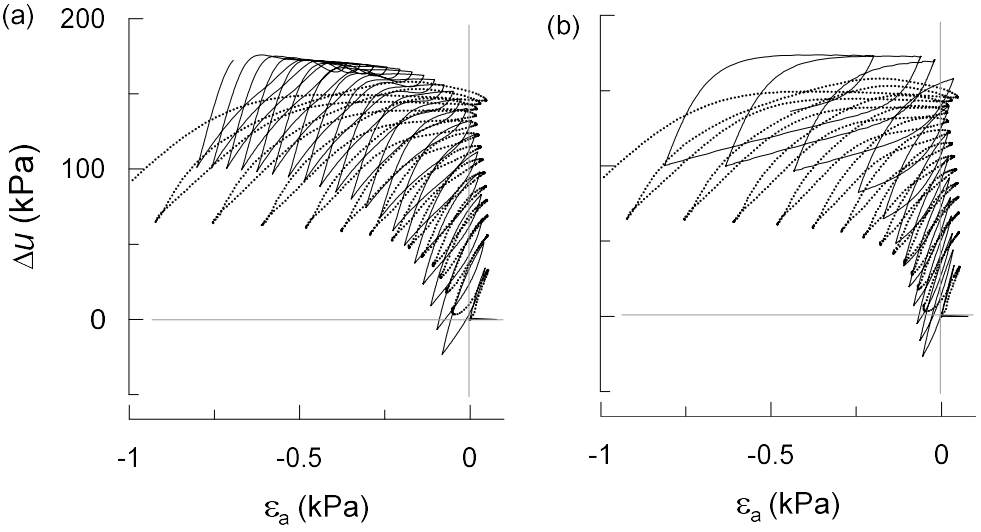

Figure 3.42: Development of the excess pore water pressure as a function the axial strain in the simulation of the test $S2$, obtained with the "dilatancy" solution (a) and the "hardening" solution (b).

simulations gave a value of $1.79 \cdot 10^5$ kPa and $1.71 \cdot 10^5$ kPa for the dilatancy and hardening solutions, respectively, with an underestimation of the initial stiffness of about 6 % and 10 %.

The optimised calibrations of the SANISAND model under cyclic conditions lead, however, to an underestimation of the volumetric strains produced under monotonic loading. As an example, Figure 3.45 shows the response of the calibrations on cyclic tests in a monotonic drained triaxial test, in which only the behaviour in the $q - \varepsilon_a$ plane can be reproduced with a good level of accuracy. Nonetheless, in the dynamic simulations carried out in OpenSees, only the displacement field of the soil-structure system induced by the propagation of the seismic motion is considered. In this way, the initial static stage serves to reproduce the effective stress state in the soil domain and the overestimation of the volumetric stiffness under monotonic loading was therefore deemed acceptable, since it did not affect the dynamic response of the system.

In virtue of the above results, the dilatancy solution gives a more accurate re-

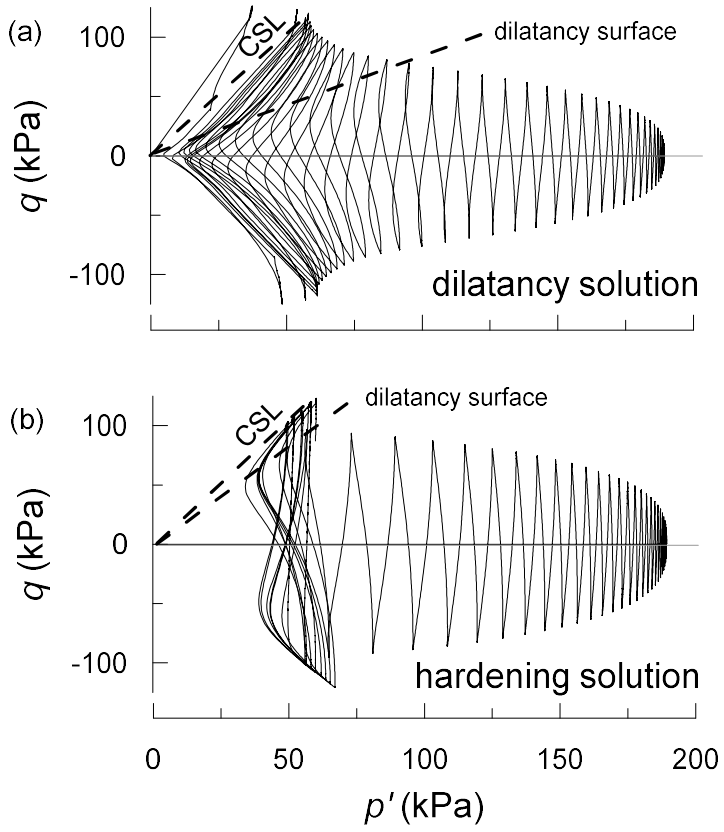

Figure 3.43: Stress paths of the undrained cyclic test carried out with an increasing amplitude of the deviatoric stress: comparison between the calibration based on (a) the dilatancy solution and (b) the hardening solution.

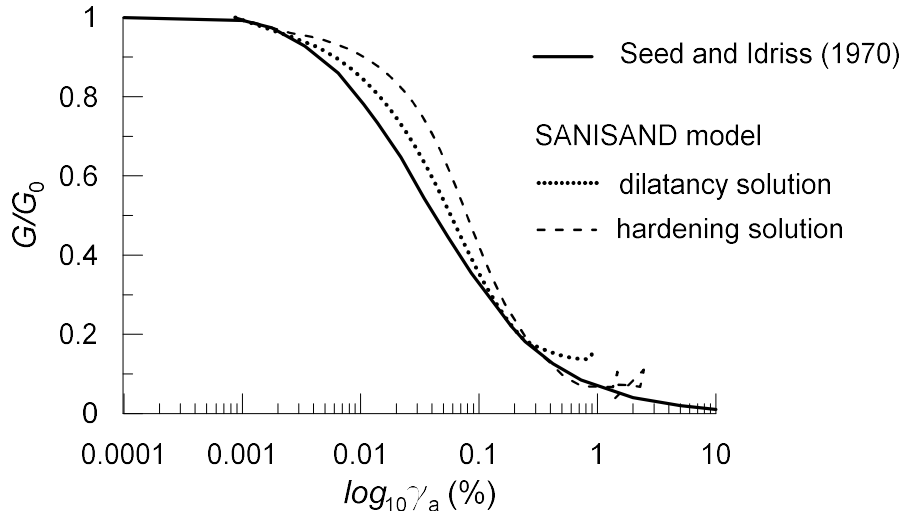

Figure 3.44: Modulus decay: comparison between the Seed and Idriss's curve adopted for the Messina Gravels and those obtained through numerical simulations on the SANISAND model.

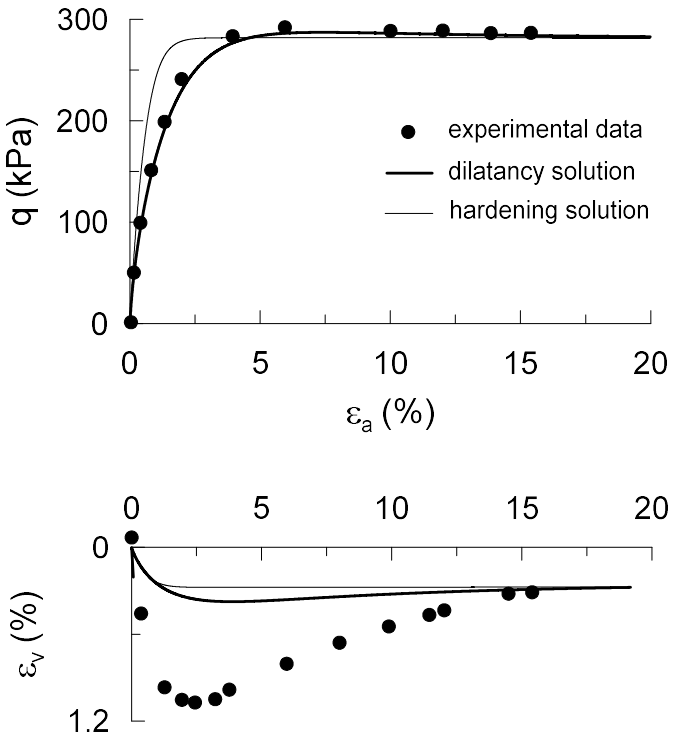

Figure 3.45: Response of the calibrations based on cyclic tests in a monotonic drained triaxial test.

production of the experimental behaviour and it was therefore taken into consideration for the dynamic analyses carried out in this study. This calibration is also deemed conceptually more valid than the hardening solution because it modifies the dilatancy parameters, that control directly the evolution of the excess pore water pressure, keeping the same hardening that instead should be an intrinsic property of a material not depending on the load conditions.

As mentioned before, also the PDMY model requires a different calibration of the input parameters under monotonic and cyclic conditions. The set of parameters adopted in the dynamic simulations in OpenSees is reported in Table 3.9, while the model response is illustrated in Figures 3.46 and 3.47.

The value of G_r, referring to a confinement stress $p'_r = 80$ kPa, was determined in order to give a small strain shear modulus G_0 equal to $1.9 \cdot 10^5$ kPa at $p'_r = 180$ kPa (see Eq. 3.19), as evaluated experimentally. The pressure dependence

Variable	Cyclic conditions
ρ_{soil} (Mg/m^3)	2.243
G_r	$1.3 \cdot 10^5$
ν	0.2
p'_r	80.0
d	0.5
$\gamma_{d,max}$	0.1
ϕ_{PTL}	17.0°
c_1	0.195
c_2	0.0
d_1	0.6
d_2	3.0
M	1.59
λ_c	0.0219
e_0	0.4478
ξ	0.7
N	40

Tabella 3.9: Parameters used for the PDMY model.

coefficient d was assumed in accordance with the observed variation of the shear modulus with depth described by the power law in Eq. 3.3. The peak shear strain $\gamma_{d,max}$ was determined through the results of the monotonic drained triaxial tests. The angle ϕ_{PTL} of the PTL in the $q - p'$ plane represents the state parameter for PDMY model, defining the transition from contractant to dilatant behaviour, and it was evaluated by trial and error. Similarly to the SANISAND model, a more contracted configuration of the PTL is required under cyclic conditions, compared to the value $\phi_{PTL} = 25°$ referred to drained monotonic conditions, to have a more gradual development of the excess pore water pressure with the number of cycles. The contraction and dilatancy parameters c_1, d_1 and d_2 were evaluated by trial and error. The code available in the OpenSees library neglects the dependency of the rate of contraction from the previous dilative phase, thus $c_2 = 0$.

It is interesting to note that the response of the PDMY model follows quite well the experimental stress path and is very similar to the response of the SANISAND model, while the latter reproduces better the deformation response, especially the progressive accumulation of permanent axial strain as the pore pressure builds up.

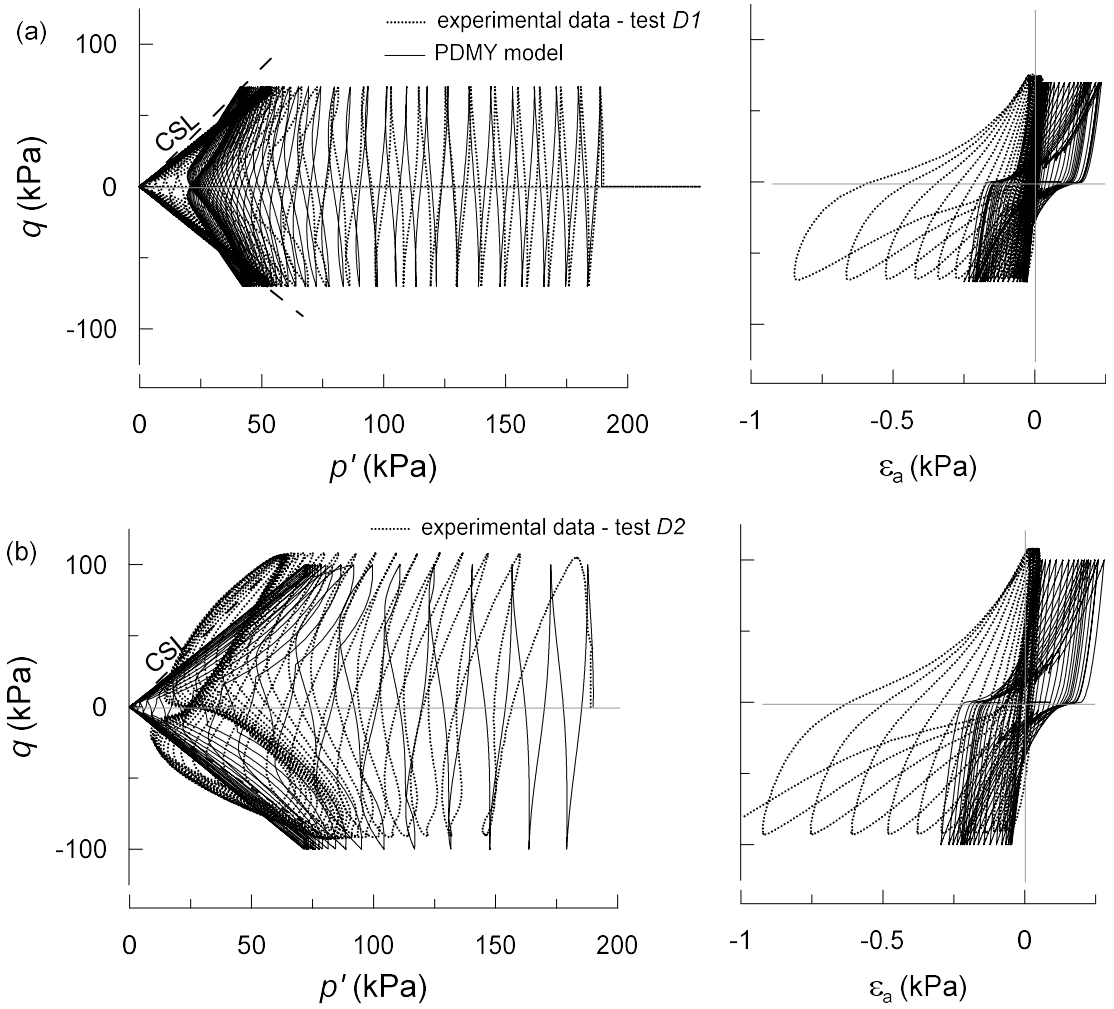

Figure 3.46: Stress path and stress-strain response of the cyclic test $S1$ (a) and $S2$ (b), obtained with the PDMY model.

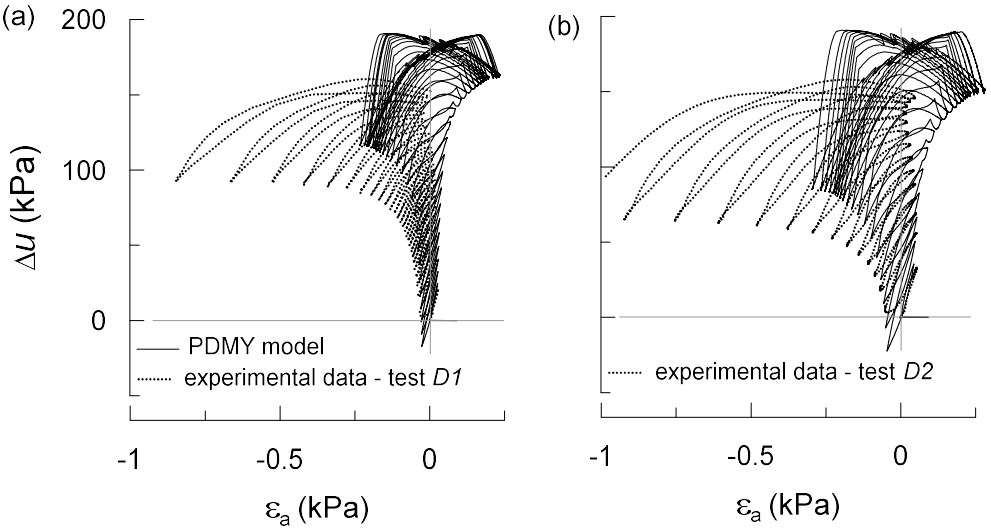

Figure 3.47: Development of the excess pore water pressure as a function the axial strain in the test $S1$ (a) and $S2$ (b), obtained with the PDMY model.

3.4 Seismic demand

The input motion of the soil-structure interaction analyses was defined according to the seismic demand for the site of the Pantano viaduct. The latter was evaluated in accordance with Italian technical provisions (*Norme Tecniche per le Costruzioni 2008*), in which four limit states must be taken into account under seismic conditions: two serviceability limit states and two ultimate limit states. In order to investigate the response of the macro-elements of the soil-abutment system and of the bridge structure when the soil exhibits a pronounced nonlinear response, the focus of the present study is on the two ultimate limit states, namely the Safety Evaluation Earthquake (SEE) with a return period $T_R = 1900$ years and a No-Collapse Earthquake (NCE) with $T_R = 2475$ years. The relative design spectra are shown in Figure 3.48, representing the design motion on a stiff outcrop (soil category A) in order to evaluate then the site effects through dynamic analyses that simulate explicitly the propagation of the seismic waves through the foundations soils.

Accordingly, four seismic records were selected as representative of the seismic

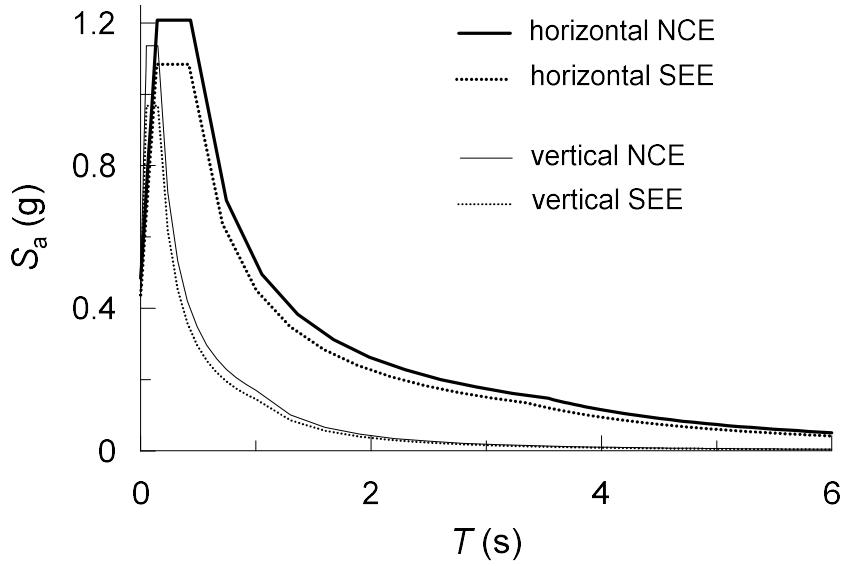

Figure 3.48: Design spectra for the NCE and SEE limit states.

Event	Record	$V_{S,30}$ (m/s)	R_{JB} (km)	M_w
Tabas (Iran, 1978)	RSN143_TABAS	767	1.8	7.35
Kobe (Japan, 1995)	RSN1108_KOBE	1043	0.9	6.90
Kocaeli (Turkey, 1999)	RSN1165_KOCAELI	811	3.6	7.51
Iwate (Japan, 2008)	RSN5618_IWATE	826	16.3	6.90

Tabella 3.10: Properties of the seismic events that originated the seismic records selected to represent the NCE and the SEE limit states.

demand, relative to the events reported in Table 3.10. The average shear wave velocity $V_{s,30}$ for the upper 30 m-depth and the moment magnitude M_w are entirely compatible with the seismo-tectonic setting of the Pantano site. The same records were chosen for both NCE and SEE scenarios, characterised by different scale factors.

The main properties of the selected seismic records are listed in Tables 3.11 and 3.12, for the NCE and SEE scenarios, respectively. The signals were low-pass filtered at 15 Hz for compatibility with the numerical computations and they are shown in Figures 3.49 to 3.52. Figures 3.53, 3.54 and 3.55 represent the comparison between the design elastic spectra and the selected spectral shapes for the three components of the seismic motion. The Tabas record follows very well the design spectra for

Record	Component	F_S	a_{max} (g)	I_A (m/s)
RSN143_TABAS	FN	0.75	0.64	12.56
	FP		0.65	10.51
	V		0.48	6.46
RSN1108_KOBE	0°	1.50	0.41	2.75
	90°		0.47	1.84
	V		0.68	1.48
RSN1165_KOCAELI	90°	2.00	0.46	3.26
	180°		0.33	2.25
	V		0.29	1.40
RSN5618_IWATE	EW	2.00	0.29	5.46
	NS		0.23	5.25
	V		0.20	2.69

Tabella 3.11: Properties of the seismic records selected to represent the NCE design earthquakes.

Record	Component	F_S	a_{max} (g)	I_A (m/s)
RSN143_TABAS	FN	0.55	0.64	9.17
	FP		0.65	7.67
	V		0.48	4.71
RSN1108_KOBE	0°	1.50	0.41	2.75
	90°		0.47	1.84
	V		0.68	1.48
RSN1165_KOCAELI	90°	1.9	0.46	3.097
	180°		0.33	2.14
	V		0.29	1.33
RSN5618_IWATE	EW	1.9	0.29	5.19
	NS		0.23	4.99
	V		0.20	2.55

Tabella 3.12: Properties of the seismic records selected to represent the SEE design earthquakes.

the entire range of periods of the seismic motion, while the other records cover the design spectral ordinates in different period intervals. Therefore, the Tabas record was widely employed to investigate the seismic response of the Pantano subsoil and to test the response of the macro-elements, while the other scenarios provided a wider validation of the methodology proposed on the full soil-bridge system.

3.5 Deconvolution of the seismic records

In the area of the Pantano abutment, the bedrock (Pezzo Conglomerate) is located at a depth of 475 m, that would lead to an unmanageable computational demand of the soil-structure numerical models. To deal with this, the selected seismic records

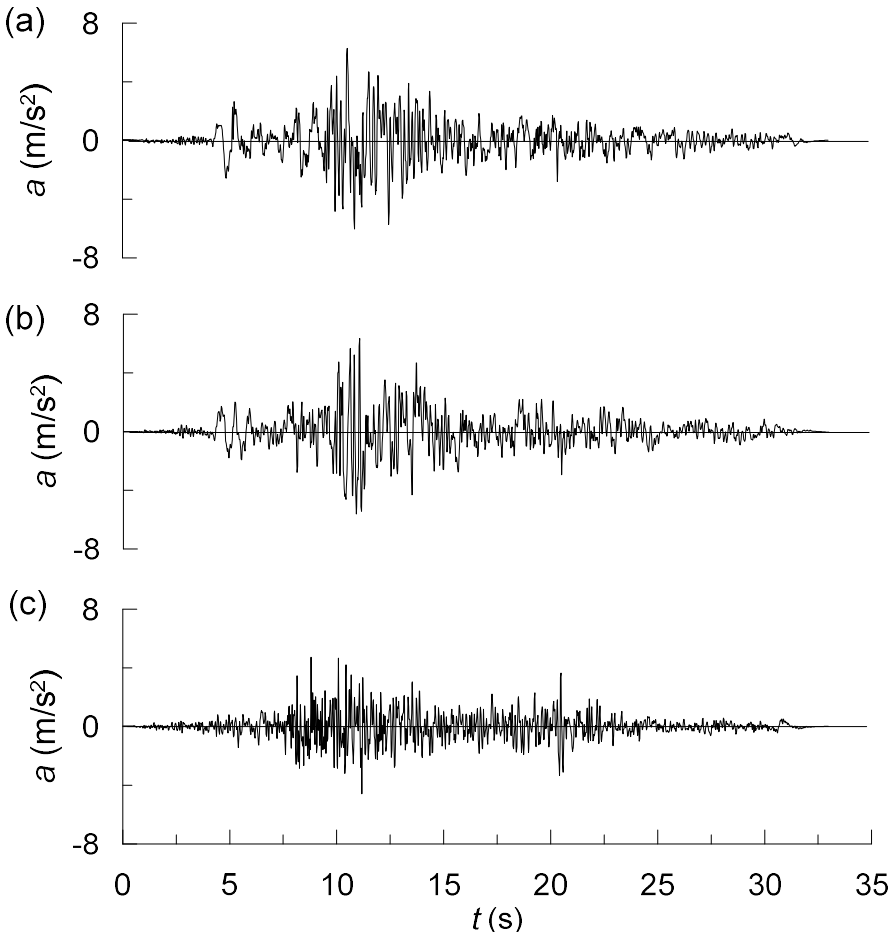

Figure 3.49: Time histories of the Tabas record in the longitudinal (a), transverse (b) and vertical (c) direction of the abutment.

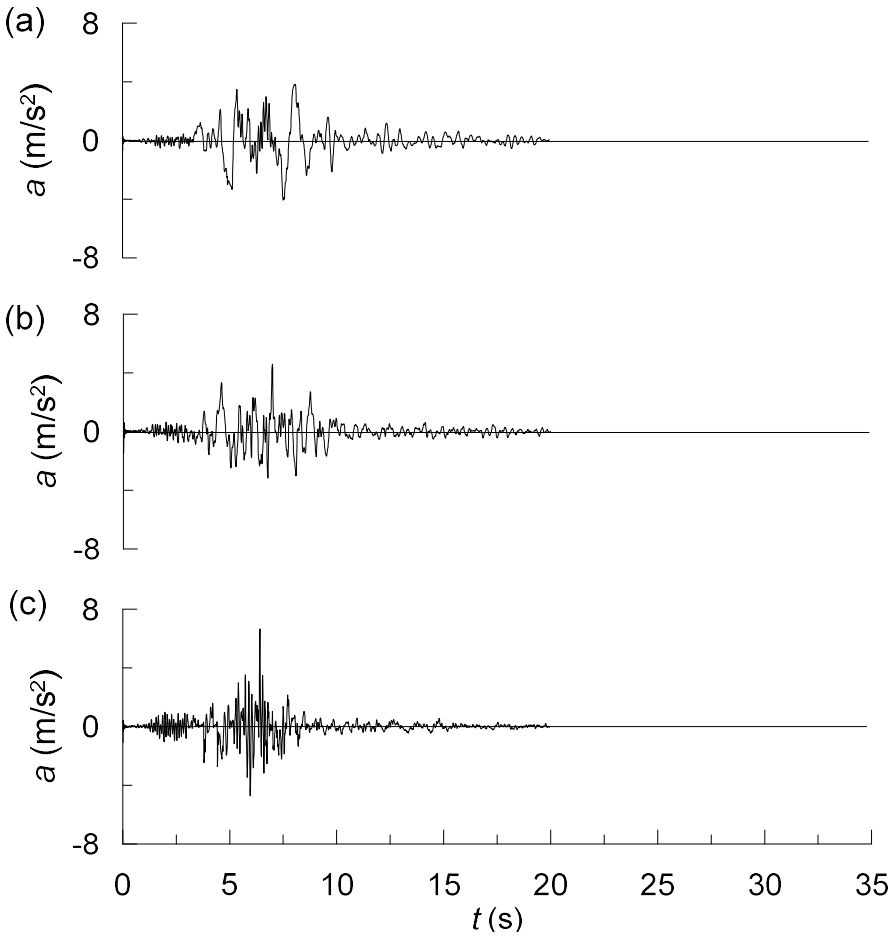

Figure 3.50: Time histories of the Kobe record in the longitudinal (a), transverse (b) and vertical (c) direction of the abutment.

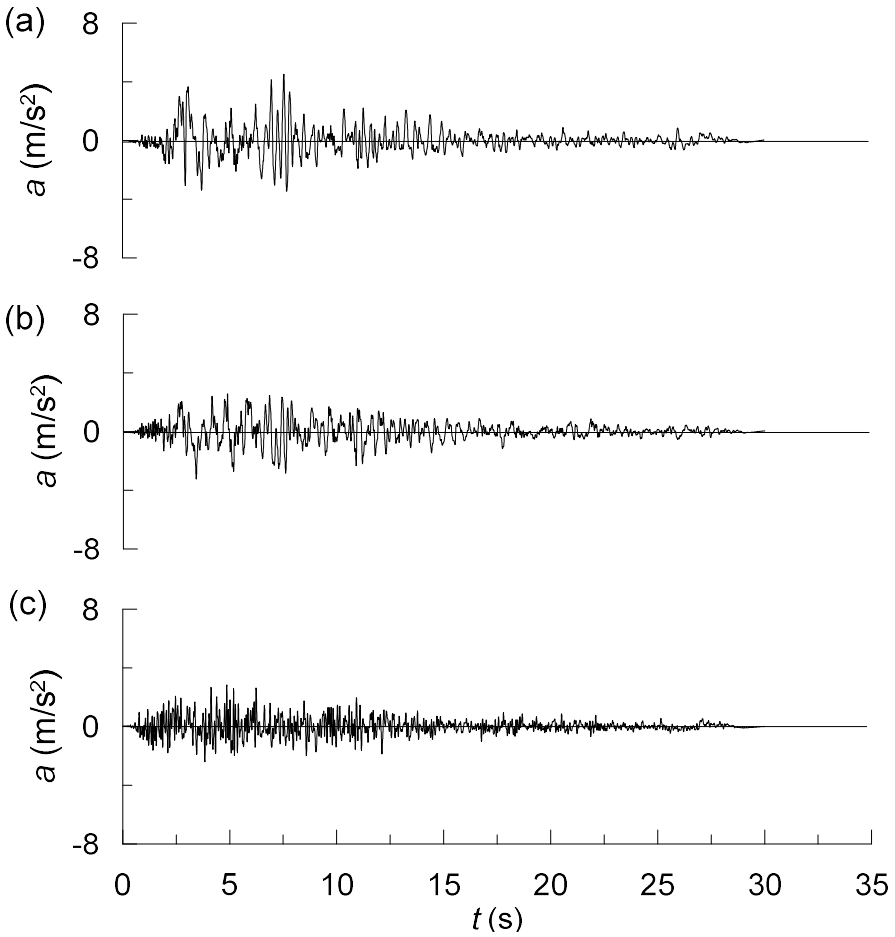

Figure 3.51: Time histories of the Kocaeli record in the longitudinal (a), transverse (b) and vertical (c) direction of the abutment.

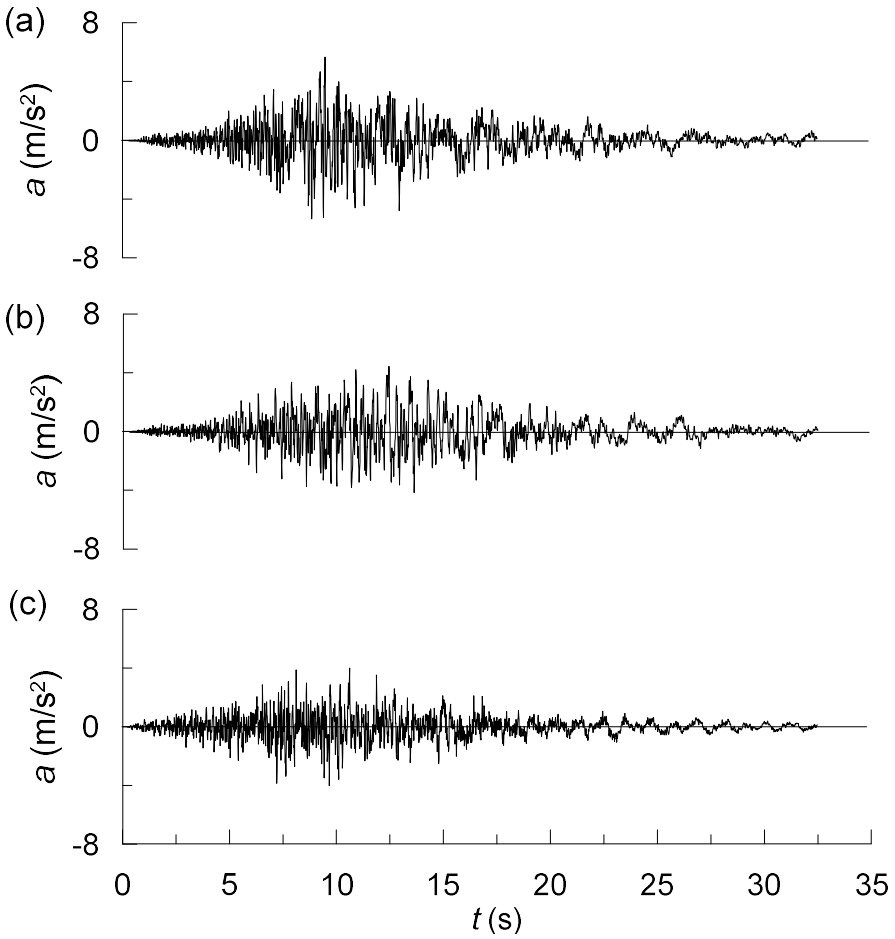

Figure 3.52: Time histories of the Iwate record in the longitudinal (a), transverse (b) and vertical (c) direction of the abutment.

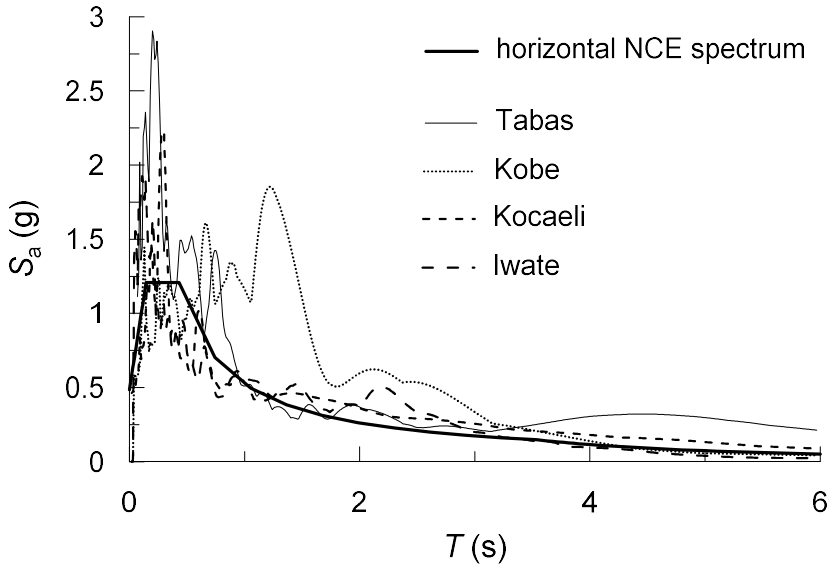

Figure 3.53: 5%-damped elastic response spectra in the longitudinal direction of the bridge associated with the records selected for the NCE and the SEE.

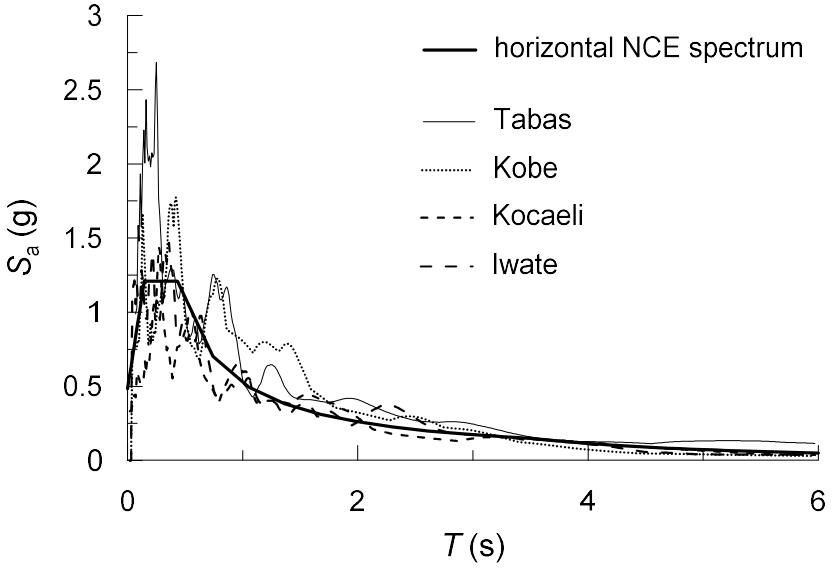

Figure 3.54: 5%-damped elastic response spectra in the transverse direction of the bridge associated with the records selected for the NCE and the SEE.

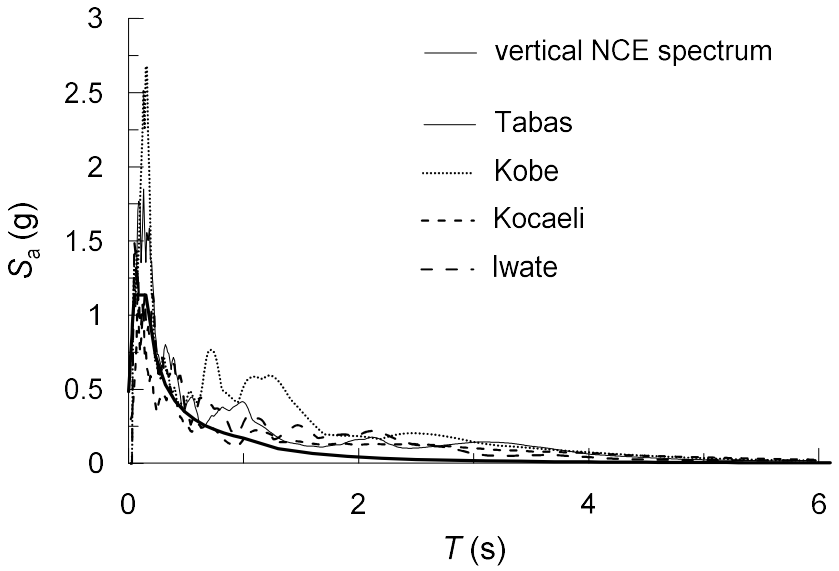

Figure 3.55: 5%-damped elastic response spectra in the vertical direction associated with the records selected for the NCE and the SEE.

were subjected to a deconvolution procedure that allowed to reduce the vertical extension of the numerical models. The deconvolution depth z_d of the seismic motion is intended as the depth beyond which the response of the soil can be regarded as linear. This technique, already used by Callisto and Rampello (2013) for the study of the towers of the Messina Strait suspension bridge, is applied here to the soil column below the Pantano abutment shown in Figure 3.56. The 1D model starts in correspondence of the abutment foundation and extends down to the Pezzo Conglomerate. The procedure consisted in carrying out one-dimensional site response analyses (1D SRA) on the entire soil column, assuming a visco-elastic behaviour of soil, in order to determine the part of the soil domain in which nonlinearities can be neglected. The seismic input was applied to the outcrop to consider explicitly in the computation the alteration of the ground motion in the bedrock due to the effective stiffness of the latter. The seismic actions obtained at the deconvolution depth were then considered as the input motion for the coupled soil-structure models.

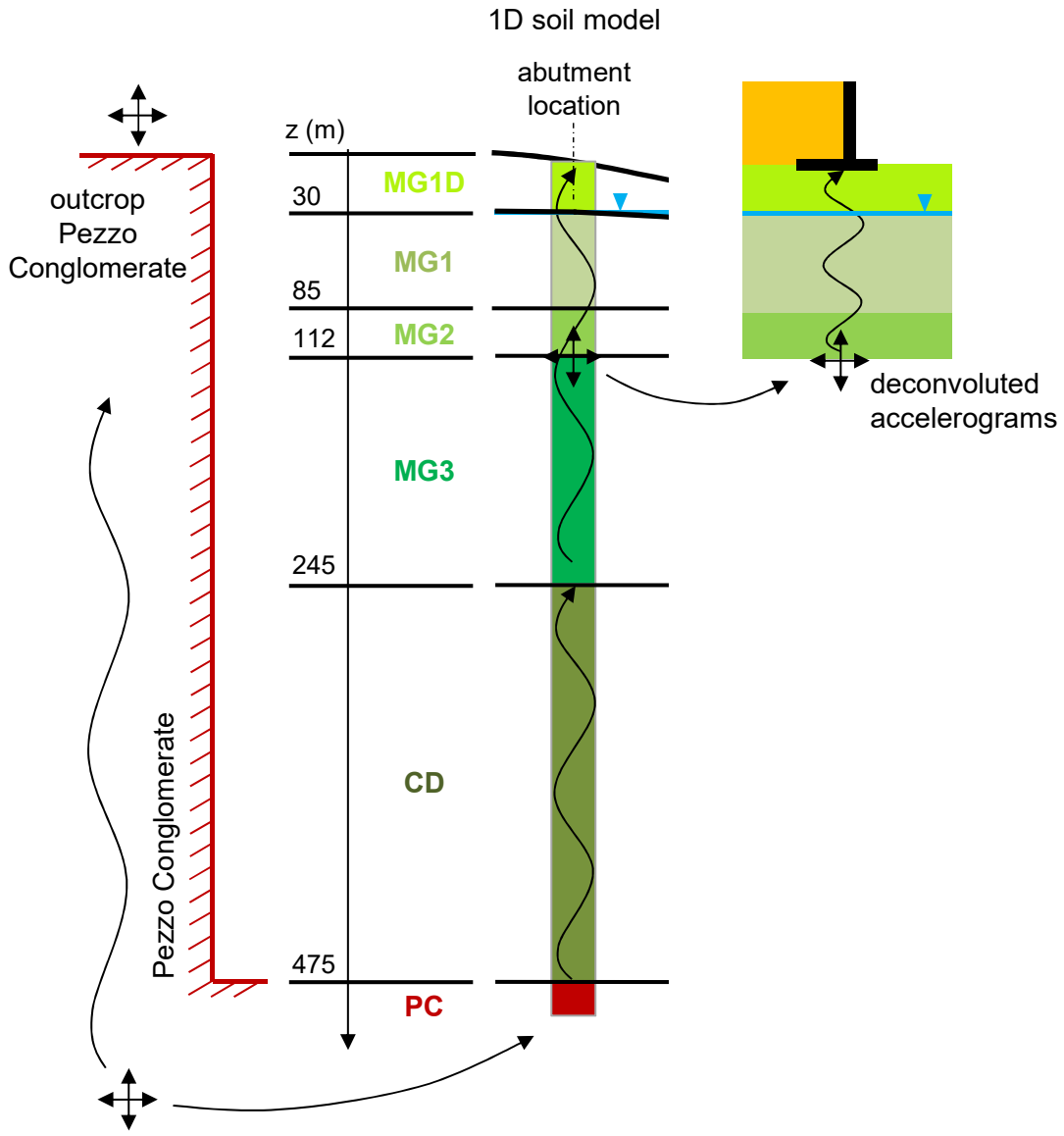

Figure 3.56: Scheme of the deconvolution procedure of the selected seismic records.

The visco-elastic analyses were carried out using the computer program MARTA (https://sites.google.com/a/uniroma1.it/luigicallisto/). The behaviour of each layer is completely described by the mass density ρ_{soil}, the shear modulus G_0 at small strains and by the evolution curves of the normalised shear modulus G/G_0 and the damping ratio ξ with the level of shear strain attained. A mean value of 2.243 Mg/m^3 was adopted for the mass density of the saturated layers, while a lower value of 2.020 Mg/m^3 was assumed for the unsaturated layer $MG1D$. The average values of G_0 for each stratum were chosen according to Table 3.3. The shear modulus decay and the variation of the damping ratio were described by the curves in Figures 3.13 and 3.14 previously defined in the geotechnical characterisation.

The results of the 1D SRA are illustrated in Figures 3.57 to 3.59, for brevity only for the most severe components of the seismic records corresponding to the NCE scenario (the fault normal component of the Tabas record, the 0 ° component of the Kobe record, the 90 ° component of the Kocaeli record and the EW component of the Iwate record). The Kobe record presents the lowest maximum acceleration a_{max} at the bedrock ($z = 475$ m) but it produces the greatest amplification of the ground motion at the foundation level ($z = 0$ m). By contrast, the Tabas record is the most severe ground motion that however leads to a maximum acceleration on the surface equal to 3.2 m/s^2, that is absolutely comparable with the values obtained for the other records of Kocaeli and Iwate. For all the seismic scenarios considered, the most evident alterations of the seismic motion occur in the soil overlying the stiff layer of Messina Gravel $MG3$. In fact, the greatest values of the maximum shear strains γ_{max} localise in the layers $MG2$ and $MG1$, for then decreasing at lower depths $z < 30$ m since the visco-elastic medium provides a null deformation for $z = 0$ (boundary condition). The shear strain attains values greater than 1 % in all the scenarios, leading to a drastic reduction of the small strain shear modulus up to $80 \div 90$ %. Accordingly, a very high damping is mobilised

in the upper layers, ranging between $12 \div 18$ %. A first important observation that can be deduced is that, for $z < 112$ m, the equivalent visco-elastic medium is completely inappropriate to represent the soil behaviour under such large seismic actions. In fact, the important shear strains occurring in the soil would lead in reality to the development of pronounced irreversible deformations that require the use of nonlinear constitutive models for the soil over the layer $MG3$. By contrast, the mobilised shear strain at greater depths is very limited by the high stiffness of the soil, with a maximum reduction of the normalised shear modulus between $0.1 \div 0.2$.

On the basis of the above results, it was assumed a deconvolution depth z_d equal to 112 m, representing the interface between the layer $MG2$ and $MG3$. The seismic actions obtained at $z = z_d$ constituted the input motion for the soil-structure models and the relative spectra are shown in Figure 3.59. It can be seen that, although the frequency content of the deonvoluted signals results very close to the original records, a modest deamplification of the motion amplitudes occurs in the range of periods $0 \div 1.5$ s, in favour of a slight amplification at larger periods.

3.6 From the real case study to a simplified structural model

A simplified soil-structure system was developed with the aim to validate the macro-elements of the soil-abutment system and of the bridge structure against dynamic analyses of the full soil-bridge model. The simplified model, depicted in Figure 3.60, is composed of an idealised structural scheme, inspired by the Pantano viaduct, resting on the Pantano subsoil, that represents the upper layers of the Messina Gravels down to the deconvolution depth. The full model is composed of 268703 elements, with 267036 solid elements for the soil and 1667 structural elements, for a whole extension of 262×72 m^2 in plan and 125.5 m in depth. The model was implemented

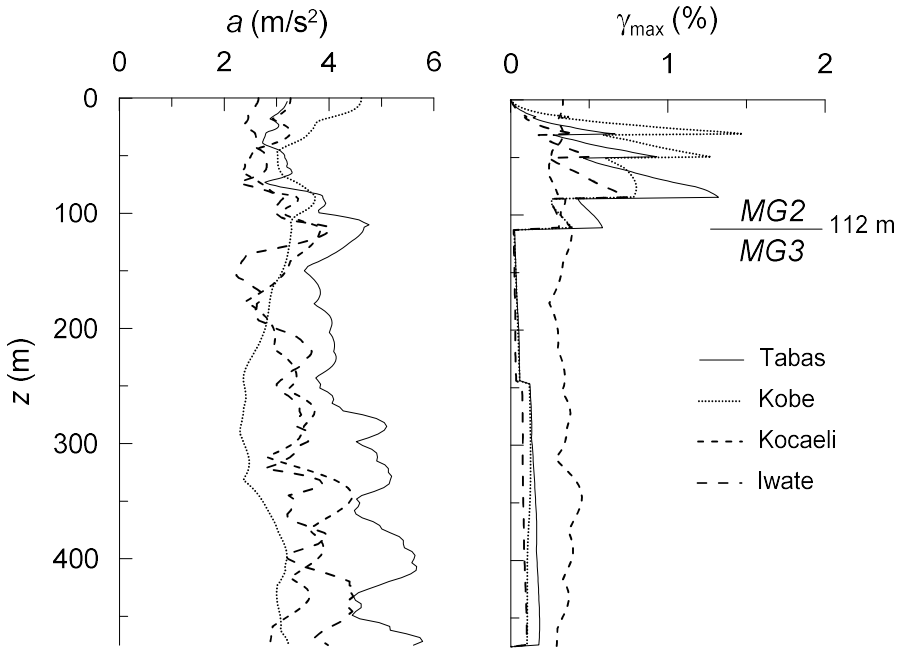

Figure 3.57: Profiles of the maximum accelerations a_{max} and of the maximum shear strains γ_{max} for the four seismic records selected for the NCE earthquake obtained through visco-elastic site response analysis.

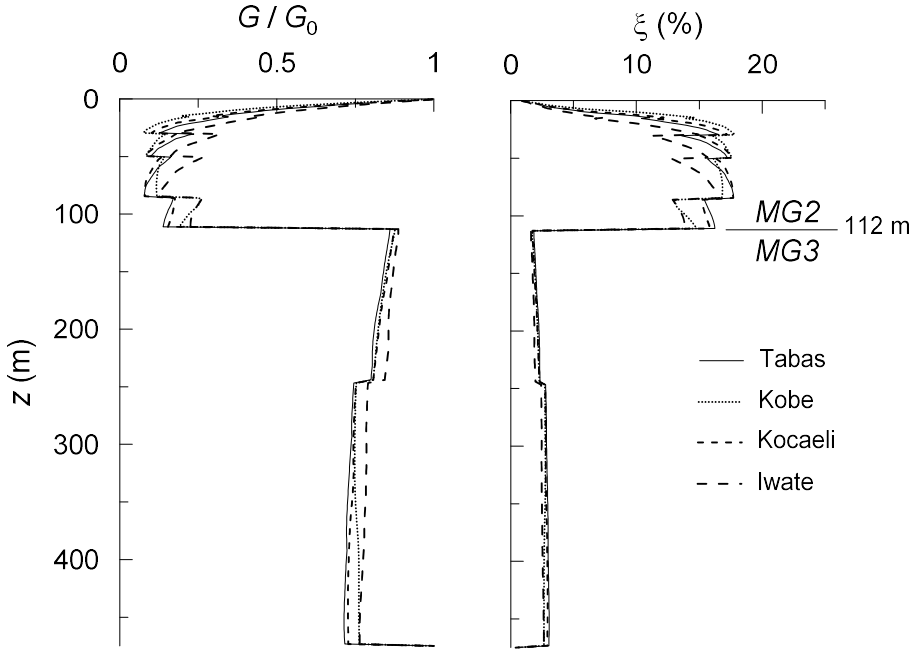

Figure 3.58: Profiles of the normalised shear modulus G/G_0 and of the damping ratio ξ for the four seismic records selected for the NCE earthquake obtained through visco-elastic site response analysis.

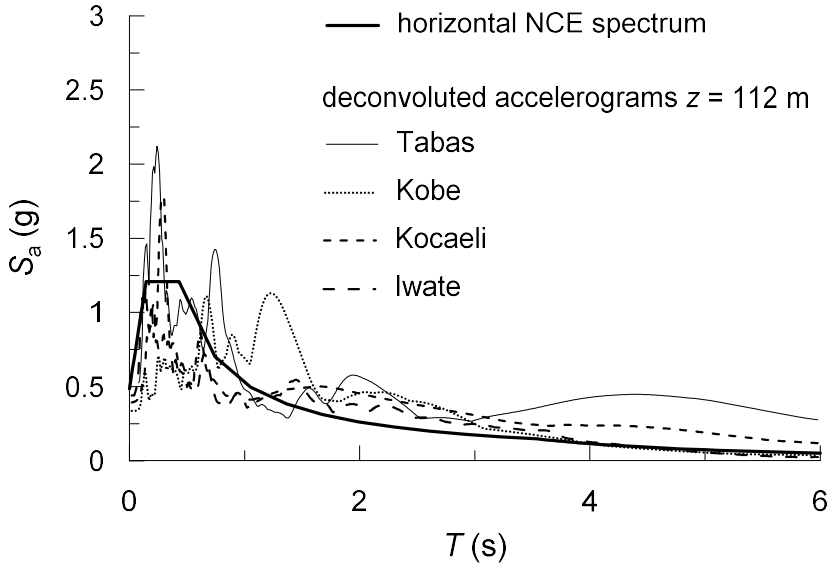

Figure 3.59: 5 %-damped elastic response spectra for the four seismic records selected for the NCE earthquake obtained through visco-elastic site response analysis.

in the analysis framework OpenSees while the mesh generation and the visualization of the results was performed in the pre/post-processor software GID.

3.6.1 Bridge structure

The bridge superstructure is composed of a continuous deck supported by two central piers and by the lateral abutments. An alternating strong and weak contact is provided between the deck and the vertical elements, intended as a three-directional bearing device (rigid constraint) and a bi-directional device (longitudinal displacements allowed), respectively, leading to an asymmetric global behaviour of the whole structure. In this way, the strong abutment carries most of the longitudinal inertial forces developing into the superstructure, representing a particularly appropriate situation for validating the macro-elements.

Each span has a length L_s of 35 m and the piers have the same height H_p equal to 13.5 m, with an aspect ratio of the bridge of $L_s/H_p \simeq 2.5$. The abutment presents

very similar properties to the case of the Pantano viaduct: it is a massive reinforced concrete structure with a 13.5 m-height wall, with a thickness of 4.0 m, resting on a shallow foundation with length and thickness of 17.5 m and 5.0 m, respectively. Because of its large strength compared to the superstructure and the soil, it is reasonable to assume that the abutment exhibits an elastic response under seismic conditions. Hence, all the structural members were modelled through the ShellMITC4 elements (Dvorkin and Bathe, 1984) with elastic behaviour, using constitutive parameters relative to a $C32/40$ strength class concrete in the European standards. A Rayleigh damping was adopted for the elements of the abutment, calibrated in order to consider a damping ratio not greater than 2 % for all the significant modes of the abutment. The deck and the piers were modelled through beam elements with visco-elastic behaviour. The elastic parameters of the deck refer to average values of the steel box cross section of the roadways of the Pantano viaduct along a span, whereas a homogenization procedure was used to get the equivalent parameters of the reinforced concrete box sections of the piers of the Pantano viaduct, in terms of axial and bending stiffness. Since the pier height of the Pantano viaduct reduces progressively towards the abutment because of the sloping ground, average parameters were finally computed for all the piers in order to consider a unique height equal to 13.5 m. Energy dissipation was reproduced by assigning a Rayleigh damping of 2 % to all the elements of the superstructure, calibrated on the significant modes of the bridge obtained through a dynamic identification of the structural system. The shallow foundations that support the piers were designed by the application of standardised procedures. The resulting dimensions are 6.0 m and 5.0 m in the longitudinal and transverse directions of the bridge, respectively, and a thickness of 2.0 m. The elastic material assigned to the pier foundations was calibrated for a $C32/40$ strength class concrete.

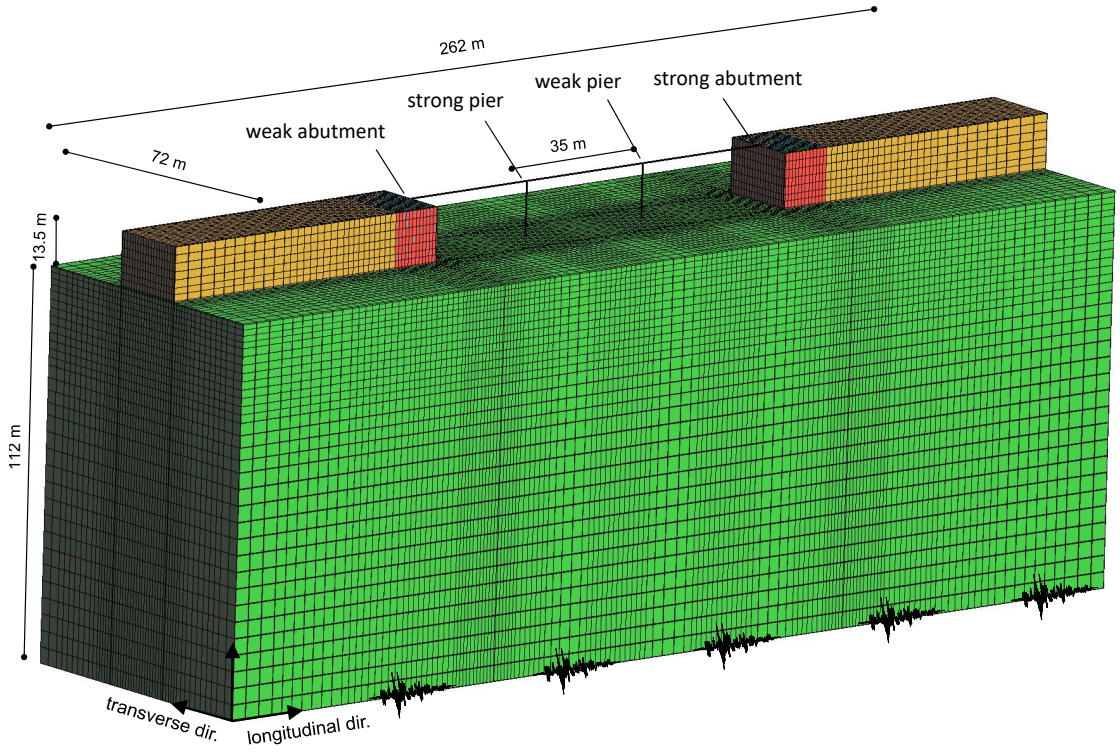

Figure 3.60: Full model of the soil-bridge system.

3.6.2 Foundation soils

The foundation soil represents the superficial layers of Messina Gravels $MG1D$, for the upper 30 m of depth, and $MG1 - MG2$ down to the depth $z_d = 112$ m. The mechanical behaviour of the foundation soils was described through the SANISAND and PDMY models and the relative constitutive parameters associated with each layer have already been discussed in Section 3.3.3. In the full soil-bridge model, the subsoil was considered for simplicity dry, hence the presence of pore water pressure was neglected in the strata $MG1$ and $MG2$. This is an approximation of the effective subsoil condition for the Pantano viaduct, that however is expected to not influence significantly the performance of the structure since the ground water table would be located a depth of 30 m from the bridge foundations. Anyway, a detailed discussion on the effects of the excess pore water pressure in the dynamic response

of the Pantano subsoil are provided in Section 7.1 regarding the nonlinear site response analysis. The assumption of dry soil allowed to adopt the SSPbrick eight node hexahedral elements (Zienkiewicz and Shiomi 1984) to discretize the entire soil domain when the PDMY model is used for the soil. These elements use a physically stabilized single-point integration, resulting in an element which is free from volumetric and shear locking. This leads to a significant reduction of the computational demand of the full model compared to the adoption of the SSPbrickUP eight node hexahedral elements (Zienkiewicz and Shiomi 1984), required when using the SANISAND model, in which instead a mixed displacement-pressure formulation is adopted with many more degrees of freedom to be solved at each time step. Both the constitutive models used for the soil are able to reproduce the effective energy dissipation as a function of the strain level, however an additional small damping ratio was introduced in the soil domain using the Rayleigh formulation only to attenuate the effects of spurious high frequencies.

3.6.3 Embankment

The embankment behind the abutment wall was regarded as a partially saturated soil, with the presence of negative pore water pressure (suction) providing non-zero stiffness and strength at small stress levels. The mix design for the soil of the embankment was determined to have a stiffness and a degree of compaction greater than the corresponding limit values imposed by technical provisions, according to the following inverse analysis procedure:

- identification of the technical requirements;
- definition of the Water Retention Curve (WRC);
- derivation of the Grain Size Distribution (GSD);
- equivalent mechanical properties.

The technical provisions taken as reference for the embankment were the *Capitolato Ferrovie* and *Testo Unico* currently in force in Italy. The design requirements for bridge embankments are aimed to minimise the settlements of the embankment due to the traffic load that might compromise the serviceability of the infrastructure. Specifically, it is prescribed that the Young's modulus E_{min} be not less than $7.2 \cdot 10^4$ kPa for the embankment body with a dry unit weight $\gamma_{d,min}$ not less than $0.95 \cdot \gamma_{d,max}$, where $\gamma_{d,max}$ is the maximum value of γ_d evaluated by a modified Proctor test. The former requirement was used as the initial constraint for the design procedure while the latter was checked a posteriori, based on the GSD curve determined.

Because of the good mechanical properties of the in-situ soil, the Messina Gravels constituted the starting mixture for the mix design. Therefore, the initial profile of the shear wave velocity with depth is described by Eq. 3.3. In this case, however, the stiffness has to be related to the Bishop's effective mean pressure in order to account for the presence of suction u_w in the soil matrix, such that

$$G(z) = A \cdot p'(z)^n = 21.82 \cdot [p(z) - S_r \cdot u_w]^{0.44} \tag{3.28}$$

in which p is the total mean pressure, u_w (< 0) is the suction relative to the atmospheric pressure and S_r the degree of saturation of soil. In practice, the embankment is compacted in-situ to reach a state that is close to the optimum degree of compaction. In this condition, the saturation degree $S_{r,opt}$ was supposed equal to 0.7 as a typical value in engineering applications. The minimum shear modulus G_{min} required by technical provisions was evaluated from E_{min} and the Poisson's ratio of the Messina Gravels, equal to 0.2, resulting equal to $3.0 \cdot 10^4$ kPa. The suction in the embankment, assumed constant with depth, was determined in order to have a shear modulus of the soil greater than G_{min} at each depth. A small value of $u_w = -4$ kPa was sufficient to satisfy the requirement on the stiffness, as illustrated

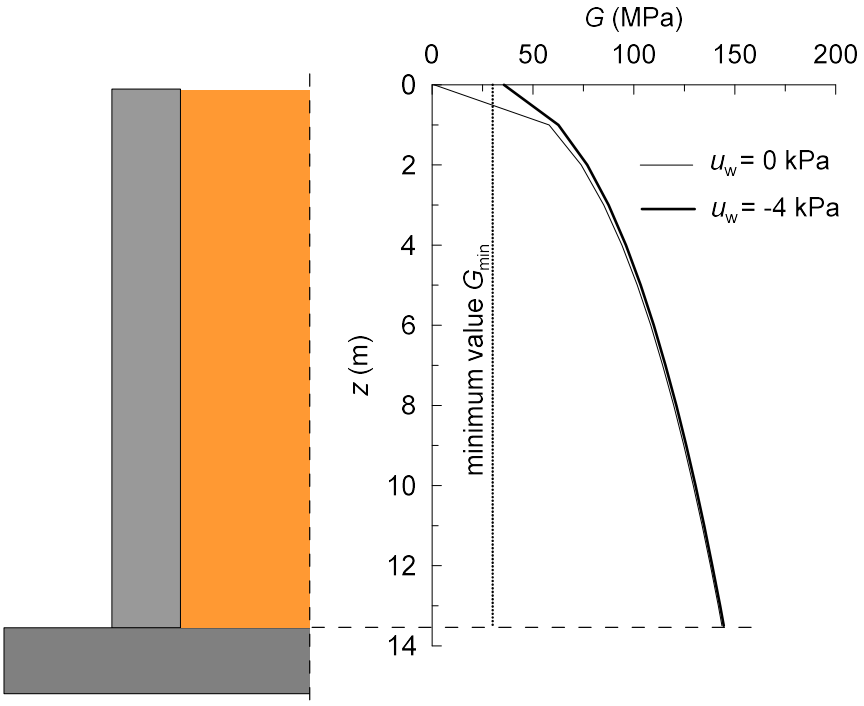

Figure 3.61: Comparison between the profile of the shear modulus of the embankment with depth and the respective minimum value G_{min} imposed by technical provisions.

in Figure 3.61.

The GSD curve was retrieved from the WRC through the inverse application of the procedure proposed by Arya and Paris (1981). The Arya and Paris model first translates a particle-size distribution into a pore-size distribution by computing the pore volume per unit sample mass $V_{v,i}$

$$V_{v,i} = \frac{w_i}{\rho_p} \cdot e, i = 1, ..., n \tag{3.29}$$

in which w_i is the solid mass obtained by the GSD, ρ_p is the particle density, e is the void ratio and n is the number of segments into which the GSD is divided. The volumes $V_{v,i}$ are assumed filled with water. The volumetric water content $\vartheta_{v,i}$ of the i-th segment of the GSD is instead determined by the cumulative pore volumes

$$\vartheta_{v,i} = \sum_{j=1}^{i} \frac{V_{v,j}}{V_b} \tag{3.30}$$

with average value $\vartheta^*_{v,i} = (\vartheta_{v,i} + \vartheta_{v,i+1})/2$. Spherical-shaped particles are considered and, accordingly, the relationship between the volumes $V_{p,i}$ and the radii R_i of the particles contained in the i-th range simply reads

$$V_{p,i} = \frac{4 \cdot \pi}{3} \cdot n_i \cdot R_i^2 = \frac{w_i}{\rho_p} \tag{3.31}$$

for n_i particles. In the case of cylindrical pores of length h_i, the equation above becomes

$$V_{v,i} = \pi \cdot r_i^2 \cdot h_i = \frac{w_i}{\rho_p} \cdot e \tag{3.32}$$

from which the mean pore radius can be obtained as follows

$$r_i = R_i^2 \cdot \left[4 \cdot e \cdot n_i^{1-\alpha}/6\right]^{0.5} \tag{3.33}$$

in which the coefficient α has to be determined empirically. Finally, the equation of capillarity is used to translate the pore size into a pore pressure u_i as reported below

$$u_i = \frac{2 \cdot \gamma \cdot cos\,(\vartheta)}{\rho_w \cdot g \cdot r_i} \tag{3.34}$$

with g the acceleration of gravity.

On the basis of the above formulation, starting from the moisture characteristics of the Messina Gravels (upper bound in Figure 3.5), the GSD was modified in order to obtain a WRC that passed through the optimum point $P_{opt} = \{u_{w,opt}; S_{r,opt}\}$, representative of the embankment state after compaction. The results of this procedure

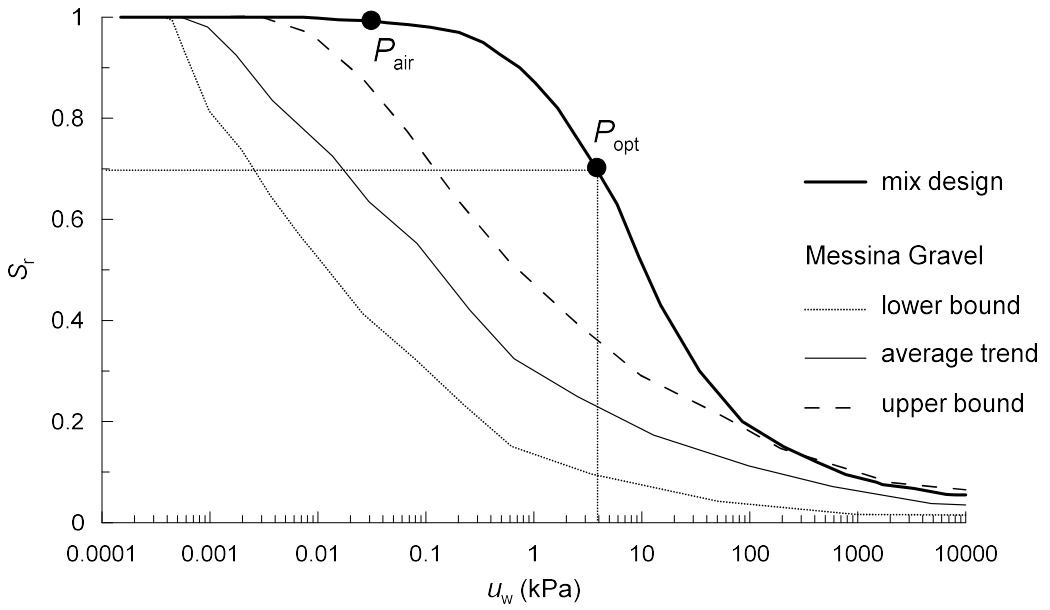

Figure 3.62: Comparison between the Water Retention Curve associated with Grain Size Distribution of the mix design chosen for the embankment and curve relative to the Messina Gravels (lower bound, upper bound and average trend).

are shown in Figures 3.62 and 3.63. The resulting mix design for the embankment is an essentially sandy soil with a minor percentage of gravel and silt. The relevant presence of sand allowed to move the air-entry point P_{air} to much greater values of the suction in order to satisfy the passage through the optimum point P_{opt}.

In accordance with the moisture characteristics found above, a friction angle of 35° was chosen for the mix design, neglecting the effect of the suction $u_{opt} = -4$ kPa on strength.

Finally, the compaction state was checked by determining the dry unit weight of the embankment γ_d. This was evaluated through the following expression

$$\gamma_d = \frac{\gamma_s}{1 + e_{max} - \Delta e \cdot D_r} = 17.3 \; kN/m^3 \tag{3.35}$$

in which the unit weight of the solid particles $\gamma_s = 26.2$ kN/m^3, the maximum void ratio $e_{max} = 0.626$, the relative density $D_r = 45\%$ and $\Delta e = e_{max} - e_{min} =$

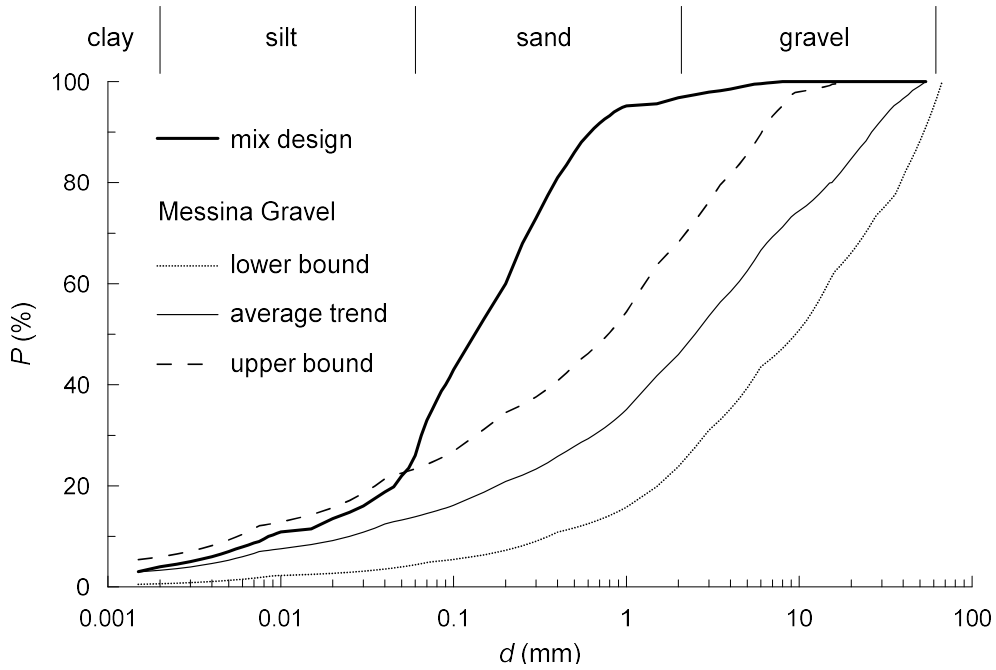

Figure 3.63: Comparison between the Grain Size Distribution curves of the mix design chosen for the embankment and of the Messina Gravels (lower bound, upper bound and average trend).

0.252, were referred for simplicity to the Messina Gravels. The maximum dry unit weight $\gamma_{d,max}$ relative to a modified Proctor test was evaluated using the empirical correlation proposed by Patra et al. (2010) and results equal to 18.08 kN/m^3. The lower bound for the dry unit weight is therefore $\gamma_{d,min} = 0.95 \cdot \gamma_{d,max} = 17.18$ kN/m^3, satisfying the requirement on the degree of compaction.

The embankment was modelled in the finite element analyses with OpenSees as an equivalent single-phase body, using both the SANISAND and PDMY models to simulate its cyclic behaviour. The properties of the mix design and the effect of suction were implicitly taken into account by assigning appropriate parameters to the constitutive models. More in detail, compared to the calibration defined for the Messina Gravels, a different stress ratio at Critical State was considered since the friction angle changed (from 38° of the Messina Gravels to 35° assumed for the sandy embankment), and a modest increment of the stiffness parameters

was introduced to account for the effect of suction according to the profile of the shear modulus illustrated in Figure 3.61. As done for the foundation soils, a small Rayleigh damping was added to these elements, calibrated on the frequency content of the seismic input, to stabilise the dynamic time stepping.

3.6.4 Soil-structure contact

The soil-structure contact was modelled by means of thin layers of solid elements interposed between the structure and the soil. Figure 3.64 shows an enlarged view of the central section of the soil-abutment model, in which the interface elements (in yellow) are placed underneath the foundation and behind the central wall and the wing walls. The main objective of the interface elements is to describe the strain concentration occurring in the soil in close proximity to the structural elements. The behaviour of the interface elements was reproduced through the same configurations of the advanced constitutive models used for the soil domain. In a preliminary stage of this study, however, a limited sensitivity analysis on the effect of the interface strength was carried out through a pushover analysis of the soil-abutment system, considering three different values of the friction angle φ_{int} of the interface: $\varphi_{int} = \varphi_{soil}$, $\varphi_{int} = 0.8 \cdot \varphi_{soil}$ and $\varphi_{int} = 0.67 \cdot \varphi_{soil}$. It was found that the variability of the friction within this range does not alter significantly the results in terms of force-displacement relationship at the deck-abutment contact. Therefore, the friction angle of the interface was set equal to that of the soil as a reasonable assumption for soil-concrete contact.

3.6.5 Solution procedure

A staged analysis procedure was adopted in which, after a first stage aimed to reproduce the lithostatic stress state in the foundation soil, the abutment structure, the embankment and then the superstructure are built sequentially in the model.

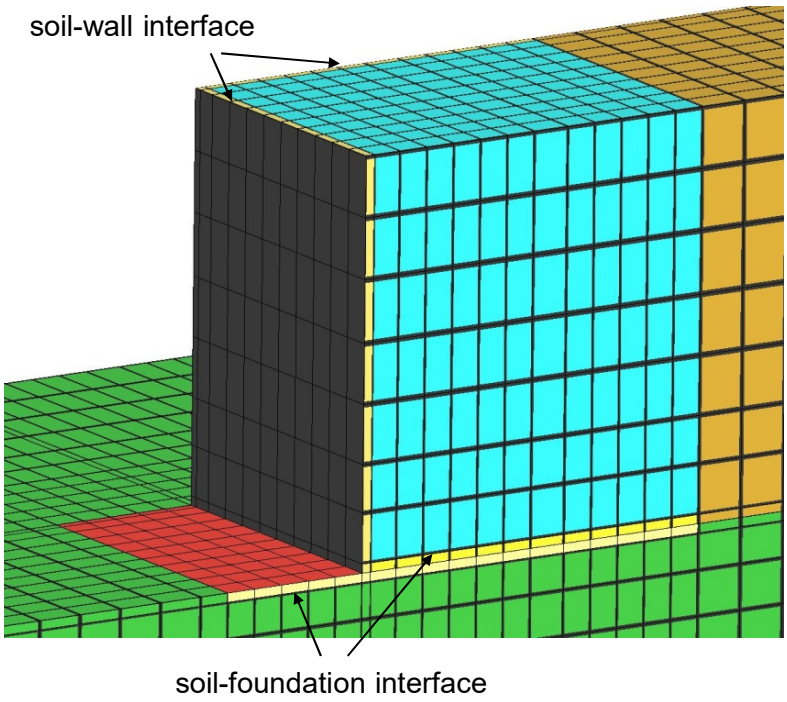

Figure 3.64: Detail of the thin layers representing the soil-structure interface.

The gravity analysis is followed by the dynamic simulation, in which the use of the parallel computing, obtained with the OpenSeesSP interpreter, was needed to get reasonable computation times.

In the static stage, the displacements at the bottom of the grid were impeded in both directions, while only the horizontal displacements normal to each boundary were restrained along the lateral sides. In the subsequent dynamic phase, the restraints in the direction of motion were removed. The longitudinal and transverse lateral boundaries were constrained to undergo the same motion, since the lateral boundaries are located far enough from the bridge to ensure the free field response.

The four seismic scenarios selected in Section 3.4 were considered to validate the macro-elements. These seismic actions were applied to the lower boundary of the model, representing the deconvolution depth, as displacement time histories. Note that the deconvoluted motion takes implicitly into account the deformability of the

underlying soil layers because it was obtained from a site response analysis of the entire soil column down to the bedrock (see Section 3.5). A considerable substepping was needed to get convergence with respect to the initial time increment of the records, with a maximum value of 10 for the Tabas motion and a minimum value of 4 for the Kobe and Kocaeli signals.

The Newmark time-stepping method was employed to integrate the equations of motion, using common values of γ and β equal to 0.5 and 0.25, respectively (average acceleration method). The Newton-Raphson algorithm was adopted to treat numerically the nonlinear response of the soil. The convergence test was based on the norm of the incremental displacement, considering a tolerance of 10^{-4}. The parallel computing was introduced in the analysis model by using the Mumps system, leading to an optimised storage and solution of the system of equations between the processors (CPU). Accordingly, the computation times become equal to $10 - 15$ % those associated with the largest simulations on the full soil-bridge model. Most of the dynamic simulations were carried out using a prefabricated workstation provided with 10 dual-core CPU working at 3.1 GHz and 48 Gbytes of RAM. Conversely, the finite element simulations on the entire soil-bridge system necessitated the use of a specific custom workstation that was assembled with 16 dual-core CPU, overclocked to 3.7 GHz, and 60 Gbytes of RAM. The resulting computation times associated with the four seismic scenarios are reported in Tables 3.13, 3.14, 3.15 and 3.16, for the different models implemented in OpenSees, from which the high computational efficiency of the methodology proposed appears clearly: the reduction of the computation times, compared to the full soil-bridge representation, was of about 55 % for the local model of abutment with macro-element of the bridge structure and up to about 98 % for the global structural model with macro-element of the soil-abutment system.

Scenario	Δt_{comp} (s)	steps (-)	t_{comp} (days)
Tabas	0.002	16450	90
Kobe	0.0025	9020	60
Kocaeli	0.00125	16056	60
Iwate	0.002	35050	180

Tabella 3.13: Full soil-bridge model: computation time interval Δt_{comp}, number of steps and duration t_{comp} of the dynamic simulation for the four seismic scenarios selected for the ultimate limit state.

Scenario	Δt_{comp} (s)	steps (-)	t_{comp} (days)
Tabas	0.002	16450	40
Kobe	0.0025	9020	28
Kocaeli	0.00125	16056	28
Iwate	0.002	35050	80

Tabella 3.14: Local soil-abutment model with macro-element of the bridge structure: computation time interval Δt_{comp}, number of steps and duration t_{comp} of the dynamic simulation for the four seismic scenarios selected for the ultimate limit state.

Scenario	Δt_{comp} (s)	steps (-)	t_{comp} (days)
Tabas	0.02	1645	0.17
Kobe	0.01	2030	0.18
Kocaeli	0.005	4014	0.2
Iwate	0.01	7010	0.34

Tabella 3.15: Linear global structural model (with dynamic impedance functions for soil-structure interaction): computation time interval Δt_{comp}, number of steps and duration t_{comp} of the dynamic simulation for the four seismic scenarios selected for the ultimate limit state.

Scenario	Δt_{comp} (s)	steps (-)	t_{comp} (days)
Tabas	0.004	1645	1.0
Kobe	0.005	2030	1.0
Kocaeli	0.0025	4014	1.5
Iwate	0.005	7010	2.0

Tabella 3.16: Non-linear global structural model (with macro-elements for soil-structure interaction): computation time interval Δt_{comp}, number of steps and duration t_{comp} of the dynamic simulation for the four seismic scenarios selected for the ultimate limit state.

3.6.6 Modal analysis of the bridge

The dynamic characteristics of the idealised bridge structure were evaluated through a modal analysis of a global structural model with a fixed base implemented in SAP2000. In a first stage, the model was tested in several static and dynamic simulations in order to verify the correct implementation of the model, taking as a reference the structural model built in OpenSees. In the following, the response of the abutments is not included in the results in order to focus on the vibration modes of the superstructure.

Although more than 100 vibration modes were analysed, the mass participation concentrates mainly in just a few significant modes in virtue of the simplicity of the structural system. The modal characteristics are listed in Table 3.17, providing the identification number of the mode, the vibration period T and the mass participation factors M_i, while the corresponding deformed shapes are illustrated in Figures 3.65 to 3.72. The structure is a somewhat stiff system since the significant modes occur in the range of periods between $0.05 \div 0.2$ s. The modes are essentially uncoupled because of the regular geometry of the structure. Nonetheless, the vibration periods are very close to each other, especially for the higher modes that however have a considerable mass participation. The maximum spectral accelerations of the input motion defined in Section 3.4 range between $0 \div 1$ s, that might lead to a considerable amplification of the structural response due to its high dynamic coupling with the frequency content of the ground motion.

The first mode shape occurs in the transverse direction and implies the in-phase deflection of all the piers with consequent important participation of the deck mass. The global rotational mode is induced by the deflection in phase-opposition of the piers with a change of curvature of the deck in proximity of the central axis of the bridge. For periods lower that 0.18 s, longitudinal and vertical modes arise, that are

Number	Vibration mode	T(s)	M_x(%)	M_y(%)	M_z(%)	M_{rx}(%)	M_{ry}(%)	M_{rz}(%)
1	*transverse*	0.2	0.0	73.0	0.0	13.8	0.0	0.0
2	*rotational*	0.18	0.0	0.0	0.0	0.0	0.0	69.3
3	*longitudinal*	0.16	55.4	0.0	0.0	0.0	2.0	0.0
4	*transverse*	0.10	0.0	5.7	0.0	0.0	0.0	0.0
5	*vertical*	0.09	4.3	7.7	7.7	0.0	19.4	0.0
6	*vertical*	0.08	4.0	0.0	7.4	0.0	42.0	0.0
7	*vertical*	0.07	1.7	0.0	42.3	0.0	0.0	0.0
10	*longitudinal*	0.05	11.5	0.0	0.0	0.0	2.0	0.0

Tabella 3.17: Significant vibration modes of the idealised bridge structure.

controlled by the deflection of the strong pier and by the higher modes of the deck. In particular, in the first longitudinal mode the strong pier deforms according to a first modal shape and the dynamic response of the deck is activated. The higher longitudinal modes follow a similar logic that therefore implies the transmission of consistent inertial forces to the abutment in the longitudinal direction at the medium to high frequencies. This consideration will constitute a crucial point to identify the macro-element of the bridge structure and to interpret the results of the dynamic simulations on the full soil-bridge system.

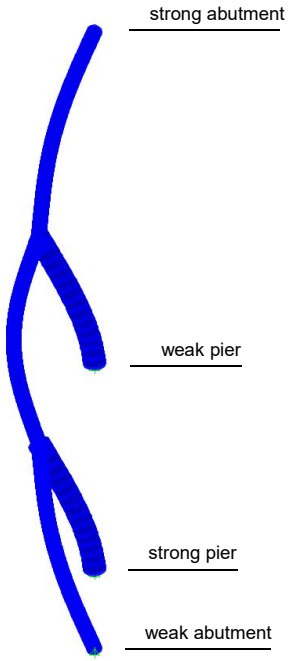

Figure 3.65: Deformed shape of the first global transverse mode (number 1).

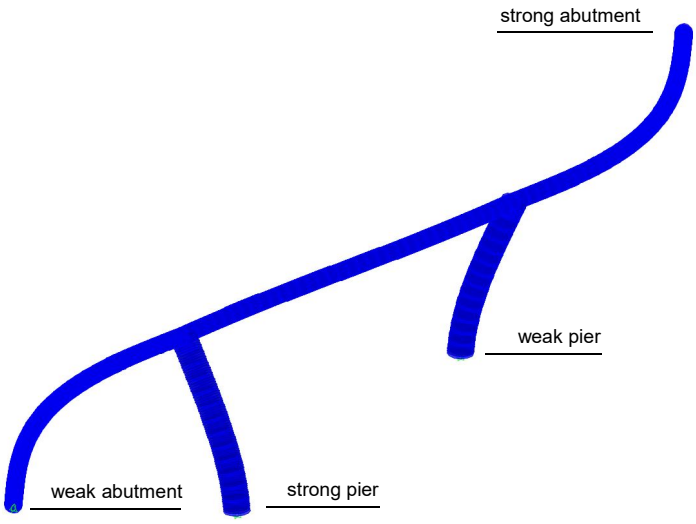

Figure 3.66: Deformed shape of the first global rotational mode (number 2).

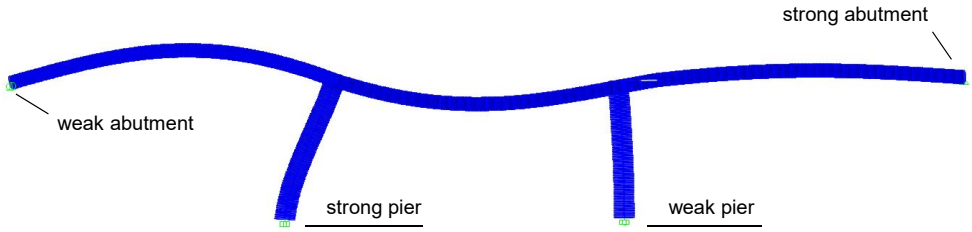

Figure 3.67: Deformed shape of the first global longitudinal mode (number 3).

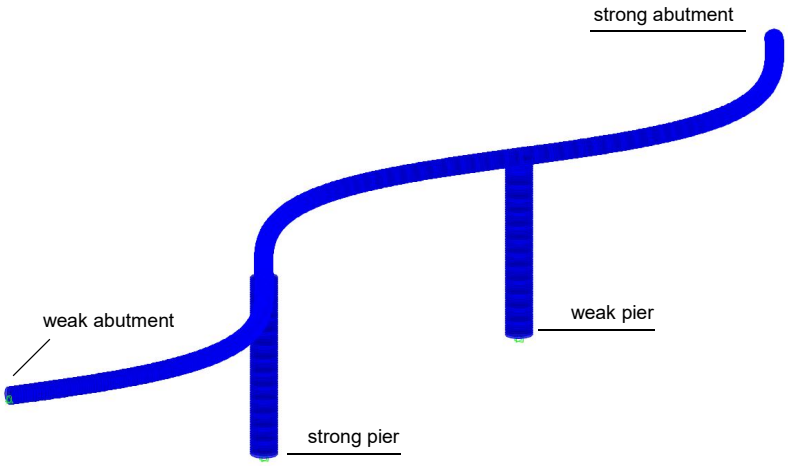

Figure 3.68: Deformed shape of the second global transverse mode (number 4).

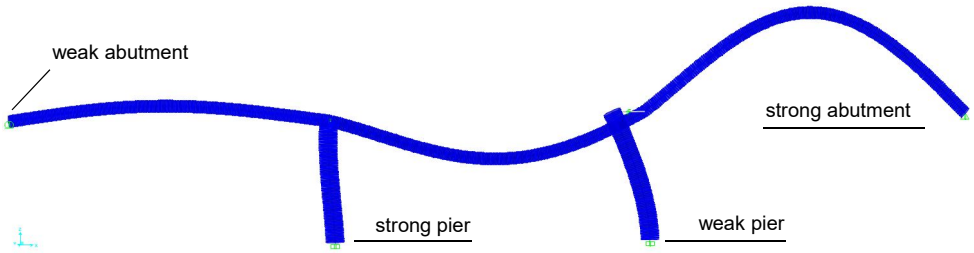

Figure 3.69: Deformed shape of the first vertical mode of the deck (number 5).

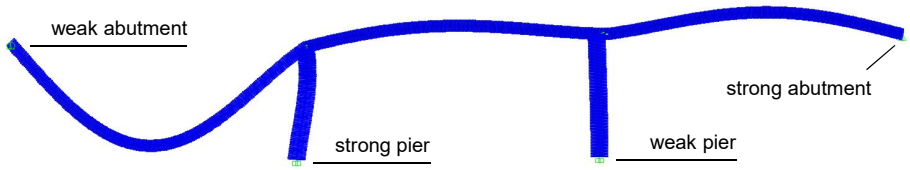

Figure 3.70: Deformed shape of the local vertical mode of the deck (number 6).

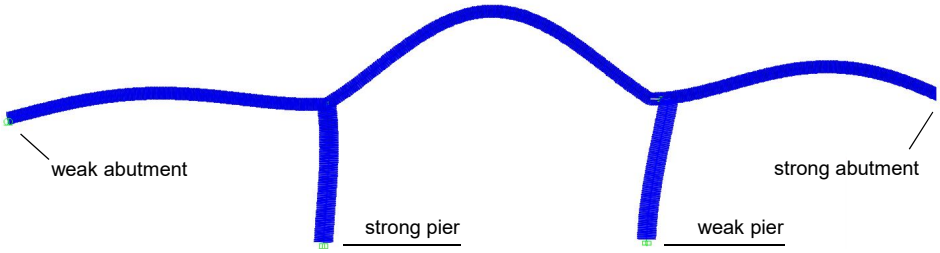

Figure 3.71: Deformed shape of the local vertical mode of the deck (number 7).

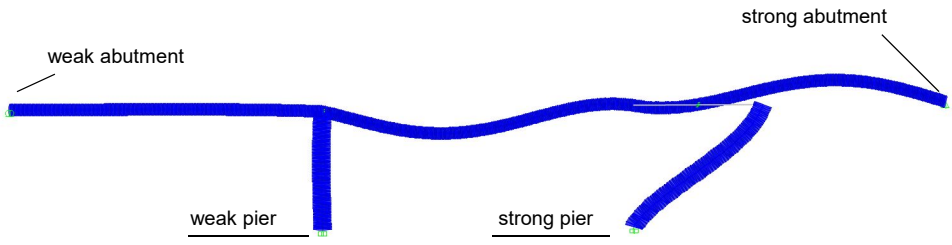

Figure 3.72: Deformed shape of the second global longitudinal mode (number 10).

Chapter 4

Dominant responses of the soil-abutment system

This section illustrates two methods for the evaluation of the significant vibration periods of the soil-abutment system, based on an analytical evaluation and a numerical investigation. The former method is a rigorous development that led to closed-form solutions for the modal characteristics of the embankment subjected to a ground motion along a generic direction, under the assumption of a linear behaviour of the mechanical system. The numerical study consisted instead in incremental dynamic analyses on soil-abutment numerical models aimed to explore the dominant responses of the abutment from small strains up to the mobilisation of a global plastic mechanism. Finally, the comparison between the predictions of the two methods, for the reference embankment defined in Section 3.6.3, provided some useful insight into the application of the analytical solutions. In addition to the evaluation of the entity and the frequency content of the inertial forces developing in the embankment, the dynamic identification of the soil-abutment system will also play a key role in the calibration of the macro-element for bridge abutments.

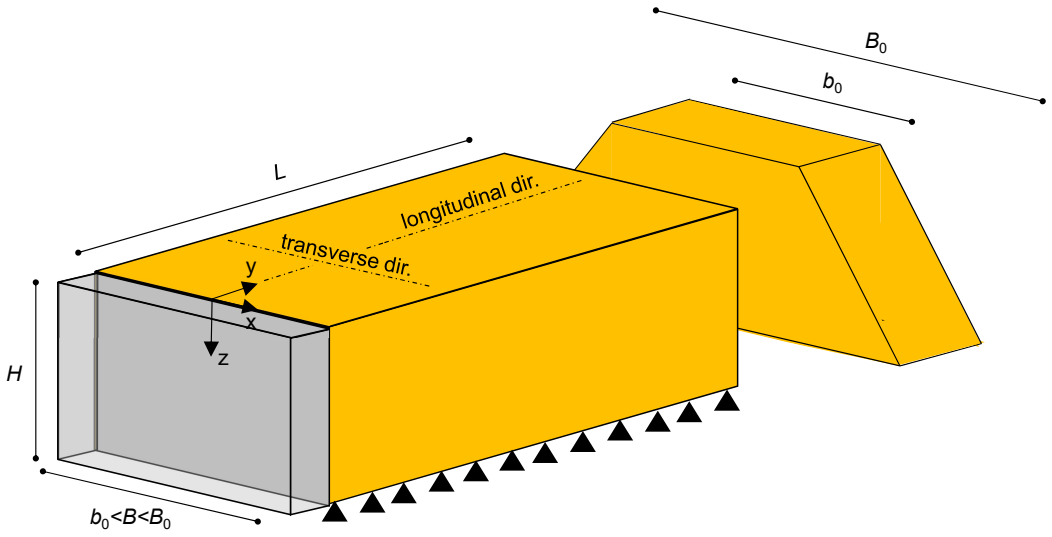

Figure 4.1: Model of embankment taken as reference for deriving the analytical formulation.

4.1 Analytical evaluation of the dominant responses

The development proposed by Kotsoglou and Pantazopoulou (2007) provides the modal characteristics of an embankment in the transverse direction of motion. In this work, the method was generalised to account for a multi-directional motion, introducing different deformation mechanisms triggered by the longitudinal and vertical components of the seismic shaking.

The physical model taken as reference is shown in Figure 4.1. For simplicity, an equivalent rectangular cross section was assumed for the embankment, of width B and height H. Kotsoglou and Pantazopoulou (2007) demonstrated through the results of finite element simulations that this is an acceptable approximation if the width is evaluated as the embankment crest width increased by $(1/4 \div 1/3)$ of the base of each inclined triangular-shaped segment of the initial trapezoidal cross section, whereas the embankment height remains unaltered. The determination of the length L of the embankment will be discussed later. Finally, the displacement field s was

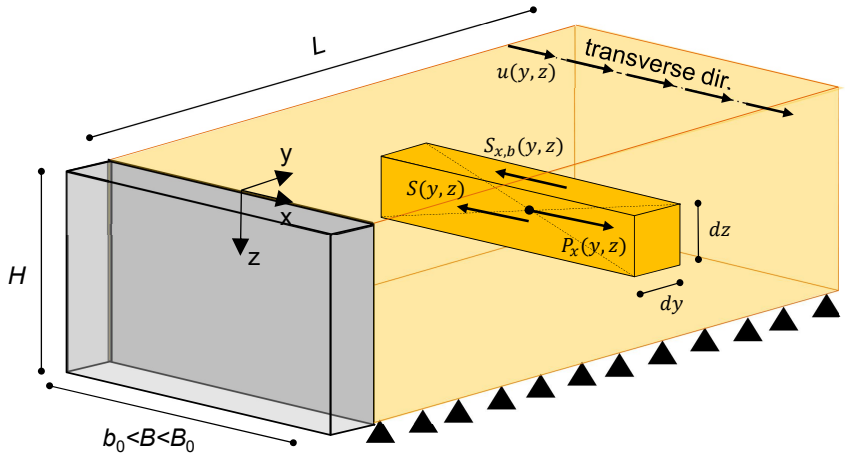

Figure 4.2: Infinitesimal soil segment considered to derive the equation of motion for embankments in the transverse direction.

considered uniform across the embankment, thus, $s(x, y, z, t) = s(y, z, t)$.

4.1.1 Transverse response

Equation of motion

In Kotsoglou and Pantazopoulou (2007), the differential equation describing the seismic response of bridge embankments was established considering an infinitesimal soil segment of height Δz and depth Δy, shown in Figure 4.2: $P_x(y, z)$ is the distributed lateral force (per unit area), $S(y, z)$ is the shear stress acting on the X-Z plane and $S_{x,b}(y, z)$ represents the shear stress acting on the X-Y plane. For the sake of conciseness, an essential description of the mathematical structure is presented below, while the reader can refer to the article by Kotsoglou and Pantazopoulou (2007) for a detailed development.

The local balance equation in the transverse direction reads

$$P_x(y, z, t) + \frac{\partial S_{x,b}(y, z, t)}{\partial z} + \frac{\partial S(y, z, t)}{\partial y} = 0 \tag{4.1}$$

with the term $P_x(y,z,t)$ that, under seismic conditions, can be regarded as the unit inertial force acting in the transverse direction, thus

$$P_x(y,z,t) = -\rho_{soil}(x,y,z,t) \cdot \frac{\partial^2 u(y,z,t)}{\partial t^2} = -\rho_{soil} \cdot u_{,tt}(y,z,t) \tag{4.2}$$

in which the soil density ρ_{soil} is assumed as a constant value. An indicial notation is used to denote derivatives, i.e. $u_{,tt}(y,z,t)$ stands for the second time derivative of the transverse displacement. Under the assumption of a linear elastic behaviour of soil, characterised by a shear modulus G, also the shear stresses can be written as a function of the displacement $u(y,z,t)$

$$S_{x,b}(y,z,t) = G \cdot \frac{\partial u(y,z,t)}{\partial z} = G \cdot u_{,z}(y,z,t) \tag{4.3}$$

$$S(y,z,t) = G \cdot \frac{\partial u(y,z,t)}{\partial y} = G \cdot u_{,y}(y,z,t). \tag{4.4}$$

Substituting Eqs. 4.2, 4.3 and 4.4 into Eq. 4.1, the latter yields

$$-\rho_{soil} \cdot u_{,tt}(y,z) + G \cdot u_{,zz}(y,z) + G \cdot u_{,yy}(y,z) = 0 \tag{4.5}$$

which, divided by ρ_{soil} gives the classical wave equation

$$u_{,tt}(y,z) - V_s \left[u_{,zz}(y,z) + u_{,yy}(y,z)\right] = 0 \tag{4.6}$$

with $V_s = \sqrt{G/\rho_{soil}}$ the shear wave velocity.

Using separation of variables $u(y,z,t) = u_y(y) \cdot u_z(z) \cdot u_t(t)$, the solution of the homogeneous case of Eq. 4.6 (free vibrations) is

$$u(y,z,t) = u(y,z,0)\cdot cos\left(t\cdot\sqrt{\frac{-(\lambda+\mu)}{a^2}}\right)+\frac{\dot{u}(y,z,0)}{\sqrt{\frac{-(\lambda+\mu)}{a^2}}}\cdot sin\left(t\cdot\sqrt{\frac{-(\lambda+\mu)}{a^2}}\right) \quad (4.7)$$

$$u(y,z,0) = A\cdot cos\left(z\cdot\sqrt{-\mu}\right)\cdot C\cdot cos\left(y\cdot\sqrt{-\lambda}\right)\cdot F \quad (4.8)$$

$$\dot{u}(y,z,0) = A\cdot\omega\cdot cos\left(z\cdot\sqrt{-\mu}\right)\cdot C\cdot cos\left(y\cdot\sqrt{-\lambda}\right)\cdot$$

$$\cdot\left[-F\cdot sin\left(\omega\cdot t\right)+J\cdot cos\left(\omega\cdot t\right)\right]_{t=0} \quad (4.9)$$

$$\omega = \sqrt{\frac{-(\lambda+\mu)}{a^2}} \quad (4.10)$$

where $a = 1/V_s^2$, while μ and λ are negative parameters that contain the order of the modal shape (counter n) in the vertical and longitudinal direction, respectively, and are so defined

$$\mu = -\frac{\pi^2\cdot(1+2\cdot n)^2}{4\cdot H^2}, n\epsilon N_0^+ \quad (4.11)$$

$$\lambda = -\frac{\pi^2\cdot(2\cdot n\pm 1)^2}{4\cdot L^2}, n\epsilon N_0^+. \quad (4.12)$$

Eq. 4.7 requires the definition of the boundary conditions in order to determine the constant values A, C, F and J. It was assumed that the relative transverse displacement u_{rel} at the base ($z = H$) is zero and, similarly, shear deformation at the top ($z = 0$) is taken equal to zero, therefore

$$u_{rel}(y, z = H) = 0 \quad (4.13)$$

$$u_{,z}(y, z = 0) = 0. \tag{4.14}$$

In the longitudinal direction, instead, the condition of free embankment was considered in correspondence of the abutment wall ($y = 0$) and a fixed boundary was supposed at the other end ($y = L$), as follows

$$u_{,y}(y = 0, z) = 0 \tag{4.15}$$

$$u(y = L, z) = 0. \tag{4.16}$$

The former equation implies that the soil directly in contact with the wall does not undergo shear strains in the longitudinal direction while the latter is representative of the embankment response at a sufficiently large distance from the abutment, starting for which the response can be reasonably approximated by the shear beam behaviour (Gazetas, 1987).

Dynamic characteristics

The dynamic characteristics of the embankment were evaluated through the following definition of the natural shapes of vibration

$$\Phi_x(y, z) = \frac{u(y, z)}{u_0(0, 0)} = cos\left(z \cdot \sqrt{-\mu}\right) \cdot cos\left(y \cdot \sqrt{-\lambda}\right) \tag{4.17}$$

with $u_0(0, 0) = A \cdot C$ the generalised coordinate (point of reference). With $u_t(t)$ the time-dependent coordinate and upon substitution of $u(y, z) = \Phi_x(y, z) \cdot u_t(t)$ in Eq. 4.5, the latter becomes

$$\rho_{soil} \cdot \Phi_x(y,z) \cdot u_{t,tt}(t) - G \cdot u_t(t) \cdot \Phi_{x,yy}(y,z) - G \cdot u_t(t) \cdot \Phi_{x,zz}(y,z) =$$

$$= -\rho_{soil} \cdot u_{g,tt}(t) \tag{4.18}$$

in which $u_g(t)$ is the ground motion at the base of the embankment. Kotsoglou and Pantazopoulou (2007) showed that the above equation can be rearranged, through the application of the principle of virtual work and integration on the entire significant volume of the embankment, as follows

$$M_n \cdot u_{t,tt}(t) - K_n \cdot u_t(t) = -\Gamma_n \cdot u_{g,tt}(t) \tag{4.19}$$

giving a canonical form of the equation of motion in which the modal mass $M_n(t)$, the modal stiffness $K_n(t)$ and the mode excitation factor $\Gamma_n(t)$ can be identified after some manipulation

$$M_n = B \cdot \int_0^L \int_0^H \rho_{soil} \cdot \Phi_x^2(y,z) \cdot dz \cdot dy, n\epsilon N_0^+ \tag{4.20}$$

$$K_n = G \cdot B \cdot \left(\int_0^L \int_0^H \Phi_x(y,z) \cdot \frac{\partial^2 \Phi_x(y,z)}{\partial z^2} \cdot dz \cdot dy + \right.$$

$$\left. + \int_0^L \int_0^H \Phi_x(y,z) \cdot \frac{\partial^2 \Phi_x(y,z)}{\partial y^2} \cdot dz \cdot dy \right), n\epsilon N_0^+ \tag{4.21}$$

$$\Gamma_n = B \cdot \int_0^L \int_0^H \rho_{soil} \cdot \Phi_x(y,z) \cdot dz \cdot dy, n\epsilon N_0^+. \tag{4.22}$$

For the case under examination illustrated in Figure 4.1, closed-form solutions can be obtained for the modal characteristics. The modal mass reads

$$M_n = B \cdot \rho_{soil} \cdot \int_0^L \int_0^H \Phi_x^2(y,z) \cdot dz \cdot dy =$$

$$= B \cdot \rho_{soil} \cdot \int_0^L \int_0^H cos^2\left(z \cdot \sqrt{-\mu}\right) \cdot cos^2\left(y \cdot \sqrt{-\lambda}\right) \cdot dz \cdot dy =$$

$$= B \cdot \rho_{soil} \cdot \int_0^L cos^2\left(y \cdot \sqrt{-\lambda}\right) \int_0^H cos^2\left(z \cdot \sqrt{-\mu}\right) \cdot dz \cdot dy =$$

$$= \frac{B \cdot \rho_{soil}}{2 \cdot \sqrt{-\lambda} \cdot \sqrt{-\mu}} \cdot \left[y \cdot \sqrt{-\lambda} + sin\left(y \cdot \sqrt{-\lambda}\right) \cdot cos\left(y \cdot \sqrt{-\lambda}\right)\right]_0^L \cdot$$

$$\cdot \left[z \cdot \sqrt{-\mu} + sin\left(z \cdot \sqrt{-\mu}\right) \cdot cos\left(z \cdot \sqrt{-\mu}\right)\right]_0^H =$$

$$= \frac{B \cdot \rho_{soil}}{2 \cdot \sqrt{-\lambda} \cdot \sqrt{-\mu}} \cdot$$

$$\cdot \left[L \cdot \sqrt{-\lambda} + sin\left(L \cdot \sqrt{-\lambda}\right) \cdot cos\left(L \cdot \sqrt{-\lambda}\right)\right] \cdot$$

$$\cdot \left[H \cdot \sqrt{-\mu} + sin\left(H \cdot \sqrt{-\mu}\right) \cdot cos\left(H \cdot \sqrt{-\mu}\right)\right], n\epsilon N_0^+ \tag{4.23}$$

having applied integration by parts. Similarly, the modal stiffness can be computed as

$$K_n = G \cdot B \cdot \left(\int_0^L \int_0^H \Phi(y,z) \cdot \frac{\partial^2 \Phi(y,z)}{\partial z^2} \cdot dz \cdot dy + \right.$$

$$\left. + \int_0^L \int_0^H \Phi(y,z) \cdot \frac{\partial^2 \Phi(y,z)}{\partial y^2} \cdot dz \cdot dy \right) =$$

$$= G \cdot B \cdot \left[\int_0^L \int_0^H cos\left(z \cdot \sqrt{-\mu}\right) \cdot cos\left(y \cdot \sqrt{-\lambda}\right) \cdot \right.$$

$$\cdot (-\mu) \cdot cos\left(z \cdot \sqrt{-\mu}\right) \cdot cos\left(y \cdot \sqrt{-\lambda}\right) \cdot dz \cdot dy +$$

$$+ \int_0^L \int_0^H cos\left(z \cdot \sqrt{-\mu}\right) \cdot cos\left(y \cdot \sqrt{-\lambda}\right) \cdot$$

$$\left. \cdot (-\lambda) \cdot cos\left(z \cdot \sqrt{-\mu}\right) \cdot cos\left(y \cdot \sqrt{-\lambda}\right) \cdot dz \cdot dy \right] =$$

$$= -\frac{G \cdot B}{2 \cdot \sqrt{-\lambda} \cdot \sqrt{-\mu}} \cdot (\mu + \lambda) \cdot \left[H \cdot \sqrt{-\mu} + sin\left(H \cdot \sqrt{-\mu}\right) \cdot cos\left(H \cdot \sqrt{-\mu}\right) \right] \cdot$$

$$\cdot \left[L \cdot \sqrt{-\lambda} + sin\left(L \cdot \sqrt{-\lambda}\right) \cdot cos\left(L \cdot \sqrt{-\lambda}\right) \right], n \epsilon N_0^+. \tag{4.24}$$

Finally, the modal frequency is derived from M_n and K_n as follows

$$\omega_n = \sqrt{\frac{K_n}{M_n}} = \left\{ -\frac{G \cdot B}{2 \cdot \sqrt{-\lambda} \cdot \sqrt{-\mu}} \cdot (\mu + \lambda) \cdot \right.$$

$$\cdot \left[H \cdot \sqrt{-\mu} + sin\left(H \cdot \sqrt{-\mu}\right) \cdot cos\left(H \cdot \sqrt{-\mu}\right) \right] \cdot$$

$$\cdot \left[L \cdot \sqrt{-\lambda} + sin\left(L \cdot \sqrt{-\lambda}\right) \cdot cos\left(L \cdot \sqrt{-\lambda}\right) \right] \cdot$$

$$\left. \cdot \frac{2 \cdot \sqrt{-\lambda} \cdot \sqrt{-\mu}}{B \cdot \rho_{soil}} \cdot \frac{1}{\left[L \cdot \sqrt{-\lambda} + sin\left(L \cdot \sqrt{-\lambda}\right) \cdot cos\left(L \cdot \sqrt{-\lambda}\right) \right]} \cdot \right.$$

$$\cdot \frac{1}{[H \cdot \sqrt{-\mu} + sin\,(H \cdot \sqrt{-\mu}) \cdot cos\,(H \cdot \sqrt{-\mu})]} \Bigg\}^{0.5} = \sqrt{-V_s^2 \cdot (\mu + \lambda)} =$$

$$= V_s \cdot \sqrt{-\left(-\frac{\pi^2 \cdot (1 + 2 \cdot n)^2}{4 \cdot H^2} - \frac{\pi^2 \cdot (2 \cdot n + 1)^2}{4 \cdot L^2}\right)} =$$

$$= \frac{V_s \cdot \pi}{2} \cdot \sqrt{\frac{(1 + 2 \cdot n)^2}{H^2} + \frac{(2 \cdot n + 1)^2}{L^2}}, n \epsilon N_0^+. \tag{4.25}$$

The expression of ω_n highlights some peculiar aspects of the transverse vibration modes of an embankment. The frequency is directly proportional to the shear wave velocity V_s of the soil while an increase of the dimensions of the embankment leads to lower modal frequencies because of the increase of deformability. Note that for very long embankments ($L \gg H$) the modal frequencies can be simply estimated, in first approximation, as

$$\omega_n = \frac{V_s \cdot \pi}{2} \cdot \sqrt{\frac{(1 + 2 \cdot n)^2}{H^2}} = \frac{V_s \cdot \pi \cdot (1 + 2 \cdot n)}{2 \cdot H}, n \epsilon N_0^+ \tag{4.26}$$

with a dynamic response governed essentially by the shear deformation of the embankment cross section.

4.1.2 Longitudinal response

Equation of motion

Consider now the case of an embankment perturbed by a longitudinal ground motion (Y direction). Figure 4.3 depicts the forces acting on an infinitesimal soil segment, where $P_y(y, z) = -\rho_{soil} \cdot v_{,tt}(y, z)$ is the punctual inertial force, $S_{y,b}(y, z)$ is the shear stress acting on the surface $B \cdot dy$, $F_y(y, z)$ is the normal distributed force on the face $B \cdot dz$ and $v(y, z)$ is the resulting longitudinal displacement, not dependent

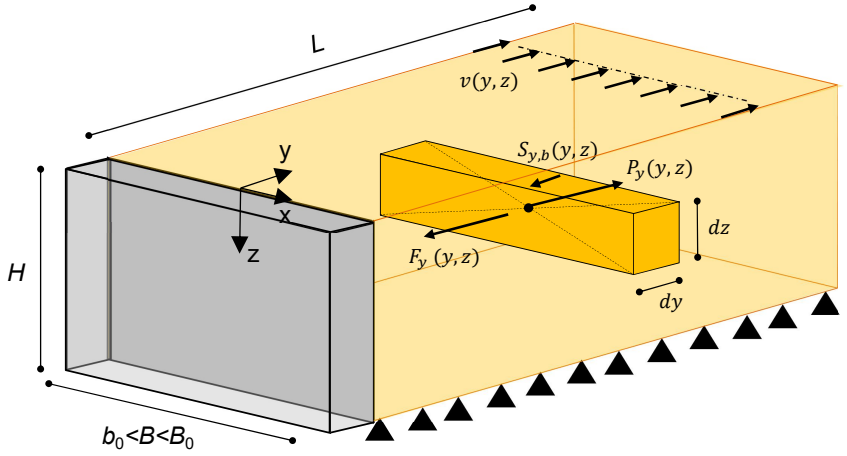

Figure 4.3: Infinitesimal soil segment considered to derive the equation of motion in the longitudinal direction.

on x by hypothesis. Differently from the response in the transverse direction, two different deformation mechanisms develop: a shear deformation due to the shear stress $S_{y,b}(y,z)$ and a volumetric deformation induced by the difference between the compressional distributed forces $F_y(y,z)$ and $F_y(y+\Delta y,z)$. The latter mechanism was not taken into account in the transverse response because, in reality, the cross section of the embankment exhibits essentially a shear-type deformed shape only, with no significant volumetric strains due to the limited width compared to the common wavelengths of the seismic motion. The variability of the displacement field in the longitudinal direction, instead, cannot be neglected and therefore a combined shear-volumetric deformation is considered.

The boundary conditions of the problem are reported below:

- zero relative displacements at the base of the embankment (uniform ground motion at the base)

$$v_{rel}(y, z = H) = 0 \tag{4.27}$$

- zero shear deformation in correspondence of the top of the embankment

$$v_{,z}(y, z = 0) = 0 \tag{4.28}$$

- free embankment in correspondence of the abutment wall

$$v_{,y}(y = 0, z) = 0 \tag{4.29}$$

- fixed embankment at an effective longitudinal distance L from the abutment

$$v(y = L, z) = 0. \tag{4.30}$$

The local balance equation of the elemental volume $dV = B \cdot dy \cdot dz$ reads

$$P_y(y, z, t) \cdot B \cdot dy \cdot dz + F_y(y + dy, z, t) \cdot B \cdot dz - F_y(y, z, t) \cdot B \cdot dz +$$

$$+ S_{y,b}(y, z + dz, t) \cdot B \cdot dy - S_{y,b}(y, z, t) \cdot B \cdot dy = 0 \tag{4.31}$$

in which the infinitesimal increment of the generic quantity $g(i)$ can be written as $g(i + di) = g(i) + dg(i)/di \cdot di$, leading to

$$-\rho_{soil} \cdot v_{,tt}(y, z, t) \cdot B \cdot dy \cdot dz + \frac{\partial F_y(y, z, t)}{\partial y} \cdot B \cdot dy \cdot dz +$$

$$+ \frac{\partial S_{y,b}(y, z, t)}{\partial z} \cdot B \cdot dy \cdot dz = 0 \tag{4.32}$$

$$-\rho_{soil} \cdot v_{,tt}(y, z, t) + \frac{\partial F_y(y, z, t)}{\partial y} + \frac{\partial S_{y,b}(y, z, t)}{\partial z} = 0. \tag{4.33}$$

In the case of a linear elastic medium and under the assumption of no vertical strains, the normal and shear distributed forces are related to the longitudinal displacement by the following relations

$$F_y(y,z,t) = E_{oed} \cdot \frac{\partial v(y,z,t)}{\partial y} = E_{oed} \cdot v_{,y}(y,z,t) \tag{4.34}$$

$$S_{y,b}(y,z,t) = G \cdot \frac{\partial v(y,z,t)}{\partial z} = G \cdot v_{,z}(y,z,t) \tag{4.35}$$

which, substituted into Eq. 4.33, gives the equation of motion

$$-\rho_{soil} \cdot v_{,tt}(y,z,t) + E_{oed} \cdot v_{,yy}(y,z,t) + G \cdot v_{,zz}(y,z,t) = 0 \tag{4.36}$$

or equivalently

$$v_{,tt}(y,z,t) - V_p^2 \cdot v_{,yy}(y,z,t) - V_s^2 \cdot v_{,zz}(y,z,t) = 0 \tag{4.37}$$

as a function of the compressional and shear wave velocities $V_p = \sqrt{E_{oed}/\rho_{soil}}$ and $V_s = \sqrt{G/\rho_{soil}}$, respectively. Note that the punctual force $F_y(y,z,t)$ is a function of the oedometric modulus E_{oed} since it produces compression and extension of the soil volume in the direction of motion. Eq. 4.37 represents a wave equation for a combined volumetric-shear mechanism induced by shear waves in the longitudinal direction Y of the embankment.

By using separation of variables, the longitudinal displacement can be decomposed as follows

$$v(y,z,t) = v_y(y) \cdot v_z(z) \cdot v_t(t) \tag{4.38}$$

which, substituted into Eq. 4.37, leads to

$$v_y(y) \cdot v_z(z) \cdot v_{t,tt}(t) - V_p^2 \cdot v_{y,yy}(y) \cdot v_z(z) \cdot v_t(t) -$$

$$-V_s^2 \cdot v_y(y) \cdot v_{z,zz}(z) \cdot v_t(t) = 0. \tag{4.39}$$

Dividing both members of the above equation by $v_y(y) \cdot v_z(z) \cdot v_t(t)$, it becomes

$$\frac{v_{t,tt}(t)}{v_t(t)} - V_p^2 \cdot \frac{v_{y,yy}(y)}{v_y(y)} - V_s^2 \cdot \frac{v_{z,zz}(z)}{v_z(z)} = 0 \tag{4.40}$$

that is equivalent to the following system of differential equations

$$\frac{v_{z,zz}(z)}{v_z(z)} = \frac{\mu}{V_s^2} = \mu_z \tag{4.41}$$

$$a^2 \cdot \frac{v_{t,tt}(y)}{v_t(t)} - \frac{v_{y,yy}(y)}{v_y(y)} = \frac{\mu}{V_p^2} = \mu_y \tag{4.42}$$

where μ is a coefficient determined from the boundary conditions and $a^2 = V_p^{-2}$.

Eq. 4.41 admits three possible solutions depending on the sign of μ: an exponential solution if $\mu > 0$, a linear solution if $\mu = 0$ and a trigonometric solution when $\mu < 0$. The acceptable solution for the boundary conditions specified before is $\mu < 0$, therefore the generic solution of Eq. 4.41 reads

$$v_z(z) = A \cdot cos\left(z \cdot \sqrt{-\mu_z}\right) + B \cdot sin\left(z \cdot \sqrt{-\mu_z}\right). \tag{4.43}$$

The coefficients A and B can be determined by invoking the relative boundary conditions, Eqs. 4.27 and 4.28. Specifically, from Eq. 4.28 one can obtain

$$v_{z,z}(0) = \left[-A \cdot \sqrt{-\mu_z} \cdot sin\left(z \cdot \sqrt{-\mu_z}\right) + B \cdot \sqrt{-\mu_z} \cdot cos\left(z \cdot \sqrt{-\mu_z}\right)\right]_{z=0} =$$

$$= B \cdot \sqrt{-\mu_z} = 0 \implies B = 0 \tag{4.44}$$

and Eq. 4.27 gives

$$v_z(z = H) = A \cdot cos\left(H \cdot \sqrt{-\mu_z}\right) = 0. \tag{4.45}$$

In addition to the trivial solution $A = 0$ (system at rest), if $A > 0$ a solution of Eq. 4.45 for μ_z can be obtained

$$cos\left(H \cdot \sqrt{-\mu_z}\right) = 0 \implies \mu_z = -\frac{\pi^2 \cdot (1 + 2 \cdot n)^2}{4 \cdot H^2} < 0, n\epsilon N_0^+ \tag{4.46}$$

by which the coefficient μ is derived

$$\mu = \mu_z \cdot V_s^2 = -V_s^2 \cdot \frac{\pi^2 \cdot (1 + 2 \cdot n)^2}{4 \cdot H^2}, n\epsilon N_0^+. \tag{4.47}$$

The expression for the z-dependent function $v_z(z)$ finally reads

$$v_z(z) = A \cdot cos\left(z \cdot \sqrt{\frac{\pi^2 \cdot (1 + 2 \cdot n)^2}{4 \cdot H^2}}\right). \tag{4.48}$$

This implies that, similarly to what happens for the transverse response, the longitudinal modes of vibration have a trigonometric distribution along the embankment height, with an increasingly order defined by the integer n.

The remaining part of the solution is computed by means of Eq. 4.42. This can be further decomposed into Eqs. 4.49 and 4.50 as reported below.

$$\frac{v_{y,yy}(y)}{v_y(y)} = \lambda \tag{4.49}$$

$$a^2 \cdot \frac{v_{t,tt}(y)}{v_t(t)} - \mu_y = \lambda \tag{4.50}$$

The former equation admits a trigonometric solution for $\lambda < 0$

$$v_y(y) = C \cdot cos\left(y \cdot \sqrt{-\lambda}\right) + D \cdot sin\left(y \cdot \sqrt{-\lambda}\right) \tag{4.51}$$

and, by imposing the relative boundary conditions Eqs. 4.29 and 4.30, Eq. 4.51 becomes

$$v_y(y) = C \cdot cos\left(y \cdot \sqrt{-\lambda}\right) \tag{4.52}$$

$$\lambda = -\frac{\pi^2 \cdot (\pm 1 + 2 \cdot n)^2}{4 \cdot L^2}, n \epsilon N_0^+. \tag{4.53}$$

The parameter λ contains the order n of the mode and it is inversely proportional to the length of the embankment. This implies that the greater the length, the smaller the modal frequency since the deformability of the embankment increases.

Eq. 4.50 allows to define the time-dependent function $v_t(t)$. This equation can be conveniently rewritten as

$$\frac{v_{t,tt}(y)}{v_t(t)} = \frac{\lambda + \mu_y}{a^2} = -\omega^2 < 0 \tag{4.54}$$

as a function of the frequency $\omega = 2 \cdot \pi / T$. The coefficient μ_y can be now computed as follows

$$\mu_y = \frac{\mu}{V_p^2} = -\frac{V_s^2}{V_p^2} \cdot \frac{\pi^2 \cdot (1 + 2 \cdot n)^2}{4 \cdot H^2}, n \epsilon N_0^+. \tag{4.55}$$

and therefore the modal frequencies assume the following form

$$\omega = \sqrt{-\frac{\lambda + \mu_y}{a^2}} = \sqrt{-V_p^2 \cdot \left[-\frac{\pi^2 \cdot (\pm 1 + 2 \cdot n)^2}{4 \cdot L^2} - \frac{V_s^2}{V_p^2} \cdot \frac{\pi^2 \cdot (1 + 2 \cdot n)^2}{4 \cdot H^2}\right]} =$$

$$= \sqrt{-\frac{\pi^2}{4} \cdot \left[-V_p^2 \cdot \frac{(\pm 1 + 2 \cdot n)^2}{L^2} - V_s^2 \cdot \frac{(1 + 2 \cdot n)^2}{H^2} \right]} =$$

$$= \frac{\pi}{2} \cdot \sqrt{V_p^2 \cdot \frac{(\pm 1 + 2 \cdot n)^2}{L^2} + V_s^2 \cdot \frac{(1 + 2 \cdot n)^2}{H^2}} \tag{4.56}$$

showing clearly how the two mechanisms, volumetric and shear deformation, concur in defining the modal characteristics of the embankment. As done before, the solution of Eq. 4.54 reads

$$v_t(t) = E \cdot cos\,(t \cdot \omega) + F \cdot sin\,(t \cdot \omega) \tag{4.57}$$

with E and F determined through the initial conditions. The total solution finally yields

$$v(y, z, t) = C \cdot cos\left(y \cdot \sqrt{-\lambda}\right) \cdot A \cdot cos\left(z \cdot \sqrt{-\mu_z}\right) \cdot$$

$$\cdot \left[E \cdot cos\,(t \cdot \omega) + F \cdot sin\,(t \cdot \omega)\right] \tag{4.58}$$

that can be also written as a function of the initial displacement $v_0(y, z, t)$ and the initial velocity $v_{0,t}(y, z, t)$ as

$$v(y, z, t) = v_0(y, z, t) \cdot cos\,(t \cdot \omega) + \frac{v_{0,t}(y, z, t)}{\omega} \cdot sin\,(t \cdot \omega)\,. \tag{4.59}$$

Dynamic characteristics

Based on the definition of $v_0(0, 0, t) = A \cdot C$ as the generalised coordinate, the natural shapes of vibration are defined through Eq. 4.60

$$\Phi_y(y, z) = \frac{v(y, z, t)}{v_0(0, 0, t)} = cos\left(z \cdot \sqrt{-\mu}\right) \cdot cos\left(y \cdot \sqrt{-\lambda}\right) \tag{4.60}$$

so that the longitudinal displacement becomes

$$v(y,z,t) = \Phi_y(y,z) \cdot v_t(t). \tag{4.61}$$

Substituting Eq. 4.61 into the equation of motion, Eq. 4.37, it follows

$$\Phi_y(y,z) \cdot v_{t,tt}(t) - V_p^2 \cdot v_t(t) \cdot \Phi_{y,yy}(y,z) - V_s^2 \cdot v_t(t) \cdot \Phi_{y,zz}(y,z) =$$

$$= -\rho_{soil} \cdot v_{g,tt}(t) \tag{4.62}$$

with $v_g(t)$ the ground motion at the base of the embankment in the longitudinal direction. As done for the transverse direction, the principle of virtual work is now applied to derive the global equation of motion. The virtual work produced by the forces acting on the system when undergoing a virtual displacement $\Phi_y(y,z)$, consistent with the boundary conditions, is calculated in the following

$$\rho_{soil} \cdot v_{t,tt}(t) \cdot \int_0^L \int_0^H \Phi_y^2(y,z) \cdot dz \cdot dy - E_{oed} \cdot v_t(t) \cdot$$

$$\cdot \int_0^L \int_0^H \Phi_y(y,z) \cdot \Phi_{,yy}(y,z) \cdot dz \cdot dy - G \cdot v_t(t) \cdot$$

$$\cdot \int_0^L \int_0^H \Phi_y(y,z) \cdot \Phi_{y,zz}(y,z) \cdot dz \cdot dy =$$

$$= -\rho_{soil} \cdot v_{g,tt}(t) \cdot \int_0^L \int_0^H \Phi_y(y,z) \cdot dz \cdot dy \tag{4.63}$$

and the above equation of motion can be written in a more compact form by recognising in it the modal mass M_n, the modal stiffness K_n and the mode excitation factor Γ_n

$$M_n \cdot v_{t,tt}(t) - K_n \cdot v_t(t) = -\Gamma_n \cdot v_{g,tt}(t) \tag{4.64}$$

$$M_n = B \cdot \rho_{soil} \cdot \int_0^L \int_0^H \Phi_y^2(y,z) \cdot dz \cdot dy, n\epsilon N_0^+ \tag{4.65}$$

$$K_n = B \cdot E_{oed} \cdot \int_0^L \int_0^H \Phi_y(y,z) \cdot \Phi_{y,yy}(y,z) \cdot dz \cdot dy +$$

$$+B \cdot G \cdot \int_0^L \int_0^H \Phi_y(y,z) \cdot \Phi_{y,zz}(y,z) \cdot dz \cdot dy, n\epsilon N_0^+ \tag{4.66}$$

$$\Gamma_n = B \cdot \rho_{soil} \cdot \int_0^L \int_0^H \Phi_y(y,z) \cdot dz \cdot dy, n\epsilon N_0^+. \tag{4.67}$$

For the schematic geometry of the embankment in Figure 4.3, the closed-form solutions for the modal characteristics are reported below.

$$M_n = B \cdot \rho_{soil} \cdot \int_0^L \int_0^H cos^2\left(z \cdot \sqrt{-\mu_z}\right) \cdot cos^2\left(y \cdot \sqrt{-\lambda}\right) \cdot dz \cdot dy =$$

$$= \frac{B \cdot \rho_{soil}}{2 \cdot \sqrt{-\lambda} \cdot \sqrt{-\mu_z}} \cdot \left[L \cdot \sqrt{-\lambda} + sin\left(L \cdot \sqrt{-\lambda}\right) \cdot cos\left(L \cdot \sqrt{-\lambda}\right)\right] \cdot$$

$$\cdot \left[H \cdot \sqrt{-\mu_z} + sin\left(H \cdot \sqrt{-\mu_z}\right) \cdot cos\left(H \cdot \sqrt{-\mu_z}\right)\right], n\epsilon N_0^+ \tag{4.68}$$

$$K_n = B \cdot E_{oed} \cdot \int_0^L \int_0^H \Phi_y(y,z) \cdot \Phi_{y,yy}(y,z) \cdot dz \cdot dy +$$

$$+B \cdot G \cdot \int_0^L \int_0^H \Phi_y(y,z) \cdot \Phi_{y,zz}(y,z) \cdot dz \cdot dy =$$

$$= -\frac{B}{2 \cdot \sqrt{-\lambda} \cdot \sqrt{-\mu_z}} \cdot (G \cdot \mu_z + E_{oed} \cdot \lambda) \cdot$$

$$\cdot \left[H \cdot \sqrt{-\mu_z} + sin\left(H \cdot \sqrt{-\mu_z}\right) \cdot cos\left(H \cdot \sqrt{-\mu_z}\right)\right] \cdot$$

$$\cdot \left[L \cdot \sqrt{-\lambda} + sin\left(L \cdot \sqrt{-\lambda}\right) \cdot cos\left(L \cdot \sqrt{-\lambda}\right)\right], n\epsilon N_0^+. \tag{4.69}$$

As a verification, the modal frequency, already evaluated in Eq. 4.56, is also computed through the modal mass and stiffness, as described in Eq. 4.70.

$$\omega_n = \sqrt{\frac{K_n}{M_n}} = \frac{\pi}{2} \cdot \sqrt{V_p^2 \cdot \frac{(\pm 1 + 2 \cdot n)^2}{L^2} + V_s^2 \cdot \frac{(1 + 2 \cdot n)^2}{H^2}}, n\epsilon N_0^+. \tag{4.70}$$

4.1.3 Vertical response

Equation of motion

Figure 4.4 depicts the forces acting on an infinitesimal soil segment induced by a vertical motion applied to the base. In this direction, the dynamic response of the embankment is conceptually similar to that associated with a longitudinal ground motion. Shear deformation occurs for the variability of the displacement along the length of the embankment, generating the shear stress $S_{z,b}(y, z)$, and it is combined with a volumetric deformation mechanism associated instead with the pressure $F_z(y, z)$. The unit inertial force in the vertical direction is given by $P_z(y, z) = -\rho_{soil} \cdot w_{,tt}(y, z, t)$. By hypothesis, the cross section of the embankment undergoes a uniform displacement at a given elevation, hence the vertical displacement $w(y, z, t)$ does not depend on x.

The local balance equation reads

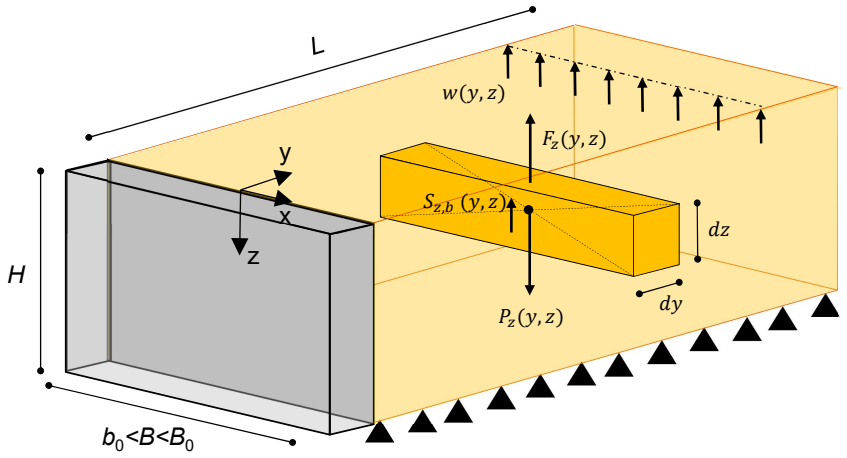

Figure 4.4: Forces acting on an infinitesimal soil segment of embankment induced by the vertical ground motion.

$$\rho_{soil} \cdot w_{,tt}(y,z,t) - \frac{\partial S_{z,b}(y,z,t)}{\partial y} - \frac{\partial F_z(y,z,t)}{\partial z} = 0 \tag{4.71}$$

and considering the following constitutive laws for a linear elastic medium with no longitudinal strains induced by the vertical motion

$$S_{z,b}(y,z,t) = G \cdot \frac{\partial w(y,z,t)}{\partial y} = G \cdot w_{,y}(y,z,t) \tag{4.72}$$

$$F_z(y,z,t) = E_{oed} \cdot \frac{\partial w(y,z,t)}{\partial z} = E_{oed} \cdot w_{,z}(y,z,t) \tag{4.73}$$

the equation of motion follows

$$-\rho_{soil} \cdot w_{,tt}(y,z) + G \cdot w_{,yy}(y,z) + E_{oed} \cdot w_{,zz}(y,z) = 0 \tag{4.74}$$

or, equivalently, it can be rearranged as

$$w_{,tt}(y,z) - V_s^2 \cdot w_{,yy}(y,z) - V_p^2 \cdot w_{,zz}(y,z) = 0. \tag{4.75}$$

By comparing Eq. 4.75 with Eq. 4.37, it can be observed that the two mechanisms associated with shearing and volumetric deformation are inverted with respect to the longitudinal dynamic response.

The solution of the equation of motion requires the definition of 6 constraints, deriving from the initial conditions (2) and from the boundary conditions (4). The same initial conditions adopted for the other directions can be considered in this case, however not affecting the derivation of the modal characteristics, while the boundary conditions are reported below:

- zero relative displacements at the base of the embankment

$$w_{rel}(y, z = H) = 0 \tag{4.76}$$

- zero vertical normal strain in correspondence of the top of the embankment

$$w_{,z}(y, z = 0) = 0 \tag{4.77}$$

- free embankment in correspondence of the abutment wall

$$w_{,y}(y = 0, z) = 0 \tag{4.78}$$

- fixed embankment at an effective longitudinal distance L from the abutment

$$w(y = L, z) = 0. \tag{4.79}$$

By applying separation of variable to the vertical displacement $w(y,z,t) = w_y(y) \cdot w_z(z) \cdot w_t(t)$, the equation of motion yields

$$w_y(y) \cdot w_z(z) \cdot w_{t,tt}(y) - V_s^2 \cdot w_{y,yy}(y) \cdot w_z(z) \cdot w_t(t) -$$

$$-V_p^2 \cdot w_y(y) \cdot w_{z,zz}(z) \cdot w_t(t) = 0. \tag{4.80}$$

The equation above can be solved by following the same strategy described for the longitudinal response and therefore only the most salient developments are presented in the following. The general integral of Eq. 4.75 is

$$w(y,z,t) = C \cdot cos\left(y \cdot \sqrt{-\lambda}\right) \cdot A \cdot cos\left(z \cdot \sqrt{-\mu_z}\right) \cdot$$

$$\cdot \left[E \cdot cos\left(t \cdot \omega\right) + F \cdot sin\left(t \cdot \omega\right)\right] \tag{4.81}$$

$$\mu_z = -\frac{\pi^2 \cdot (1+2\cdot n)^2}{4 \cdot H^2} < 0, n\epsilon N_0^+ \tag{4.82}$$

$$\lambda = -\frac{\pi^2 \cdot (\pm 1+2\cdot n)^2}{4 \cdot L^2} < 0, n\epsilon N_0^+ \tag{4.83}$$

and the modal frequency can be computed through the coefficients μ_z and λ as reported below

$$\omega = \sqrt{-\frac{\lambda+\mu_y}{V_s^{-2}}} = \sqrt{-V_s^2 \cdot \left[-\frac{\pi^2 \cdot (\pm 1+2\cdot n)^2}{4 \cdot L^2} - \frac{V_p^2}{V_s^2} \cdot \frac{\pi^2 \cdot (1+2\cdot n)^2}{4 \cdot H^2}\right]} =$$

$$= \sqrt{-\frac{\pi^2}{4} \cdot \left[-V_s^2 \cdot \frac{(\pm 1+2\cdot n)^2}{L^2} - V_p^2 \cdot \frac{(1+2\cdot n)^2}{H^2}\right]} =$$

$$= \frac{\pi}{2} \cdot \sqrt{V_s^2 \cdot \frac{(\pm 1+2\cdot n)^2}{L^2} + V_p^2 \cdot \frac{(1+2\cdot n)^2}{H^2}}. \tag{4.84}$$

It can be observed that the shear waves affect the longitudinal development of

the vibration modes of the embankment, while the vertical response is modelled by the compressional waves.

Dynamic characteristics

The natural shapes of vibration are defined by $\Phi_z(y,z)$

$$\Phi_z(y,z) = \frac{w(y,z,t)}{w_0(0,0,t)} = cos\left(z \cdot \sqrt{-\mu_z}\right) \cdot cos\left(y \cdot \sqrt{-\lambda}\right) \tag{4.85}$$

so that the displacement field can be regarded as the product between a shape function $\Phi_z(y,z)$ and a time-dependent function $w_t(t)$.

By applying the principle of virtual work, the global equation of motion can be derived, that is formally identical to Eqs. 4.19 and 4.64, with the following expressions for the modal characteristics

$$M_{n,z} = B \cdot \rho_{soil} \cdot \int_0^L \int_0^H \Phi_z^2(y,z) \cdot dz \cdot dy, n\epsilon N_0^+ \tag{4.86}$$

$$K_{n,z} = B \cdot G \cdot \int_0^L \int_0^H \Phi_z(y,z) \cdot \Phi_{z,zz}(y,z) \cdot dz \cdot dy +$$

$$+B \cdot E_{oed} \cdot \int_0^L \int_0^H \Phi_z(y,z) \cdot \Phi_{z,yy}(y,z) \cdot dz \cdot dy, n\epsilon N_0^+ \tag{4.87}$$

$$\Gamma_{n,z} = B \cdot \rho_{soil} \cdot \int_0^L \int_0^H \Phi_z(y,z) \cdot dz \cdot dy, n\epsilon N_0^+. \tag{4.88}$$

For the case under examination (Figure 4.4), the solutions of the equations above are reported below.

$$M_{n,z} = B \cdot \rho_{soil} \cdot \int_0^L \int_0^H cos^2\left(z \cdot \sqrt{-\mu_z}\right) \cdot cos^2\left(y \cdot \sqrt{-\lambda}\right) \cdot dz \cdot dy =$$

$$= \frac{B \cdot \rho_{soil}}{2 \cdot \sqrt{-\lambda} \cdot \sqrt{-\mu_z}} \cdot \left[L \cdot \sqrt{-\lambda} + sin\left(L \cdot \sqrt{-\lambda} \right) \cdot cos\left(L \cdot \sqrt{-\lambda} \right) \right] \cdot$$

$$\cdot \left[H \cdot \sqrt{-\mu_z} + sin\left(H \cdot \sqrt{-\mu_z} \right) \cdot cos\left(H \cdot \sqrt{-\mu_z} \right) \right], n\epsilon N_0^+ \tag{4.89}$$

$$K_{n,z} = B \cdot E_{oed} \cdot \int_0^L \int_0^H \Phi(y,z) \cdot \Phi_{,zz}(y,z) \cdot dz \cdot dy +$$

$$+ B \cdot G \cdot \int_0^L \int_0^H \Phi(y,z) \cdot \Phi_{,yy}(y,z) \cdot dz \cdot dy =$$

$$= -\frac{B}{2 \cdot \sqrt{-\lambda} \cdot \sqrt{-\mu_z}} \cdot (E_{oed} \cdot \mu_z + G \cdot \lambda) \cdot$$

$$\cdot \left[H \cdot \sqrt{-\mu_z} + sin\left(H \cdot \sqrt{-\mu_z} \right) \cdot cos\left(H \cdot \sqrt{-\mu_z} \right) \right] \cdot$$

$$\cdot \left[L \cdot \sqrt{-\lambda} + sin\left(L \cdot \sqrt{-\lambda} \right) \cdot cos\left(L \cdot \sqrt{-\lambda} \right) \right], n\epsilon N_0^+. \tag{4.90}$$

$$\omega_{n,z} = \sqrt{\frac{K_n}{M_n}} = \frac{\pi}{2} \cdot \sqrt{V_s^2 \cdot \frac{(2 \cdot n + 1)^2}{L^2} + V_p^2 \cdot \frac{(1 + 2 \cdot n)^2}{H^2}} =$$

$$= \sqrt{-\frac{\lambda + \mu_y}{V_s^{-2}}}, n\epsilon N_0^+. \tag{4.91}$$

4.1.4 Generic direction of motion

The local equations of motion of bridge embankments in the three coordinate directions and the resulting modal frequencies are summarised in Table 4.1. The transverse motion induces only shear strains for the assumption that the displacement field is uniform across the embankment, hence it does not depend on the

Motion	Local equation of motion	Modal frequency
Transv.	$u_{,tt}(y,z) - V_s \cdot u_{,yy}(y,z) - V_s \cdot u_{,zz}(y,z) = 0$	$\frac{V_s \cdot \pi}{2} \cdot \sqrt{\frac{(1+2\cdot n)^2}{H^2} + \frac{(2\cdot n+1)^2}{L^2}}$
Long.	$v_{,tt}(y,z) - V_p^2 \cdot v_{,yy}(y,z) - V_s^2 \cdot v_{,zz}(y,z) = 0$	$\frac{\pi}{2} \cdot \sqrt{V_p^2 \cdot \frac{(2\cdot n+1)^2}{L^2} + V_s^2 \cdot \frac{(1+2\cdot n)^2}{H^2}}$
Vert.	$w_{,tt}(y,z) - V_s^2 \cdot w_{,yy}(y,z) - V_p^2 \cdot w_{,zz}(y,z) = 0$	$\frac{\pi}{2} \cdot \sqrt{V_s^2 \cdot \frac{(2\cdot n+1)^2}{L^2} + V_p^2 \cdot \frac{(1+2\cdot n)^2}{H^2}}$

Tabella 4.1: Local equations of motion and modal frequencies of bridge embankments.

compressional wave velocity of soil. The other components of the seismic motion provoke instead a combined volumetric-shear deformation with different expressions of the modal frequencies. The horizontal motion is generally caused by S-waves while, when the vertical motion is mainly induced by P-waves propagating in a saturated soil ($V_p/V_s \gg 1$), the modal frequencies in the vertical direction are essentially controlled by the compressional wave velocity and can be also evaluated, in first approximation, as

$$\omega_n = \frac{\pi}{2} \cdot V_p \cdot \sqrt{\frac{(1+2\cdot n)^2}{H^2}}, \textit{vertical direction.} \tag{4.92}$$

The effect of the P-waves on the longitudinal motion is instead much more limited, since it is inversely proportional to the square of the effective length of the embankment (Eq. 4.70). It is worth bearing in mind however that embankments are generally partially saturated soils in which the P-wave velocity is therefore relative to the soil skeleton. Consequently, the ratio V_p/V_s is not much greater than 1 and, as a result, also in the vertical direction the effect of shear deformation on the modal characteristics cannot be neglected.

Taking advantage of the assumption of linear behaviour of the embankment, the displacement field induced by a multi-component seismic motion is obtained by superposition

$$s(y,z,t) \cdot e_i = u(y,z,t) \cdot e_x + v(y,z,t) \cdot e_y + w(y,z,t) \cdot e_z \tag{4.93}$$

with e_i the versor of the axis i. Analogously, the mass participation and the modal stiffness can be obtained through the respective quantities in three orthogonal directions. This method was implemented in Matlab and will constitute a central aspect in calibrating the dynamic properties of the macro-element for bridge abutments.

4.2 Numerical evaluation of the nonlinear dominant responses of the soil-abutment system

The dynamic response of the soil-abutment system is now studied through a soil-abutment interaction model implemented in OpenSees, shown in Figure 4.5. The model constitutes a part of the global soil-bridge representation illustrated in Figure 3.60 and is composed of 99744 elements for a whole plan extension of 135.0×72.0 m^2. It includes the abutment, the embankment and a homogeneous subsoil, representing the superficial layers of Messina Gravel $MG1D$ and $MG1$. The soil domain extends down to a depth of 60 m from the abutment foundation, for a vertical extension equal to about 3.0 times the greatest size of the foundation. The horizontal extension of the model is equal to 3.6 and 7.7 times the transverse and longitudinal dimensions of the abutment. Through preliminary dynamic pushover analyses on such a model, it was verified the negligible interaction between the significant soil volume involved in the abutment response and the lateral boundaries. Because of the large amount of simulations carried out in the dynamic identification of the abutment, the PDMY model was preferred to the SANISAND model to describe the behaviour of the foundation soil and of the embankment, in virtue of its computational efficiency. A detailed description of the constitutive parameters and the finite element modelling is given in Section 3.3 and Section 3.6, respectively.

A staged analysis procedure was adopted with gravity loads applied first, in which the construction of the abutment and of the embankment was simulated in

a sequential manner, and followed by the dynamic simulation, in which the use of the parallel computing was needed to get manageable computation times. The dynamic perturbation consisted of a distributed force to the top of the central wall of the abutment that varies in time as a harmonic function of period T for 10 cycles of loading. The force was applied separately for each loading direction at the deck-abutment contact, with a constant amplitude during a single analysis. Different amplitudes were considered and also the period T ranged between $0.05 \div 5.0$ s, for a total of 160 analyses for each load direction. The smallest amplitude refers to a reversible response of the abutment, hence with no appreciable permanent displacements developed at the deck-abutment contact during the analysis. The highest external force was instead determined as that perturbation producing a steady dominant response of the abutment, as described in detail later. The results are expressed in terms of a relationship between the external force per unit length of the wall and the corresponding average displacement computed at the top of the central wall.

Consider for instance the abutment perturbed by a longitudinal distributed force Q_1. Focusing on the lowest external force equal to 600 kN/m (reversible behaviour), Figure 4.6 depicts the time evolution of the longitudinal displacement v at the deck-abutment contact for three periods of the external force. The time scale is normalised with respect to the duration T_f of the dynamic perturbation. As expected, the amplitudes of the displacements are somewhat limited so that the plastic response of the soil is not relevant, with negligible permanent displacements at the end of the analysis.

It can be observed that the maximum displacement does not increase monotonically as the period rises. In fact, if the maximum displacement for each curve is plotted as a function of the period T of the respective external force, one can obtain the dynamic amplification curve illustrated in Figure 4.7. Three peaks can be

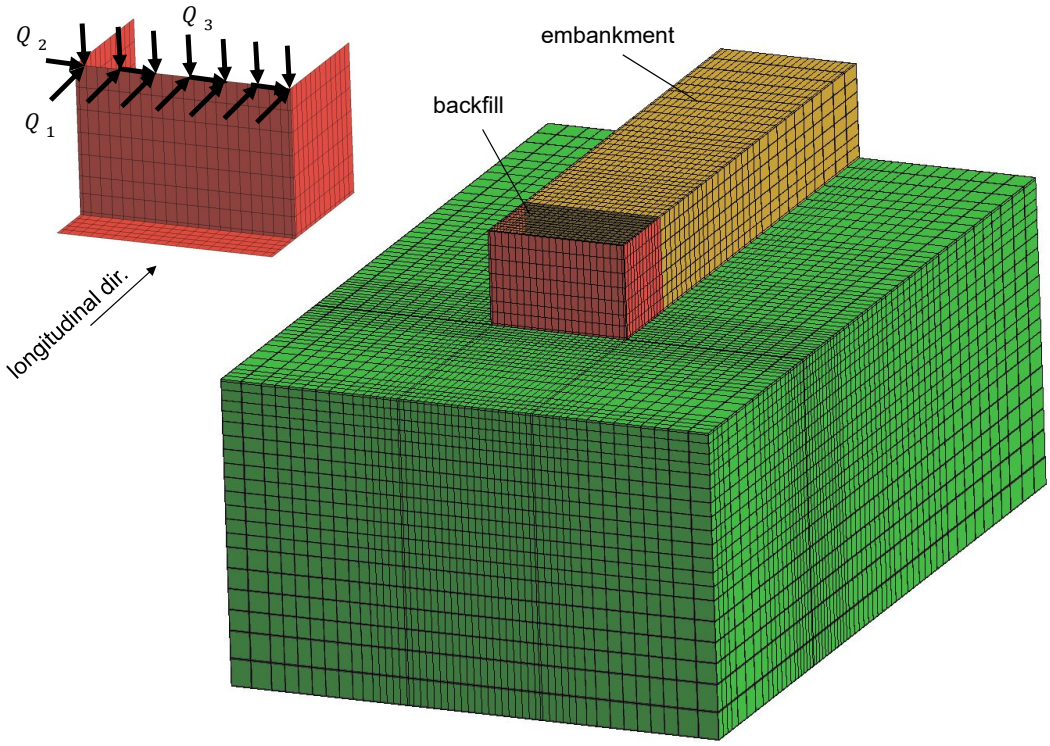

Figure 4.5: Soil-abutment interaction model implemented in OpenSees.

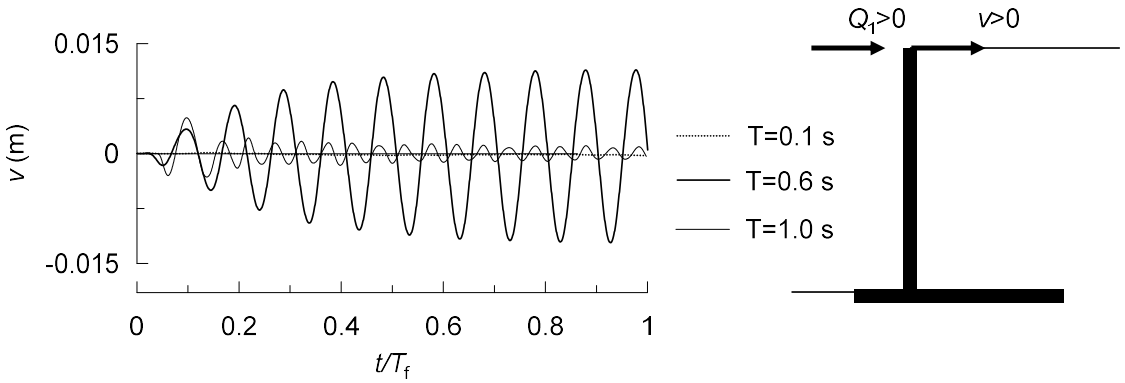

Figure 4.6: Time evolution of the displacements at the deck-abutment contact in the longitudinal direction for Q_1 equal to 600 kN/m.

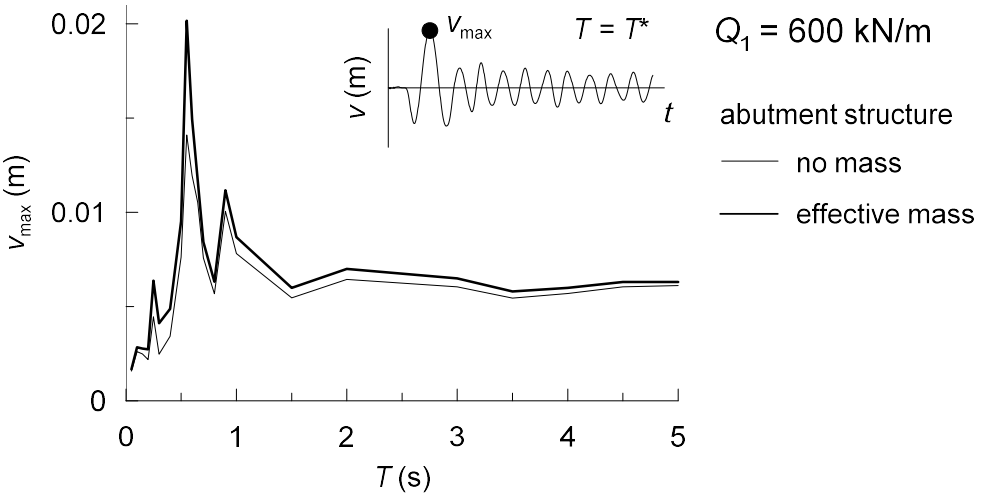

Figure 4.7: Dynamic amplification curve (reversible regime) of the soil-abutment system in the longitudinal direction.

recognised with amplification of the response in the range between $0.4 \div 1.0$ s. For lower periods the response is progressively attenuated because the abutment and the soil are too deformable compared to the oscillations of the external force and, as a result, the system tends to vibrate in phase opposition. For periods beyond 1.5 s, instead, the dynamic effects become negligible and the external force acts as a static perturbation. The maximum amplification occurs in correspondence of a period of 0.6 s, identifying the dominant response of the soil-abutment system at this level of deformation, while the other two minor peaks occur at 0.9 s and 0.3 s. The structural mass of the abutment has a minor effect on the response, leading to a modest further increase of the displacements, confined in the region of the maximum amplification, without altering the dominant periods of the system. It follows that the dynamic amplification of the soil-abutment system is mainly controlled by the participating mass of the embankment, that therefore appears to be much greater than the abutment mass.

Figure 4.8 shows the dynamic amplification curves associated with an increasing

level of the force Q_1. A higher intensity of the external force causes an increment of deformability and a longer dominant response of the abutment. These effects can be concisely described by two non-dimensional parameters: the period elongation $T_D/T_{D,0}$, that is the ratio of the dominant period T_D for a given force Q_1 to the dominant period $T_{D,0}$ associated with the reversible response ($Q_1 < Q_{1,y}$) and the ratio $v_{max}/v_{max,y}$ between the corresponding maximum displacements. The relationship of these two parameters with the normalised amplitude $Q_1/Q_{1,y}$, where $Q_{1,y}$ is intended as the amplitude that produces the first shift of the dominant period, gives the curves of the period elongation and of the maximum displacements shown in Figure 4.9, which highlight some peculiar aspects of the dynamic response of the soil-abutment system.

For values of $Q_1/Q_{1,y}$ less than 1, the maximum displacement $v_{max}/v_{max,y}$ increases quasi-linearly with a modest gradient and the dominant period keeps unaltered, delimiting a range of the normalised amplitude in which the behaviour of the soil-abutment system is essentially reversible governed by the elastic stiffness of the soil. For higher intensities of the external force, the behaviour changes, leading to an increment of deformability and a significant increase of the dominant period up to $1.3 \cdot T_{D,0}$. This is a transition phase in which the period elongation goes up as a consequence of an increasingly more pronounced plastic response of the soil. In fact, in this zone the growth of the maximum displacements is accompanied by a marked increase of the permanent displacements as well, the latter depicted in Figure 4.10. The latter accumulate progressively in time and are directed downstream due to the mobilization of the active resistance in the embankment, as also demonstrated by the time histories of the displacements produced by a level of force $Q_1/Q_{1,y} = 3.0$ in Figure 4.11. Moving beyond the transition zone ($Q_1/Q_{1,y} > 3.0$), even though the maximum displacements keep increasing more than linearly, the dominant period stabilises at a value of 0.78 s. This is caused by a diffused plastic response in

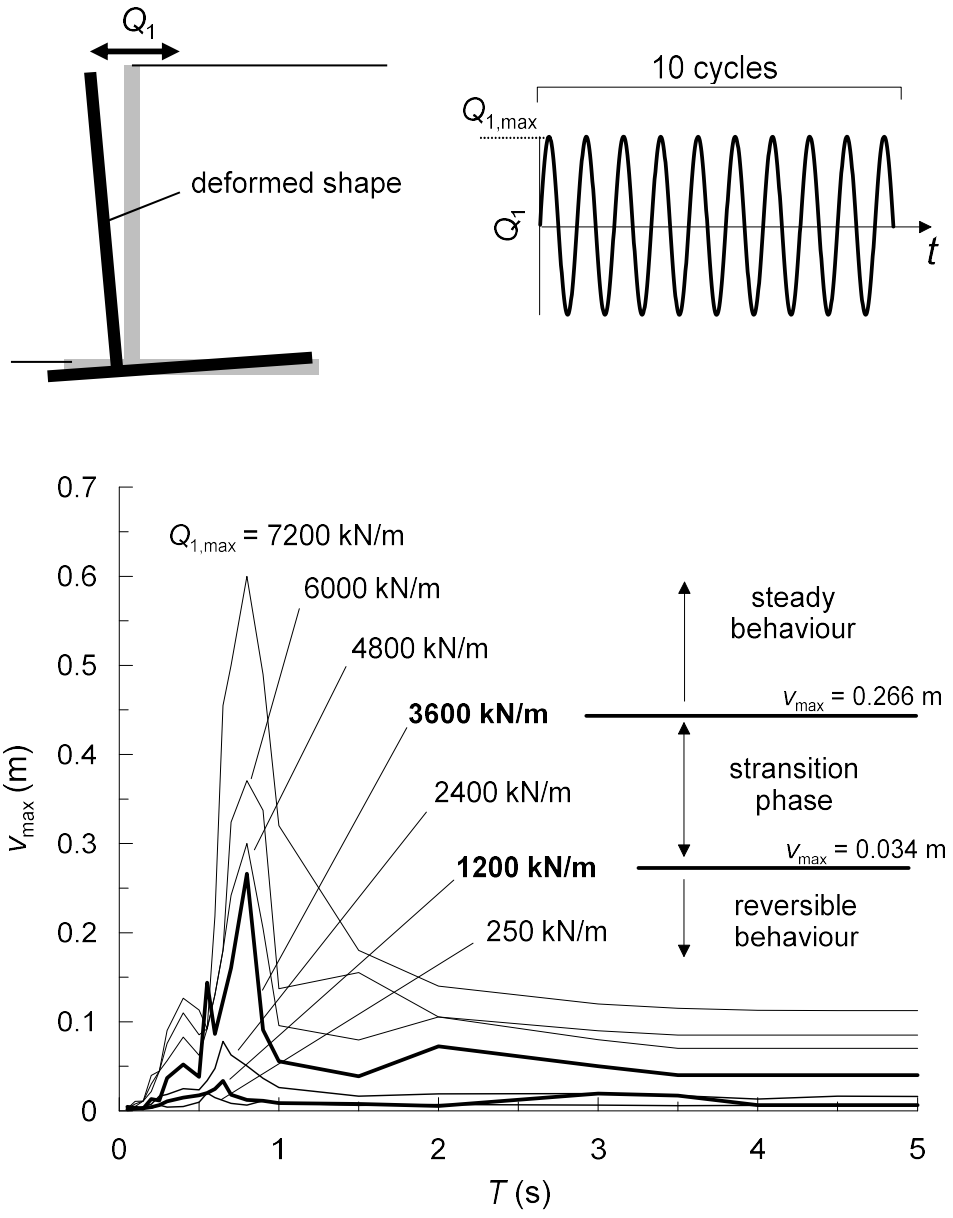

Figure 4.8: Dynamic amplification curves of the soil-abutment system for an increasing amplitude of the external force Q_1 in the longitudinal direction.

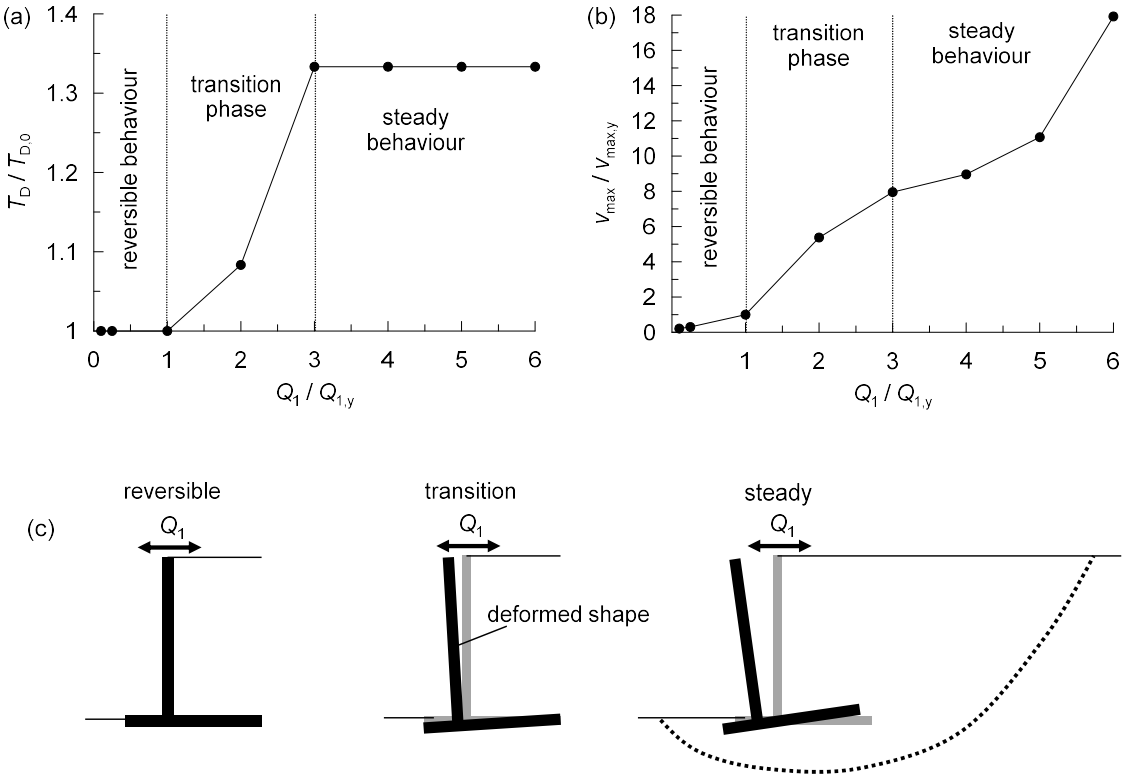

Figure 4.9: Curves of the period elongation (a) and of the maximum displacements (b).

the soil with activation of a global plastic mechanism of the soil-abutment system. Accordingly, the participating mass of the embankment becomes bounded by the edges of the plastic volume and cannot increase further for higher intensities of the perturbation, leading to a steady dominant response. A non-dimensional representation of the dynamic amplification curves, including both the effects of the period elongation and the increment of the maximum displacements, is shown in Figure 4.12.

In the vertical direction, the incremental dynamic analysis was carried out monitoring the mean vertical displacement w on the top of the central wall caused by a vertical force Q_3 applied to the same nodes. The results of the dynamic identification are shown in Figures 4.13, 4.14 and 4.15. The reversible behaviour occurs in the same interval of the external force detected for the longitudinal response.

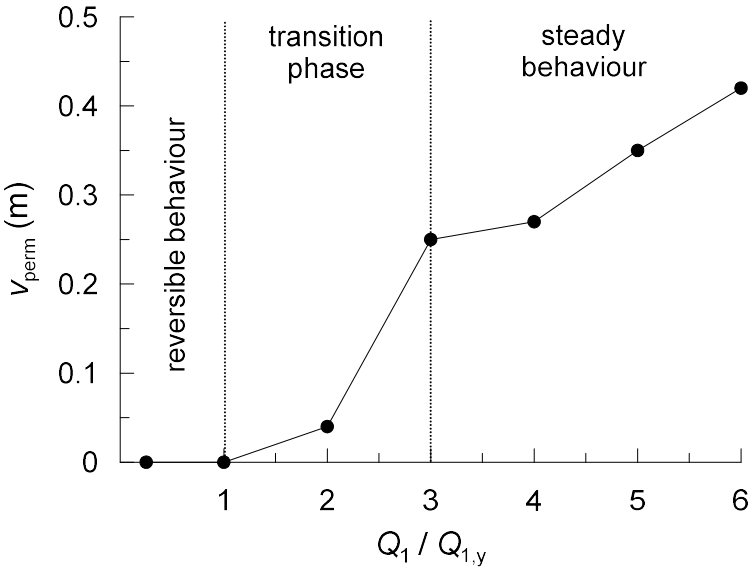

Figure 4.10: Permanent displacements of the abutment top plotted as a function of the normalised load $Q_1/Q_{1,y}$.

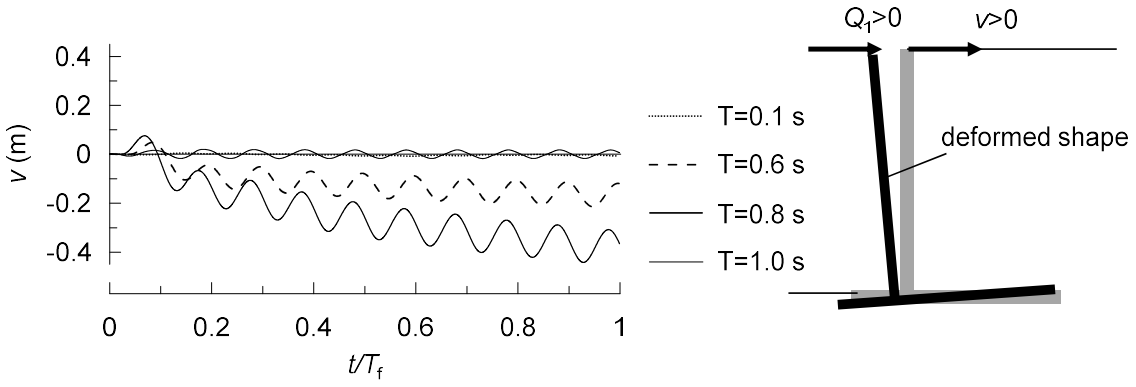

Figure 4.11: Time evolution of the displacements at the deck-abutment contact in the longitudinal direction for Q_1 equal to 3600 kN/m.

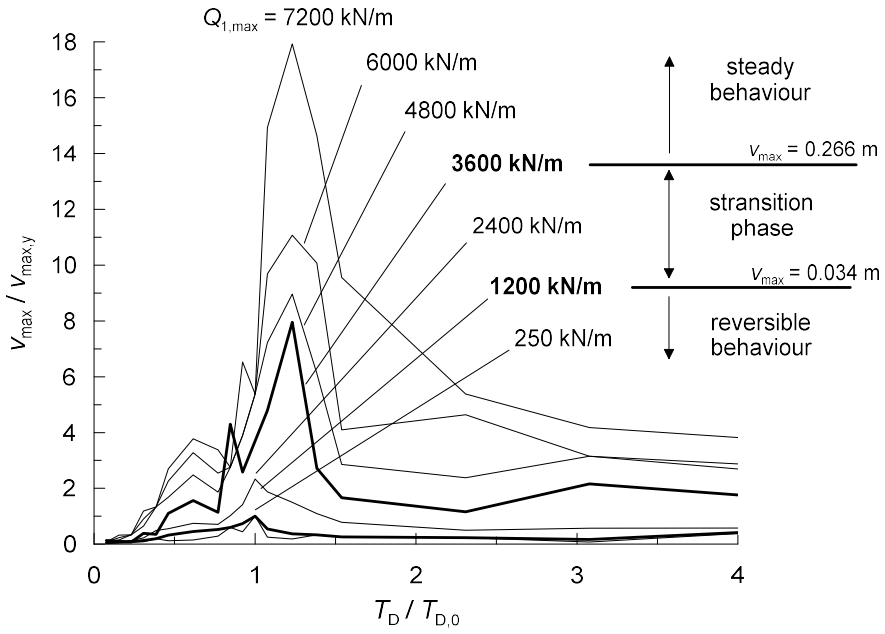

Figure 4.12: Non-dimensional representation of the dynamic amplification curves of the soil-abutment system in the longitudinal direction.

The corresponding maximum displacements are very small, less than 2 cm, of the same order of magnitude of those obtained in the longitudinal response. However, the dominant period occurs at 0.4 s, resulting in a stiffer response compared to the longitudinal one, with a ratio $T_{D,0}^{vert}/T_{D,0}^{long} = 0.67$. The reversible regime holds up to a vertical force equal to 1200 kN/m, with a slight increase of the maximum displacement and negligible permanent effects in the post-shaking condition. Afterwards, the dominant period starts rising up to a period of 0.5 s, attained in correspondence of $Q_3 = 2400$ kN/m, with a period elongation of $T_D/T_{D,0} = 1.25$. In this transition phase, the displacements increase markedly, as well as the permanent ones. The dominant period keeps unaltered in the range $Q_3 = 2400 \div 4800$ kN/m, in which the maximum displacements increase more than linearly due to the progressively more pronounced plastic response of the soil interacting with the abutment. Until this level of force, the two curves of the period elongation in the longitudinal and vertical

directions present a similar trend, though the respective displacement fields show completely different amplitudes. In the vertical response, however, a new transition phase was detected at very high levels of the perturbation ($Q_3 > 4800$ kN/m) in which the shape of the dynamic amplification curve modify. More specifically, the dominant period decreases to the initial value of 0.4 s, for $Q_3 = 6000$ kN/m, because the displacement at 0.5 s reduces while that at 0.6 s increases progressively, leading to the formation of a new vibration mode that becomes the dominant one for extremely severe external forces ($Q_3 > 8400$ kN/m). This phenomenon (mode switch) was not observed in the longitudinal direction probably because of the different deformation modes that develop in the soil. A much higher magnitude of the external force is required to activate a global plastic mechanism in the vertical direction, compared to the longitudinal limit load that mobilises the active resistance in the embankment. As it will be described in detail in Section 5.9.1, this happens because the bearing capacity of the abutment foundation involves a large volume of soil in which the resistance is mobilised, with part of the soil downstream and upstream in addition to the foundation soil. This implies a more complex response of the abutment, with a possible alternating mobilization of the soil resistance in different parts of the subsoil interacting with the abutment before reaching the ultimate condition, that might be responsible of the multiple oscillations of the dominant period observed above.

Looking at the transverse response, the identification of the dominant response is shown only for the reversible regime, since this is an ongoing research. In Figure 4.16, the dynamic amplification curve obtained by applying a transverse force $Q_2 = 600$ kN/m is compared with the curves in the longitudinal and vertical directions. The transverse response follows quite closely the curve relative to the longitudinal direction, with a comparable amplitude of the displacements, but it presents a slightly larger dominant period $T_{D,0}^{tran}$ equal to 0.7 s. The longer dynamic response might be

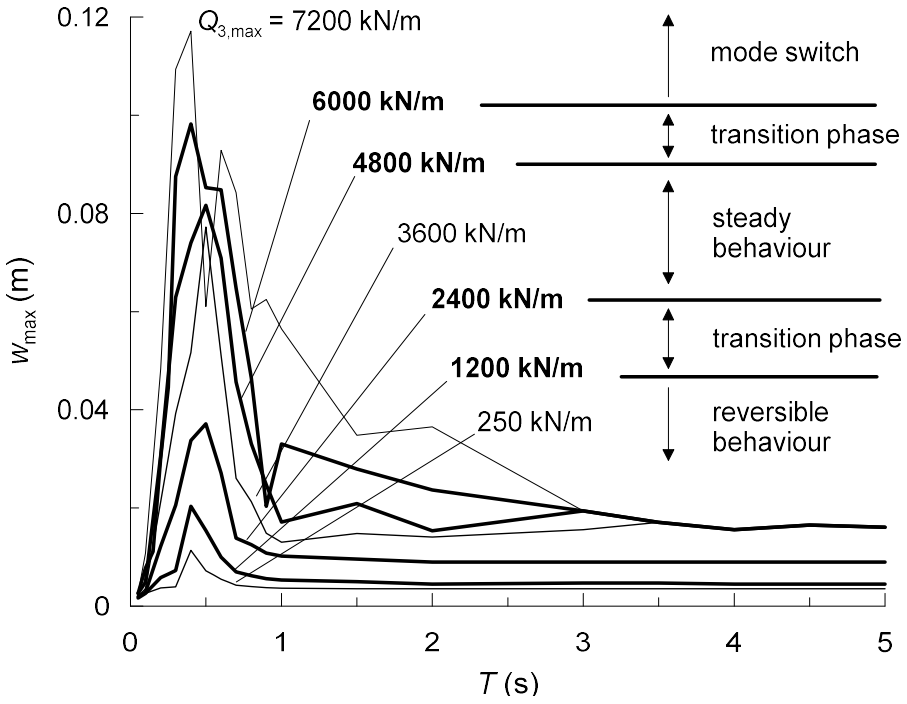

Figure 4.13: Dynamic amplification curves of the soil-abutment system for an increasing amplitude of the vertical external force Q_3.

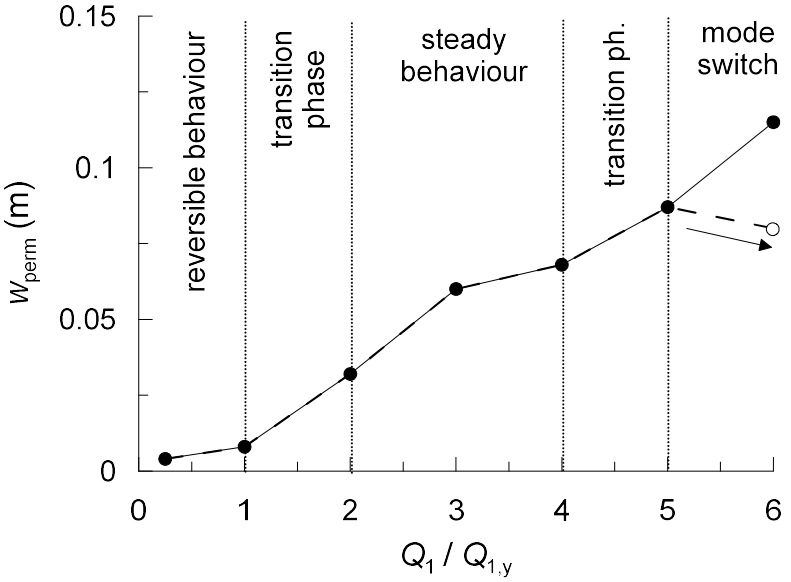

Figure 4.14: Permanent displacements of the abutment top plotted as a function of the normalised load $Q_3/Q_{3,y}$.

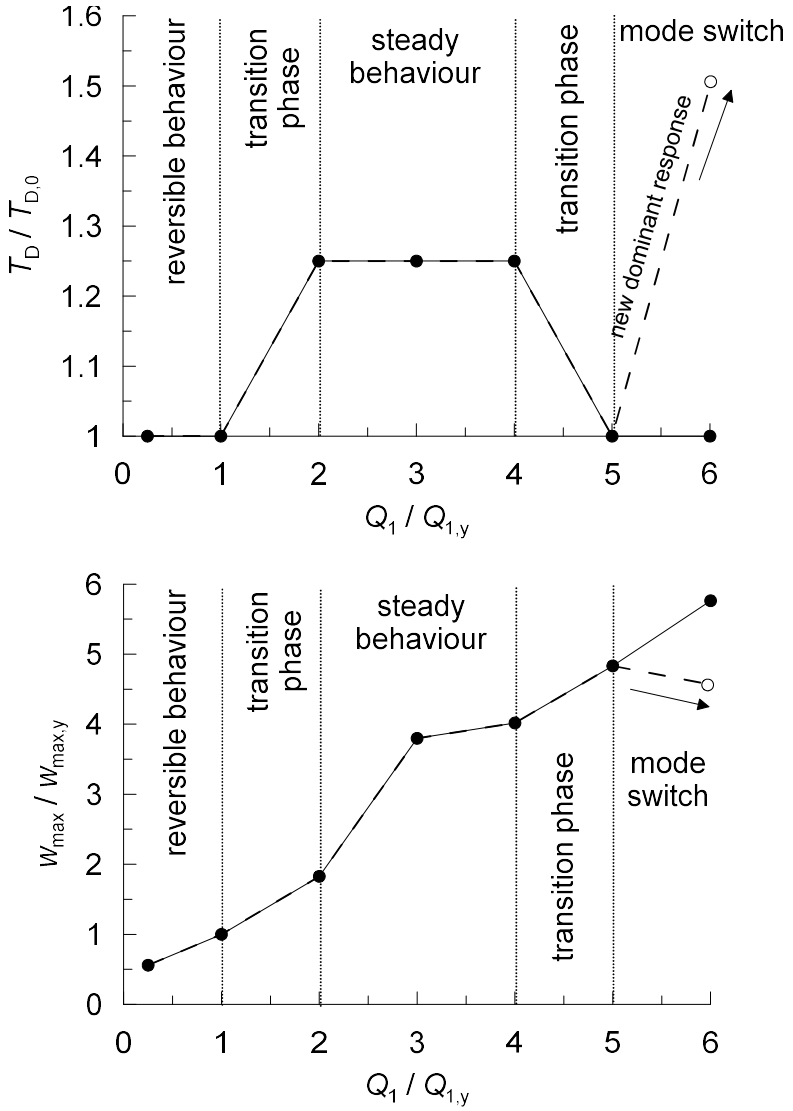

Figure 4.15: Curves of the period elongation (a) and of the maximum displacements at resonance (b) in the vertical direction.

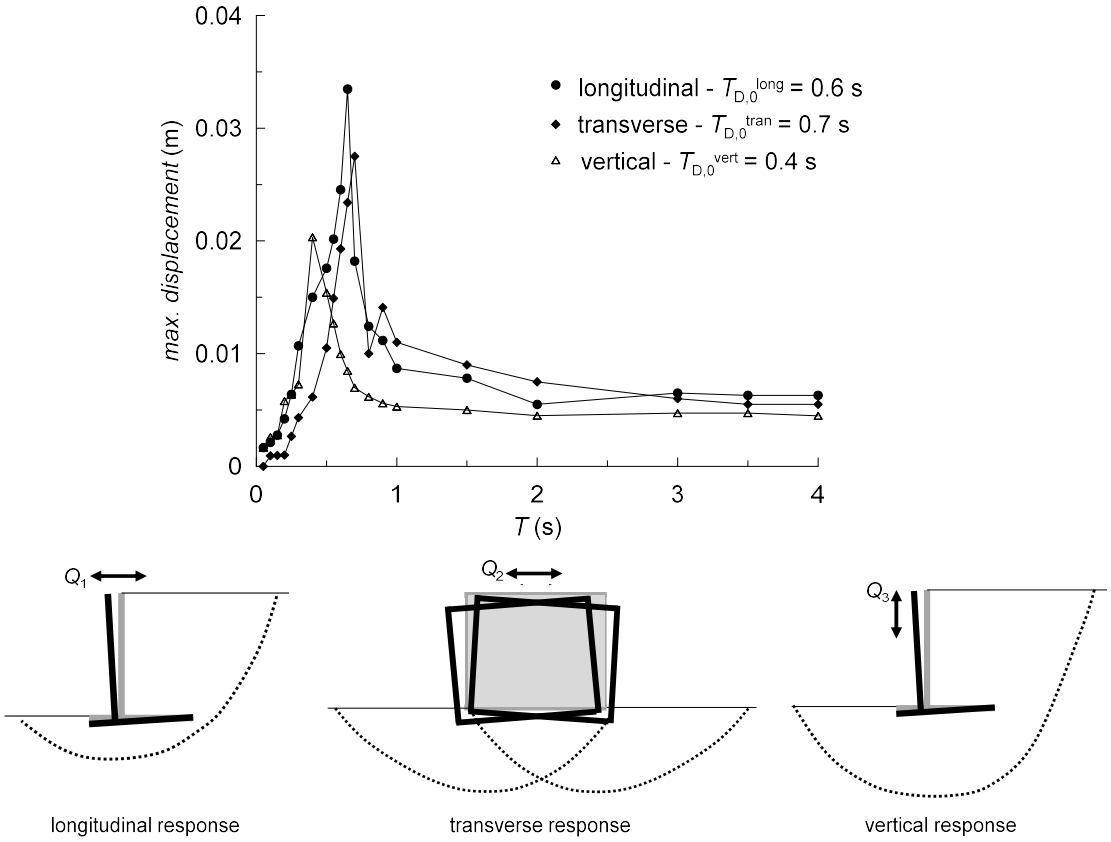

Figure 4.16: Dynamic amplification curves of the soil-abutment system for $Q_i = Q_{i,y} = 1200$ kN/m (upper bound of the reversible regime).

due to the different kinematics associated with the three directions (Figure 4.16). Differently from the other directions, in the transverse direction there is no lateral confinement to the abutment wall and therefore the oscillations of the abutment are mainly controlled by the soil-foundation interaction, that might cause the slight increment of deformability observed above. At this low level of the external force, the static displacements are contained in a quite narrow range because the response is primarily elastic.

4.3 Comparison between analytical predictions and numerical evaluations

The numerical results obtained above for the reference embankment are now compared with the analytical predictions. Eqs. 4.26, 4.70 and 4.91 give the analytical solutions for the vibration periods along the three coordinate directions. In these solutions, the height H of the embankment was taken equal to its original value of 13.5 m while the length L was assumed equal to $3 \cdot H = 40.5$ m, since for greater values of L the modal frequencies become much less dependent on the aspect ratio L/H (long embankment condition). Theoretically, the length of the embankment to be considered should be representative of the volume of soil that interacts dynamically with the abutment, also called effective length of the embankment, whose identification is not straightforward. In dynamic simulations, in fact, the mass of the soil involved in the dynamic response of the abutment is referred to part of the embankment and of the foundation soil, whose contributions are hardly distinguishable. Moreover the mass participation varies with the frequency of the dynamic perturbation and, consequently, also the effective length should reflect these features. A first evaluation of the effective embankment length for the problem at hand will be provided in Section 5.14.2, devoted to the calibration of the macro-element of bridge abutment, but further investigations are needed to reach a more general understanding on it. The compressional and shear wave velocities of the soil are equal to $V_p = 407$ m/s and $V_s = 220$ m/s, respectively, where the former refers to the soil skeleton because the embankment is regarded as a partially saturated soil.

Figure 4.17 shows the vibration periods of the embankment in the three coordinate directions of motion. Let $T_{R,1}^{long}$, $T_{R,1}^{tran}$ and $T_{R,1}^{vert}$ be the first resonance periods in the longitudinal, transverse and vertical direction, respectively. In all directions, after the first resonance the vibration period decreases rapidly, tending to a horizon-

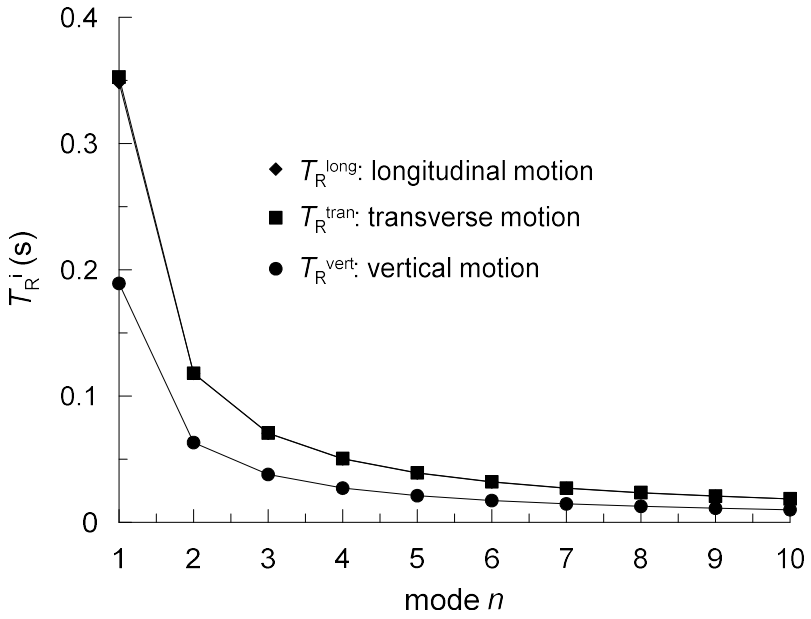

Figure 4.17: Analytical evaluation of the vibration periods of the reference embankment in the transverse, longitudinal and vertical directions of motion.

tal asymptote for $n > 8$, which is different for the vertical and the horizontal modes. The vertical response results to be much stiffer than the horizontal one, with ratios $T_{R,1}^{vert}/T_{R,1}^{long}$ and $T_{R,1}^{vert}/T_{R,1}^{tran}$ equal to 0.54 and 0.56. The longitudinal response is slightly more stiffer than the transverse response because involves a combined shear and volumetric deformation mechanism, while the transverse modes are affected only by the shear wave velocity.

The analytical results above are now compared with the dominant responses obtained through the numerical interaction models in OpenSees. The comparison is initially referred to the dynamic amplification curves in the reversible regime (Figure 4.16). It is evident that the analytical method leads to a considerable underestimation of the dominant periods in all the directions of motion, with the following ratios between the analytical $T_{R,1}^{(ana)}$ and the numerical $T_{R,1}^{(num)}$ predictions

$$\frac{T_{R,1}^{(num)}}{T_{R,1}^{(ana)}} = \begin{cases} 1.70, & \textit{longitudinal direction} \\ 2.05, & \textit{transverse direction} \\ 2.12, & \textit{vertical direction} \end{cases} .$$

The reason of this discrepancy is deemed to be mainly due to the different physical problems considered by the two methods. The finite element models in OpenSees give a more accurate description of the soil-abutment system, especially with a more likely reproduction of the displacement field induced by the seismic excitation. The analytical solutions, instead, are derived through a rigorous mathematical formulation but refer to a more simplified mechanical system, as schematically shown in Figures 4.18 and 4.19 for the longitudinal and vertical response, respectively. This implies a different kinematics of the embankment interacting with the abutment under dynamic excitation.

In the numerical models, in fact, the abutment undergoes a roto-translational motion involving part of the embankment and also part of the soil underneath the footing, while the analytical method does not take into account the deformability of the foundation soil and the soil-abutment interaction is more simply regarded as an appropriate boundary condition. In spite of these important simplifications, the analytical solutions may represent a very useful tool for a prompt estimation of the dominant responses of embankments and, to overcome the above limitations, the following simple modification was introduced to the analytical method in order to obtain a good match between the two methods.

As observed before, the most limiting simplification of the analytical model is that it neglects completely the deformability of the foundation soil. Without modifying the mathematical formulation, a greater effective height H_{eff} of the embankment was introduced in the solutions of the modal characteristics. Calibrating H_{eff} against the numerical results by trial and error, it was found that the effective height depends on

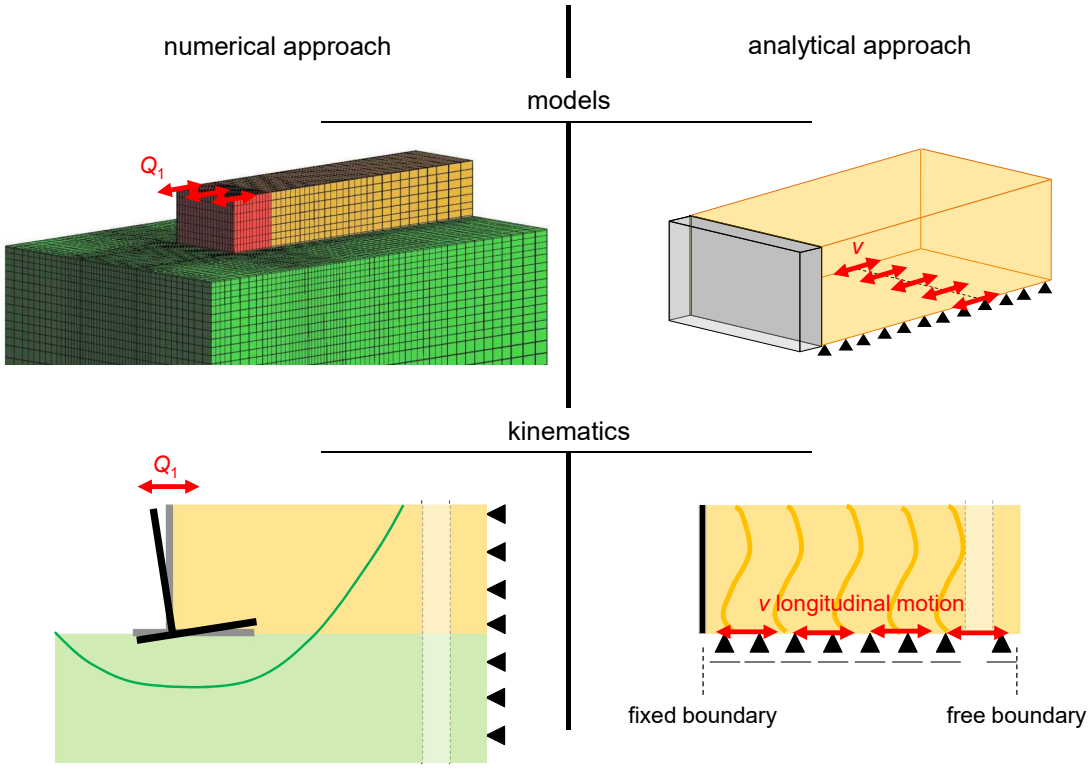

Figure 4.18: Longitudinal response: physical models used in the analytical and numerical methods.

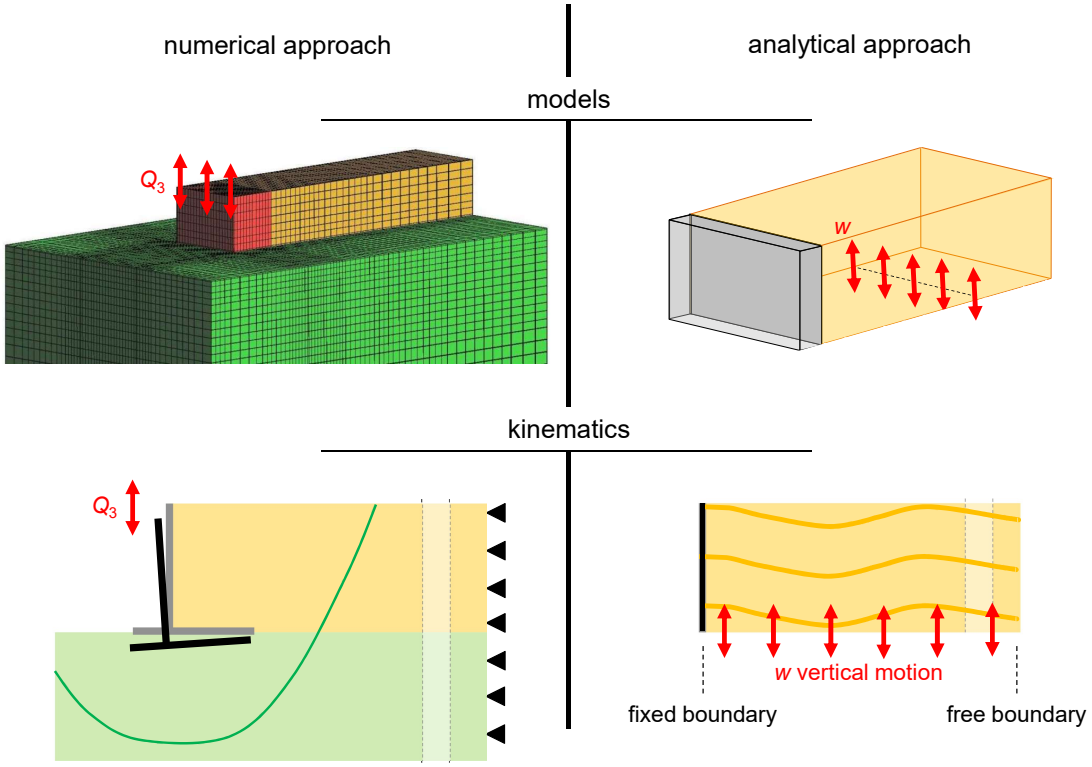

Figure 4.19: Vertical response: physical models used in the analytical and numerical methods.

the direction of motion. In detail, the expression of the effective height was related to the length of the abutment foundation L_f, obtaining the following relations

$$H_{eff} = \begin{cases} H + L_f, \ longitudinal \ direction \\ H + 1.5 \cdot L_f, \ transverse \ direction \\ H + 1.5 \cdot L_f, \ vertical \ direction \end{cases} . \tag{4.94}$$

The above expressions seem to be representative of the volume of soil beneath the foundation that is involved in the response of the abutment, according to the different deformation mechanisms induced by the horizontal and vertical ground motion (see Figure 4.16). In this way, the analytical solutions match very well the numerical results, as illustrated in Figure 4.20, and can be therefore employed for a prompt assessment of the modal characteristics of bridge embankments along a

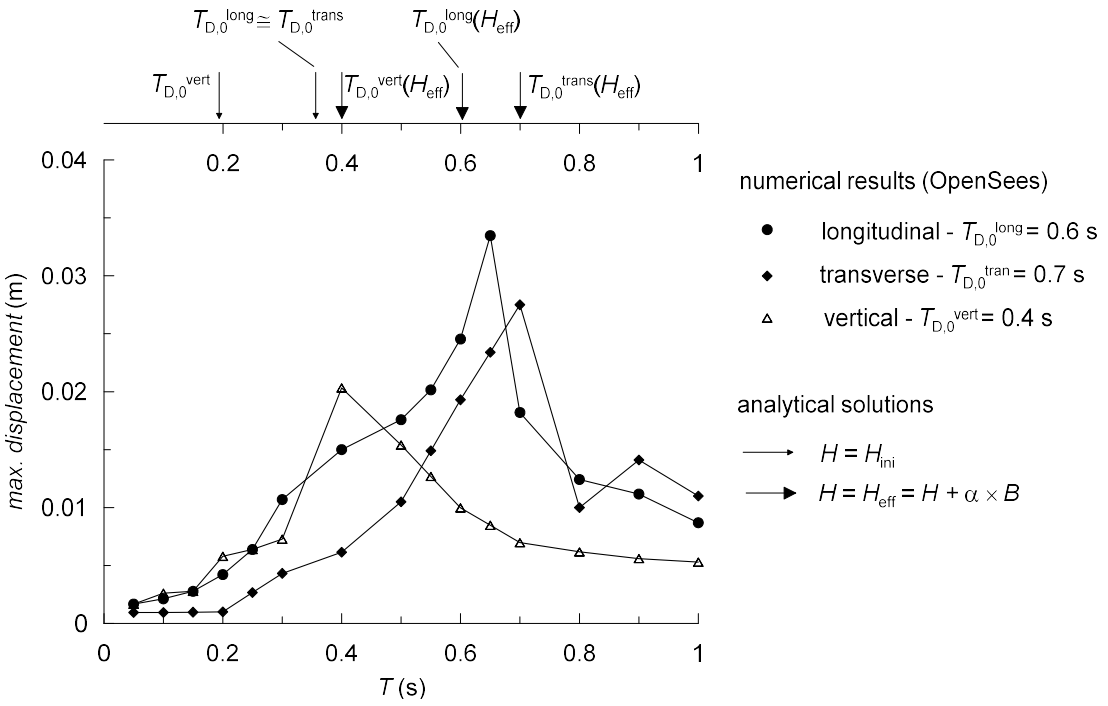

Figure 4.20: Comparison between the analytical prediction of the dominant periods and the dynamic amplification curves retrieved through the numerical soil-abutment interaction models in the reversible regime.

generic direction of motion.

The analytical method was developed under the assumption of linear behaviour of soil, which theoretically holds only in the reversible region of the curve of the period elongation, thus for a very modest external perturbation. In a simplified manner, the analytical approach might be also used to predict the dominant periods beyond the small strain regime, regarding the progressive, nonlinear reduction of the soil stiffness with the level of strain as an equivalent linear behaviour, referring to appropriate values of the normalised shear modulus G/G_0. As an example, consider the dynamic amplification curves in Figures 4.8 and 4.13. It was found that the optimum values of G/G_0 to be used in the analytical method (Eqs. 4.26, 4.70 and 4.91) in order to reproduce the shift of the dominant period in the transition phase and in the steady state are 0.75 and 0.5, respectively. The relative results are shown

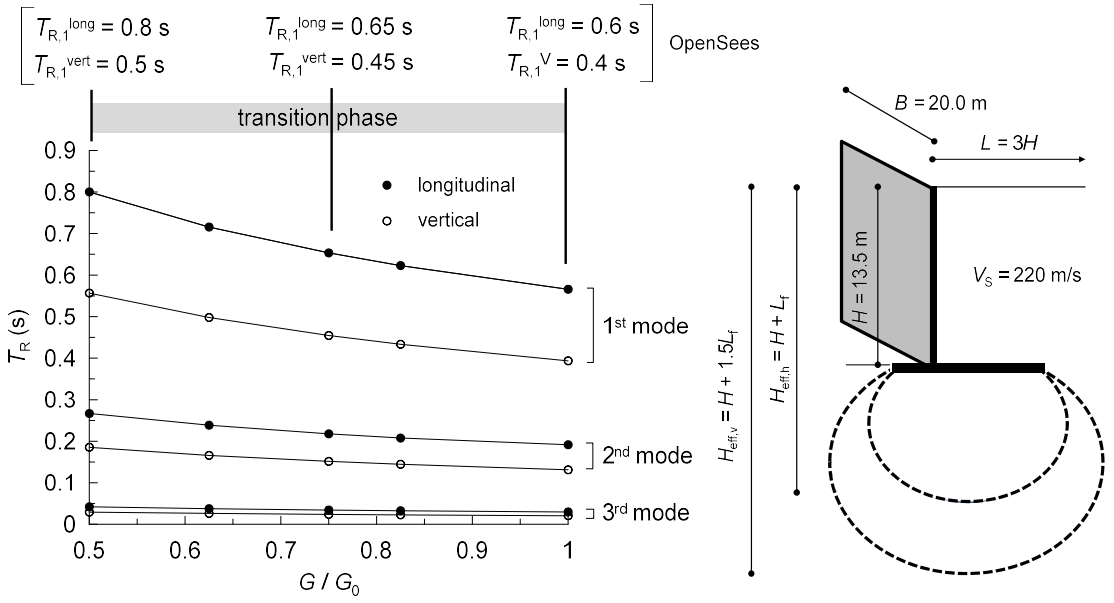

Figure 4.21: Analytical prediction of the dominant periods of the embankment, considering a reduction of the elastic moduli of 0.75, in the transition zone identified by the numerical results.

in Figure 4.21.

Chapter 5

A macro-element for bridge abutments

5.1 Conceptual framework

In the following, the effects of the soil-structure interaction occurring at the abutment locations are taken into account by introducing in the global structural model a macro-element representation of the soil-abutment system, leading to a drastic limitation of the degrees of freedom of the numerical models. The macro-element is aimed to reproduce the highly nonlinear interaction between the soil and the abutment under general multi-axial loading conditions. The force-displacement relationship of the model is elastic-plastic, derived from a rigorous thermodynamic approach. It is conceived to relate the forces Q_i exchanged at the deck-abutment contact to the corresponding displacements q_j through a second-order stiffness matrix H_{ij}:

$$Q_i = H_{ij} \cdot q_j. \tag{5.1}$$

In the model, the capacity of the soil-abutment system is described by a limit

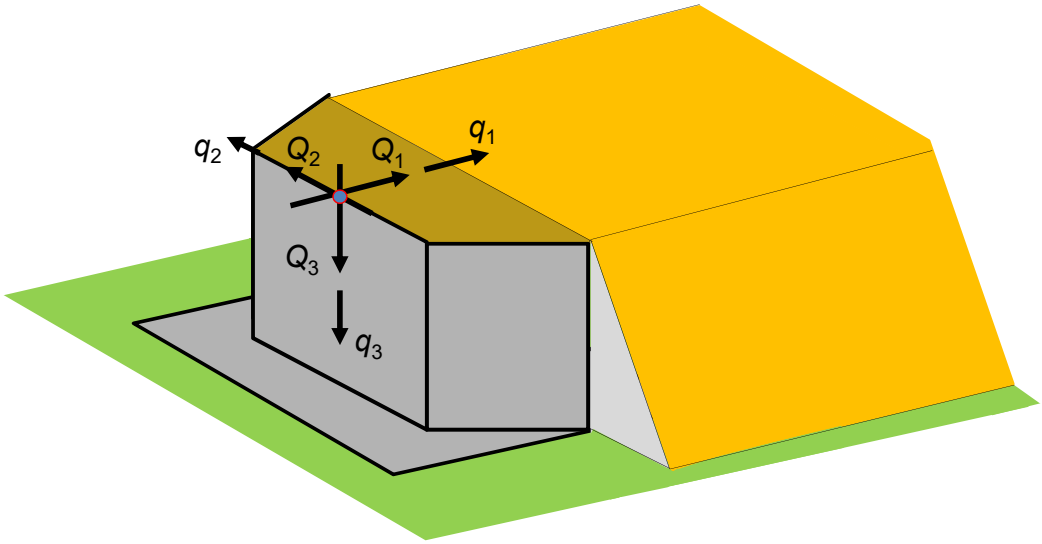

Figure 5.1: Forces Q_i and corresponding displacements q_i representing the significant degrees of freedom of the deck-abutment contact considered in the macro-element formulation.

surface in the force space, while the inertial effects are taken into account through the introduction of appropriate participating masses.

The physical quantities of the macro-element and their positive signs are depicted in Figure 5.1. The formulation is restricted to the significant degrees of freedom of the deck-abutment contact, that are the three interaction forces Q_i, $i = 1, 2, 3$, while the moment contribution is neglected for the following reasons. The moment Q_{r2} along the transverse axis 2 constitutes the main source of rotation for an abutment compared to the other components of moment. Nonetheless, the transmission of the moment Q_{r2} occurs only in the case of fully integral bridges. In such cases, the superstructure and the substructure are constructed monolithically, with no movement joints between spans and abutments, and the bridge movement is accommodated at the ends of the approach slabs. This structural solution can be used to minimise maintenance costs of the superstructure of the bridge but it is usually adopted for short-span bridges only, due to some issues mainly relative to soil-structure effects at

the abutments (concrete creep and shrinkage), temperature movements and attainment of the passive resistance under earthquake loads. The longitudinal moment Q_{r1} is produced by the tendency of the deck to rotate around the longitudinal axis. This leads to different forces transmitted to the bearing devices placed along the top of the central wall. Although always present in both seat-type girder bridges and integral bridges, this moment produces a much stiffer response compared to the moment Q_{r2} because its intensity is strongly controlled by the distance between the bearing devices that is however limited by the width of the deck. Moreover, these forces are further limited for seat-type girder bridges because the bearing devices represent unilateral constraints in the vertical direction and hence only vertical forces directed downwards can be transferred to the abutment. Finally, the moment around the vertical axis Q_{r3} is associated with the stiffest response of the abutment since it involves the torsional stiffness of the soil-abutment system, producing appreciable displacements only for very high skew angles between the deck and the abutment.

In the following, a brief introduction to the thermodynamic framework used to derive the macro-model is presented. Then, for the sake of clarity, the mathematical formulation is initially described for the one-dimensional case, for then developing the general multi-axial response. Finally, a calibration procedure of the macro-element is presented.

5.2 The thermodynamic approach

The constitutive law of the macro-element was derived within a rigorous and consistent framework based on what is often termed *generalised thermomechanics*, also known in soil mechanics as hyperplasticity (Collins and Houlsby, 1997). It places strong emphasis on the use of internal variables to describe the past history of the

material. The First and Second Laws of Thermodynamics are enforced directly in this formulation so that any model defined within this framework will automatically obey these laws. The use of this framework constitutes a first step forward with respect to the existing macro-element representations in geomechanics, leading to a more robust mathematical formulation with consistent deformation processes. A second advantage in using a thermodynamic approach is that the framework makes considerable use of potential functions, that is closely related to variational and extremum principles. In this light, the constitutive behaviour of a dissipative material can be completely defined through the specification of just two potential functions, with the incremental response being derived by application of standardized procedures. Hence the potentials are derived to obtain the dependent variables of the problem, thus the forces Q_i and the corresponding displacements q_i associated with the deck-abutment contact. In the following, the central aspects needed to develop an energetically compatible material are presented, specialising the entire framework, commonly defined for the element of volume, to the dissipative response of a macro-system.

The first potential is the energy function, conveniently expressed in terms of the Gibbs free energy g or the Helmholtz free energy f for a mechanical continuum, which are interchangeable state quantities related by the Legendre transformation. These functions derive from the First Law of Thermodynamics, which states that the rate of the internal energy $\dot{u}$ is equal to the sum of the heat flow $\dot{h}$ into the system from the surroundings and the mechanical power $\dot{w}$ also from the surroundings, thus

$$\dot{h} + \dot{w} = \dot{u}. \tag{5.2}$$

In applying thermodynamics to solids undergoing small strains, the rate of the mechanical work input can be written as $\dot{w} = Q_i \cdot \dot{q}_i$ and the heat supply to an element

of volume is $\dot{h} = -q_{k,k}$, with q_k the heat flux in the k direction (recall that the comma notation indicates a spatial differential). The internal energy can be expressed as a function of appropriately chosen internal variables. For thermomechanical continua, it can be convenient to consider the displacement vector q_i and entropy s as internal variables, thus $u = u(q_i, s)$. From the internal energy, other energy functions can be derived as different forms of the Legendre transform, namely the enthalpy h, the Helmholtz free energy f and the Gibbs free energy g. These functions are defined as follows

$$h(Q_i, s) = u - Q_i \cdot q_i \tag{5.3}$$

$$f(q_i, \vartheta) = u - s \cdot \vartheta \tag{5.4}$$

$$g(Q_i, \vartheta) = h - s \cdot \vartheta \tag{5.5}$$

where ϑ is the temperature. The important role of the energy functions is that they serve as a potential from which one can determine the reversible constitutive response of the material. In particular, from the above equations it can be noticed that the Helmholtz and Gibbs functions are related by the following expression of the Legendre transform

$$g(Q_i, \vartheta) + f(q_i, \vartheta) = Q_i \cdot q_i \tag{5.6}$$

which gives a clear physical interpretation of the two state quantities: the Helmholtz free energy represents the reversible mechanical work done in a deformation process, expressed in terms of displacements, and the Gibbs free energy is the complementary work. As an example, Figure 5.2 illustrates the two functions in a linear elastic

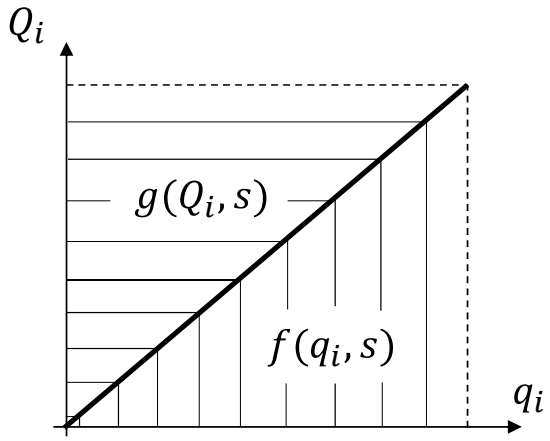

Figure 5.2: Helmholtz free energy $f(q_i, s)$ and Gibbs free energy $g(Q_i, s)$ for a linear elastic medium.

behaviour.

However, the response of a dissipative material depends not only on the current values of the state variables, such as the energy functions already introduced, but also on the history of the material state. The latter is encapsulated within certain internal variables α_i, which are tensorial in form. The internal variables of the model are passive variables in the transformation and, when there is no elastic-plastic coupling, play the role of plastic displacements. It follows that the internal energy $u(q_i, \alpha_i, s)$ is also a function of the internal variables, as well as for the other energy functions.

The second potential is either the dissipation function d or the yield function y, also in this case related by a specific form of the Legendre transformation. The Second Law states that there is a property s (the entropy) such that

$$\dot{s} \geq \left(\frac{q_k}{\vartheta}\right)_{,k} \tag{5.7}$$

and, developing the gradient of the entropy flux q_k/ϑ, Eq. 5.7 becomes

$$\vartheta \cdot \dot{s} + q_{k,k} - \frac{q_k \cdot \vartheta_{,k}}{\vartheta} \geq 0 \tag{5.8}$$

in which the first two terms $\vartheta \cdot \dot{s} + q_{k,k} = d$ are named mechanical dissipation, while the third term $q_k \cdot \vartheta_{,k}/\vartheta$ is the thermal dissipation. The latter is always non-negative because heat flux is always in the direction of the negative thermal gradient. This term becomes small by comparison with the first two for slow processes, so it is widely accepted that the two sources of dissipation must be non-negative

$$\vartheta \cdot \dot{s} + q_{k,k} = d \geq 0 \tag{5.9}$$

$$\frac{q_k \cdot \vartheta_{,k}}{\vartheta} \geq 0. \tag{5.10}$$

For a bridge, thermal effects derive mainly from temperature gradients in the structure, due to daily and seasonal cycles of temperature, but the thermal variations in the abutment and in the soil interacting with it do not affect sensibly the performance of the bridge. Hence, the thermal response is not taken into account in the formulation of the macro-element and the total dissipation coincides with the mechanical dissipation d. From the First Law, Eq. 5.2, and the definition of dissipation d, it follows that

$$\dot{u} = Q_i \cdot \dot{q}_i - q_{k,k} = Q_i \cdot \dot{q}_i + \vartheta \cdot \dot{s} - d. \tag{5.11}$$

The differential of $u = (q_i, \alpha_i, s)$ reads

$$\dot{u} = \frac{\partial u}{\partial q_i} \cdot \dot{q}_i + \frac{\partial u}{\partial \alpha_i} \cdot \dot{\alpha}_i + \frac{\partial u}{\partial s} \cdot \dot{s} \tag{5.12}$$

in which the quantity $\partial u/\partial \alpha_i$ represents the negative value of the so-called generalised force $\bar{\chi}_i$, by definition. Comparing Eq. 5.11 and Eq. 5.12, it follows that

$$d\left(q_i, \alpha_i, s, \dot{\alpha}_i\right) = \bar{\chi}_i \cdot \dot{\alpha}_i \tag{5.13}$$

which represents the mechanical power produced by the generalised force $\bar{\chi}_i$ in the plastic strain α_i. In general, the dissipation function results to be a function of the state of the material and also of the rate of change of state.

Equivalently to the definition of the generalised force $\bar{\chi}_i$, one can define a dissipative generalised force χ_i that is instead obtained by deriving the dissipation function. In this regard, it is worth clarifying the difference between the generalised force $\bar{\chi}_i$, the dissipative generalised force χ_i and their relation with the effective (or true) force Q_i. All these forces are obtained by deriving the potential functions as reported below

$$Q_i = -\frac{\partial f(q_i, \alpha_i)}{\partial q_i} \tag{5.14}$$

$$\bar{\chi}_i = -\frac{\partial f(q_i, \alpha_i)}{\partial \alpha_i} = -\frac{\partial g(Q_i, \alpha_i)}{\partial \alpha_i} \tag{5.15}$$

$$\chi_i = \frac{\partial d\left(q_i, \alpha_i, s, \dot{\alpha}_i\right)}{\partial \dot{\alpha}_i} \tag{5.16}$$

and, in general, $\bar{\chi}_i$ differs from χ_i. In fact, for a homogeneous first-order function, Euler's theorem gives

$$\frac{\partial d\left(q_i, \alpha_i, s, \dot{\alpha}_i\right)}{\partial \dot{\alpha}_i} \cdot \dot{\alpha}_i = \chi_i \cdot \dot{\alpha}_i = d \tag{5.17}$$

and comparing Eq. 5.11 with Eq. 5.17 the following expression holds

$$(\bar{\chi}_i - \chi_i) \cdot \dot{\alpha}_i = 0. \tag{5.18}$$

In general, the dissipative force can be a function of the rate of the internal variables, so that one can draw from Eq. 5.18 the conclusion that $(\bar{\chi}_i - \chi_i)$ is or-

thogonal to $\dot{\alpha}_i$; however, under the assumption that χ_i does not depend on $\dot{\alpha}_i$, hypothesis known as orthogonality principle (Ziegler 1977), the much stronger conclusion $\bar{\chi}_i = \chi_i$ can be made. The Ziegler's assumption was proved to provide realistic descriptions of the behaviour of many materials, especially those involving frictional dissipation.

As a consequence of the elastic-plastic uncoupling, Collins and Houlsby (1997) showed that, by a suitable choice of α_i, it is possible to write the Gibbs free energy as the sum of three terms

$$g(Q_i, \alpha_i) = g_1(Q_i) + g_2(\alpha_i) - Q_i \cdot \alpha_i \tag{5.19}$$

in which the only term that involves both Q_i and α_i is linear in α_i. Taking this one step further, differentiation of Eq. 5.15 gives

$$\bar{\chi}_i = -\frac{\partial g(Q_i, \alpha_i)}{\partial \alpha_i} = -\frac{\partial g_2(\alpha_i)}{\partial \alpha_i} + Q_i \tag{5.20}$$

from which it can be desumed that the generalised force differs from the true force Q_i only by the term $\rho_i = \partial g_2(\alpha_i)/\partial \alpha_i$, known as the back stress in conventional constitutive modelling. In kinematic hardening plasticity, the back stress ρ_i is associated with the coordinates of the center of the yield surface in the space of the forces. As an example, Figure 5.3 shows an elastic-plastic response (St. Venant model) with kinematic hardening represented in true space and in generalised stress space.

The macro-element of bridge abutments was formulated as a rate-independent macro-material, because mainly aimed to reproduce the behaviour of the system under seismic conditions. Under this assumption, the dissipation function must be a homogeneous first-order function in the rates $\dot{\alpha}_i$ because the magnitude of dissipated energy must be directly proportional to the magnitude of deformation.

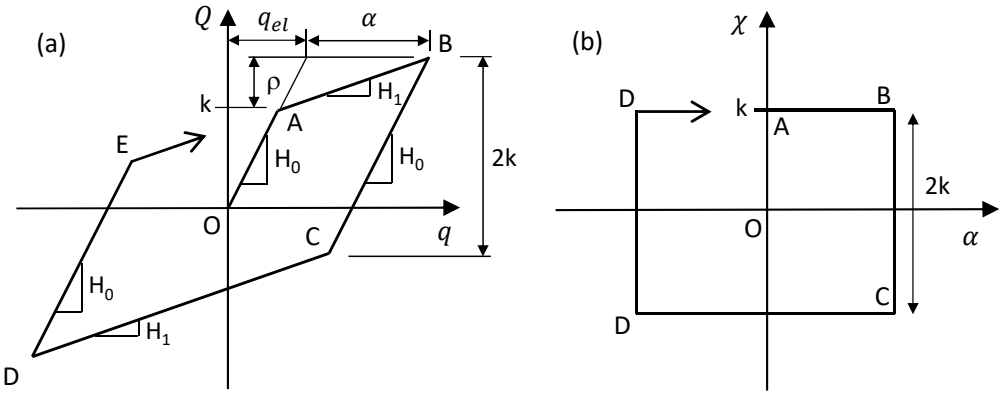

Figure 5.3: Cyclic stress-strain behaviour of an elastic-perfectly plastic material with linear hardening in true stress space (a) and in generalised stress space (b).

The formulation was completed by the Ziegler's orthogonality principle (1977), which is equivalent to the assumption $\bar{\chi}_i = \chi_i$. In this way, the dissipation function acts as a potential, so that the dissipative generalised force is orthogonal to level surfaces of the dissipation. This principle can be viewed as a stronger statement than the Second Law of Thermodynamics: the Second Law requires that energy be dissipated whereas the orthogonality principal requires dissipation to be maximal. The dissipative response of the macro-element was reproduced by a series of yield surfaces with kinematic hardening that evolve in the plastic domain of the model, bounded by a limit locus of ultimate loads and by the innermost surface of first yield. The generic yield surface y_n appears in the following form

$$y_n = y_n\left(\alpha_i, \chi_i\right) = 0 \tag{5.21}$$

with no dependence on the true force Q_i in virtue of the associativity of the plastic flow (Houlsby and Puzrin, 2006). In general, in fact, the rate of the plastic displacement $\dot{\alpha}_i$ can be determined from the flow rule

$$\dot{\alpha}_i = \lambda_n \cdot \frac{\partial y_n \left(Q_i, \alpha_i, \chi_i\right)}{\partial \chi_i} \tag{5.22}$$

and the plastic flow is said associated in the generalised stress space but not in the true stress space. Under the orthogonality assumption, $\bar{\chi}_i = \chi_i = -\partial g(Q_i, \alpha_i)/\partial \alpha_i$, the yield function can be also represented in the true stress space as follows

$$y_n^* = y_n \left[\alpha_i, \chi_i \left(Q_i, \alpha_i\right)\right] = y_n^* \left(Q_i, \alpha_i\right) = 0. \tag{5.23}$$

Differentiating y_n^*, after some manipulation one can obtain

$$\frac{\partial y_n}{\partial Q_i} \cdot dQ_i + \frac{\partial y_n}{\partial \alpha_i} \cdot d\alpha_i + \frac{\partial y_n}{\partial \chi_i} \cdot d\chi_i =$$

$$= \frac{\partial y_n^*}{\partial Q_i} \cdot dQ_i + \frac{\partial y_n^*}{\partial \alpha_i} \cdot d\alpha_i \tag{5.24}$$

and equating terms in dQ_i then gives

$$\frac{\partial y_n}{\partial Q_i} + \frac{\partial y_n}{\partial \chi_i} = \frac{\partial y_n^*}{\partial Q_i}. \tag{5.25}$$

If $\partial y_n/\partial Q_i = 0$, from Eq. 5.25 follows that $\partial y_n/\partial \chi_i = \partial y_n^*/\partial Q_i$ and consequently the plastic displacement increments are associated in the conventional sense, thus both in true and generalised force spaces. The choice of an associative flow rule was dictated by the lack of experimental evidences on the development of irreversible displacements of bridge abutments under multi-axial loading conditions. As mentioned before, the yield surface can be determined from dissipation through a specific expression of the Legendre transform and vice versa, that reads

$$w_n = \chi_i \cdot \dot{\alpha}_i - d = 0. \tag{5.26}$$

Since $w_n = 0$, it can be determined only to within an arbitrary multiplicative constant. Therefore, it is convenient to decompose w_n as $w_n = \lambda_n \cdot y_n = 0$, where λ_n is an arbitrary non-negative multiplier, called plastic multiplier. Note that this biunivocal relationship is valid only for a material with uncoupled elastic-plastic response.

Once the analytical expressions for the energy and dissipation functions are defined, the constitutive laws can be obtained through standardised procedures. This has the great advantage that all the salient aspects of the response can be included in the potentials in an energetically compatible form with constitutive relations that follow the structure of conventional plasticity. The formal expressions for the dependent variables used in the following are reported below

$$q_i = -\frac{\partial g(Q_i, \alpha_i)}{\partial Q_i} \tag{5.27}$$

$$Q_i = \frac{\partial f(q_i, \alpha_i)}{\partial q_i} \tag{5.28}$$

$$\bar{\chi}_i = -\frac{\partial g(Q_i, \alpha_i)}{\partial Q_i} = -\frac{\partial f(q_i, \alpha_i)}{\partial \alpha_i} \tag{5.29}$$

$$\chi_i = \frac{\partial d(q_i, \alpha_i)}{\partial \dot{\alpha}_i} \tag{5.30}$$

$$\dot{\alpha}_i = \lambda_n \cdot \frac{\partial y_n \left(Q_i, \alpha_i, \chi_i\right)}{\partial \chi_i}. \tag{5.31}$$

5.3 One-dimensional formulation

The macro-element was formulated within the multi-surface plasticity theory with

constitutive relations derived according to the thermodynamic approach described in Section 5.2. Although not strictly necessary in the one-dimensional version (1D model), for the sake of clarity the model is presented following the same thermodynamic structure used for the general multi-axial formulation, regarding the 1D model as a degenerate case of the latter.

The one-dimensional representation of the macro-element is depicted in Figure 5.4. The model represents an extension of the well-known Iwan model (Iwan 1967) and consists of a series connection of devices with different properties that provide the elastic-plastic response. The elastic spring with stiffness $H^{(0)}$, named spring 0, represents essentially the response of the soil-abutment system at small strain levels. A set of sliders, each connected in parallel with a spring, gives the plastic behaviour with kinematic hardening. The R device incorporates the ratcheting phenomenon into the plastic response of the model, as proposed by Houlsby et al. (2017) for deep foundations: it is conceived as a small increment of the total plastic displacement occurring when the model undergoes loading and unloading cycles induced by a non-symmetric external perturbation (force or displacement). In order to account for the salient aspects of the soil-abutment interaction, two significant modifications were introduced with respect to the original Iwan model: a dissymmetric behaviour of the sliders and an inertial response. The former is a crucial feature to capture the dependence of the abutment capacity on the load direction. In the longitudinal direction, for example, the abutment exhibits a different strength in compression and extension, which is associated with the attainment of the passive and active resistance in the backfill, respectively. The inertial response, instead, is intended to reproduce the inertial effects that arise in the part of the embankment interacting dynamically with the wall and that are transferred to the superstructure of the bridge, which have been already discussed in Chapter 4. This is achieved through the introduction of some participating masses of the embankment that are, in principle,

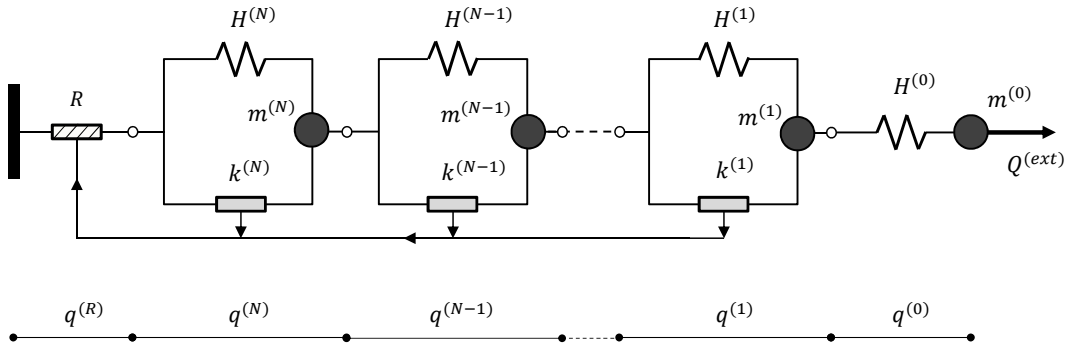

Figure 5.4: Inertial multi-surface plasticity model with kinematic hardening

associated with each plastic flow.

The model is expressed in terms of conjugate forces and displacements acting on the top of the central wall of the abutment. Note that the displacements are referred to an initial condition of the system at rest in which all the internal devices are overlapped. In this way, the elongations of the devices correspond to the respective displacements. The physical quantities involved in the model and the relative dimensions are reported here below:

- external force

$$[Q^{(ext)}] = [F] = [M \cdot L \cdot T^{-2}]$$

- internal force in the spring 0

$$[Q^{(0)}] = [F] = [M \cdot L \cdot T^{-2}]$$

- internal force in the n-th combined spring-slider device

$$[Q^{(n)}] = [F] = [M \cdot L \cdot T^{-2}], n = 1, ..., N$$

- total displacement

$$[q] = [L]$$

- elongation of the spring 0

$$[q^{(0)}] = [L]$$

- elongation of the n-th slider (equal to the elongation of the spring in parallel)

$$[q^{(n)}] = [L], n = 1, ..., N.$$

- elongation of the ratcheting device

$$[q^{(R)}] = [L]$$

- mass associated with the sping 0

$$[m^{(0)}] = [M]$$

- mass associated with the n-th combined spring-slider device

$$[m^{(n)}] = [M], n = 1, ..., N$$

- stiffness of the spring 0

$$[H^{(0)}] = [F \cdot L^{-1}] = [M \cdot T^{-2}]$$

- stiffness of the n-th spring

$$[H^{(n)}] = [F \cdot L^{-1}] = [M \cdot T^{-2}], n = 1, ..., N$$

- strength of the n-th slider

$$[k^{(n)}] = [F] = [M \cdot L \cdot T^{-2}], n = 1, ..., N.$$

In virtue of the elastic-plastic uncoupling, the plastic deformations $q^{(n)}$ play exactly the role of the internal variables $\alpha^{(n)}$ of the model. The ratcheting device computes the rate of the ratcheting displacement as a function of the rate of the plastic displacements developing in the sliders through n factors $R^{(n)}$ (Houslby et al. 2017), as reported below

$$\dot{\alpha}^{(R)} = S\left(Q^{(ext)}\right) \cdot \sum_{n=1}^{N} R^{(n)} \cdot \dot{\alpha}^{(n)} \tag{5.32}$$

in which $S\left(Q^{(ext)}\right)$ is a modified signum function that allows to develop ratcheting only under nonsymmetric external perturbations

$$S\left(Q^{(ext)}\right) = \begin{cases} 1, Q^{(ext)} > 0 \\ 0, Q^{(ext)} = 0 \\ -1, Q^{(ext)} < 0 \end{cases} . \tag{5.33}$$

This is a simplified, although general, strategy to reproduce ratcheting in the cyclic response of abutments: an additional ratcheting displacement develops during loading and unloading cycles with a rate of accumulation that, as a first approximation, can be considered not dependent on the strain level, thus $R^{(n)}$ are constant values, or that can reduce gradually as the number of cycles increases, $R^{(n)}$ taken as a function of the plastic displacements $\alpha^{(n)}$. For a bridge abutment, however, the dissymmetry of the displacement field is mainly caused by the peculiar geometry of the system rather than the ratcheting phenomenon. For this reason, in the present formulation the parameters $R^{(n)}$ were assumed constant during cycles.

5.3.1 Balance and compatibility

The global balance equation reads:

$$Q^{(ext)} + Q^{(M,0)} + \sum_{1}^{N} Q^{(M,n)} + Q^{(int)} = 0 \tag{5.34}$$

in which the external force $Q^{(ext)}$ and the sum of the inertial forces $Q^{(M,n)}$ developing in the masses are equilibrated by the internal force $Q^{(int)}$ acting in the fixed node of the model. It is worth noticing that the inertial forces $Q^{(M,n)}$ alter the forces $Q^{(n)}$ in the internal devices according to the following local balance equation of the

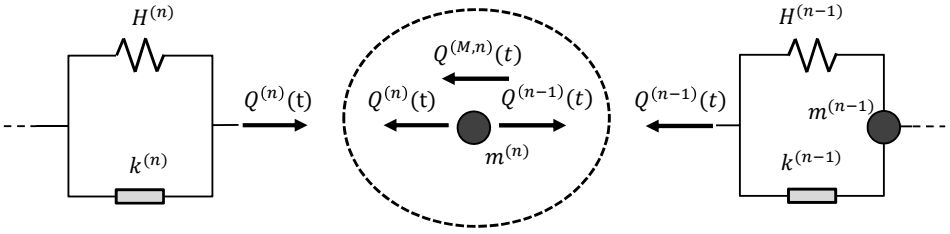

Figure 5.5: Local equilibrium of the one-dimensional macro-element

n-th mass

$$Q^{(M,n)} = Q^{(n-1)} - Q^{(n)}, n = 1, .., N \tag{5.35}$$

in which the force acting in the n-th device is equal to

$$Q^{(n)} = k^{(n)} + H^{(n)} \cdot \alpha^{(n)}, n = 1, .., N. \tag{5.36}$$

Eqs. 5.35 and 5.36 describe the internal equilibrium of the macro-element, schematically illustrated in Figure 5.5. It is worth noticing that the strength $k^{(n)}$ represents the dissipative force $\chi^{(n)}$ while $H^{(n)} \cdot \alpha^{(n)}$ is the back stress ratio.

This implies that, when the external perturbation is able to excite the masses in the model, the forces acting on the two end nodes of the macro-element are different.

Compatibility is expressed by the following equation

$$q = q^{(0)} + \sum_{1}^{N} q^{(n)} + q^{(R)} = \sum_{0}^{N} q^{(n)} + q^{(R)} \tag{5.37}$$

with the total displacement q obtained as the sum of the elongations of the linear and nonlinear internal devices, $q^{(0)}$ and $\sum_1^N q^{(n)} + q^{(R)}$ respectively.

5.4 Energy function

The energy function represents the work done by the system, which can be expressed in terms of displacements (Helmholtz free energy) or forces (Gibbs free energy). The two state functions are determined initially through the definition of the mechanical work and then, as a verification, through the application of the Legendre transform.

The elastic contribution to the total work is due to the elongation of the elastic spring 0 and it can be computed by the following quadratic form

$$L^{(0)}\left(q^{(0)}\right) = \int_0^{q^{(0)}} Q^{(0)} \cdot dq = \int_0^{q^{(0)}} H^{(0)} \cdot q^{(0)} \cdot dq = \frac{1}{2} \cdot H^{(0)} \cdot \left(q^{(0)}\right)^2 \tag{5.38}$$

or expressed as a function of the generalized forces

$$L^{(0)}\left(Q^{(0)}\right) = \frac{1}{2} \cdot C^{(0)} \cdot Q^{(0)2} \tag{5.39}$$

in which $C^{(0)} = H^{(0)-1}$.

When the strength of the n-th slider is attained, the internal force, equal to $k^{(n)}$, works in the sliding $\alpha^{(n)}$, giving the following plastic work

$$L^{(k,n)} = \int_0^{\alpha^{(n)}} Q^{(n)} \cdot dq = Q^{(n)} \cdot \alpha^{(n)} = k^{(n)} \cdot \alpha^{(n)} \tag{5.40}$$

which can be easily extended to the work done by the entire set of N sliders

$$\sum_{n=1}^{N} L^{(k,n)} = \sum_{n=1}^{N} k^{(n)} \cdot \alpha^{(n)}. \tag{5.41}$$

The work produced during the compression and elongation of the springs in parallel to the sliders is conceptually analogous to Eq. 5.38, thus

$$L^{(H,n)} = \int_0^{\alpha^{(n)}} Q^{(n)} \cdot dq = \int_0^{\alpha^{(n)}} H^{(n)} \cdot q^{(n)} \cdot dq = \frac{1}{2} \cdot H^{(n)} \cdot \alpha^{(n)2} \tag{5.42}$$

$$\sum_{n=1}^{N} L^{(H,n)} = \frac{1}{2} \cdot \sum_{n=1}^{N} H^{(n)} \cdot \alpha^{(n)2}. \tag{5.43}$$

The work done by the "ratcheting" force is simply

$$L^{(R)} = \int_0^{\alpha^{(R)}} Q^{(R)} \cdot dq = Q^{(R)} \cdot \alpha^{(R)}. \tag{5.44}$$

The inertial force $Q^{(M,n)}$ that develops in the n-th mass works in the respective absolute displacement $\sum_{h=n}^{N} q^{(h)}$. The expression of the work reads

$$L^{(M,n)} = \int_0^{\sum_{h=n}^{N} q^{(h)}} Q^{(M,n)} \cdot dq = \int_0^{\sum_{h=n}^{N} q^{(h)}} m^{(n)} \cdot \ddot{q} \cdot dq =$$

$$= \int_0^{\sum_{h=n}^{N} q^{(h)}} m^{(n)} \cdot \dot{q} \cdot d\dot{q} = \frac{1}{2} \cdot m^{(n)} \cdot \left(\sum_{h=n}^{N} \dot{q}^{(h)} \right)^2 \tag{5.45}$$

which represents the kinetic energy of the n-th material point. It is important to note that the work done by the n-th inertial force is a function of the absolute velocity of that point $\sum_{h=n}^{N} \dot{q}^{(h)}$, that is obtained as the sum of the motion of the devices behind the mass under examination. The sum of the "inertial" works is straightforward

$$\sum_{n=0}^{N} L^{(M,n)} = \frac{1}{2} \cdot \sum_{n=0}^{N} m^{(n)} \cdot \left(\sum_{h=n}^{N} \dot{q}^{(h)} \right)^2 \tag{5.46}$$

in which the summation starts from $n = 0$ because it includes the response of the mass associated with the elastic spring 0. Separating the elastic displacements from the plastic displacements, Eq. 5.46 reads

$$\sum_{n=0}^{N} L^{(M,n)} = \frac{1}{2} \cdot m^{(0)} \cdot \dot{q}^2 + \frac{1}{2} \cdot \sum_{n=1}^{N} m^{(n)} \cdot \left(\sum_{h=n}^{N} \dot{\alpha}^{(h)} \right)^2 \tag{5.47}$$

and, by introducing Eq. 5.37 in the definition of the total displacement q, the inertial work can be further developed as follows

$$\sum_{n=0}^{N} L^{(M,n)} = \frac{1}{2} \cdot m^{(0)} \cdot \left(\dot{q}^{(0)} + \sum_{n=1}^{N} \dot{\alpha}^{(n)} \right)^2 + \frac{1}{2} \cdot \sum_{n=1}^{N} m^{(n)} \cdot \left(\sum_{h=n}^{N} \dot{\alpha}^{(h)} \right)^2 =$$

$$= \frac{1}{2} \cdot m^{(0)} \cdot \left(\frac{\dot{Q}^{(0)}}{H_0} + \sum_{n=1}^{N} \dot{\alpha}^{(n)} \right)^2 + \frac{1}{2} \cdot \sum_{n=1}^{N} m^{(n)} \cdot \left(\sum_{h=n}^{N} \dot{\alpha}^{(h)} \right)^2 \tag{5.48}$$

in which the elastic elongation was expressed as $q^{(0)} = Q^{(0)}/H_0$. The convenience of the above expression will become apparent later. This work can be used to derive the Helmholtz free energy while the complementary work $L_{comp}^{(M,n)}\left(Q^{(M,n)}\right)$, needed to determine the Gibbs free energy, can be computed by using the Legendre transform in Eq. 5.49.

$$\sum_{n=0}^{N} L_{comp}^{(M,n)} = \sum_{n=0}^{N} Q^{(M,n)} \cdot \sum_{h=n}^{N} q^{(h)} - \sum_{n=0}^{N} L^{(M,n)} \tag{5.49}$$

With some further development, the complementary work can be written as a function of the elastic displacement and of the internal variables describing the plastic deformation as follows

$$\sum_{n=0}^{N} L_{comp}^{(M,n)} = \sum_{n=0}^{N} m^{(n)} \cdot \sum_{h=n}^{N} \ddot{q}^{(h)} \cdot \sum_{k=n}^{N} q^{(k)} - \frac{1}{2} \cdot \sum_{n=0}^{N} m^{(n)} \cdot \left(\sum_{h=n}^{N} \dot{q}^{(h)} \right) =$$

$$= m^{(0)} \cdot \ddot{q}^{(0)} \cdot q^{(0)} + \sum_{n=1}^{N} m^{(n)} \cdot \sum_{h=n}^{N} \ddot{\alpha}^{(h)} \cdot \sum_{k=n}^{N} \alpha^{(k)} -$$

$$-\frac{1}{2}\cdot m^{(0)}\cdot\left(\dot{q}^{(0)}\right)^2-\frac{1}{2}\cdot\sum_{n=1}^{N}m^{(n)}\cdot\left(\sum_{h=n}^{N}\dot{\alpha}^{(h)}\right)^2. \tag{5.50}$$

As done in Eq. 5.48, the reversible contribution can be further rewritten in terms of the elastic force $Q^{(0)}$

$$\sum_{n=0}^{N}L_{comp}^{(M,n)}=m^{(0)}\cdot\left(\frac{\ddot{Q}^{(0)}}{H^{(0)}}+\sum_{n=1}^{N}\ddot{\alpha}^{(n)}\right)\cdot\left(\frac{Q^{(0)}}{H^{(0)}}+\sum_{n=1}^{N}\alpha^{(n)}\right)+$$

$$+\sum_{n=1}^{N}m^{(n)}\cdot\sum_{h=n}^{N}\ddot{q}^{(h)}\cdot\sum_{k=n}^{N}q^{(k)}-\frac{1}{2}\cdot m^{(0)}\cdot\left(\dot{q}^{(0)}\right)^2-\frac{1}{2}\cdot\sum_{n=1}^{N}m^{(n)}\cdot\left(\sum_{h=n}^{N}\dot{\alpha}^{(h)}\right)^2. \tag{5.51}$$

5.4.1 Gibbs free energy

The Gibbs free energy can be obtained as the sum of the works determined above, expressed in terms of internal forces $Q^{(j)}$ and internal variables $\alpha^{(n)}$

$$g(Q^{(j)},\alpha^{(n)},m^{(j)})=-L^{(0)}\left(Q^{(0)}\right)-\sum_{n=1}^{N}L^{(k,n)}(Q^{(n)},\alpha^{(n)})+$$

$$+\sum_{n=1}^{N}L^{(H,n)}(Q^{(n)},\alpha^{(n)})-L^{(R)}(Q^{(n)},\alpha^{(n)})-\sum_{n=0}^{N}L^{(M,n)}(Q^{(j)},\alpha^{(n)},m^{(n)}). \tag{5.52}$$

Note that the Gibbs free energy of the macro-element is also a function of the masses $m^{(n)}$ included in the inertial work $L^{(M,n)}(Q^{(j)},\alpha^{(n)},m^{(n)})$. By introducing Eqs. 5.39, 5.41, 5.43, 5.44 and 5.48 into Eq. 5.52, this becomes

$$g(Q^{(j)},\alpha^{(n)},m^{(n)})=-\frac{1}{2\cdot H^{(0)}}\cdot\left(Q^{(0)}\right)^2-\sum_{n=1}^{N}Q^{(n)}\cdot\alpha^{(n)}+\frac{1}{2}\cdot\sum_{n=1}^{N}H^{(n)}\cdot\left(\alpha^{(n)}\right)^2-$$

$$-Q^{(R)}\cdot\alpha^{(R)}-m^{(0)}\cdot\left(\frac{\ddot{Q}^{(0)}}{H^{(0)}}+\sum_{n=1}^{N}\ddot{\alpha}^{(n)}\right)\cdot\left(\frac{Q^{(0)}}{H^{(0)}}+\sum_{n=1}^{N}\alpha^{(n)}\right)-$$

$$-\sum_{n=1}^{N}m^{(n)}\cdot\sum_{h=n}^{N}\ddot{\alpha}^{(h)}\cdot\sum_{k=n}^{N}\alpha^{(k)}+\frac{1}{2}\cdot m^{(0)}\cdot\left(\frac{\dot{Q}_0}{H_0}+\sum_{j=1}^{N}\dot{\alpha}^{(j)}\right)^2+$$

$$+\frac{1}{2}\cdot\sum_{n=1}^{N}m^{(n)}\cdot\left(\sum_{j=n}^{N}\dot{\alpha}^{(j)}\right)^2 \tag{5.53}$$

or, equivalently, it can be written in a more compact form as follows

$$g(Q^{(j)},\alpha^{(n)},m^{(n)})=-\frac{1}{2\cdot H^{(0)}}\cdot\left(Q^{(0)}\right)^2-\sum_{n=1}^{N}Q^{(n)}\cdot\alpha^{(n)}+$$

$$+\frac{1}{2}\cdot\sum_{n=1}^{N}H^{(n)}\cdot\left(\alpha^{(n)}\right)^2-Q^{(R)}\cdot\alpha^{(R)}-\sum_{n=0}^{N}m^{(n)}\cdot\sum_{h=n}^{N}\ddot{q}^{(h)}\cdot\sum_{k=n}^{N}q^{(k)}+$$

$$+\frac{1}{2}\cdot\sum_{n=0}^{N}m^{(n)}\cdot\left(\sum_{j=n}^{N}\dot{q}^{(j)}\right)^2. \tag{5.54}$$

As already discussed in Section 5.2, for an uncoupled material the Gibbs free energy can be rearranged as the sum of three terms

$$g(Q^{(j)},\alpha^{(n)},m^{(n)})=g_1(Q^{(j)},0,m^{(n)})+g_2(0,\alpha^{(n)},m^{(n)})-Q^{(n)}\cdot\alpha^{(n)} \tag{5.55}$$

$$g_1(Q^{(j)},0,m^{(n)})=-\frac{1}{2\cdot H^{(0)}}\cdot\left(Q^{(0)}\right)^2 \tag{5.56}$$

$$g_2(0,\alpha^{(n)},m^{(n)})=\frac{1}{2}\cdot\sum_{n=1}^{N}H^{(n)}\cdot\left(\alpha^{(n)}\right)^2-\sum_{n=0}^{N}m^{(n)}\cdot\sum_{h=n}^{N}\ddot{q}^{(h)}\cdot\sum_{k=n}^{N}q^{(k)}+$$

$$+\frac{1}{2}\cdot\sum_{n=0}^{N} m^{(n)}\cdot\left(\sum_{j=n}^{N}\dot{q}^{(j)}\right)^{2}. \tag{5.57}$$

In particular, the term $g_2(0,\alpha^{(n)},m^{(n)})$ is a function of the history of load through the plastic displacements $\alpha^{(n)}$ and therefore it confers kinematic hardening to the plastic response of the macro-element. This decomposition will appear particularly useful in deriving the incremental response of the model.

Moreover, the inertial terms, related to the dynamic response of the masses, can be collected into an inertial function

$$g_{in}(Q^{(j)},\alpha^{(n)},m^{(n)}) = -\sum_{n=0}^{N} m^{(n)}\cdot\sum_{h=n}^{N}\ddot{q}^{(h)}\cdot\sum_{k=n}^{N} q^{(k)}+\frac{1}{2}\cdot\sum_{n=0}^{N} m^{(n)}\cdot\left(\sum_{j=n}^{N}\dot{q}^{(j)}\right)^{2} \tag{5.58}$$

and Eq. 5.54 simply reads

$$g(Q^{(j)},\alpha^{(n)},m^{(n)}) = g_{st}(Q^{(j)},\alpha^{(n)},0)+g_{in}(Q^{(j)},\alpha^{(n)},m^{(n)}) \tag{5.59}$$

as the sum of the inertial function and of the so-called "static" energetic contribution $g_{st}(Q^{(j)},\alpha^{(n)},0)$. The latter is a frequency-independent quantity composed of the non-inertial terms

$$g_{st}(Q^{(j)},\alpha^{(n)},0) = -\frac{1}{2\cdot H^{(0)}}\cdot\left(Q^{(0)}\right)^{2}-\sum_{n=1}^{N} Q^{(n)}\cdot\alpha^{(n)}+$$

$$+\frac{1}{2}\cdot\sum_{n=1}^{N} H^{(n)}\cdot\left(\alpha^{(n)}\right)^{2}-Q^{(R)}\cdot\alpha^{(R)} \tag{5.60}$$

which is exactly the Gibbs function of the classical Iwan model.

5.4.2 Helmholtz free energy

The Helmholtz free energy represents the elastic mechanical work of the system expressed in terms of displacements $q^{(n)}$

$$f(q^{(j)}, \alpha^{(n)}, m^{(n)}) = L_{comp}(q^{(j)}, \alpha^{(n)}, m^{(n)}) = \frac{1}{2} \cdot H^{(0)} \cdot \left(q^{(0)}\right)^2 +$$

$$+\frac{1}{2} \cdot \sum_{n=1}^{N} H^{(n)} \cdot \left(\alpha^{(n)}\right)^2 + \frac{1}{2} \cdot \sum_{n=0}^{N} m^{(n)} \cdot \left(\sum_{h=n}^{N} \dot{q}_j^{(h)}\right)^2 . \tag{5.61}$$

In order to find and explicit expression of the Helmholtz function in the total displacement q, Eq. 5.61 can be written as

$$f(q^{(j)}, \alpha^{(n)}, m^{(n)}) = \frac{1}{2} \cdot H^{(0)} \cdot \left(q - \sum_{n=1}^{N} \alpha^{(n)} - \alpha^{(R)}\right)^2 + \frac{1}{2} \cdot \sum_{n=1}^{N} H^{(n)} \cdot \left(\alpha^{(n)}\right)^2 +$$

$$+\frac{1}{2} \cdot m^{(0)} \cdot q^2 + \frac{1}{2} \cdot \sum_{n=1}^{N} m^{(n)} \cdot \left(\sum_{h=n}^{N} \dot{\alpha}_j^{(h)}\right)^2 . \tag{5.62}$$

As done for the Gibbs free energy, also the Helmholtz free energy is the sum of a frequency-independent term $f_{st}(q^{(j)}, \alpha^{(n)}, 0)$ and of an inertial function $f_{in}(q^{(j)}, \alpha^{(n)}, m^{(n)})$

$$f(q^{(j)}, \alpha^{(n)}, m^{(n)}) = f_{st}(q^{(j)}, \alpha^{(n)}, 0) + f_{in}(q^{(j)}, \alpha^{(n)}, m^{(n)}) \tag{5.63}$$

with

$$f_{st}(q^{(j)}, \alpha^{(n)}, 0) = \frac{1}{2} \cdot H^{(0)} \cdot \left(q - \sum_{n=1}^{N} \alpha^{(n)} - \alpha^{(R)}\right)^2 + \frac{1}{2} \cdot \sum_{n=1}^{N} H^{(n)} \cdot \left(\alpha^{(n)}\right)^2 \tag{5.64}$$

$$f_{in}(q^{(j)},\alpha^{(n)},m^{(n)}) = \frac{1}{2}\cdot m^{(0)}\cdot q^2 + \frac{1}{2}\cdot\sum_{n=1}^{N} m^{(n)}\cdot\left(\sum_{h=n}^{N}\dot{\alpha}_j^{(h)}\right)^2. \tag{5.65}$$

As a verification, the Helmholtz free energy is now derived by applying the Legendre transform as reported below

$$f(q^{(j)},\alpha^{(n)},m^{(n)}) = g(Q^{(j)},\alpha^{(n)},m^{(n)}) + Q^{(j)}\cdot q^{(j)} =$$

$$= -\frac{1}{2\cdot H^{(0)}}\cdot\left(Q^{(0)}\right)^2 - \sum_{n=1}^{N} Q^{(n)}\cdot\alpha^{(n)} + \frac{1}{2}\cdot\sum_{n=1}^{N} H^{(n)}\cdot\left(\alpha^{(n)}\right)^2 -$$

$$-Q^{(R)}\cdot\alpha^{(R)} - \sum_{n=0}^{N} m^{(n)}\cdot\sum_{h=n}^{N}\ddot{q}^{(h)}\cdot\sum_{k=n}^{N} q^{(k)} + \frac{1}{2}\cdot\sum_{n=0}^{N} m^{(n)}\cdot\left(\sum_{j=n}^{N}\dot{q}^{(j)}\right)^2 +$$

$$+Q^{(0)}\cdot q^{(0)} + \sum_{n=1}^{N} Q^{(n)}\cdot\alpha^{(n)} +$$

$$+Q^{(R)}\cdot\alpha^{(R)} + \sum_{n=0}^{N} Q^{(M,n)}\cdot\sum_{h=n}^{N} q^{(h)} =$$

$$= \frac{1}{2}\cdot H^{(0)}\cdot\left(q^{(0)}\right)^2 + \frac{1}{2}\cdot\sum_{n=1}^{N} H^{(n)}\cdot\left(\alpha^{(n)}\right)^2 -$$

$$-\sum_{n=0}^{N} m^{(n)}\cdot\sum_{h=n}^{N}\ddot{q}^{(h)}\cdot\sum_{k=n}^{N} q^{(k)} + \frac{1}{2}\cdot\sum_{n=0}^{N} m^{(n)}\cdot\left(\sum_{j=n}^{N}\dot{q}^{(j)}\right)^2 +$$

$$+\sum_{n=0}^{N} m^{(n)}\cdot\sum_{h=n}^{N}\ddot{q}^{(h)}\cdot\sum_{k=n}^{N} q^{(k)} =$$

$$= \frac{1}{2} \cdot H^{(0)} \cdot \left(q - \sum_{n=1}^{N} \alpha^{(n)} - \alpha^{(R)} \right)^2 + \frac{1}{2} \cdot \sum_{n=1}^{N} H^{(n)} \cdot \left(\alpha^{(n)} \right)^2 +$$

$$+ \frac{1}{2} \cdot \sum_{n=0}^{N} m^{(n)} \cdot \left(\sum_{j=n}^{N} \dot{q}^{(j)} \right)^2 \tag{5.66}$$

obtaining again the expression found in Eq. 5.61.

5.5 Dissipative response

5.5.1 Yield functions

The second potential is the dissipation function or, equivalently, the yield function. In this model, the former was derived from the specific function adopted to describe the yield surfaces of the soil-abutment system. This procedure was particularly useful to derive the dissipative response of the multi-axial macro-element but it has some advantages also in the one-dimensional case. The macro-element is a multi-surface plasticity model with pure kinematic hardening. In the one-dimensional problem, the n-th yield function $y^{(n)}$ represents simply a plastic threshold that increases from the first yield, $n = 1$, to the last yield $n = N$, the latter representing the ultimate condition of the soil-abutment system.

When the sliders exhibit a symmetric behaviour, the dissipative part of the model degenerates in the well-known Iwan model and, for this case, Houlsby et al. (2017) determined the analytical expression for the yield functions

$$y^{(n)}(Q^{(ext)}, \alpha^{(n)}, \chi^{(n)}) = \left|\chi^{(n)}\right| - k^{(n)} + R^{(n)} \cdot (\left|\chi^{(R)}\right| - \left|\chi^{(n)}\right|) = 0, n = 1, ..., N \tag{5.67}$$

in which $\chi^{(n)}$ and $\chi^{(R)}$ are the dissipative forces in the n-th slider and in the

ratcheting device, respectively, and $R^{(n)}$ is the ratcheting factor (Eq. 5.32).

In the macro-element of abutment, however, the sliders present a non-symmetric behaviour, with strength in compression $k_+^{(n)}$ different from that in extension $k_-^{(n)}$, that can be expressed analytically in the following form

$$k^{(n)}[S(\dot{\alpha}^{(n)})] =< k_+^{(n)} \cdot S(\dot{\alpha}^{(n)}) > + < -k_-^{(n)} \cdot S(-\dot{\alpha}^{(n)}) >, n = 1, .., N. \quad (5.68)$$

in which the Macaulay brackets $y =< x >$ operate such that the variable $y = x$ if $x \geq 0$ and $y = 0$ if $x < 0$. For instance, looking at the longitudinal direction of the abutment this assumption allows to reproduce the different mobilization of the active and passive resistance in the backfill, as well as the different mechanisms associated with the attainment of the bearing capacity and the uplift of the foundation when the abutment is loaded in the vertical direction instead. Accordingly, the final version of the yield surfaces follows

$$y^{(n)}(\alpha^{(n)}, \chi^{(n)}) = \left|\chi^{(n)}\right| - k^{(n)}[S(\dot{\alpha}_n)] + R^{(n)} \cdot (|\left|\chi^{(R)}\right| - \left|\chi^{(n)}\right|) = 0, n = 1, ..., N. \quad (5.69)$$

Note that the yield function is not dependent on the true force $Q^{(n)}$, since the associativity of the plastic flow, and is not affected directly by the presence of the masses. However, the masses influence the whole dissipative response because the plastic multiplier contains the inertial effects induced by their motion, as it will appear evident in the derivation of the constitutive relation.

5.5.2 Dissipation function

Under the assumption of associated flow and validity of the Ziegler's principle (1977), the dissipation function can be uniquely determined from the yield functions. This

implies that the flow rule is associated in true force space and in generalised force space. Starting from the analytical expression for the dissipation function d, obtained by Houlsby et al. (2017) for the Iwan model, and considering the dependency of the strength $k^{(n)}$ on the sign of $\dot{\alpha}_n$ (Eq. 5.68), the dissipation reads

$$d(\alpha^{(n)}, \dot{\alpha}^{(n)}) = \sum_{n=1}^{N} \chi^{(n)} \cdot |\dot{\alpha}_n| + \chi^{(R)} \cdot \dot{\alpha}^{(R)} =$$

$$= \sum_{n=1}^{N} k^{(n)}[S(\dot{\alpha}_n)] \cdot |\dot{\alpha}_n| + Q^{(R)} \cdot S\left(Q^{(ext)}\right) \sum_{n=1}^{N} R^{(n)} \cdot \dot{\alpha}^{(n)} \tag{5.70}$$

which expresses the power dissipated during a generic transformation.

The ratcheting displacement is introduced in the mathematical formulation as a constraint (Houlsby et al. 2017)

$$c = \dot{\alpha}^{(R)} - S\left(Q^{(ext)}\right) \cdot \sum_{n=1}^{N} R^{(n)} \cdot \dot{\alpha}^{(n)} = 0 \tag{5.71}$$

that is taken into account by using the method of Lagrangian multipliers. Instead of using d, a new function d^* is defined as

$$d^* = d + \Lambda \cdot c = \sum_{n=1}^{N} k^{(n)}[S(\dot{\alpha}_n)] \cdot |\dot{\alpha}_n| + Q^{(R)} \cdot S\left(Q^{(ext)}\right) \sum_{n=1}^{N} R^{(n)} \cdot \dot{\alpha}^{(n)} +$$

$$+ \Lambda \cdot \left(\dot{\alpha}^{(R)} - S\left(Q^{(ext)}\right) \cdot \sum_{n=1}^{N} R^{(n)} \cdot \dot{\alpha}^{(n)} \right) \tag{5.72}$$

which by virtue of the condition $c = 0$ is numerically equal to d. The Lagrangian multiplier Λ enforces the condition imposed by the constraint c. In this way, the incremental response of the model can be derived through the unconstrained function d^*. Note that, as expected, dissipation is a homogeneous function of order one of

the plastic displacement rate $\dot{\alpha}^{(n)}$ because the assumption of rate-independency.

5.6 Incremental response

For the numerical implementation, the response needs to be expressed in an incremental form. The relationship between the external force $Q^{(ext)}$ and the total displacement q can be obtained by differentiating either the Gibbs free energy or the Helmholtz free energy according to Eqs. 5.27 and 5.28, respectively.

In the present case, the constitutive law was obtained from the Helmholtz free energy as follows

$$Q^{(ext)} = \frac{\partial}{\partial q}\left[\frac{1}{2}\cdot H^{(0)}\cdot\left(q-\sum_{n=1}^{N}\alpha^{(n)}-\alpha^{(R)}\right)^2+\right.$$

$$\left.+\frac{1}{2}\cdot\sum_{n=1}^{N}H^{(n)}\cdot\left(\alpha^{(n)}\right)^2+\frac{1}{2}\cdot m^{(0)}\cdot\dot{q}^2+\frac{1}{2}\cdot\sum_{n=1}^{N}m^{(n)}\cdot\left(\sum_{j=n}^{N}\dot{\alpha}^{(j)}\right)^2\right]=$$

$$=H^{(0)}\cdot\left(q-\sum_{n=1}^{N}\alpha^{(n)}-\alpha^{(R)}\right)+m^{(0)}\cdot\ddot{q}^2 \tag{5.73}$$

having separated the contribution of the mass associated with the elastic spring 0 from that of the other masses, as done in Eq. 5.47. The desired incremental response therefore reads

$$\dot{Q}^{(ext)}=\frac{\partial}{\partial t}\left[\frac{\partial f(q^{(j)},\alpha^{(n)},m^{(n)})}{\partial q}\right]=H^{(0)}\cdot\left(\dot{q}-\sum_{n=1}^{N}\dot{\alpha}^{(n)}-\dot{\alpha}^{(R)}\right)+m^{(0)}\cdot\dddot{q}^2 \tag{5.74}$$

whose solution requires the definition of the flow rule, given below

$$\dot{\alpha}^{(n)} = \lambda_n \cdot \frac{\partial y^{(n)}(\alpha^{(n)}, \chi^{(n)})}{\partial \chi^{(n)}} =$$

$$= \lambda_n \cdot \frac{\partial}{\partial \chi^{(n)}} \left[|\chi^{(n)}| - k^{(n)}[S(\dot{\alpha}_n)] + R^{(n)} \cdot (|\chi^{(R)}| - |\chi^{(ext)}|) \right] =$$

$$= \lambda_n \cdot S(\chi^{(n)}), n = 1, .., N \tag{5.75}$$

with $S(\chi^{(n)})$ is the modified signum function (Eq. 5.33) of the dissipative force in the n-th slider and λ_n is the non-negative plastic multiplier associated with the n-th yield surface. By introducing Eq. 5.75 in the definition of the ratcheting displacement Eq. 5.32, the latter becomes

$$\dot{\alpha}^{(R)} = S\left(Q^{(ext)}\right) \cdot \sum_{n=1}^{N} R^{(n)} \cdot |\dot{\alpha}^{(n)}| =$$

$$= S\left(Q^{(ext)}\right) \cdot \sum_{n=1}^{N} R^{(n)} \cdot |\lambda_n \cdot S(\chi^{(n)})|. \tag{5.76}$$

As in conventional plasticity, in the description of the incremental response of a thermodynamic material, two possibilities exist: the material is within the yield surface ($y^{(n)}(\alpha^{(n)}, \chi^{(n)}) < 0$), in which case no dissipation occurs and $\lambda_n = 0$, or the material point lies on the yield surface ($y^{(n)}(\alpha^{(n)}, \chi^{(n)}) = 0$), then plastic deformation can occur provided that $\lambda_n \geq 0$. The plastic multiplier is determined by invoking the consistency condition of the yield surface

$$\dot{y}^{(n)}(\alpha^{(n)}, \chi^{(n)}) = \frac{\partial y^{(n)}}{\partial \alpha^{(n)}} \cdot \dot{\alpha}^{(n)} + \frac{\partial y^{(n)}}{\partial \chi^{(n)}} \cdot \dot{\chi}^{(n)} = 0, n = 1, .., N. \tag{5.77}$$

in which the dissipative generalised force $\chi^{(n)}$ results equal to the generalised force $\bar{\chi}^{(n)}$ for the orthogonality principle of Ziegler (1977), so that

$$\chi^{(n)} = \bar{\chi}^{(n)} = -\frac{\partial g(Q^{(j)}, \alpha^{(n)}, m^{(n)})}{\partial \alpha^{(n)}}. \tag{5.78}$$

By virtue of the elastic-plastic uncoupling, Eq. 5.78 can be rewritten by introducing the decomposition of the Gibbs free energy in Eq. 5.55

$$\chi^{(n)} = \bar{\chi}^{(n)} = -\frac{\partial}{\partial \alpha^{(n)}} \left[g_1(Q^{(j)}, m^{(n)}) + g_2(\alpha^{(n)}, m^{(n)}) - Q^{(n)} \cdot \alpha^{(n)} \right] =$$

$$= -\frac{\partial g_2(\alpha^{(n)}, m^{(n)})}{\partial \alpha^{(n)}} + Q^{(n)}, n = 1, .., N \tag{5.79}$$

and differentiation of Eq. 5.79 gives

$$\dot{\chi}^{(n)} = -\frac{\partial^2 g_2(\alpha^{(n)}, m^{(n)})}{\partial \alpha^{(n)2}} \cdot \dot{\alpha}^{(n)} + \dot{Q}^{(n)} =$$

$$= -\frac{\partial^2 g_2(\alpha^{(n)}, m^{(n)})}{\partial \alpha^{(n)2}} \cdot \lambda_n \cdot \frac{\partial y^{(n)}(\alpha^{(n)}, \chi^{(n)})}{\partial \chi^{(n)}} + \dot{Q}^{(n)}, n = 1, .., N. \tag{5.80}$$

Substitution of Eqs. 5.76 and 5.80 into Eq. 5.77 gives the solution for the plastic multiplier:

$$\dot{y}^{(n)}(\alpha^{(n)}, \chi^{(n)}) = \frac{\partial y^{(n)}}{\partial \alpha^{(n)}} \cdot \lambda_n \cdot \frac{\partial y^{(n)}(\alpha^{(n)}, \chi^{(n)})}{\partial \chi^{(n)}} +$$

$$+ \frac{\partial y^{(n)}}{\partial \chi^{(n)}} \cdot \left(-\frac{\partial^2 g_2(\alpha^{(n)}, m^{(n)})}{\partial \alpha^{(n)2}} \cdot \lambda_n \cdot \frac{\partial y^{(n)}(\alpha^{(n)}, \chi^{(n)})}{\partial \chi^{(n)}} + \dot{Q}^{(n)} \right) = 0, n = 1, .., N. \tag{5.81}$$

$$\lambda_n = \frac{\frac{\partial y^{(n)}}{\partial \chi^{(n)}} \cdot \dot{Q}^{(n)}}{\frac{\partial y^{(n)}}{\partial \chi^{(n)}} \cdot \frac{\partial^2 g_2}{\partial \alpha^{(n)2}} \cdot \frac{\partial y^{(n)}}{\partial \chi^{(n)}} - \frac{\partial y^{(n)}}{\partial \alpha^{(n)}} \cdot \frac{\partial y^{(n)}}{\partial \chi^{(n)}}}, n = 1, .., N. \tag{5.82}$$

In the equation above, the derivative of the yield function with respect to $\chi^{(n)}$ is

straightforward

$$\frac{\partial y^{(n)}}{\partial \chi^{(n)}} = S(\chi^{(n)}) = \begin{cases} -1 & \chi^{(n)} < 0 \\ 0 & 0 \\ 1 & \chi^{(n)} > 0 \end{cases} , n = 1, ..., N \tag{5.83}$$

and the term $\partial y_n / \partial \alpha_n$ is identically equal to zero. Some developments are instead needed to calculate the derivative of the function $g_2(\alpha^{(n)}, m^{(n)})$. Taking advantage of the decomposition of the Gibbs free energy into its static and inertial terms (Eq. 5.59), the sub-function g_2 can be differentiated as follows

$$\frac{\partial^2 g_2(\alpha^{(n)}, m^{(n)})}{\partial \alpha^{(n)2}} = \frac{\partial^2 g_{2,0}(\alpha^{(n)}, 0)}{\partial \alpha^{(n)2}} + \frac{\partial^2 g_{2,in}(\alpha^{(n)}, m^{(n)})}{\partial \alpha^{(n)2}} \tag{5.84}$$

in which the static part can be simply developed

$$\frac{\partial^2 g_{2,0}(\alpha^{(n)}, 0)}{\partial \alpha^{(n)2}} = \frac{\partial^2}{\partial \alpha^{(n)2}} \left[-\frac{1}{2 \cdot H^{(0)}} \cdot \left(Q^{(0)}\right)^2 - \sum_{n=1}^{N} Q^{(n)} \cdot \alpha^{(n)} + \right.$$

$$\left. + \frac{1}{2} \cdot \sum_{n=1}^{N} H^{(n)} \cdot \left(\alpha^{(n)}\right)^2 - Q^{(R)} \cdot \alpha^{(R)} \right] = H^{(n)} \tag{5.85}$$

so it results equal to the stiffnesses of the springs that produce kinematic hardening. The differentiation of the inertial part, instead, can be achieved through some manipulation

$$\frac{\partial^2 g_{2,in}(\alpha^{(n)}, m^{(n)})}{\partial \alpha^{(n)2}} = \frac{\partial^2}{\partial \alpha^{(n)2}} \left[-\sum_{n=0}^{N} m^{(n)} \cdot \sum_{h=n}^{N} \ddot{q}^{(h)} \cdot \sum_{k=n}^{N} q^{(k)} + \right.$$

$$\left. + \frac{1}{2} \cdot \sum_{n=0}^{N} m^{(n)} \cdot \left(\sum_{j=n}^{N} \dot{q}^{(j)} \right)^2 \right] =$$

$$= \frac{\partial^2}{\partial \alpha^{(n)2}} \left[-m^{(0)} \cdot \sum_{h=0}^{N} \ddot{q}^{(h)} \cdot \sum_{k=0}^{N} q^{(k)} + \frac{1}{2} \cdot m^{(0)} \cdot \left(\sum_{j=0}^{N} \dot{q}^{(j)} \right)^2 \right] +$$

$$+ \frac{\partial^2}{\partial \alpha^{(n)2}} \left[-m^{(n)} \cdot \sum_{h=n}^{N} \ddot{q}^{(h)} \cdot \sum_{k=n}^{N} q^{(k)} + \frac{1}{2} \cdot m^{(n)} \cdot \left(\sum_{j=n}^{N} \dot{q}^{(j)} \right)^2 \right] \tag{5.86}$$

in which the term relative to the mass $m^{(0)}$ has been separated by the masses of the sliders. For compatibility, the total displacement is $q = q^{(0)} + \sum_{n=1}^{N} \alpha^{(n)}$ and, if it is substituted into Eq. 5.86, the latter becomes

$$\frac{\partial^2 g_{2,in}(\alpha^{(n)}, m^{(n)})}{\partial \alpha^{(n)2}} = \frac{\partial^2}{\partial \alpha^{(n)2}} \left[-m^{(0)} \cdot \sum_{h=1}^{N} \ddot{\alpha}^{(h)} \cdot \sum_{k=1}^{N} \alpha^{(k)} + \frac{1}{2} \cdot m^{(0)} \cdot \left(\sum_{j=1}^{N} \dot{\alpha}^{(j)} \right)^2 \right] +$$

$$+ \frac{\partial^2}{\partial \alpha^{(n)2}} \left[-m^{(n)} \cdot \sum_{h=n}^{N} \ddot{q}^{(h)} \cdot \sum_{k=n}^{N} q^{(k)} + \frac{1}{2} \cdot m^{(n)} \cdot \left(\sum_{j=n}^{N} \dot{q}^{(j)} \right)^2 \right] =$$

$$= -m^{(0)} \cdot \frac{\partial^2}{\partial \alpha^{(n)2}} \left[\sum_{h=1}^{N} \ddot{\alpha}^{(h)} \cdot \sum_{k=1}^{N} \alpha^{(k)} \right] + \frac{1}{2} \cdot m^{(0)} \cdot \frac{\partial^2}{\partial \alpha^{(n)2}} \left[\left(\sum_{j=1}^{N} \dot{\alpha}^{(j)} \right)^2 \right] +$$

$$- m^{(n)} \cdot \frac{\partial^2}{\partial \alpha^{(n)2}} \left[\sum_{h=n}^{N} \ddot{\alpha}^{(h)} \cdot \sum_{k=n}^{N} \alpha^{(k)} \right] + \frac{1}{2} \cdot m^{(n)} \cdot \frac{\partial^2}{\partial \alpha^{(n)2}} \left[\left(\sum_{j=n}^{N} \dot{\alpha}^{(j)} \right)^2 \right] =$$

$$= -m^{(0)} \cdot \frac{\partial^2 A^{(n)}}{\partial \alpha^{(n)2}} + \frac{1}{2} \cdot m^{(0)} \cdot \frac{\partial^2 B^{(n)}}{\partial \alpha^{(n)2}} - m^{(n)} \cdot \frac{\partial^2 C^{(n)}}{\partial \alpha^{(n)2}} + \frac{1}{2} \cdot m^{(n)} \cdot \frac{\partial^2 D^{(n)}}{\partial \alpha^{(n)2}}. \tag{5.87}$$

The terms $A^{(n)}, B^{(n)}, C^{(n)}$ and $D^{(n)}$ include the time derivatives of the plastic displacements $\alpha^{(n)}$ and a change of variable is necessary to differentiate them, which

can be generalised for the first and second mixed derivative of the internal variable α as reported below

$$\frac{\partial}{\partial \alpha} \cdot \frac{\partial^k \alpha}{\partial t^k} = \frac{\partial}{\dot{\alpha} \cdot \partial t} \cdot \frac{\partial^k \alpha}{\partial t^k} = \frac{1}{\dot{\alpha}} \cdot \frac{\partial^{k+1} \alpha}{\partial t^{k+1}} \tag{5.88}$$

$$\frac{\partial^2}{\partial \alpha^2} \cdot \frac{\partial^k \alpha}{\partial t^k} = \frac{\partial}{\partial \alpha} \cdot \frac{\partial}{\partial \alpha} \cdot \frac{\partial^k \alpha}{\partial t^k} = \frac{\partial}{\partial \alpha} \cdot \left[\frac{1}{\dot{\alpha}} \cdot \frac{\partial^{k+1} \alpha}{\partial t^{k+1}} \right] =$$

$$= \frac{\partial^{k+2} \alpha}{\partial t^{k+2}} \cdot \frac{1}{\dot{\alpha}^2} - \frac{\partial^{k+1} \alpha}{\partial t^{k+1}} \cdot \frac{\ddot{\alpha}}{\dot{\alpha}^3}. \tag{5.89}$$

In light of the above, the terms $A^{(n)}, B^{(n)}, C^{(n)}$ and $D^{(n)}$ can be developed as follows

- term $A^{(n)}$:

$$\frac{\partial A^{(n)}}{\partial \alpha^{(n)}} = \frac{\partial}{\partial \alpha^{(n)}} \left[\sum_{h=1}^{N} \ddot{\alpha}^{(h)} \cdot \sum_{k=1}^{N} \alpha^{(k)} \right] =$$

$$= \frac{\partial}{\partial \alpha^{(n)}} \left[\sum_{h=1}^{N} \ddot{\alpha}^{(h)} \right] \cdot \sum_{k=1}^{N} \alpha^{(k)} + \sum_{h=1}^{N} \ddot{\alpha}^{(h)} \cdot \frac{\partial}{\partial \alpha^{(n)}} \left[\sum_{k=1}^{N} \alpha^{(k)} \right] =$$

$$= \frac{1}{\dot{\alpha}^{(n)}} \cdot \frac{\partial^3 \sum_{h=1}^{N} \alpha^{(h)}}{\partial t^3} \cdot \sum_{k=1}^{N} \alpha^{(k)} + \sum_{h=1}^{N} \ddot{\alpha}^{(h)} = \frac{1}{\dot{\alpha}^{(n)}} \cdot \sum_{h=1}^{N} \dddot{\alpha}^{(h)} \cdot \sum_{k=1}^{N} \alpha^{(k)} + \sum_{h=1}^{N} \ddot{\alpha}^{(h)} \tag{5.90}$$

$$\frac{\partial^2 A^{(n)}}{\partial \alpha^{(n)2}} = \frac{\partial}{\partial \alpha^{(n)}} \left[\frac{1}{\dot{\alpha}^{(n)}} \cdot \sum_{h=1}^{N} \dddot{\alpha}^{(h)} \cdot \sum_{k=1}^{N} \alpha^{(k)} + \sum_{h=1}^{N} \ddot{\alpha}^{(h)} \right] =$$

$$= \frac{\partial}{\partial \alpha^{(n)}} \left[\frac{1}{\dot{\alpha}^{(n)}} \cdot \sum_{h=1}^{N} \dddot{\alpha}^{(h)} \cdot \sum_{k=1}^{N} \alpha^{(k)} \right] + \frac{\partial}{\partial \alpha^{(n)}} \left[\sum_{h=1}^{N} \ddot{\alpha}^{(h)} \right] =$$

$$= \frac{\partial}{\partial \alpha^{(n)}} \left[\frac{1}{\dot{\alpha}^{(n)}} \cdot \sum_{h=1}^{N} \dddot{\alpha}^{(h)} \right] \cdot \sum_{k=1}^{N} \alpha^{(k)} + \frac{1}{\dot{\alpha}^{(n)}} \cdot \sum_{h=1}^{N} \dddot{\alpha}^{(h)} \cdot \frac{\partial}{\partial \alpha^{(n)}} \left[\sum_{k=1}^{N} \alpha^{(k)} \right] +$$

$$+ \frac{1}{\dot{\alpha}^{(n)}} \cdot \sum_{h=1}^{N} \dddot{\alpha}^{(h)} =$$

$$= \frac{\frac{\partial}{\partial \alpha^{(n)}} \left[\sum_{h=1}^{N} \dddot{\alpha}^{(h)} \right] \cdot \dot{\alpha}^{(n)} - \sum_{h=1}^{N} \dddot{\alpha}^{(h)} \cdot \frac{\partial \dot{\alpha}^{(n)}}{\partial \alpha^{(n)}}}{\dot{\alpha}^{(n)2}} \cdot \sum_{k=1}^{N} \alpha^{(k)} +$$

$$+ \frac{1}{\dot{\alpha}^{(n)}} \cdot \sum_{h=1}^{N} \dddot{\alpha}^{(h)} + \frac{1}{\dot{\alpha}^{(n)}} \cdot \sum_{h=1}^{N} \dddot{\alpha}^{(h)} =$$

$$= \frac{\frac{1}{\dot{\alpha}^{(n)}} \cdot \sum_{h=1}^{N} \ddddot{\alpha}^{(h)} \cdot \dot{\alpha}^{(n)} - \sum_{h=1}^{N} \dddot{\alpha}^{(h)} \cdot \frac{1}{\dot{\alpha}^{(n)}} \cdot \ddot{\alpha}^{(n)}}{\dot{\alpha}^{(n)2}} \cdot \sum_{k=1}^{N} \alpha^{(k)} +$$

$$+ 2 \cdot \frac{1}{\dot{\alpha}^{(n)}} \cdot \sum_{h=1}^{N} \dddot{\alpha}^{(h)} =$$

$$= \frac{1}{\dot{\alpha}^{(n)2}} \cdot \sum_{h=1}^{N} \ddddot{\alpha}^{(h)} \cdot \sum_{k=1}^{N} \alpha^{(k)} - \frac{1}{\dot{\alpha}^{(n)3}} \cdot \sum_{h=1}^{N} \dddot{\alpha}^{(h)} \cdot \ddot{\alpha}^{(n)} \cdot \sum_{k=1}^{N} \alpha^{(k)} + 2 \cdot \frac{1}{\dot{\alpha}^{(n)}} \cdot \sum_{h=1}^{N} \dddot{\alpha}^{(h)}. \quad (5.91)$$

- term $B^{(n)}$:

$$\frac{\partial B^{(n)}}{\partial \alpha^{(n)}} = \frac{\partial}{\partial \alpha^{(n)}} \left[\left(\sum_{j=1}^{N} \dot{\alpha}^{(j)} \right)^2 \right] = 2 \cdot \sum_{j=1}^{N} \dot{\alpha}^{(j)} \cdot \frac{\partial}{\partial \alpha^{(n)}} \left[\sum_{j=1}^{N} \dot{\alpha}^{(j)} \right] =$$

$$= 2 \cdot \sum_{j=1}^{N} \dot{\alpha}^{(j)} \cdot \frac{1}{\dot{\alpha}^{(n)}} \cdot \frac{\partial}{\partial t} \left[\sum_{j=1}^{N} \dot{\alpha}^{(j)} \right] = 2 \cdot \frac{1}{\dot{\alpha}^{(n)}} \cdot \sum_{j=1}^{N} \dot{\alpha}^{(j)} \cdot \sum_{j=1}^{N} \ddot{\alpha}^{(j)} \quad (5.92)$$

$$\frac{\partial^2 B^{(n)}}{\partial \alpha^{(n)2}} = \frac{\partial}{\partial \alpha^{(n)2}} \left[2 \cdot \frac{1}{\dot{\alpha}^{(n)}} \cdot \sum_{j=1}^{N} \dot{\alpha}^{(j)} \cdot \sum_{j=1}^{N} \ddot{\alpha}^{(j)} \right] =$$

$$= 2 \cdot \frac{\partial}{\partial \alpha^{(n)}} \left[\frac{1}{\dot{\alpha}^{(n)}} \cdot \sum_{j=1}^{N} \dot{\alpha}^{(j)} \right] \cdot \sum_{j=1}^{N} \ddot{\alpha}^{(j)} + 2 \cdot \frac{1}{\dot{\alpha}^{(n)}} \cdot \sum_{j=1}^{N} \dot{\alpha}^{(j)} \cdot \frac{\partial}{\partial \alpha^{(n)}} \left[\sum_{j=1}^{N} \ddot{\alpha}^{(j)} \right] =$$

$$= 2 \cdot \frac{\frac{\partial}{\partial \alpha^{(n)}} \left[\sum_{j=1}^{N} \dot{\alpha}^{(j)} \right] \cdot \dot{\alpha}^{(n)} - \sum_{j=1}^{N} \dot{\alpha}^{(j)} \cdot \frac{\partial \dot{\alpha}^{(n)}}{\partial \alpha^{(n)}}}{\dot{\alpha}^{(n)2}} \cdot \sum_{j=1}^{N} \ddot{\alpha}^{(j)} +$$

$$+ 2 \cdot \frac{1}{\dot{\alpha}^{(n)}} \cdot \sum_{j=1}^{N} \dot{\alpha}^{(j)} \cdot \frac{1}{\dot{\alpha}^{(n)}} \cdot \sum_{j=1}^{N} \dddot{\alpha}^{(j)} =$$

$$= 2 \cdot \frac{\frac{1}{\dot{\alpha}^{(n)}} \cdot \sum_{j=1}^{N} \ddot{\alpha}^{(j)} \cdot \dot{\alpha}^{(n)} - \sum_{j=1}^{N} \dot{\alpha}^{(j)} \cdot \frac{1}{\dot{\alpha}^{(n)}} \cdot \ddot{\alpha}^{(n)}}{\dot{\alpha}^{(n)2}} \cdot \sum_{j=1}^{N} \ddot{\alpha}^{(j)} +$$

$$+ 2 \cdot \frac{1}{\dot{\alpha}^{(n)}} \cdot \sum_{j=1}^{N} \dot{\alpha}^{(j)} \cdot \frac{1}{\dot{\alpha}^{(n)}} \cdot \sum_{j=1}^{N} \dddot{\alpha}^{(j)} =$$

$$= 2 \cdot \frac{1}{\dot{\alpha}^{(n)2}} \cdot \sum_{j=1}^{N} \ddot{\alpha}^{(j)} \cdot \sum_{j=1}^{N} \ddot{\alpha}^{(j)} - 2 \cdot \frac{\ddot{\alpha}^{(n)}}{\dot{\alpha}^{(n)3}} \cdot \sum_{j=1}^{N} \dot{\alpha}^{(j)} \cdot \sum_{j=1}^{N} \ddot{\alpha}^{(j)} +$$

$$+ 2 \cdot \frac{1}{\dot{\alpha}^{(n)2}} \cdot \sum_{j=1}^{N} \dot{\alpha}^{(j)} \cdot \sum_{j=1}^{N} \dddot{\alpha}^{(j)} \tag{5.93}$$

- term $C^{(n)}$ (formally identical to term $A^{(n)}$):

$$\frac{\partial C^{(n)}}{\partial \alpha^{(n)}} = \frac{\partial}{\partial \alpha^{(n)}} \left[\sum_{h=n}^{N} \ddot{\alpha}^{(h)} \cdot \sum_{k=n}^{N} \alpha^{(k)} \right] = \frac{1}{\dot{\alpha}^{(n)}} \cdot \sum_{h=n}^{N} \dddot{\alpha}^{(h)} \cdot \sum_{k=n}^{N} \alpha^{(k)} + \sum_{j=1}^{N} \ddot{\alpha}^{(j)} \tag{5.94}$$

$$\frac{\partial^2 C^{(n)}}{\partial \alpha^{(n)2}} = \frac{\partial}{\partial \alpha^{(n)}} \left[\frac{1}{\dot{\alpha}^{(n)}} \cdot \sum_{h=n}^{N} \dddot{\alpha}^{(h)} \cdot \sum_{k=n}^{N} \alpha^{(k)} + \sum_{j=1}^{N} \ddot{\alpha}^{(j)} \right] =$$

$$= \frac{1}{\dot{\alpha}^{(n)2}} \cdot \sum_{h=n}^{N} \dddot{\alpha}^{(h)} \cdot \sum_{k=n}^{N} \alpha^{(k)} - \frac{1}{\dot{\alpha}^{(n)3}} \cdot \sum_{h=n}^{N} \dddot{\alpha}^{(h)} \cdot \ddot{\alpha}^{(n)} \cdot \sum_{k=n}^{N} \alpha^{(k)} + 2 \cdot \frac{1}{\dot{\alpha}^{(n)}} \cdot \sum_{j=n}^{N} \dddot{\alpha}^{(j)}. \tag{5.95}$$

- term $D^{(n)}$ (formally identical to term $B^{(n)}$):

$$\frac{\partial D}{\partial \alpha^{(n)}} = \frac{\partial}{\partial \alpha^{(n)}} \left[\left(\sum_{h=n}^{N} \dot{\alpha}^{(h)} \right)^2 \right] = 2 \cdot \frac{1}{\dot{\alpha}^{(n)}} \cdot \sum_{h=n}^{N} \dot{\alpha}^{(h)} \cdot \sum_{k=n}^{N} \ddot{\alpha}^{(k)} \tag{5.96}$$

$$\frac{\partial^2 D}{\partial \alpha^{(n)2}} = \frac{\partial}{\partial \alpha^{(n)2}} \left[2 \cdot \frac{1}{\dot{\alpha}^{(n)}} \cdot \sum_{h=n}^{N} \dot{\alpha}^{(h)} \cdot \sum_{k=n}^{N} \ddot{\alpha}^{(k)} \right] =$$

$$= 2 \cdot \frac{1}{\dot{\alpha}^{(n)2}} \cdot \sum_{h=n}^{N} \ddot{\alpha}^{(h)} \cdot \sum_{k=n}^{N} \ddot{\alpha}^{(k)} - 2 \cdot \frac{\ddot{\alpha}^{(n)}}{\dot{\alpha}^{(n)3}} \cdot \sum_{h=n}^{N} \dot{\alpha}^{(h)} \cdot \sum_{k=n}^{N} \ddot{\alpha}^{(k)} +$$

$$+2 \cdot \frac{1}{\dot{\alpha}^{(n)2}} \cdot \sum_{h=n}^{N} \dot{\alpha}^{(h)} \cdot \sum_{k=n}^{N} \dddot{\alpha}^{(k)}. \tag{5.97}$$

By substituting the above expressions for the terms $A^{(n)}, B^{(n)}, C^{(n)}$ and $D^{(n)}$ in Eq. 5.87, it becomes

$$\frac{\partial^2 g_{2,in}(\alpha^{(n)}, m^{(n)})}{\partial \alpha^{(n)2}} = -m^{(0)} \cdot \frac{\partial^2 A^{(n)}}{\partial \alpha^{(n)2}} + \frac{1}{2} \cdot m^{(0)} \cdot \frac{\partial^2 B^{(n)}}{\partial \alpha^{(n)2}} -$$

$$-m^{(n)} \cdot \frac{\partial^2 C^{(n)}}{\partial \alpha^{(n)2}} + \frac{1}{2} \cdot m^{(n)} \cdot \frac{\partial^2 D^{(n)}}{\partial \alpha^{(n)2}} =$$

$$= -m^{(0)} \cdot \left(\frac{1}{\dot{\alpha}^{(n)2}} \cdot \sum_{h=1}^{N} \dddot{\alpha}^{(h)} \cdot \sum_{k=1}^{N} \alpha^{(k)} - \frac{1}{\dot{\alpha}^{(n)3}} \cdot \sum_{h=1}^{N} \ddot{\alpha}^{(h)} \cdot \ddot{\alpha}^{(n)} \cdot \sum_{k=1}^{N} \alpha^{(k)} + \right.$$

$$\left. +2 \cdot \frac{1}{\dot{\alpha}^{(n)}} \cdot \sum_{h=1}^{N} \dddot{\alpha}^{(h)} \right) +$$

$$+\frac{1}{2} \cdot m^{(0)} \cdot (2 \cdot \frac{1}{\dot{\alpha}^{(n)2}} \cdot \sum_{j=1}^{N} \ddot{\alpha}^{(j)} \cdot \sum_{j=1}^{N} \ddot{\alpha}^{(j)} - 2 \cdot \frac{\ddot{\alpha}^{(n)}}{\dot{\alpha}^{(n)3}} \cdot \sum_{j=1}^{N} \dot{\alpha}^{(j)} \cdot \sum_{j=1}^{N} \ddot{\alpha}^{(j)} +$$

$$+2\cdot\frac{1}{\dot{\alpha}^{(n)2}}\cdot\sum_{j=1}^{N}\dot{\alpha}^{(j)}\cdot\sum_{j=1}^{N}\dddot{\alpha}^{(j)}\Bigg)-$$

$$-m^{(n)}\cdot\Bigg(\frac{1}{\dot{\alpha}^{(n)2}}\cdot\sum_{h=n}^{N}\dddot{\alpha}^{(h)}\cdot\sum_{k=n}^{N}\alpha^{(k)}-\frac{1}{\dot{\alpha}^{(n)3}}\cdot\sum_{h=n}^{N}\ddot{\alpha}^{(h)}\cdot\ddot{\alpha}^{(n)}\cdot\sum_{k=n}^{N}\alpha^{(k)}+$$

$$+2\cdot\frac{1}{\dot{\alpha}^{(n)}}\cdot\sum_{j=n}^{N}\ddot{\alpha}^{(j)}\Bigg)+$$

$$+\frac{1}{2}\cdot m^{(n)}\cdot\big(2\cdot\frac{1}{\dot{\alpha}^{(n)2}}\cdot\sum_{h=n}^{N}\ddot{\alpha}^{(h)}\cdot\sum_{k=n}^{N}\ddot{\alpha}^{(k)}-2\cdot\frac{\ddot{\alpha}^{(n)}}{\dot{\alpha}^{(n)3}}\cdot\sum_{h=n}^{N}\dot{\alpha}^{(h)}\cdot\sum_{k=n}^{N}\ddot{\alpha}^{(k)}+$$

$$+2\cdot\frac{1}{\dot{\alpha}^{(n)2}}\cdot\sum_{h=n}^{N}\dot{\alpha}^{(h)}\cdot\sum_{k=n}^{N}\dddot{\alpha}^{(k)}\Bigg)=$$

$$=m^{(0)}\cdot\Bigg(-\frac{1}{\dot{\alpha}^{(n)2}}\cdot\sum_{h=1}^{N}\dddot{\alpha}^{(h)}\cdot\sum_{k=1}^{N}\alpha^{(k)}+\frac{1}{\dot{\alpha}^{(n)3}}\cdot\sum_{h=1}^{N}\ddot{\alpha}^{(h)}\cdot\ddot{\alpha}^{(n)}\cdot\sum_{k=1}^{N}\alpha^{(k)}-$$

$$-2\cdot\frac{1}{\dot{\alpha}^{(n)}}\cdot\sum_{h=1}^{N}\ddot{\alpha}^{(h)}+\frac{1}{\dot{\alpha}^{(n)2}}\cdot\sum_{h=n}^{N}\ddot{\alpha}^{(h)}\cdot\sum_{k=n}^{N}\ddot{\alpha}^{(k)}-$$

$$-\frac{\ddot{\alpha}^{(n)}}{\dot{\alpha}^{(n)3}}\cdot\sum_{h=n}^{N}\dot{\alpha}^{(h)}\cdot\sum_{k=n}^{N}\ddot{\alpha}^{(k)}+\frac{1}{\dot{\alpha}^{(n)2}}\cdot\sum_{h=n}^{N}\dot{\alpha}^{(h)}\cdot\sum_{k=n}^{N}\dddot{\alpha}^{(k)}\Bigg)+$$

$$+m^{(n)}\cdot\Bigg(-\frac{1}{\dot{\alpha}^{(n)2}}\cdot\sum_{h=n}^{N}\dddot{\alpha}^{(h)}\cdot\sum_{k=n}^{N}\alpha^{(k)}+\frac{1}{\dot{\alpha}^{(n)3}}\cdot\sum_{h=n}^{N}\dddot{\alpha}^{(h)}\cdot\ddot{\alpha}^{(n)}\cdot\sum_{k=n}^{N}\alpha^{(k)}-$$

$$-2\cdot\frac{1}{\dot{\alpha}^{(n)}}\cdot\sum_{j=n}^{N}\dddot{\alpha}^{(j)}+\frac{1}{\dot{\alpha}^{(n)2}}\cdot\sum_{h=n}^{N}\ddot{\alpha}^{(h)}\cdot\sum_{k=n}^{N}\ddot{\alpha}^{(k)}-\frac{\ddot{\alpha}^{(n)}}{\dot{\alpha}^{(n)3}}\cdot\sum_{h=n}^{N}\dot{\alpha}^{(h)}\cdot\sum_{k=n}^{N}\ddot{\alpha}^{(k)}+$$

$$+\frac{1}{\dot{\alpha}^{(n)2}}\cdot\sum_{h=n}^{N}\dot{\alpha}^{(h)}\cdot\sum_{k=n}^{N}\dddot{\alpha}^{(k)}\Bigg),n=1,...,N. \tag{5.98}$$

having included the contribution of the mass 0 in the summations. For clarity, the terms representing the time derivatives of the internal variables can be grouped as

$$G_{M,0}^{(4)}=-\frac{1}{\dot{\alpha}^{(n)2}}\cdot\sum_{h=1}^{N}\ddddot{\alpha}^{(h)}\cdot\sum_{k=1}^{N}\alpha^{(k)} \tag{5.99}$$

$$G_{M,0}^{(3)}=\frac{1}{\dot{\alpha}^{(n)3}}\cdot\sum_{h=1}^{N}\dddot{\alpha}^{(h)}\cdot\ddot{\alpha}^{(n)}\cdot\sum_{k=1}^{N}\alpha^{(k)}-2\cdot\frac{1}{\dot{\alpha}^{(n)}}\cdot\sum_{h=1}^{N}\ddddot{\alpha}^{(h)}+$$

$$+\frac{1}{\dot{\alpha}^{(n)2}}\cdot\sum_{h=1}^{N}\dot{\alpha}^{(h)}\cdot\sum_{k=1}^{N}\dddot{\alpha}^{(k)} \tag{5.100}$$

$$G_{M,0}^{(2)}=\frac{1}{\dot{\alpha}^{(n)2}}\cdot\sum_{h=1}^{N}\ddot{\alpha}^{(h)}\cdot\sum_{k=1}^{N}\ddot{\alpha}^{(k)}-\frac{\ddot{\alpha}^{(n)}}{\dot{\alpha}^{(n)3}}\cdot\sum_{h=1}^{N}\dot{\alpha}^{(h)}\cdot\sum_{k=1}^{N}\ddot{\alpha}^{(k)} \tag{5.101}$$

$$G_{M,n}^{(4)}=-\frac{1}{\dot{\alpha}^{(n)2}}\cdot\sum_{h=n}^{N}\ddddot{\alpha}^{(h)}\cdot\sum_{k=n}^{N}\alpha^{(k)} \tag{5.102}$$

$$G_{M,n}^{(3)}=\frac{1}{\dot{\alpha}^{(n)3}}\cdot\sum_{h=n}^{N}\dddot{\alpha}^{(h)}\cdot\ddot{\alpha}^{(n)}\cdot\sum_{k=n}^{N}\alpha^{(k)}-2\cdot\frac{1}{\dot{\alpha}^{(n)}}\cdot\sum_{j=n}^{N}\ddddot{\alpha}^{(j)}+$$

$$+\frac{1}{\dot{\alpha}^{(n)2}}\cdot\sum_{h=n}^{N}\dot{\alpha}^{(h)}\cdot\sum_{k=n}^{N}\dddot{\alpha}^{(k)} \tag{5.103}$$

$$G_{M,n}^{(2)}=\frac{1}{\dot{\alpha}^{(n)2}}\cdot\sum_{h=n}^{N}\ddot{\alpha}^{(h)}\cdot\sum_{k=n}^{N}\ddot{\alpha}^{(k)}-\frac{\ddot{\alpha}^{(n)}}{\dot{\alpha}^{(n)3}}\cdot\sum_{h=n}^{N}\dot{\alpha}^{(h)}\cdot\sum_{k=n}^{N}\ddot{\alpha}^{(k)} \tag{5.104}$$

where the superscript j indicates the highest order of the time derivatives included in the term $G_{M,n}^{(j)}$, while the subscript identifies the n-th mass. Therefore

$$\frac{\partial^2 g_{2,in}(\alpha^{(n)}, m^{(n)})}{\partial \alpha^{(n)2}} = m^{(0)} \cdot \left(G_{M,0}^{(4)} + G_{M,0}^{(3)} + G_{M,0}^{(2)} \right) +$$

$$+ m^{(n)} \cdot \left(G_{M,n}^{(4)} + G_{M,n}^{(3)} + G_{M,n}^{(2)} \right), n = 1, ..., N \tag{5.105}$$

and finally the second derivative of the function g_2, that coincides with the plastic modulus in the one-dimensional case, reads

$$\frac{\partial^2 g_2(\alpha^{(n)}, m^{(n)})}{\partial \alpha^{(n)2}} = H^{(n)} + m^{(0)} \cdot \left(G_{M,0}^{(4)} + G_{M,0}^{(3)} + G_{M,0}^{(2)} \right) +$$

$$+ m^{(n)} \cdot \left(G_{M,n}^{(4)} + G_{M,n}^{(3)} + G_{M,n}^{(2)} \right), n = 1, ..., N. \tag{5.106}$$

as the sum of a frequency-independent term $H^{(n)}$ and an inertial term in which the contribution of the masses is modelled by the time derivatives of the internal variables. Though its quite articulated form, the inertial term constitutes an important feature of the present formulation because it is a rigorous, analytical manner to include the inertial effects arising from the soil-abutment system in the response of the macro-constitutive law. It was shown that the inertial effects affect both the energy and dissipation potentials through the sub-function $g_2(\alpha^{(n)}, m^{(n)})$ that has a double effect: providing energy to the macro-element in virtue of the kinetic energy of the masses and, at the same time, dissipating energy since the inertial forces work in the plastic flow. From a numerical point of view, Eq. 5.106 can be integrated in time by application of standardised methods, such as the finite difference method.

Now, the expression of the n-th plastic muliplier can be finally obtained

$$\lambda_n = \frac{\frac{\partial y^{(n)}}{\partial \chi^{(n)}} \cdot \dot{Q}^{(n)}}{\frac{\partial y^{(n)}}{\partial \chi^{(n)}} \cdot \frac{\partial^2 g_2}{\partial \alpha^{(n)2}} \cdot \frac{\partial y^{(n)}}{\partial \chi^{(n)}} - \frac{\partial y^{(n)}}{\partial \alpha^{(n)}} \cdot \frac{\partial y^{(n)}}{\partial \chi^{(n)}}} =$$

$$= S(\chi^{(n)}) \cdot \frac{\dot{Q}^{(n)}}{H^{(n)} + m^{(0)} \cdot \left(G^{(4)}_{M,0} + G^{(3)}_{M,0} + G^{(2)}_{M,0}\right) + m^{(n)} \cdot \left(G^{(4)}_{M,n} + G^{(3)}_{M,n} + G^{(2)}_{M,n}\right)} =$$

$$= S(\chi^{(n)}) \cdot \frac{\dot{Q}^{(n)}}{H^{(n)} + H^{(n)}_{in}}, n = 1, .., N. \tag{5.107}$$

In some cases the plastic multiplier assumes a simpler form. For example, when the model is subjected to a static or a pseudo-static external perturbation, the dynamic response of the masses is not activated or can be neglected. It follows that the plastic multiplier simplifies as

$$\lambda_n = S(\chi^{(n)}) \cdot \frac{\dot{Q}^{(n)}}{H^{(n)}}, n = 1, .., N \tag{5.108}$$

in which the plastic response is controlled only by the stiffnesses $H^{(n)}$ associated with the kinematic hardening.

In dynamic simulations, instead, the inertial response can be reproduced through two techniques: the masses can be included implicitly in the response of the macro-element or they can be modelled explicitly in the numerical model. The former strategy is more elegant because the inertial formulation described so far would be encapsulated into a unique finite element for a prompt use in numerical simulations, at cost of a greater implementation effort. Otherwise, each mass could be associated with a separated element, the latter modelled to reproduce the n-th plastic flow according to the frequency-independent formulation of the macro-element. In other words, the macro-element could be also conveniently modelled as a series connection of a number of sub-models, that contain the non-inertial response of the macro-element, each combined with a mass that confers the frequency-dependent response. This leads to a straightforward implementation of the model, at least in

the one-dimensional case but, by contrast, the numerical modelling of the macro-element becomes a bit more articulated, especially in the multi-axial formulation and when the number of yield surfaces rises.

A reasonable assumption in using the macro-element consists in setting equal to zero the mass $m^{(0)}$, because this is located at the same point where the external perturbation is applied. For example, in a non-linear dynamic analysis, the perturbation is represented by a history of displacements applied to the node of the mass $m^{(0)}$ that therefore cannot alter the global response because its motion is imposed by the boundary condition. This leads to the following simpler form of the plastic multiplier, although conceptually identical to Eq. 5.107, that is

$$\lambda_n = S(\chi^{(n)}) \cdot \frac{\dot{Q}^{(n)}}{H^{(n)} + m^{(n)} \cdot \left(G_{M,n}^{(4)} + G_{M,n}^{(3)} + G_{M,n}^{(2)} \right)}, n = 1, .., N. \tag{5.109}$$

This assumption will be kept in the calibration and validation of the macro-element discussed in Chapter 5 and 7, respectively.

In the general case of Eq. 5.107, the evolution law for the internal variables, previously defined in Eq. 5.75, reads

$$\dot{\alpha}^{(n)} = \lambda_n \cdot S(\chi^{(n)}) = \frac{\dot{Q}^{(n)}}{H^{(n)} + H_{dyn}^{(n)}}, n = 1, .., N \tag{5.110}$$

$$\dot{\alpha}^{(R)} = S\left(Q^{(ext)}\right) \cdot \sum_{n=1}^{N} R^{(n)} \cdot \left|\dot{\alpha}^{(n)}\right| = S(Q^{(ext)}) \cdot \sum_{n=1}^{N} R^{(n)} \cdot \left| \frac{\dot{Q}^{(n)}}{H^{(n)} + H_{dyn}^{(n)}} \right|. \tag{5.111}$$

The substitution of Eqs. (5.110) and (5.111) into Eq. (5.74) gives the incremental form of the one-dimensional model, represented below

$$\dot{Q}^{(ext)} = H^{(0)} \cdot \left(\dot{q} - \sum_{n=1}^{N} \dot{\alpha}^{(n)} - \dot{\alpha}^{(R)} \right) + m^{(0)} \cdot \ddot{q}^2 =$$

$$= H^{(0)} \cdot \left(\dot{q} - \sum_{n=1}^{N} \frac{\dot{Q}^{(n)}}{H^{(n)} + H_{dyn}^{(n)}} - S(Q^{(ext)}) \cdot \sum_{n=1}^{N} R^{(n)} \cdot \left| \frac{\dot{Q}^{(n)}}{H^{(n)} + H_{dyn}^{(n)}} \right| \right) +$$

$$+ m^{(0)} \cdot \ddot{q}^2. \tag{5.112}$$

The unknowns of the problem are the force $Q^{(ext)}$ (or the total displacement q), that is the output quantity for the macro-element, and the internal forces $Q^{(n)}$ in the n dissipative devices, which are related to the inertial forces $Q^{(M,n)}$ by the local balance equations in Eq. 5.35. The solution of the incremental form in Eq. 5.112 requires therefore the introduction of the n local equations of motion of the masses, represented by Eqs. 5.35 and 5.36 previously defined. The incremental form of the local equations of motion reads

$$m^{(n)} \cdot \sum_{j=n}^{N} \ddot{\alpha}^{(j)} = H^{(n)} \cdot \dot{\alpha}^{(n)} - H^{(n-1)} \cdot \dot{\alpha}^{(n-1)}, n = 1, ..., N \tag{5.113}$$

that, solved at each time step together with Eq. (5.112), make the mathematical model well-posed because composed of $N + 1$ unknowns $\left\{ Q^{(ext)}, Q^{(n)} \right\}$ and $N + 1$ equations. The considerations above are still valid when the model is perturbed by a time history of the force $Q^{(ext)}$ and considering the total displacement q as the response quantity.

5.7 Multi-axial formulation

In the tensorial form, the forces and the displacements are grouped into two first-

order tensors in which the generic terms $Q_i^{(l)}$ and $q_i^{(l)}$ are the force and displacement, respectively, acting in the i direction, while the superscript l identifies the device which they refer to. Each mass is represented by a diagonal second-order tensor $m_{ij}^{(l)}$. This implies that there is no directional coupling of the inertial effects: the effect of a mass $m_{11}^{(n)}$ is only on the displacement $q_{11}^{(n)}$ developing in the same direction. Under the assumption of no moment transmission at the deck-abutment contact, this seems a reasonable hypothesis since the directional coupling of the displacement field should be mainly due to the peculiar geometry of the abutment and not caused by the inertial coupling.

5.7.1 Balance and compatibility

The derivation of the global balance equation is straightforward:

$$Q_i^{(ext)} + Q_i^{(M,0)} + \sum_1^N Q_i^{(M,n)} + Q_i^{(int)} = 0, i = 1, 2, 3 \tag{5.114}$$

with inertial forces $Q_i^{(M,n)}$ determined by the local equilibrium

$$Q_i^{(M,n)} = Q_i^{(n-1)} - Q_i^{(n)}, n = 1, .., N, i = 1, 2, 3 \tag{5.115}$$

combined with the constitutive law of the so-called generalised Voight model

$$Q_i^{(n)} = k_i^{(n)} + H_{ij}^{(n)} \cdot \alpha_j^{(n)}, n = 1, .., N, i = 1, 2, 3. \tag{5.116}$$

The strength $k_i^{(n)}$ associated with the activation of the n-th plastic flow depends on the load direction, relation that will be defined later in deriving the yield surfaces of the soil-abutment system under multi-axial loading paths. Also the stiffness $H_{ij}^{(n)}$ presents directional properties that are described by the generalised hardening rule adopted for the model at hand (see Section 5.9.3). Finally, as for the one-dimensional

model, the plastic deformations are assumed as internal variables $\alpha_j^{(n)} = q_j^{(n)}$,$n = 1, ..., N$, which allow to take into consideration the past history of the macro-element on its current response.

Also compatibility is simply the multi-directional generalisation of Eq. 5.37

$$q_j = q_j^{(0)} + \sum_1^N q_j^{(n)} + q_j^{(R)} = \sum_0^N q_j^{(n)} + q_j^{(R)}, j = 1, 2, 3 \tag{5.117}$$

with the total displacement characterised by the norm q

$$q = \sqrt{q_1^2 + q_2^2 + q_3^2}. \tag{5.118}$$

and by the orientation obtained through the direction cosines $cos\,(\theta_i) = q_i/q$.

5.8 Energy function

As presented for the one-dimensional model (1D model), each contribution to the mechanical work is now computed in order to evaluate the multi-axial formulation of the energy functions:

- work associated with the elastic response (spring 0 in the one-dimensional model)

$$L^{(0)} = \int_0^{q_i^{(0)}} Q_i^{(0)} \cdot dq_i = \int_0^{q_i^{(0)}} H_{ij}^{(0)} \cdot q_j \cdot dq_i =$$

$$= \frac{1}{2} \cdot H_{ij}^{(0)} \cdot q_j^{(0)} \cdot q_i^{(0)} = \frac{1}{2} \cdot C_{ji}^{(0)} \cdot Q_i^{(0)} \cdot Q_j^{(0)} \tag{5.119}$$

with $C_{ji}^{(0)} = H_{ji}^{(0)-1}$ the second-order initial tangent compliance matrix.

- work associated wih the n-th plastic flow, also called plastic work (sliders in the 1D model)

$$\sum_{n=1}^{N} L^{(k,n)} = \sum_{n=1}^{N} \int_0^{q_i^{(n)}} Q_i^{(n)} \cdot dq_i = \sum_{n=1}^{N} Q_i^{(n)} \cdot q_i^{(n)} =$$

$$= \sum_{n=1}^{N} k_i^{(n)} \cdot \alpha_i^{(n)}, n = 1, ..., N \tag{5.120}$$

in which the n-th internal force $Q_i^{(n)}$ is equal to the corresponding strength when the n-th yield is attained.

- work done by the "hardening" forces (kinematic hardening springs in the 1D model)

$$\sum_{n=1}^{N} L^{(H,n)} = \sum_{n=1}^{N} \int_0^{q_j^{(n)}} Q_i^{(n)} \cdot dq_i = \sum_{n=1}^{N} \int_0^{q_n} H_{ij}^{(n)} \cdot q_j^{(n)} \cdot dq_i =$$

$$= \sum_{n=1}^{N} \frac{1}{2} \cdot H_{ij}^{(n)} \cdot q_j^{(n)} \cdot q_i^{(n)}. \tag{5.121}$$

- work produced by ratcheting

$$L^{(R)} = \int_0^{q_i^{(R)}} Q_i^{(R)} \cdot dq_i = Q_i^{(R)} \cdot q_i^{(R)} = Q_i^{(R)} \cdot \alpha_i^{(R)}. \tag{5.122}$$

- work done by the inertial forces (from the mass 0 to the last mass N)

$$\sum_{n=0}^{N} L^{(M,n)} = \sum_{n=0}^{N} \int_0^{\sum_{h=n}^{N} q_j^{(h)}} Q_i^{(M,n)} \cdot dq_i = \sum_{n=0}^{N} \int_0^{\sum_{j=n}^{N} q_j^{(h)}} m_{ij}^{(n)} \cdot \ddot{q}_j \cdot dq_i =$$

$$= \sum_{n=0}^{N} \int_0^{\sum_{j=n}^{N} q_j^{(h)}} m_{ij}^{(n)} \cdot \dot{q}_j \cdot d\dot{q}_i = \frac{1}{2} \cdot \sum_{n=0}^{N} m_{ij}^{(n)} \cdot \left(\sum_{h=n}^{N} \dot{q}_j^{(h)} \right) \cdot \left(\sum_{h=n}^{N} \dot{q}_i^{(h)} \right). \tag{5.123}$$

By separating the elastic and the plastic displacements, Eq. 5.123 reads

$$\sum_{n=0}^{N} L^{(M,n)} = \frac{1}{2} \cdot \sum_{n=0}^{N} m_{ij}^{(n)} \cdot \left(\sum_{h=n}^{N} \dot{q}_j^{(h)} \right) \cdot \left(\sum_{h=n}^{N} \dot{q}_i^{(h)} \right) = \frac{1}{2} \cdot m_{ij}^{(0)} \cdot \dot{q}_j^{(0)} \cdot \dot{q}_i^{(0)} +$$

$$+\frac{1}{2}\cdot\sum_{n=1}^{N} m_{ij}^{(n)}\cdot\left(\sum_{h=n}^{N}\dot{q}_j^{(h)}\right)\cdot\left(\sum_{h=n}^{N}\dot{q}_i^{(h)}\right) \tag{5.124}$$

and recognising that the absolute velocity $\sum_{h=n}^{N}\dot{q}_j^{(h)}$ can be written as $\dot{q}_j^{(0)} + \sum_{n=1}^{N}\dot{\alpha}_j^{(n)} = C_{ji}^{(0)}\cdot\dot{Q}_i^{(0)} + \sum_{n=1}^{N}\dot{\alpha}_j^{(n)}$ for compatibility, Eq. 5.124 becomes

$$\sum_{n=0}^{N} L^{(M,n)} = \frac{1}{2}\cdot m_{ij}^{(0)}\cdot\left(C_{ji}^{(0)}\cdot\dot{Q}_i^{(0)} + \sum_{n=1}^{N}\dot{\alpha}_j^{(n)}\right)\cdot$$

$$\cdot\left(C_{ij}^{(0)}\cdot\dot{Q}_j^{(0)} + \sum_{n=1}^{N}\dot{\alpha}_i^{(n)}\right) + \frac{1}{2}\cdot\sum_{n=1}^{N} m_{ij}^{(n)}\cdot\left(\sum_{h=n}^{N}\dot{\alpha}_j^{(h)}\right)\cdot\left(\sum_{h=n}^{N}\dot{\alpha}_i^{(h)}\right). \tag{5.125}$$

The complementary work can be computed by using the Legendre transform and assumes the following form

$$\sum_{n=0}^{N} L_{comp}^{(M,n)} = \sum_{n=0}^{N} Q_i^{(M,n)}\cdot\sum_{h=n}^{N} q_i^{(h)} - \sum_{n=0}^{N} L^{(M,n)} =$$

$$= m_{ij}^{(0)}\cdot\ddot{q}_j^{(0)}\cdot q_i^{(0)} + \sum_{n=1}^{N} m_{ij}^{(n)}\cdot\sum_{h=n}^{N}\ddot{q}_j^{(h)}\cdot\sum_{k=n}^{N} q_i^{(k)} -$$

$$-\frac{1}{2}\cdot m_{ij}^{(0)}\cdot\dot{\alpha}_j^{(0)}\cdot\dot{\alpha}_i^{(0)} - \frac{1}{2}\cdot\sum_{n=1}^{N} m_{ij}^{(n)}\cdot\left(\sum_{h=n}^{N}\dot{\alpha}_j^{(h)}\right)\cdot\left(\sum_{h=n}^{N}\dot{\alpha}_i^{(h)}\right) =$$

$$= m_{ij}^{(0)}\cdot\left(C_{ji}^{(0)}\cdot\ddot{Q}_i^{(0)} + \sum_{n=1}^{N}\ddot{\alpha}_j^{(n)}\right)\cdot\left(C_{ij}^{(0)}\cdot Q_j^{(0)} + \sum_{n=1}^{N}\alpha_i^{(n)}\right) +$$

$$+\sum_{n=1}^{N} m_{ij}^{(n)}\cdot\sum_{h=n}^{N}\ddot{q}_j^{(h)}\cdot\sum_{k=n}^{N} q_i^{(k)} - \frac{1}{2}\cdot m_{ij}^{(0)}\cdot\dot{\alpha}_j^{(0)}\cdot\dot{\alpha}_i^{(0)} -$$

$$-\frac{1}{2}\cdot\sum_{n=1}^{N} m_{ij}^{(n)}\cdot\left(\sum_{h=n}^{N}\dot{\alpha}_j^{(h)}\right)\cdot\left(\sum_{h=n}^{N}\dot{\alpha}_i^{(h)}\right). \tag{5.126}$$

5.8.1 Gibbs free energy

Based on the above expressions, the Gibbs free energy is given below

$$g(Q_i^{(n)},\alpha_i^{(n)},m_{ij}^{(n)}) = -L(Q_i^{(n)},\alpha_i^{(n)},m_{ij}^{(n)}) =$$

$$= -L^{(0)}\left(Q_i^{(0)}\right) - \sum_{n=1}^{N} L^{(k,n)}(Q_i^{(n)},\alpha_i^{(n)}) + \sum_{n=1}^{N} L^{(H,n)}(Q_i^{(n)},\alpha_i^{(n)}) -$$

$$-L^{(R)}(Q_i^{(n)},\alpha_i^{(n)}) - \sum_{n=1}^{N} L^{(M,n)}(Q_i^{(n)},\alpha_i^{(n)},m_{ij}^{(n)}) =$$

$$= -\frac{1}{2}\cdot C_{ji}^{(0)}\cdot Q_i^{(0)}\cdot Q_j^{(0)} - \sum_{n=1}^{N} Q_i^{(n)}\cdot\alpha_i^{(n)} +$$

$$+\frac{1}{2}\cdot\sum_{n=1}^{N} H_{ij}^{(n)}\cdot\alpha_j^{(n)}\cdot\alpha_i^{(n)} - Q_i^{(R)}\cdot\alpha_i^{(R)} - m_{ij}^{(0)}\cdot\sum_{h=0}^{N}\ddot{q}_j^{(h)}\cdot\sum_{k=0}^{N} q_i^{(k)} +$$

$$-\sum_{n=1}^{N} m_{ij}^{(n)}\cdot\sum_{h=n}^{N}\ddot{\alpha}_j^{(h)}\cdot\sum_{k=n}^{N}\alpha_i^{(k)} + \frac{1}{2}\cdot m_{ij}^{(0)}\cdot\left(\sum_{h=0}^{N}\dot{\alpha}_j^{(h)}\right)\cdot\left(\sum_{h=0}^{N}\dot{\alpha}_i^{(h)}\right) +$$

$$+\frac{1}{2}\cdot\sum_{n=1}^{N} m_{ij}^{(n)}\cdot\left(\sum_{h=n}^{N}\dot{\alpha}_j^{(h)}\right)\cdot\left(\sum_{h=n}^{N}\dot{\alpha}_i^{(h)}\right). \tag{5.127}$$

In virtue of the elastic-plastic uncoupling, the Gibbs free energy can be rewritten as the sum of the three separated terms in Eq. 5.55 and, in particular, the function

$g_2(0, \alpha_i^{(n)}, m_{ij}^{(n)})$, important for deriving the plastic multiplier, reads

$$g_2(0, \alpha_i^{(n)}, m_{ij}^{(n)}) = \frac{1}{2} \cdot \sum_{n=1}^{N} H_{ij}^{(n)} \cdot \alpha_j^{(n)} \cdot \alpha_i^{(n)} - m_{ij}^{(0)} \cdot \sum_{h=0}^{N} \ddot{q}_j^{(h)} \cdot \sum_{k=0}^{N} q_i^{(k)} -$$

$$- \sum_{n=1}^{N} m_{ij}^{(n)} \cdot \sum_{h=n}^{N} \ddot{\alpha}_j^{(h)} \cdot \sum_{k=n}^{N} \alpha_i^{(k)} + \frac{1}{2} \cdot m_{ij}^{(0)} \cdot \left(\sum_{h=0}^{N} \dot{\alpha}_j^{(h)} \right) \cdot \left(\sum_{h=0}^{N} \dot{\alpha}_i^{(h)} \right) +$$

$$+ \frac{1}{2} \cdot \sum_{n=1}^{N} m_{ij}^{(n)} \cdot \left(\sum_{h=n}^{N} \dot{\alpha}_j^{(h)} \right) \cdot \left(\sum_{h=n}^{N} \dot{\alpha}_i^{(h)} \right). \tag{5.128}$$

As for the 1D model, the inertial addenda can be grouped into the inertial function $g_{in}(m_{ij}^{(n)})$

$$g_{in}(m_{ij}^{(n)}) = - \sum_{n=0}^{N} m_{ij}^{(n)} \cdot \sum_{h=n}^{N} \ddot{q}_j^{(h)} \cdot \sum_{k=n}^{N} q_i^{(k)} +$$

$$+ \frac{1}{2} \cdot \sum_{n=0}^{N} m_{ij}^{(n)} \cdot \left(\sum_{h=n}^{N} \dot{\alpha}_j^{(h)} \right) \cdot \left(\sum_{h=n}^{N} \dot{\alpha}_i^{(h)} \right) \tag{5.129}$$

and the Gibbs free energy results to be the sum of the so-called "static" function g_{st}, not dependent on the mass tensors $m_{ij}^{(n)}$, and the inertial function g_{in}, that confers a frequency-dependent response to the model, thus

$$g(Q_i^{(n)}, \alpha_i^{(n)}, m_{ij}^{(n)}) = g_{st}(Q_i^{(n)}, \alpha_i^{(n)}, 0) + g_{in}(Q_i^{(n)}, \alpha_i^{(n)}, m_{ij}^{(n)}). \tag{5.130}$$

5.8.2 Helmholtz free energy

The generalization of the Helmholtz free energy is given by the following equation

$$f(q_i^{(n)}, \alpha_i^{(n)}, m_{ij}^{(n)}) = L_{comp}(q_i^{(n)}, \alpha_i^{(n)}, m_{ij}^{(n)}) =$$

$$= \frac{1}{2} \cdot H_{ij}^{(0)} \cdot q_j^{(0)} \cdot q_i^{(0)} + \frac{1}{2} \cdot \sum_{n=1}^{N} H_{ij}^{(n)} \cdot \alpha_j^{(n)} \cdot \alpha_i^{(n)} +$$

$$+ \frac{1}{2} \cdot \sum_{n=0}^{N} m_{ij}^{(n)} \cdot \left(\sum_{h=n}^{N} \dot{q}_j^{(h)} \right) \cdot \left(\sum_{h=n}^{N} \dot{q}_i^{(h)} \right) = \frac{1}{2} \cdot H_{ij}^{(0)} \cdot q_j^{(0)} \cdot q_i^{(0)} +$$

$$+ \frac{1}{2} \cdot \sum_{n=1}^{N} H_{ij}^{(n)} \cdot \alpha_j^{(n)} \cdot \alpha_i^{(n)} + \frac{1}{2} \cdot m_{ij}^{(0)} \cdot \dot{q}_j \cdot \dot{q}_i +$$

$$+ \frac{1}{2} \cdot \sum_{n=1}^{N} m_{ij}^{(n)} \cdot \left(\sum_{h=n}^{N} \dot{q}_j^{(h)} \right) \cdot \left(\sum_{h=n}^{N} \dot{q}_i^{(h)} \right) =$$

$$= f_{st}(q_i^{(n)}, \alpha_i^{(n)}, 0_{ij}) + f_{in}(q_i^{(n)}, \alpha_i^{(n)}, m_{ij}^{(n)}) \tag{5.131}$$

in which the static and inertial functions read

$$f_{st}(q_i^{(n)}, \alpha_i^{(n)}, 0_{ij}) = \frac{1}{2} \cdot H_{ij}^{(0)} \cdot q_j^{(0)} \cdot q_i^{(0)} + \frac{1}{2} \cdot \sum_{n=1}^{N} H_{ij}^{(n)} \cdot \alpha_j^{(n)} \cdot \alpha_i^{(n)} \tag{5.132}$$

$$f_{in}(q_i^{(n)}, \alpha_i^{(n)}, m_{ij}^{(n)}) = \frac{1}{2} \cdot \sum_{n=0}^{N} m_{ij}^{(n)} \cdot \left(\sum_{h=n}^{N} \dot{q}_j^{(h)} \right) \cdot \left(\sum_{h=n}^{N} \dot{q}_i^{(h)} \right) =$$

$$= \frac{1}{2} \cdot m_{ij}^{(0)} \cdot \dot{q}_j \cdot \dot{q}_i + \frac{1}{2} \cdot \sum_{n=1}^{N} m_{ij}^{(n)} \cdot \left(\sum_{h=n}^{N} \dot{q}_j^{(h)} \right) \cdot \left(\sum_{h=n}^{N} \dot{q}_i^{(h)} \right). \tag{5.133}$$

5.9 Yield functions

The plastic domain is confined by two important loci: the surface of first yield and the surface of ultimate conditions. The former refers to the locus from which the nonlinear response of the system is no longer negligible, while the latter represents the locus of activation of global plastic mechanisms of the soil-abutment system.

The entire configuration of the yield surfaces of the macro-element is based on the identification of these two boundary surfaces, that are therefore initially presented for then defining the inner surfaces and their evolution.

5.9.1 Ultimate conditions of the soil-abutment system

Under the large forces transmitted by a bridge structure during an earthquake, a bridge abutment may undergo significant displacements deriving from the mobilisation of both the soil and the structural strength. The potential plastic mechanisms that can occur under complex loading patterns are here examined to derive a general framework for the ultimate conditions of the soil-abutment system. On the basis of the results presented in the following, the concept of dissipative abutment, with possibility to have a plastic response of the abutment structure and introduction to a new anti-seismic technology for the abutment system, is explored in Appendix 1.

Due to its asymmetry, the capacity of the abutment is expected to be highly dependent on the load direction. In this study, the capacity of bridge abutments under general loading paths was analysed through the application of the theorems of limit analysis in finite element simulations (Sloan 1988, 1989) by using the software Optum G2 and Optum G3 (OptumCE 2016), related to bi- and three-dimensional modelling, respectively. Limit analysis allows for a rapid assessment of the stability or bearing capacity of geostructures without having to perform an exhaustive step-by-step elastoplastic analysis. The theorems of limit analysis can be proved for material that conform to perfect plasticity with a convex yield criterion and with deformation governed by the normality rule.

5.9.1.1 Limit analysis and numerical modelling

Figure 5.6 shows the geometry of the abutment taken as reference in this study, inspired by the abutment of the Pantano viaduct (Gorini and Callisto 2017) already

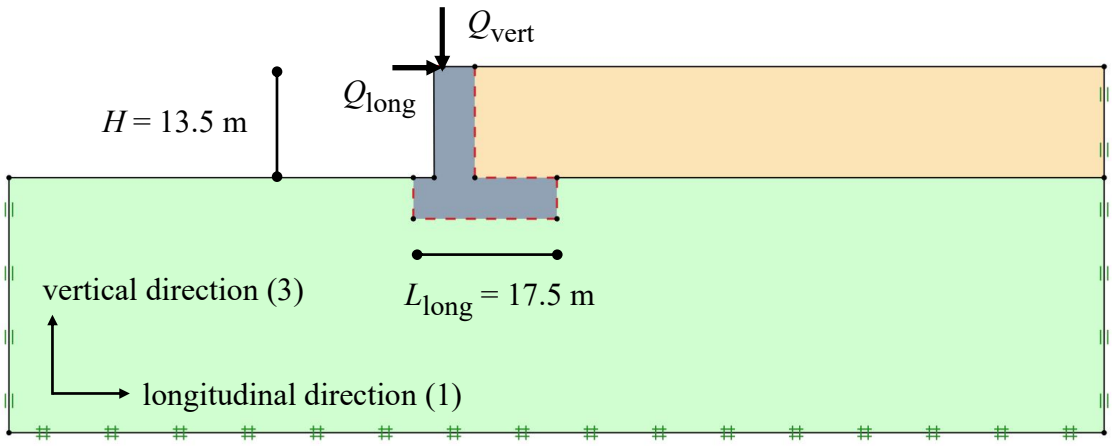

Figure 5.6: Reference configuration of the abutment: two-dimensional model implemented in Optum G2.

described in Section 3.6. As mentioned before, the main objective pursued in this section is to define a general model describing the ultimate conditions of bridge abutments. Hence, starting from the geometry of the abutment above, employed in the reference global soil-bridge model, several generic configurations of the abutment were analysed, considering more typical values of the strength parameters of soil and also varying the geometry of the system.

The soil domain is composed of a homogeneous foundation soil and the embankment behind the wall. The fixed boundaries of the model are located far enough from the abutment in order to guarantee that the response of the latter is not affected by the boundary conditions. All the elements in the numerical models were represented by solid elements with rigid-perfectly plastic behaviour described by the Mohr-Coulomb failure criterion with associated flow rule. The interface between soil and structure was modelled as a frictional connection (shear joint in Optum) in the two-dimensional models and through a thin layer meshed by solid elements in the three-dimensional models, with appropriate strength properties.

The external perturbation for the abutment is represented by a set of forces

applied to the top of the central wall (distributed forces in the three-dimensional representations), representative of the load coming from the deck. The positive signs of the forces are those shown in Figure 5.6. The numerical simulations consist in determining the value of the so-called collapse multiplier, intended as the intensity of the external force that causes the failure of the system. Each analysis is composed of several iterations with mesh adaptivity in order to concentrate the discretization of the domain where plastic strains occur. The calculation stops when the two limit solutions (provided by the lower-bound and upper-bound plasticity solutions) stabilise at a constant value, identifying a sufficiently narrow range for a good approximation of the exact solution. The results shown in the following are related to upper bound solutions to also analyse the kinematics associated with the plastic modes. In order to compare the response of the three-dimensional models with that obtained by the two-dimensional models, the failure loads are expressed in terms of forces per unit length of the central wall.

5.9.1.2 Non-dimensional formulation

The variability of the ultimate surface in different configurations of the soil-abutment system was studied through the definition of a rigorous non-dimensional formulation of the problem. In this way, the main factors that control the shape and the size of the ultimate locus were highlighted ensuring the general validity of the results. In accordance with Buckingham theorem, from the 18 physical quantities that describe the problem (Table 5.1), one can derive the 16 non-dimensional groups, listed in Table 5.2, that characterise completely the mechanical model.

Some reasonable assumptions were made to reduce the quantities of the system and accordingly the number of groups. The backfill and the embankment were assumed to be composed of the same frictional material ($\mu_{back} = \mu_{emb}$, $c_{back} = c_{emb} = 0$) but, in general, with different properties from the foundation soil (μ_{soil},

Symbol	Dimension	Description
μ_{soil}	-	*Friction coefficient of the foundation soil*
μ_{emb}	-	*Friction coefficient of the embankment*
μ_{int}	-	*Friction coefficient of the soil-structure interface*
H	L	*Height of the abutment*
L_{long}	L	*Foundation length in the longitudinal direction*
L_{tr}	L	*Foundation length in the transverse direction*
μ_{abut}	-	*Friction coefficient of the abutment structure*
c_{abut}	$\mathrm{M{\cdot}L^{-1}{\cdot}T^{-2}}$	*Cohesion of the abutment structure*
i_{long}	L	*Distance between piles in the longitudinal direction*
i_{tr}	L	*Distance between piles in the transverse direction*
L_p	L	*Length of piles*
D_p	L	*Diameter of piles*
μ_p	-	*Friction coefficient of piles*
c_p	$\mathrm{M{\cdot}L^{-1}{\cdot}T^{-2}}$	*Cohesion of piles*
Q_1	$\mathrm{M{\cdot}L{\cdot}T^{-2}}$	*External force in the longitudinal direction*
Q_2	$\mathrm{M{\cdot}L{\cdot}T^{-2}}$	*External force in the transverse direction*
Q_3	$\mathrm{M{\cdot}L{\cdot}T^{-2}}$	*External force in the vertical direction*
Q_{r2}	$\mathrm{M{\cdot}L^{2}{\cdot}T^{-2}}$	*External moment around the transverse axis*

Tabella 5.1: Physical quantities characterising the soil-abutment system.

Number	Group	Definition
1	μ_{soil}	*Friction coefficient of the foundation soil*
2	μ_{emb}	*Friction coefficient of the embankment*
3	μ_{int}	*Friction coefficient of the soil-structure interface*
4	μ_{abut}	*Friction coefficient of the abutment*
5	$c_{abut} \cdot H^2/Q_1$	*Dimensionless abutment cohesion*
6	H/L_{long}	*Longitudinal aspect ratio of the abutment*
7	H/L_{tr}	*Transverse aspect ratio of the abutment*
8	Q_2/Q_1	*Skew load*
9	$Q_3/(\gamma_{soil} \cdot H \cdot L_{long})$	*Dimensionless vertical external force*
10	$Q_{r2}/(Q_1 \cdot H)$	*Dimensionless transverse moment*
11	i_{long}/D_p	*Normalised longitudinal interax of piles*
12	i_{tr}/D_p	*Normalised transverse interax of piles*
13	μ_p	*Friction coefficient of piles*
14	$c_p \cdot D_p^2/Q_1$	*Strength factor of piles*
15	L_p/D_p	*Slenderness of piles*
16	L_p/H	*Abutment-pile length ratio*

Tabella 5.2: Non-dimensional groups of the soil-abutment system.

$c_{soil} = 0$). A unit weight of 20 kN/m^3 was considered for the entire soil domain, while the abutment and the piles were designed as reinforced concrete elements with unit weight equal to 25 kN/m^3 (Appendix 1 devoted to dissipative abutments). For soil-concrete contact, the friction coefficient along the interface can be reasonably taken equal to that of the soil. With all these assumptions, the behaviour of an abutment resting on a shallow foundation is controlled by 10 non-dimensional groups (n. 1 to n. 10 in Table 5.2) while the remaining groups link the properties of the pile group beneath the raft to the characteristics of the abutment and the load pattern. Some groups are a function of the geometry of the abutment, n. 5 and 6, and of the pile group, n. 14 and 15, while there are several linking groups that combine the strength parameters of the system with the external forces, n. 8, 9 and 13, and with the geometric quantities, n. 4 and 13.

5.9.1.3 Bi-axial load

Consider the two-dimensional model of the reference abutment described above (Figure 5.6) loaded by a combined longitudinal-vertical force (L-V plane) on the top of the central wall. The structure is assumed to have infinite strength, in order to focus on failure of soil, while the foundation soil and the embankment present the same friction coefficient equal to 0.577 (friction angle $\varphi_{soil} = \varphi_{emb} = 30°$). Figure 5.7 shows, in the space of the forces $\{Q_1, Q_3\}$, the points representing the activation of global plastic mechanisms of the system for different ratios Q_3/Q_1 of the vertical to the longitudinal force.

It is evident that the failure points can be well described by an ellipse, characterised by a specific orientation δ with respect to the vertical axis Q_3, that identifies the ratio Q_3/Q_1 correspondent to the maximum capacity Q_{max}. In the longitudinal direction ($Q_3 = 0$), the positive and negative limit forces are associated with the attainment of the passive and active resistance in the soil behind the wall, respec-

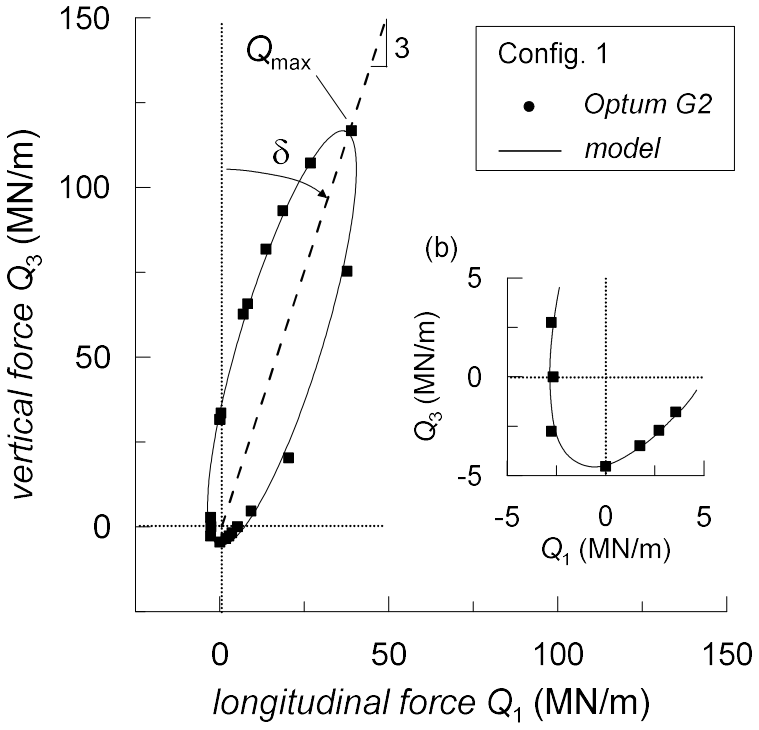

Figure 5.7: Failure points for the combined longitudinal-vertical load and their fitting with an ellipse-shaped model.

tively. In the vertical direction instead ($Q_1 = 0$), the positive limit value represents the bearing capacity of the foundation while the negative limit value is the force directed upwards that produces the uplift of the abutment and part of the soil sitting on the footing.

The ellipse is almost entirely located in the first quadrant of the positive forces, reflecting the highly asymmetric response of the abutment: the simultaneous application of the two components of the load leads to a noticeable increase of the capacity when the forces are directed downwards and towards the backfill while it causes a drastic reduction of the resistance when they push away the abutment from the soil, as highlighted in the zoomed-in graph in Figure 5.7(b). The orientation δ of the ellipse is strongly controlled by the friction coefficient at the soil-abutment interface, as it will be better described later. The maximum capacity is instead dependent on

the soil strength and the abutment geometry. The failure mode associated with the maximum capacity is illustrated in Figure 5.8(a) in which the strength is attained largely in the soil behind the wall, with a logarithmic spiral-shaped sliding surface that extends downstream beyond the footing. This failure mode can be therefore regarded as the combined mobilization of the passive resistance of the embankment and the bearing capacity of the foundation soil. In correspondence with the minimum capacity instead, the failure mechanism, shown in Figure 5.8(b), reveals that the abutment and part of the backfill tend to rotate as a rigid body around the downstream end of the footing.

5.9.1.4 Moment transmission at the deck-abutment contact

For integral abutments, the deck-abutment joint allows the transmission of moment between them. As already described in detail in Section 5.1, the bending moment Q_{r2} acting in the L-V plane is often the most relevant source of rotation for an abutment, compared to the longitudinal and vertical moments, and therefore it is the only component taken into consideration in the following. The effect of a clockwise moment Q_{r2} on failure is shown in Figure 5.9, for different levels of Q_{r2} with respect to the limit value $Q_{r2,lim}$, the latter referred to the case in which the moment is the only external force acting on the abutment. It can be observed that the presence of moment essentially causes a rotation of the ellipse around a point close to the maximum capacity, without altering the shape of the ultimate locus. It follows that the greatest effect occurs on the limit values of the longitudinal force, as highlighted in the magnified representation in Figure 5.9(b). More in detail, the effect of a clockwise moment Q_{r2} depends on how it combines with the longitudinal force Q_1: it reduces the positive limit value of Q_1 (longitudinal force pushing the abutment towards the backfill) and increases the negative value of Q_1. This happens because the moment favours the activation of the mechanism produced by the longitudinal force

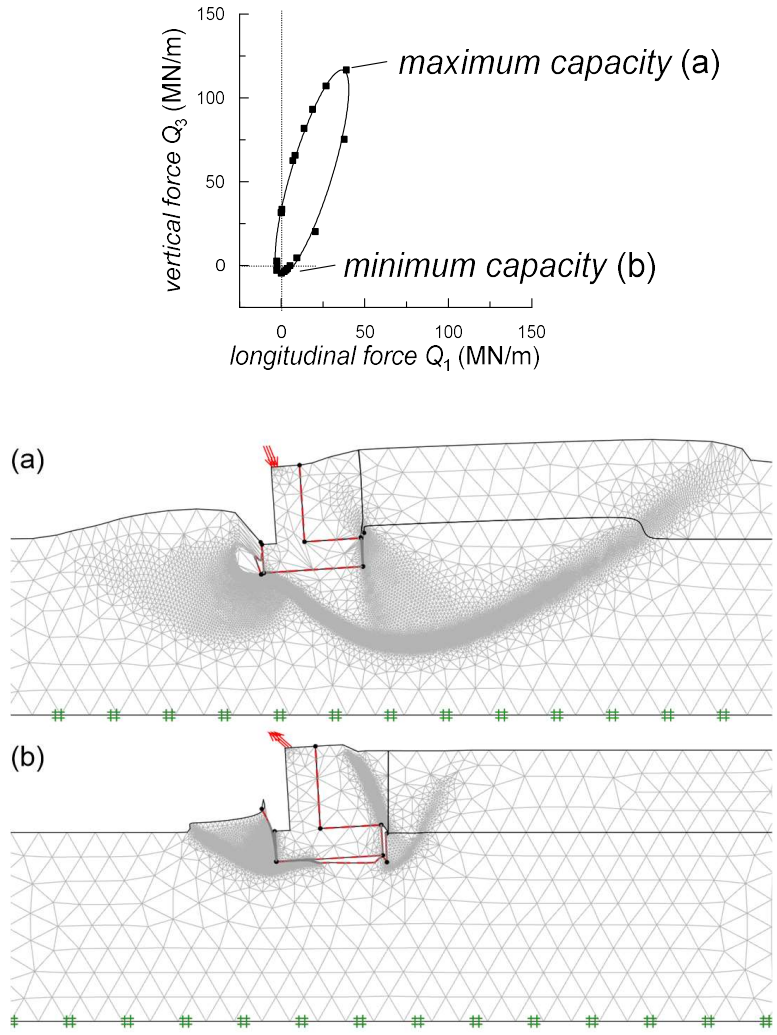

Figure 5.8: Failure mechanisms of the abutment in correspondence of the maximum (a) and minimum (b) capacity.

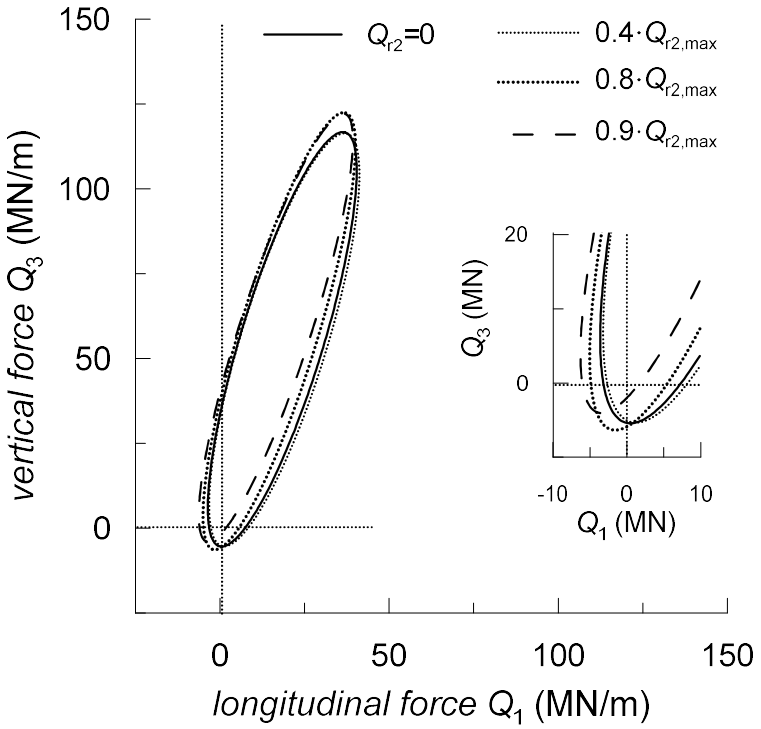

Figure 5.9: Failure surfaces in the Q_1-Q_3 plane for different levels of the clockwise external moment Q_{r2} ($Q_{r2,max} = 3.7{\cdot}10^5$ kN·m/m) acting in the longitudinal-vertical plane of the abutment.

in the first case while it contrasts the counter-clockwise rotation of the abutment due to a negative longitudinal force. The opposite situation occurs when a counter-clockwise moment is considered and the relative results are not shown herein for the sake of conciseness.

Moreover, in Figure 5.10 it is shown that the mechanisms produced by the longitudinal force are very similar to those caused by the bending moment: the abutment undergoes a roto-translation in both cases, with nearly identical sliding surfaces, around a centre of rotation C placed underneath the foundation. In light of the above results, the effect of the external moment Q_{r2} can be regarded to a pair of identical couple of longitudinal forces $Q_{1,eq}$ applied to the top of the abutment wall and at a depth h_r proportional to the height of the wall through an equivalent factor a. The latter is a function of the soil strength and the abutment geometry and it

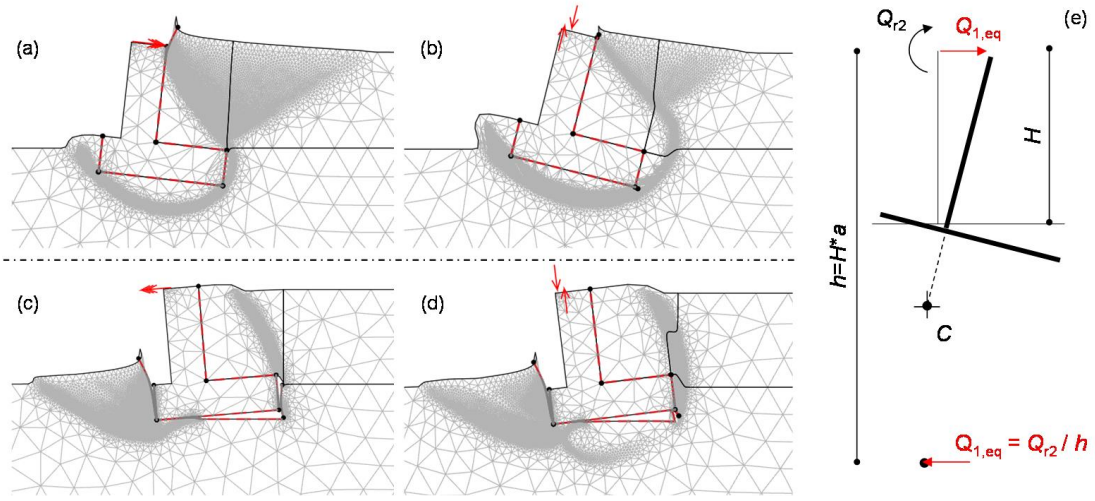

Figure 5.10: Comparison between the failure modes produced by the longitudinal external force Q_1, (a) and (c), and those related to the external moment Q_{r2}, (b) and (d); (e) physical interpretation of failure due to Q_{r2} as an equivalent couple of horizontal forces $Q_{1,eq}$.

results equal to 3.9 and 7.3 for the cases (b) and (d), respectively. This manner to account for the presence of moments through couples of forces is in line with the normalisation schemes usually used in the macro-elements for shallow foundations (Nova and Montrasio 1991, Martin 1994, Chazichogos et al 2001, Venanzi et al. 2014). This is an important assumption because it allows to work with homogeneous physical quantities and, accordingly, also the surface of ultimate loads is defined in a homogeneous space.

Nonetheless, it is worth noticing that the deck-abutment moment can constitute a relevant source of reduction of the capacity only at very high levels of moment (Figure 5.9), hardly reachable due to the effective resistance of the deck-abutment joint. Hence, even for integral abutments, moments transmitted to the abutment seem not to affect considerably the failure of the soil-abutment system, which supports the assumption of having neglected the rotational degrees of freedom in the macro-element formulation.

5.9.1.5 Inertial effects

Under seismic conditions, the inertial effects that develop in the soil and the abutment can alter the activation of the plastic mechanisms of the system. A simplified method to study this phenomenon consists in representing the effects induced by the seismic excitation through pseudo-static forces F_e (Mononobe-Okabe theory 1924) defined as

$$F_e = m \cdot k_h \cdot g \tag{5.134}$$

where m is the mass of the volume which the force is applied to, while k_h is the horizontal seismic coefficient representing an acceleration normalised to the acceleration of gravity g. These forces were reproduced in the software Optum as a uniform field of acceleration, considered purely horizontal, applied to the entire domain through the seismic coefficient ($k_h > 0$ when the inertial forces are directed towards the backfill).

From the results illustrated in Figure 5.11 it is evident that the inertial forces provoke a contraction and a rotation of the limit surface, without altering its shape. More in detail, the dimension of the admissible domain always reduces as the seismic coefficient rises but more evidently when the inertial forces are directed upstream, because they favour the activation of the plastic mechanism associated with the maximum capacity.

The corresponding sliding surfaces are depicted in Figure 5.12, limiting the lateral extension of the soil domain for the sake of a better graphical representation: the surfaces move progressively upstream with the normalised pseudo-static acceleration while the opposite situation occurs when the inertial forces are directed downstream. Moreover, the effect on the orientation of the ellipse is emisymmetric and slightly more pronounced when the inertial forces are directed downstream,

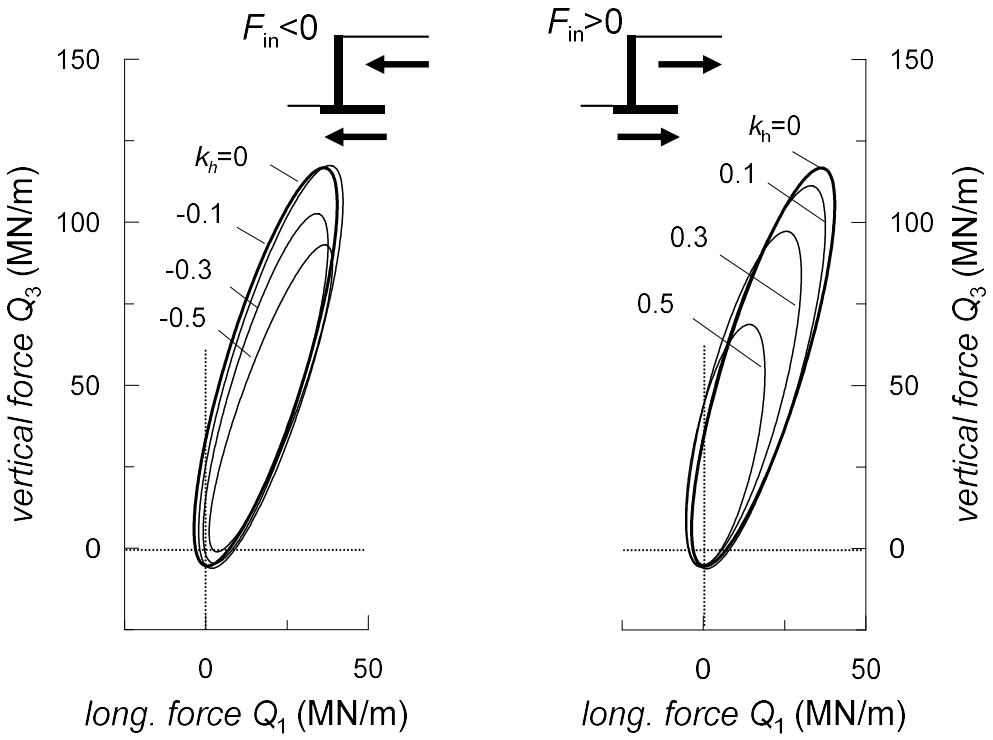

Figure 5.11: Inertial effects: comparison between the ultimate surface retrieved under static conditions ($k_h = 0$) and those obtained for different values of the seismic coefficient ($k_h > 0$ if directed towards the backfill).

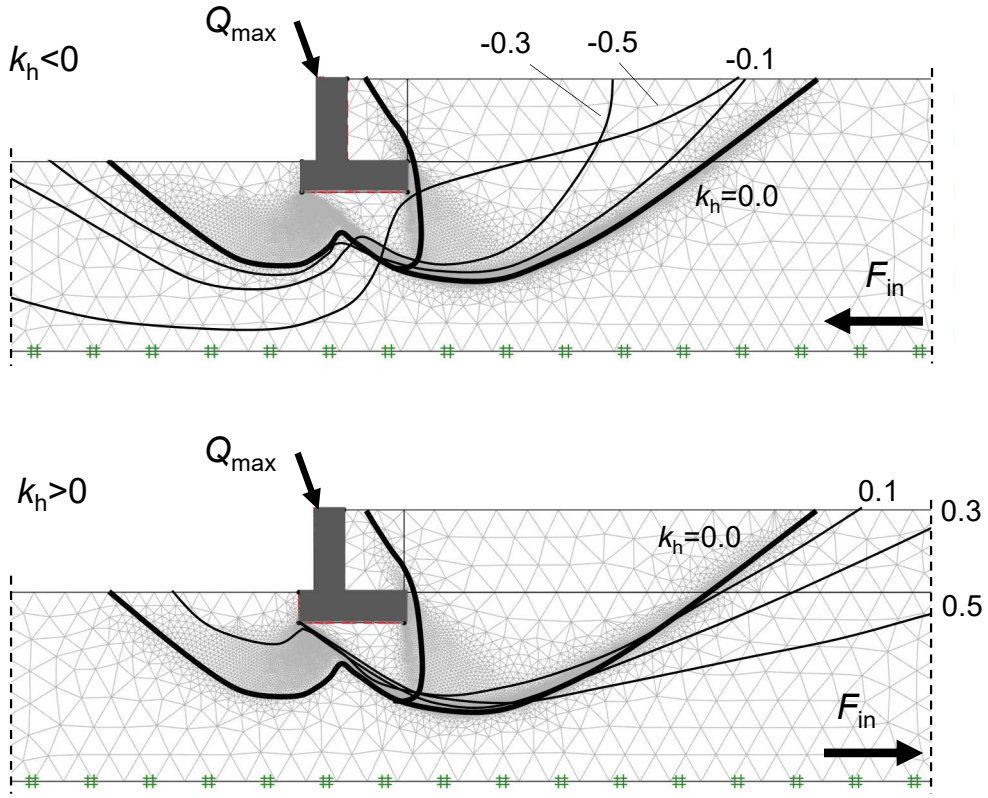

Figure 5.12: Effect of the seismic coefficient on the global plastic mechanisms correspondent to the maximum capacity of the soil-abutment system.

leading especially to a relevant reduction of the longitudinal force associated with the attainment of the active resistance in the backfill. More in detail, the failure surface undergoes a counter-clockwise rotation up to $-5.6°$ (-0.098 rad) when $k_h > 0$, reducing the positive limit force in longitudinal direction, while a clockwise rotation occurs, up to $7.3°$ (0.124 rad), for negative seismic coefficients.

Figure 5.13 also shows two dimensionless parameters, $d_d(k_h)/H$ and $d_u(k_h)/H$ describing concisely the extension of the failure modes occurring in correspondence of the maximum capacity, which reflect the considerations made above. Up to an absolute value of k_h equal to 0.3, that is usually the upper bound for the seismic motion, a unique gradient can be recognised for the dimensionless parameters, while for higher levels of k_h the extension of the mechanism increases remarkably.

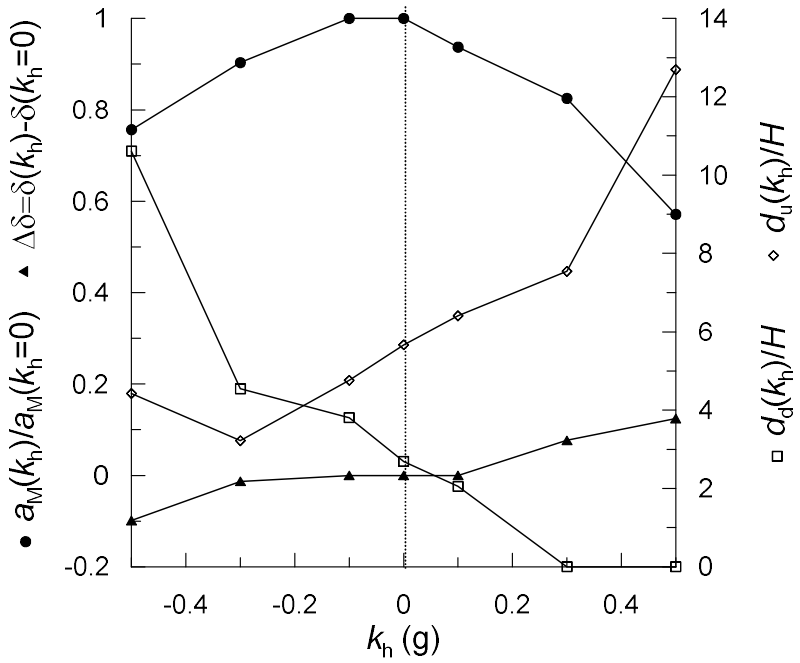

Figure 5.13: Parameters describing the geometry of the mechanisms under pseudo-static conditions.

5.9.1.6 General formulation of the ultimate surface

The results shown in the previous paragraph are referred to plane strain conditions. An effective width of the foundation is now considered to analyse the influence of the three-dimensional response of the abutment on failure. A full model of abutment is illustrated in Figure 5.14, in which the backfill is retained by the central wall and the wing walls of the abutment, that in turn are supported by a raft foundation. Laterally to the wing walls, rigid diaphragms are placed to guarantee the stability of the sides of the embankment in the longitudinal direction, resting on two slabs connected to the raft.

Simulations on such models were carried out in Optum G3, considering a transverse aspect ratio H/L_{tr} of 0.7, and the relative results are shown in Figure 5.15. The failure locus in the L-V plane retrieved in absence of the transverse force, continuous line with $Q_2/Q_1 = 0$, is larger than the respective locus under plane strain

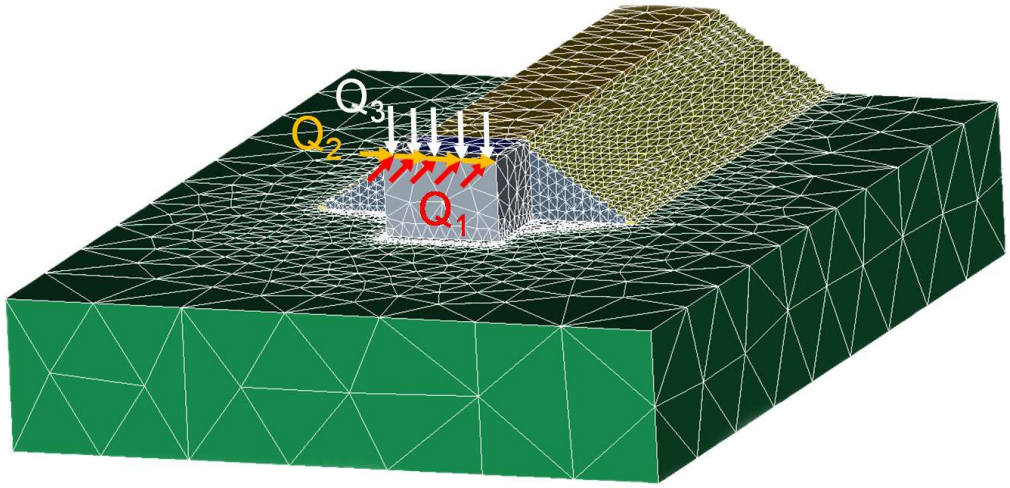

Figure 5.14: Three-dimensional model implemented in Optum G3 and positive signs of the forces applied to the abutment.

conditions (2D model), with maximum increase of the limit load in the region where the capacity attains the maximum values. This is due to a different mobilization of the soil strength and, in fact, focusing on failure in correspondence of the maximum capacity, Figure 5.16 shows the lines of equal work dissipated by the stresses in the domain: the mechanism is nearly identical to the 2D failure along the central section of the abutment, in terms of mobilization of strength and deformed shape, but in plan the sliding surface surrounds the abutment structure for then involving part of the embankment that leads to the increment of the capacity observed above.

When also a transverse force Q_2 is applied to the central wall, the size of the limit locus reduces progressively as the ratio Q_2/Q_1 rises but the ellipse keeps the same orientation, as illustrated in Figure 5.15(a). Moreover, looking at the effect of the transverse force in the transverse-vertical plane (Figure 5.15(b)), it is evident that every ultimate locus can be again represented by an ellipse with different size. More in detail, from the plane $Q_1 = 0$ MN/m, the size of the ellipse increases up to a limit value, close to $Q_1 = 10$ MN/m, for then reducing towards the maximum

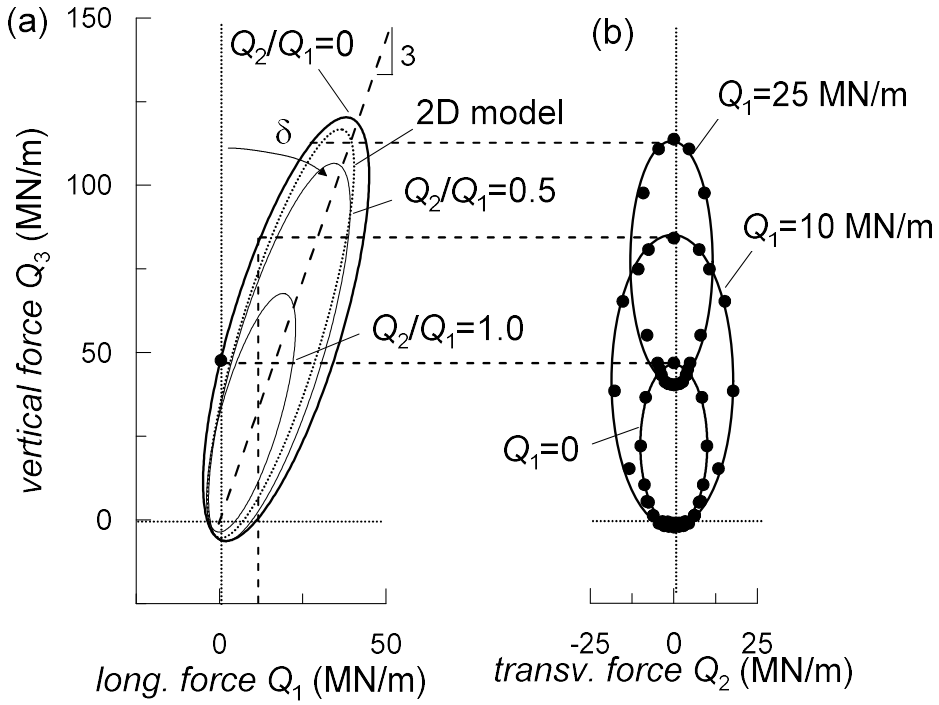

Figure 5.15: (a) Traces of the failure surface in the plane $\{Q_1, Q_3\}$ obtained through three-dimensional simulations for different values of the skew load Q_2/Q_1; (b) traces of the surface in the plane $\{Q_2, Q_3\}$.

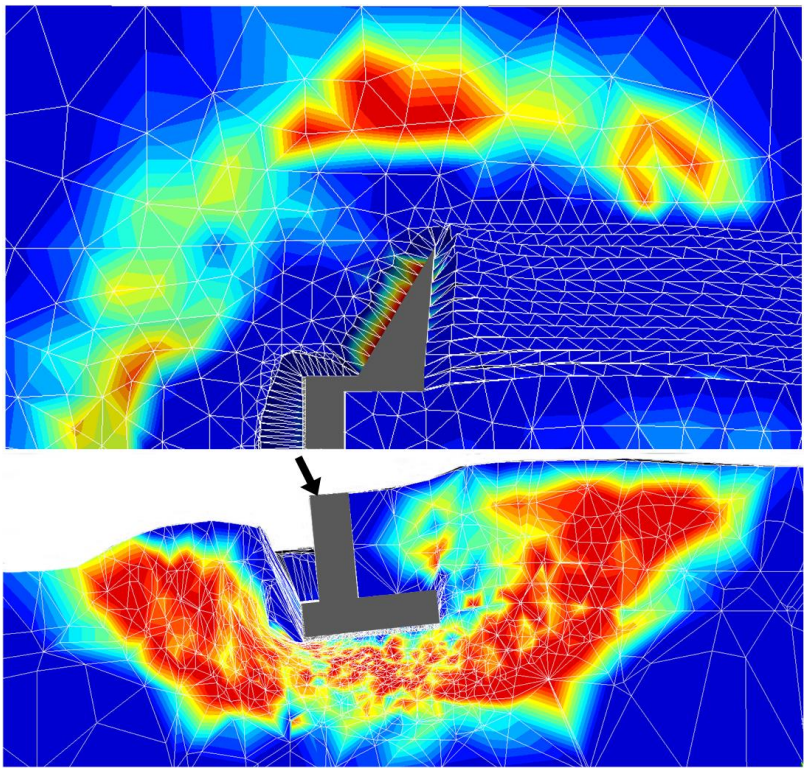

Figure 5.16: Three-dimensional failure mode correspondent to the maximum capacity: contours of the shear dissipation from 0 kJ (blue) up to 1 kJ (red).

capacity.

Accordingly, the ultimate surface of an abutment can be described by an ellipsoid, almost entirely located in the first quadrant and inclined with respect to the coordinate axes, whose analytical expression reads

$$\frac{\left[(Q_3 - c_3) \cdot cos\left(\delta\right) + (Q_1 - c_1) \cdot sin\left(\delta\right)\right]^2}{a_M^2} + \frac{Q_2^2}{a_i^2} +$$

$$+ \frac{\left[-(Q_3 - c_3) \cdot sin\left(\delta\right) + (Q_1 - c_1) \cdot cos\left(\delta\right)\right]^2}{a_m^2} - 1 = 0. \tag{5.135}$$

The ellipsoid is centred at $C = \{c_1, 0, c_3\}$ and is rotated of an angle $\delta = arctg\left(Q_1/Q_3\right)$ in the plane $\{Q_1, Q_3\}$. It is symmetric with respect to the Q_2-axis for the symmetry

of the problem. The major semi-axis is denoted as a_M, the minor one a_m while a_i indicates the intermediate value.

In Section 5.9.1.4, it was seen how the moment transmission at the deck-abutment contact can be introduced in the formulation of the ultimate surface as an equivalent couple of longitudinal forces $Q_{1,eq} = Q_{r2}/h_{2,eq}$. Hence, the total longitudinal force applied on top of the wall results equal to

$$Q_{1,tot} = Q_1 + Q_{1,eq} = Q_1 + Q_{r2}/h_{2,eq} \tag{5.136}$$

and Eq. 5.135 can be easily extended to the case of 4 degrees of freedom of the deck-abutment contact $\{Q_1, Q_2, Q_3, Q_{r2}\}$ as follows

$$\frac{\left[(Q_3 - c_3) \cdot cos\left(\delta\right) + (Q_1 + Q_{r2}/h_{2,eq} - c_1) \cdot sin\left(\delta\right)\right]^2}{a_M^2} + \frac{Q_2^2}{a_i^2} +$$

$$+ \frac{\left[-\left(Q_3 - c_3\right) \cdot sin\left(\delta\right) + (Q_1 + Q_{r2}/h_{2,eq} - c_1) \cdot cos\left(\delta\right)\right]^2}{a_m^2} - 1 = 0. \tag{5.137}$$

Following the same logic above, a 5 degrees of freedom ultimate surface $\{Q_1, Q_2, Q_3, Q_{r1}, Q_{r2}\}$ might be theoretically written in the following form

$$\frac{\left[(Q_3 - c_3) \cdot cos\left(\delta\right) + (Q_1 + Q_{r2}/h_{2,eq} - c_1) \cdot sin\left(\delta\right)\right]^2}{a_M^2} +$$

$$+ \frac{\left(Q_2 + Q_{r1}/h_{1,eq}\right)^2}{a_i^2} +$$

$$+ \frac{\left[-\left(Q_3 - c_3\right) \cdot sin\left(\delta\right) + (Q_1 + Q_{r2}/h_{2,eq} - c_1) \cdot cos\left(\delta\right)\right]^2}{a_m^2} - 1 = 0. \tag{5.138}$$

Group	Config. 1	Config. 2	Config. 3	Config. 4	Config. 5
μ_{soil}	0.577	0.577	0.466	0.577	0.466
μ_{emb}	0.577	0.577	0.466	0.577	0.577
μ_{int}	0.577	0.0	0.466	0.577	0.577
H/L_{long}	0.77	0.77	0.77	0.9	0.77
$Q_3/(\gamma_{soil} \cdot H \cdot L_{long})$	$2.1 \cdot 10^{-4}$	$2.1 \cdot 10^{-4}$	$2.1 \cdot 10^{-4}$	$1.8 \cdot 10^{-4}$	$2.1 \cdot 10^{-4}$

Tabella 5.3: Non-dimensional groups associated with different configurations of the soil-abutment system.

in which the term $h_{1,eq}$ is the equivalent height associated with the longitudinal moment Q_{r1}, that alters the transverse response of the abutment. The moment Q_{r3} along the z-axis, instead, would affect both the longitudinal and transverse response and further investigations on the skew effects would be needed in order to include these effects in the formulation of the ultimate surface of bridge abutments. Anyway, as already discussed in Section 5.1, taking into account moment transmission in the equation of the ultimate surface would lead to a greater completeness of the mathematical formulation of the macro-element but their effects are probably negligible for the behaviour of bridge abutments, except for rare cases characterised by highly irregular structures such as very high skew angle at the deck-abutment contact.

5.9.1.7 Normalised representation and calibration

The results of a limited parametric study are now shown in order to analyse the applicability of the capacity model proposed above in different configurations of the soil-abutment system. Specifically, in addition to the reference configuration considered so far, other three models are taken into account, characterised by the non-dimensional groups listed in Table 5.3.

In Config. 2, a smooth interface between soil and structure is considered while a perfectly rough interface ($\mu_{int} = \mu_{soil}$) is assumed for the other configurations. Config. 3 accounts for a lower strength of the soil compared to the reference configuration n. 1. Two geometries of the abutment are examined relative to a longitudinal aspect

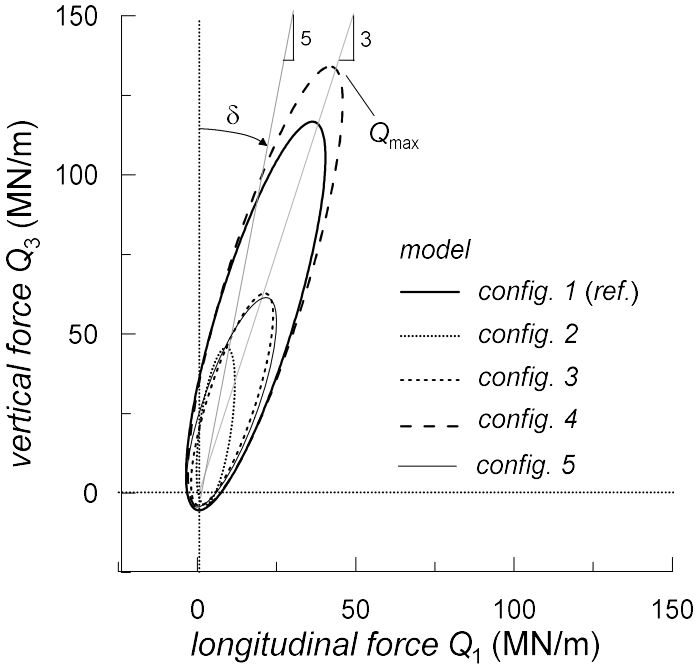

Figure 5.17: Ellipse-shaped failure surfaces in the plane $\{Q_1, Q_3\}$ for the configurations of the soil-abutment system listed in Table 5.3.

ratio H/L_{long} of 0.77 (Config. 1, 2, 3 and 5) and 0.9 (Config. 4). A lower strength of the foundation soil $\mu_{soil} = 0.466$ compared to that of the reference embankment $\mu_{emb} = 0.577$ is considered in Config. 5. Figure 9 shows the ultimate surfaces obtained as an interpolation of the failure points associated with the models above.

The first evidence is that, in each configuration, failure can be still represented by an elliptic locus. The orientation δ of the ellipse is essentially controlled by the friction along the soil-structure interface, which ranges from 11° for a smooth interface to 18° for a perfectly rough interface, hence when the vertical force is 5 and 3 times the longitudinal force, respectively. A smooth interface also causes a noticeable decrement of the maximum capacity and an almost null limit value of the negative force Q_1. However, the friction coefficient along the interface is a function of the properties of the materials in contact and, for soil-concrete contact, it can be assumed

approximately equal to the strength parameter of soil. Soil strength and the aspect ratio modify the size of the ellipse: the capacity rises with the soil strength and with the longitudinal aspect ratio of the abutment structure. The latter consideration can be explained as an increment of the whole resistance of the backfill for taller abutments, keeping the same length of the footing, due to a larger volume of soil interacting with the wall. Keeping the strength of the embankment in the reference Config. 1, a decrease of the strength in the foundation soil causes a contraction of the ultimate surface. The resulting ultimate locus is almost overlapped to that of Config. 3, in which $\mu_{soil} = \mu_{emb} = 0.466$, and therefore the capacity of the system is mainly controlled by the strength of the soil underneath the abutment foundation. In the zone of the maximum capacity, in fact, occurring for ratios $Q_3/Q_1 = 1 \div 5$, the global plastic mechanisms are conceptually similar to that already shown in Figure 5.8: there is an important mobilisation of the soil strength surrounding the footing and, at the same time, the attainment of the passive resistance in the embankment. The strength of the foundation soil is mobilised in a much larger volume compared to the plastic volume behind the wall and, as a result, the capacity of the system depends essentially on the properties of the foundation soil.

It can be convenient to represent the failure points in a normalised space in which the external forces are divided by the maximum capacity $Q_{max} = max\left\{\sqrt{Q_1^2 + Q_3^2}\right\}$. By plotting the results above in this space, shown in Figure 5.18, only two failure loci can be distinguished relative to different friction angles along the soil-structure contact. All the surfaces present the same size with orientation δ_a defined by the properties of the soil-structure interface, as observed before. It follows that the failure surface can be completely defined by evaluating its maximum capacity Q_{max} and by assuming the friction angle of the interface between soil and structure. The quantity Q_{max} can be determined either by carrying out a sole failure analysis on a soil-abutment model in correspondence of the maximum capacity or by correlating it

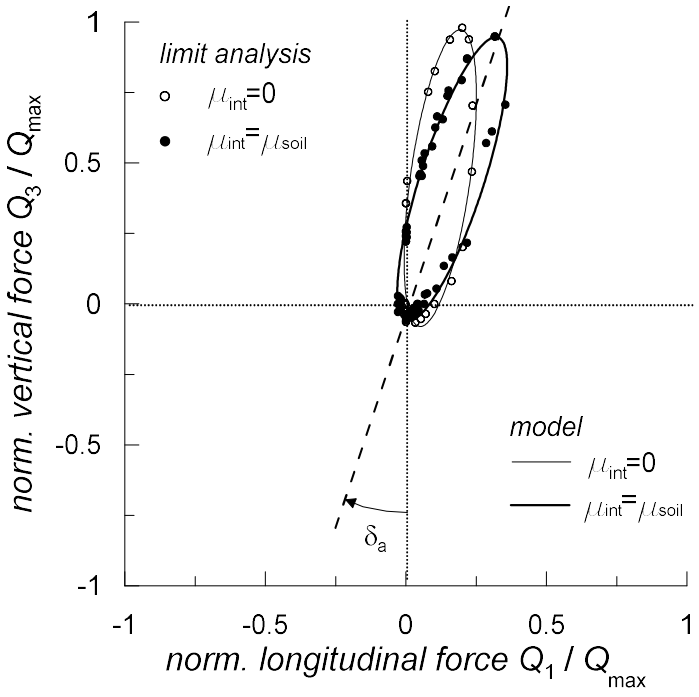

Figure 5.18: Representation of the failure surfaces in the normalised plane $\{Q_1/Q_{max}, Q_3/Q_{max}\}$.

to the vertical limit load $Q_{3,max}$ representing the bearing capacity of the foundation. In fact, the ratio $Q_{max}/Q_{3,max}$ ranges between 3.0 and 3.5 for all the configurations examined above. The three-dimensional ultimate surfaces of these systems follow the considerations made in Section 5.9.1.6, regarding the effects of the three-dimensional geometry of the abutment, and the relative results are therefore omitted for the sake of conciseness.

As a result, the following ratios can be assumed for the ellipsoid of ultimate loads:

- coordinate of the centre:

$$c_3 = 0.9 \cdot a_M \tag{5.139}$$

$$c_3/c_1 = 3.0 \tag{5.140}$$

- shape factors:

$$a_M/a_m = 5.0 \tag{5.141}$$

$$a_M/a_i = 2.3 \tag{5.142}$$

$$2 \cdot a_M = 0.95 \cdot Q_{max}. \tag{5.143}$$

Hence, once the maximum capacity of the abutment is evaluated, or equivalently the vertical limit value, the ultimate surface can be completely defined by using Eqs. 5.135 to 5.143.

Using the normalization scheme introduced before, it is now possible to define a normalised version of the ellipsoid as follows

$$\frac{\left[(Q_3/Q_{max} - c_{3,a}) \cdot cos\left(\delta_a\right) + (Q_1/Q_{max} - c_{1,a}) \cdot sin\left(\delta_a\right)\right]^2}{a_{M,a}^2} + \frac{Q_{2,a}^2}{a_{i,a}^2} +$$

$$+ \frac{\left[-\left(Q_3/Q_{max} - c_{3,a}\right) \cdot sin\left(\delta_a\right) + (Q_1/Q_{max} - c_{1,a}) \cdot cos\left(\delta_a\right)\right]^2}{a_{m,a}^2} - 1 = 0 \tag{5.144}$$

with $c_{i,a} = c_i/Q_{max}$ and $a_{M,a} = 1$ for the normalization scheme adopted. Note that the orientation δ_a of the ultimate surface in the normalised space coincides with the orientation δ in the true force space

$$\delta_a = arctg\left(\frac{Q_1}{Q_{max}} \cdot \frac{Q_{max}}{Q_3}\right) = arctg\left(\frac{Q_1}{Q_3}\right) = \delta. \tag{5.145}$$

5.9.2 Identification of the elastic domain

The ultimate surface found above represents the outermost yield surface of the macro-element, while the boundary of the elastic domain was determined looking at the results of pushover analyses on a local model of the abutment developed

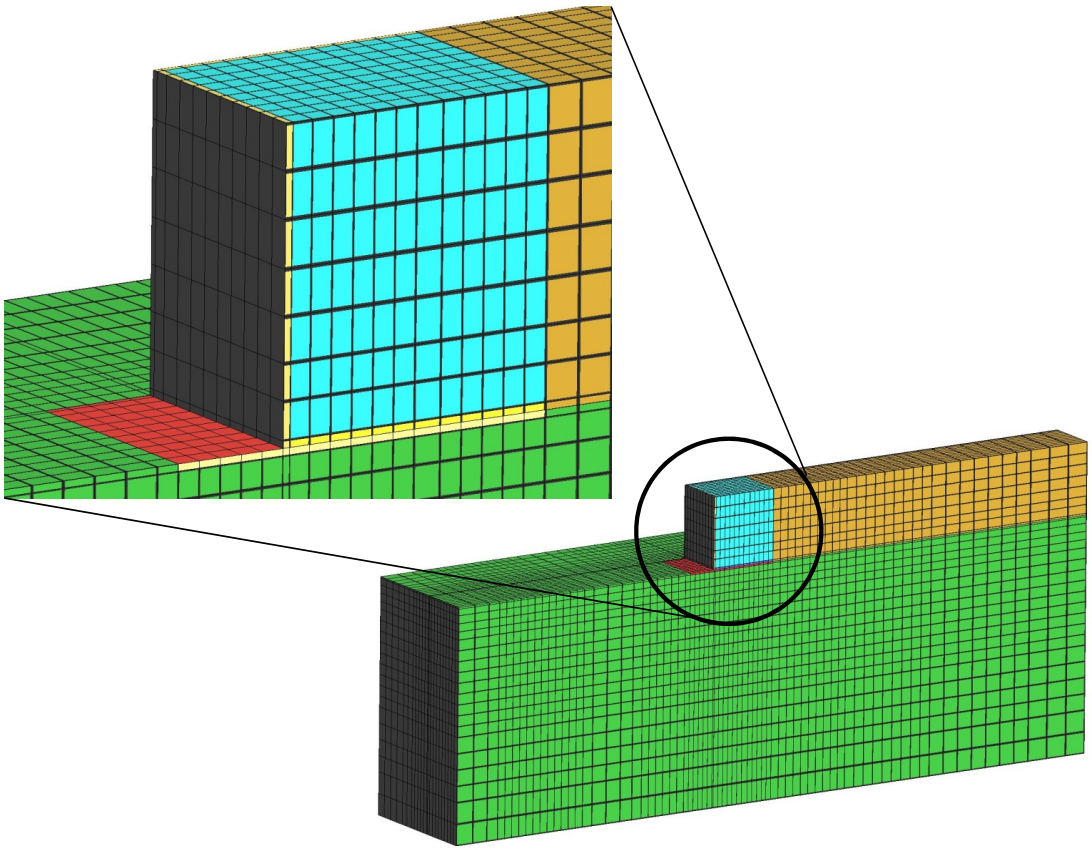

Figure 5.19: (a) Central section of the soil-abutment interaction model implemented in OpenSees and (b) detail of the soil-structure interface.

in OpenSees, shown in Figure 5.19. In this case, the numerical representation in OpenSees is equivalent to the Optum 3D model discussed in the previous section, in terms of geometry and strength parameters.

A brief argumentation of the peculiar aspects of the model is discussed in the following. The model is composed of a uniform layer of foundation soil, the approaching embankment and the abutment structure. The former reflects the properties the superficial layer of Messina Gravel $MG1$, except for a different friction angle of 30°, that extends down to a depth of 70 m from the ground level because the focus is on the local behaviour of the abutment perturbed by dynamic forces on top and not by seismic waves coming from the foundation soil. The extension of the model in plan

was instead defined in order to ensure that the lateral boundaries are distant enough so that the response of the abutment not being altered by the model dimensions. To this end, the following ratios were used

$$\frac{L_{long}}{B_{long}} = 4.0 \tag{5.146}$$

$$\frac{L_{tran}}{B_{tran}} = 3.0 \tag{5.147}$$

where the geometric quantities above are illustrated in Figure 5.20. The boundary conditions consisted in fixed constraints at the base of the model, while only the horizontal displacements were impeded along the vertical boundaries, allowing the soil to settle under gravity loads.

The subsoil was assumed to be dry and, therefore, all the soil domain was discretised through the SSPbrick eight node hexahedral elements (Zienkiewick et al. 1984), coupled with the PDMY model (Yang et al. 2003) to reproduce the mechanical behaviour of the foundation soil and of the embankment. Identical parameters were used for the interface layers interposed between the abutment and the soil except for the friction angle. In fact, two values of the latter were considered in the computation: a friction angle of the interface φ_{int} equal to that of the soil φ_{soil} and $\varphi_{int} = 2/3 \cdot \varphi_{soil}$. It was seen that the variability of the friction angle of the interface within this range does not alter significantly the results in terms of pushover curves, hence just the case of a perfectly rough interface is discussed in the following. The behaviour of the structure is represented by a visco-elastic material with parameters relative to a C32/40 strength class concrete in European standard.

A staged analysis procedure was adopted, with gravity loads applied first followed by the pushover analysis. The static phase consisted in a first stage aimed to initialise the lithostatic stress state in the foundation soil and then the abutment structure and

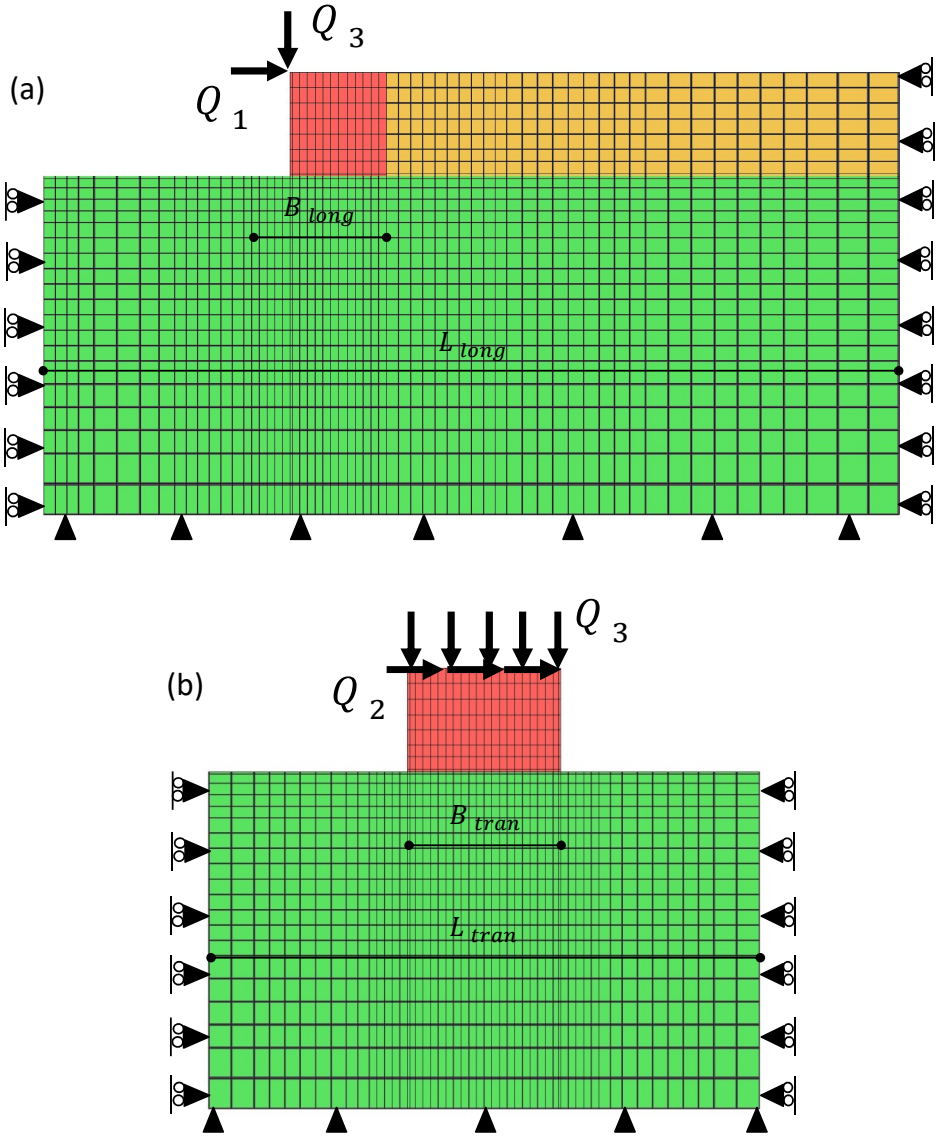

Figure 5.20: Representation of the boundary conditions in the longitudinal (a) and transverse (b) plane.

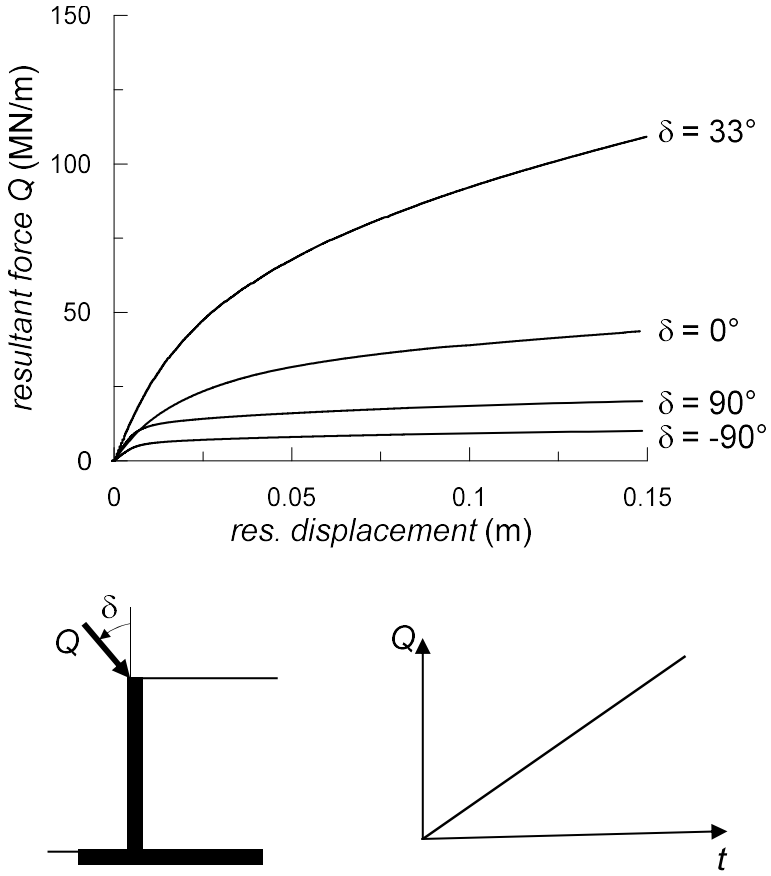

Figure 5.21: Pushover curves for different directions of the load on top of the wall.

the embankment were built sequentially into the model. In the subsequent pushover analysis, a distributed force was applied to the top of the central wall, whose intensity was progressively amplified until reaching the ultimate load of the soil-abutment system, corresponding to the activation of a global plastic mechanism. Within the context of the macro-element of bridge abutment, the response of the numerical models was quantified by monitoring the displacements of the nodes on the top of the wall. In this way, it was possible to compute the pushover curves in Figure 5.21, referred to different ratios Q_1/Q_3 of the external force in the longitudinal-vertical plane of the abutment. The curves relate the force per unit length of the wall to the resulting average displacement of the wall top in the same direction.

For each curve in Figure 5.21, the point corresponding to the first variation of the stiffness with respect to the initial value was identified (first yield). Figure 5.22 plots the points of first yield along different loading paths and it is evident that they can be very well interpolated by an ellipse. The configuration of the ellipse of first yield can be obtained by correlating its size and orientation to the characteristics of the ultimate surface, the latter obtained by the limit analysis solutions in 5.9.1.3, as reported below

$$\frac{a^{(1)}}{a^{(N)}} = 0.1 \tag{5.148}$$

$$\frac{c_3^{(1)}}{c_1^{(1)}} = \frac{c_3^{(N)}}{c_1^{(N)}} = tg\,(\delta) \tag{5.149}$$

$$\frac{a^{(1)}}{b^{(1)}} = \frac{a^{(N)}}{b^{(N)}}. \tag{5.150}$$

Hence, the first surface have the same shape and orientation as the ultimate surface but presents a much smaller dimension.

If also a transverse force is introduced, the resulting elastic domain is shown in Figure 5.23: it can be still represented by an ellipse with ratio $a_{el}^{tran}/a_{ult}^{tran} = 0.15$ between the size of the elastic domain a_{el}^{tran} and that associated with the ultimate locus a_{ult}^{tran}.

The two extreme boundaries of the plastic domain are finally illustrated in the three-dimensional space of the interaction forces in Figure 5.24.

5.9.3 Generalised hardening rule

The plastic domain is now entirely bounded by the two fundamental surfaces of first yield and ultimate loads. Taking this one step further, the inner yield surfaces

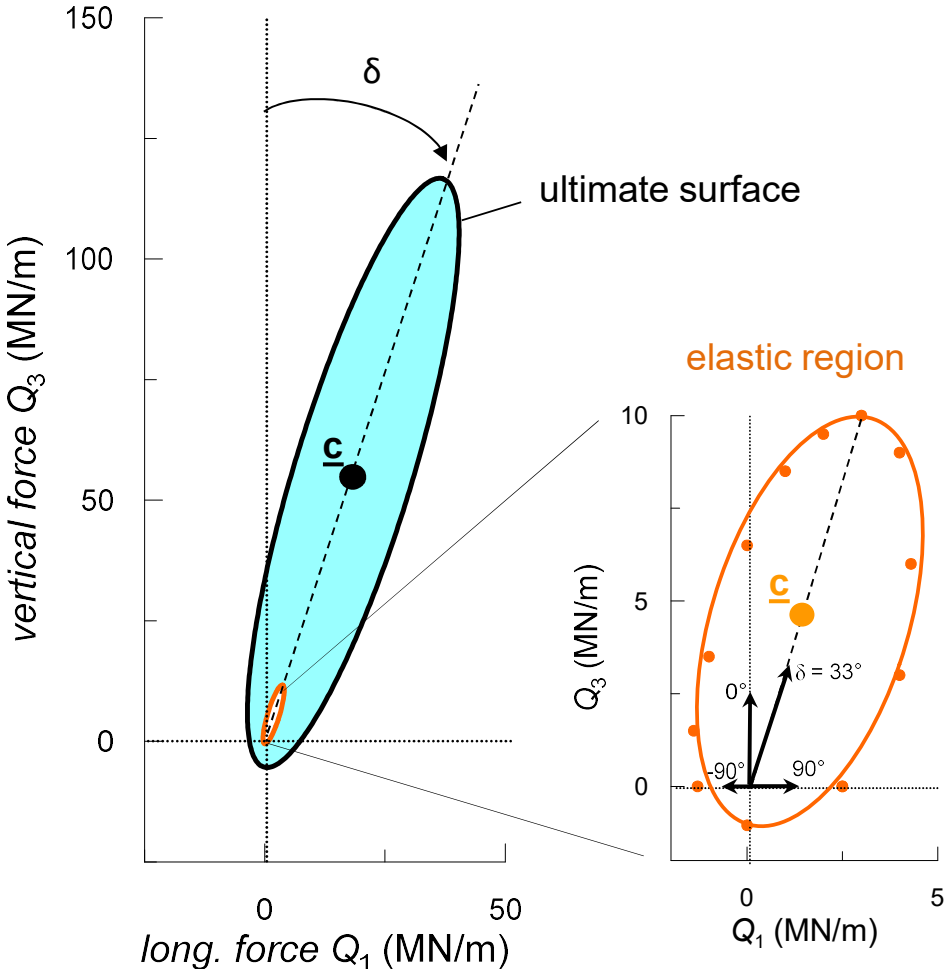

Figure 5.22: Boundary of the plastic domain: the surfaces of ultimate loads and first yield.

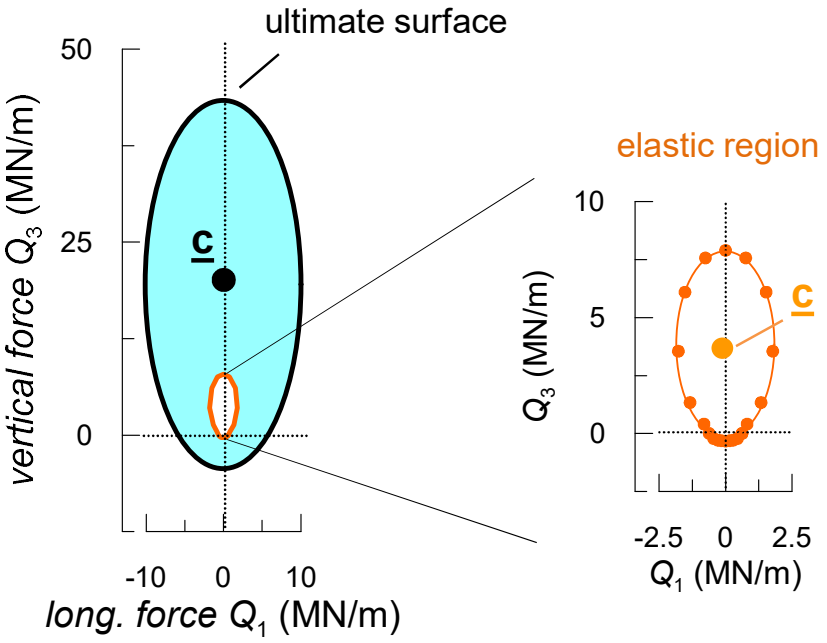

Figure 5.23: Trace of the surface of first yield in the $\{Q_2, Q_3\}$plane.

are conceived to be homothetic to the boundary surfaces. In the thermodynamic approach, however, the yield surfaces are a function of the dissipative forces $\chi_i^{(n)}$, related to the true forces $Q_i^{(n)}$ by Eq. 5.20. Therefore a change of variable is needed and the generic yield surface is described by the following equation

$$y^{(n)}(\chi_i^{(n)}) = \frac{\left[\left(\chi_3^{(n)} - c_3^{(n)}\right) \cdot cos\,(\delta) + \left(\chi_1^{(n)} - c_1^{(n)}\right) \cdot sin\,(\delta)\right]^2}{a_M^{(n)2}} +$$

$$+ \frac{\chi_2^{(n)2}}{a_i^{(n)2}} + \frac{\left[-\left(\chi_3^{(n)} - c_3^{(n)}\right) \cdot sin\,(\delta) + \left(\chi_1^{(n)} - c_1^{(n)}\right) \cdot cos\,(\delta)\right]^2}{a_m^{(n)2}} -$$

$$-1 = 0, n = 1, ..., N. \tag{5.151}$$

Note that, when the n-th plastic flow is activated, the surfaces contained within the n-th surface follow the force state in virtue of the kinematic hardening. This is an essential feature for the response of the model under cyclic conditions because, in

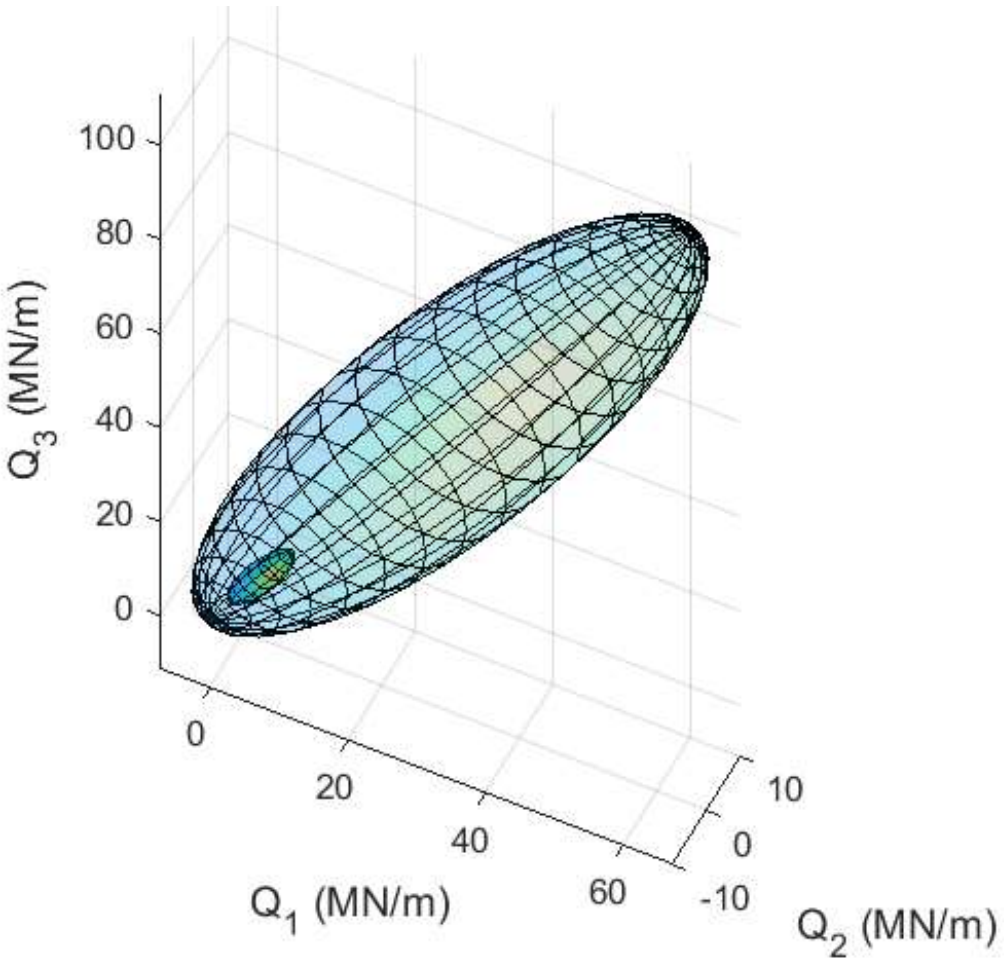

Figure 5.24: Representation of the first and ultimate yield surface in the space of the interaction forces at the deck-abutment contact.

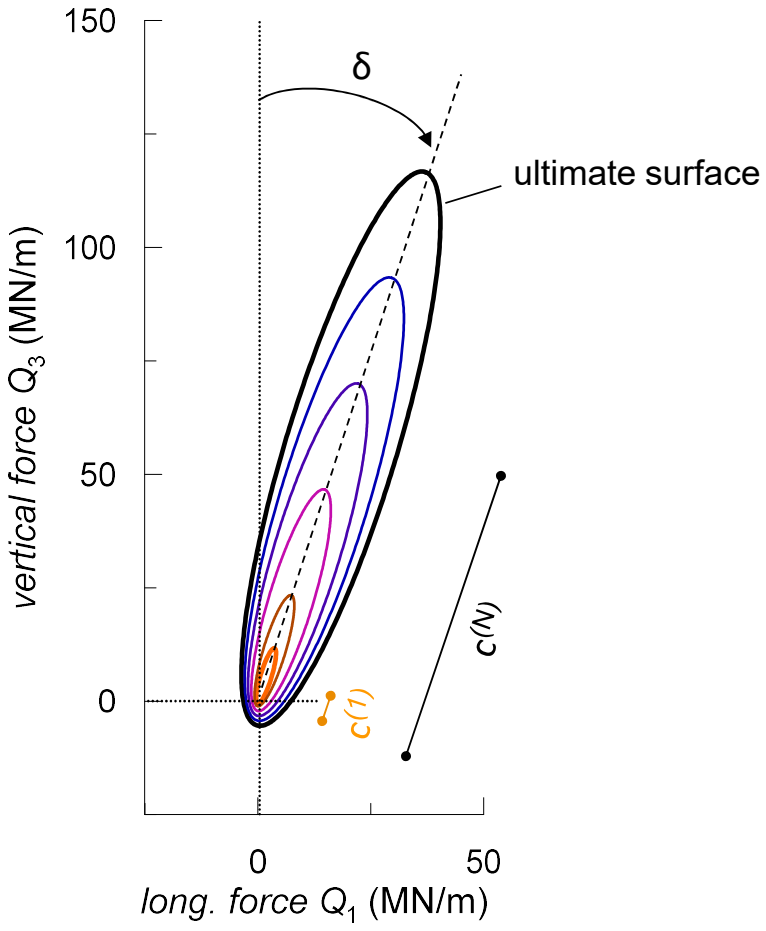

Figure 5.25: Configuration of the yield surfaces.

this way, during plastic loading the elastic region and the lower order surfaces move in the space of the interaction forces, together with the point representative of the state of the macro-element, and when a load reversal occurs plastic displacements start developing again for a different plastic threshold. The configuration of the yield surfaces of the macro-element is represented in Figure 5.25.

All the surfaces respect the following conditions

$$\frac{c_3^{(1)}}{c_1^{(1)}} = \frac{c_3^{(N)}}{c_1^{(N)}} = tg\left(\delta\right), n = 1, ..., N \tag{5.152}$$

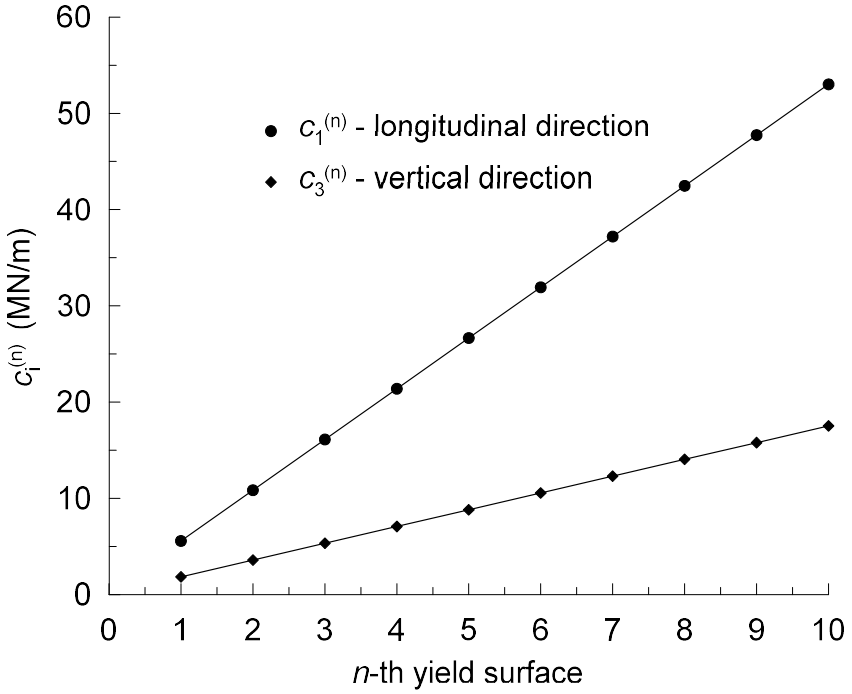

Figure 5.26: Variation of the centers of the yield surfaces in the initial configuration of the macro-element.

$$\frac{a^{(n)}}{b^{(n)}} = const, n = 1, ..., N \tag{5.153}$$

and with centre of the n-th surface that moves linearly from the first locus to the ultimate locus, as described in Figure 5.26. Therefore, the plastic domain is composed of a series of homothetic yield surfaces that, starting from the small elastic region, evolve with kinematic hardening until reaching the ultimate surface, keeping the same shape ratio $a^{(n)}/b^{(n)}$ and orientation $tg\,(\delta)$. Kinematic hardening is controlled by the stiffness tensors $H_{ij}^{(n)}$ associated with each plastic flow. The evaluation of the kinematic hardening terms $H_{ij}^{(n)}$ will be described later in the calibration of the macro-element.

Differently from a nested surface plasticity model in which the non-intersection condition must be satisfied, in the present multiple surface plasticity model the yield

surfaces can intersect with each other, likely situation along general loading paths (variable load ratio $Q_i^{(n)}/Q_j^{(n)}$), such as those induced by the seismic motion. It follows that the increment of the plastic displacement is computed as the vector sum of the plastic increments associated with the surfaces for which the plastic flow is activated (plastic multiplier $\lambda^{(n)} > 0$); when $\lambda^{(n)} = 0$, instead, the response is purely elastic and, finally, the increment of the total displacement $\dot{q}$ derives from Eq. 5.117. Plastic hardening is obtained by Eq. 5.80, in which the term

$$\dot{c}_i^{(n)} = \frac{\partial^2 g_2(\alpha_i^{(n)})}{\partial \alpha_i^{(n)2}} \cdot \dot{\alpha}_i^{(n)} \tag{5.154}$$

represents the translation of the center $c_i^{(n)}$ of the n-th surface. This is conceptually identical to the Prager's translation rule (1949), in which the center of the yield surface moves in the direction of the rate of the plastic displacement.

5.10 Dissipation function

The dissipation function represents the plastic power of the system, hence the rate of the work done by the dissipative forces only. It reflects the directional properties introduced in the model by the peculiar shape of the yield surfaces found before and, moreover, is altered by the inertial effects that appear in the expression of the plastic multiplier (see Eq. 5.107 in the one-dimensional formulation). By definition, the dissipation function d is given by the following inequality

$$d(\alpha_i^{(n)}, \dot{\alpha}_i^{(n)}) = \chi_i^{(n)} \cdot \dot{\alpha}_i^{(n)} \geq 0 \tag{5.155}$$

which must be verified for every transformation in accordance with the Second Law of Thermodynamics. As done for the one-dimensional model, the contribution of the ratcheting displacement was introduced in the dissipation function as a

constraint c, leading to a new function d^* that reads

$$d^* = d + \Lambda \cdot c = \left| \chi_i^{(n)} \cdot \dot{\alpha}_i^{(n)} \right| +$$

$$+ \Lambda \cdot \left(\dot{\alpha}^{(R)} - S\left(Q^{(ext)}\right) \cdot \sum_{n=1}^{N} R^{(n)} \cdot \dot{\alpha}^{(n)} \right) \tag{5.156}$$

with Λ the Lagrange multiplier. In this way, the incremental response of the model can be derived through the unconstrained function d^*.

The expression above requires to develop the flow rule for the internal variables $\dot{\alpha}_i^{(n)}$, especially for the plastic multiplier $\lambda^{(n)}$ that will be defined later to write the constitutive law in incremental form. The complete derivation of each term of the dissipation function is therefore shown in the next paragraph, obtaining directly the response of the macro-element. Starting from the analytical expressions of the yield surfaces in Eq. 5.151, the initial function d can be also derived through the following form of the Legendre transformation

$$\lambda^{(n)} \cdot y^{(n)}(\alpha_i^{(n)}, \chi_i^{(n)}) = \chi_i^{(n)} \cdot \dot{\alpha}_i^{(n)} - d(\alpha_i^{(n)}, \dot{\alpha}_i^{(n)}) = 0 \tag{5.157}$$

which can be conveniently rearranged as

$$d(\alpha_i^{(n)}, \dot{\alpha}_i^{(n)}) = \lambda^{(n)} \cdot \left[\chi_i^{(n)} \cdot \frac{\partial y^{(n)}(\alpha_i^{(n)}, \chi_i^{(n)})}{\partial \chi_i^{(n)}} - y^{(n)}(\alpha_i^{(n)}, \chi_i^{(n)}) \right] = \chi_i^{(n)} \cdot \dot{\alpha}_i^{(n)}. \tag{5.158}$$

5.11 Incremental response

Analogously to the one-dimension model, the incremental response of the multi-axial macro-element was obtained by differentiating the Helmholtz free energy as follows

$$\dot{Q}_i^{(ext)} = \frac{\partial}{\partial t}\left[\frac{\partial f(q_j^{(n)}, \alpha_j^{(n)}, m_{ij}^{(n)})}{\partial q_j}\right] = H_{ij}^{(0)} \cdot \dot{q}_j^{(0)}\,(q_j) + m_{ij}^{(0)} \cdot \frac{\partial}{\partial t}[\ddot{q}_j] =$$

$$= H_{ij}^{(0)} \cdot \left(\dot{q}_j - \sum_{n=1}^{N} \dot{\alpha}_j^{(n)} - \dot{\alpha}_j^{(R)}\right) + m_{ij}^{(0)} \cdot \dddot{q}_j. \tag{5.159}$$

Keeping the assumption made for the one-dimensional model that $m_{ij}^{(0)} = 0_{ij}$ because it is associated with the node which the external perturbation is applied to, the second addendum in the equation above vanishes. Eq. 5.159 can be developed by introducing the evolution law for the internal variables (Eq. 5.75)

$$\dot{Q}_i^{(ext)} = H_{ij}^{(0)} \cdot \left[\dot{q}_j - \sum_{n=1}^{N} \lambda_n \cdot \frac{\partial y_n^g(\chi_j^{(n)}, \alpha_j^{(n)}, \chi_j^{(n)})}{\partial \chi_j^{(n)}} - \right.$$

$$\left. - S\left(Q_i^{(ext)}\right) \cdot \sum_{n=1}^{N} R^{(n)} \cdot \lambda_n \cdot \frac{\partial y_n^g(\chi_j^{(n)}, \alpha_j^{(n)}, \chi_j^{(n)})}{\partial \chi_j^{(n)}}\right]. \tag{5.160}$$

Eq. 5.160, together with $n \cdot i$ equations of the flow rule and with $n \cdot i$ local balance equations of the masses $m_{ij}^{(n)}$, constitutes a system of $(2 \cdot n + 1) \cdot i$ equations in $(2 \cdot n + 1) \cdot i$ unknowns $\left\{Q_i^{(ext)}\ (or\ q_i), \alpha_i^{(n)}, Q_i^{(n)}\right\}$. The local balance equations read

$$Q_i^{(n)} = Q_i^{(n-1)} - Q_i^{(M,n)} = Q_i^{(n-2)} - Q_i^{(M,n-1)} - Q_i^{(M,n)} =$$

$$= Q_i^{(n-3)} - Q_i^{(M,n-2)} - Q_i^{(M,n-1)} - Q_i^{(M,n)} = Q_i^{(ext)} - \sum_{k=1}^{n} Q_i^{(M,k)}, n = 1, .., N. \tag{5.161}$$

while the flow rule requires the solution for the plastic multiplier (Eq. 5.107), that is generalised here below to multi-axial conditions

$$\lambda_n = \frac{\frac{\partial y^{(n)}}{\partial \chi_i^{(n)}} \cdot \dot{Q}_i{}^{(n)}}{\frac{\partial y^{(n)}}{\partial \chi_i^{(n)}} \cdot \frac{\partial^2 g_2}{\partial \alpha_i^{(n)2}} \cdot \frac{\partial y^{(n)}}{\partial \chi_i^{(n)}} - \frac{\partial y^{(n)}}{\partial \alpha_i^{(n)}} \cdot \frac{\partial y^{(n)}}{\partial \chi_i^{(n)}}}, n = 1, .., N. \tag{5.162}$$

The term $\partial y^{(n)}/\partial \alpha_i^{(n)}$ is identically equal to zero because the yield functions do not depend on the internal variables. Therefore the n-th plastic multiplier reads

$$\lambda_n = \frac{\frac{\partial y^{(n)}}{\partial \chi_i^{(n)}} \cdot \dot{Q}_i{}^{(n)}}{\frac{\partial y^{(n)}}{\partial \chi_i^{(n)}} \cdot \frac{\partial^2 g_2}{\partial \alpha_i^{(n)2}} \cdot \frac{\partial y^{(n)}}{\partial \chi_i^{(n)}}} =$$

$$= \frac{\frac{\partial y^{(n)}}{\partial \chi_1^{(n)}} \cdot \dot{Q}_1{}^{(n)} + \frac{\partial y^{(n)}}{\partial \chi_2^{(n)}} \cdot \dot{Q}_2{}^{(n)} + \frac{\partial y^{(n)}}{\partial \chi_3^{(n)}} \cdot \dot{Q}_3{}^{(n)}}{\frac{\partial y^{(n)}}{\partial \chi_1^{(n)}} \cdot \frac{\partial^2 g_2}{\partial \alpha_1^{(n)2}} \cdot \frac{\partial y^{(n)}}{\partial \chi_1^{(n)}} + \frac{\partial y^{(n)}}{\partial \chi_2^{(n)}} \cdot \frac{\partial^2 g_2}{\partial \alpha_2^{(n)2}} \cdot \frac{\partial y^{(n)}}{\partial \chi_2^{(n)}} + \frac{\partial y^{(n)}}{\partial \chi_3^{(n)}} \cdot \frac{\partial^2 g_2}{\partial \alpha_3^{(n)2}} \cdot \frac{\partial y^{(n)}}{\partial \chi_3^{(n)}}}. \tag{5.163}$$

The derivative of the yield functions $\partial y^{(n)}/\partial \chi_i^{(n)}$ are developed below:

- derivative of the yield functions with respect to $\chi_1^{(n)}$

$$\frac{\partial y^{(n)}\left(\chi_i^{(n)}\right)}{\partial \chi_1^{(n)}} = \frac{\partial}{\partial \chi_1^{(n)}} \left\{ \frac{\left[\left(\chi_3^{(n)} - c_3^{(n)}\right) \cdot cos\left(\delta\right) + \left(\chi_1^{(n)} - c_1^{(n)}\right) \cdot sin\left(\delta\right)\right]^2}{a_M^{(n)2}} + \right.$$

$$\left. + \frac{\chi_2^{(n)2}}{a_i^{(n)2}} + \frac{\left[-\left(\chi_3^{(n)} - c_3^{(n)}\right) \cdot sin\left(\delta\right) + \left(\chi_1^{(n)} - c_1^{(n)}\right) \cdot cos\left(\delta\right)\right]^2}{a_m^{(n)2}} - 1 \right\} =$$

$$= \frac{2}{a_M^{(n)2}} \cdot \left[\left(\chi_3^{(n)} - c_3^{(n)}\right) \cdot cos\left(\delta\right) + \left(\chi_1^{(n)} - c_1^{(n)}\right) \cdot sin\left(\delta\right)\right] \cdot sin\left(\delta\right) \cdot S(\chi_1^{(n)}) +$$

$$+ \frac{2}{a_m^{(n)2}} \cdot \left[-\left(\chi_3^{(n)} - c_3^{(n)}\right) \cdot sin\left(\delta\right) + \left(\chi_1^{(n)} - c_1^{(n)}\right) \cdot cos\left(\delta\right)\right] \cdot cos\left(\delta\right) \cdot S(\chi_1^{(n)}); \tag{5.164}$$

- derivative of the yield functions with respect to $\chi_2^{(n)}$

$$\frac{\partial y^{(n)}\left(\chi_i^{(n)}\right)}{\partial \chi_2^{(n)}} = \frac{2\cdot}{a_i^{(n)2}} \cdot \chi_2^{(n)} \cdot S(\chi_2^{(n)}); \tag{5.165}$$

- derivative of the yield functions with respect to $\chi_3^{(n)}$

$$\frac{\partial y^{(n)}\left(\chi_i^{(n)}\right)}{\partial \chi_3^{(n)}} = \frac{2}{a_M^{(n)2}} \cdot \left[\left(\chi_3^{(n)} - c_3^{(n)}\right) \cdot cos\left(\delta\right) + \left(\chi_1^{(n)} - c_1^{(n)}\right) \cdot sin\left(\delta\right)\right] \cdot$$

$$\cdot cos\left(\delta\right) \cdot S(\chi_3^{(n)}) - \frac{2}{a_m^{(n)2}} \cdot \left[-\left(\chi_3^{(n)} - c_3^{(n)}\right) \cdot sin\left(\delta\right) + \left(\chi_1^{(n)} - c_1^{(n)}\right) \cdot cos\left(\delta\right)\right] \cdot$$

$$\cdot sin\left(\delta\right) \cdot S(\chi_3^{(n)}). \tag{5.166}$$

The second derivative of the sub-function $g_2(0, \alpha_i^{(n)}, m_{ij}^{(n)})$ of the Gibbs free energy reads

$$\frac{\partial^2 g_2\left(0, \alpha_i^{(n)}, m_{ij}^{(n)}\right)}{\partial \alpha_i^{(n)2}} = \frac{\partial^2 g_{2,st}\left(0, \alpha_i^{(n)}, 0_{ij}\right)}{\partial \alpha_i^{(n)2}} + \frac{\partial^2 g_{2,in}\left(0, \alpha_i^{(n)}, m_{ij}^{(n)}\right)}{\partial \alpha_i^{(n)2}} \tag{5.167}$$

having decomposed the function g_2 into its static and inertial part, thus

$$g_{2,st}(\alpha_i^{(n)}, 0) = \frac{1}{2} \cdot H_{ij}^{(n)} \cdot \alpha_j^{(n)} \cdot \alpha_i^{(n)} \tag{5.168}$$

$$g_{2,in}(\alpha_i^{(n)}, m_{ij}^{(n)}) = g_2(\alpha_i^{(n)}, m_{ij}^{(n)}) = -m_{ij}^{(n)} \cdot \sum_{h=n}^{N} \ddot{q}_j^{(h)} \cdot \sum_{k=n}^{N} q_i^{(k)} +$$

$$+\frac{1}{2} \cdot m_{ij}^{(n)} \cdot \left(\sum_{h=n}^{N} \dot{\alpha}_j^{(h)}\right) \cdot \left(\sum_{h=n}^{N} \dot{\alpha}_i^{(h)}\right). \tag{5.169}$$

The derivation of the term $g_{2,st}(\alpha_i^{(n)})$ reads

$$\frac{\partial^2 g_{2,0}(\alpha_i^{(n)})}{\partial \alpha_i^{(n)2}} = \frac{\partial^2}{\partial \alpha_i^{(n)2}} \left[\frac{1}{2} \cdot H_{ij}^{(n)} \cdot \alpha_j^{(n)} \cdot \alpha_i^{(n)} \right] = H_{ij}^{(n)} \tag{5.170}$$

which is equal to the stiffness tensors that provide kinematic hardening. Some further developments are needed for the inertial term

$$\frac{\partial^2 g_{2,in}(\alpha_i^{(n)}, m_{ij}^{(n)})}{\partial \alpha_i^{(n)2}} = \frac{\partial^2}{\partial \alpha_i^{(n)2}} \left[-m_{ij}^{(n)} \cdot \sum_{h=n}^{N} \ddot{\alpha}_j^{(h)} \cdot \sum_{k=n}^{N} \alpha_i^{(k)} + \right.$$

$$\left. + \frac{1}{2} \cdot m_{ij}^{(n)} \cdot \left(\sum_{h=n}^{N} \dot{\alpha}_j^{(h)} \right) \cdot \left(\sum_{k=n}^{N} \dot{\alpha}_j^{(k)} \right) \right] =$$

$$= -m_{ij}^{(n)} \cdot \frac{\partial^2}{\partial \alpha_i^{(n)2}} \left[\sum_{h=n}^{N} \ddot{\alpha}_j^{(h)} \cdot \sum_{k=n}^{N} \alpha_i^{(k)} \right] +$$

$$+ \frac{1}{2} \cdot m_{ij}^{(n)} \cdot \frac{\partial^2}{\partial \alpha_i^{(n)2}} \left[\left(\sum_{h=n}^{N} \dot{\alpha}_j^{(h)} \right) \cdot \left(\sum_{k=n}^{N} \dot{\alpha}_j^{(k)} \right) \right] =$$

$$= -m_{ij}^{(n)} \cdot \frac{\partial^2 C^{(n)}}{\partial \alpha_i^{(n)} \cdot \partial \alpha_j^{(n)}} + \frac{1}{2} \cdot m_{ij}^{(n)} \cdot \frac{\partial^2 D^{(n)}}{\partial \alpha_i^{(n)} \cdot \partial \alpha_j^{(n)}}. \tag{5.171}$$

By using the change of variable introduced in Eqs. 5.88 and 5.89, the terms $C^{(n)}$ and $D^{(n)}$ can be derived as follows:

- term $C^{(n)}$:

$$\frac{\partial C^{(n)}}{\partial \alpha_i^{(n)}} = \frac{\partial}{\partial \alpha_i^{(n)}} \left[\sum_{h=n}^{N} \ddot{\alpha}_j^{(h)} \cdot \sum_{k=n}^{N} \alpha_i^{(k)} \right] =$$

$$= \frac{\partial}{\partial \alpha_i^{(n)}} \left[\sum_{h=n}^{N} \ddot{\alpha}_j^{(h)} \right] \cdot \sum_{k=n}^{N} \alpha_i^{(k)} + \sum_{h=n}^{N} \ddot{\alpha}_j^{(h)} \cdot \frac{\partial}{\partial \alpha_i^{(n)}} \left[\sum_{k=n}^{N} \alpha_i^{(k)} \right] =$$

$$= \left[\alpha_i^{(n)} \right]^{-1} \cdot \frac{\partial^3 \sum_{h=n}^{N} \alpha_i^{(h)}}{\partial t^3} \cdot \sum_{k=n}^{N} \alpha_i^{(k)} + \sum_{h=n}^{N} \ddot{\alpha}_j^{(h)} =$$

$$= \left[\alpha_i^{(n)}\right]^{-1} \cdot \sum_{h=n}^{N} \dddot{\alpha}_i^{(h)} \cdot \sum_{k=n}^{N} \alpha_i^{(k)} + \sum_{h=n}^{N} \ddot{\alpha}_h \tag{5.172}$$

$$\frac{\partial^2 C^{(n)}}{\partial \alpha_i^{(n)2}} = \frac{\partial}{\partial \alpha_i^{(n)}} \left[\left[\alpha_i^{(n)}\right]^{-1} \cdot \sum_{h=n}^{N} \dddot{\alpha}_i^{(h)} \cdot \sum_{k=n}^{N} \alpha_i^{(k)} + \sum_{h=n}^{N} \ddot{\alpha}^{(h)} \right] =$$

$$= \frac{\partial}{\partial \alpha_i^{(n)}} \left[\left[\alpha_i^{(n)}\right]^{-1} \cdot \sum_{h=n}^{N} \dddot{\alpha}_i^{(h)} \cdot \sum_{k=n}^{N} \alpha_i^{(k)} \right] + \frac{\partial}{\partial \alpha_i^{(n)}} \left[\sum_{h=n}^{N} \ddot{\alpha}^{(h)} \right] =$$

$$= \left[\dot{\alpha}_i^{(n)}\right]^{-2} \cdot \sum_{h=n}^{N} \ddddot{\alpha}_i^{(h)} \cdot \sum_{k=n}^{N} \alpha_i^{(k)} - \left[\dot{\alpha}_i^{(n)}\right]^{-3} \cdot \sum_{h=n}^{N} \dddot{\alpha}_i^{(h)} \cdot \ddot{\alpha}_i^{(n)} \cdot \sum_{k=n}^{N} \alpha_i^{(k)} +$$

$$+2 \cdot \left[\dot{\alpha}_i^{(n)}\right] \cdot \sum_{h=n}^{N} \dddot{\alpha}_i^{(h)}. \tag{5.173}$$

- term $D^{(n)}$:

$$\frac{\partial D^{(n)}}{\partial \alpha_i^{(n)}} = \frac{\partial}{\partial \alpha_i^{(n)}} \left[\left(\sum_{h=n}^{N} \dot{\alpha}_j^{(h)} \right) \cdot \left(\sum_{k=n}^{N} \dot{\alpha}_j^{(k)} \right) \right] = 2 \cdot \left[\dot{\alpha}_i^{(n)}\right]^{-1} \cdot \sum_{h=n}^{N} \dot{\alpha}_i^{(h)} \cdot \sum_{k=n}^{N} \ddot{\alpha}_i^{(k)} \tag{5.174}$$

$$\frac{\partial^2 D^{(n)}}{\partial \alpha_i^{(n)2}} = \frac{\partial}{\partial \alpha_i^{(n)}} \left[2 \cdot \left[\dot{\alpha}_i^{(n)}\right]^{-1} \cdot \sum_{h=1}^{N} \dot{\alpha}_i^{(h)} \cdot \sum_{k=1}^{N} \ddot{\alpha}_i^{(k)} \right] =$$

$$= 2 \cdot \left[\dot{\alpha}_i^{(n)}\right]^{-2} \cdot \sum_{h=1}^{N} \ddot{\alpha}_i^{(h)} \cdot \sum_{k=1}^{N} \ddot{\alpha}_i^{(k)} - 2 \cdot \left[\dot{\alpha}_i^{(n)}\right]^{-3} \cdot \ddot{\alpha}_i^{(n)} \cdot \sum_{h=1}^{N} \dot{\alpha}_i^{(h)} \cdot \sum_{k=1}^{N} \ddot{\alpha}_i^{(k)} +$$

$$+2 \cdot \left[\dot{\alpha}_i^{(n)}\right]^{-2} \cdot \sum_{h=1}^{N} \dot{\alpha}_i^{(h)} \cdot \sum_{k=1}^{N} \dddot{\alpha}_i^{(k)}. \tag{5.175}$$

By substituting the expressions for the terms $C^{(n)}$ and $D^{(n)}$ in Eq. 5.171, the latter becomes

$$\frac{\partial^2 g_{2,in}(\alpha_i^{(n)}, m_{ij}^{(n)})}{\partial \alpha_i^{(n)2}} = -m_{ij}^{(n)} \cdot \frac{\partial^2 C^{(n)}}{\partial \alpha_i^{(n)} \cdot \partial \alpha_j^{(n)}} + \frac{1}{2} \cdot m_{ij}^{(n)} \cdot \frac{\partial^2 D^{(n)}}{\partial \alpha_i^{(n)} \cdot \partial \alpha_j^{(n)}} =$$

$$= -m_{ij}^{(n)} \cdot \left\{ \left[\dot{\alpha}_i^{(n)}\right]^{-2} \cdot \sum_{h=n}^{N} \dddot{\alpha}_i^{(h)} \cdot \sum_{k=n}^{N} \alpha_i^{(k)} - \left[\dot{\alpha}_i^{(n)}\right]^{-3} \cdot \sum_{h=n}^{N} \ddot{\alpha}_i^{(h)} \cdot \ddot{\alpha}_i^{(n)} \cdot \sum_{k=n}^{N} \alpha_i^{(k)} + \right.$$

$$\left. + 2 \cdot \left[\dot{\alpha}_i^{(n)}\right] \cdot \sum_{h=n}^{N} \ddot{\alpha}_i^{(h)} \right\} + \frac{1}{2} \cdot m_{ij}^{(n)} \cdot \left\{ 2 \cdot \left[\dot{\alpha}_i^{(n)}\right]^{-2} \cdot \sum_{h=n}^{N} \ddot{\alpha}_i^{(h)} \cdot \sum_{k=n}^{N} \ddot{\alpha}_i^{(k)} - \right.$$

$$\left. - 2 \cdot \left[\dot{\alpha}_i^{(n)}\right]^{-3} \cdot \ddot{\alpha}_i^{(n)} \cdot \sum_{h=n}^{N} \dot{\alpha}_i^{(h)} \cdot \sum_{k=n}^{N} \ddot{\alpha}_i^{(k)} + 2 \cdot \left[\dot{\alpha}_i^{(n)}\right]^{-2} \cdot \sum_{h=n}^{N} \dot{\alpha}_i^{(h)} \cdot \sum_{k=n}^{N} \dddot{\alpha}_i^{(k)} \right\} =$$

$$+ m_{ij}^{(n)} \cdot \left\{ \left[\dot{\alpha}_i^{(n)}\right]^{-2} \cdot \sum_{h=n}^{N} \dddot{\alpha}_i^{(h)} \cdot \sum_{k=n}^{N} \alpha_i^{(k)} - \left[\dot{\alpha}_i^{(n)}\right]^{-3} \cdot \sum_{h=n}^{N} \ddot{\alpha}_i^{(h)} \cdot \ddot{\alpha}_i^{(n)} \cdot \sum_{k=n}^{N} \alpha_i^{(k)} + \right.$$

$$+ \left[\dot{\alpha}_i^{(n)}\right] \cdot \sum_{h=n}^{N} \ddot{\alpha}_i^{(h)} + \left[\dot{\alpha}_i^{(n)}\right]^{-2} \cdot \sum_{h=n}^{N} \ddot{\alpha}_i^{(h)} \cdot \sum_{k=n}^{N} \ddot{\alpha}_i^{(k)} -$$

$$\left. - \left[\dot{\alpha}_i^{(n)}\right]^{-3} \cdot \ddot{\alpha}_i^{(n)} \cdot \sum_{h=n}^{N} \dot{\alpha}_i^{(h)} \cdot \sum_{k=n}^{N} \ddot{\alpha}_i^{(k)} + \left[\dot{\alpha}_i^{(n)}\right]^{-2} \cdot \sum_{h=n}^{N} \dot{\alpha}_i^{(h)} \cdot \sum_{k=n}^{N} \dddot{\alpha}_i^{(k)} \right\}. \qquad (5.176)$$

Following the notation used for the one-dimensional case, the time derivatives of the internal variables are collected into the terms $G_{M,n}^{(j)}$, where the superscript j indicates the order of the maximum time derivative, as reported below

$$G_{M,n,i}^{(4)} = -\frac{1}{\dot{\alpha}_i^{(n)2}} \cdot \sum_{h=n}^{N} \dddot{\alpha}_i^{(h)} \cdot \sum_{k=n}^{N} \alpha_i^{(k)} \tag{5.177}$$

$$G_{M,n,i}^{(3)} = \frac{1}{\dot{\alpha}_i^{(n)3}} \cdot \sum_{h=n}^{N} \ddot{\alpha}_i^{(h)} \cdot \ddot{\alpha}_i^{(n)} \cdot \sum_{k=n}^{N} \alpha_i^{(k)} - \frac{1}{\dot{\alpha}^{(n)}} \cdot \sum_{h=n}^{N} \dddot{\alpha}_i^{(h)} + \\ + \frac{1}{\dot{\alpha}_i^{(n)2}} \cdot \sum_{h=n}^{N} \dot{\alpha}_i^{(h)} \cdot \sum_{k=n}^{N} \dddot{\alpha}_i^{(k)} \tag{5.178}$$

$$G_{M,n,i}^{(2)} = \frac{1}{\dot{\alpha}_i^{(n)2}} \cdot \sum_{h=n}^{N} \ddot{\alpha}_i^{(h)} \cdot \sum_{k=n}^{N} \ddot{\alpha}_i^{(k)} - \frac{\ddot{\alpha}_i^{(n)}}{\dot{\alpha}_i^{(n)3}} \cdot \sum_{h=n}^{N} \dot{\alpha}_i^{(h)} \cdot \sum_{k=n}^{N} \ddot{\alpha}_i^{(k)} \tag{5.179}$$

so that Eq. 5.176 can be written in the following more compact form

$$\frac{\partial^2 g_{2,in}(\alpha_i^{(n)}, m_{ij}^{(n)})}{\partial \alpha_i^{(n)2}} = m_{ij}^{(n)} \cdot \left(G_{M,n,j}^{(4)} + G_{M,n,j}^{(3)} + G_{M,n,j}^{(2)} \right), n = 1, ..., N. \tag{5.180}$$

The second derivative of the function $g_2(\alpha_i^{(n)}, m_{ij}^{(n)})$ is finally reported below and constitutes the generalization of Eq. 5.106 obtained for the one-dimensional model

$$\frac{\partial^2 g_2(\alpha_i^{(n)}, m_{ij}^{(n)})}{\partial \alpha_i^{(n)2}} = H_{ij}^{(n)} + m_{ij}^{(n)} \cdot \left(G_{M,n,j}^{(4)} + G_{M,n,j}^{(3)} + G_{M,n,j}^{(2)} \right), n = 1, ..., N. \tag{5.181}$$

Substituting the above results in Eq. 5.162 of the plastic multiplier, the latter can be developed as

$$\lambda_n = \frac{\frac{\partial y^{(n)}}{\partial \chi_1^{(n)}} \cdot \dot{Q_1}^{(n)} + \frac{\partial y^{(n)}}{\partial \chi_2^{(n)}} \cdot \dot{Q_2}^{(n)} + \frac{\partial y^{(n)}}{\partial \chi_3^{(n)}} \cdot \dot{Q_3}^{(n)}}{\frac{\partial y^{(n)}}{\partial \chi_1^{(n)}} \cdot \frac{\partial^2 g_2}{\partial \alpha_1^{(n)2}} \cdot \frac{\partial y^{(n)}}{\partial \chi_1^{(n)}} + \frac{\partial y^{(n)}}{\partial \chi_2^{(n)}} \cdot \frac{\partial^2 g_2}{\partial \alpha_2^{(n)2}} \cdot \frac{\partial y^{(n)}}{\partial \chi_2^{(n)}} + \frac{\partial y^{(n)}}{\partial \chi_3^{(n)}} \cdot \frac{\partial^2 g_2}{\partial \alpha_3^{(n)2}} \cdot \frac{\partial y^{(n)}}{\partial \chi_3^{(n)}}} = \\ = \frac{N_1^{(n)} + N_2^{(n)} + N_3^{(n)}}{D_1^{(n)} + D_2^{(n)} + D_3^{(n)}}, n = 1, .., N \tag{5.182}$$

in which each term reads

$$N_1^{(n)} = \frac{\partial y^{(n)}}{\partial \chi_1^{(n)}} \cdot \dot{Q_1}^{(n)} =$$

$$= \left\{ \frac{2 \cdot sin\,(\delta) \cdot S(\chi_1^{(n)})}{a_M^{(n)2}} \cdot \left[\left(\chi_3^{(n)} - c_3^{(n)} \right) \cdot cos\,(\delta) + \left(\chi_1^{(n)} - c_1^{(n)} \right) \cdot sin\,(\delta) \right] + \right.$$

$$+ \frac{2 \cdot cos\,(\delta) \cdot S(\chi_1^{(n)})}{a_m^{(n)2}} \cdot$$

$$\left. \cdot \left[- \left(\chi_3^{(n)} - c_3^{(n)} \right) \cdot sin\,(\delta) + \left(\chi_1^{(n)} - c_1^{(n)} \right) \cdot cos\,(\delta) \right] \right\} \cdot \dot{Q_1}^{(n)} \tag{5.183}$$

$$N_2^{(n)} = \frac{\partial y^{(n)}}{\partial \chi_2^{(n)}} \cdot \dot{Q_2}^{(n)} = \frac{1}{a_i^{(n)2}} \cdot 2 \cdot \chi_2^{(n)} \cdot S(\chi_2^{(n)}) \cdot \dot{Q_2}^{(n)} \tag{5.184}$$

$$N_3^{(n)} = \frac{\partial y^{(n)}}{\partial \chi_3^{(n)}} \cdot \dot{Q_3}^{(n)} = \left\{ \frac{2 \cdot cos\,(\delta) \cdot S(\chi_3^{(n)})}{a_M^{(n)2}} \cdot \left[\left(\chi_3^{(n)} - c_3^{(n)} \right) \cdot cos\,(\delta) + \right. \right.$$

$$\left. + \left(\chi_1^{(n)} - c_1^{(n)} \right) \cdot sin\,(\delta) \right] - \frac{2 \cdot sin\,(\delta) \cdot S(\chi_3^{(n)})}{a_m^{(n)2}} \cdot$$

$$\left. \cdot \left[- \left(\chi_3^{(n)} - c_3^{(n)} \right) \cdot sin\,(\delta) + \left(\chi_1^{(n)} - c_1^{(n)} \right) \cdot cos\,(\delta) \right] \right\} \cdot \dot{Q_3}^{(n)} \tag{5.185}$$

$$D_1^{(n)} = \frac{\partial y^{(n)}}{\partial \chi_1^{(n)}} \cdot \frac{\partial^2 g_2}{\partial \alpha_1^{(n)2}} \cdot \frac{\partial y^{(n)}}{\partial \chi_1^{(n)}} =$$

$$= \left\{ \frac{2 \cdot sin\,(\delta) \cdot S(\chi_1^{(n)})}{a_M^{(n)2}} \cdot \left[\left(\chi_3^{(n)} - c_3^{(n)} \right) \cdot cos\,(\delta) + \left(\chi_1^{(n)} - c_1^{(n)} \right) \cdot sin\,(\delta) \right] + \right.$$

$$+\frac{2\cdot cos\left(\delta\right)\cdot S(\chi_1^{(n)})}{a_m^{(n)2}}\cdot\left[-\left(\chi_3^{(n)}-c_3^{(n)}\right)\cdot sin\left(\delta\right)+\left(\chi_1^{(n)}-c_1^{(n)}\right)\cdot cos\left(\delta\right)\right]\Bigg\}\cdot$$

$$\cdot\left[H_{11}^{(n)}+m_{11}^{(n)}\cdot\left(G_{M,n,1}^{(4)}+G_{M,n,1}^{(3)}+G_{M,n,1}^{(2)}\right)\right]\cdot$$

$$\cdot\left\{\frac{2\cdot sin\left(\delta\right)\cdot S(\chi_1^{(n)})}{a_M^{(n)2}}\cdot\left[\left(\chi_3^{(n)}-c_3^{(n)}\right)\cdot cos\left(\delta\right)+\left(\chi_1^{(n)}-c_1^{(n)}\right)\cdot sin\left(\delta\right)\right]+\right.$$

$$\left.+\frac{2\cdot cos\left(\delta\right)\cdot S(\chi_1^{(n)})}{a_m^{(n)2}}\cdot\left[-\left(\chi_3^{(n)}-c_3^{(n)}\right)\cdot sin\left(\delta\right)+\left(\chi_1^{(n)}-c_1^{(n)}\right)\cdot cos\left(\delta\right)\right]\right\} \quad (5.186)$$

$$D_2^{(n)}=\frac{\partial y^{(n)}}{\partial\chi_2^{(n)}}\cdot\frac{\partial^2 g_2}{\partial\alpha_2^{(n)2}}\cdot\frac{\partial y^{(n)}}{\partial\chi_2^{(n)}}=\frac{1}{a_i^{(n)2}}\cdot 2\cdot\chi_2^{(n)}\cdot S(\chi_2^{(n)})\cdot$$

$$\cdot\left[H_{22}^{(n)}+m_{22}^{(n)}\cdot\left(G_{M,n,2}^{(4)}+G_{M,n,2}^{(3)}+G_{M,n,2}^{(2)}\right)\right]\cdot\frac{1}{a_i^{(n)2}}\cdot 2\cdot\chi_2^{(n)}\cdot S(\chi_2^{(n)}) \quad (5.187)$$

$$D_3^{(n)}=\frac{\partial y^{(n)}}{\partial\chi_3^{(n)}}\cdot\frac{\partial^2 g_2}{\partial\alpha_3^{(n)2}}\cdot\frac{\partial y^{(n)}}{\partial\chi_3^{(n)}}=$$

$$=\left\{\frac{2\cdot cos\left(\delta\right)\cdot S(\chi_3^{(n)})}{a_M^{(n)2}}\cdot\left[\left(\chi_3^{(n)}-c_3^{(n)}\right)\cdot cos\left(\delta\right)+\left(\chi_1^{(n)}-c_1^{(n)}\right)\cdot sin\left(\delta\right)\right]+\right.$$

$$-\frac{2\cdot sin\left(\delta\right)\cdot S(\chi_3^{(n)})}{a_m^{(n)2}}\cdot\left[-\left(\chi_3^{(n)}-c_3^{(n)}\right)\cdot sin\left(\delta\right)+\left(\chi_1^{(n)}-c_1^{(n)}\right)\cdot cos\left(\delta\right)\right]\Bigg\}\cdot$$

$$\cdot\left[H_{33}^{(n)}+m_{33}^{(n)}\cdot\left(G_{M,n,3}^{(4)}+G_{M,n,3}^{(3)}+G_{M,n,3}^{(2)}\right)\right]\cdot$$

$$\cdot\left\{\frac{2\cdot cos\left(\delta\right)\cdot S(\chi_3^{(n)})}{a_M^{(n)2}}\cdot\left[\left(\chi_3^{(n)}-c_3^{(n)}\right)\cdot cos\left(\delta\right)+\left(\chi_1^{(n)}-c_1^{(n)}\right)\cdot sin\left(\delta\right)\right]-\right.$$

$$\left.-\frac{2\cdot sin\left(\delta\right)\cdot S(\chi_3^{(n)})}{a_m^{(n)2}}\cdot\left[-\left(\chi_3^{(n)}-c_3^{(n)}\right)\cdot sin\left(\delta\right)+\left(\chi_1^{(n)}-c_1^{(n)}\right)\cdot cos\left(\delta\right)\right]\right\}.$$

(5.188)

The constant ratios found for the ellipsoid in Eq. 5.152 and 5.153 can be introduced in the equations above to give the final version of the plastic multiplier in the general formulation of the macro-element

$$N_1^{(n)}=\frac{2\cdot S(\chi_1^{(n)})\cdot\dot{Q}_1{}^{(n)}}{a_M^{(n)2}}\cdot\left\{sin\left(\delta\right)\cdot\left[\left(\chi_3^{(n)}-c_3^{(n)}\right)\cdot cos\left(\delta\right)+\right.\right.$$

$$\left.+\left(\chi_1^{(n)}-c_1^{(n)}\right)\cdot sin\left(\delta\right)\right]+$$

$$\left.+\frac{cos\left(\delta\right)}{\varepsilon_m^2}\cdot\left[-\left(\chi_3^{(n)}-c_3^{(n)}\right)\cdot sin\left(\delta\right)+\left(\chi_1^{(n)}-c_1^{(n)}\right)\cdot cos\left(\delta\right)\right]\right\} \tag{5.189}$$

$$N_2^{(n)}=\frac{1}{a_i^{(n)2}}\cdot 2\cdot\chi_2^{(n)}\cdot S(\chi_2^{(n)})\cdot\dot{Q}_2{}^{(n)} \tag{5.190}$$

$$N_3^{(n)} = \frac{2 \cdot S(\chi_3^{(n)})}{a_M^{(n)2}} \cdot \Big\{ cos\,(\delta) \cdot \Big[\Big(\chi_3^{(n)} - c_3^{(n)} \Big) \cdot cos\,(\delta) + \\ + \Big(\chi_1^{(n)} - c_1^{(n)} \Big) \cdot sin\,(\delta) \Big] +$$

$$- \frac{sin\,(\delta)}{\varepsilon_m^2} \cdot \Big[- \Big(\chi_3^{(n)} - c_3^{(n)} \Big) \cdot sin\,(\delta) + \Big(\chi_1^{(n)} - c_1^{(n)} \Big) \cdot cos\,(\delta) \Big] \Big\} \cdot \dot{Q}_3{}^{(n)} \tag{5.191}$$

$$D_1^{(n)} = \frac{\partial y^{(n)}}{\partial \chi_1^{(n)}} \cdot \frac{\partial^2 g_2}{\partial \alpha_1^{(n)2}} \cdot \frac{\partial y^{(n)}}{\partial \chi_1^{(n)}} =$$

$$= \frac{2 \cdot S(\chi_1^{(n)}) \cdot \dot{Q}_1{}^{(n)}}{a_M^{(n)2}} \cdot \Big\{ sin\,(\delta) \cdot \Big[\Big(\chi_3^{(n)} - c_3^{(n)} \Big) \cdot cos\,(\delta) + \\ + \Big(\chi_1^{(n)} - c_1^{(n)} \Big) \cdot sin\,(\delta) \Big] +$$

$$+ \frac{cos\,(\delta)}{\varepsilon_m^2} \cdot \Big[- \Big(\chi_3^{(n)} - c_3^{(n)} \Big) \cdot sin\,(\delta) + \Big(\chi_1^{(n)} - c_1^{(n)} \Big) \cdot cos\,(\delta) \Big] \Big\} \cdot$$

$$\cdot \Big[H_{11}^{(n)} + m_{11}^{(n)} \cdot \Big(G_{M,n,1}^{(4)} + G_{M,n,1}^{(3)} + G_{M,n,1}^{(2)} \Big) \Big] \cdot$$

$$\cdot \frac{2 \cdot S(\chi_1^{(n)}) \cdot \dot{Q}_1{}^{(n)}}{a_M^{(n)2}} \cdot \Big\{ sin\,(\delta) \cdot \Big[\Big(\chi_3^{(n)} - c_3^{(n)} \Big) \cdot cos\,(\delta) + \\ + \Big(\chi_1^{(n)} - c_1^{(n)} \Big) \cdot sin\,(\delta) \Big] +$$

$$+ \frac{cos\,(\delta)}{\varepsilon_m^2} \cdot \Big[- \Big(\chi_3^{(n)} - c_3^{(n)} \Big) \cdot sin\,(\delta) + \Big(\chi_1^{(n)} - c_1^{(n)} \Big) \cdot cos\,(\delta) \Big] \Big\} \tag{5.192}$$

$$D_2^{(n)} = \frac{\partial y^{(n)}}{\partial \chi_2^{(n)}} \cdot \frac{\partial^2 g_2}{\partial \alpha_2^{(n)2}} \cdot \frac{\partial y^{(n)}}{\partial \chi_2^{(n)}} = \frac{1}{a_i^{(n)2}} \cdot 2 \cdot \chi_2^{(n)} \cdot S(\chi_2^{(n)}) \cdot$$

$$\cdot \left[H_{22}^{(n)} + m_{22}^{(n)} \cdot \left(G_{M,n,2}^{(4)} + G_{M,n,2}^{(3)} + G_{M,n,2}^{(2)} \right) \right] \cdot \frac{1}{a_i^{(n)2}} \cdot 2 \cdot \chi_2^{(n)} \cdot S(\chi_2^{(n)}) \tag{5.193}$$

$$D_3^{(n)} = \frac{\partial y^{(n)}}{\partial \chi_3^{(n)}} \cdot \frac{\partial^2 g_2}{\partial \alpha_3^{(n)2}} \cdot \frac{\partial y^{(n)}}{\partial \chi_3^{(n)}} =$$

$$= \frac{2 \cdot S(\chi_3^{(n)}) \cdot \dot{Q_3}^{(n)}}{a_M^{(n)2}} \cdot \left\{ cos\,(\delta) \cdot \left[\left(\chi_3^{(n)} - c_3^{(n)} \right) \cdot cos\,(\delta) + \right. \right.$$

$$\left. + \left(\chi_1^{(n)} - c_1^{(n)} \right) \cdot sin\,(\delta) \right] -$$

$$\left. - \frac{sin\,(\delta)}{\varepsilon_m^2} \cdot \left[- \left(\chi_3^{(n)} - c_3^{(n)} \right) \cdot sin\,(\delta) + \left(\chi_1^{(n)} - c_1^{(n)} \right) \cdot cos\,(\delta) \right] \right\} \cdot$$

$$\cdot \left[H_{33}^{(n)} + m_{33}^{(n)} \cdot \left(G_{M,n,3}^{(4)} + G_{M,n,3}^{(3)} + G_{M,n,3}^{(2)} \right) \right] \cdot$$

$$\cdot \frac{2 \cdot S(\chi_3^{(n)}) \cdot \dot{Q_3}^{(n)}}{a_M^{(n)2}} \cdot \left\{ cos\,(\delta) \cdot \left[\left(\chi_3^{(n)} - c_3^{(n)} \right) \cdot cos\,(\delta) + \right. \right.$$

$$\left. + \left(\chi_1^{(n)} - c_1^{(n)} \right) \cdot sin\,(\delta) \right] -$$

$$\left. - \frac{sin\,(\delta)}{\varepsilon_m^2} \cdot \left[- \left(\chi_3^{(n)} - c_3^{(n)} \right) \cdot sin\,(\delta) + \left(\chi_1^{(n)} - c_1^{(n)} \right) \cdot cos\,(\delta) \right] \right\}. \tag{5.194}$$

The result above shows that the inertial effects, produced by the motion of the masses, affect the plastic response of the macro-element. Based on the above expressions, the evolution laws for the internal variables can be derived through Eq. 5.75, as well as the dissipation function, here omitted for brevity. The complete derivation of the incremental response for the three-dimensional macro-element is provided in Appendix 2.

The general formulation degenerates into the one-dimensional case when the model is perturbed by a mono-component external force (or displacement). Consider for example the macro-element composed of n masses and n yield surfaces, perturbed by a longitudinal force Q_1. According to Eq. 5.160, the incremental response of the model reads

$$\dot{Q}_1^{(ext)} = H_{11}^{(0)} \cdot \left[\dot{q}_1 - \sum_{n=1}^{N} \lambda_n \cdot \frac{\partial y_n^g(Q_1^{(n)}, \alpha_1^{(n)}, \chi_1^{(n)})}{\partial \chi_1^{(n)}} \right]. \tag{5.195}$$

The yield functions in Eq. 5.137 just becomes

$$y^{(n)}(\chi_1^{(n)}) = \frac{\left[\left(\chi_3^{(n)} - c_3^{(n)} \right) \cdot cos\left(\delta\right) + \left(\chi_1^{(n)} - c_1^{(n)} \right) \cdot sin\left(\delta\right) \right]^2}{a_M^{(n)2}} +$$

$$+ \frac{\chi_2^{(n)2}}{a_i^{(n)2}} + \frac{\left[- \left(\chi_3^{(n)} - c_3^{(n)} \right) \cdot sin\left(\delta\right) + \left(\chi_1^{(n)} - c_1^{(n)} \right) \cdot cos\left(\delta\right) \right]^2}{a_m^{(n)2}} - 1 =$$

$$+ \frac{\left[\left(\chi_1^{(n)} - c_1^{(n)} \right) \right]^2}{a_m^{(n)2}} = 0 \tag{5.196}$$

from which n dissymmetric plastic thresholds can be obtained

$$\chi_1^{(n)} = k_1^{(n)} = \pm a_m^{(n)} + c_1^{(n)}$$

identical to the yield functions of the 1D model. The values $a_m^{(n)} + c_1^{(n)}$ and $-a_m^{(n)} +$

$c_1^{(n)}$ would represent the passive and active resistance of the backfill, respectively. The plastic multiplier (Eq. 5.163) is given by

$$\lambda_n = \frac{\frac{\partial y^{(n)}}{\partial \chi_1^{(n)}} \cdot \dot{Q_1}^{(n)}}{\frac{\partial y^{(n)}}{\partial \chi_1^{(n)}} \cdot \frac{\partial^2 g_2}{\partial \alpha_1^{(n)2}} \cdot \frac{\partial y^{(n)}}{\partial \chi_1^{(n)}}} = \frac{N_1^{(n)}}{D_1^{(n)}}, n = 1, .., N \tag{5.197}$$

$$N_1^{(n)} = \frac{\partial y^{(n)}}{\partial \chi_1^{(n)}} \cdot \dot{Q_1}^{(n)} = \frac{2 \cdot S(\chi_1^{(n)}) \cdot \dot{Q_1}^{(n)}}{a_m^{(n)2}} \cdot \left(\chi_1^{(n)} - c_1^{(n)}\right) \tag{5.198}$$

$$D_1^{(n)} = \frac{\partial y^{(n)}}{\partial \chi_1^{(n)}} \cdot \frac{\partial^2 g_2}{\partial \alpha_1^{(n)2}} \cdot \frac{\partial y^{(n)}}{\partial \chi_1^{(n)}} =$$

$$= \frac{4}{a_m^{(n)4}} \cdot \left(\chi_1^{(n)} - c_1^{(n)}\right)^2 \cdot \left[H_{11}^{(n)} + m_{11}^{(n)} \cdot \left(G_{M,n,1}^{(4)} + G_{M,n,1}^{(3)} + G_{M,n,1}^{(2)}\right)\right] \tag{5.199}$$

$$\lambda_n = \frac{S(\chi_1^{(n)}) \cdot a_m^{(n)2} \cdot \left(\chi_1^{(n)} - c_1^{(n)}\right) \cdot \dot{Q_1}^{(n)}}{2 \cdot \left(\chi_1^{(n)} - c_1^{(n)}\right)^2 \cdot \left[H_{11}^{(n)} + m_{11}^{(n)} \cdot \left(G_{M,n,1}^{(4)} + G_{M,n,1}^{(3)} + G_{M,n,1}^{(2)}\right)\right]}, n = 1, .., N \tag{5.200}$$

and the evolution law for the internal variables is reported below

$$\dot{\alpha}_1^{(n)} = \lambda_n \cdot \frac{\partial y_1(\chi_1^{(n)})}{\partial \chi_1^{(n)}} =$$

$$= \frac{S(\chi_1^{(n)}) \cdot a_m^{(n)2} \cdot \left(\chi_1^{(n)} - c_1^{(n)}\right)}{2 \cdot \left(\chi_1^{(n)} - c_1^{(n)}\right)^2 \cdot \left[H_{11}^{(n)} + m_{11}^{(n)} \cdot \left(G_{M,n,1}^{(4)} + G_{M,n,1}^{(3)} + G_{M,n,1}^{(2)}\right)\right]} \cdot \dot{Q_1}^{(n)} \cdot$$

$$\cdot \frac{2 \cdot S(\chi_1^{(n)})}{a_m^{(n)2}} \cdot \left(\chi_1^{(n)} - c_1^{(n)}\right) =$$

$$= \frac{\dot{Q_1}^{(n)}}{\left[H_{11}^{(n)} + m_{11}^{(n)} \cdot \left(G_{M,n,1}^{(4)} + G_{M,n,1}^{(3)} + G_{M,n,1}^{(2)}\right)\right]}, n = 1, .., N. \tag{5.201}$$

that leads to the incremental form of the 1D model reported here below

$$\dot{Q}_1^{(ext)} = H_{11}^{(0)} \cdot \left[\dot{q_1} - \sum_{n=1}^{N} \frac{\dot{Q_1}^{(n)}}{\left[H_{11}^{(n)} + m_{11}^{(n)} \cdot \left(G_{M,n,1}^{(4)} + G_{M,n,1}^{(3)} + G_{M,n,1}^{(2)}\right)\right]}\right]. \tag{5.202}$$

Finally, if the masses are set equal to zero, Eq. 5.202 simplifies in the incremental form of a generalised Iwan model with dissymmetric behaviour

$$\dot{Q}_1^{(ext)} = H_{11}^{(0)} \cdot \left[\dot{q_1} - \sum_{n=1}^{N} \frac{\dot{Q_1}^{(n)}}{H_{11}^{(n)}}\right]. \tag{5.203}$$

5.12 Implementation

The macro-element for bridge abutments was coded in Matlab and OpenSees. These environments are based on two different programming languages, requiring a distinct structuring of the source code. Matlab is a programming platform designed for numerical computations and statistical analysis written mainly in the homonym programming language created by MathWorks but including also the syntax of the language C. As already described in Section 2.2, OpenSees is instead a software framework built according to the logic of object-oriented programming and written in C and C++. Therefore, although the mathematical relationships of the macro-element be the same, they are differently structured in the two codes. In Matlab, the macro-element constitutes a single, independent routine, while in OpenSees the model was coded as a new sub-class and inserted in a large object-oriented environment.

In the following, the finite difference approximation of the incremental form of

the macro-element is developed, that represents the basic structure implemented in Matlab. Afterwards, the implementation of the macro-element in the OpenSees environment is presented: the one-dimensional formulation was coded as a new material while the multi-axial formulation constituted a new finite element for the OpenSees library. In its present form, the new finite element does not include the inertial effects produced by the masses, that hence need to be modelled explicitly in the numerical soil-structure model. The introduction of the masses in the multi-axial formulation will constitute a forthcoming development of the present research.

5.12.1 Numerical integration of the equations of motion

Eqs. 5.112 and 5.113 can be integrated numerically in time through, for example, the finite difference method. Since the mathematical structure of the three-dimensional macro-element is conceptually identical to that in one-dimension, for the sake of conciseness the integration of the equations of motion is shown for the one-dimensional model only.

The finite difference approximation of the incremental response reads

$$\frac{Q^{(ext)}(t+\Delta t)-Q^{(ext)}(t)}{\Delta t}=H^{(0)}\cdot\left(\frac{q(t+\Delta t)-q(t)}{\Delta t}-\right.$$

$$-\sum_{n=1}^{N}\frac{Q^{(n)}(t+\Delta t)-Q^{(n)}(t)}{\Delta t}\cdot\frac{1}{H_n+m^{(n)}\cdot\left(\partial G^{(4)}_{M,n}+\partial G^{(3)}_{M,n}+\partial G^{(2)}_{M,n}\right)}-$$

$$-S(Q^{(ext)})\cdot\sum_{n=1}^{N}R_n\cdot\left|\frac{Q^{(n)}(t+\Delta t)-Q^{(n)}(t)}{\Delta t}\cdot\right.$$

$$\left.\left.\cdot\frac{1}{H_n+m^{(n)}\cdot\left(\partial G^{(4)}_{M,n}+\partial G^{(3)}_{M,n}+\partial G^{(2)}_{M,n}\right)}\right|\right) \tag{5.204}$$

and, multiplying both members by Δt, it gives

$$Q^{(ext)}(t+\Delta t) - Q^{(ext)}(t) = H^{(0)} \cdot (q(t+\Delta t) - q(t) -$$

$$- \sum_{n=1}^{N} \frac{Q^{(n)}(t+\Delta t) - Q^{(n)}(t)}{H_n + m^{(n)} \cdot \left(\partial G^{(4)}_{M,n} + \partial G^{(3)}_{M,n} + \partial G^{(2)}_{M,n} \right)} -$$

$$- S(Q^{(ext)}) \cdot \sum_{n=1}^{N} R_n \cdot \left| \frac{Q^{(n)}(t+\Delta t) - Q^{(n)}(t)}{H_n + m^{(n)} \cdot \left(\partial G^{(4)}_{M,n} + \partial G^{(3)}_{M,n} + \partial G^{(2)}_{M,n} \right)} \right| \Bigg) \tag{5.205}$$

in which the mass $m^{(0)}$ is set equal to zero. The n-th internal force $Q^{(n)}(t)$ is obtained by the local balance equation in Eq. 5.35, that can be rewritten in incremental form for the mass $m^{(1)}$ of the first slider as

$$\dot{Q}^{(1)}(t) = \dot{Q}^{(ext)}(t) - \dot{Q}^{(M,1)}(t) = \dot{Q}^{(ext)}(t) - m^{(1)} \cdot \sum_{n=1}^{N} \ddot{\alpha}^{(n)}(t) =$$

$$= \dot{Q}^{(ext)}(t) - m^{(1)} \cdot \left[\ddot{q}(t) - \ddot{q}^{(0)}(t) \right] \tag{5.206}$$

and for the other masses

$$\dot{Q}^{(n)}(t) = \dot{Q}^{(n-1)}(t) - \dot{Q}^{(M,n)}(t) = \dot{Q}^{(n-2)}(t) - \dot{Q}^{(M,n-1)}(t) - \dot{Q}^{(M,n)}(t) =$$

$$= \dot{Q}^{(n-3)}(t) - \dot{Q}^{(M,n-2)}(t) - \dot{Q}^{(M,n-1)}(t) - \dot{Q}^{(M,n)}(t) =$$

$$= \dot{Q}^{(ext)}(t) - \sum_{h=1}^{n} \dot{Q}^{(M,h)}(t) = \dot{Q}^{(ext)}(t) - \sum_{h=1}^{n} m^{(h)} \cdot \ddot{\alpha}^{(n)}(t), n > 1. \tag{5.207}$$

which can be easily integrated numerically. The finite difference approximations of the inertial terms $\partial G^{(4)}_{M,n}$, $\partial G^{(3)}_{M,n}$ and $\partial G^{(2)}_{M,n}$ are developed here below:

$$\partial G^{(4)}_{M,n}(t) = -\frac{1}{\dot{\alpha}^{(n)2}} \cdot \sum_{h=n}^{N} \dddot{\alpha}^{(h)} \cdot \sum_{k=n}^{N} \alpha^{(k)} = -\left(\frac{\Delta t}{\alpha^{(n)}(t+\Delta t) - \alpha^{(n)}(t)}\right)^2 \cdot$$

$$\cdot \frac{1}{\Delta t^3} \cdot \sum_{h=n}^{N} \left[\alpha^{(h)}(t - 2 \cdot \Delta t) - 4 \cdot \alpha^{(h)}(t - \Delta t) + 6 \cdot \alpha^{(h)}(t) - \right.$$

$$\left. -4 \cdot \alpha^{(h)}(t + \Delta t) + \alpha^{(h)}(t + 2 \cdot \Delta t)\right] \cdot \sum_{k=n}^{N} \alpha^{(k)} \tag{5.208}$$

$$\partial G^{(3)}_{M,n}(t) = \frac{1}{\dot{\alpha}^{(n)3}} \cdot \sum_{h=n}^{N} \ddot{\alpha}^{(h)} \cdot \ddot{\alpha}^{(n)} \cdot \sum_{k=n}^{N} \alpha^{(k)} - 2 \cdot \frac{1}{\dot{\alpha}^{(n)}} \cdot \sum_{j=n}^{N} \ddot{\alpha}^{(j)} +$$

$$+ \frac{1}{\dot{\alpha}^{(n)2}} \cdot \sum_{h=n}^{N} \dot{\alpha}^{(h)} \cdot \sum_{k=n}^{N} \ddot{\alpha}^{(k)} =$$

$$= \left(\frac{\Delta t}{\alpha^{(n)}(t+\Delta t) - \alpha^{(n)}(t)}\right)^3 \cdot \frac{1}{\Delta t^3} \cdot \sum_{h=n}^{N} \left[-0.5 \cdot \alpha^{(h)}(t - 2 \cdot \Delta t) + \alpha^{(h)}(t - \Delta t) - \right.$$

$$\left. -\alpha^{(h)}(t + \Delta t) + 0.5 \cdot \alpha^{(h)}(t + 2 \cdot \Delta t)\right] \cdot$$

$$\cdot \frac{\alpha^{(n)}(t)(t + \Delta t) - 2 \cdot \alpha^{(n)}(t)(t_0) + \alpha^{(n)}(t)(t - \Delta t)}{\Delta t^2} \cdot \sum_{k=n}^{N} \alpha^{(k)} -$$

$$-2 \cdot \frac{\Delta t}{\alpha^{(n)}(t+\Delta t) - \alpha^{(n)}(t)} \cdot$$

$$\cdot \sum_{j=n}^{N} \frac{-0.5 \cdot \alpha^{(j)}(t-2\cdot\Delta t) + \alpha^{(j)}(t-\Delta t) - \alpha^{(j)}(t+\Delta t) + 0.5 \cdot \alpha^{(j)}(t+2\cdot\Delta t)}{\Delta t^3} +$$

$$+ \left(\frac{\Delta t}{\alpha^{(n)}(t+\Delta t) - \alpha^{(n)}(t)} \right)^2 \cdot \sum_{h=n}^{N} \frac{\alpha^{(h)}(t+\Delta t) - \alpha^{(h)}(t)}{\Delta t} \cdot$$

$$\cdot \sum_{k=n}^{N} \frac{-0.5 \cdot \alpha^{(k)}(t-2\cdot\Delta t) + \alpha^{(k)}(t-\Delta t) - \alpha^{(k)}(t+\Delta t) + 0.5 \cdot \alpha^{(k)}(t+2\cdot\Delta t)}{\Delta t^3} =$$

$$= \sum_{h=n}^{N} \left\{ \frac{-0.5 \cdot \alpha^{(h)}(t-2\cdot\Delta t) + \alpha^{(h)}(t-\Delta t) - \alpha^{(h)}(t+\Delta t) + 0.5 \cdot \alpha^{(h)}(t+2\cdot\Delta t)}{\left[\alpha^{(n)}(t+\Delta t) - \alpha^{(n)}(t)\right]^3} \right\} \cdot$$

$$\cdot \frac{\alpha^{(n)}(t)(t+\Delta t) - 2\cdot\alpha^{(n)}(t)(t_0) + \alpha^{(n)}(t)(t-\Delta t)}{\Delta t^2} \cdot \sum_{k=n}^{N} \alpha^{(k)} -$$

$$-\frac{2}{\Delta t^2} \cdot \sum_{j=n}^{N} \frac{-0.5 \cdot \alpha^{(j)}(t-2\cdot\Delta t) + \alpha^{(j)}(t-\Delta t) - \alpha^{(j)}(t+\Delta t) + 0.5 \cdot \alpha^{(j)}(t+2\cdot\Delta t)}{\alpha^{(n)}(t+\Delta t) - \alpha^{(n)}(t)} +$$

$$+ \sum_{h=n}^{N} \frac{\alpha^{(h)}(t+\Delta t) - \alpha^{(h)}(t)}{\alpha^{(n)}(t+\Delta t) - \alpha^{(n)}(t)} \cdot$$

$$\cdot \sum_{k=n}^{N} \frac{-0.5 \cdot \alpha^{(k)}(t-2\cdot\Delta t) + \alpha^{(k)}(t-\Delta t) - \alpha^{(k)}(t+\Delta t) + 0.5\cdot\alpha^{(k)}(t+2\cdot\Delta t)}{\Delta t^2} \tag{5.209}$$

$$G^{(2)}_{M,n} = \frac{1}{\dot{\alpha}^{(n)2}} \cdot \sum_{h=n}^{N} \ddot{\alpha}^{(h)} \cdot \sum_{k=n}^{N} \ddot{\alpha}^{(k)} - \frac{\ddot{\alpha}^{(n)}}{\dot{\alpha}^{(n)3}} \cdot \sum_{h=n}^{N} \dot{\alpha}^{(h)} \cdot \sum_{k=n}^{N} \ddot{\alpha}^{(k)} =$$

$$= \left(\frac{\Delta t}{\alpha^{(n)}(t+\Delta t) - \alpha^{(n)}(t)} \right)^2 \cdot \sum_{h=n}^{N} \frac{\alpha^{(h)}(t-\Delta t) - 2\cdot\alpha^{(h)}(t+\Delta t) + \alpha^{(h)}(t+2\cdot\Delta t)}{\Delta t^2} \cdot$$

$$\cdot \sum_{k=n}^{N} \frac{\alpha^{(k)}(t-\Delta t) - 2\cdot\alpha^{(k)}(t+\Delta t) + \alpha^{(k)}(t+2\cdot\Delta t)}{\Delta t^2} -$$

$$- \frac{\alpha^{(n)}(t-\Delta t) - 2\cdot\alpha^{(n)}(t+\Delta t) + \alpha^{(n)}(t+2\cdot\Delta t)}{\Delta t^2} \cdot$$

$$\cdot \left(\frac{\Delta t}{\alpha^{(n)}(t+\Delta t) - \alpha^{(n)}(t)} \right)^3 \cdot \sum_{h=n}^{N} \frac{\alpha^{(h)}(t+\Delta t) - \alpha^{(h)}(t)}{\Delta t} \cdot$$

$$\cdot \sum_{k=n}^{N} \frac{\alpha^{(k)}(t-\Delta t) - 2\cdot\alpha^{(k)}(t+\Delta t) + \alpha^{(k)}(t+2\cdot\Delta t)}{\Delta t^2} =$$

$$= \sum_{h=n}^{N} \frac{\alpha^{(h)}(t-\Delta t) - 2\cdot\alpha^{(h)}(t+\Delta t) + \alpha^{(h)}(t+2\cdot\Delta t)}{\left[\alpha^{(n)}(t+\Delta t) - \alpha^{(n)}(t)\right]^2} \cdot$$

$$\cdot \sum_{k=n}^{N} \frac{\alpha^{(k)}(t-\Delta t) - 2\cdot\alpha^{(k)}(t+\Delta t) + \alpha^{(k)}(t+2\cdot\Delta t)}{\Delta t^2} -$$

$$- \left[\alpha^{(n)}(t-\Delta t) - 2\cdot\alpha^{(n)}(t+\Delta t) + \alpha^{(n)}(t+2\cdot\Delta t)\right] \cdot$$

$$\cdot \sum_{h=n}^{N} \frac{\alpha^{(h)}(t+\Delta t) - \alpha^{(h)}(t)}{\left[\alpha^{(n)}(t+\Delta t) - \alpha^{(n)}(t)\right]^3} \cdot$$

$$\cdot \sum_{k=n}^{N} \frac{\alpha^{(k)}(t-\Delta t) - 2 \cdot \alpha^{(k)}(t+\Delta t) + \alpha^{(k)}(t+2\cdot\Delta t)}{\Delta t^2}. \tag{5.210}$$

Eqs. 5.205, 5.207 and 5.208, with the aid of Eqs. 5.208, 5.209 and 5.210, can be integrated in time to give the response of the macro-element in terms of the total displacement $q(t+\Delta t)$ or the force in the free node $Q^{(ext)}(t+\Delta t)$, according to the method of analysis used. In this regard, with some further manipulation, the explicit expressions for the total displacement and the force in the free node are given below

$$q(t+\Delta t) = \left[1 + 0.5 \cdot \frac{m^{(1)}}{\left[H^{(n)} + H^{(n)}_{dyn}\right] \cdot \Delta t^2}\right]^{-1} \cdot$$

$$\cdot \left\{ q(t) \cdot \left[1 + \frac{m^{(1)}}{\Delta t^2} \cdot \sum_{n=1}^{N} \frac{1}{H^{(n)} + H^{(n)}_{dyn}}\right] - q(t-2\cdot\Delta t) \cdot \right.$$

$$\cdot \left[\frac{m^{(1)}}{\Delta t^2} \cdot \sum_{n=1}^{N} \frac{1}{H^{(n)} + H^{(n)}_{dyn}}\right] + q(t-3\cdot\Delta t) \cdot \left[0.5 \cdot \frac{m^{(1)}}{\Delta t^2} \cdot \sum_{n=1}^{N} \frac{1}{H^{(n)} + H^{(n)}_{dyn}}\right] +$$

$$+ Q^{(ext)}(t+\Delta t) \cdot \left[\frac{1}{H^{(0)}} + \sum_{n=1}^{N} \frac{1}{H^{(n)} + H^{(n)}_{dyn}} + 0.5 \cdot \frac{m^{(1)}}{H^{(0)} \cdot \Delta t^2} \cdot \sum_{n=1}^{N} \frac{1}{H^{(n)} + H^{(n)}_{dyn}}\right] -$$

$$- Q^{(ext)}(t) \cdot \left[\frac{1}{H^{(0)}} + \sum_{n=1}^{N} \frac{1}{H^{(n)} + H^{(n)}_{dyn}} + \frac{m^{(1)}}{H^{(0)} \cdot \Delta t^2} \cdot \sum_{n=1}^{N} \frac{1}{H^{(n)} + H^{(n)}_{dyn}}\right] +$$

$$+Q^{(ext)}(t-2\cdot\Delta t)\cdot\left[\frac{m^{(1)}}{H^{(0)}\cdot\Delta t^2}\cdot\sum_{n=1}^{N}\frac{1}{H^{(n)}+H_{dyn}^{(n)}}\right]-$$

$$-Q^{(ext)}(t-3\cdot\Delta t)\cdot\left[0.5\cdot\frac{m^{(1)}}{H^{(0)}\cdot\Delta t^2}\cdot\sum_{n=1}^{N}\frac{1}{H^{(n)}+H_{dyn}^{(n)}}\right]-$$

$$-\sum_{n=1}^{N}\frac{m^{(n)}}{H^{(n)}\cdot\Delta t^2}\cdot\left[-0.5\cdot q^{(n)}(t-4\cdot\Delta t)+q^{(n)}(t-3\cdot\Delta t)-\right.$$

$$\left.-q^{(n)}(t-\Delta t)+0.5\cdot q^{(n)}(t)\right]\Big\} \tag{5.211}$$

$$Q^{(ext)}(t+\Delta t)=\left[\frac{1}{H^{(0)}}+\sum_{n=1}^{N}\frac{1}{H^{(n)}+H_{dyn}^{(n)}}+0.5\cdot\frac{m^{(1)}}{H^{(0)}\cdot\Delta t^2}\cdot\sum_{n=1}^{N}\frac{1}{H^{(n)}+H_{dyn}^{(n)}}\right]^{-1}\cdot$$

$$\cdot\left\{q(t+\Delta t)\cdot\left[1+0.5\cdot\frac{m^{(1)}}{\Delta t^2}\cdot\sum_{n=1}^{N}\frac{1}{H^{(n)}+H_{dyn}^{(n)}}\right]-\right.$$

$$-q(t)\cdot\left[1+\frac{m^{(1)}}{\Delta t^2}\cdot\sum_{n=1}^{N}\frac{1}{H^{(n)}+H_{dyn}^{(n)}}\right]+$$

$$+q(t-2\cdot\Delta t)\cdot\left[\frac{m^{(1)}}{\Delta t^2}\cdot\sum_{n=1}^{N}\frac{1}{H^{(n)}+H_{dyn}^{(n)}}\right]-q(t-3\cdot\Delta t)\cdot$$

$$\cdot\left[0.5\cdot\frac{m^{(1)}}{\Delta t^2}\cdot\sum_{n=1}^{N}\frac{1}{H^{(n)}+H_{dyn}^{(n)}}\right]+Q^{(ext)}(t)\cdot$$

$$\cdot\left[\frac{1}{H^{(0)}}+\sum_{n=1}^{N}\frac{1}{H^{(n)}+H_{dyn}^{(n)}}+\frac{m^{(1)}}{H^{(0)}\cdot\Delta t^2}\cdot\sum_{n=1}^{N}\frac{1}{H^{(n)}+H_{dyn}^{(n)}}\right]-$$

$$-Q^{(ext)}(t-2\cdot\Delta t)\cdot\left[\frac{m^{(1)}}{H^{(0)}\cdot\Delta t^2}\cdot\sum_{n=1}^{N}\frac{1}{H^{(n)}+H^{(n)}_{dyn}}\right]+$$

$$+Q^{(ext)}(t-3\cdot\Delta t)\cdot\left[0.5\cdot\frac{m^{(1)}}{H^{(0)}\cdot\Delta t^2}\cdot\sum_{n=1}^{N}\frac{1}{H^{(n)}+H^{(n)}_{dyn}}\right]+$$

$$+\sum_{n=1}^{N}\frac{m^{(n)}}{H^{(n)}\cdot\Delta t^2}\cdot\left[-0.5\cdot q^{(n)}(t-4\cdot\Delta t)+q^{(n)}(t-3\cdot\Delta t)-\right.$$

$$\left.-q^{(n)}(t-\Delta t)+0.5\cdot q^{(n)}(t)\right]\Big\}. \tag{5.212}$$

The explicit time-integration algorithm above is not unconditionally stable and, therefore, it requires an appropriate choice of the time step. However, convergence can be obtained with a limited sub-stepping that is a function of the level of mobilised strength of the macro-element. The maximum reduction of the time step of the input motion needed for the dynamic simulations carried out in the present thesis was of about 10, that was comparable with the sub-stepping adopted for the dynamic analyses of the full soil-bridge system.

When the dynamic response of the masses is negligible, the above equations simplify as follows

$$q(t+\Delta t)=q(t)+\left[Q^{(ext)}(t+\Delta t)-Q^{(ext)}(t)\right]\cdot\left(\frac{1}{H^{(0)}}+\sum_{n=1}^{N}\frac{1}{H^{(n)}}\right) \tag{5.213}$$

$$Q^{(ext)}(t+\Delta t)=Q^{(ext)}(t)+\left[q(t+\Delta t)-q(t)\right]\cdot\left(H^{(0)}+\sum_{n=1}^{N}H^{(n)}\right) \tag{5.214}$$

leading to the incremental response of the classical Iwan model.

5.12.2 A new material in OpenSees: one-dimensional macro-element

The macro-element of bridge abutment is a method for the structural analysis: it is conceived to represent the behaviour of bridge abutments, under both static and dynamic conditions, in the global model of the structure, according to the scheme illustrated in Figure 5.27(a). The one-dimensional formulation was introduced in the OpenSees environment as a new Uniaxial material that reproduces the response of the fundamental device shown in Figure 5.27(b). In fact, taking advantage of the rheological representation of the one-dimensional macro-element, it can be regarded as the assembly of a certain number N of elemental devices, each representing a generalised version of the Voight model with a dissymmetric behaviour of the slider and the introduction of a mass. Hence, the elemental device can have a different strength and stiffness in compression and extension, which is an essential feature for simulating the behaviour of abutments. The model was written with the aim to carry out either force- or displacement-controlled analyses.

In Figure 5.28, the cyclic response of the macro-element with only one dissipative device, in addition to the elastic spring 0, is presented in which the bias parameters for strength $A_k = k_-^{(1)}/k_+^{(1)}$ and stiffness $A_H = H_-^{(1)}/H_+^{(1)}$ are less than one. Figure 5.29 shows instead a qualitative cyclic response of the macro-element composed of 10 dissipative devices in a displacement-controlled analysis. At the end of the first cycle, the model develops a permanent internal force that moves the following cycles upwards. The plastic thresholds evolve during the first cycle according to the kinematic hardening prescribed, leading to the overlapped response of the next cycles.

5.12.3 A new finite element in OpenSees: multi-axial formulation

The three-dimensional formulation was coded as a new ZeroLength-class finite el-

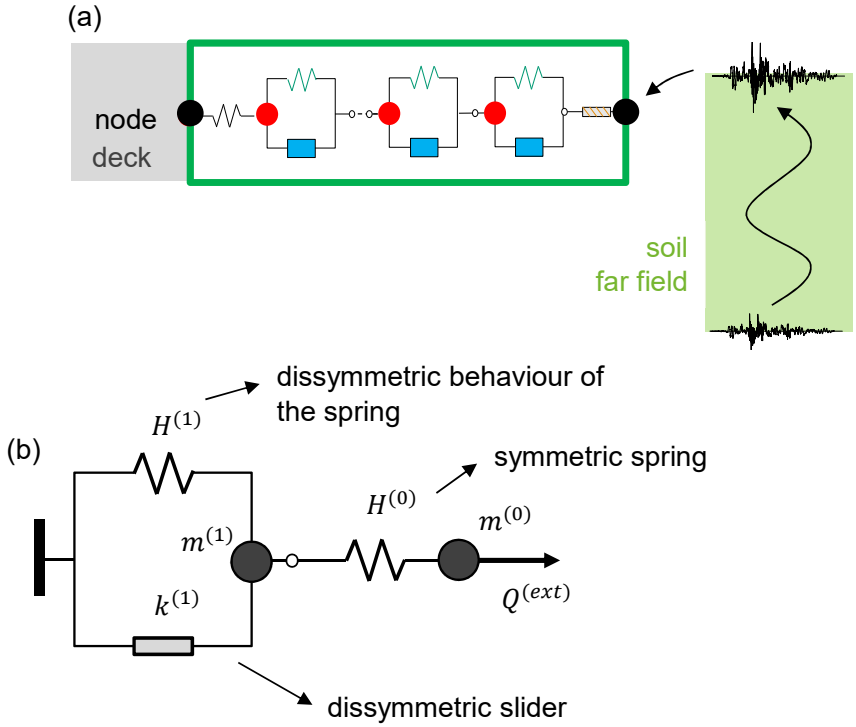

Figure 5.27: Representation of the 1D macro-element as a part of the global structural model (a) and of the new material coded in the OpenSees library (b).

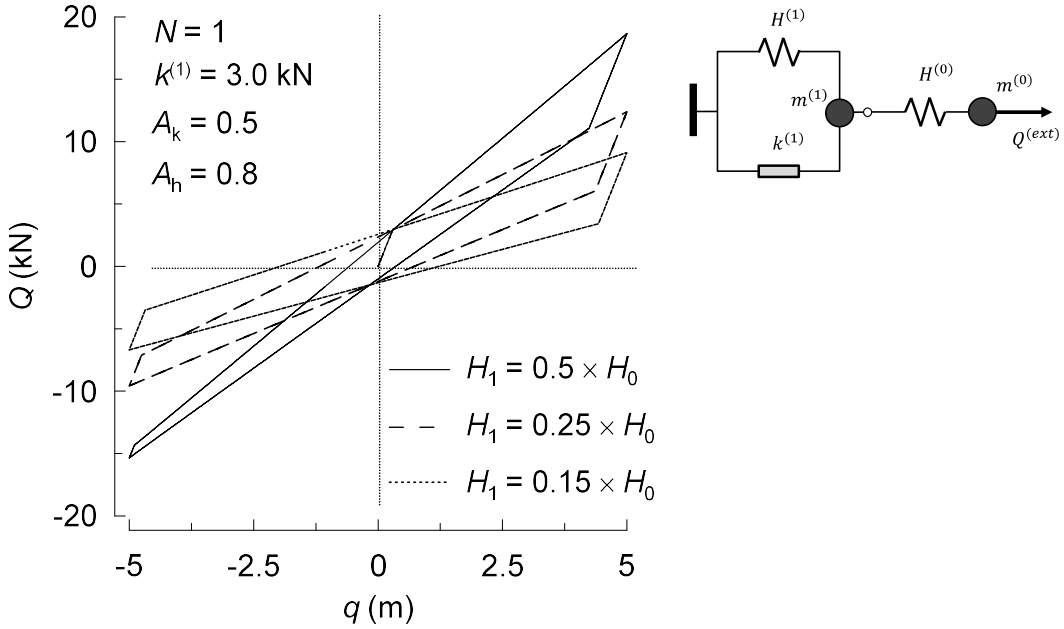

Figure 5.28: Qualitative responses of the one-dimensional macro-element considering a dissymmetric behaviour on the strength and stiffness of the elemental devices.

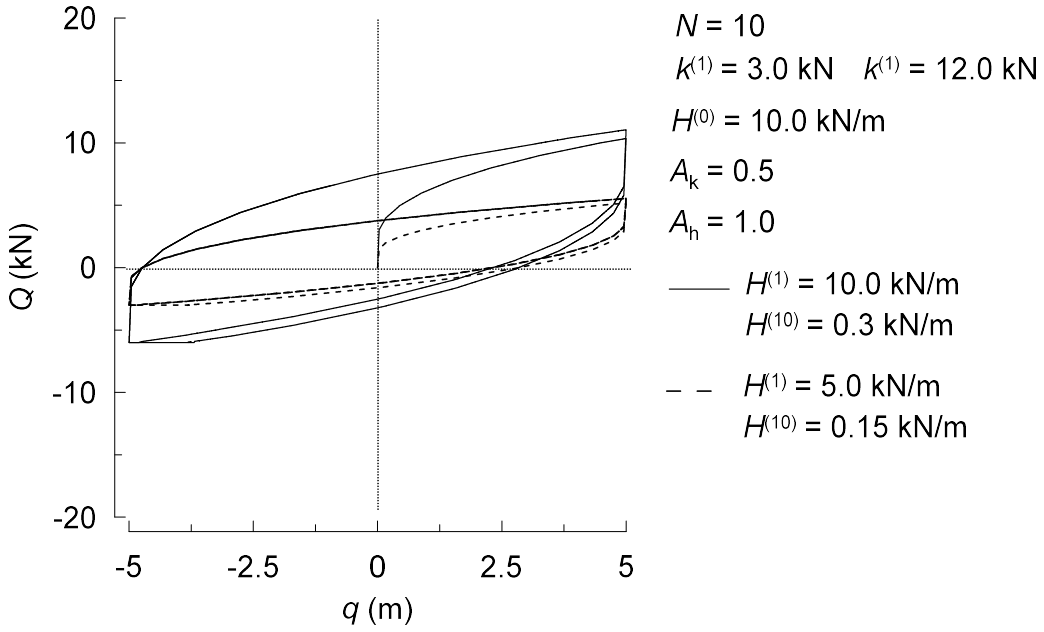

Figure 5.29: Cyclic response of the 1D macro-element considering 10 cycles of loading.

ement in the OpenSees library. The code was written in C++ based on the logic of object-oriented programming: the source code was included into the OpenSees framework as a sub-class opportunely linked to the other objects according to the typical hierarchical structure of this method of programming. The source code is composed of two files: a header file (.h), containing the general setting of the model, and a main file (.cpp), in which the model formulation is developed. Currently, the inertial effects are not included into the formulation of the finite element, therefore the masses have to be modelled explicitly in the numerical model, associating each of them with a specific yield surface. This can be accomplished by representing each plastic flow through a separated finite element combined with a mass. Nonetheless, as it will be shown in Section 5.14, only a few masses are needed to reproduce with a good level of accuracy the frequency-dependent response of the soil-abutment system. In first approximation, the finite element including the multi-surface elastic-plastic response of the macro-element can be coupled with the sole diagonal mass

tensor $m_{ii}^{(1)}$ associated with the first yield, with an acceptable reproduction of the dynamic response of the abutment.

In the header file, all the attributes needed and linked to the new source code are recalled. The public and private methods used to compute the response of the finite element are stated and linked to the relative source codes. In the general constructor all the variables are declared, specifying their dimensions and precision. All the stiffness $H_1^{(n)}$ and strength parameters $k_1^{(n)}$ in a specific coordinate direction associated with the N plastic flows can be defined as input quantities, in order to choose the more appropriate configuration of the yield surface and the kinematic hardening rule for the problem under examination. Based on this information, the ellipsoidal yield function, that is implemented in the main file, generates the entire plastic domain.

In the main file, the finite element is completely defined, starting from its geometry: it is composed of two coincident nodes, with three degrees of freedom each, that interact according to the general formulation of the model. The main constructor initialises the variables previously defined in the header file and contains some derived quantities, such as the equivalent stiffnesses associated with activation of the plastic flows. The constitutive relations are implemented in incremental form according to the following procedure. The code takes the nodal displacements as the input quantities for the main routine of the constitutive relationships. The relative displacement between the two nodes is therefore computed, projecting it along the local axes of the finite element through the definition of an appropriate coordinate-transformation object. A trial elastic force vector is therefore determined as the inner product between the relative displacement and the initial elastic stiffness of the model $H_{ii}^{(0)}$. An iterative check on the distance between the trial force and the yield surfaces follows, in order to specialise the constitutive relations according to

the resistance mobilised. In case of plastic flow, the tangent stiffness matrix (Appendix 2) is assembled and the effective force vector is finally computed. The model can be employed in both force- or displacement-controlled analyses. At present, the source code of the model is available as a dynamic-link library (DLL file) with the intention to submit it for review to the scientific committee of OpenSees in order to make it available in the OpenSees library.

5.13 Application in numerical analysis

The conceptual structure of the macro-element is illustrated in Figure 5.30. The soil domain is divided in two parts, namely the far field and the near field (Cremer et al. 2002). The macro-element is conceived to reproduce the response of the abutment and the soil interacting with it, which constitute the near field where all material and geometric nonlinearities are lumped. The far field refers instead to the area of soil not affected by soil-structure interaction, in which seismic waves propagate under free field conditions as in the absence of the abutment.

A first distinction is needed when using the macro-element in static or dynamic analyses. In a gravity analysis, the loads coming from the superstructure of the bridge are transmitted to the macro-element which in turn deforms. Hence a simple force-based approach would be envisaged to analyse the static configuration of the bridge. In this case, the mechanical properties of the soil volume to be considered for calibrating the macro-element would be those of the embankment and of the foundation soil. For the latter, a vertical extension equal to the effective height of the embankment (see Section 3.3) can be assumed as representative of the mechanical properties of the soil interacting with the footing.

However, the principal domain of application of the macro-element consists in carrying out efficient nonlinear dynamic soil-structure analyses, in virtue of the drastic

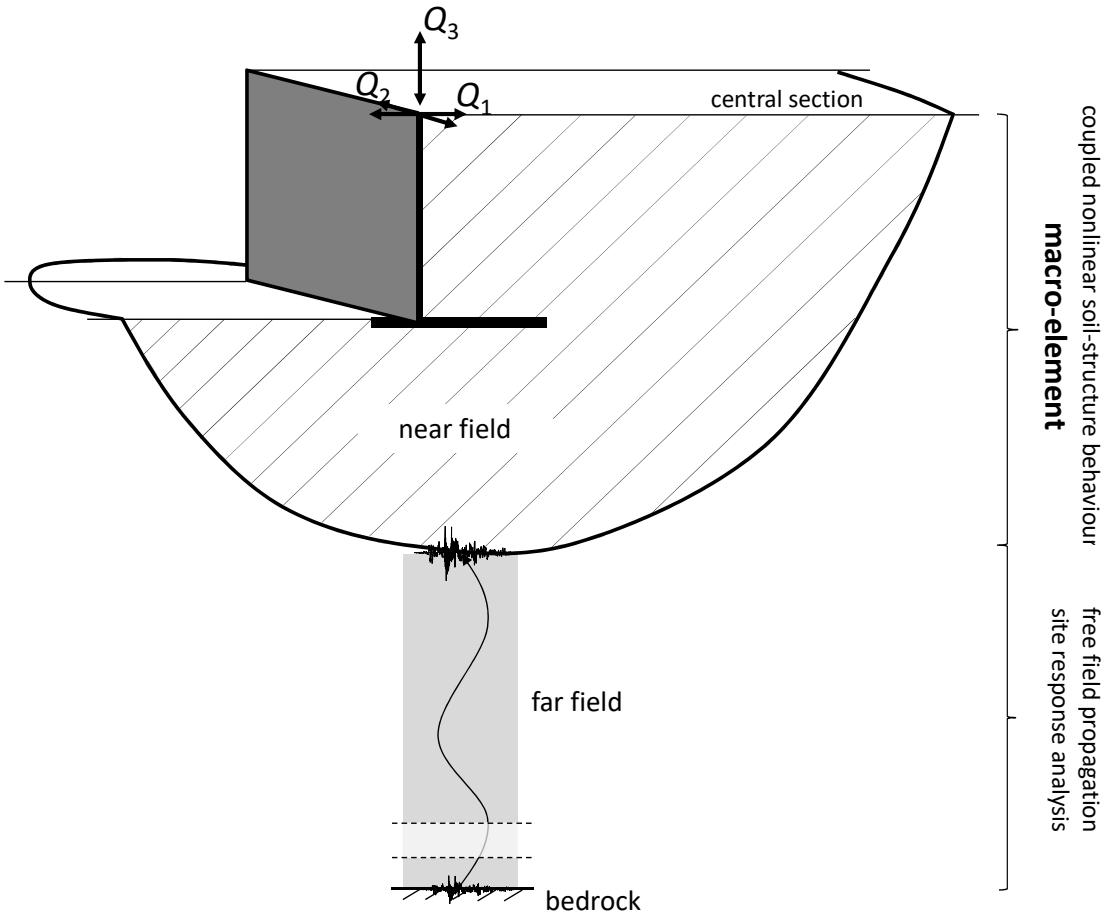

Figure 5.30: Analysis procedure of the macro-element approach.

reduction of the degrees of freedom of the global structural models accounting for soil-structure interaction. Under seismic conditions, the ground motion coming up from the far field is transferred to the superstructure through the macro-element, which in turn is also perturbed by the seismic actions generated by the dynamic response of the superstructure. In this condition, the input motion for the macro-element needs to be characterised by means of time histories of the seismic motion. In this view, the propagation of the seismic waves from the bedrock up to the lower boundary of the near field can be studied through a free field site response analysis. The free field seismic motion is then applied to the free node of the macro-element and a nonlinear time domain analysis can be performed, as shown in Figure 5.31. After evaluating the static or dynamic response of the global structural model accounting for soil-structure interaction, the macro-element response, in terms of force-displacement relationships, can be also used for a prompt evaluation of the stability of the soil-abutment system. Under static conditions, the stability of the system is guaranteed by a sufficient distant of the state of the abutment, in terms of interaction forces exchanged at the deck-abutment contact, from the ultimate surface of the soil-abutment system. This distance represents a safety factor against failure and it is provided by technical provisions. Under dynamic conditions, instead, the ultimate conditions of the abutment might be theoretically attained in order to limit the seismic actions transferred to the superstructure, at the cost of a certain amount of permanent displacements of the geotechnical system that must be compatible with the performance levels prescribed for the entire bridge structure.

It is worth noticing that the soil-structure interaction effects occurring at different locations of a bridge should be modelled with a comparable level of accuracy in order to have consistent results. This implies that, in a plasticity-based macro-element approach, appropriate macro-element representations for the pier foundations should be adopted in conjunction with the macro-elements of the abutments.

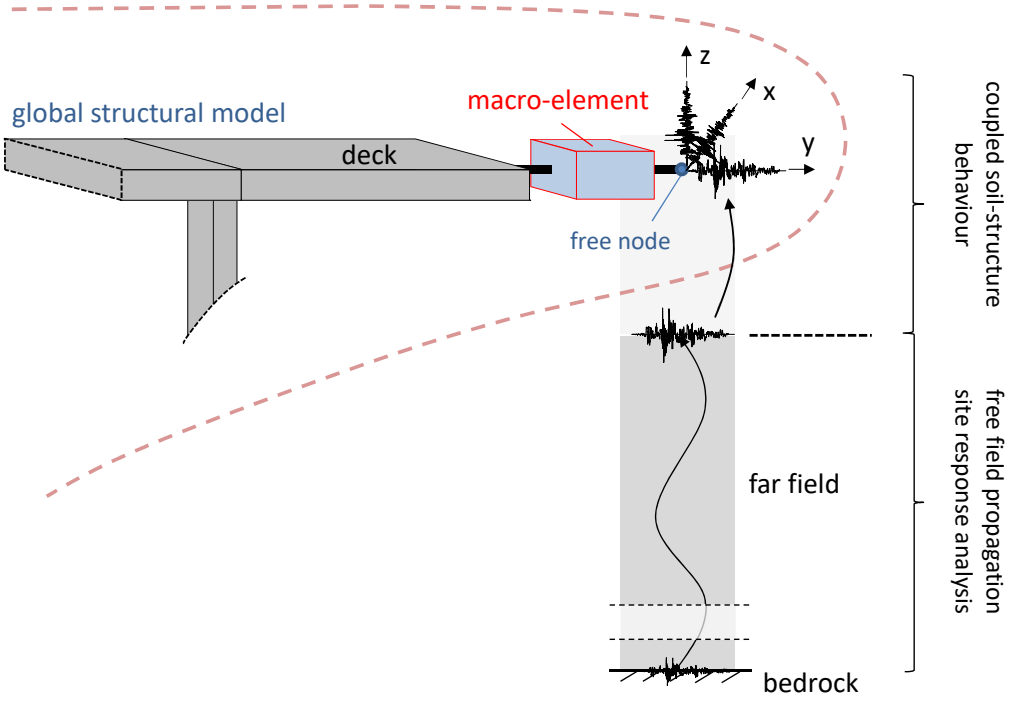

Figure 5.31: Schematic representation of the macro-element in the global structural model.

In the following section, a straightforward strategy to calibrate the input parameters of the macro-element of bridge abutment is proposed, starting from the so-called static configuration of the model, with no mass, that can be employed in static simulations, for then assigning dynamic properties to the model with the aim to carry out non-linear dynamic analyses. In Chapter 7, a complete application of the macro-element will be presented for the girder bridge taken as reference in this study.

5.14 Calibration

The macro-element is completely defined through the specification of the following constitutive parameters

- capacity of the soil-abutment system in a reference direction;

- initial stiffness of the soil-abutment system in a reference direction;
- mass of the macro-element.

The first two points refer to the so-called static parameters of the model, while the latter focuses on the calibration of the masses that play the role of dynamic parameters in the sense that confer frequency-dependent features to the response of the macro-element. The calibration procedure consists in defining first the static parameters for then identifying the additional masses. For the sake of clarity, in the following the macro-element is initially calibrated for the one-dimensional case, describing step by step the strategy used to set the parameters, for then generalising the calibration to the three-dimensional model. All the parameters were calibrated against the results of static and dynamic simulations on the soil-abutment interaction model taken as reference in this study, previously shown in Figure 4.5.

The macro-element for bridge abutments can be employed in the numerical evaluation of the structural behaviour according to two different modelling techniques: one can use the general three-dimensional formulation (Section 5.7) or, in a simplified manner, three uncoupled one-dimensional macro-elements (Section 5.3). It is obvious that the former represents the rigorous way to reproduce the soil-abutment interaction effects under multi-axial loading conditions but the latter can however constitute a useful tool for a prompt application in numerical simulations in virtue of its simplified formulation, especially when the multi-directional coupling of the deck-abutment response is not so important (e. g. mono-directional bearing devices at the deck-abutment contact). The calibration procedure presented in the following looks at the fundamental physical quantities characterising a soil-abutment system and therefore it can be used in both the representation strategies above.

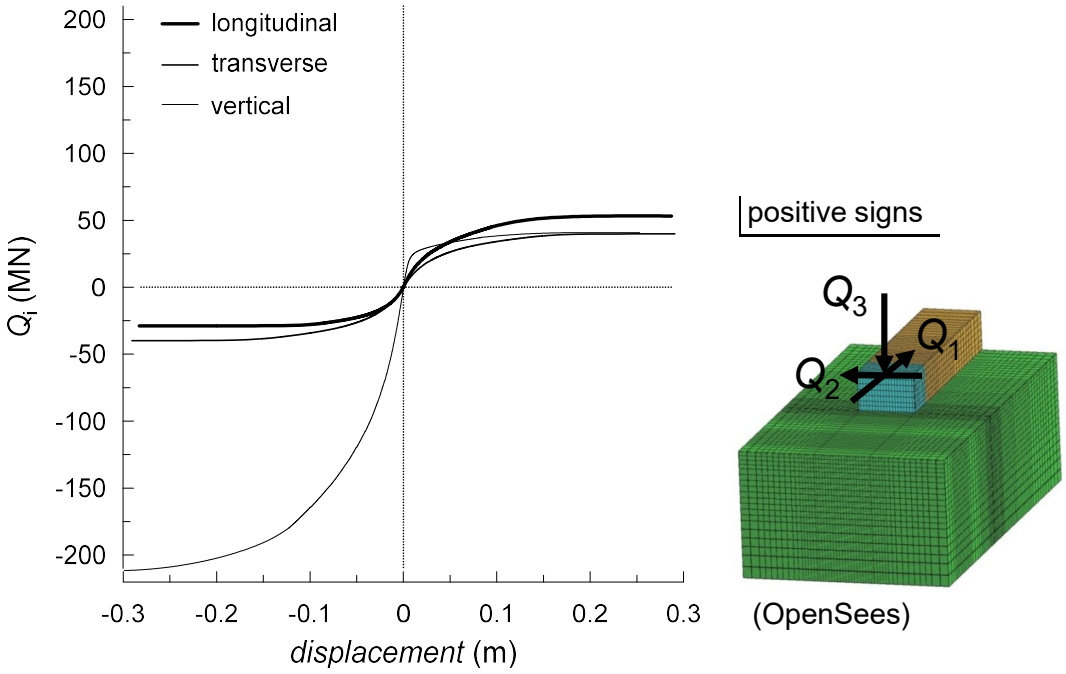

Figure 5.32: Pushover curves in the three coordinate directions obtained through the soil-structure interaction model in OpenSees.

5.14.1 Static parameters

The force-displacement relations on the abutment top obtained by pushover analyses on the soil-abutment model described in Section 4.2, that is part of the reference global soil-bridge model, were considered to calibrate the macro-element. Several directions of the force on top of the wall were considered and the backbone curves along the three coordinate directions of the deck-abutment contact are illustrated in Figure 5.32. Note that the ultimate capacity shown by these curves is in agreement with the results of the limit analysis in Section 5.9.1.

The first evident result is that the longitudinal and vertical curves show a marked dissymmetric behaviour, with a strength bias parameter $Q_-^{(ult)}/Q_+^{(ult)}$ (i. e. positive capacity over negative capacity) of 0.35 and 0.18 in the longitudinal and vertical direction, respectively, while as expected $Q_-^{(ult)}/Q_+^{(ult)}$ is equal to 1 for the transverse response. More in detail, the extreme values of the capacity are associated with the

vertical response: the highest strength is attained for a vertical load directed downwards (bearing capacity of the foundation) while the minimum capacity is associated with the uplift of the system (vertical force directed upwards). In the longitudinal direction, the passive $Q_+^{(ult)}$ and active $Q_-^{(ult)}$ resistance of the embankment constitute the upper and lower bounds for the backbone curve, respectively. The behaviour in the transverse direction does not show particular features reflecting the symmetry of the abutment with respect to the central section of the system.

For the sake of clarity, the longitudinal response of the abutment is initially analysed. From the relative backbone curve, the ultimate strength towards the backfill (passive resistance) results to be $Q_+^{(ult)} = 70$ MN, with a bias parameter $Q_-^{(ult)}/Q_+^{(ult)} = 0.35$, and the initial stiffness is $H^{(0)} = 10^3$ MN/m. Moreover, the behaviour of the soil-abutment system can be regarded as linear for positive forces lower than $Q^{(1)} = 9$ MN, that is about $0.13 \cdot Q_+^{(ult)}$, and negative values of about 3.4 MN. These parameters are represented on the longitudinal backbone curve in Figure 5.33 and the remaining parameters can be derived according to the following procedure.

The 1D macro-element (Figure 5.2) is composed of an initial spring with stiffness $H^{(0)}$, connected in series with N dissipative devices, each characterised by a stiffness $H^{(n)}$ and a plastic threshold $k^{(n)}$. The strength parameters range between the ultimate strength $k^{(N)} = Q^{(ult)}$ and the first yield $k^{(1)} = Q^{(1)} = \zeta \cdot Q^{(ult)}$. Accordingly, the stiffness varies from the initial value $H^{(1)} = H^{(0)}$ at first field to $H^{(N)} = 0$ MN/m at failure. The size of the elastic region reflects the properties of the specific constitutive model used in the analyses, that is the PDMY model in this case, but, more in general, it seems a reasonable assumption to choose as an elastic domain the fraction of the ultimate domain ζ between $0.05 \div 0.15$.

The plastic domain is now well bounded by the first and last yield. In between, the plastic flow evolves according to the specific set of stiffness and strength parameters

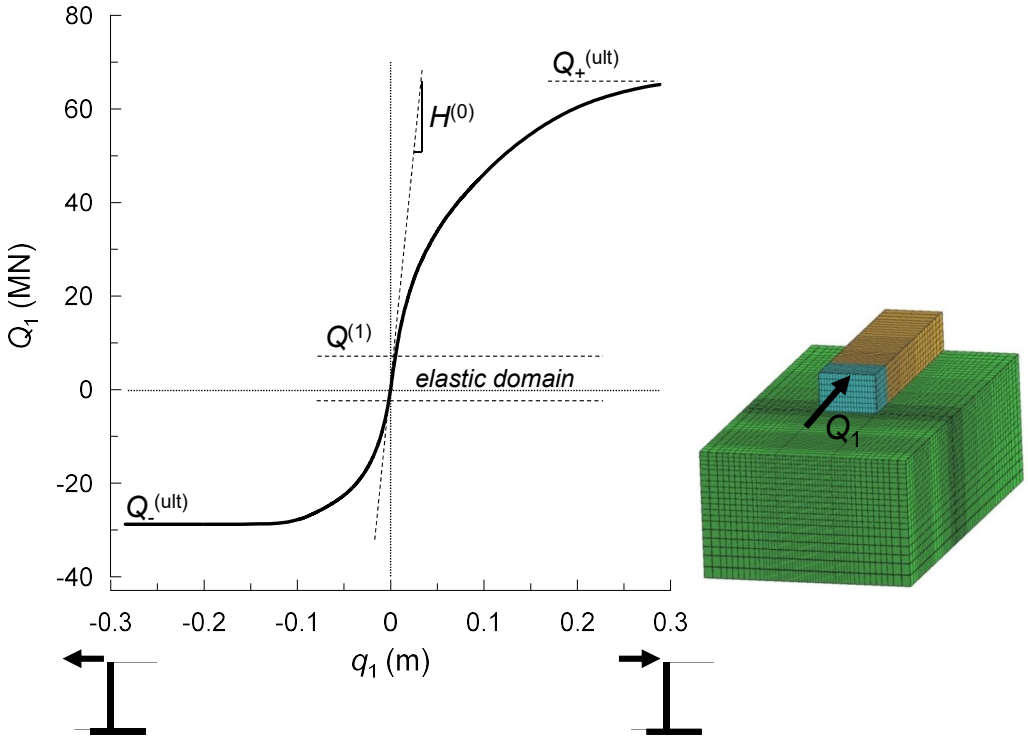

Figure 5.33: Force-displacement relationship at the deck-abutment contact in the longitudinal direction, obtained through a pushover analysis on the reference soil-abutment interaction model.

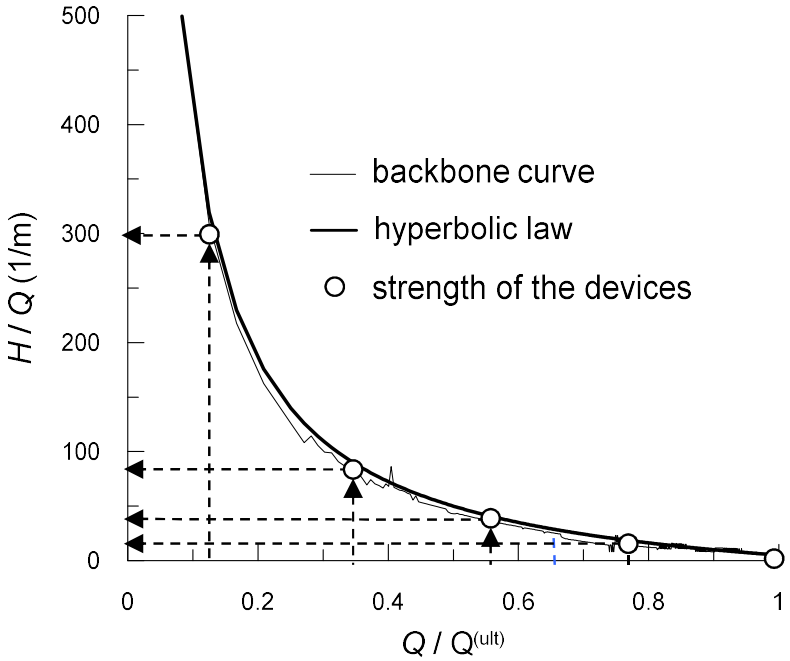

Figure 5.34: Representation of the normalised tangent stiffness H/Q of the force-displacement relationship at the deck-abutment contact plotted as a function of the mobilised strength Q/Q_{ult}.

assigned to the internal devices. The generic dissipative device (mass set equal to zero) is a generalization of the classical Voight model, made up of a parallel connection of a slider and a spring that exhibit a dissymmetric behaviour. The stiffness of the n-th spring, that confers kinematic hardening to the plastic response, activates when the strength of the respective slider is mobilised. Hence the term $H^{(n)}$ has to be associated with a specific interval of the internal force in the macro-element. To this end, in Figure 5.34 the normalised tangent stiffness H/Q of the longitudinal backbone curve is plotted as a function of the mobilised strength $Q/Q^{(ult)}$.

It is evident that the trend obtained can be very well described by a hyperbole of equation

$$\frac{H}{Q} = \alpha + \frac{\beta}{\frac{Q}{Q_{ult}}} \tag{5.215}$$

with α and β positive constants. The hyperbole's equation must satisfy the following boundary conditions

$$\frac{H}{Q} = \left[\frac{H}{Q}\right]_{in}, \frac{Q}{Q_{ult}} = 0.13 \tag{5.216}$$

$$\frac{H}{Q} = \left[\frac{H}{Q}\right]_{fin}, \frac{Q}{Q_{ult}} = 1 \tag{5.217}$$

that are related to the first yield and the ultimate strength of the macro-element, respectively. Introducing Eqs. 5.216 and 5.217 in Eq. 5.215, after some manipulation the latter can be rearranged in the following form

$$\frac{H}{Q} = \left[\frac{H}{Q}\right]_{in} - \left\{\left[\frac{H}{Q}\right]_{in} - \left[\frac{H}{Q}\right]_{fin}\right\} \cdot \left[\frac{1}{0.9} - \frac{1}{\left(9 \cdot \frac{Q}{Q_{ult}}\right)}\right]. \tag{5.218}$$

For the case at hand, $[H/Q]_{in} = 300$ 1/m whereas $[H/Q]_{fin}$ is close to zero (set equal to $H^{(N)} = 0.01$ MN/m for numerical stability). Accordingly, once an interpolation law for the strength parameters is chosen (linear or hyperbolic), the hyperbolic formula in Eq. 5.218 gives the corresponding stiffness parameters to be assigned to each spring of the dissipative devices.

The resulting backbone curve is shown in Figure 5.35, for different values of N. It can be seen that for a number of devices greater than 5 the piecewise linear curve of the macro-element gives a good approximation of the backbone curve obtained through the interaction model. Hence, the macro-element composed of an elastic spring on top and 5 dissipative devices was assumed as the reference configuration for the case under examination, with relative properties summarised in Table 5.4.

The above procedure was then used to calibrate the 1D macro-elements along the other two coordinate directions, transverse and vertical. The resulting backbone curves are depicted in Figure 5.36, considering 5 dissipative devices in each direction.

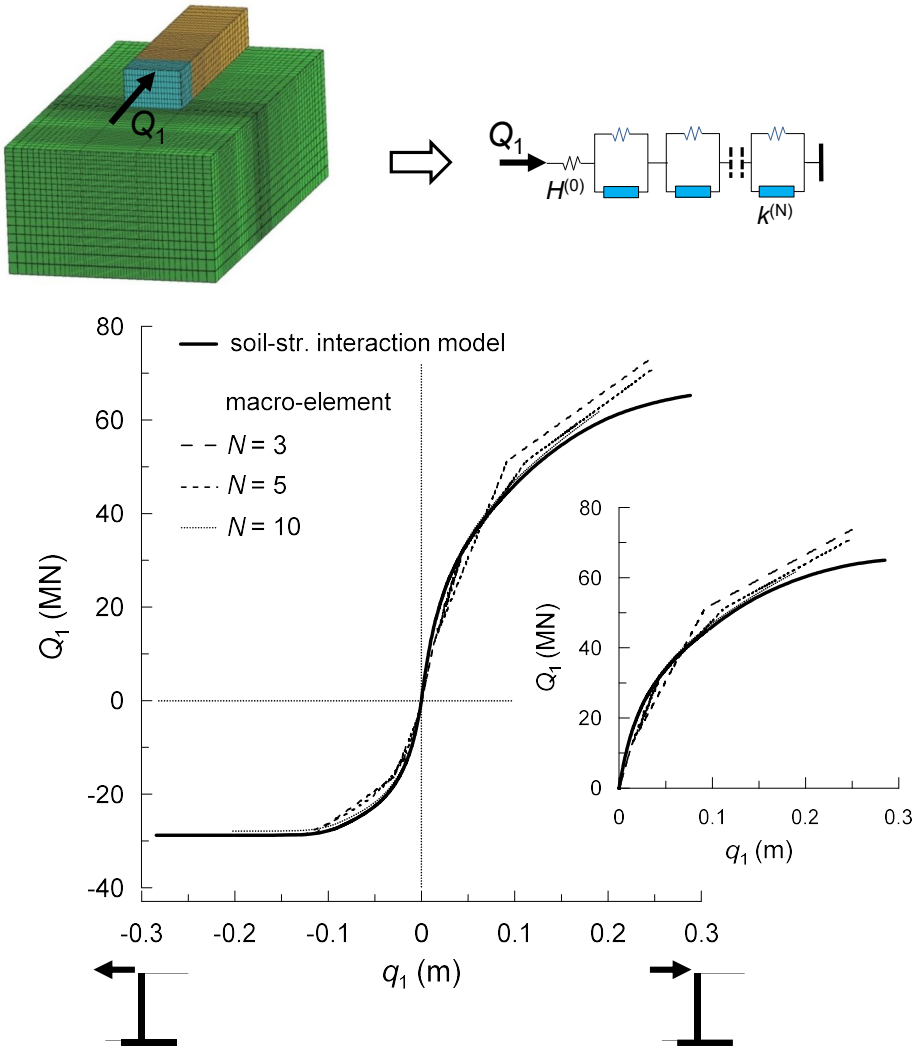

Figure 5.35: Comparison between the longitudinal pushover curve obtained by the soil-abutment model in OpenSees and that reproduced by means of the macro-element.

Device	$H^{(n)}$ (MN/m)	$k_+^{(n)}$ (MN)	$k_-^{(n)}$ (MN)
0	10^3	–	–
1	10^3	9.7	3.4
2	$5 \cdot 10^2$	24.8	8.7
3	$3 \cdot 10^2$	39.8	13.9
4	$1.5 \cdot 10^2$	54.9	19.2
5	10^{-2}	70.0	24.5

Tabella 5.4: Stiffness $H^{(n)}$ and strength $k^{(n)}$ parameters assigned to the macro-element.

In light of the above, the calibration of the macro-element is primarily based on the definition of the force-displacement relation at the deck-abutment contact. More specifically, the ultimate resistance of the system and the relative bias parameter can be also evaluated through basic approaches such as Earth Pressure Theory, but the initial stiffness of the whole system necessitates the determination of the backbone curve of the geotechnical system. Without performing an advanced elastoplastic analysis on soil-abutment interaction models, in the longitudinal direction one can also refer to some experimental and numerical studies, carried out with the specific aim of quantifying the passive backfill response for seat-type abutments. In this regard, a fairly detailed review of the literature is provided in the report by Stewart et al. (2007): two relevant experimental tests on full-scale specimens were conducted at UC-Davis (Romstad et al. 1995) and at UCLA (Stewart et al. 2007) and also significant modelling efforts were devoted to the generalisation of the experimental results above (Martin et al. 1996, Siddharthan et al. 1997, Shamsabadi et al. 2005, Shamsabadi et al. 2007, Shamsabadi et al. 2010).

Taking this one step further, the sole backbone curve in the longitudinal direction can be sufficient to determine the static configuration of the general three-dimensional macro-element and, accordingly, also of the three uncoupled 1D macro-elements. In fact, the dependence of the ultimate capacity of the soil-abutment system on the load direction is described by the ellipsoidal yield function in Eq. 5.135. This surface can be in turn identified by the only information on the maximum capacity or, equivalently, the bearing capacity of the abutment foundation, giving a correlation between the plastic thresholds $k_i^{(n)}$ acting in different directions. The initial stiffness matrix $H_{ii}^{(0)}$ is a diagonal matrix by definition and, in accordance with the results shown in Section 5.9.2, the same ellipsoidal relationship used for the capacity can be assumed also for the initial stiffness as a first approximation. It is worth noticing that, despite being a strong assumption because not verified

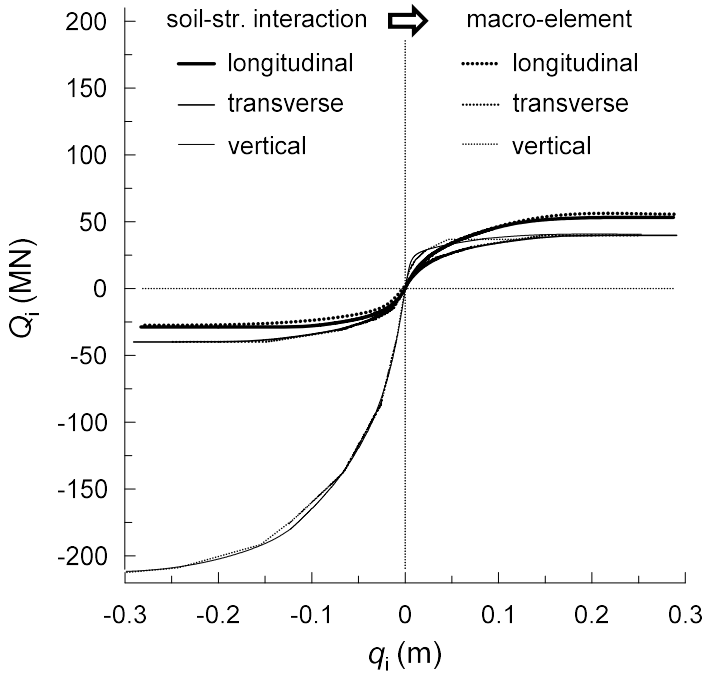

Figure 5.36: Pushover curves in the three coordinate directions: comparison between the results of the soil-abutment interaction model and the macro-element response.

for different configurations of the abutment, the effect of the initial stiffness on the response is somewhat limited because the elastic response is bounded by the small-sized first yield surface, starting from which the plastic flow governs essentially the response of the macro-element.

5.14.2 Mass of the macro-element

The abutment and the volume of soil that interacts dynamically with it has a significant mass which, under seismic excitation, can produce relevant frequency-dependent inertial effects. In order to account for this phenomenon, some participating masses were introduced into the macro-element with the aim to reproduce the desired dynamic properties of the soil-abutment system. More specifically, the masses were calibrated to replicate the dominant responses of the system from small to large strain levels, in terms of dominant periods and amplification of the dis-

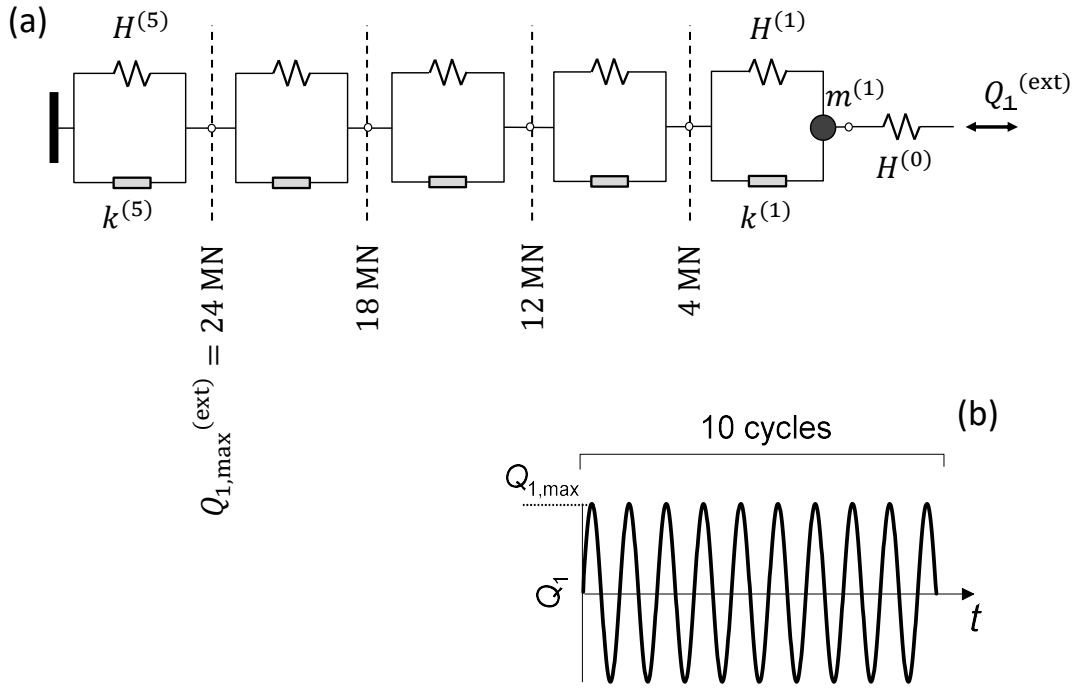

Figure 5.37: (a) Relation between the levels of the external force $Q_1^{(ext)}$ and the activation of the sliders of the macro-element; (b) time history of the external force.

placement field, previously evaluated in the numerical investigation in Chapter 4. It will be shown that the definition of the first mass is the most crucial point in the calibration because it centers the dynamic response of the macro-element on the dominant response of the system at small strains. The role of the other masses consists instead of reproducing the progressive shift of the dominant period as the level of strain rises, having however a minor effect on the whole dynamic response of the macro-element.

Consider the static configuration of the macro-element defined in the previous paragraph. A first mass $m^{(1)}$ was introduced in the model associated with the first slider. In this case, the free node of the macro-element does not have mass because it is the point of application of the external perturbation, hence it would not produce any inertial effects if perturbed by a displacement time history. Nonetheless,

as mentioned before, the first yield occurs for low internal forces, $k^{(1)} = 9.7$ MN, and therefore the response of the elastic spring on top is quite immediately combined with the plastic response for activation of the first slider. A preliminary parametric study on the effect of the first mass is shown, varying the mass $m^{(1)}$ and the intensity of the external force applied to the macro-element. The analysis procedure is schematically illustrated in Figure 5.37. In order to replicate the dynamic amplification curves obtained with the soil-abutment models in OpenSees, the macro-element was perturbed by a harmonic force, for 10 loading-unloading cycles and in the range of periods between $T = 0.2 \div 4.0$ s. Four values of the external force were considered equal to 4000 kN, 12000 kN, 18000 kN and 24000 kN, which correspond to the activation of the first, second, third and the fourth slider, respectively. Figures 5.38 to 5.43 show the dynamic amplification curves of the macro-element, considering a variability of the mass of seven orders of magnitude. Up to $m^{(1)} = 1$ Mg, the system is too rigid and the amplification curves show a flat trend of the maximum displacements on the abutment top $q_{1,max}$ not dependent on the period T, hence with negligible inertial effects.

A moderate dynamic amplification of the displacement field begins for a value of the mass equal to 100 Mg. At this point, the dominant response occurs at a period of 0.3 s with an increase of the maximum displacement $q_{max}/q_{max,st}$ of 1.4 with respect of the displacement $q_{max,st}$ at large periods (static response). For greater values of the mass, the dynamic amplification becomes increasingly more pronounced and the dominant response moves progressively to larger periods.

Note that, for a given mass, the dominant period tends to increase with the intensity of the force, that is particularly evident in Figures 5.41, 5.42 and 5.43. The amplitude-dependence of the dominant period is produced by the increment of deformability associated with the activation of the sliders at higher levels of the internal force. In fact, when the strength of a slider is attained, the spring associated with

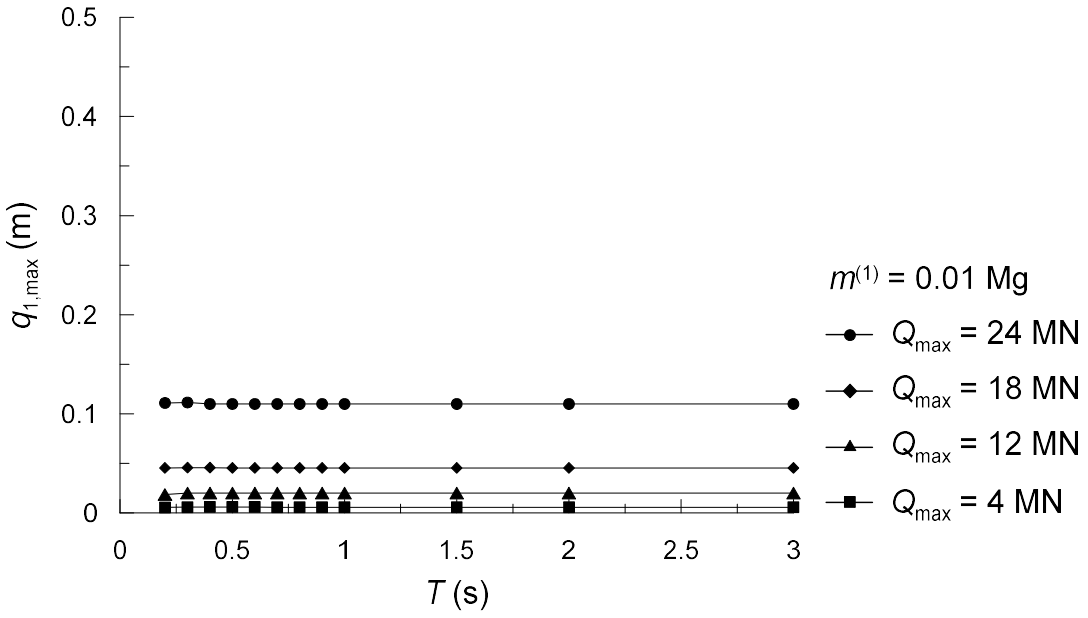

Figure 5.38: Dynamic amplification curves of the macro-element with mass $m^{(1)} = 0.01$ Mg.

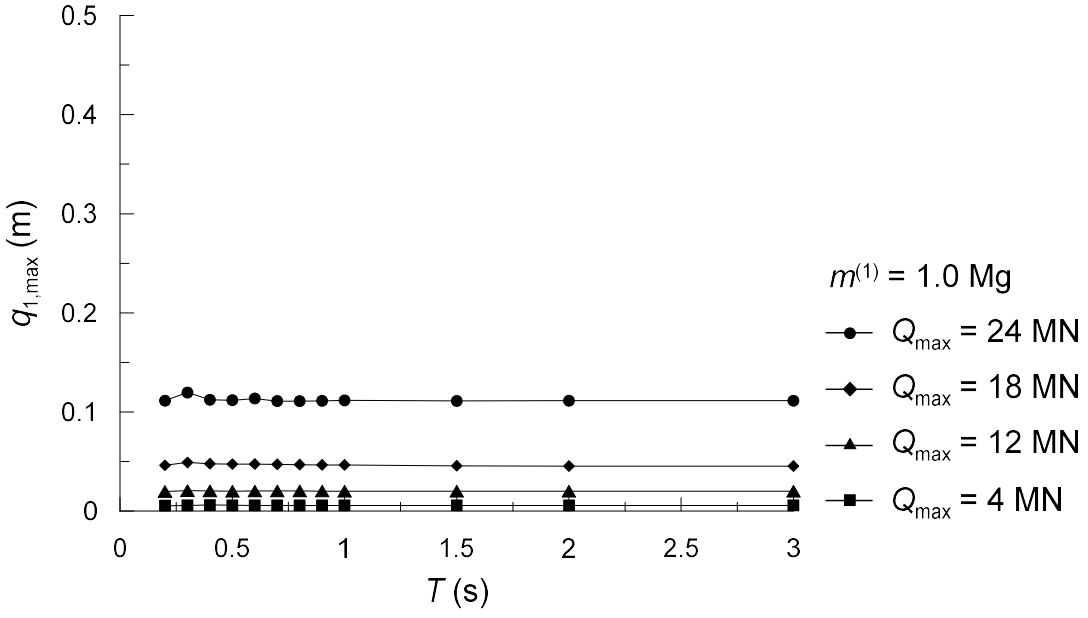

Figure 5.39: Dynamic amplification curves of the macro-element with mass $m^{(1)} = 1.0$ Mg.

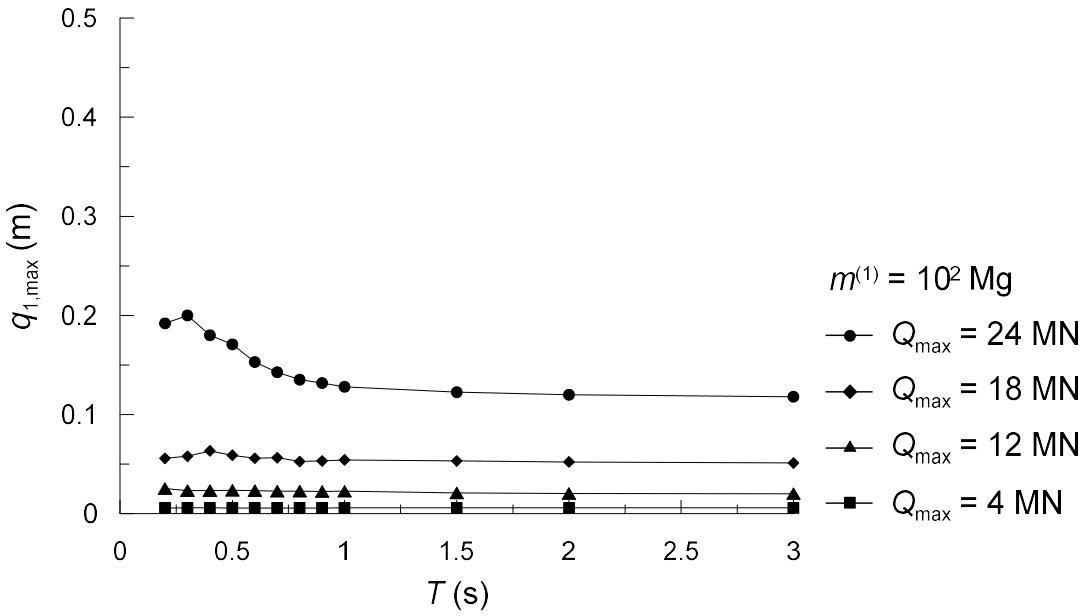

Figure 5.40: Dynamic amplification curves of the macro-element with mass $m^{(1)} = 10^2$ Mg.

it begins loading up, modifying the whole stiffness of the system (kinematic hardening). As a result, the deformability of the macro-element reduces progressively with the number of sliders activated, leading to an increasingly longer dynamic response.

Based on the results above, the value of the first mass for the case under examination should be of the order of 10^4 Mg. Without the necessity to perform a parametric study to identify the optimum value of $m^{(1)}$, an expeditious strategy is described below based on some basic considerations. Consider the response of the macro-element in which only the first slider is activated. In this condition, the macro-element behaves as a single degree of freedom system and the first mass can be estimated by the following basic equation

$$m^{(1)} = \frac{T_0^2}{4 \cdot \pi^2} \cdot H^{(1)} = \frac{(0.6s)^2}{4 \cdot \pi^2} \cdot 10^6 kN/m = 9.1 \cdot 10^3 Mg \tag{5.219}$$

giving a value that is very close to the that obtained through the parametric study. The dominant period at small strains T_0 can be evaluated through the analytical

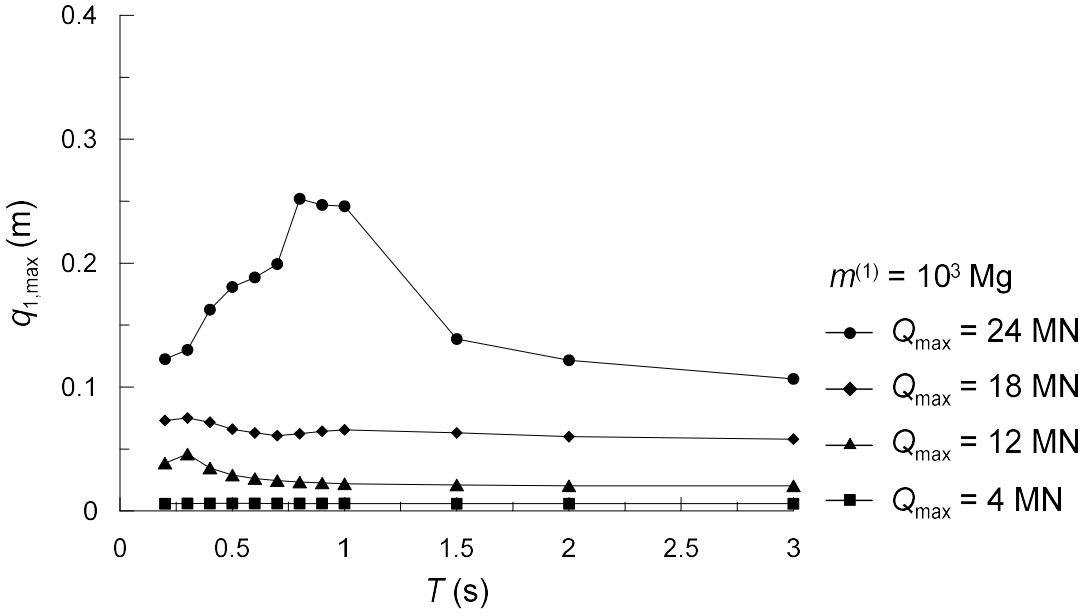

Figure 5.41: Dynamic amplification curves of the macro-element with mass $m^{(1)} = 10^3$ Mg.

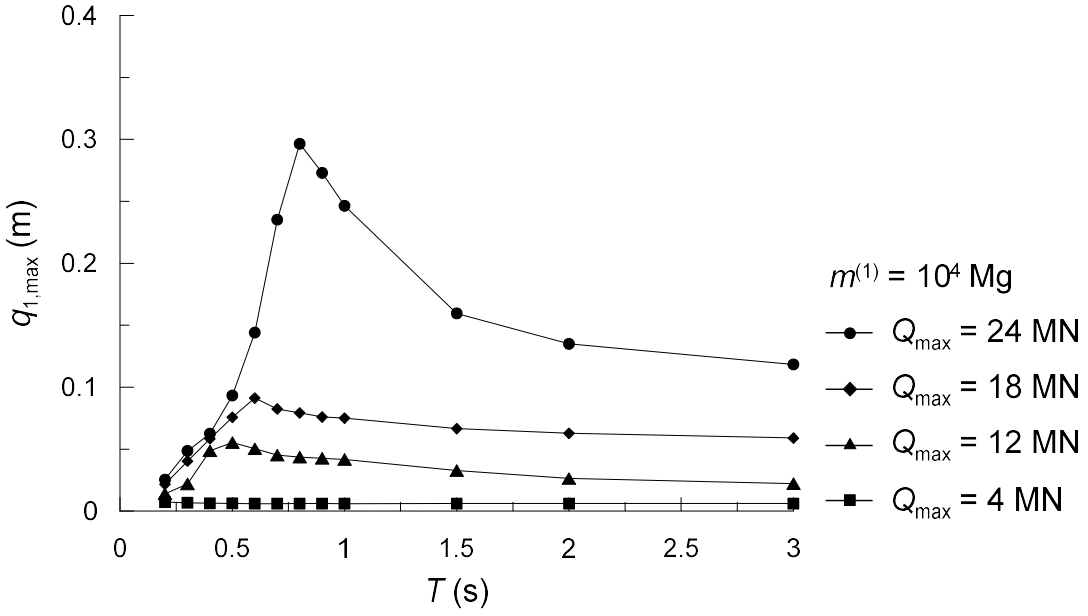

Figure 5.42: Dynamic amplification curves of the macro-element with mass $m^{(1)} = 10^4$ Mg.

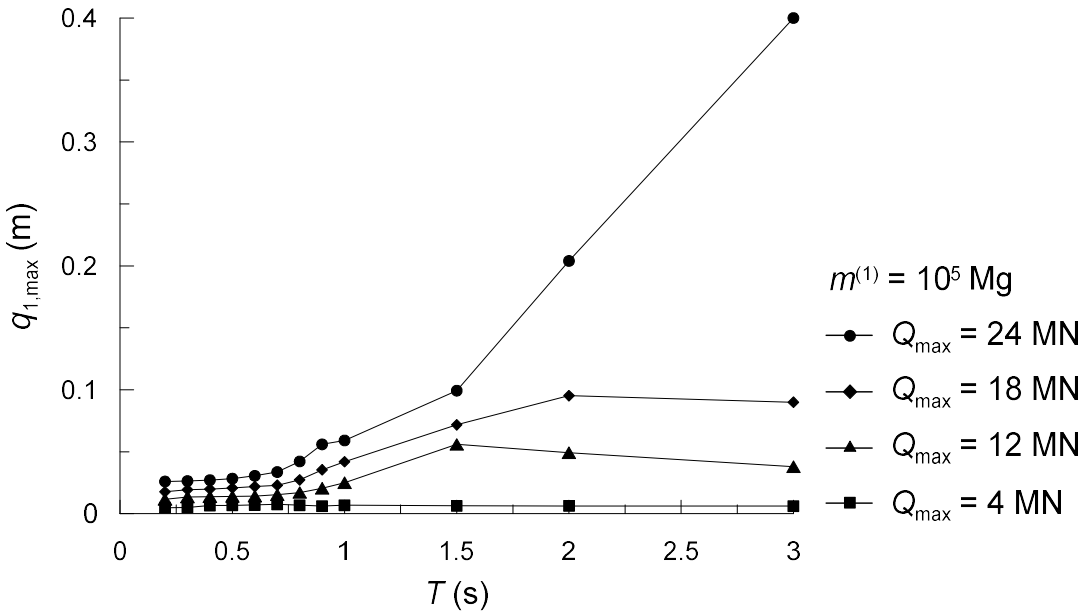

Figure 5.43: Dynamic amplification curves of the macro-element with mass $m^{(1)} = 10^5$ Mg.

or the numerical method used to identify the soil-abutment system (see Chapter 4), while the stiffness $H^{(1)}$ associated with the first slider derives from the calibration of the static parameters of the model. The following physical interpretation can be given to the mass $m^{(1)}$. The masses of the abutment m_{abut} and the backfill m_{back}, the latter intended as the volume of soil contained between the central wall and the wing walls, are equal to $3.6 \cdot 10^3$ Mg and $3.4 \cdot 10^3$ Mg, respectively. It follows that the participating mass $m^{(1)}$ is equal to $1.29 \cdot (m_{abut} + m_{back})$. This proves that part of the soil behind and beneath the abutment contributes to the dynamic response of the latter, with important inertial effects for the relevant mass involved. Assuming for simplicity that the inertial effects would be essentially induced by the dynamic response of the soil behind the wall, a participating mass of the embankment $m_{e,e}$ can be computed as

$$m_{e,e} = m^{(1)} - (m_a + m_b) = 2.0 \cdot 10^3 Mg \tag{5.220}$$

that is relative to a volume of the embankment $V_{e,e}$ equal to

$$V_{e,e} = \frac{m_{e,e}}{\rho_{soil}} = \frac{2.0 \cdot 10^3}{2.039} = 2.0 \cdot 10^3 m^3. \tag{5.221}$$

In light of the above, an effective length of the embankment L_{eff} interacting dynamically with the abutment can be defined as follows

$$L_{eff} = L_{back} + \frac{V_{e,e}}{H \cdot B} = \frac{2.0 \cdot 10^3}{13.5 \cdot 20.0} = 12.5 + 7.4 = 19.9m. \tag{5.222}$$

Hence, in this case, the ratio L_{eff}/H between the effective length and the height of the abutment is equal to 1.5.

Figure 5.44 represents the response of the macro-element with the mass $m^{(1)}$ computed above. The dynamic amplification is quite well captured by the macro-element up to $Q_1 = 12$ MN, corresponding to the transition phase in the period elongation curve of the soil-abutment system (see Section 4.2), but the dominant response occurs at slightly lower periods. For higher intensities of the external force, the underestimation of the maximum displacements rises, even if the significant range of periods for the dynamic amplification is well centred on the maximum response of the interaction models. For $Q_1 = 24$ MN, corresponding to a steady dominant response of the system, the dynamic amplification curve of the macro-element reproduces quite well the response of the interaction model but, after the dominant period at 0.8 s, it presents a slower decrease of the maximum displacement.

In order to improve the response of the macro-element, especially for Q_1 between $12 \div 18$ MN, a second mass $m^{(2)}$ was introduced in the model, associated with the second dissipative device. As a result of a parametric study aimed to find the optimum value for the mass $m^{(2)}$, the latter was set equal to the first mass. The new amplification curves are shown in Figure 5.45. The first curve, obtained for a force of 4 MN, keeps unaltered because the response of the mass $m^{(2)}$ begins when

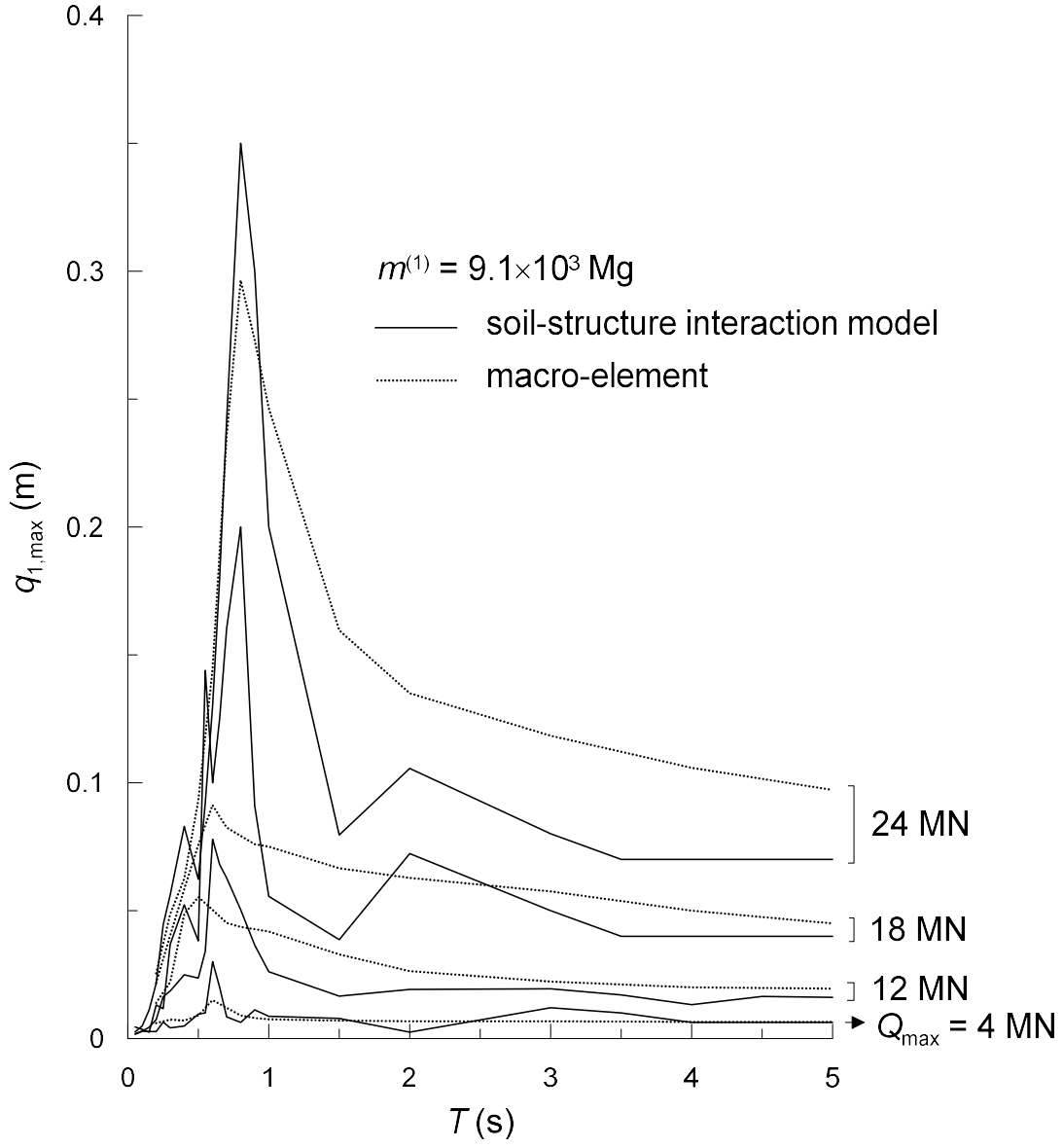

Figure 5.44: Comparison between the dynamic amplification curves of the macro-element with mass $m^{(1)} = 9.1 \cdot 10^3$ Mg and that obtained with the numerical models (OpenSees) from the reversible regime (activation of the first slider) to the steady behaviour (activation of the fourth slider).

the strength of the second slider $k_{-}^{(2)} = 8.7$ MN is attained. The effect of the second mass becomes evident in the transition phase, leading to a better matching with the response of the interaction models.

The response of the macro-element could be further improved by adding other masses to the other sliders but, as it was shown, a limited number of masses opportunely calibrated can be sufficient to reproduce the response of the entire soil-abutment system from small to large strain levels. In this way, in fact, the calibration of the macro-element is based on general principles that allow to identify the first masses in a simple and immediate manner. It was shown that a proper identification of the first mass leads to a good reproduction of the dynamic response of the abutment system and it can be evaluated with good approximation by referring to the dynamic characteristics of a single degree of freedom system. The second mass is able to improve the response of the macro-element, with a better reproduction of the period elongation, and it appears of the same order of magnitude of the first mass, at least for the case study under examination. In any case, a very low computational demanding sensitivity analysis on the effect of each mass introduced into the macro-element can be easily carried out to have an accurate evaluation of their optimum values in any configurations of the soil-abutment system.

5.15 An energetically compatible macro-element for shallow foundations

The thermodynamic formulation of the macro-element for bridge abutments was specialised to the case of shallow foundations, in order to reach a representation of the soil-foundation system promptly applicable in the global structural model of the bridge, together with the macro-element of bridge abutment. This model constitutes a first step in the derivation of an equivalent 6 degrees of freedom system

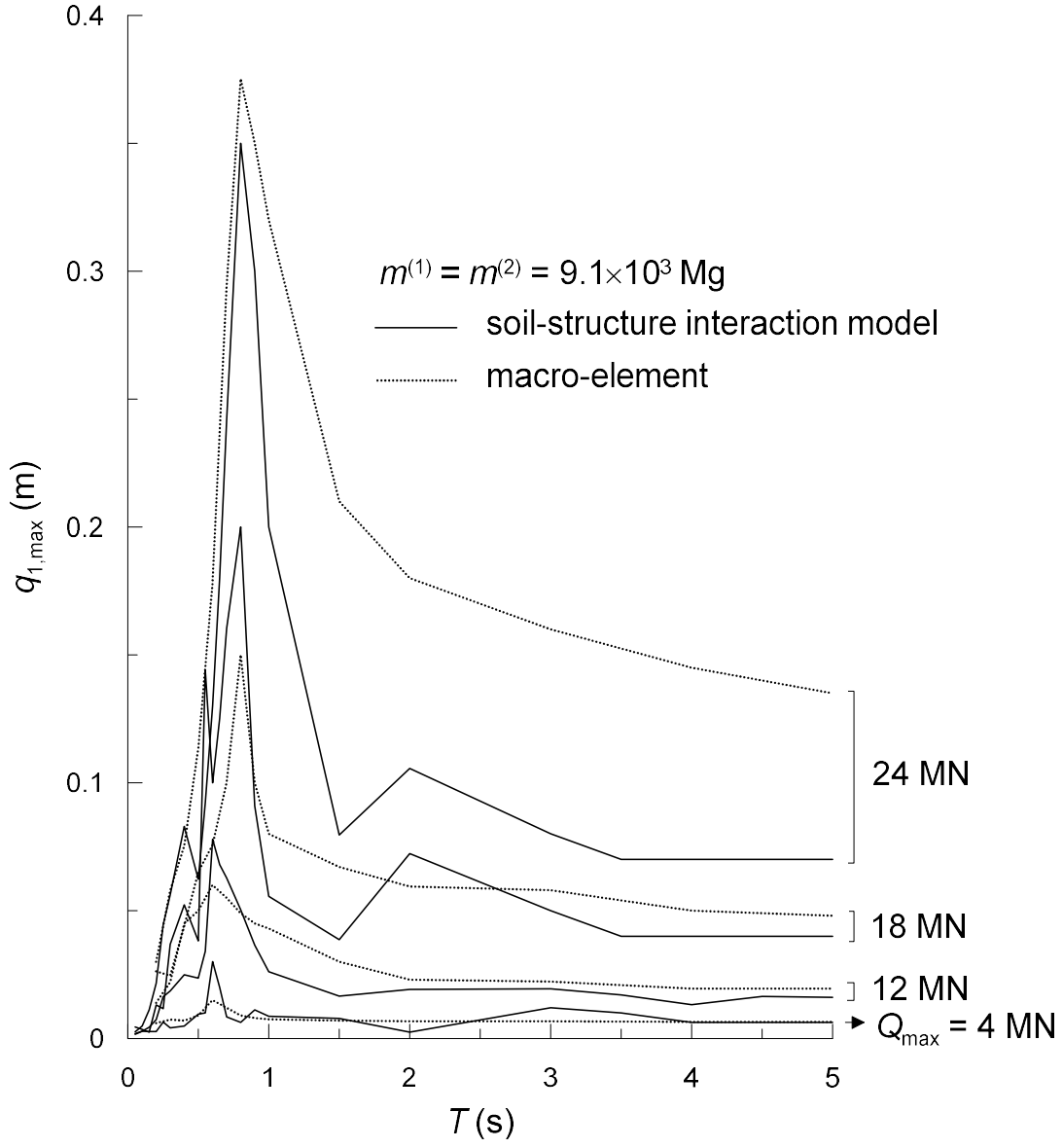

Figure 5.45: Comparison between the dynamic amplification curves of the macro-element with mass $m^{(1)} = m^{(2)} = 9.1 \cdot 10^3$ Mg and that obtained with the numerical models (OpenSees) from the reversible regime (activation of the first slider) to the steady behaviour (activation of the fourth slider).

for shallow foundations consistent with the dictates of Thermodynamics. This is an ongoing research that aims to reinterpret the main features of the multi-axial response of the foundations, already included in several existing models, according to an energetically compatible framework.

5.15.1 Mathematical formulation

The model is formally identical to the macro-element for bridge abutments, composed of multiple yield surfaces that evolve in the space of the generalised forces according to a prescribed kinematic hardening rule, but it is bounded by a more appropriate version of the ultimate surface for shallow foundations that, consequently, modifies also the shape of the internal yield surfaces. Another relevant difference between the two representations is that the inertial effects of the soil underneath the foundation can be reasonably neglected. Therefore the only mass needed in this case is the mass of the footing whose contribution can be modelled explicitly in the finite element model without being included in the constitutive response.

The foundation is regarded as a body with infinite stiffness and strength. The present formulation is aimed at describing the translational and rotational motion of a shallow foundation along the three-coordinate directions illustrated in Figure 5.46: the generalised forces (3 forces and 3 moments) are denoted as $Q_{i,0}$ and the corresponding generalised displacements as $q_{i,0}$.

The generalised forces $Q_{i,0}$ and displacements $q_{i,0}$ are grouped into two first-order tensors composed of non-homogeneous quantities

$$Q_{i,0} = \{Q_{1,0}, Q_{2,0}, Q_{3,0}, Q_{r1,0}, Q_{r2,0}, Q_{r3,0}\} \tag{5.223}$$

$$q_{i,0} = \{q_{1,0}, q_{2,0}, q_{3,0}, q_{r1,0}, q_{r2,0}, q_{r3,0}\}\,. \tag{5.224}$$

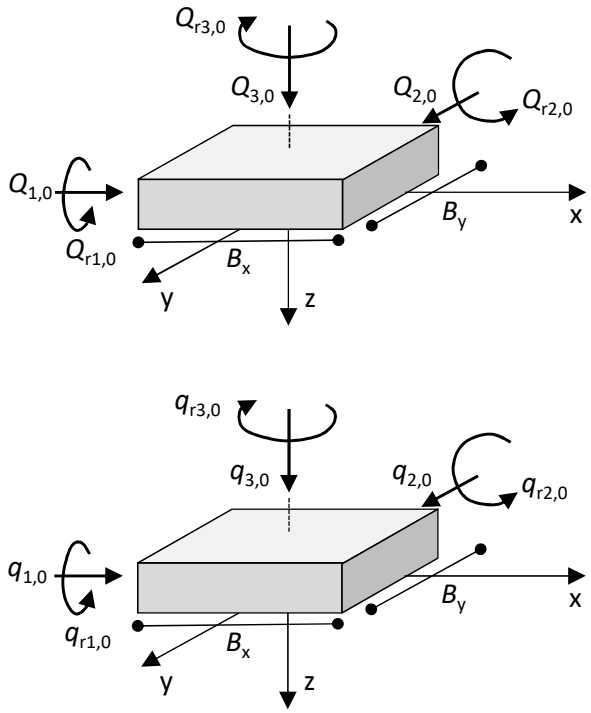

Figure 5.46: Notation adopted for the generalised forces $Q_{i,0}$ and the generalised displacements $q_{i,0}$.

In order to consider consistent forces and displacements, two vectors composed of homogeneous quantities are defined as

$$Q_i = \left\{ Q_{1,0}, Q_{2,0}, Q_{3,0}, Q_{r1,0}/B_y, Q_{r2,0}/B_x, Q_{r3,0}/\sqrt{B_x \cdot B_y} \right\} \tag{5.225}$$

$$q_i = \left\{ q_{1,0}, q_{2,0}, q_{3,0}, q_{r1,0}/B_y, q_{r2,0}/B_x, q_{r3,0}/\sqrt{B_x \cdot B_y} \right\} \tag{5.226}$$

in which the dimension of the generic terms Q_i and q_i are a force and a length, respectively. It can be also convenient to express the generalised forces Q_i in the following normalised form (Venanzi et al. 2014)

$$\overline{Q}_i = \left\{ Q_{1,0}/Q_{3,0}^{max}, Q_{2,0}/Q_{3,0}^{max}, Q_{3,0}/Q_{3,0}^{max}, Q_{r1,0}/\left(B_y \cdot Q_{3,0}^{max}\right), \right.$$

$$, Q_{r2,0}/\left(B_x \cdot Q_{3,0}^{max}\right), Q_{r3,0}/\left(\sqrt{B_x \cdot B_y} \cdot Q_{3,0}^{max}\right)\Big\} \tag{5.227}$$

where $Q_{3,0}^{max}$ represents the bearing capacity of the foundation.

The balance equation simply reads

$$Q_i^{(ext)} = Q_i^{(int)} = Q_i^{(n)}, i = 1, 2, 3 \tag{5.228}$$

hence the internal force $Q_i^{(n)}$ associated with the n-th plastic flow is equal to the external one $Q_i^{(ext)}$. Compatibility is instead described by Eq. 5.117 written for the case of bridge abutments, in which the plastic deformations are assumed as internal variables.

For this mechanical system, the Gibbs free energy and the Helmholtz free energy are reported below

$$g(Q_i^{(n)}, \alpha_i^{(n)}) = -\frac{1}{2} \cdot C_{ji}^{(0)} \cdot Q_i^{(0)} \cdot Q_j^{(0)} - \sum_{n=1}^{N} Q_i^{(n)} \cdot \alpha_i^{(n)} -$$

$$-\frac{1}{2} \cdot \sum_{n=1}^{N} H_{ij}^{(n)} \cdot \alpha_j^{(n)} \cdot \alpha_i^{(n)} - Q_i^{(R)} \cdot \alpha_i^{(R)} \tag{5.229}$$

$$f(q_i^{(n)}, \alpha_i^{(n)}) = \frac{1}{2} \cdot H_{ij}^{(0)} \cdot \left(q_j - \sum_{n=1}^{N} \alpha_j^{(n)} - \alpha_j^{(R)}\right) \cdot \left(q_i - \sum_{n=1}^{N} \alpha_i^{(n)} - \alpha_i^{(R)}\right) +$$

$$+\frac{1}{2} \cdot \sum_{n=1}^{N} H_{ij}^{(n)} \cdot \alpha_j^{(n)} \cdot \alpha_i^{(n)} \tag{5.230}$$

which represent the energy functions of the classical Iwan model with six degrees of freedom (Houlsby and Puzrin 2006), in the case of no elastic-plastic coupling. Note that the true force $Q_i^{(n)}$ is related to the generalised force $\bar{\chi}_i^{(n)}$, that is equal to

the dissipative force $\chi_i^{(n)}$ for the Ziegler's principle, by the following equation

$$\bar{\chi}_i^{(n)} = -\frac{\partial g(\alpha_i^{(l)})}{\partial \alpha_i^{(n)}} = -\frac{\partial g_2(\alpha_i^{(l)})}{\partial \alpha_i^{(n)}} + Q_i^{(n)} = -H_i^{(n)} \cdot \alpha_i^{(n)} + Q_i^{(n)} \tag{5.231}$$

while the dissipative ratcheting force reads

$$\bar{\chi}_i^{(R)} = -\frac{\partial f(\alpha_i^{(l)})}{\partial \alpha_i^{(R)}} = \frac{1}{2} \cdot H_{ij}^{(0)} \cdot \left(q_j - \sum_{n=1}^{N} \alpha_j^{(n)} - \alpha_j^{(R)} \right) =$$

$$= H_{ij}^{(0)} \cdot q_j^{(0)} = Q_j^{(0)} = Q_j^{(n)} = Q_j^{(ext)} \tag{5.232}$$

having considered the global balance equation (Eq. 5.228).

By comparing Eq. 5.231 with Eq. 5.116, the latter describing the local behaviour of the n-th dissipative device, it follows that $\bar{\chi}_i = \chi_i = k_i^{(n)}$ during plastic loading.

The plastic domain of the macro-element is confined between the surface of first yield and the surface of ultimate conditions, within which the other surfaces are placed in accordance with Eqs. 5.152 and 5.153. Except for the ultimate locus, the other surfaces evolve in the space of the forces with kinematic hardening defined by the second-order tensors $H_{ij}^{(n)}$ associated with each plastic flow. As for the dissipative response of the abutments, all the yield loci are assumed to have the same shape, hence the configuration of the plastic domain can be completely defined by the specification of the surface of ultimate loads. In the present model, the ultimate surface for a 6-DoF shallow foundation proposed by Martin (1994) is used. Accordingly, the generic yield surface reads

$$y^{(n)}(\chi_i^{(n)}) = \left(\frac{\chi_1^{(n)}}{h_0^{(n)}} \right)^2 + \left(\frac{\chi_2^{(n)}}{h_0^{(n)}} \right)^2 + \left(\frac{\chi_{r1}^{(n)}}{l_0^{(n)}} \right)^2 + \left(\frac{\chi_{r2}^{(n)}}{l_0^{(n)}} \right)^2 + \left(\frac{\chi_{r3}^{(n)}}{x_0^{(n)}} \right)^2 -$$

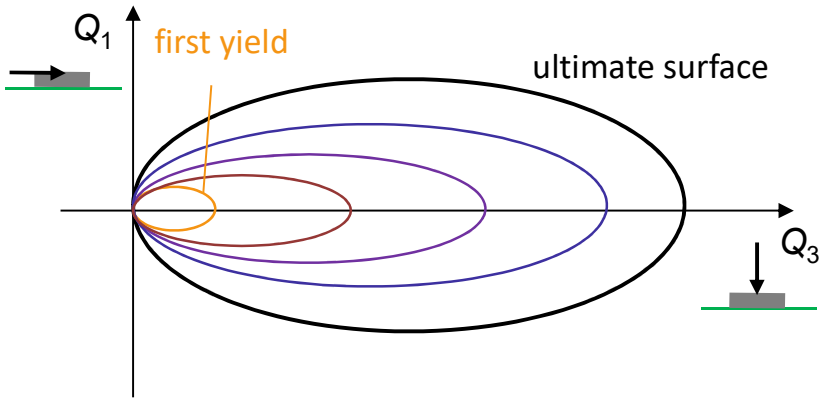

Figure 5.47: Configuration of the yield surfaces.

$$-\frac{2\cdot a^{(n)}}{h_0^{(n)}\cdot l_0^{(n)}}\cdot\left(\chi_2^{(n)}\cdot\chi_{r1}^{(n)}-\chi_1^{(n)}\cdot\chi_{r2}^{(n)}\right)-$$

$$-\chi_3^{(n)2\cdot\beta_1^{(n)}}\cdot\left(1-\frac{\chi_3^{(n)}}{Q_{3,0}^{max}}\right)^{2\cdot\beta_2^{(n)}}\cdot Q_{3,0}^{max(2-2\cdot\beta_1^{(n)})}=0, n=1,...,N. \tag{5.233}$$

where $h_0^{(n)}$, $l_0^{(n)}$, $x_0^{(n)}$, $a^{(n)}$, $\beta_1^{(n)}$ and $\beta_2^{(n)}$ are model constants; see Martin (1994) and Bienen et al. (2006) for explanation on their physical meaning. The configuration of the yield surfaces in the $Q_1 - Q_3$ plane is represented in Figure 5.47.

The maximum capacity of the foundation is represented by the vertical limit load $Q_{3,0}^{max}$, when only the vertical force is applied on the footing. From the ultimate surface, the size of the inner surfaces reduces linearly to the surface of first yield. Similarly to the macro-element of bridge abutment, the size of the first yield was assumed to be equal to $0.1 \cdot a_N$, hence as a small fraction of the size a_N of the ultimate surface.

The dissipation function is obtained from the specific expression used to describe the yield functions of the model. By definition, dissipation reads

$$d(\alpha_i^{(n)}, \dot{\alpha}_i^{(n)}) = \chi_i^{(n)} \cdot \dot{\alpha}_i^{(n)} \geq 0 \tag{5.234}$$

that must be positive in accordance with the Second Law of Thermodynamics. The rates of the plastic strains $\dot{\alpha}_i^{(n)}$ and $\dot{\alpha}_i^{(R)}$ are computed through the flow rule as follows

$$\dot{\alpha}_i^{(n)} = \lambda_n \cdot \frac{\partial y_n^g(\chi_i^{(n)})}{\partial \chi_i^{(n)}} \tag{5.235}$$

$$\dot{\alpha}_i^{(R)} = S\left(\dot{Q}_i{}^{(ext)}\right) \cdot \sum_{n=1}^{N} R_n \cdot \lambda_n \cdot \frac{\partial y_n^g(\chi_i^{(n)})}{\partial \chi_i^{(n)}} \tag{5.236}$$

in which the plastic multiplier is given below

$$\lambda_n = \frac{\frac{\partial y^{(n)}}{\partial \chi_i^{(n)}} \cdot \dot{Q}_i{}^{(n)}}{\frac{\partial y^{(n)}}{\partial \chi_i^{(n)}} \cdot \frac{\partial^2 g_2}{\partial \alpha_i^{(n)2}} \cdot \frac{\partial y^{(n)}}{\partial \chi_i^{(n)}} - \frac{\partial y^{(n)}}{\partial \alpha_i^{(n)}} \cdot \frac{\partial y^{(n)}}{\partial \chi_i^{(n)}}}, n = 1, .., N. \tag{5.237}$$

The terms $\partial y^{(n)}/\partial \alpha_i^{(n)}$ are identically equal to zero because the yield surfaces are only a function of the dissipative forces. Hence, Eq. 5.237 can be written in the following form

$$\lambda_n = \frac{\frac{\partial y^{(n)}}{\partial \chi_i^{(n)}} \cdot \dot{Q}_i{}^{(n)}}{\frac{\partial y^{(n)}}{\partial \chi_i^{(n)}} \cdot \frac{\partial^2 g_2}{\partial \alpha_i^{(n)2}} \cdot \frac{\partial y^{(n)}}{\partial \chi_i^{(n)}}} = \frac{N_i^{(n)}}{D_i^{(n)}}, n = 1, .., N. \tag{5.238}$$

The derivatives of the yield functions $\frac{\partial y^{(n)}}{\partial \chi_i^{(n)}}$ are developed here below

$$\frac{\partial y^{(n)}\left(\chi_i^{(n)}\right)}{\partial \chi_1^{(n)}} = \frac{\partial}{\partial \chi_1^{(n)}} \left\{ \left(\frac{\chi_1^{(n)}}{h_0^{(n)}}\right)^2 + \left(\frac{\chi_2^{(n)}}{h_0^{(n)}}\right)^2 + \left(\frac{\chi_{r1}^{(n)}}{l_0^{(n)}}\right)^2 + \left(\frac{\chi_{r2}^{(n)}}{l_0^{(n)}}\right)^2 + \right.$$

$$+\left(\frac{\chi_{r3}^{(n)}}{x_0^{(n)}}\right)^2-\frac{2\cdot a^{(n)}}{h_0^{(n)}\cdot l_0^{(n)}}\cdot\left(\chi_2^{(n)}\cdot\chi_{r1}^{(n)}-\chi_1^{(n)}\cdot\chi_{r2}^{(n)}\right)-$$

$$-{\chi_3^{(n)}}^{2\cdot\beta_1^{(n)}}\cdot\left(1-\frac{\chi_3^{(n)}}{Q_{3,0}^{max}}\right)^{2\cdot\beta_2^{(n)}}\cdot{Q_{3,0}^{max}}^{(2-2\cdot\beta_1^{(n)})}-1\Bigg\}=$$

$$=\frac{2}{h_0^{(n)}}\cdot\chi_1^{(n)}+\frac{2\cdot a^{(n)}}{h_0^{(n)}\cdot l_0^{(n)}}\cdot\chi_{r2}^{(n)} \tag{5.239}$$

$$\frac{\partial y^{(n)}\left(\chi_i^{(n)}\right)}{\partial\chi_2^{(n)}}=\frac{2}{h_0^{(n)}}\cdot\chi_2^{(n)}-\frac{2\cdot a^{(n)}}{h_0^{(n)}\cdot l_0^{(n)}}\cdot\chi_{r1}^{(n)} \tag{5.240}$$

$$\frac{\partial y^{(n)}\left(\chi_i^{(n)}\right)}{\partial\chi_3^{(n)}}=-{Q_{3,0}^{max}}^{(2-2\cdot\beta_1^{(n)})}\cdot\Bigg[2\cdot\beta_1^{(n)}\cdot{\chi_3^{(n)}}^{(2\cdot\beta_1^{(n)}-1)}\cdot\left(1-\frac{\chi_3^{(n)}}{Q_{3,0}^{max}}\right)^{2\cdot\beta_2^{(n)}}+$$

$$+{\chi_3^{(n)}}^{2\cdot\beta_1^{(n)}}\cdot 2\cdot\beta_2^{(n)}\cdot\left(1-\frac{\chi_3^{(n)}}{Q_{3,0}^{max}}\right)^{(2\cdot\beta_2^{(n)}-1)}\cdot\left(-\frac{1}{Q_{3,0}^{max}}\right)\Bigg]=$$

$$=-2\cdot{Q_{3,0}^{max}}^{(2-2\cdot\beta_1^{(n)})}\cdot\frac{1}{\chi_3^{(n)}}\cdot\left(1-\frac{\chi_3^{(n)}}{Q_{3,0}^{max}}\right)^{2\cdot\beta_2^{(n)}}\cdot$$

$$\cdot\left[\beta_1^{(n)}\cdot{\chi_3^{(n)}}^{2\cdot\beta_1^{(n)}}-\beta_2^{(n)}\cdot{\chi_3^{(n)}}^{2\cdot\beta_1^{(n)}}\cdot\left(1-\frac{\chi_3^{(n)}}{Q_{3,0}^{max}}\right)^{-1}\cdot\left(\frac{1}{Q_{3,0}^{max}}\right)\right] \tag{5.241}$$

$$\frac{\partial y^{(n)}\left(\chi_i^{(n)}\right)}{\partial\chi_{r1}^{(n)}}=\frac{2}{l_0^{(n)}}\cdot\chi_{r1}^{(n)}-\frac{2\cdot a^{(n)}}{h_0^{(n)}\cdot l_0^{(n)}}\cdot\chi_2^{(n)} \tag{5.242}$$

$$\frac{\partial y^{(n)}\left(\chi_i^{(n)}\right)}{\partial \chi_{r2}^{(n)}} = \frac{2}{l_0^{(n)}} \cdot \chi_{r2}^{(n)} + \frac{2 \cdot a^{(n)}}{h_0^{(n)} \cdot l_0^{(n)}} \cdot \chi_1^{(n)} \tag{5.243}$$

$$\frac{\partial y^{(n)}\left(\chi_i^{(n)}\right)}{\partial \chi_{r3}^{(n)}} = \frac{2}{x_0^{(n)}} \cdot \chi_{r3}^{(n)}. \tag{5.244}$$

The second derivative of the sub-function $g_2(0, \alpha_i^{(n)})$ of the Gibbs freee energy reads

$$\frac{\partial^2 g_2(0, \alpha_i^{(n)})}{\partial \alpha_i^{(n)2}} = \frac{\partial^2}{\partial \alpha_i^{(n)2}} \left[\frac{1}{2} \cdot H_{ij}^{(n)} \cdot \alpha_j^{(n)} \cdot \alpha_i^{(n)}\right] = H_{ij}^{(n)}. \tag{5.245}$$

Based on the above results, each addendum in Eq. 5.238 can be derived

$$N_1^{(n)} = \frac{\partial y^{(n)}}{\partial \chi_1^{(n)}} \cdot \dot{Q_1}^{(n)} = \left(\frac{2}{h_0^{(n)}} \cdot \chi_1^{(n)} + \frac{2 \cdot a^{(n)}}{h_0^{(n)} \cdot l_0^{(n)}} \cdot \chi_{r2}^{(n)}\right) \cdot \dot{Q_1}^{(n)} \tag{5.246}$$

$$N_2^{(n)} = \frac{\partial y^{(n)}}{\partial \chi_2^{(n)}} \cdot \dot{Q_2}^{(n)} = \left(\frac{2}{h_0^{(n)}} \cdot \chi_2^{(n)} - \frac{2 \cdot a^{(n)}}{h_0^{(n)} \cdot l_0^{(n)}} \cdot \chi_{r1}^{(n)}\right) \cdot \dot{Q_2}^{(n)} \tag{5.247}$$

$$N_3^{(n)} = \frac{\partial y^{(n)}}{\partial \chi_3^{(n)}} \cdot \dot{Q_3}^{(n)} = \left\{-2 \cdot Q_{3,0}^{max(2-2\cdot\beta_1^{(n)})} \cdot \frac{1}{\chi_3^{(n)}} \cdot \left(1 - \frac{\chi_3^{(n)}}{Q_{3,0}^{max}}\right)^{2\cdot\beta_2^{(n)}} \cdot \right.$$

$$\left. \cdot \left[\beta_1^{(n)} \cdot \chi_3^{(n)2\cdot\beta_1^{(n)}} - \beta_2^{(n)} \cdot \chi_3^{(n)2\cdot\beta_1^{(n)}} \cdot \left(1 - \frac{\chi_3^{(n)}}{Q_{3,0}^{max}}\right)^{-1} \cdot \left(\frac{1}{Q_{3,0}^{max}}\right)\right]\right\} \cdot \dot{Q_3}^{(n)} \tag{5.248}$$

$$N_{r1}^{(n)} = \frac{\partial y^{(n)}}{\partial \chi_{r1}^{(n)}} \cdot \dot{Q}_{r1}^{(n)} = \left(\frac{2}{l_0^{(n)}} \cdot \chi_{r1}^{(n)} - \frac{2 \cdot a^{(n)}}{h_0^{(n)} \cdot l_0^{(n)}} \cdot \chi_2^{(n)}\right) \cdot \dot{Q}_{r1}^{(n)} \tag{5.249}$$

$$N_{r2}^{(n)} = \frac{\partial y^{(n)}}{\partial \chi_{r2}^{(n)}} \cdot \dot{Q}_{r2}^{(n)} = \left(\frac{2}{l_0^{(n)}} \cdot \chi_{r2}^{(n)} + \frac{2 \cdot a^{(n)}}{h_0^{(n)} \cdot l_0^{(n)}} \cdot \chi_1^{(n)} \right) \cdot \dot{Q}_{r2}^{(n)} \tag{5.250}$$

$$N_{r3}^{(n)} = \frac{\partial y^{(n)}}{\partial \chi_{r3}^{(n)}} \cdot \dot{Q}_{r3}^{(n)} = \left(\frac{2}{x_0^{(n)}} \cdot \chi_{r3}^{(n)} \right) \cdot \dot{Q}_{r3}^{(n)}. \tag{5.251}$$

$$D_1^{(n)} = \frac{\partial y^{(n)}}{\partial \chi_1^{(n)}} \cdot \frac{\partial^2 g_2}{\partial \alpha_1^{(n)2}} \cdot \frac{\partial y^{(n)}}{\partial \chi_1^{(n)}} = \left(\frac{2}{h_0^{(n)}} \cdot \chi_1^{(n)} + \frac{2 \cdot a^{(n)}}{h_0^{(n)} \cdot l_0^{(n)}} \cdot \chi_{r2}^{(n)} \right)^2 \cdot H_{11}^{(n)} \tag{5.252}$$

$$D_2^{(n)} = \frac{\partial y^{(n)}}{\partial \chi_2^{(n)}} \cdot \frac{\partial^2 g_2}{\partial \alpha_2^{(n)2}} \cdot \frac{\partial y^{(n)}}{\partial \chi_2^{(n)}} = \left(\frac{2}{h_0^{(n)}} \cdot \chi_2^{(n)} - \frac{2 \cdot a^{(n)}}{h_0^{(n)} \cdot l_0^{(n)}} \cdot \chi_{r1}^{(n)} \right)^2 \cdot H_{22}^{(n)} \tag{5.253}$$

$$D_3^{(n)} = \frac{\partial y^{(n)}}{\partial \chi_3^{(n)}} \cdot \frac{\partial^2 g_2}{\partial \alpha_3^{(n)2}} \cdot \frac{\partial y^{(n)}}{\partial \chi_3^{(n)}} = \left\{ -2 \cdot Q_{3,0}^{max(2-2\cdot\beta_1^{(n)})} \cdot \frac{1}{\chi_3^{(n)}} \cdot \left(1 - \frac{\chi_3^{(n)}}{Q_{3,0}^{max}} \right)^{2\cdot\beta_2^{(n)}} \cdot \right.$$

$$\left. \cdot \left[\beta_1^{(n)} \cdot \chi_3^{(n)2\cdot\beta_1^{(n)}} - \beta_2^{(n)} \cdot \chi_3^{(n)2\cdot\beta_1^{(n)}} \cdot \left(1 - \frac{\chi_3^{(n)}}{Q_{3,0}^{max}} \right)^{-1} \cdot \left(\frac{1}{Q_{3,0}^{max}} \right) \right] \right\}^2 \cdot H_{33}^{(n)} \tag{5.254}$$

$$D_{r1}^{(n)} = \frac{\partial y^{(n)}}{\partial \chi_{r1}^{(n)}} \cdot \frac{\partial^2 g_2}{\partial \alpha_{r1}^{(n)2}} \cdot \frac{\partial y^{(n)}}{\partial \chi_{r1}^{(n)}} = \left(\frac{2}{l_0^{(n)}} \cdot \chi_{r1}^{(n)} - \frac{2 \cdot a^{(n)}}{h_0^{(n)} \cdot l_0^{(n)}} \cdot \chi_2^{(n)} \right)^2 \cdot H_{r1r1}^{(n)} \tag{5.255}$$

$$D_{r2}^{(n)} = \frac{\partial y^{(n)}}{\partial \chi_{r2}^{(n)}} \cdot \frac{\partial^2 g_2}{\partial \alpha_{r2}^{(n)2}} \cdot \frac{\partial y^{(n)}}{\partial \chi_{r2}^{(n)}} = \left(\frac{2}{l_0^{(n)}} \cdot \chi_{r2}^{(n)} + \frac{2 \cdot a^{(n)}}{h_0^{(n)} \cdot l_0^{(n)}} \cdot \chi_1^{(n)} \right)^2 \cdot H_{r2r2}^{(n)} \tag{5.256}$$

$$D_{r3}^{(n)} = \frac{\partial y^{(n)}}{\partial \chi_{r3}^{(n)}} \cdot \frac{\partial^2 g_2}{\partial \alpha_{r3}^{(n)2}} \cdot \frac{\partial y^{(n)}}{\partial \chi_{r3}^{(n)}} = \frac{4}{x_0^{(n)2}} \cdot \chi_{r3}^{(n)2} \cdot H_{r3r3}^{(n)}. \tag{5.257}$$

The kinematic hardening matrix $H_{ij}^{(n)}$ associated with the n-th plastic flow is assumed to be diagonal. This is the primary assumption that differentiates the macro-response of a shallow foundation from that of an embedded foundation.

In light of the above, in the case of a complete six-dimensional loading pattern, the plastic multiplier assumes a quite articulated expression, in which all the terms $N_i^{(n)}$ and $D_i^{(n)}$ are different from zero. Nonetheless, each contribution to λ_n has a simple form that can be easily integrated through the application of standardised procedures, such as the finite difference method. The solution of the plastic multiplier allows to determine the flow rule, which in turn can be substituted in Eq. 5.234 to give the general expression of the dissipation function. When also an additional ratcheting displacement is considered, following the procedure already described in Section 5.5.2, a modified dissipation function $d^* = d + \Lambda \cdot c$ is introduced in the formulation that includes the ratcheting effect in the constraint $c = \dot{\alpha}^{(R)} - S\left(Q^{(ext)}\right) \cdot \sum_{n=1}^{N} R^{(n)} \cdot \dot{\alpha}^{(n)}$ through the Lagrangian multiplier $\Lambda > 0$.

There are some cases, however, in which dissipation assumes a much easier form. Consider, for example, the macro-element subjected to a purely horizontal load $Q_1^{(ext)}$. For simplicity, no ratcheting displacement develops during plastic flow. In this case, the N yield surfaces degenerate in n-th plastic thresholds $k_1^{(n)}$ with an eventual dissymmetric behaviour (Eq. 5.68). In this case, the plastic multiplier simply reads

$$\lambda_n = \frac{\frac{\partial y^{(n)}}{\partial \chi_1^{(n)}} \cdot \dot{Q}_1^{(n)}}{\frac{\partial y^{(n)}}{\partial \chi_1^{(n)}} \cdot \frac{\partial^2 g_2}{\partial \alpha_1^{(n)2}} \cdot \frac{\partial y^{(n)}}{\partial \chi_1^{(n)}}} = \frac{N_1^{(n)}}{D_1^{(n)}} = \frac{h_0^{(n)}}{2 \cdot \chi_1^{(n)} \cdot H_{11}^{(n)}} \cdot \dot{Q}_1^{(n)}, n = 1, .., N \tag{5.258}$$

and the flow rule yields

$$\dot{\alpha}_1^{(n)} = \lambda_n \cdot \frac{\partial y_n^g(\chi_1^{(n)})}{\partial \chi_1^{(n)}} = \frac{h_0^{(n)}}{2 \cdot \chi_1^{(n)} \cdot H_{11}^{(n)}} \cdot \dot{Q_1}^{(n)} \cdot \frac{2}{h_0^{(n)}} \cdot \chi_1^{(n)} =$$

$$= \frac{1}{H_{11}^{(n)}} \cdot \dot{Q_1}^{(n)}, n = 1, .., N. \tag{5.259}$$

The dissipation function assumes the following compact form

$$d(\alpha_1^{(n)}, \dot{\alpha}_1^{(n)}) = \sum_{n=1}^{N} \chi_1^{(n)} \cdot \dot{\alpha}_1^{(n)} = \sum_{n=1}^{N} k_1^{(n)} \cdot \dot{\alpha}_1^{(n)} = \sum_{n=1}^{N} \frac{k_1^{(n)}}{H_{11}^{(n)}} \cdot \dot{Q_1}^{(n)} \tag{5.260}$$

having recognised that, during plastic flow, the dissipative force is equal to the plastic threshold $k_1^{(n)} = \chi_1^{(n)}$.

The incremental response of the model can be obtained by differentiating the Helmholtz free energy

$$\dot{Q}_1^{(ext)} = \frac{\partial f\left(q, \alpha_1^{(n)}\right)}{\partial q} = H_{11}^{(0)} \cdot \dot{q}_1^{(0)}(q_1) = H_{11}^{(0)} \cdot \left(\dot{q}_1 - \sum_{n=1}^{N} \dot{\alpha}_1^{(n)}\right) =$$

$$= H_{11}^{(0)} \cdot \left(q_1 - \sum_{n=1}^{N} \lambda_n \cdot \frac{\partial y_n}{\partial \chi_1^{(n)}}\right) = H_{11}^{(0)} \cdot \left(q_1 - \sum_{n=1}^{N} \frac{\dot{Q_1}^{(n)}}{H_{11}^{(n)}}\right) =$$

$$= H_{11}^{(0)} \cdot \left(q_1 - \sum_{n=1}^{N} \frac{\dot{Q_1}^{(ext)}}{H_{11}^{(n)}}\right) \tag{5.261}$$

that can be easily integrated through the finite difference method for instance. Hence, the one-dimensional response of the model is formally identical to that of the macro-element of bridge abutments with no mass, except for a different calibration of the plastic thresholds, or better of the ultimate capacity of the foundation. This allows to use the new Uniaxial material implemented in OpenSees in Section 5.12.2

for a prompt use of the 1D macro-element in the structural analysis of the reference bridge, while the implementation of the multi-axial formulation will constitute a forthcoming development of the present research.

5.15.2 Application to the case study

The macro-element of shallow foundations was used, together with the macro-element of bridge abutments, in the global structural model of the reference bridge in order to develop a complete nonlinear representation of the soil-structure interaction. For simplicity, a one-dimensional macro-element was applied to the foundation of the strong pier, aligned with the direction of motion, with the primary aim to reproduce the permanent displacements developing in the foundation soil.

Following the calibration procedure described in Section 5.14.1, the macro-element is completely defined by the specification of the initial stiffness $H^{(1)}$ and the ultimate strength $k^{(N)}$. The former was evaluated by the elastic solutions for the static stiffness of rigid footings at the ground surface proposed by Gazetas (1991), reported here below

$$H^{(1)} = \frac{2 \cdot G \cdot l}{2 - \nu} \cdot \left[2 + 2.5 \cdot \left(\frac{b}{l} \right)^{0.85} \right] - \frac{0.2 \cdot G \cdot l}{0.75 - \nu} \cdot \left(1 - \frac{b}{l} \right). \tag{5.262}$$

In this case, the shear modulus of soil G is referred to the behaviour at small strains because it was used to calculate the initial stiffness of the macro-element. It was assumed to be equal to $9.5 \cdot 10^4$ kPa, representing the average value of the elastic modulus adopted in the superficial layer $MG1D$. The Poisson's ratio was set equal to 0.2, associated with the small-strain response of the soil. The semi-length of the foundation in the longitudinal and transverse directions of the bridge are 3 m and 2.5 m, respectively. Accordingly, the initial stiffness of the macro-element results to be equal to $1.3 \cdot 10^6$ kN/m, that is comparable with the initial stiffness assigned to

the macro-element of the soil-abutment system in the same direction, equal to 10^6 kN/m, in spite of the completely different geometry of the two geotechnical systems. This result can be due to the elastic response of the soil exhibited at small strains, that controls the response with no significant dependence on the load conditions.

The capacity of the soil-foundation system in the longitudinal direction, thus the external force that produces the attainment of the ultimate strength of the macro-element $k^{(N)}$, was instead determined as the minimum value between the limit force associated with the attainment of the bearing capacity and the mobilisation of the sliding capacity at the soil-foundation contact. The former was obtained by simply applying the Brinch-Hansen formula. More specifically, it was determined the limit value of the longitudinal force $Q^b_{1,lim}$ that mobilises the ultimate strength of the geotechnical system. The foundation is initially considered loaded by the static actions transmitted by the superstructure, evaluated through the gravity analysis of the full soil-bridge system. Focusing on the foundation of the strong pier, the resulting load pattern is shown in Figure 5.48: in addition to the important vertical load $Q_3 = 2331$ kN, a modest longitudinal load $Q_1 = 34$ kN and a significant moment $Q_{r2} = 290$ kNm are transferred to the foundation. Starting from this configuration, the Brinch-Hansen formula was applied, increasing the longitudinal force until the attainment of the bearing capacity. In order to account for the increase of moment associated with the increment of the shear force at the base of the column, the moment Q_{r2} was increased as the product between the the longitudinal force acting on the foundation and the height of the pier. The resulting limit value $Q^b_{1,lim}$ is equal to 335 kN (oriented towards the weak abutment), corresponding to a vertical force $Q_3 = 2331$ kN and a moment $Q_{r2} = 4522$ kNm, that is equal to about 1 % the limit force on the abutment top corresponding to the attainment of the active resistance in the backfill. The limit value in the opposite direction results equal to $Q^b_{1,lim} = 381$ kN (oriented towards the strong abutment), associated with a moment

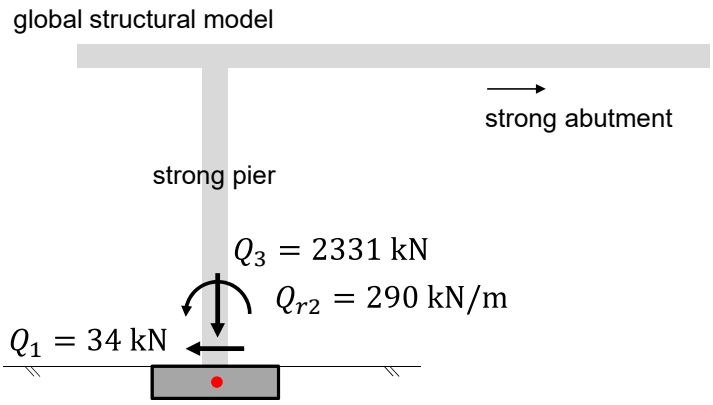

Figure 5.48: Load pattern of the foundation of the strong pier under gravity loads.

$Q_{r2} = 4394$ kNm, giving a bias parameter on strength of 0.88.

The limit force that produces the sliding at the soil-foundation contact was computed, in first approximation, as

$$Q_{1,lim}^{shear} = Q_{3,st} \cdot tg\,(\varphi') = 2331 \cdot tg\,(\varphi') = 1821 \text{ kN} \tag{5.263}$$

as the foundation was placed on the ground surface. Therefore the ultimate condition of the foundation is controlled by the attainment of the bearing capacity of the foundation and the ultimate strength of the macro-element was set as a equal to $k_{-}^{(N)} = 335$ kN, towards the weak abutment, and $k_{+}^{(N)} = 381$ kN, towards the strong abutment.

The 1D macro-element was supposed to be composed of 5 dissipative devices, each characterised by a stiffness $H^{(n)}$ and a plastic threshold $k^{(n)}$ ranging between the ultimate strength $k^{(N)}$ and the first yield $k^{(1)}$. The latter was assumed as a small fraction of the ultimate strength, thus $k^{(1)} = 0.15 \cdot k^{(N)}$. The entire set of stiffness and strength parameters is listed in Table 5.5, having considered a linear variation of the parameters from the first yield up to the ultimate conditions.

The resulting backbone curve is depicted in Figure 5.49, showing the comparison with the force-displacement law obtained for a number of devices equal to 10.

Device	$H^{(n)}$ (kN/m)	$k_+^{(n)}$ (kN)	$k_-^{(n)}$ (kN)
0	$1.3 \cdot 10^6$	–	–
1	10^5	57	49
2	10^4	143	126
3	$4.3 \cdot 10^3$	228	201
4	$2.1 \cdot 10^3$	315	278
5	10^{-1}	381	335

Tabella 5.5: Stiffness $H^{(n)}$ and strength $k^{(n)}$ parameters assigned to the macro-element of shallow foundation.

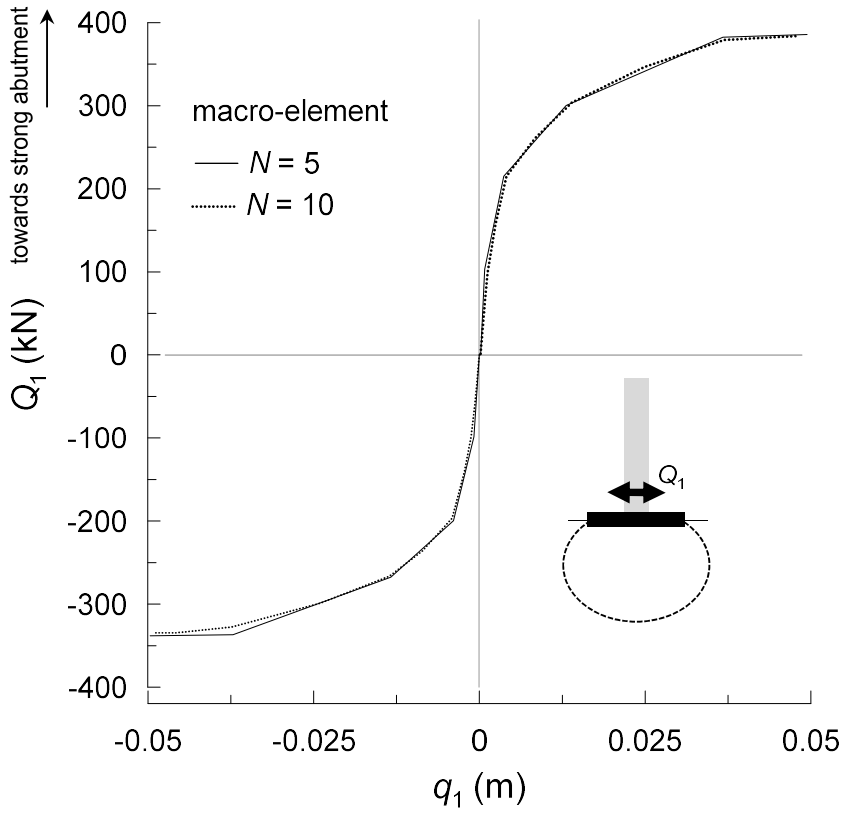

Figure 5.49: Force-displacement relation in the longitudinal direction obtained through the macro-element of shallow foundation.

Chapter 6

A macro-element of the bridge structure

6.1 Conceptual framework

The cardinal point of the present thesis consists in analysing the soil-abutment-superstructure interaction, looking for a better understanding of this phenomenon and providing a methodology to predict the relative effects on the entire soil-bridge system. In this view, in the previous chapter an advanced representation of the soil-abutment system has been proposed to incorporate into the global structural response the nonlinear and multi-axial interaction occurring at the abutment locations. A complementary view of this problem would be to study the influence of the dynamic behaviour of the bridge structure on the seismic performance of the abutments. The response of a bridge abutment, in fact, is affected by its interaction with the superstructure, with a reciprocal frequency-dependent exchange of inertial forces at the deck-abutment contact under seismic conditions. These forces can become important in the case of strong shaking and therefore can modify significantly the stress-strain state in the abutment structure and in the soil interacting with it. In

order to account for this phenomenon, an original approach is proposed to the study of the seismic behaviour of bridge abutments, in which a simplified description of the dynamic response of the bridge is introduced into a finite-element model of the soil-abutment system. Specifically, the dynamic behaviour of the bridge structure is described by an expressly conceived elastic-plastic macro-element, that simulates the complex loading pattern transferred to the abutment during the seismic event. This approach improves the current analysis methods based on sub-structuring, limiting at the same time the computational demand needed for an otherwise complete study of the soil-structure interaction for this type of problems. The validity of the procedure is demonstrated on a simple structural scheme, comparing the results of the simplified approach with the results obtained from dynamic analyses of the full soil-structure system. Based on these results, a strategy is devised for the calibration of the bridge macro-element, making use of a limited number of input parameters. In Chapter 7, the method will be applied to the reference soil-bridge system (Section 3.6), carrying out full three-dimensional dynamic analyses.

Figure 6.1 depicts the conceptual scheme of the macro-element of the bridge structure. While the structural elements of the abutment are represented explicitly in the soil-abutment model, the response of the bridge structure is simulated through the introduction of an equivalent macro-element. This system is formally described by a second-order transfer tensor TT_{ij} which expresses a frequency-dependent relationship between the vector of the generalised displacements at the foundation level u_j and the resulting vector of the generalised forces Q_i at the deck-abutment contact, that can be written as:

$$Q_i = TT_{ij} \cdot u_j. \tag{6.1}$$

For a linear structural system, the transfer tensor is an intrinsic property of the

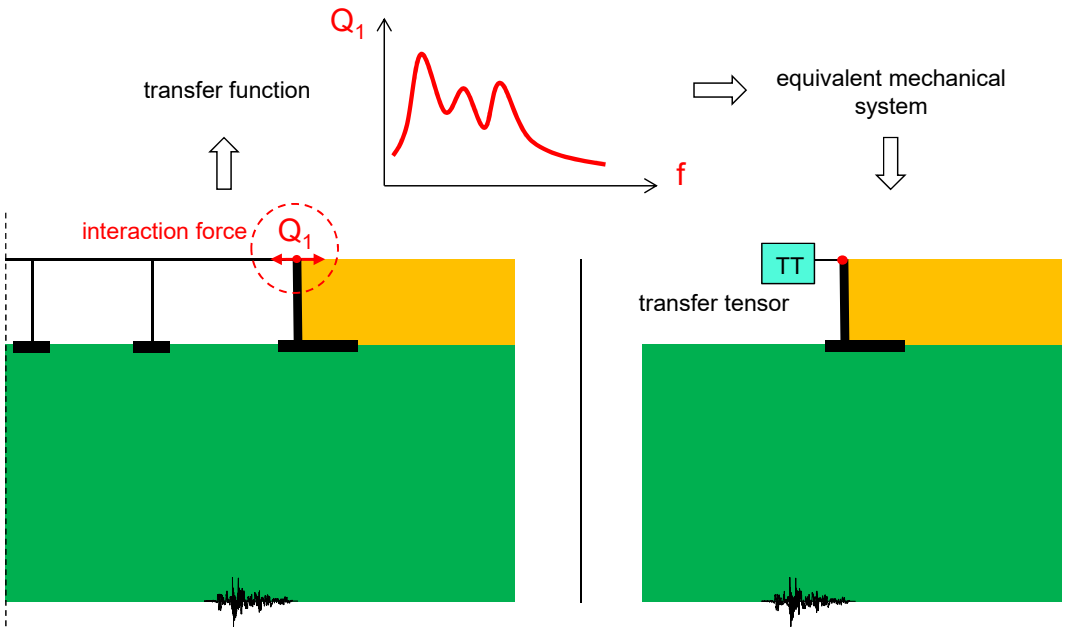

Figure 6.1: Conceptual scheme of the method of the transfer tensor.

structure: it is not affected by the presence of the soil and depends only on the mechanical properties of the bridge. In other words, it describes the filtering effect of the bridge structure on the interaction forces exchanged between the abutment and the superstructure, taking explicitly into consideration their effective connection. The generic term of the tensor TT_{ij} is a transfer function, whose calibration procedure will be described in the following. The mathematical formulation of a transfer function specialises according to the expected level of nonlinearity of the structural response. When the dynamic response of the structure can be regarded as linear, the transfer functions is not dependent on the amplitude of the external excitation and the macro-element is also called elastic transfer tensor. When the nonlinearities of the bridge structure become important, instead, the transfer functions are represented by nonlinear relationships reproducing the amplitude-dependent response of the whole structure. The nonlinear macro-element represents the generalisation of the elastic transfer tensor and it is calibrated starting from the structural parameters

in the elastic regime.

In spite of its general formulation, the transfer tensor is mainly devoted to represent the significant degrees of freedom of the deck-abutment contact (see Section 5.1), hence the validation is focused on the translational motion of the deck-abutment joint, neglecting the transmission of moment.

6.2 Calibration of the elastic transfer tensor

The elastic transfer tensor is conceived as a simplified structural system able to reproduce the global effects of the multi-directional dynamic response of the bridge, in terms of inertial forces transferred to the geotechnical system. As mentioned in the previous paragraph, it is an intrinsic property of a structure not affected by the soil characteristics, assumption that will be demonstrated later. Figure 6.2 shows the identification procedure of a generic transfer function: a global numerical model of the structure, including the structural members and the abutments, is perturbed by a frequency sweep at the base of the piers and at the abutments foundations, and for each frequency the maximum value of the interaction forces produced at the deck-abutment contact is determined; the transfer function is evaluated at each frequency as the ratio of the interaction force to the amplitude of the input motion. Generally, the transfer functions present a multi-modal distribution in the frequency domain that can be easily reproduced in numerical modelling through some masses connected by simple rheological systems. This modelling technique is conceptually identical to the procedure used to include the inertial effects in the macro-element of the soil-abutment system: in that case the masses were calibrated to reproduce the dominant responses of the soil-abutment system representing the fundamental vibration modes.

The masses of the macro-element of the bridge structure are aimed to repro-

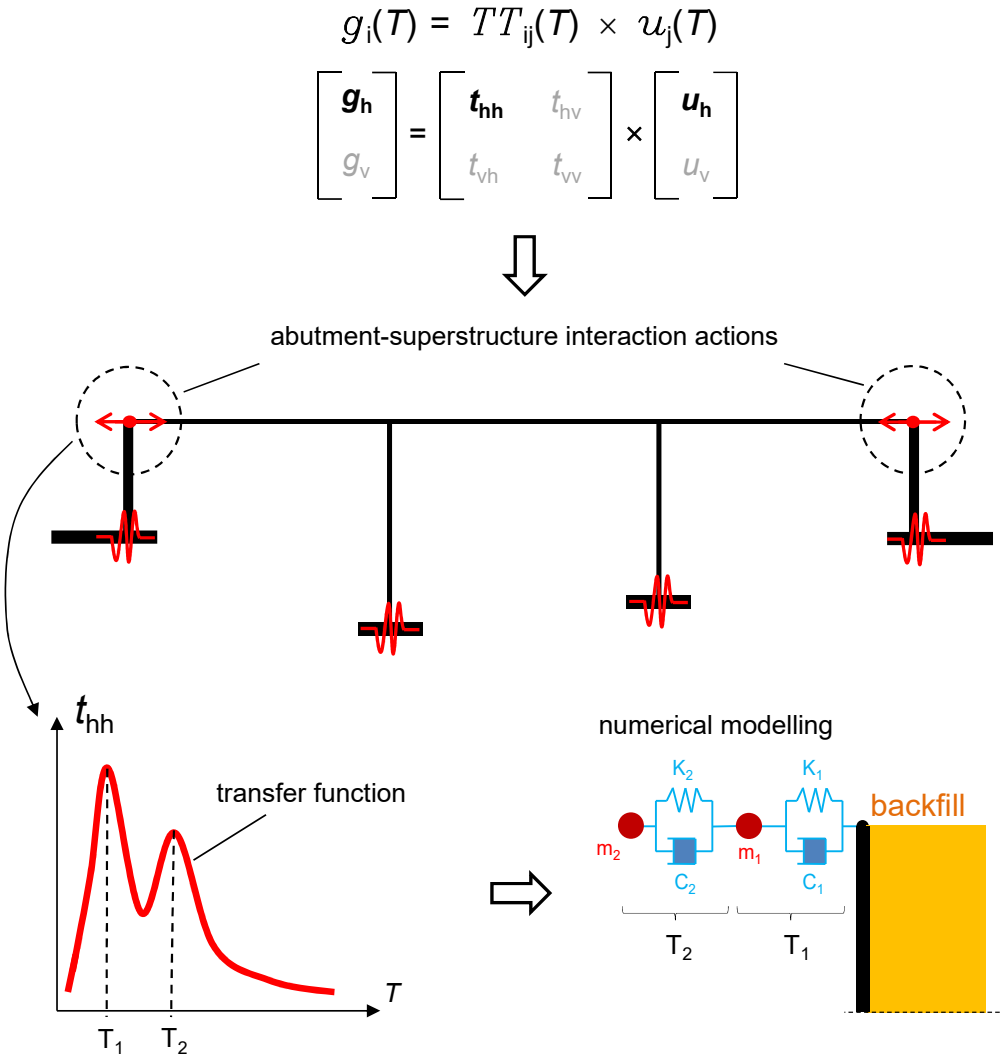

Figure 6.2: Identification procedure of the generic transfer function t_{hh}.

duce the peaks of the transfer functions, which depend on the dynamic response of the superstructure. More specifically, the peaks can be associated with the significant vibration modes of the bridge structure for the degree of freedom of the deck-abutment contact considered and, consequently, the transfer functions can be obtained starting from the modal information of the bridge.

6.3 Validation

The response of the macro-element was initially tested in a simple, idealised soil-bridge system with the aim to have a robust and clear understanding on its applicability. This allowed to carry out a number of nonlinear dynamic analyses of the full soil-structure system, considering the multi-directionality of the ground motion and different seismic scenarios. The structural behaviour varied from linear elastic to highly nonlinear, employing appropriate finite-element representations of the structural members.

6.3.1 Uni-axial elastic macro-element

Consider the three-dimensional model of the idealised soil-structure system depicted in Figure 6.3, including a framed structure in contact with the soil through the pier foundation and the abutment. The analysis of this system was performed by using the analysis framework OpenSees, adopting appropriate formulations for the finite elements and assuming a visco-elastic behaviour for both the soil and the structural elements. The numerical model is composed of 3689 finite elements, of which 92 relative to the structure. The model was built with a three-dimensional mesh, with a unit length in the direction out of plane. Hence, the response of the soil domain and the abutment is under plane strain conditions while the effective geometry of

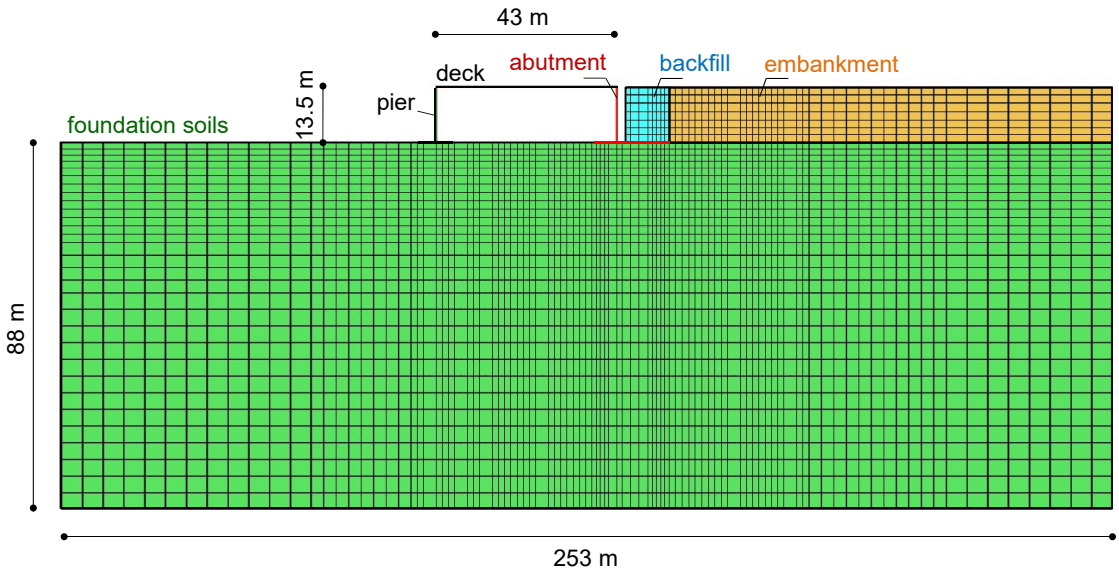

Figure 6.3: Mesh of the full soil-abutment-superstructure interaction model implemented in OpenSees.

the superstructure was reproduced in the model.

The structure is made up of a deck connected by a hinge to the abutment and by a rigid constraint to the pier. The vertical elements are in turn in contact with the foundation soil through the respective foundations. Thinking about multi-span girder bridges with a discontinuous deck, this simplified structural configuration is aimed at representing the part of the structure that interacts with the abutment. The abutment presents a very similar geometry to that of the Pantano viaduct: it has 13.5 m-height wall, with a thickness of 4 m, resting on a shallow foundation with length and thickness of 17.5 m and 5 m, respectively. A visco-elastic behaviour was assigned to every finite element of the structure, with elastic moduli relative to a $C32/40$ strength class concrete in European standards; a Rayleigh damping was used in order to have a damping ratio not greater than 5 % for all the significant modes of the structure, the latter evaluated through a preliminary modal analysis of the structural model with fixed base. The entire soil domain was initially assumed to be dry and, accordingly, every element was discretised through the SSPbrick

finite elements available in OpenSees. The backfill, placed behind the abutment wall, extends to the entire length of the foundation, followed by the embankment representing the approaching structure to the bridge. The backfill has a Young's modulus and a Poisson's ratio equal to 10^6 kPa and 0.3, respectively, while the values of $2.75 \cdot 10^5$ kPa and 0.2 were assigned to the embankment, reflecting common values prescribed by technical provisions. The unit weight was assumed equal to 20 kN/m^3 for both materials. The foundation soil consists of a uniform layer starting from the structure foundations down to the bedrock placed at 88 m from the foundation level; the soil considered is characterised by a unit weight of 22 kN/m^3 and a shear wave velocity of 205 m/s. The soil elements were provided with a proportional viscous damping, defined to have a damping ratio not greater than 2 % for frequencies between $0.05 \div 15$ Hz, representative of the frequency content of the ground motion.

Consider the identification of a simplified structural system equivalent to the deck, the pier and its foundation, in the longitudinal direction only. Figure 6.4 shows the transfer function of the structure (dotted line) for the longitudinal interaction force Q_1 at the deck-abutment contact, obtained by applying the procedure described in Section 6.2. Note that the maximum amplitude of the harmonic input motion for the structural model is taken equal to 1 m, therefore the transfer function coincides with the trend in the frequency domain of the maximum interaction force produced at the deck-abutment contact. The transfer function presents the largest amplitudes at high frequencies, because the interaction force Q_1 is mainly governed by the dynamic axial response of the deck. Specifically, the dynamic response of the deck is activated by the second vibration mode of the abutment wall occurring at a period T of 0.01 s, leading to the maximum amplification of the interaction force. The second peak, occurring at $T = 0.2$ s, is instead related to the first global mode of the structure involving both the vertical elements but not able to excite the deck in its axial direction. The transfer function of the deck (dashed line), in fact, shows a sole peak

at 0.05 s with a noticeable increase of the maximum interaction force with respect to the response of the whole structure. This means that calibrating the macro-element on the mechanical properties of the deck, i. e. based on the mass and the axial stiffness of the deck, would lead to a considerable overestimation of the inertial forces transferred to the abutment and also to an incorrect determination of the dominant period. Therefore, the vertical elements must be included in the evaluation of the transfer function because they lead to the desired increase of deformability of the system necessary to attenuate partially the axial vibrations of the deck. The dominant period, however, moves to lower values since, for the structure under examination, the axial mode of the deck combines with the higher modes of the vertical elements.

The transfer function can be approximated by the mono-modal curve in Figure 6.4 (continuous line). This simple shape can be modelled inserting in the soil-abutment interaction model a single degree of freedom (SDOF) system, calibrating its mass $m^{(1)}$, stiffness $h^{(1)}$ and damping $\xi^{(1)}$ in order to follow the transfer function of the structure. As a result of a trial and error procedure, the optimum mass and stiffness of the macro-element results to be $m^{(1)} = 0.15 \cdot m^{(deck)}$ and $h^{(1)} = 3.9 \cdot h^{(deck)}$, in which $m^{(deck)}$ and $h^{(deck)}$ are the mass and the axial stiffness of the deck, respectively. A viscous damping ratio of 2 % was assigned to the macro-element, evaluated on the effective Rayleigh damping of the structure. By comparing the results of the identification procedure with the modal information of the structure, it was found that the mass of the macro-element can be set equal to the mass associated with the second mode of the deck that occurs at 0.05 s. Note that this is not the fundamental axial mode of the deck but it refers to the higher mode of the vertical elements (abutment in this case) that activates the second vibration mode of the deck. The stiffness required to localise the response of the macro-element at 0.05 s was instead found to be much higher than the axial stiffness of the deck. This is a further

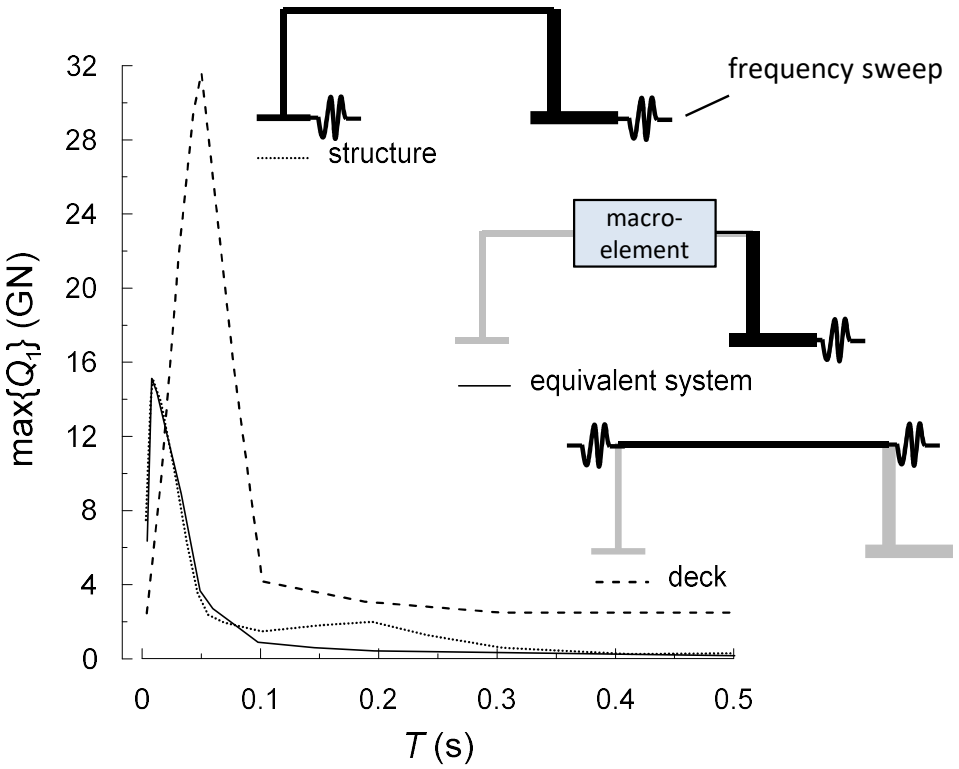

Figure 6.4: Frequency-dependent trends of the maximum longitudinal interaction force at the abutment-deck contact obtained for a maximum amplitude of the input motion equal to 1 m: comparison between the response of the full soil-structure model (dots), that obtained applying the equivalent mechanical system to the abutment (continuous line) and the sole deck (dashed line).

evidence that the characteristics of the macro-elements differ considerably from the static properties of the deck, in a way that depends on the specific structural scheme under examination.

In order to test the effectiveness of the macro-element, time-domain dynamic analyses were carried out applying to the base of the soil domain the longitudinal component of the wideband seismic record of Tabas (Figure 3.49). The response of the local model of abutment including the macro-element is compared with that obtained by the full soil-structure interaction model. Figure 6.5 compares the time-histories of the interaction force Q_1 and the corresponding Fourier spectra. It is evident that for this simple one-dimensional case the macro-element is able to repro-

duce quite correctly the inertial effects of the pier-deck system. Looking at Figures 6.6 and 6.7, representing the longitudinal displacement of the top of the wall and of the center of gravity of the foundation, respectively, it can be seen that also the kinematics of the abutment is not altered by the presence of the macro-element. The elastic response spectra at the foundation level show a very good agreement between the response of the full soil-structure model and the local model of the abutment. Hence, in this simple soil-structure system, the macro-element of the bridge structure can be used to evaluate the local dynamic response of the abutment, taking efficiently into account the interaction with the superstructure of the bridge, but it also allows a good prediction of the seismic actions acting on the bottom and on the top of the wall that can be used in the structural analysis of the entire bridge.

The response of the abutment with application of the macro-element is now compared in Figures 6.8, 6.9 and 6.10 with other classical strategies to represent the abutment-superstructure connection in the geotechnical analysis. The results are restricted to the significant time interval ($5 \div 25$ s) and to the frequency content ($T = 0 \div 6$ s) of the Tabas record in order to highlight the differences between these techniques. For the same reason, only the interaction force Q_1 induced by the seismic shaking is represented. The first evident result is that the use of a macro-element calibrated on the mechanical properties of the deck leads to a marked overestimation of the inertial forces transferred to the soil-abutment system, in a completely different range of frequencies associated with the axial mode of the deck. It follows that the displacement on the abutment top is amplified and consequently also the foundation motion changes sensibly: the foundation undergoes a greater longitudinal displacement induced by the amplified oscillations of the wall top and the maximum spectral accelerations at the base move to longer periods. This implies that also the stress-strain state in the soil surrounding the abutment is altered with an erroneous evaluation of the abutment stability, especially the eventual attainment of the re-

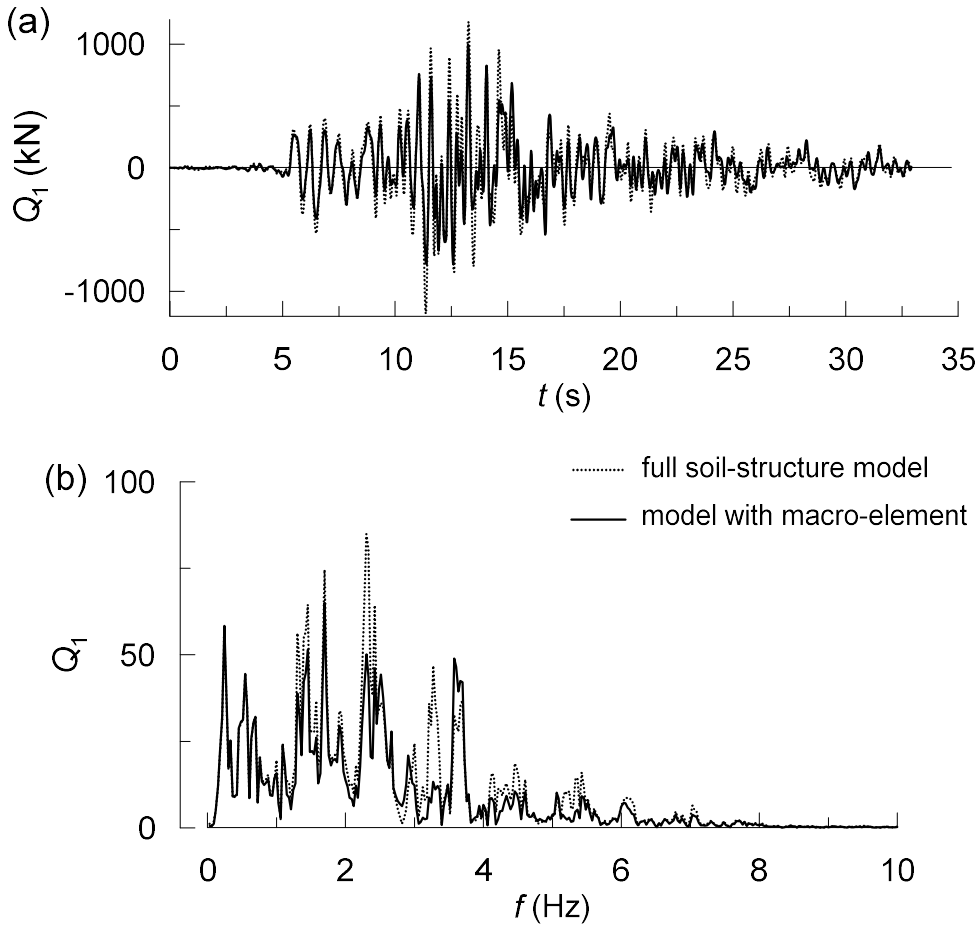

Figure 6.5: Time evolution of the interaction force Q_1 (a) and relative Fourier spectrum (b) in the longitudinal direction recorded at the abutment-deck contact: comparison between the full soil-structure model and the local soil-abutment model with macro-element.

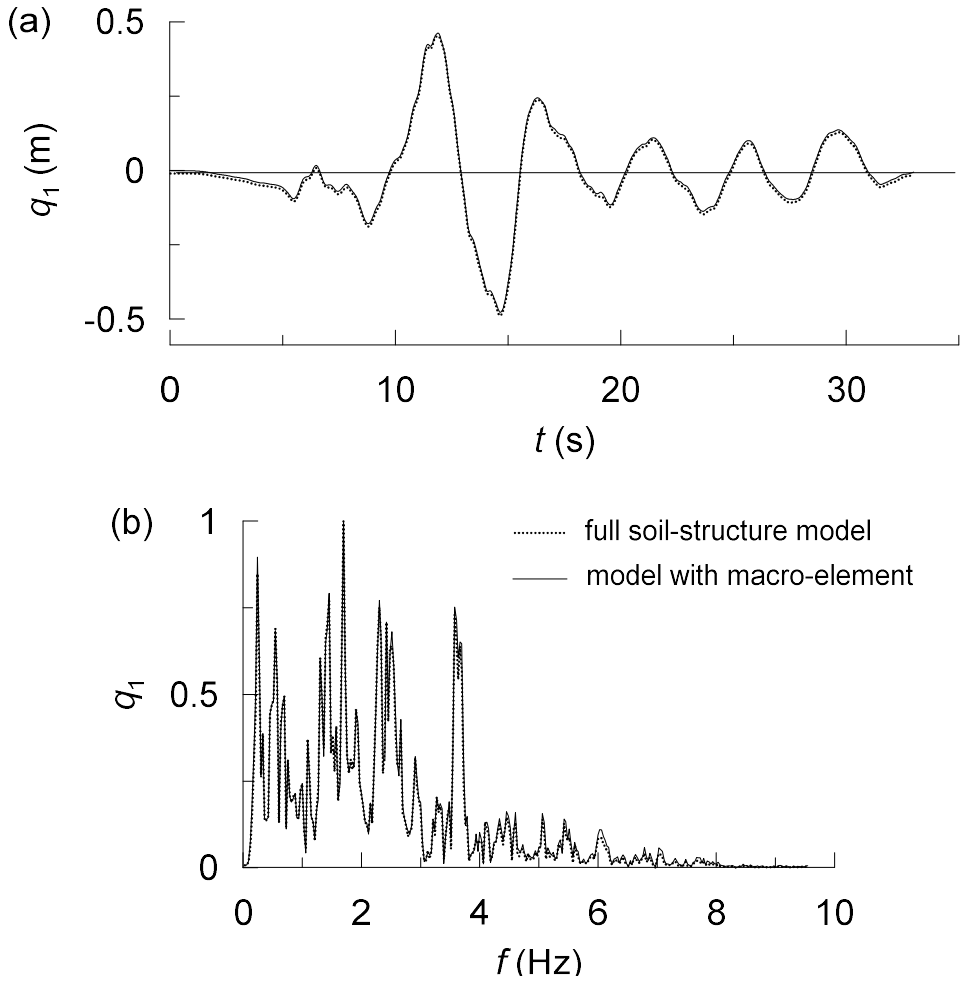

Figure 6.6: Time evolution of the displacement on top q_1 (a) and Fourier spectrum of the relative accelerogram (b) in the longitudinal direction recorded at the abutment-deck contact: comparison between the full soil-structure model and the local soil-abutment model with macro-element.

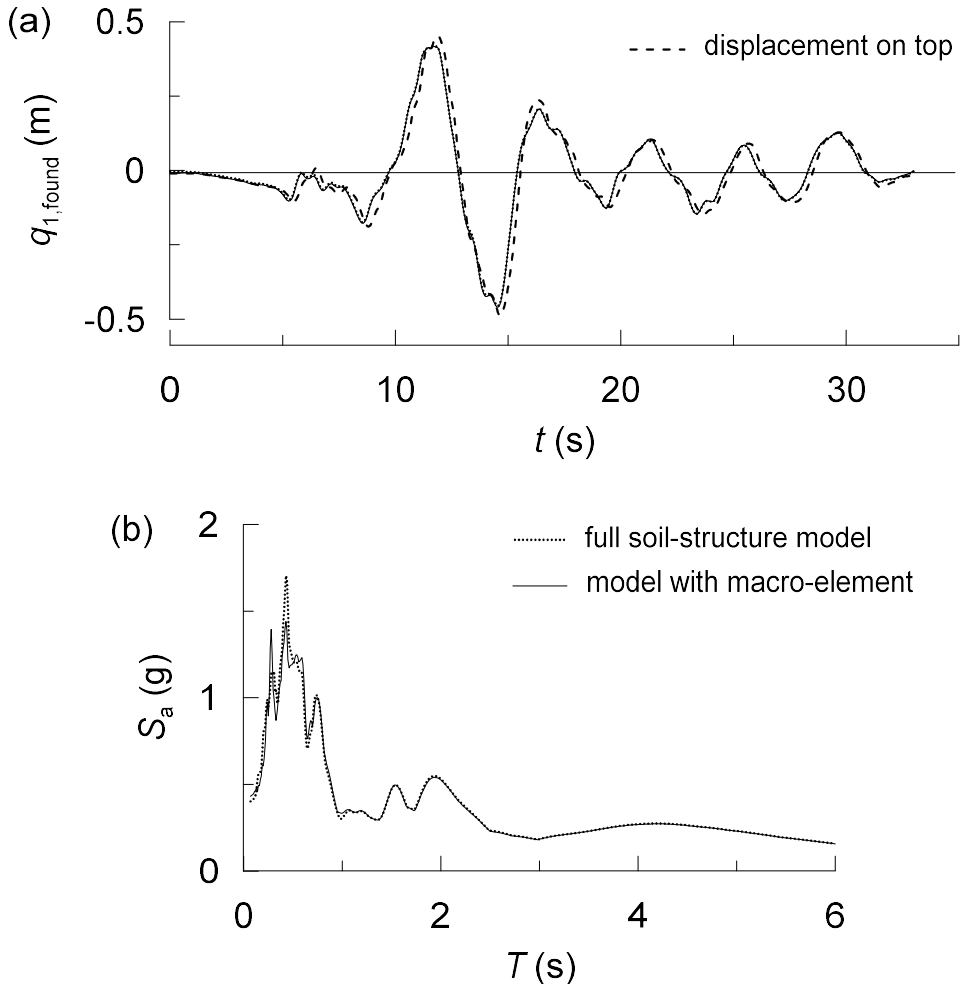

Figure 6.7: Time evolution of the displacement of the barycenter of the foundation $q_{1,found}$ (a) and 5 %-damped elastic response spectrum of the relative accelerogram (b) in the longitudinal direction: comparison between the full soil-structure model and the local soil-abutment model with macro-element.

sistance in the backfill with development of permanent settlements of the transition slab.

Another standard technique of modelling the dynamic interaction between the abutment and the bridge structure consists in applying an equivalent static force (thin continuous line) at the top of the abutment, intended as the inertial force associated with the first significant vibration mode of the bridge for the degree of freedom considered at the deck-abutment contact. Hence, the longitudinal pseudo-static force refers to the dominant period of the transfer function of the whole structure at 0.01 s. The resulting time-independent interaction force Q_1 presents a magnitude of about 750 kN, with some minor oscillations due to the variation of the internal force in the finite element placed on the abutment top. It is evident that, despite giving a rough estimation of the maximum interaction force transferred to the abutment with an underestimation of about 38 %, this technique neglects completely the time-dependent effects at the deck-abutment contact. Nonetheless, the displacement field of the abutment is quite similar to that of the full model with a maximum increase of q_1 and $q_{1,found}$ of about 10 %.

In the simplest case, the interaction with the superstructure can be completely neglected in the local model of the abutment by simply assuming no constraints at the abutment top (thin dotted lines). This leads to a response of the system that is conceptually identical to that described above using the equivalent static force, with the only difference that the interaction force Q_1 is approximately equal to zero.

Hence it seems that the dynamic response of the superstructure influences mainly the stress state in the soil-abutment system and only to a more limited extent the displacement field. This might be due to the fact that also the structure moves together with the abutment under seismic excitation, not altering considerably the abutment motion but generating however relevant inertial forces transmitted to the abutment according to its dynamic characteristics.

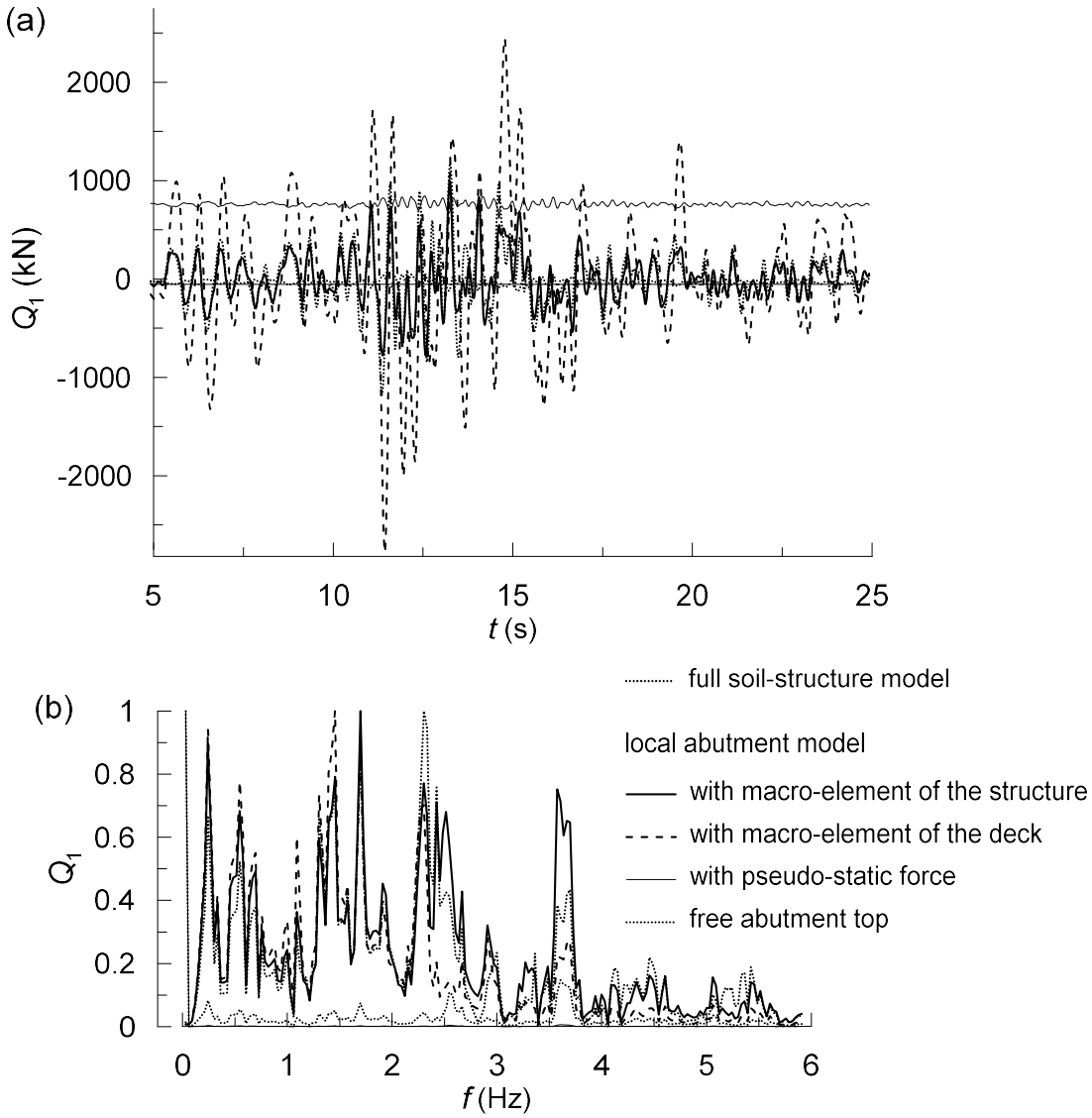

Figure 6.8: Time evolution of the interaction force Q_1 (a) and relative Fourier spectrum (b) in the longitudinal direction. Comparison between different representations of the abutment-superstructure interaction: full soil-structure model, macro-element of the structure, macro-element of the sole deck, free wall top and equivalent pseudo-static force.

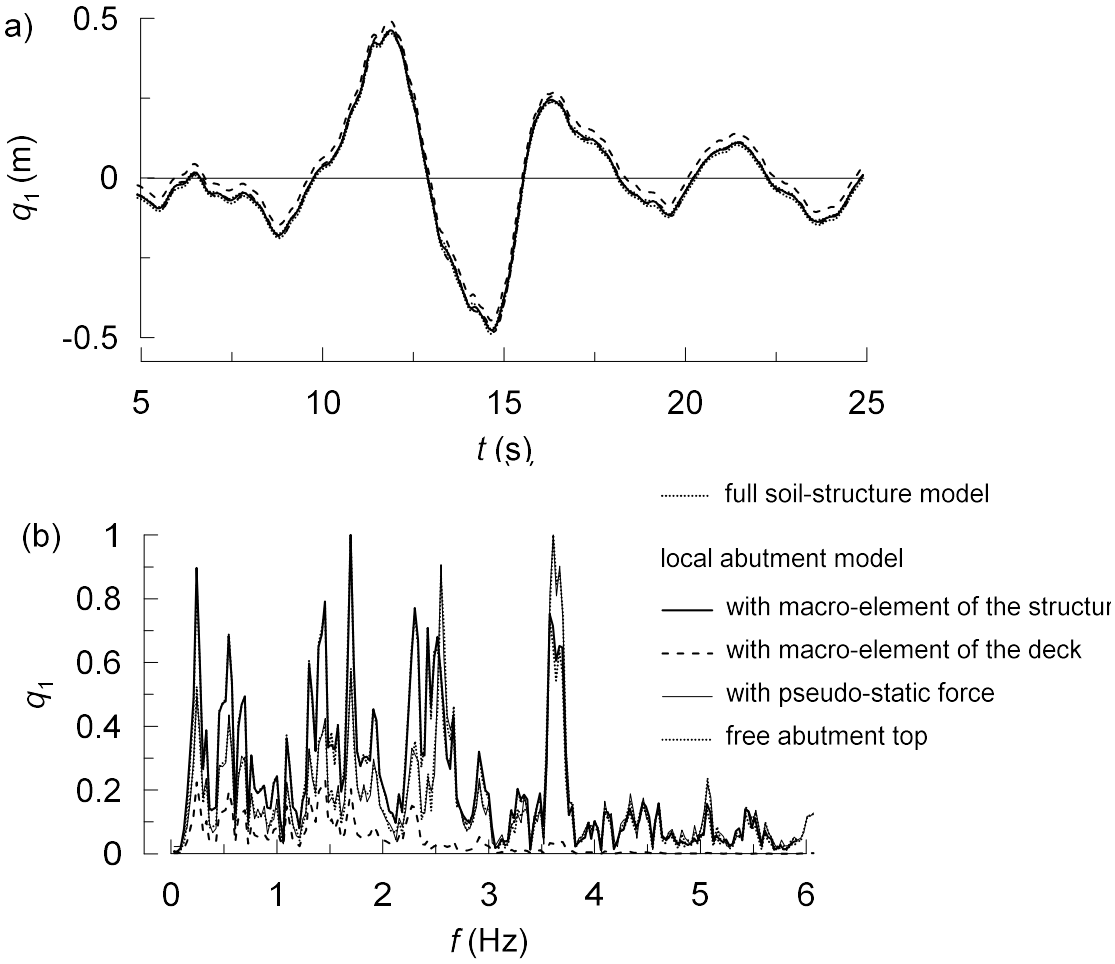

Figure 6.9: Time evolution of the displacement on the abutment top q_1 (a) and Fourier spectrum of the relative accelerogram (b) in the longitudinal direction. Comparison between different representations of the abutment-superstructure interaction: full soil-structure model, macro-element of the structure, macro-element of the sole deck, free wall top and equivalent pseudo-static force.

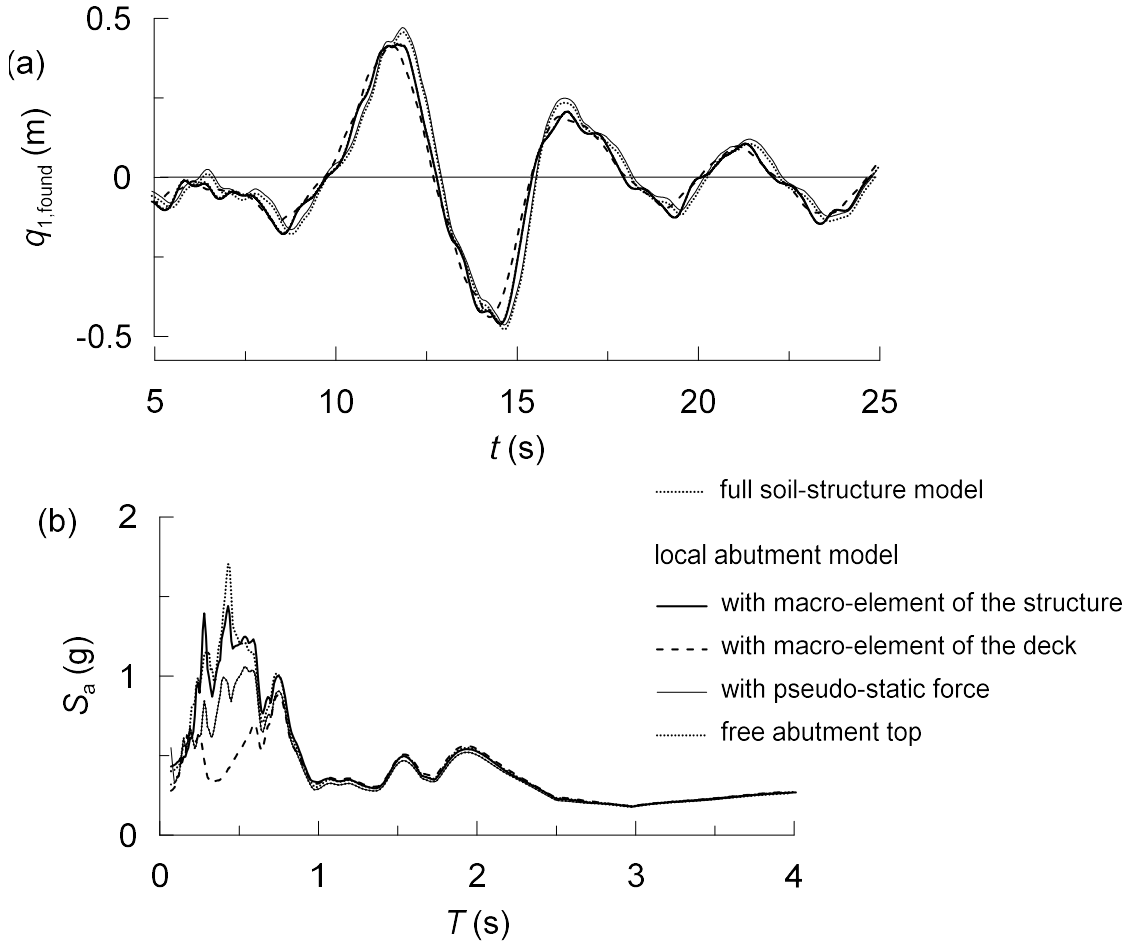

Figure 6.10: Time evolution of the displacement of the barycenter of the foundation $q_{1,found}$ (a) and 5 %-damped elastic response spectrum of the relative accelerogram (b) in the longitudinal direction. Comparison between different representations of the abutment-superstructure interaction: full soil-structure model, macro-element of the structure, macro-element of the sole deck, free wall top and equivalent pseudo-static force.

In principle, the proposed calibration procedure is of general validity, at least for a linear system, and can be easily extended to the remaining horizontal and vertical components of the earthquake motion, monitoring the resulting forces and moments at the deck-abutment joint.

6.3.2 Bi-axial elastic macro-element

The reference soil-structure system illustrated before is now perturbed by a bi-component seismic motion composed of the longitudinal and the vertical components of the Tabas record (Figure 3.49), as illustrated in Figure 6.11. The deck-abutment joint was regarded as a multi-directional device with no transmission of moments. In this case, the macro-element is composed of two transfer functions as follows

$$\begin{bmatrix} Q_1 \\ Q_3 \end{bmatrix} = \begin{bmatrix} TT_{11} & TT_{13} \\ TT_{31} & TT_{33} \end{bmatrix} \cdot \begin{bmatrix} q_1 \\ q_3 \end{bmatrix} = \begin{bmatrix} TT_{11} & 0 \\ 0 & TT_{33} \end{bmatrix} \cdot \begin{bmatrix} u_1 \\ u_3 \end{bmatrix}. \tag{6.2}$$

The coupled terms TT_{13} and TT_{31} were set equal to zero, neglecting for simplicity the directional coupling of the response. Otherwise, these transfer functions should have determined by following the general identification procedure described before, retrieving the force Q_3 produced by the displacement field u_1 at the foundation level and the force Q_1 induced by u_3.

The longitudinal transfer function determined in Section 6.3.1 is therefore combined with the vertical transfer function TT_{33}, the latter obtained by following the general identification procedure. Figure 6.12 compares the transfer functions of the structure in the two coordinate directions, together with the respective functions associated with the deck. The vertical response presents a bi-modal trend with a dominant peak at 0.07 s and a second peak at 0.5 s. The former is a global mode in which the second vibration mode of the deck, in the vertical direction, combines

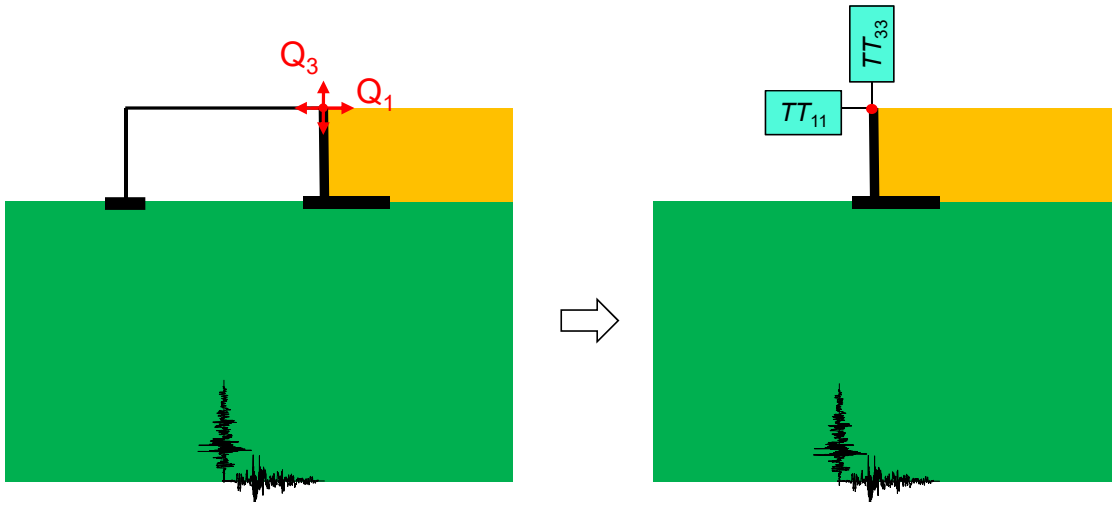

Figure 6.11: Bi-component seismic motion: from the full soil-structure model to the local model with macro-element.

with the higher vertical modes of the abutment and the pier, leading to a very stiff response with a high value of the interaction force Q_3. The second peak is instead associated with the first vertical mode of the deck without involving the vertical elements, leading to a longer but more deformable response; as a result, the maximum value of the interaction force is much lower. This second mode does not appear in the function TT_{11} because the longitudinal response is strongly controlled by the axial modes of the deck while the vertical response involves mainly its bending stiffness. In fact, looking at the dynamic amplification of the deck in the two directions (dashed lines in Figure 6.12), the corresponding peaks are close to those of the transfer functions of the structure, with amplitudes attenuated by the response of the vertical elements.

From a numerical point of view, the vertical transfer function was modelled by either a SDoF system or by a two degrees of freedom (2DoF) system. In both cases, the modal mass and damping associated with the peaks in the transfer functions were used in the two representations of the macro-element. The SDoF system was aimed to reproduce the dominant response of the structural system and presents

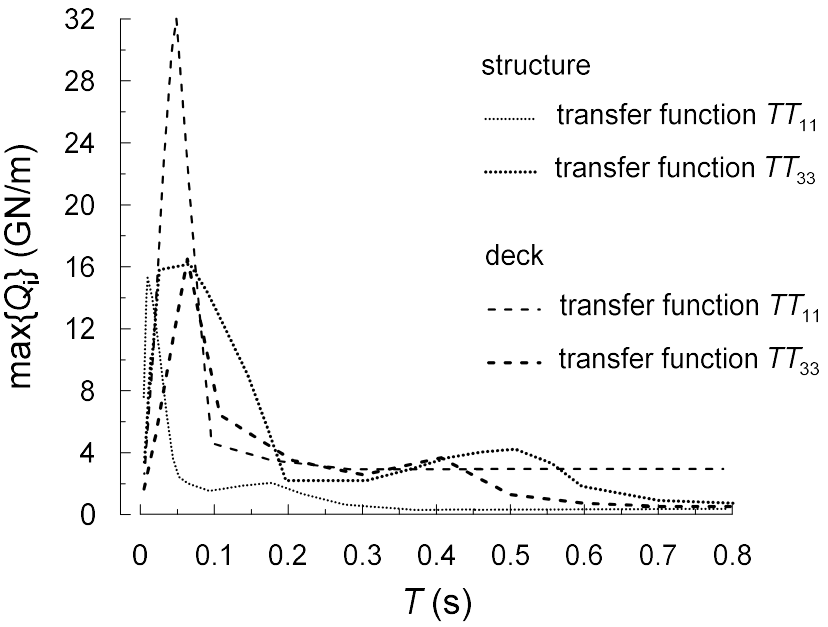

Figure 6.12: Comparison between the transfer functions of the structure (dotted lines) and of the deck (dashed lines), in the longitudinal TT_{11} and vertical TT_{33} directions.

a mass equal to $0.6 \cdot m_d$, with m_d the deck mass, which is combined in the 2DoF system with a second mass equal to $0.9 \cdot m_d$ that is the first mass participation of the deck in the vertical direction (peak at 0.5 s). The stiffness was instead defined by trial and error, modifying the deck stiffness in order to have a good reproduction of the maximum amplitudes. The resulting transfer functions are shown in Figure 6.13.

The vertical responses of the abutment considering the two vertical equivalent systems are compared in Figure 6.14, in terms of spectral accelerations in correspondence of the top and the foundation of the abutment. In order to focus on the vertical response, the soil domain is perturbed by the vertical component of the Tabas record. It is evident that the 2DoF system is able to follow much more closely the response of the full soil-structure system. The SDoF system is very stiff, because it is aimed to reproduce only the dominant vertical mode of the structure, and this leads to a remarkable overestimation of the spectral amplitudes up to a

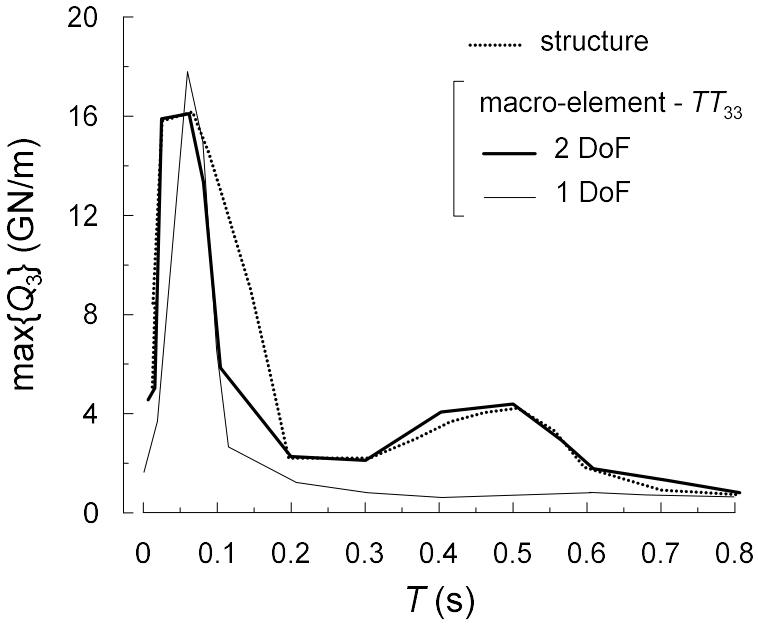

Figure 6.13: Transfer functions in the vertical direction: full structure (dotted line), abutment with SDoF macro-element (thin continuous line) and abutment with 2DoF macro-element (thick continuous line).

period of about 1.2 s. Because of the high stiffness of the structure under examination, the response of the abutment is mainly controlled by the deformability of the surrounding soil. Based on the above results, the bi-modal representation of the macro-element was taken as a reference in the following simulations with a combined longitudinal-vertical input motion.

Figure 6.15 shows the time histories of the longitudinal interaction force and the relative Fourier amplitudes in the case of a bi-component seismic motion applied to the base of the soil domain. The bi-directionality of the seismic motion leads to a decrease of the maximum interaction force, compared to the mono-directional propagation of the seismic motion (Figure 6.5), caused by the directional coupling of the displacement field for the non-symmetric geometry of the abutment. The macro-element reproduces pretty well the frequency content of the force Q_1 but underestimates its maximum amplitudes. Similar considerations can be inferred for the vertical interaction force Q_3, shown in Figure 6.16, but with a more detailed

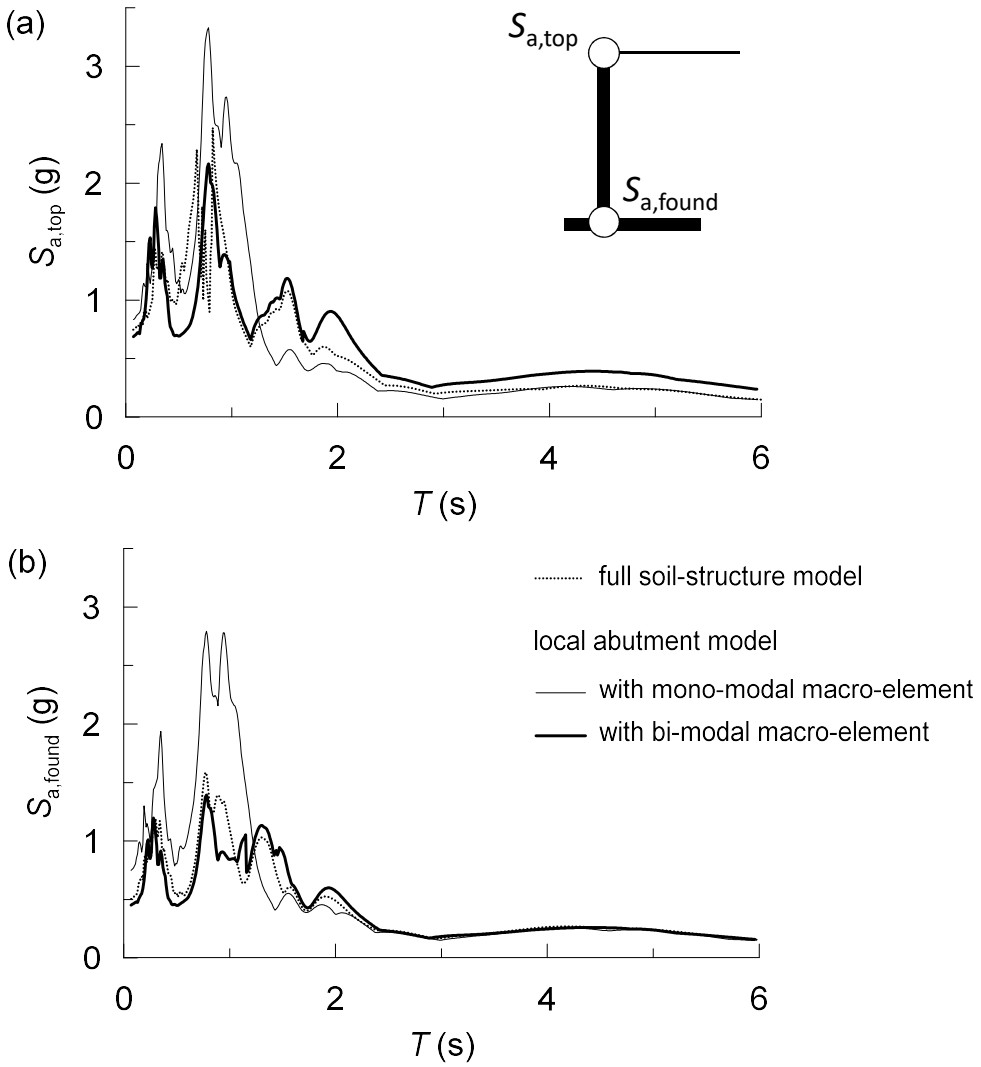

Figure 6.14: Comparison between the vertical response of the abutment with a mono-modal macro-element and a bi-modal macro-element: 5%-damped elastic response spectra at the abutment top (a) and at the foundation level (b) in the vertical direction.

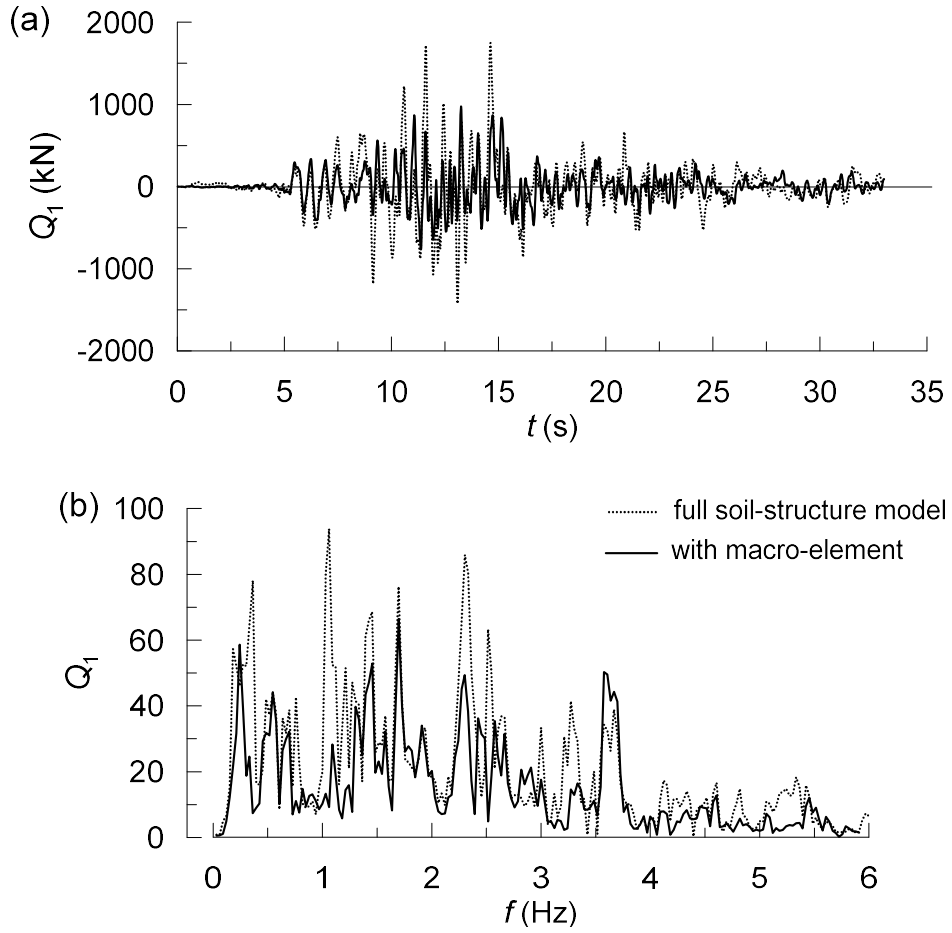

Figure 6.15: Time evolution of the interaction force Q_1 (a) and relative Fourier spectrum (b) in the longitudinal direction recorded at the abutment-deck contact: comparison between the full soil-structure model and the model with macro-element.

reproduction of the maximum inertial effects.

Figures 6.17 and 6.18 depict the elastic response spectra at the deck-abutment contact in the longitudinal and vertical direction, respectively. The spectral accelerations of the full model in the case of a bi-component motion decrease and, more evidently in the vertical direction, the dominant peaks of the spectra move to larger periods for the higher deformability of soil induced by the multi-directionality of the seismic motion.

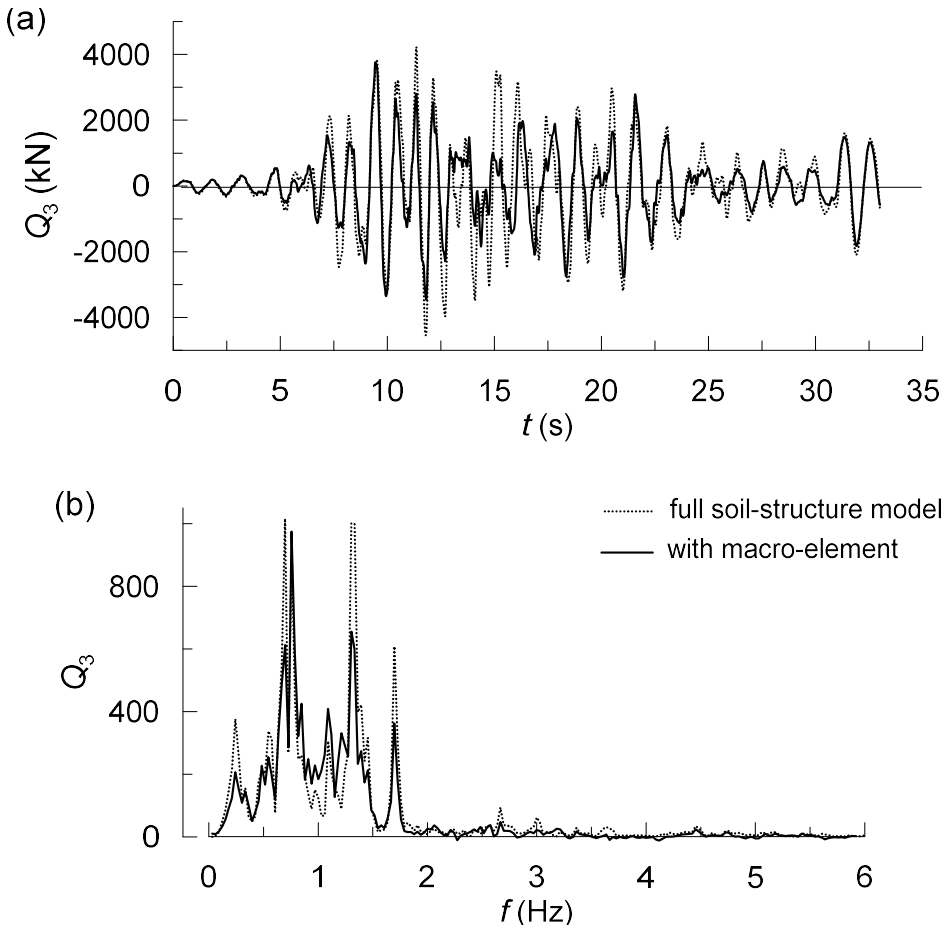

Figure 6.16: Time evolution of the interaction force Q_3 (a) and relative Fourier spectrum (b) in the vertical direction recorded at the abutment-deck contact: comparison between the full soil-structure model and the model with macro-element.

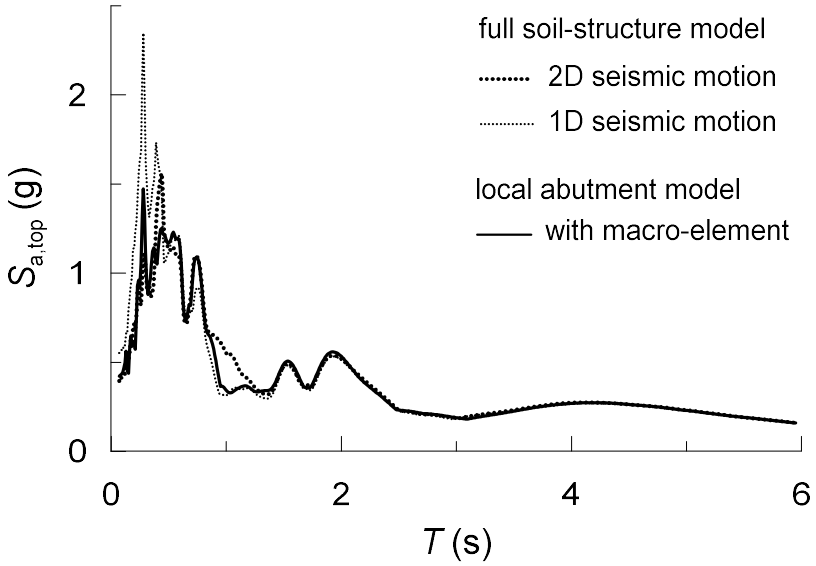

Figure 6.17: 5%-damped elastic response spectra at the abutment top in the longitudinal direction: comparison between the full soil-structure model and the model with macro-element.

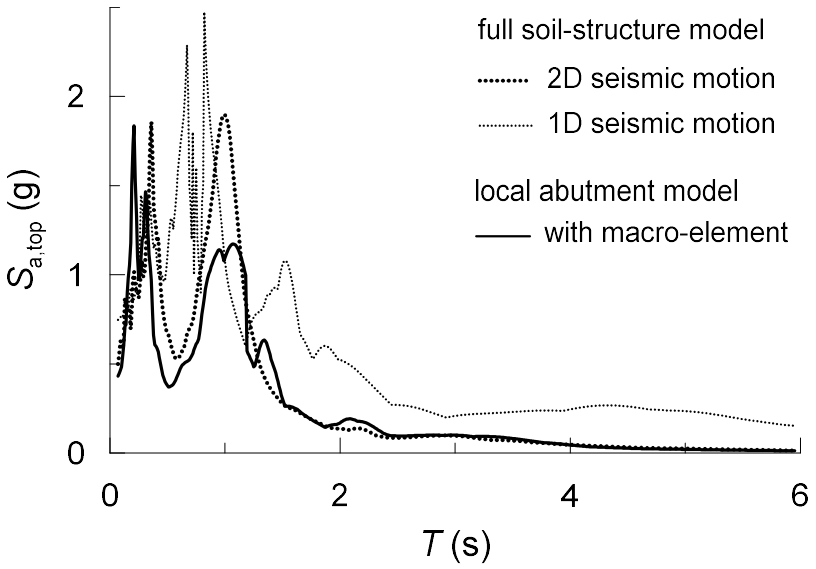

Figure 6.18: 5%-damped elastic response spectra at the abutment top in the vertical direction: comparison between the full soil-structure model and the model with macro-element.

6.4 Effect of the dynamic response of the embankment

The identification procedure of the transfer tensor takes for granted that the macro-element is an intrinsic property of a structure, not depending on the behaviour of the soil-abutment system. In order to verify this assumption, a parametric study on the stiffness of the embankment was carried out, varying the shear modulus of soil of two orders of magnitude with respect to the reference case exposed so far, while the mechanical properties of the foundation soil were kept constant. For the sake of clarity, the longitudinal component of the Tabas record was assumed as the input motion for all the configurations analysed. Hence, only the longitudinal transfer function of the macro-element is considered, with the properties determined in Section 6.3. The behaviour of the macro-element was quantified looking at its internal force Q_1, in its time evolution and frequency content, and at the spectral accelerations of the abutment top $S_{a,top}$. Four values of the shear modulus ratio $G_{emb}/G_{emb,ref} = 0.1, 0.5, 2.0, 10.0$ were analysed, with $G_{emb,ref}$ the modulus of the embankment in the reference case (Section 6.1).

From the time histories of the interaction force obtained by the full soil-structure model, shown in Figure 6.19, it can be observed that the maximum amplitudes increase with the stiffness of the embankment up to a factor of roughly 1.5 for $G_{emb} \geq 2 \cdot G_{emb,ref}$. The macro-element reproduces quite well the inertial effects transmitted to the abutment in all the configurations, even if for very stiff embankments, $G_{emb} = 10 \cdot G_{emb,ref}$, the equivalent system leads to an underestimation the maximum interaction force of about 30 %. This behaviour in the time domain is accompanied by a redistribution of the frequencies when the soil stiffness changes, as it appears apparent in Figure 6.20: the stiffest embankment leads to a slight deamplification of the interaction force for frequencies lower than about 2.5 Hz, compared to the case $G_{emb} = 0.1 \cdot G_{emb,ref}$, in favour of a sensible amplification of the inertial

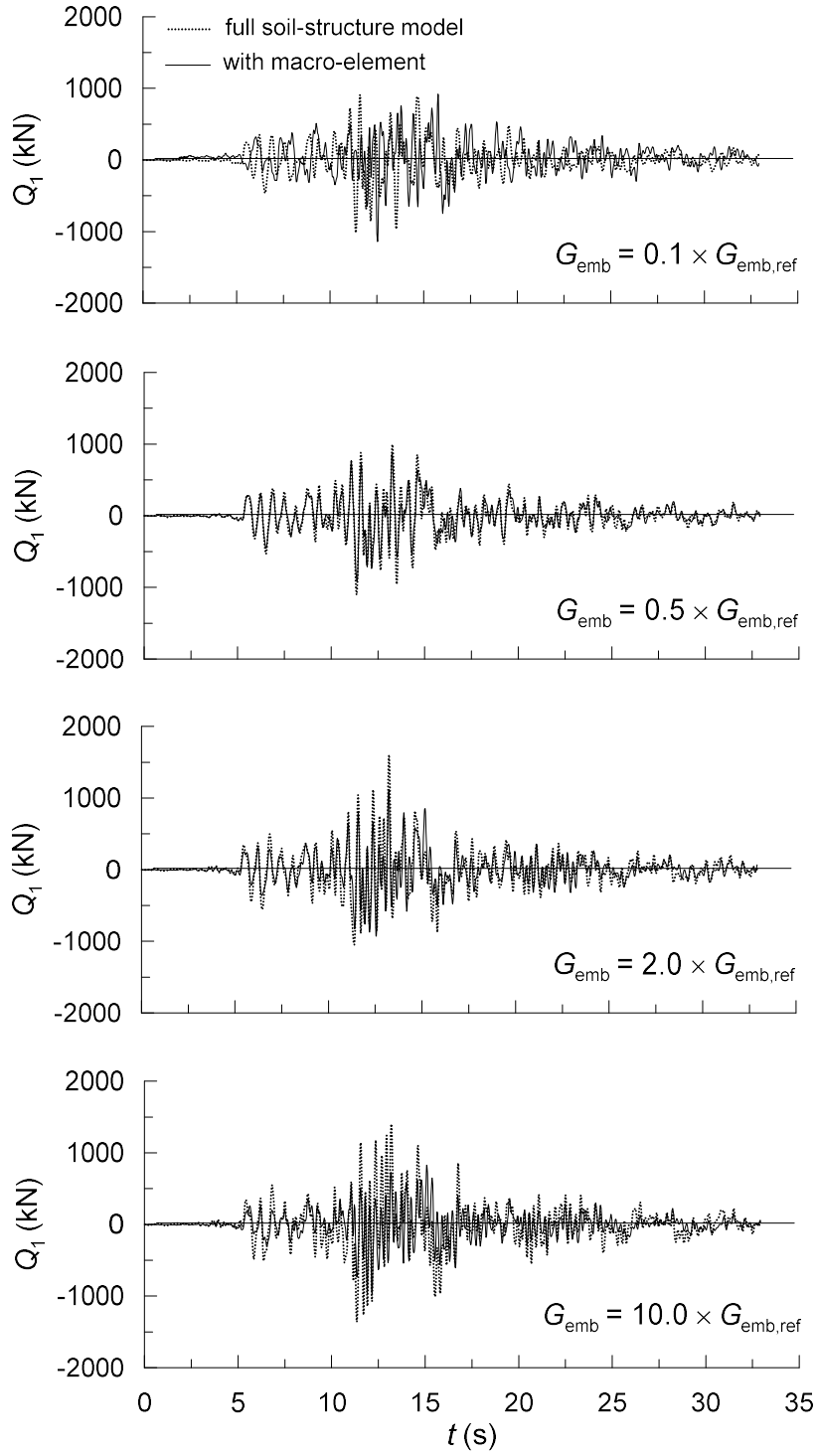

Figure 6.19: Time histories of the longitudinal interaction force at the deck-abutment contact for different values of the embankment stiffness G_{emb}.

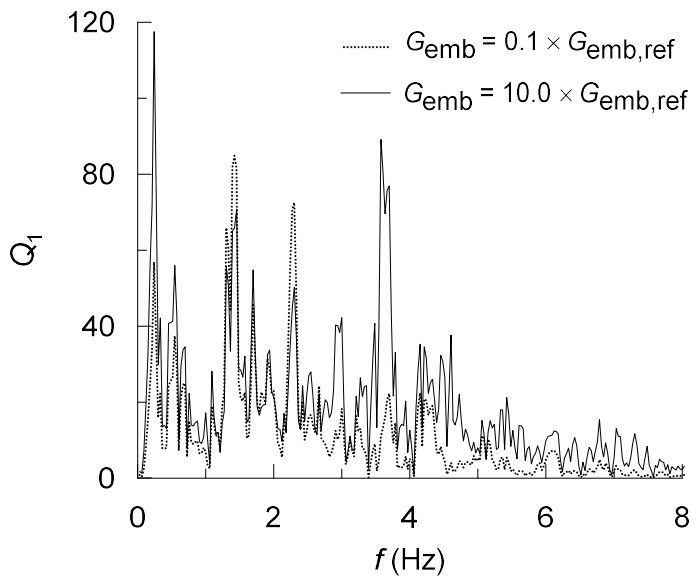

Figure 6.20: Fourier spectra of the interaction force Q_1 for a stiffness of the embankment of $G_{emb} = 0.1 \cdot G_{emb,ref}$ and $G_{emb} = 10 \cdot G_{emb,ref}$.

effects for higher frequencies.

Finally, Figure 6.21 shows the response spectra at the abutment top. There is a good agreement between the full model and local model with macro-element, although the model with the macro-element appears to be less sensitive to variations of the embankment stiffness. In the full model, the dominant peak of the spectrum, occurring at about 0.5 s, tends to disappear as the soil stiffness goes up while the amplitudes at high frequencies increase progressively. The response of the local model of the abutment presents the same tendency but especially the dominant peak reduces more slowly.

In light of the above results, it can be inferred that, for common values of the embankment stiffness, the definition of the macro-element does not depend on the response of the soil-abutment system. Only for extremely stiff embankments the macro-element response starts being affected by the dynamic behaviour of the embankment because the deformability of the abutment becomes comparable with the stiffness of the embankment. In these cases, the determination of the transfer func-

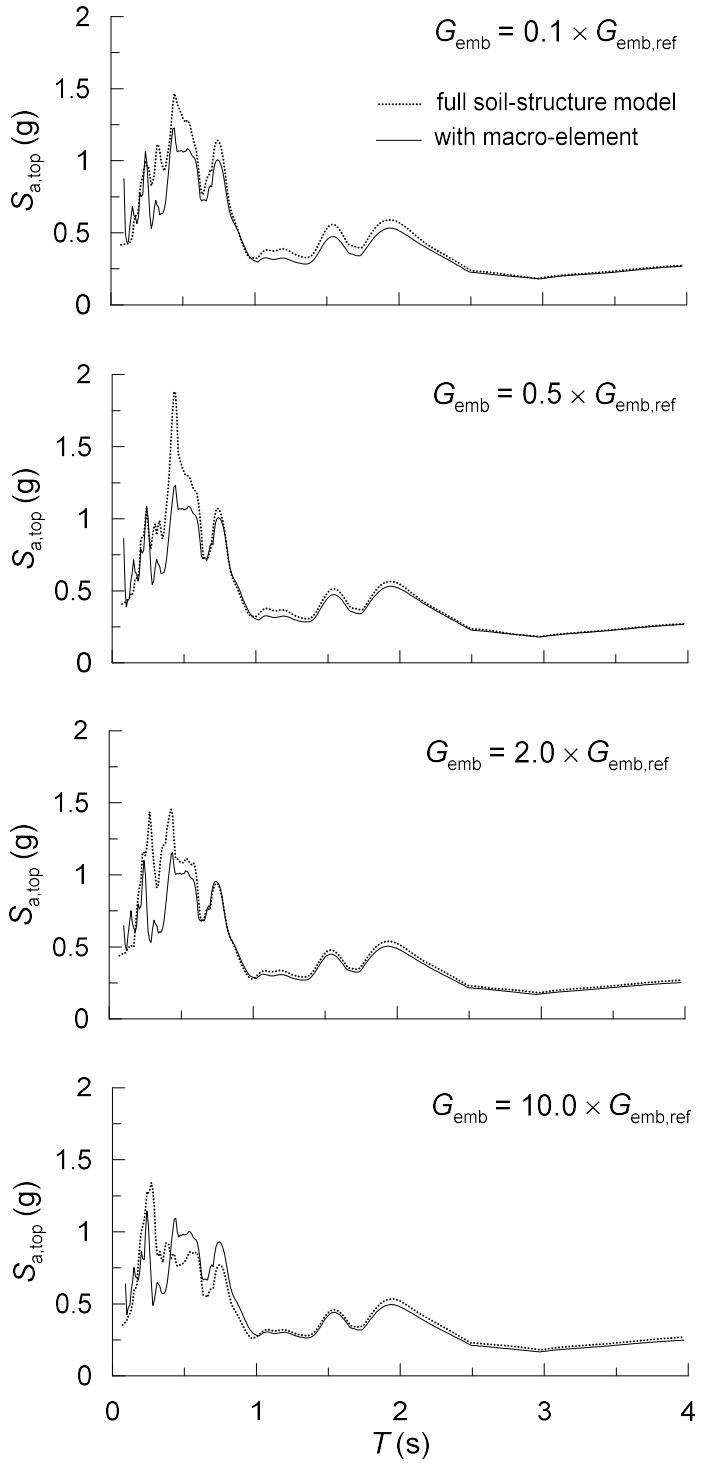

Figure 6.21: 5%-damped elastic response spectra at the deck-abutment contact for different values of the embankment stiffness.

tions based on a global structural model only would lead to a too deformable macro-element with moderate underestimation of the seismic actions exchanged at the deck-abutment contact. It is worth noticing, however, that the stiffness of the reference embankment reflects common values used in practice and therefore these extreme cases in which sub-structuring would partially lose its effectiveness are hardly obtainable.

6.5 Effect of the elastic-plastic behaviour of the foundation soil

The main concern about the assumption of a visco-elastic behaviour for the soil is that it is completely reversible and, consequently, the post-earthquake configuration of the structure coincides with the initial state. This is a strong assumption that is now removed to investigate the performance of the macro-element of the bridge structure when the soil develops permanent displacements. In the reference soil-structure system (Section 6.3), the PDMY model (Yang et al. 2003) was adopted to reproduce the elastic-plastic behaviour of soil, calibrated in order to have the same initial tangent of the elastic material used so far. After the first yield, the stiffness of the PDMY model decreases progressively until reaching the ultimate strength. The input parameters of the PDMY model chosen for the foundation soil and the embankment are listed in Table 6.1. The embankment presents a lower mass density and a slightly higher stiffness because it is regarded as a partially saturated soil. For the same reason, different parameters that control the rate of contraction and dilation were assigned to the two soils, while a unique projection of the Critical State Line on the compressibility plane was considered for both materials. The Critical stress ratio M is instead the variable quantity in the parametric study since it is a primary factor controlling the development of permanent strains due to shearing in the soil, with a friction angle ranged between $30 \div 39$ °. The structure is still

Variable	Foundation soil	Embankment
ρ_{soil} (Mg/m^3)	2.243	2.039
G_r	$9.5 \cdot 10^4$	$1.15 \cdot 10^5$
ν	0.2	0.2
p'_r	80.0	80.0
d	0.5	0.5
$\gamma_{d,max}$	0.1	0.1
ϕ_{PTL}	26°	26°
c_1	0.045	0.013
c_2	5.0	5.0
d_1	0.06	0.3
d_2	3.0	3.0
M	$1.2 \div 1.59$	$1.2 \div 1.59$
λ_c	0.02	0.02
e_0	0.9	0.9
ξ	0.7	0.7
N	40	40

Tabella 6.1: Parameters of the PDMY model adopted for the foundation soil and the embankment.

assumed as a linear visco-elastic body, represented by the macro-element previously defined (Section 6.2). For simplicity, the sole longitudinal component of the Tabas record was employed in this study.

As a first result, consider the entire soil domain characterised by a Critical stress ratio of 1.55 ($\varphi' = 38$ °). The response of the soil-abutment model with macro-element is compared with that of the full soil-structure system in Figures 6.22, 6.23 and 6.24. It can be observed that the displacement field of the abutment keeps being well reproduced by the macro-element of the bridge structure, while the latter is not able to reproduce the progressive development of the permanent internal force at the deck-abutment contact due to the attainment of the soil strength underneath the abutment and the pier. In fact, the plastic strains developing in the soil lead to a different behaviour of the two foundations and, as a result, to a deformed permanent configuration of the entire structure after the shaking: the relative displacement $q_{1,rel}$ between the abutment and the pier foundations (Figure 6.22(b)) show that the distance between the two element increases progressively in time from about 5 s to 15 s, in which the Tabas record attains the maximum amplitudes. These relative

displacements are accommodated by the structure, resulting in a very similar development of the offset in the interaction force. Note that the plastic response of the soil has a minor effect on the frequency content of the interaction force, that is still well reproduced by the macro-element. In the following, the development of this permanent effect at the deck-abutment contact is analysed in detail in order to reach a clear understanding on its relevance in the local behaviour of the abutment.

6.5.1 Soil plasticity curves of the transfer tensor

The results of the parametric study on the soil strength are concisely expressed in terms of three output quantities of the structural system: the permanent displacements of the pier and the abutment foundations, $q^{p}_{1,found}$ and $q^{a}_{1,found}$ respectively, and the permanent interaction force Q_1 on the abutment top in the longitudinal direction. A normalised version of these quantities, divided by the respective maximum values, is plotted as a function of the soil strength $tg(\varphi')$ in Figure 6.25, from which one can deduce some general information about the permanent effects associated with the abutment-superstructure interaction. The trend of the permanent interaction force with the soil strength is named soil plasticity curve of the transfer tensor since it shows the effect of the soil plasticity on the deck-abutment interaction. In other words, this curve gives a direct evaluation of the permanent effect that should be added to the response of the macro-element. The other two curves show the progressive increase of the permanent effects at the foundations level giving information about the variability of the relative pier-abutment displacement after the earthquake.

In high-strength soils, in spite of the development of important permanent forces induced by the relative motion between pier and abutment, the absolute permanent displacements at the foundation level are very small. The lower the soil strength, the higher the permanent interaction force since the relative displacement increases,

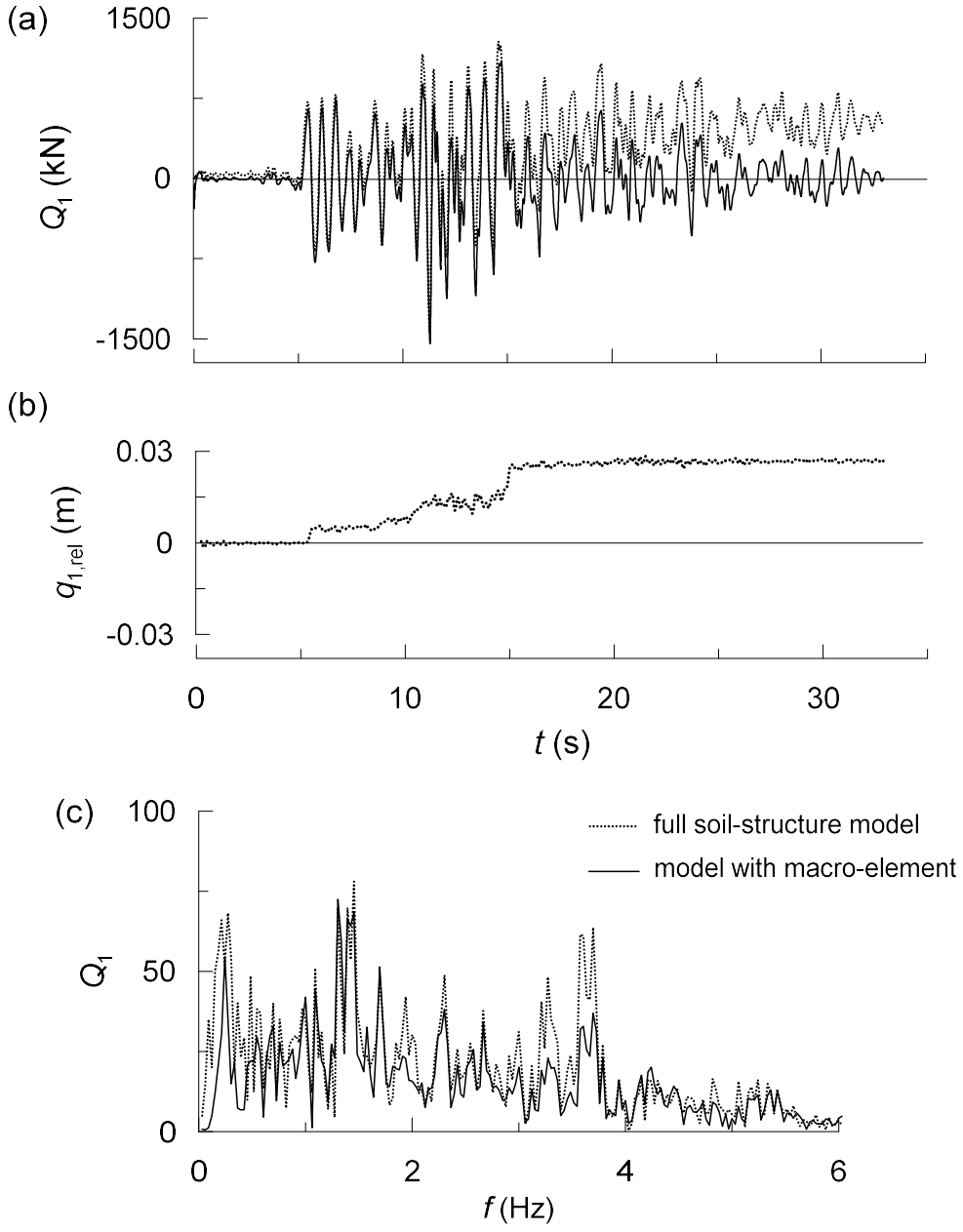

Figure 6.22: (a) Time histories of the longitudinal interaction force Q_1 at the deck-abutment contact; (b) time history of the relative displacement $q_{1,rel}$ between the abutment and the pier; (c) Fourier spectra of the interaction force Q_1.

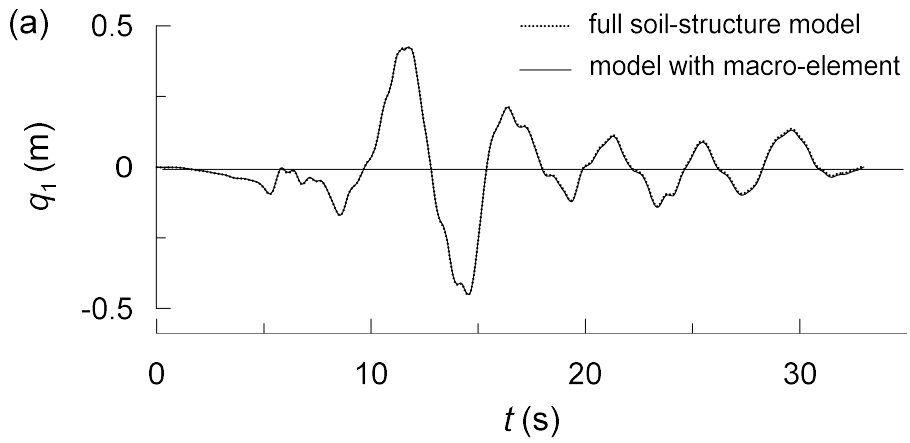

Figure 6.23: Time histories of the longitudinal displacement of the top of the abutment.

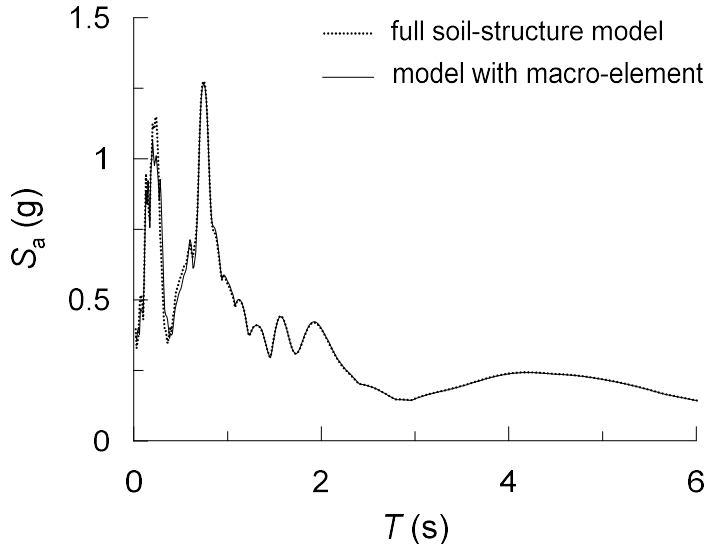

Figure 6.24: 5%-damped elastic response spectra of the longitudinal acceleration of the abutment foundation.

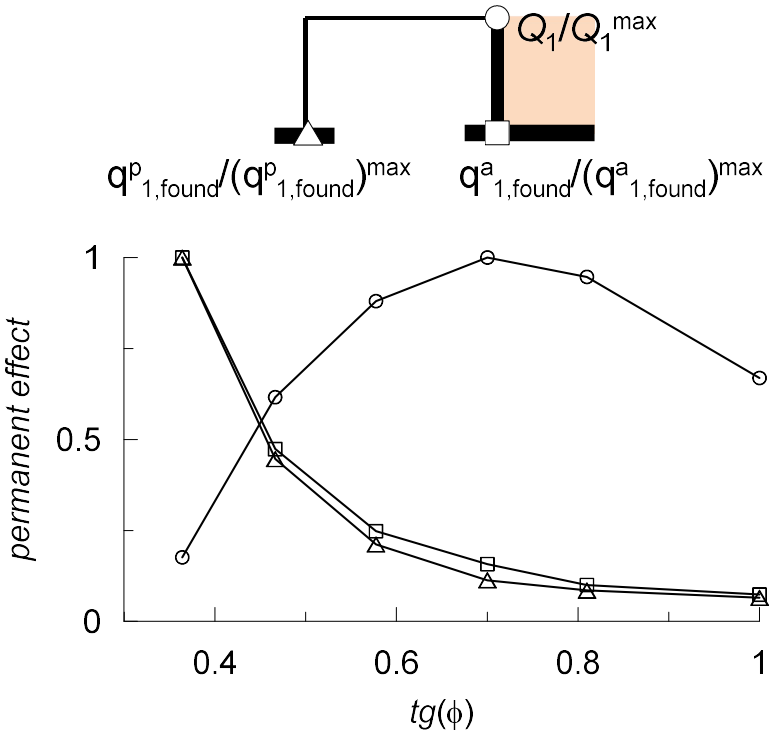

Figure 6.25: Soil plasticity curve of the macro-element.

but not in a monotonic manner because when the irreversible displacements of the foundation soil start increasing more than linearly, $tg(\varphi') < 0.7$, the interaction force reduces with a similar gradient. This leads to assume that in the case of low-strength soils, the plastic deformation processes occur mainly in depth, in the far field where there is no appreciable interaction between soil and structure. Accordingly, the seismic action that reaches the foundations result to be somewhat uniform because limited by the soil strength, giving a modest permanent interaction force. By contrast, in presence of high-strength soils, the plastic displacements localise mainly in the volume of soil that interacts with the foundations. This leads to a different response between the pier and the abutment and, accordingly, relevant permanent interaction forces.

By entering the soil plasticity curve with the specific friction coefficient of the foundation soil, one can include the effect of the plastic response of soil in the re-

sponse of the macro-element of the bridge structure. For a generic soil-structure system, the following procedure can be utilised to determine the soil plasticity curve without performing an exhaustive parametric study on complex soil-structure numerical models. The basic hypothesis is that the shape of the soil plasticity curve and the displacement curves does not vary in the normalised space. The identification of these curves is based on the definition of some cardinal points illustrated in Figure 6.26. Considering a unique trend for both the foundation displacements, $q^a_{1,found}$ and $q^p_{1,found}$, and recognising that appreciable irreversible displacements of soil develop only when the soil strength is lower than a critical value $tg(\varphi')_{cr}$, the displacement curve can be determined by carrying out nonlinear free field site response analyses of the soil domain (soil column) varying the soil strength. As a result, one can obtain an estimation of $tg(\varphi')_{cr}$, starting from which the plastic response of soil becomes much more pronounced with development of significant permanent displacements, and of the permanent displacement associated with the lowest strength. The critical value $q_{adim,cr}$ of the soil displacement can be taken in first approximation equal to $0.1 \div 0.15$, consistent with the value obtained for the system under examination. In this way, the displacement curve is completely defined. Finally, the effective value of the permanent interaction force at the critical strength, representing the scale factor of the soil plasticity curve, can be obtained by a sole elastoplastic analysis on the entire soil-structure system or, in a simplified manner, it can be related to the shear strength of the foundation soil.

6.5.2 Relevance in engineering applications

The permanent effects arising in the deck-abutment interaction can occur when there is a coupled behaviour between the abutment and the pier foundations. The resulting permanent forces on the abutment top are therefore proportional to the stiffness of the structural system. The structure considered in this study is a very

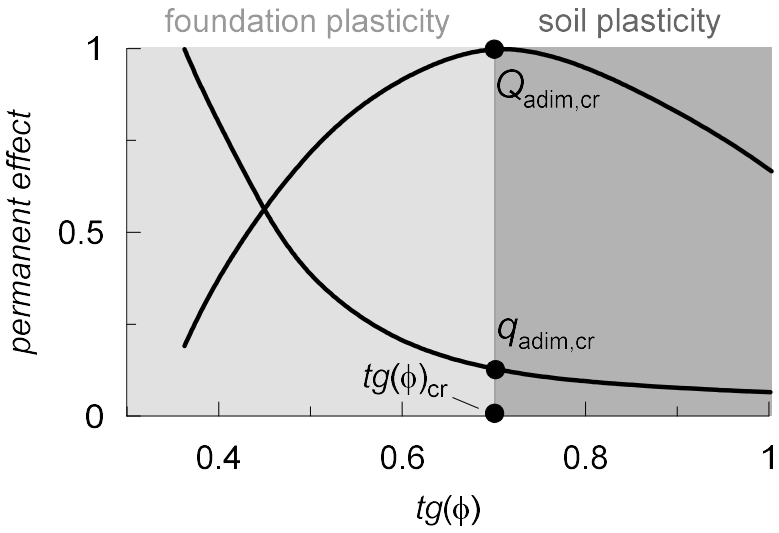

Figure 6.26: Cardinal points of the soil plasticity curve.

stiff system and consequently the permanent effects are not negligible. Hence, it is interesting to explore the actual significance of the permanent interaction forces in common girder bridges. In order to give a first answer, a sensitivity analysis on the stiffness of the structure at hand was performed. In Figure 6.27, the permanent force is plotted as a function of the stiffness of the structure, both normalised to the respective values $Q_{1,perm}^{(ref)}$ and $h_{d,p}^{(ref)}$ relative to the reference configuration of the structure. The axial stiffness of the deck h_d and the bending stiffness of the pier h_p were changed separately giving the two curves shown in Figure 6.27. These curves present a very similar trend and, as expected, the idealised system taken as reference in this study maximises the permanent interaction force because of its very high stiffness. For $h_{d,p}/h_{d,p}^{(ref)} < 0.6$, the permanent forces start decreasing very rapidly.

In order to make this result comparable with real girder bridges, Figure 6.28 plots the normalised permanent force as a function of the fundamental period of the structure $T_{st,d}$. The two curves are associated with the variation of the stiffness in the deck and in the pier, in which for each configuration the dominant period in the

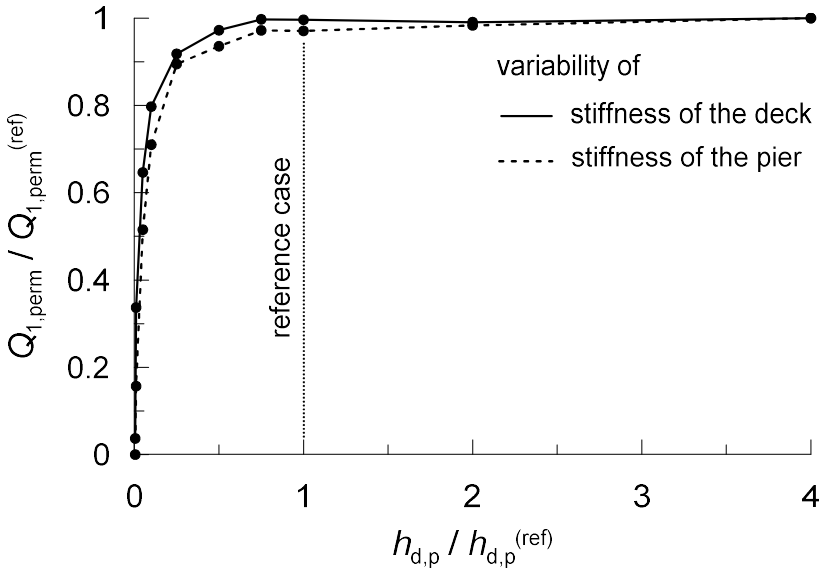

Figure 6.27: Permanent interaction force Q_1 at the deck-abutment contact plotted as a function of the normalised stiffness of the structure $h_{d,p}/h_{d,p}^{max}$.

direction of the ground motion was determined, i. e. the global mode that maximise the interaction force on the abutment top. Also in this plane, these curves show a very similar trend in which, after a first narrow range at very low periods where the permanent force assumes essentially a constant value, approximatively equal to that in the reference case, the permanent effect starts decreasing more than linearly as the period rises. In particular, focusing on the representative interval of periods for girder bridges (shadow zone), the permanent force reduces of about 30 % at $T_{st,d} = 1$ s and 75 % at $T_{st,d} = 3$ s, making this effect much less important.

To sum up, the permanent forces at the deck-abutment contact are caused by the development of irreversible differential displacements in the respective foundation soils. It was found that the permanent forces cannot be reproduced by the macro-element of the bridge structure but they can be relevant only in the case of very stiff structural systems.

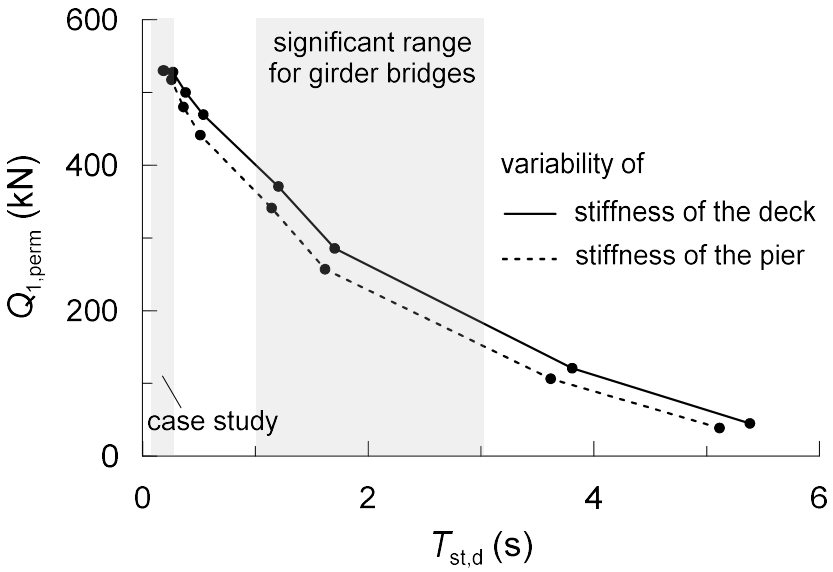

Figure 6.28: Permanent interaction force Q_1 at the deck-abutment contact plotted as a function of the fundamental structural period $T_{st,d}$.

6.6 Different seismic scenarios

In addition to the Tabas record, the macro-element was tested in other two seismic scenarios, namely Ducze (Turkey, 1999) and Denaly (Alaska, 2002) (Record references: NGA_8165DUZCE and NGA_2114DENALY in the PEER Ground Motion Database, Section NGA-West2, https://ngawest2.berkeley.edu), chosen with a completely different frequency content. With reference to the longitudinal motion, the respective records were scaled in order to keep the same Arias intensity (Arias, 1970) as that of the Tabas record used in the reference analyses, equal to 12.56 m/s, and the resulting elastic response spectra are shown in Figure 6.29. The Duzce record is characterised by a short duration and spectral accelerations localised at high frequencies compared to the Denaly record that is instead a long motion with a predominant period at about 1.0 s.

The time histories of the longitudinal interaction force Q_1 are depicted in Figure 6.30. The Denaly scenario generates much higher interaction forces than the high

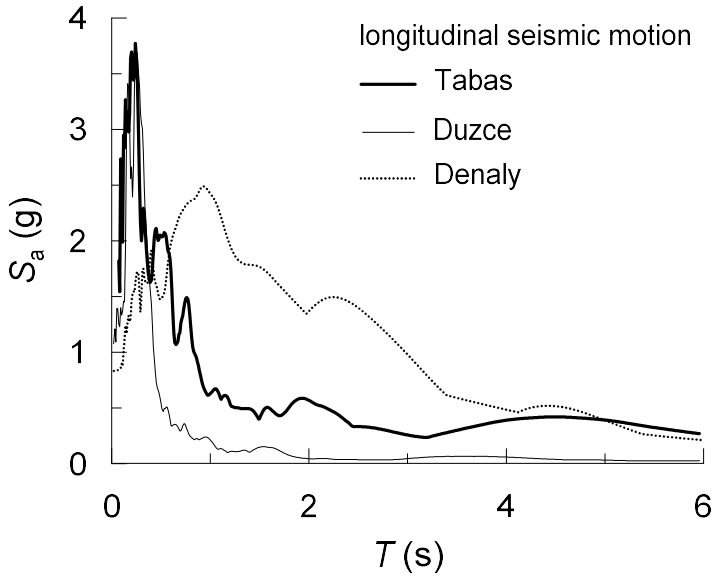

Figure 6.29: 5%-damped elastic response spectra in the longitudinal direction of the Tabas, Duzce and Denaly records.

frequency signal of Ducze, whose trends are in both cases well reproduced by the macro-element placed on the abutment top. Nonetheless, the post-earthquake interaction forces are of the same order of magnitude: they result equal to 421 kN and 445 kN for the Denaly and Duzce record, respectively, and a value of 501 kN was instead recorded for the Tabas scenario. Therefore, the permanent force on the abutment appears mainly linked to the energy content of the seismic motion rather than to its frequency content. In effect, the results of a sensitivity analysis varying the Arias intensity of the three seismic records considered, not shown for brevity, showed that the permanent deck-abutment force for the structural system at hand increases with the square of the Arias intensity.

The displacement of the abutment top, illustrated in Figure 6.31, is much more pronounced for the low-frequency seismic signal of Denaly, giving a permanent displacement of about 0.074 m compared to 0.045 m and 0.035 m developed in the case of the Duzce and Tabas records, respectively. In this regard, a satisfying agree-

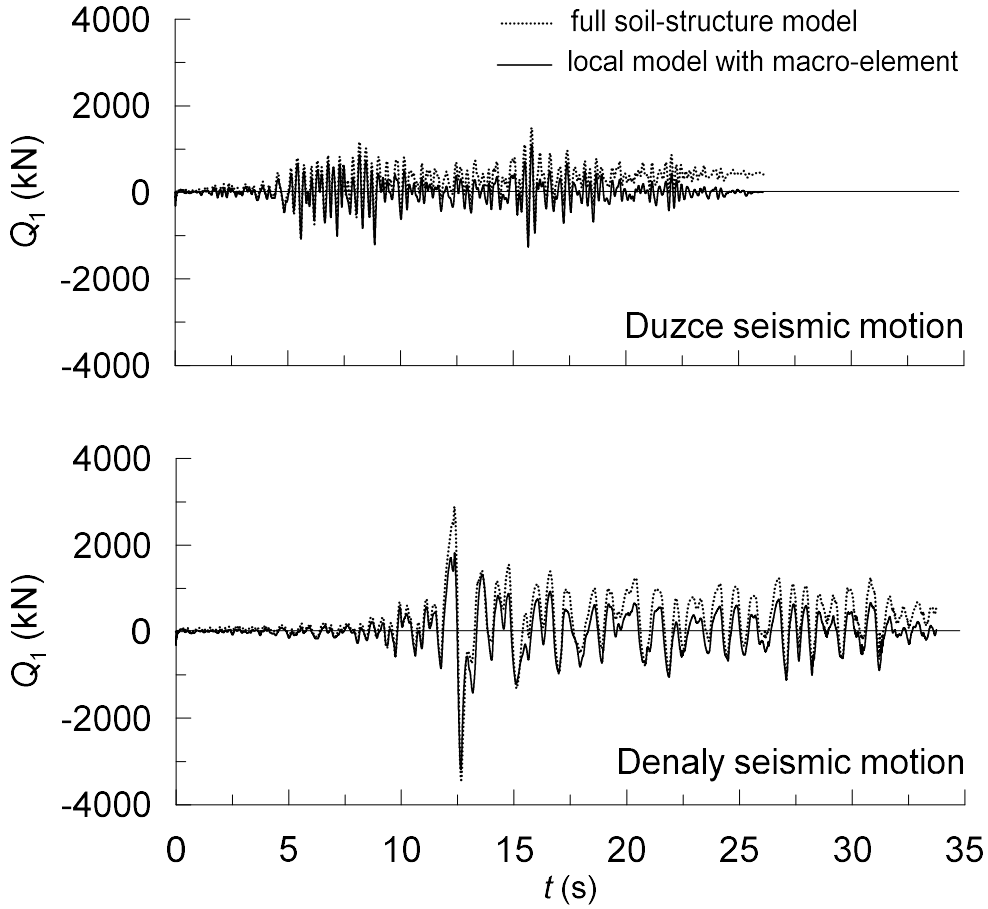

Figure 6.30: Time evolution of the interaction force Q_1 in the longitudinal direction recorded at the deck-abutment contact.

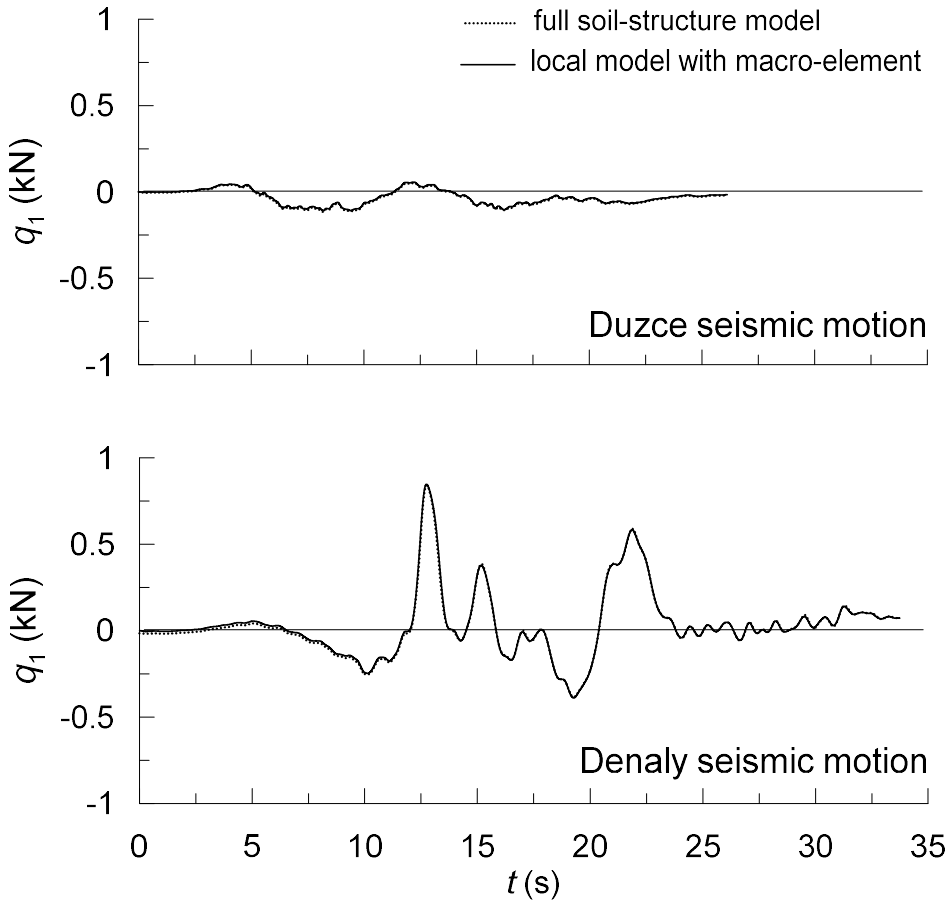

Figure 6.31: Time histories of the longitudinal displacements of the abutment top.

ment can be observed between the response of the abutment in the full soil-structure model and in the local model with macro-element, as well as in terms of spectral accelerations acting on the deck-abutment joint, represented in Figure 6.32, and at the foundation level, Figure 6.33. By comparing the foundation input motion with the motion at the abutment top, it can be noticed an opposite tendency: the spectral accelerations of Denaly are significantly amplified by the abutment response while the motion attenuates in the case of Duzce. This might be due to the fact that the volume of soil interacting dynamically with the abutment filters the seismic motion according to its own dynamic characteristics and, as a result, tends to attenuate the amplitudes at medium-high frequencies.

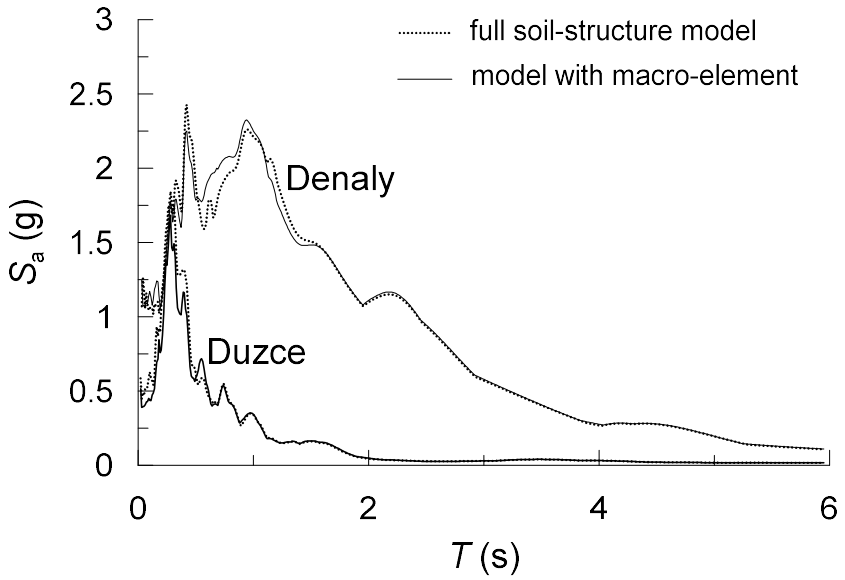

Figure 6.32: 5%-damped elastic response spectra of the longitudinal accelerograms recorded at the deck-abutment contact.

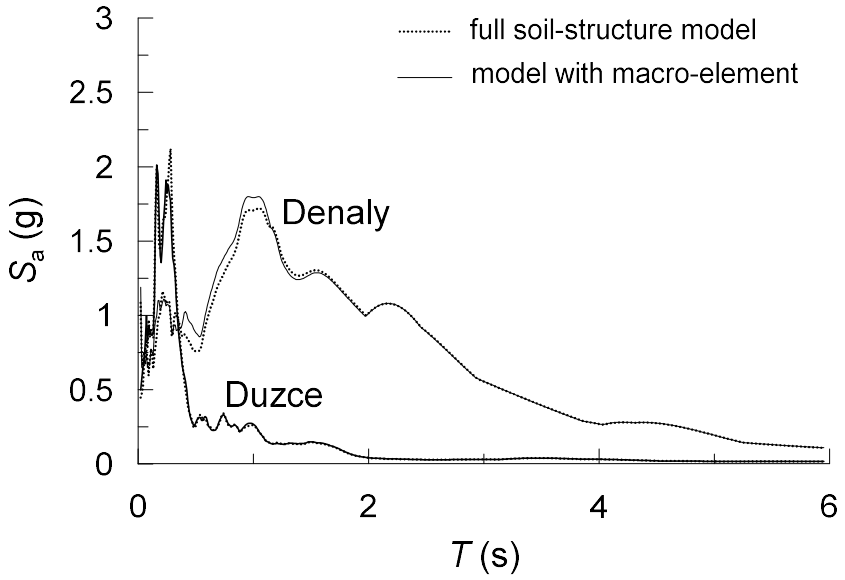

Figure 6.33: 5%-damped elastic response spectra of the longitudinal accelerograms recorded at the abutment foundation.

6.7 Effect of pore water pressure

Pore water pressures alter the stiffness and strength of soil and, accordingly, the abutment response. Nonetheless, in Section 6.4 it has been demonstrated that the macro-element can be reasonably regarded as an intrinsic property of the structure and therefore its formulation does not depend on the degree of saturation of soil.

As an example, consider the reference configuration of the soil-structure system shown in Section 6.3, in which now the foundation soil is assumed saturated. The embankment was instead kept dry since, in reality, it is a partially saturated medium. The elastic-plastic behaviour of soil was reproduced through the PDMY model as described in detail in Section 6.5. The longitudinal component of the seismic motion of Tabas was considered in the computation and the macro-element of the structure was composed of a sole equivalent mechanical system, placed on the abutment top in the longitudinal direction, with the mechanical properties defined in Section 6.3.1. The efficiency of the macro-element is quantified in Figure 6.34 looking at the interaction force and the elastic response spectrum at the abutment top. In the full soil-structure model, the presence of pore water pressures in the foundation soil leads to a decrease of the maximum seismic actions exchanged at the deck-abutment contact, either in terms of interaction forces or spectral accelerations. This is mainly due to the reduction of the soil strength beneath the foundation that limits the maximum amplitudes of the seismic motion in the soil domain, without however an appreciable variation of its frequency content. Apart from neglecting the development of the permanent offset of the interaction force, the response of the local model of the abutment with macro-element reproduces with a good level of accuracy of the effects above, providing a further confirmation that the macro-element of the bridge structure is mainly dependent on the structural features only.

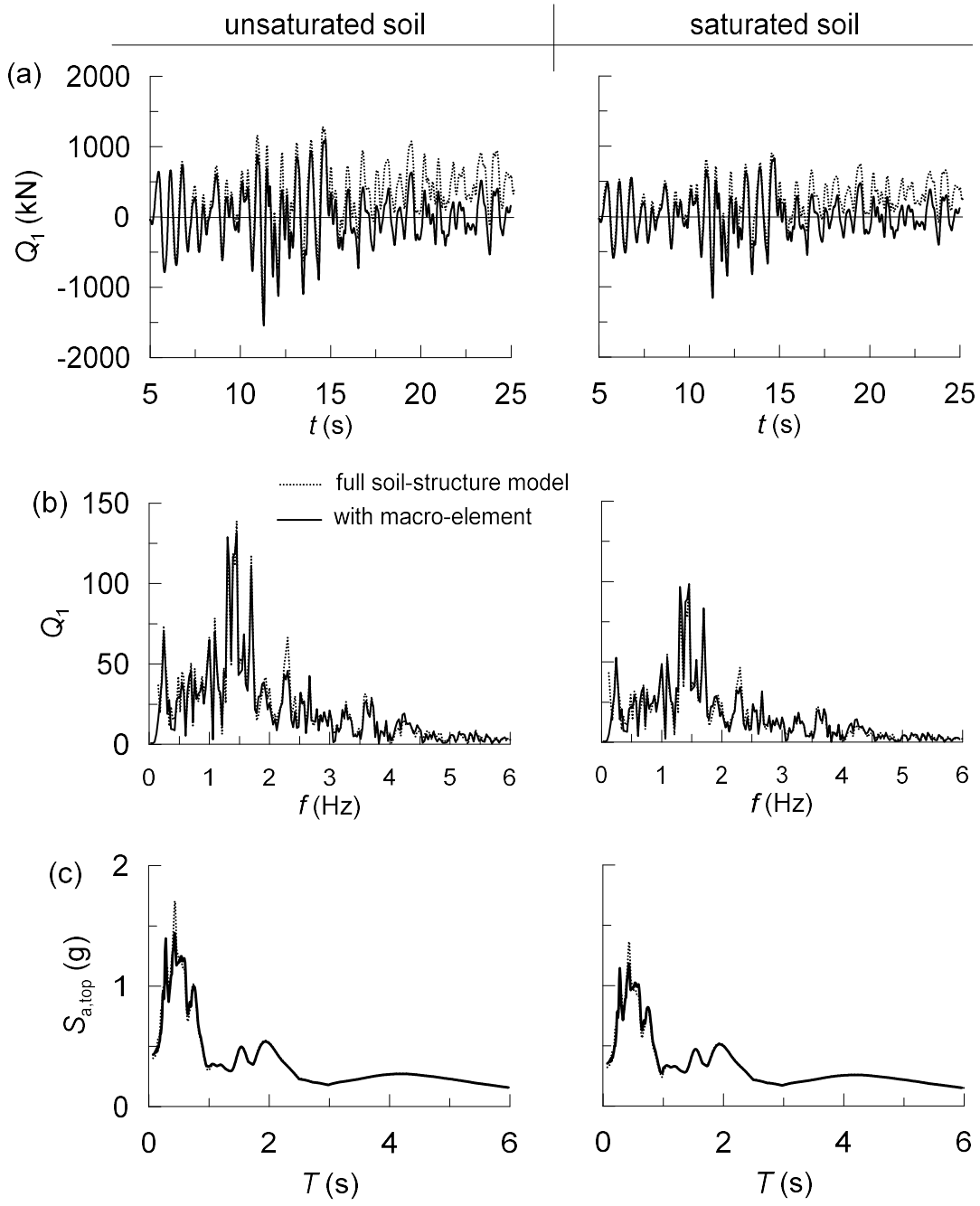

Figure 6.34: Effect of the pore water pressure in soil: representation of (a) the time evolution of the interaction force Q_1, (b) the relative Fourier spectrum and (c) the 5 %-damped elastic response spectrum in the longitudinal direction recorded at the deck-abutment contact.

6.8 Nonlinear structural behaviour

The transfer functions composing the linear macro-element are amplitude-independent because they are conceived to reproduce a visco-elastic response of the bridge structure. Under severe ground shaking, however, the structural response can become markedly nonlinear and the transfer tensor needs to be modified to catch the progressive modification of the dynamic characteristics of the structure with the intensity of the ground motion. The amplitude-dependent features can be taken into account in the macro-element representation according to two approaches: the global nonlinear behaviour of the structure can be regarded as an equivalent linear elastic behaviour or the macro-element should be reformulated according to an appropriate nonlinear force-displacement relationship. The former option would simply imply that the transfer functions be reduced, keeping the same shape, as a function of the level of mobilisation of the overall resistance of the superstructure. This can be a useful expeditious for a prompt application of the elastic transfer tensor, keeping the same mathematical formulation and with an immediate application in numerical computations. However, this is an approximate manner to account for material nonlinearities, hardly applicable in case of a highly nonlinear behaviour or in presence of lumped dissipative sources in the structural scheme, such as anti-seismic devices. Therefore, the latter option was exploited, in which, starting from the definition of the elastic transfer tensor, shape functions were introduced in the transfer tensor in order to incorporate the amplitude-dependent effects.

Let us consider the reference idealised structural scheme (Section 6.3), in which the nonlinear behaviour of the structure was introduced by using the 3D fiber-section force-based beam-column elements with an elastic-perfectly plastic fiber material available in the OpenSees library. An appropriate discretization of about one fiber every 0.1 m was adopted for the cross sections of the structural members, determined

through a sensitivity analysis varying the number of fibers in the sections. The elastic properties of the fibers were chosen to have the same behaviour of the elastic reference structure. A unique yield force was considered for all the fibers, equal to 10^4 kN, that however gives a different global strength for the sections of the abutment, the deck and the pier because the latter are characterised by a different area. In detail, the abutment foundation has a cross section per unit length of 1×5 m^2, discretised in 320 fibers; the abutment wall cross section, per unit length, is 1×4 m^2, with 256 fibers; the deck section presents 264 fibers placed in 1×4 m^2; the pier cross section measures 1×5.4 m^2, with 352 fibers; the 1×5 m^2 cross section of the pier foundation per unit length has 320 fibers.

An incremental dynamic analysis was carried out perturbing the structure through a harmonic excitation represented by imposed displacements applied to the abutment and pier foundations in the longitudinal direction. The periods of the harmonic signal ranged between 0.005 and 1.0 s, including the peaks of the elastic transfer function. The minimum amplitude $u_{1,el}$ of the input motion was of 0.01 m, corresponding to a linear response of the structure, while the maximum amplitude $u_{1,max}$ refers to the attainment of the ultimate capacity of the system. The resulting transfer functions are shown in Figure 6.35, delimiting the range in which the structural response is elastic-plastic. The dominant peak of the elastic transfer function, at 0.01 s, rises up rapidly to an ultimate interaction force of about $1.7 \cdot 10^6$ kN. This value represents the ultimate condition of the structure, associated with the activation of a global plastic mechanism. It results to be the limit value for all the significant peaks of the function, as demonstrated by the trends of the maximum values of the interaction force Q_1 with the amplitude u_1 in Figure 6.36. All the curves tend to the same limit value $Q_{1,ult}$ because it depends on the whole resistance of the structure, that in turn is defined by the strength parameters of the structural members.

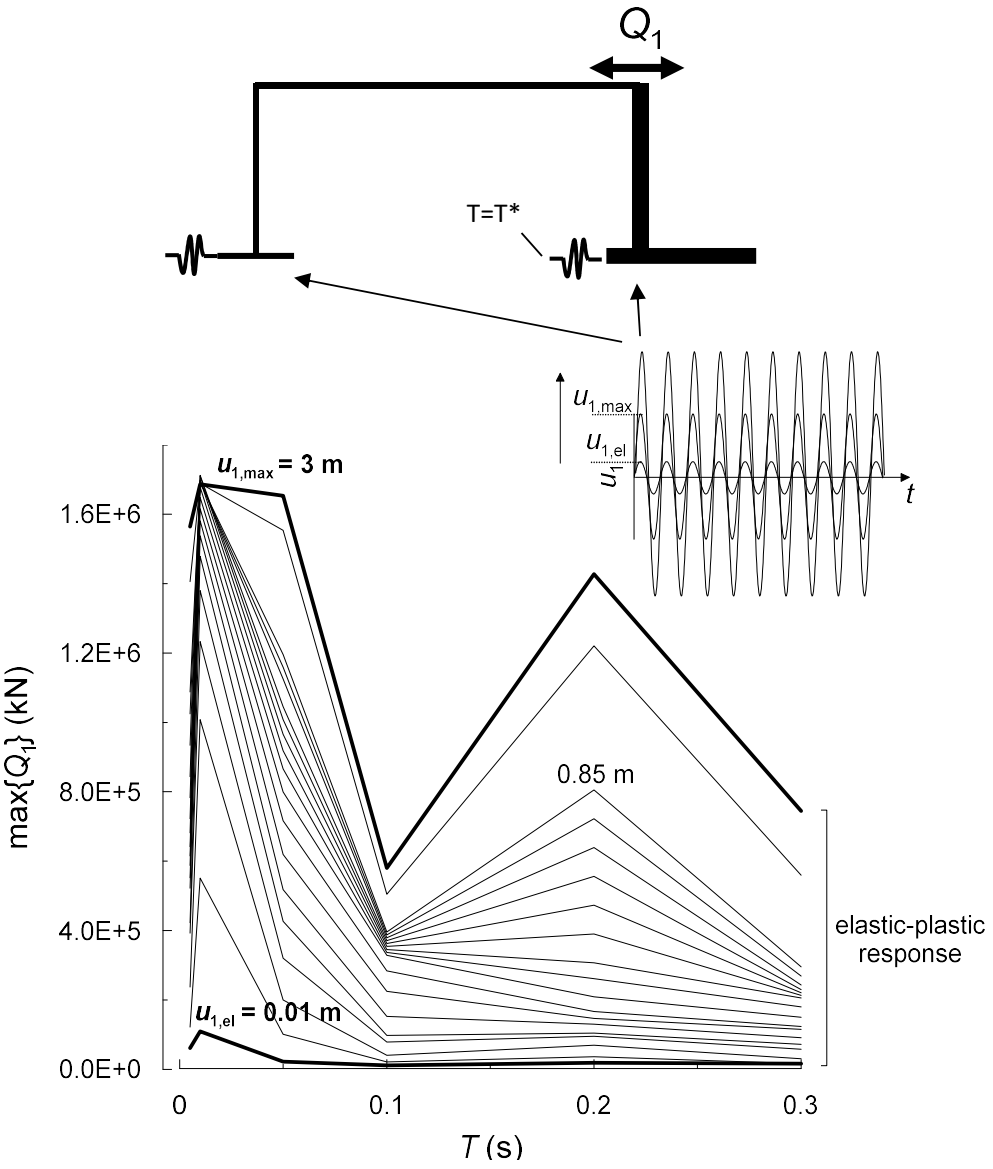

Figure 6.35: Nonlinear structural response: dependence of transfer function TT_{11} on the intensity of the input motion.

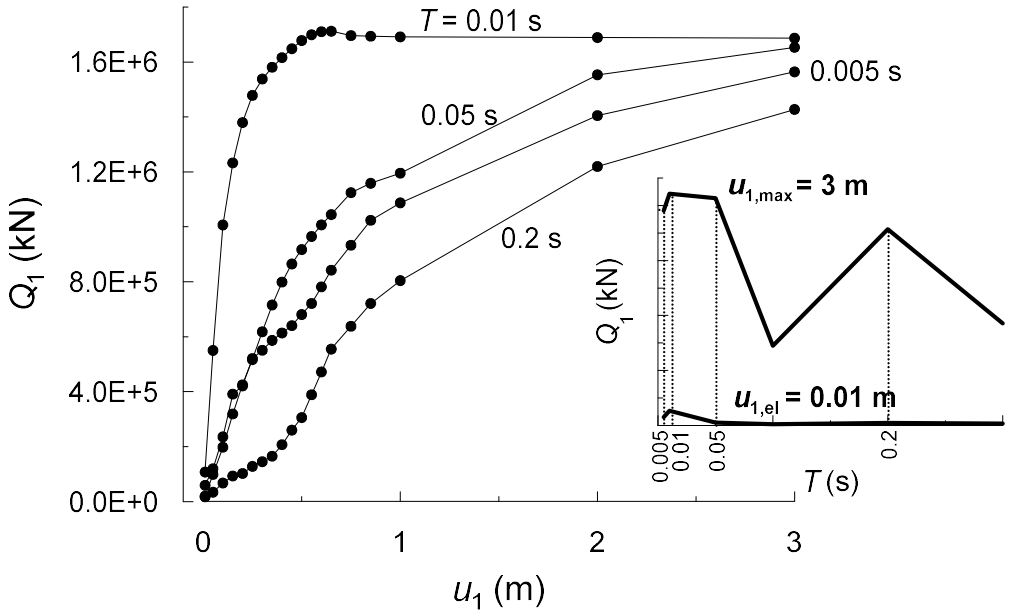

Figure 6.36: Nonlinear structural response: maximum interaction force Q_1 plotted as a function of the amplitude of the input motion.

6.8.1 Nonlinear macro-element

The curves shown in Figure 6.36 constitute the so-called nonlinear shape functions of the transfer tensor that account for the amplitude-dependent effects of the interaction forces at the deck-abutment contact. It can be convenient to represent these trends in the normalised plane in Figure 6.37: the normalised interaction force $Q_{1,ad} = Q_1/Q_{1,ult}$ is related to the normalised input displacement $u_{1,ad} = u_1/u_{1,ult}$, where $u_{1,ult}$ is the maximum amplitude of the input associated with the attainment of $Q_{1,ult}$. In this modified metric, all the curves follow a similar trend, thus a similar way to reach failure. As a result, a unique trend can be recognised as a descriptor of the shape function of the transfer tensor, that can be well approximated by the hyperbole-shaped function illustrated in Figure 6.38, whose general equation reads

$$Q_{1,ad} = \frac{h_{TT,in} \cdot u_{1,ad}}{1 + u_{1,ad}/a}. \tag{6.3}$$

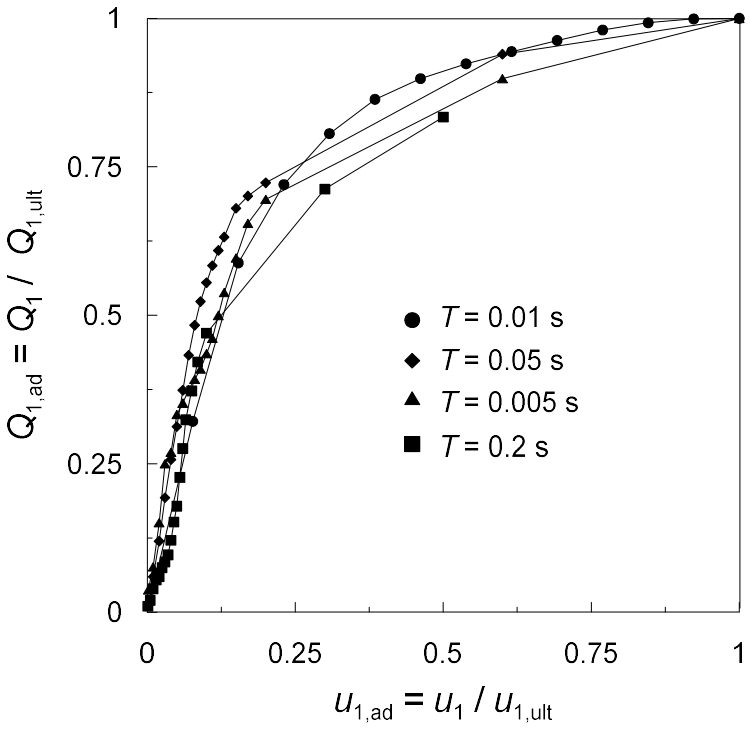

Figure 6.37: Normalised maximum interaction force $Q_{1,ad}$ plotted as a function of the intensity factor $u_{1,ad}$, considering a yield internal force of 10^4 kN.

The coefficient a was found by imposing the passage of the curve for the point $\{1, 1\}$, giving the following relationship

$$Q_{1,ad} = \frac{h_{TT,in} \cdot u_{1,ad}}{1 + u_{1,ad} \cdot (h_{TT,in} - 1)} \tag{6.4}$$

in which $h_{TT,in}$ represents the initial stiffness of the model. The effective relationship of the shape function therefore reads

$$Q_1 = \frac{Q_{1,ult}}{u_{ult}} \cdot \frac{h_{TT,in} \cdot u_1}{1 + u_1 \cdot (h_{TT,in} - 1) / u_{1,ult}} \tag{6.5}$$

that is completely defined by the specification of the initial tangent $h_{TT,in}$ and the ultimate condition of the system, intended as ultimate interaction force and corresponding input displacement.

The initial stiffness of the nonlinear macro-element can be obtained from the

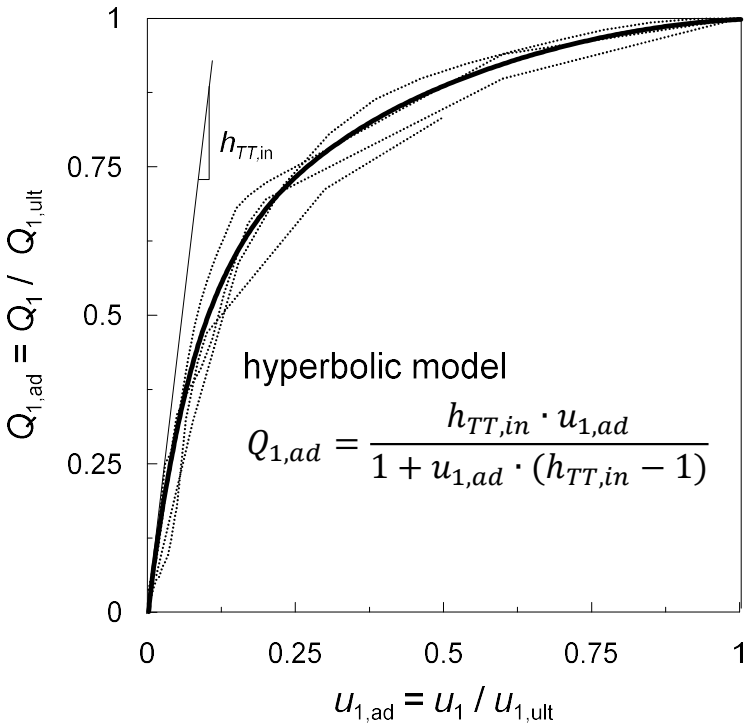

Figure 6.38: Hyperbolic law of the nonlinear macro-element.

elastic transfer function as $h_{TT,in} = Q_1/u_1$. The failure point, instead, requires the determination of the ultimate capacity of the structure, in terms of interaction force exchanged between the deck and the abutment, in the direction of motion. This can be evaluated through a simple static pushover analysis of the bridge structure or by means of an incremental dynamic analysis describing the entire development of the shape function.

The nonlinear macro-element presents a quite versatile formulation and an easy calibration, conceptually valid for all the degrees of freedom of the deck-abutment contact. In the case of the reference idealised structural system, an analytical expression was found to model the amplitude-dependent effects of the inertial forces transferred to the abutment. However, considering a generic bridge structure, a single incremental dynamic analysis in correspondence of the dominant period of the elastic transfer function seems to be sufficient to generate a unique nonlinear shape

function to be combined with the elastic properties of the transfer tensor.

6.8.2 Bi-linear representation

Although its simple mathematical formulation, the hyperbolic macro-element cannot be introduced in a finite element model of abutment as an assembly of rheological systems but it requires the implementation of an *ad hoc* finite element, incorporating the transfer tensor and the nonlinear shape functions. In a simplified manner, the macro-element could also be approximated by a bi-linear trend, shown in Figure 6.39, that is instead susceptible of a rheological representation useful in numerical modelling: the elastic transfer tensor, usually modelled as the assembly of basic rheological systems, is combined with a fuse calibrated to reproduce the ultimate capacity of the structural system. Hence, this simplified bi-linear version is completely defined by following the procedure described in Section 6.8.1 for the hyperbolic formulation, recalled in Figure 6.40, and can be promptly employed in finite element analyses. This solution can be particularly representative of all those cases in which the structure is provided with devices that limit the maximum internal forces, such as in presence of isolated-base anti-seismic devices or fuses. This alternative representation is used in the following to validate the non-linear macro-element of the bridge structure.

6.8.3 Validation

As a last step, the macro-element of the bridge structure is now tested in time domain dynamic analyses on the idealised reference system in which both the soil and the structure exhibit a nonlinear behaviour. The seismic record of Tabas, in its longitudinal component, was taken as the reference scenario for the validation, in virtue of its wideband frequency spectrum and extremely high energetic content. The full soil-structure model and the local model of abutment with macro-element

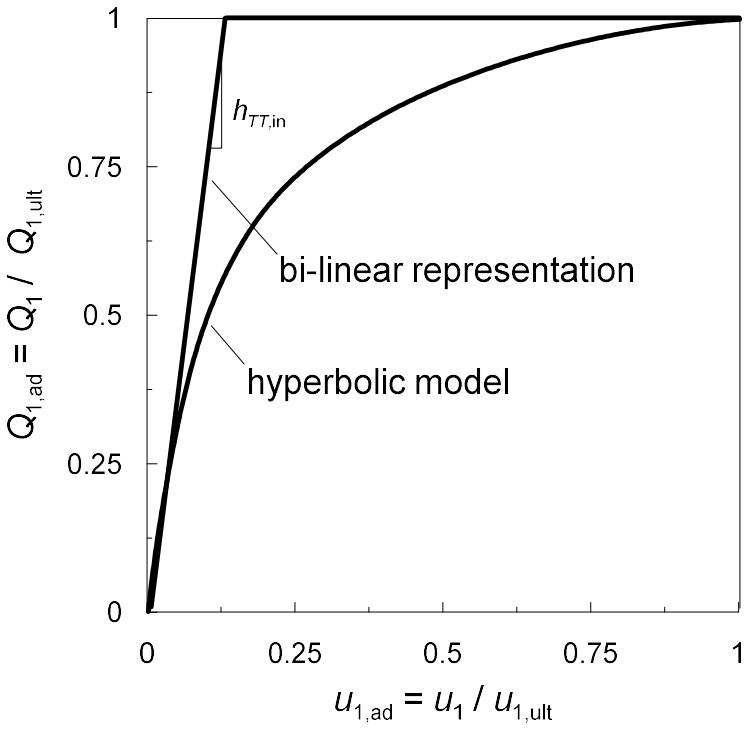

Figure 6.39: Bi-linear representation of the hyperbolic macro-element.

are compared. The performance of the abutment is quantified by the time evolution of the interaction force at the top of the wall in Figure 6.41, that is the internal force in the deck in contact with the abutment wall in the full model and the internal force in the macro-element in the local model, and by the elastic response spectra at the abutment top in Figure 6.42.

The combined nonlinear response of the soil and the structure leads to a visible reduction of the maximum interaction forces at the deck-abutment contact of about 40 % with respect to the forces produced by a linear elastic structural system. Also the permanent force $Q_{1,perm}$ undergoes a reduction of 48 % due to the full nonlinear response that increases the global deformability of the system accommodating more easily the differential displacements between the foundations of the pier and of the abutment. The bi-linear macro-element provides a good reproduction of the effects above, except for the permanent force that is however attenuated by nonlinearity.

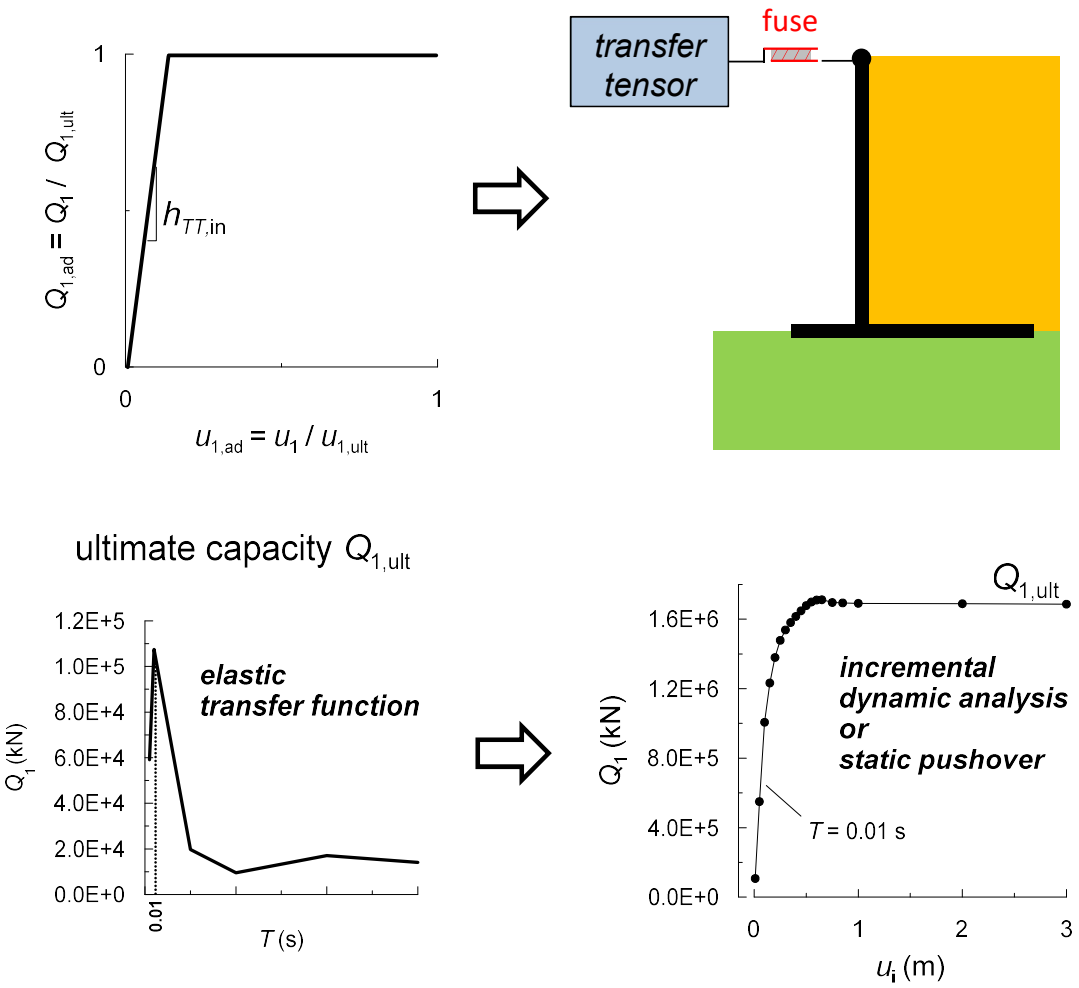

Figure 6.40: Physical representation of the bi-linear macro-element and calibration procedure.

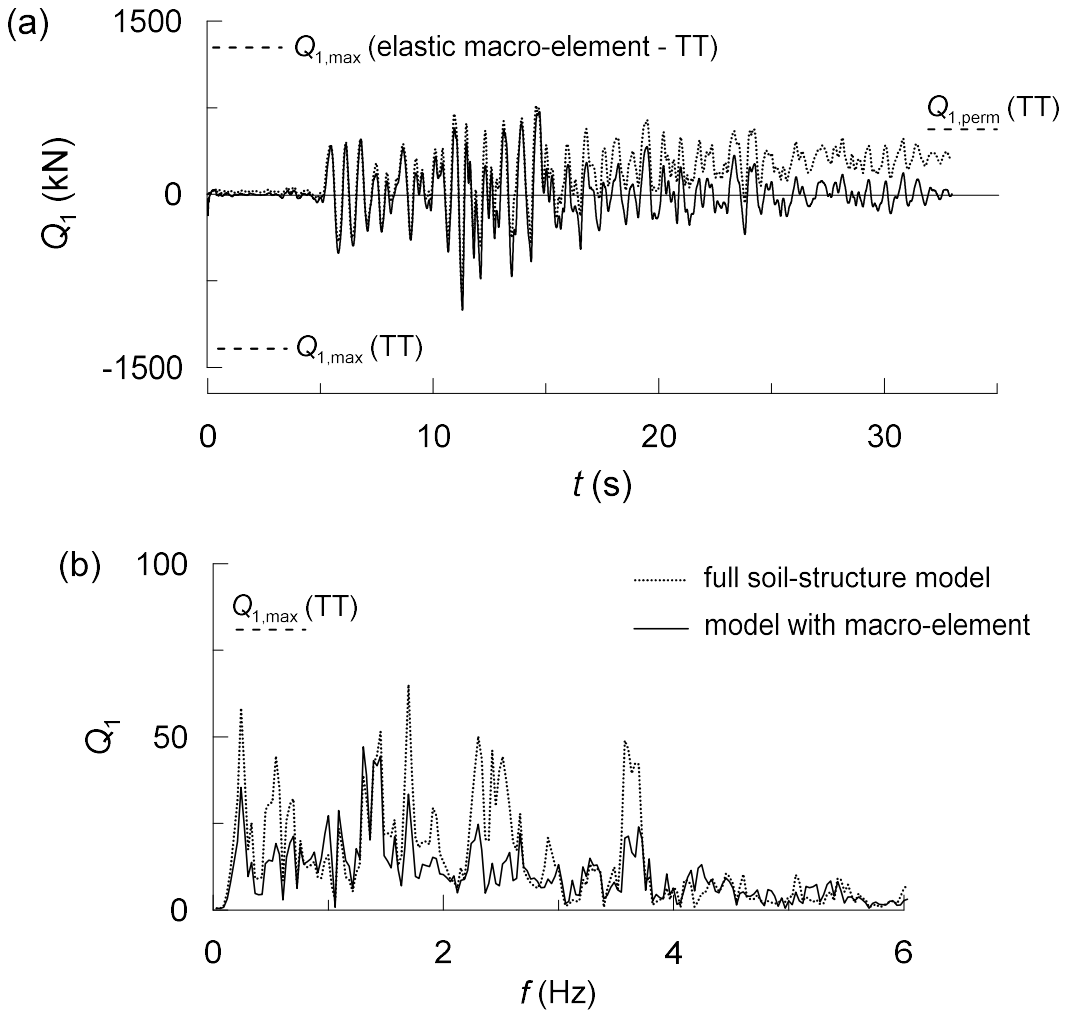

Figure 6.41: Time evolution of the interaction force Q_1 (a) and relative Fourier spectrum (b) in the longitudinal direction recorded at the deck-abutment contact: comparison between the fully nonlinear soil-structure model and the model with bi-linear macro-element.

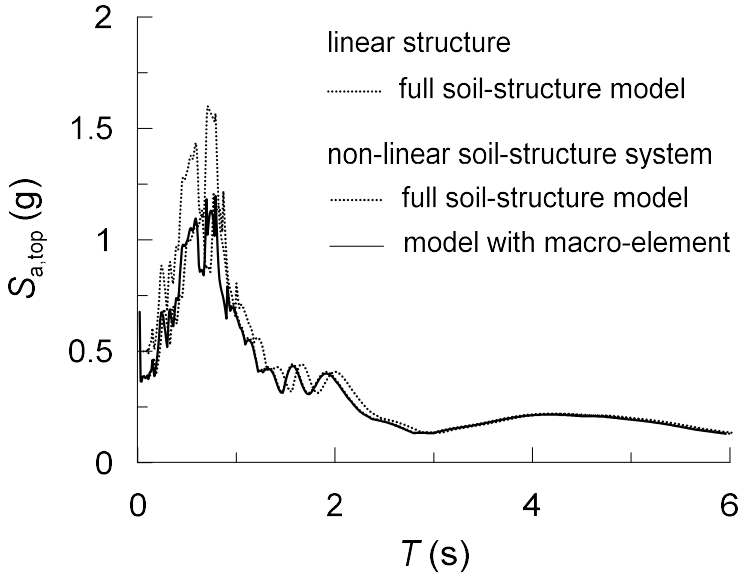

Figure 6.42: 5%-damped elastic response spectrum of the relative accelerogram in the longitudinal direction recorded at the deck-abutment contact: comparison between the fully nonlinear soil-structure model and the model with bi-linear macro-element.

The spectral accelerations on the abutment top, not altered by the presence of the macro-element, are limited at a value of about 1.2 g, instead of about 1.6 g obtained in the case of linear structural behaviour. The nonlinear structural response does not alter the frequency content of the seismic actions exchanged at the deck-abutment contact.

On the whole, the macro-element seems to be able to study with a good level of accuracy the local seismic performance of a bridge abutment, considering also the inertial effects deriving from the superstructure, with a significant gain in computational efficiency: the execution time of the nonlinear dynamic analyses on the full soil-structure models under plain strain conditions was about 7 days each, while the local model of abutment with macro-element run in not more than 2 days.

6.9 Macro-element for the reference multi-span girder bridge

A uni-axial elastic macro-element is here computed for the multi-span girder bridge in Section 3.6, that constitutes the soil-structure system used for validating the macro-elements of the soil-abutment system and of the structure. A longitudinal seismic input was used to test the model, hence the macro-element is composed of the sole longitudinal transfer function according to the following relationship

$$Q_1 = TT_{11} \cdot u_1. \tag{6.6}$$

The function TT_{11} was obtained carrying out dynamic simulations on the global structural model represented in Figure 6.43. The model was implemented in OpenSees and in SAP2000, verifying the identical response of the two representations. The foundations of the piers and of the abutments were perturbed by a harmonic excitation in a range of periods between $0.01 \div 1.5$ s, in order to contain the significant modes of the system. The resulting transfer function, provided in Figure 6.44 (dot-

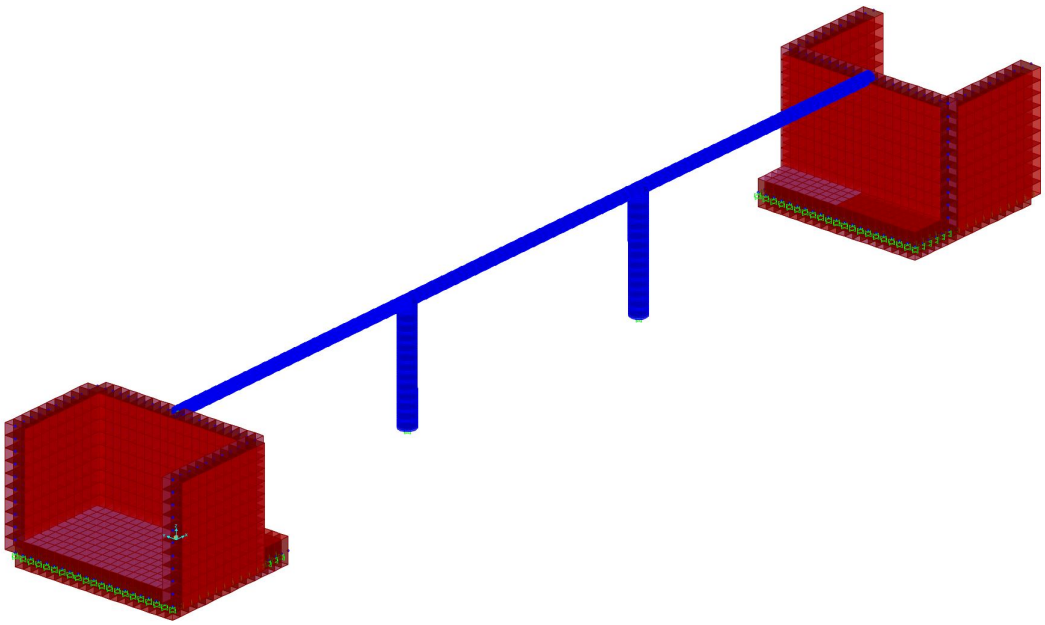

Figure 6.43: Mesh of the global structural model used to determine the transfer function TT_{11}.

ted line), is characterised by a peculiar bi-modal response. As it was found for the simple structural scheme in Section 6.3, the dominant peak is associated with a combined global response, in which the higher modes of the vertical elements trigger the dynamic axial response of the deck. The associated mass participation factor is equal to 11.5 %, that corresponds approximately to the mass of the deck. A second peak with lower amplitude occurs at about 0.15 s, produced by the first global mode in the longitudinal direction. In this mode, the strong pier bends according to a first mode shape, carrying a lower amount of the deck mass. Although the greater mass participation, equal to 55.4 %, this mode produces a more limited effect in terms of inertial forces transferred to the abutment, compared to the dominant peak, because the bending of the strong pier occurs at too long periods and therefore the axial response of the deck is not activated.

These global inertial effects were reproduced in the numerical model of the abutment through an equivalent two degrees of freedom system calibrated on the peaks

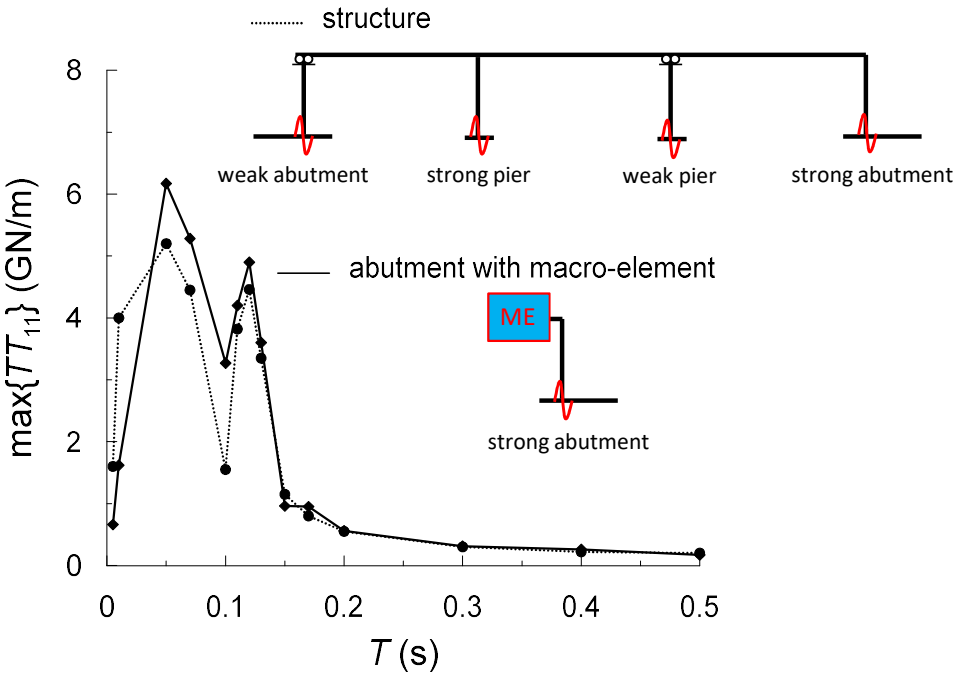

Figure 6.44: Transfer function TT_{11} in terms of longitudinal interaction force at the deck-abutment contact.

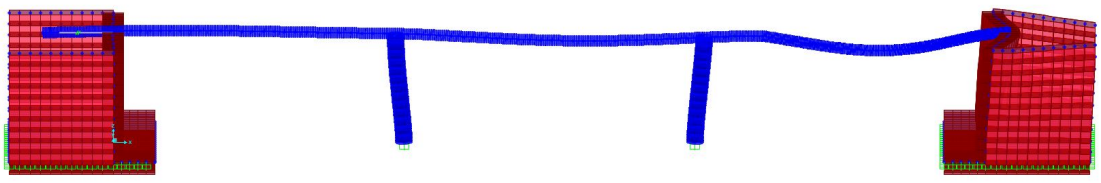

Figure 6.45: Mode shape of the structure at 0.05 s.

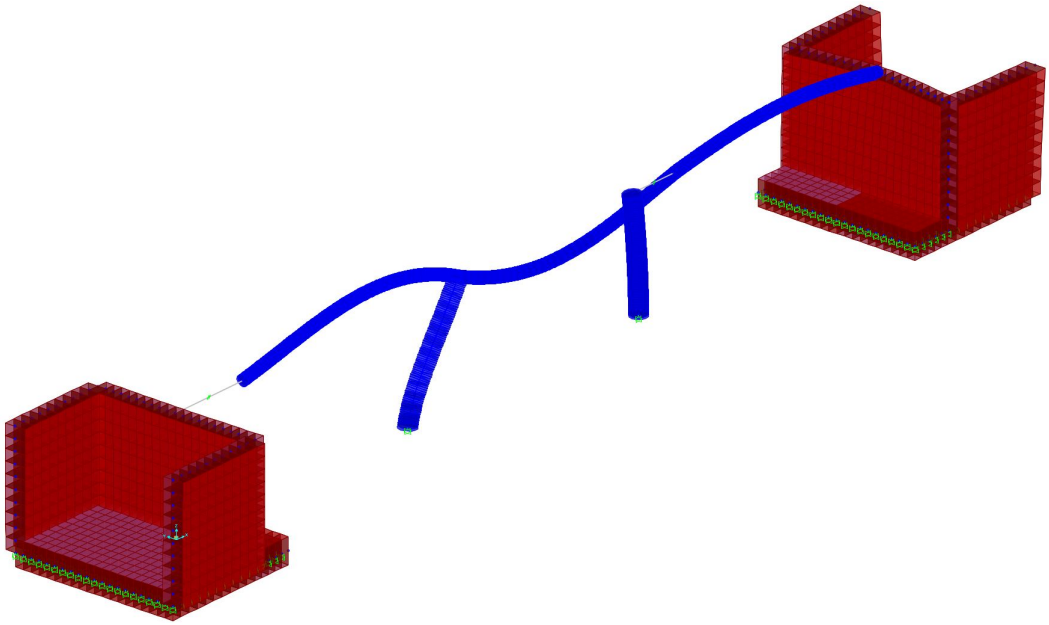

Figure 6.46: Mode shape of the structure at 0.15 s.

of the function TT_{11} of the structure, with relative transfer function given in Figure 6.44 (continuous line). The masses of the equivalent model represent the modal masses, whereas the optimum values of the stiffness were found by trial and error.

Chapter 7

Seismic performance of the soil-bridge system

The validation of the proposed macro-element method is now presented, assuming the response of the full soil-bridge model taken as reference in this study (Section 3.6) as the target behaviour to be reproduced.

7.1 Site response analysis

As a first evaluation of the dynamic response of the subsoil, site response analysis of the Pantano subsoil is presented in the following. For brevity, the focus is on the seismic record of Tabas, that is the most severe seismic scenario among the records selected as representative of the seismic demand for the Pantano subsoil (see Se. 3.4). A three-dimensional soil column was implemented in OpenSees, representing the soil layers in the area of the Pantano abutment located above the deconvolution depth. Hence, the model reproduces the superficial layer of Messina Gravels $MG1D$ and the layers $MG1$ and $MG2$ down to a depth of 112 m. The SANISAND and PDMY models were used to model the soil behaviour, according to the calibration

described in Section 3.3.3. The ground water table is located at a depth of 30 m from the abutment foundation, thus at the interface between the strata $MG1D$ and $MG1$. The soil domain was discretised through the SSPbrickUP elements available in the OpenSees library to account for the coupled hydro-mechanical behaviour of the original configuration of the Pantano subsoil.

A first gravity analysis recreated the lithostatic stress state in the soil, which is allowed to settle under its self weight. In a second stage, periodic constraints were assigned to the nodes at the same depth in the direction of motion. The deconvoluted time histories of the Tabas record, shown in Section 3.5, were applied to the nodes on the lower boundary of the column as imposed displacements. The Joyner and Chen procedure (1975) was not employed in the application of the input motion because the deconvoluted time histories take already implicitly into account the deformability of the soil at greater depths.

The original configuration of the Pantano subsoil is initially taken into consideration, analysing the one-dimensional propagation of seismic waves with adoption of the SANISAND and of the PDMY constitutive models. Some insight into the multi-directional site response of the Pantano subsoil is instead provided in Appendix 3.

7.1.1 One-dimensional site response

The longitudinal component of Tabas (fault normal) produces the displacement time histories shown in Figure 7.1. In the first 30 m-depth, the longitudinal soil displacements are markedly magnified compared to the base of the model, with no significant modification of the ground motion above the ground water table. The corresponding displacements of the ground surface after the earthquake, equal to 0.26 m, demonstrate the important role of the plastic response of the soil. By contrast, the displacements for $z > 85$ m follow closely the input motion with no appreciable permanent displacements. Therefore, the primary irreversible deformations of the

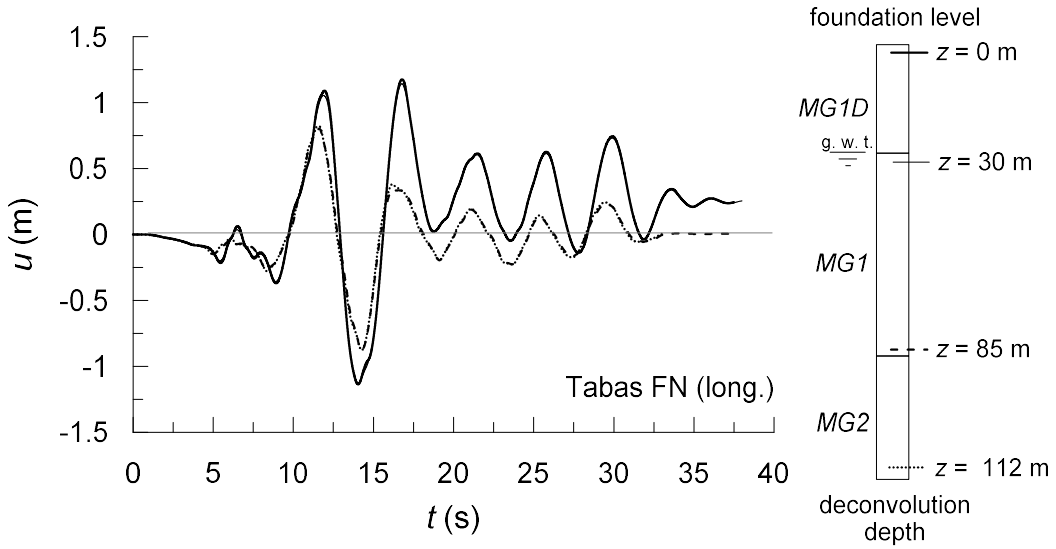

Figure 7.1: Time histories of the longitudinal displacements at significant depths of the soil column using the SANISAND model.

soil column localise in the layer $MG1$.

The above response, obtained by using the SANISAND material for the soil elements, is compared in Figure 7.2 with the behaviour obtained with the PDMY model. The discrepancy on the maximum displacements, occurring in the time interval between $12 \div 15$ s, is around of $10 \div 13$ % for the two highest peaks. In the second part of the signal, for $t > 15$ s, the response of the PDMY model presents a moderate reduction of the displacements, especially at the ground level. The stiffer response of the PDMY model leads to a permanent displacement equal to 0.21 m at $z = 0$ m, thus equal to 80 % that computed with the SANISAND model.

The development of excess pore water pressures is concisely described by the time evolution of the pore pressure coefficient $r_u = u_w/\sigma_z$, shown in Figure 7.3, with u_w the pore water pressure and σ_z the total vertical stress, recorded at the base of the layer $MG1$ undergoing the highest plastic distorsions. The rise of the excess pore water pressure is rather similar between the two models, with the greatest gradient of the coefficient r_u between 6 s and 17.5 s, corresponding to the significant

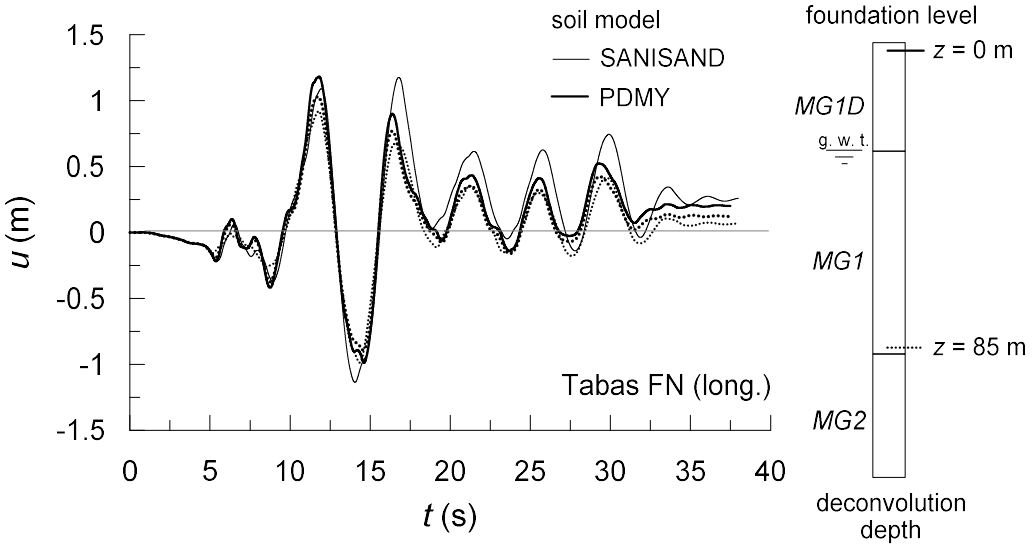

Figure 7.2: Comparison between the responses of the SANISAND model and of the PDMY model: time histories of the longitudinal displacements at $z = 0$ m (foundation level) and $z = 85$ m.

duration (Bommer and Martinez-Pereira 1999) of the Tabas record. In this zone, the increase of the pore water pressure is slightly more rapid in the case of the SANISAND model, resulting in a final value of the pore pressure coefficient equal to 0.81 instead of 0.70 computed with the PDMY model. Hence, the effective stress in depth reduces significantly in both cases with a consequent relevant reduction of the shear strength of soil in the lower part of the layer $MG1$, that is the main cause of the large permanent displacements recorded at the ground level.

The spectral shapes at the ground level, illustrated in Figure 7.4, reflect the considerations above. The maximum amplitudes of the deconvoluted seismic input (dashed line) are localised in the range of periods between 0 s and 0.8 s for the high stiffness of the deposits below the deconvolution depth. For both models, instead, the seismic actions at $z = 0$ m increase markedly for periods greater than about 0.9 s due to the higher deformability of the upper layers. More in detail, the PDMY model leads to a marked increment of the spectral ordinates in the range of periods associated with the main dynamic amplification of the superficial

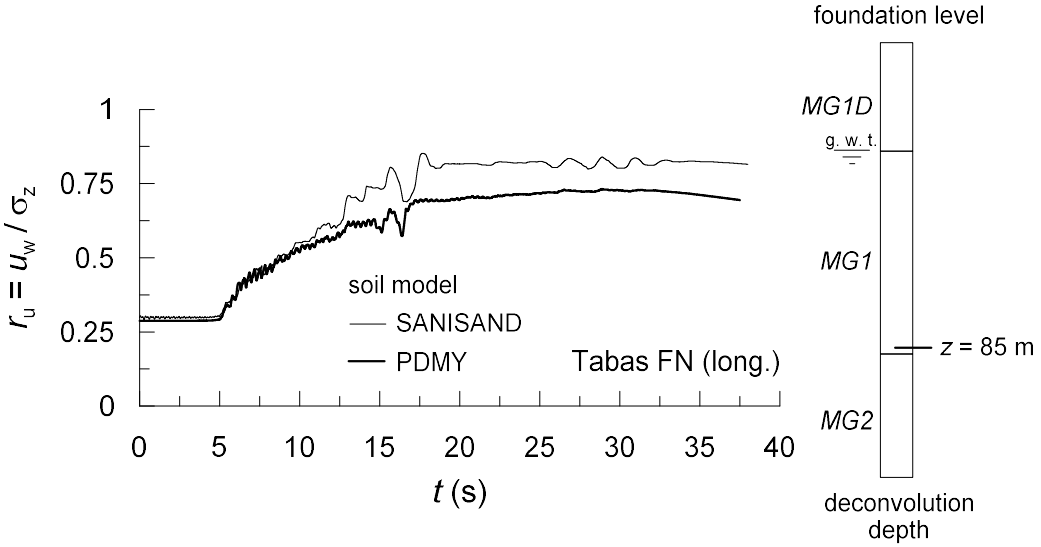

Figure 7.3: Comparison between the responses of the SANISAND model and of the PDMY model: time evolution of the pore pressure coefficient r_u at $z = 85$ m.

deposits, between $1.3 \div 2.4$ s. The response of the SANISAND model is slightly longer, with a less pronounced amplification between $1.3 \div 2.4$ s in favour of a slightly more exalted response for larger periods. For periods lower that 0.9 s, the PDMY model returns a moderately amplified response between $0.4 \div 0.7$ s against the deamplified response provided by the SANISAND model, especially at medium to high frequencies ($T < 0.5$ s), hence in the spectral region where the dynamic responses of the soil and the structure are coupled. In fact, the significant range of periods for the superstructure is $0 \div 0.2$ s (see Section 3.6.6) and that associated with the vibration modes of the soil-abutment system is $0.6 \div 0.8$ s (see Section 4.3) in the longitudinal direction. Therefore, the PDMY model is expected to produce a more amplified dynamic response of the structural system. These differences between the two models of soil are however not particularly pronounced and, moreover, tend to attenuate with depth, as demonstrated by the response spectra at the ground water table.

The site response examined so far is relative to the effective configuration of

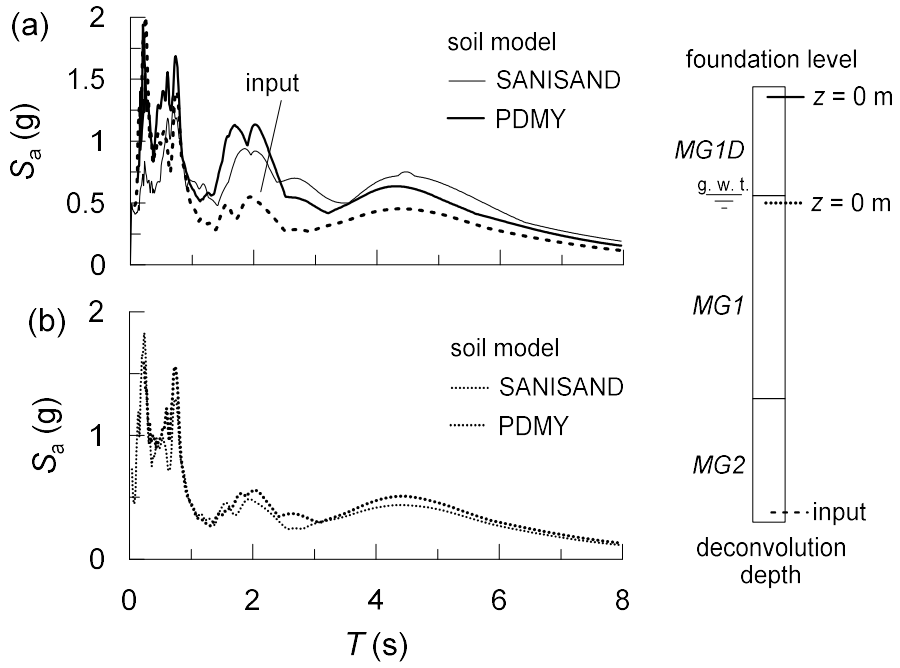

Figure 7.4: Comparison between the responses of the SANISAND model and of the PDMY model: 5 %-damped elastic response spectra at (a) $z = 0$ m (foundation level) and (b) $z = 30$ m (ground water table).

the Pantano subsoil. In the reference soil-structure system used to validate the methodology proposed, the soil domain differs from the Pantano subsoil for the absence of pore water pressures. This simplification was introduced to reduce the extremely high computation times of the numerical simulations and to focus on the dynamic response of the two macro-elements. The resulting ground motion at the foundation level is shown in Figure 7.5. The main difference consists in a reduction of the permanent displacement after the earthquake of about 46 %, due to the higher shear strength of the dry soil, while the time evolution and the maximum values of the longitudinal displacement are not particularly influenced by the presence of pore water pressures in the soil. Accordingly, the spectral accelerations of the dry soil, represented in Figure 7.6, result moderately magnified, especially for periods lower than 2.4 s, with no significant alteration of the relative frequency content. It follows that the dry subsoil in the reference soil-bridge model is expected to give a

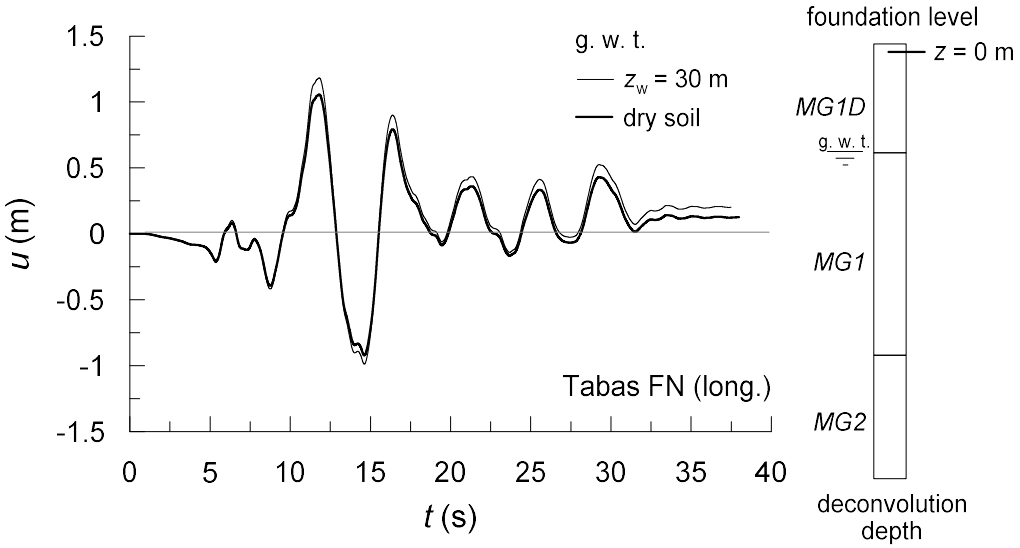

Figure 7.5: Comparison between the time histories of the longitudinal displacements at $z = 0$ m (foundation level) of the original soil column and the dry soil domain used in the soil-structure interaction analyses.

moderate, although not excessive, overestimation of the seismic actions that reach the foundation level, without modifying the dynamic coupling between soil and structure.

7.2 Different representations of the soil-abutment interaction

The validation of the macro-elements refers to the case of a mono-directional seismic motion. In the global structural model, in addition to the macro-element of the soil-abutment system, some other existing strategies are employed as an element of comparison. Also the soil-foundation interaction is modelled according to different methods, with an increasing level of complexity, from a dynamic impedance function to the macro-element formulation proposed in the present work (see Section 5.15).

In a complementary manner, the local dynamic behaviour of the abutment is studied by including the macro-element of the bridge structure into the soil-abutment model. In this regard, several comparisons against existing methods have already

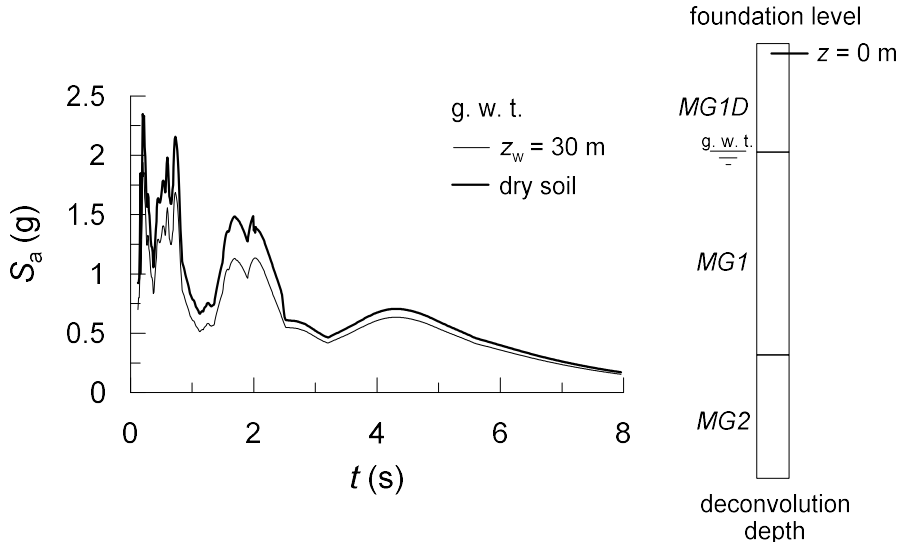

Figure 7.6: Comparison between the 5 %-damped elastic response spectra at $z = 0$ m (foundation level) of the original soil column and the dry soil domain used in the soil-structure interaction analyses.

been shown in detail in Section 6.6, thus in this case the purpose of the following application is twofold: testing the accuracy of the solution of the simplified model with respect to the results of the full soil-bridge representation and analysing in depth the relationship between the internal responses of the two macro-elements, representing the core of the soil-abutment-superstructure interaction.

7.2.1 Structural model with dynamic impedance functions

The validation of the macro-elements is presented in the one-dimensional case, therefore a single dynamic impedance function was applied to the end node of the deck in contact with the strong abutment. A classical Kelvin-Voight model was used to represent the impedance function in the finite element model of the bridge structure, depicted in Figure 7.7. Because of the lack of specific solutions for bridge abutments, the stiffness h_{abut} of the impedance function was set equal to 50 % the modulus $H^{(0)}$ of the initial elastic spring of the macro-element of bridge abutment (see Section 5.14.1), representing an effective stiffness according to the profiles of the normalised

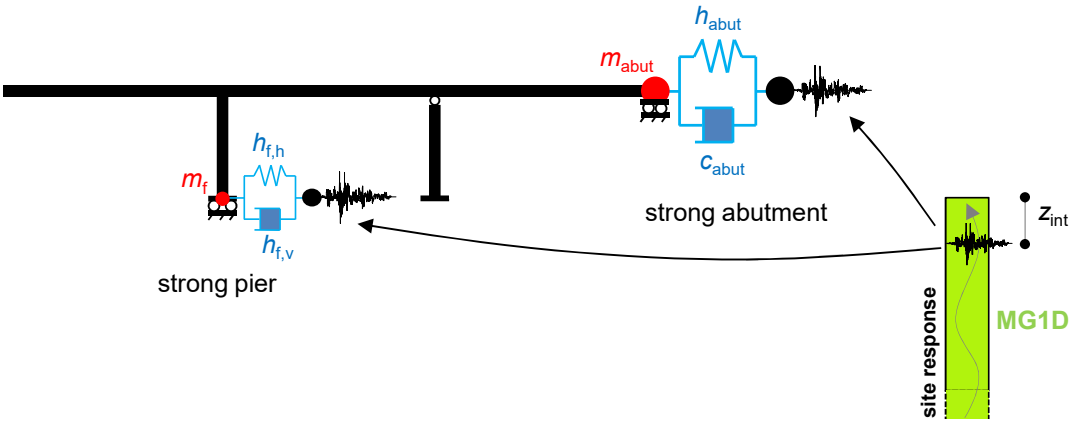

Figure 7.7: Global structural model with dynamic impedance functions for the soil-abutment and the soil-foundation interaction.

shear modulus of soil obtained in Section 3.5 (the average value of G/G_0 is about 0.5 in the significant depth interval for the soil-abutment interaction); the damping coefficient c_{abut} was instead evaluated through the solutions proposed by Gazetas (1991) for shallow foundations, considering the same reduction of the small strain shear modulus of soil. The model was provided with a mass equal to the first mass of the macro-element of bridge abutment, in order to include the inertial effects developing in the soil-abutment system at small strains (see Section 4.14.2).

In order to have a comparable level of accuracy, a longitudinal dynamic impedance was used to reproduce the soil-structure interaction effects occurring at the foundation of the strong pier as well. The latter is represented by a translational Kelvin-Voight model placed in the longitudinal direction. The mechanical properties of the model were evaluated by using the classical solutions proposed by Gazetas (1991) for shallow foundations, calibrating the stiffness and damping on the fundamental period of the superstructure in the direction of motion (longitudinal), that is equal to 0.16 s (see Section 3.6.6). The foundation mass is assigned to the node connecting the base of the pier to the dynamic impedance model.

The seismic input for the structural model derives from the site response analysis

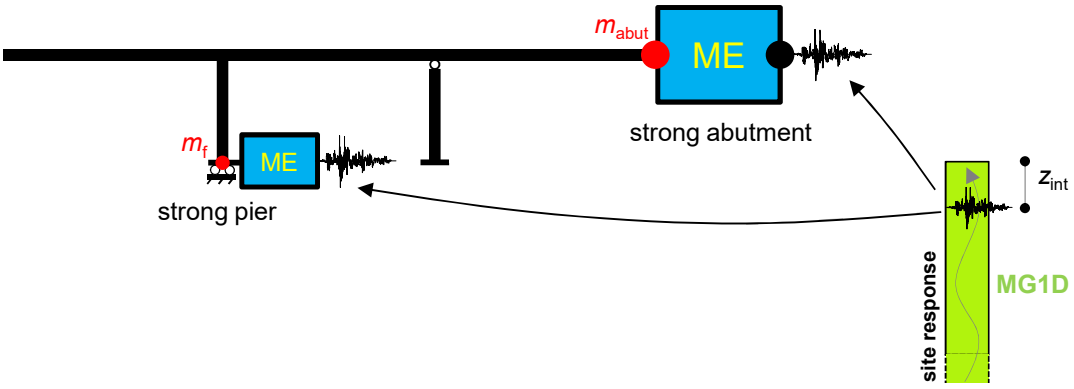

Figure 7.8: Global structural model with thermodynamic macro-elements for the soil-abutment and the soil-foundation interaction.

described in Section 7.1, carried out on the Pantano subsoil in the absence of pore water pressures. More in detail, the time histories applied to the free nodes of the impedance models refer to the depth z_{int} of the base of the volume of soil that interacts with the structure. At the abutment location, the interaction depth was set equal to the effective height of the soil-abutment system (see Section 4.3), that is equal to $z_{int} = H + L_{found} = 31$ m in the longitudinal direction, with H and L_{found} the height of the wall and the length of the foundation. The interaction depth for the pier foundation was instead assumed equal to the foundation length $l_{found} = 6$ m.

7.2.2 Structural model with macro-elements

The conceptual scheme of the nonlinear dynamic analysis of the global structural model with macro-elements is illustrated in Figure 7.8. It follows the same prescriptions on the input motion defined in the case of the application of dynamic impedance functions. The two one-dimensional macro-elements are placed in the direction of motion. The configurations of the two macro-elements have already been defined in Section 5.14 and Section 5.15.

7.3 Seismic performance of the structure

7.3.1 Foundation input motion

Consider the dynamic response of the soil-bridge model subjected to the longitudinal component of the Tabas record. As a first result, in Figure 7.9 the seismic motion at the level of the pier foundations obtained from the full soil-structure interaction analysis is compared with the free field motion at the ground level; in the same figure it is also shown the displacement time history of a node placed on the lateral boundary of the soil domain (grey dotted line), representative of the ground motion far from the structure. Starting from the latter, it can be observed that the seismic response of the soil along the boundary of the soil-structure model reproduces quite well the free field conditions (black dotted line), both in its time evolution and in the permanent displacement after the seismic event. This response is however substantially different from the seismic motion of the foundations of the strong abutment and of the piers. Despite being of a comparable order of magnitude, the motion of the foundations tends to accumulate irreversible displacements in the opposite direction of that involved in the free field response. This is mainly caused by the response of the strong abutment that, in virtue of its considerable mass participating to the dynamic response of the bridge, tends to control the displacements. The foundation of the strong abutment undergoes a permanent displacement of 0.37 m against the value of 0.18 m recorded at the pier foundations, since the pier can accommodate partially the displacements of the abutment with its flexural deformability. This appears evident looking at the qualitative deformed shape of the bridge in the post-earthquake condition, illustrated in Figure 7.10. It is evident that the two abutments move inwards, pushed by the inertial effects developing in the volume of embankment interacting with the walls. More in detail, the strong abutment undergoes a more pronounced permanent displacement and rotation, compared to

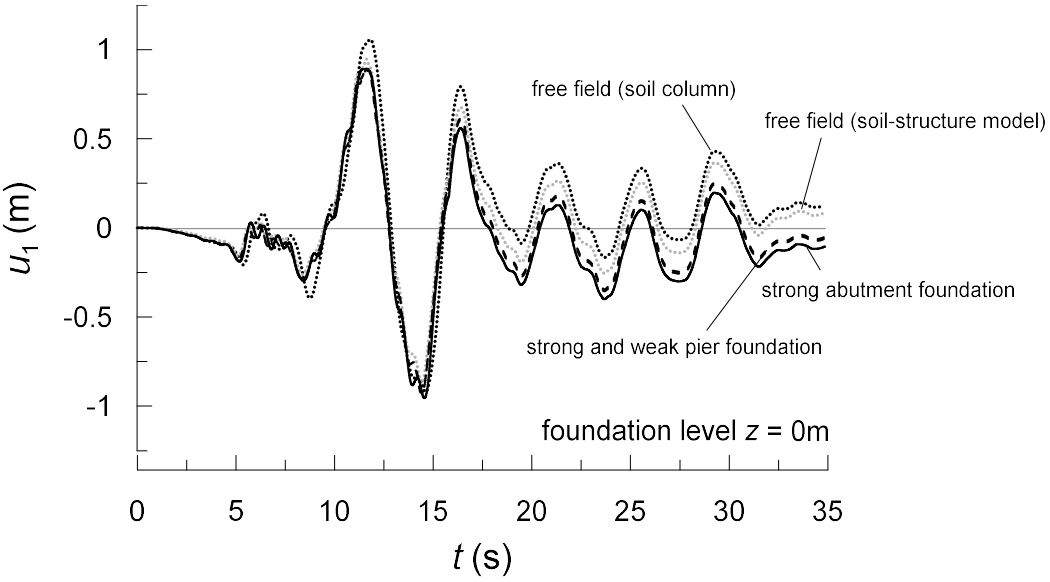

Figure 7.9: Foundation input motion for the abutments and the piers.

the weak abutment, for its interaction with the superstructure of the bridge. The inertial effects arising from the dynamic response of the superstructure, in fact, are transferred to the soil-abutment system producing an increment of the stress state in the soil and, hence, facilitating the attainment of the soil strength. This leads to the more marked permanent displacement of the strong abutment in Figure 7.10, that is only in part absorbed by the strong pier. This is a crucial result because it highlights the effect of the soil-abutment-superstructure interaction on the seismic demand of the bridge, in terms of residual displacements. The soil-structure interaction at the strong abutment location is therefore the result of the reciprocal exchange of inertial forces between the superstructure and the soil interacting with the bridge that, on one hand, increases the irreversible deformation processes in the embankment and, on the other hand, affects the internal forces in the superstructure.

Analysing more in detail the last concept, Figures 7.11 and 7.12 show how the spectral accelerations of the strong abutment change for its interaction with the remaining part of the bridge structure and with the embankment. The free field

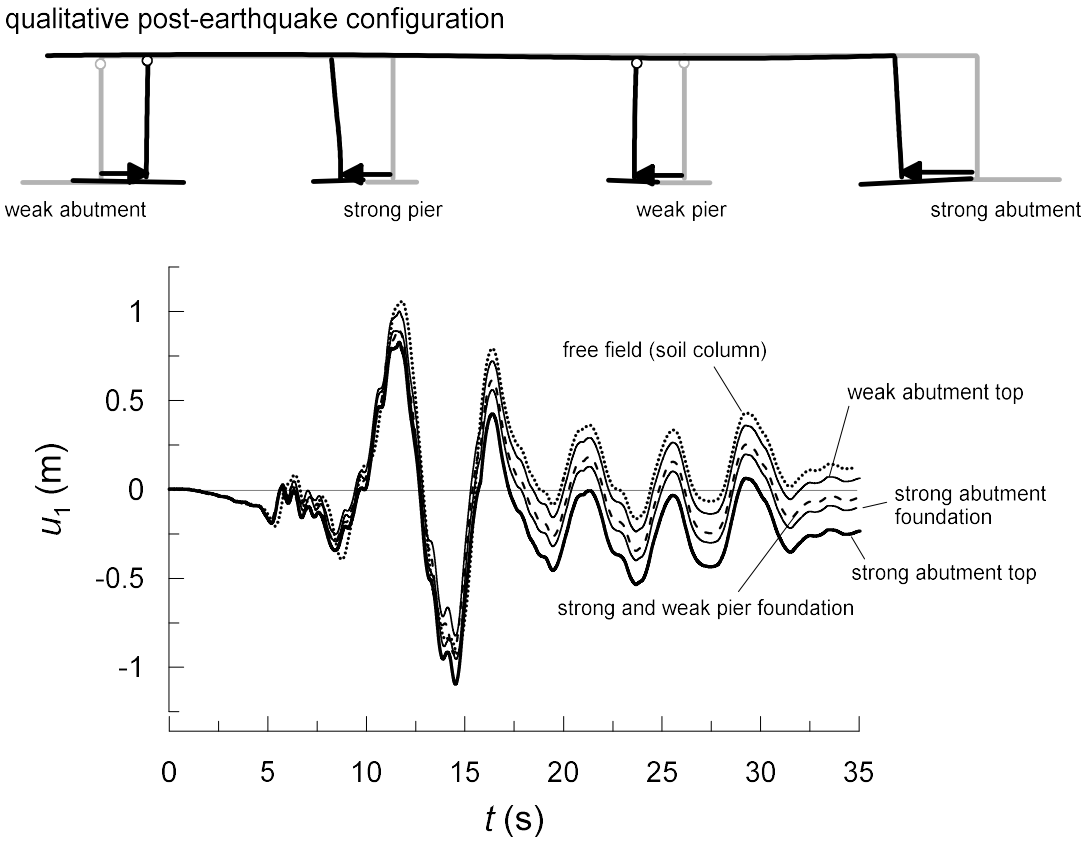

Figure 7.10: Time histories of the longitudinal displacements of the pier foundations and of the abutments top.

response (Figure 7.11(a)) follows quite closely the amplitudes of the input motion up to a period of 0.8 s, while a consistent amplification of the ordinates occurs between 1.1 s and 2.5 s, that is therefore associated with the dynamic excitation of the soil deposit. In correspondence of the pier foundations (dashed lines), a much stiffer response is observed: a marked amplification of the spectral accelerations happens for periods lower than about 1.0 s. The foundations of both the piers present the greatest amplification at 0.75 s but the weak pier differs for a dominant peak at about 0.25 s. This change in the frequency content of the foundation input motion is caused by the interaction of the soil with the structure. A similar result can be observed in Figure 7.11(b) referred to the foundations of the abutments, in which however a unique well-defined range of amplification periods can be localised between $0.5 \div 1.0$ s. In this range, for both the abutments, the increment of the maximum amplification is of about 17 % with respect to the pier foundations and, consequently, it can only be due to the resonance of the embankment-abutment system. In effect, this range has been recognised in Chapter 4 as the significant range including the dominant responses of the soil-abutment system for small to large strain levels.

Moving on to the top of the strong abutment, shown in Figure 7.12, the spectral shape differs from the motion at the base only at low periods, $0.2 \div 0.7$ s, with a considerable increment of the spectral accelerations. The dominant period keeps unaltered and presents a modest increase of the associated peak of about 7 %. The noticeable increment between $0.2 \div 0.7$ s can be directly associated with the presence of the structural members of the central and wing walls, that are very stiff elements emphasising the dynamic behaviour at high frequencies. The fundamental contribution of the dynamic response of the embankment, instead, can be seen in the spectrum computed in a node at the top of the embankment but placed in close vicinity to the lateral boundary of the model (dashed line in Figure 7.12).

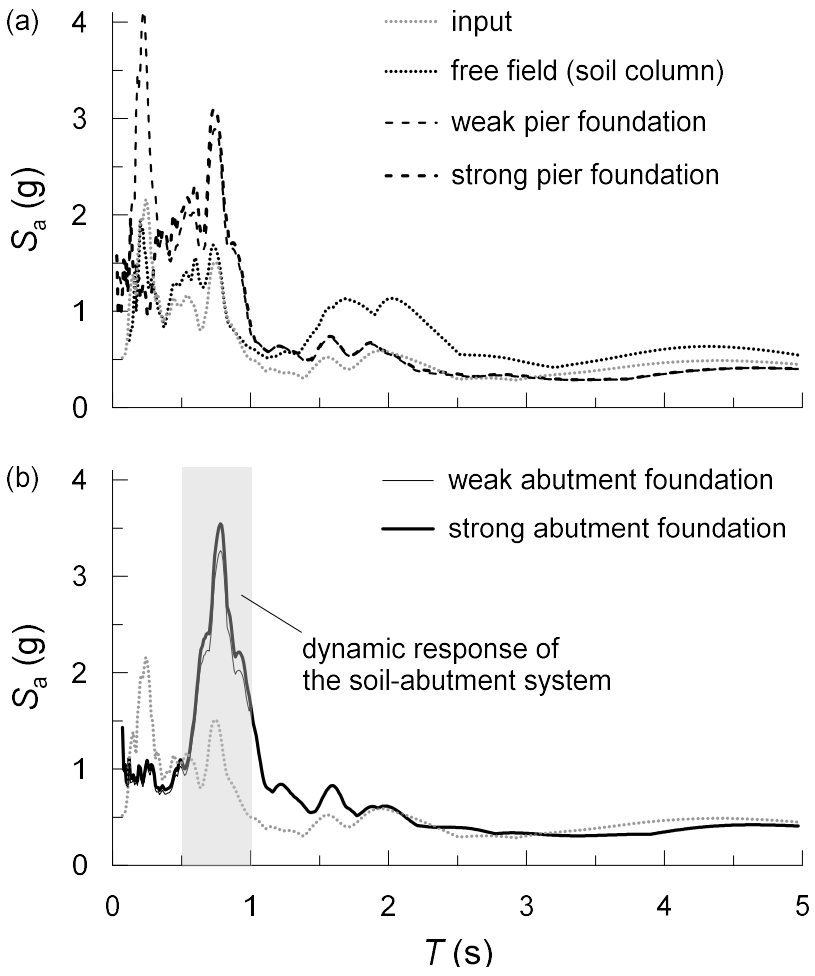

Figure 7.11: 5 %-damped elastic response spectra at the foundation level of the piers (a) and of the abutments (b).

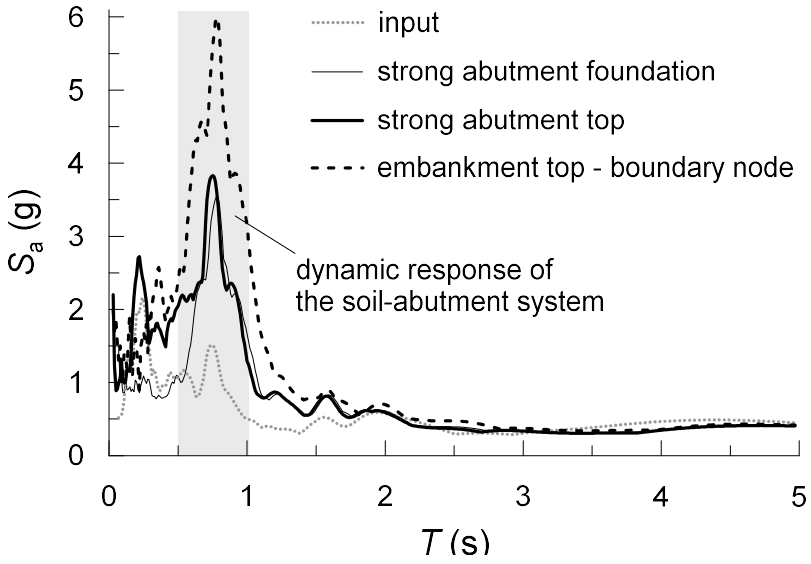

Figure 7.12: 5 %-damped elastic response spectra of the strong abutment and of the embankment.

Despite keeping the same dominant period, the corresponding spectral acceleration increases by about 60 % with respect to the maximum spectral acceleration at the abutment top, whereas the other regions of the spectrum shows a similar trend. This discrepancy can be directly associated with the resonance of the embankment far from the abutment. When the embankment starts interacting with the abutment structure, instead, the high stiffness of the latter attenuates partially the dominant peak, leading to a slight amplification at higher frequencies.

7.3.2 Seismic performance of the bridge

The seismic performance of the whole structure is concisely quantified looking at the output quantities depicted in Figure 7.13. For the peculiar structural layout considered, the longitudinal seismic loading is transferred to the superstructure through the strong abutment and the strong pier. Hence, the relative longitudinal displacement between the top of the abutment and the top of the strong pier can be regarded as an indicator of how the relative position between the two resistant vertical elements

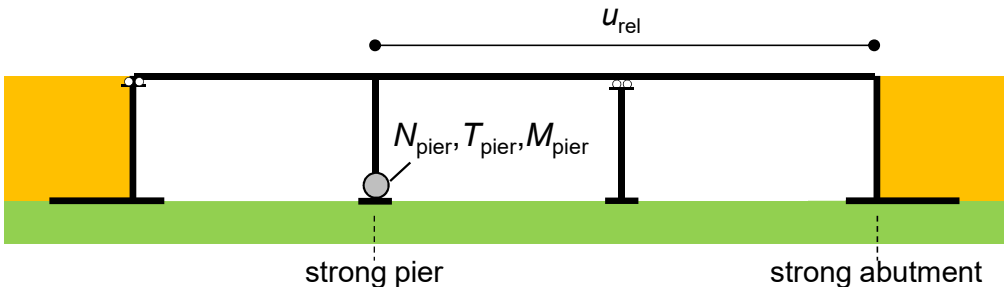

Figure 7.13: Output quantities used to quantify the effect of soil-structure interaction on the seismic performance of the bridge.

changes during ground motion. The base of the strong pier is the other scrutiny point of the dynamic response of the bridge, monitoring the relative internal forces, that are the normal force N_{pier}, the shear force T_{pier} and the moment M_{pier} along the axis out of plane.

Referring to the propagation of the longitudinal seismic motion of the Tabas record, Figure 7.14 shows the time evolution of the output quantities obtained with the full soil-bridge model. In the significant time interval of the input motion, between about $5 \div 15$ s, the superstructure shows the maximum dynamic amplification. The maximum amplitudes of the relative abutment-pier displacement in the direction of motion are lower than 0.1 m but an irreversible contribution develops progressively in time, giving an offset of about 0.18 m at the end of the earthquake. As observed in Section 7.3.1, this means that the strong abutment moves inwards the bridge, pushed by the dynamic response of the embankment, but is partially constrained by the flexural stiffness of the strong pier, generating a permanent axial force in the deck. The latter translates in permanent interaction forces at the deck-abutment contact due to the nonlinear behaviour of the soil, phenomenon already analysed in detail in Section 6.5. The flexural forces T_{pier} and M_{pier} in the strong pier (Figure 7.14(c)) show a noticeable variation in time, with a more pronounced permanent value after the earthquake in the case of the moment. The axial force in

the pier instead, that is the vertical load for the foundation, undergoes minor variations with respect to the initial condition at rest: the maximum amplitudes induced by the ground motion are somewhat limited, leading however to a moderate permanent increase of N_{pier} after the earthquake of about 37 %. For all quantities, the maximum and permanent effects localise in the critical time interval of the Tabas record between 5 s and 15 s.

The above results are now compared with the response of the global structural model in which different representations are employed for the soil-abutment interaction. As a first comparison, consider three structural models so defined: the global structural model with fixed base, the model with a non-inertial impedance function at the deck-abutment contact and with the non-inertial macro-element of bridge abutment, both applied in the direction of motion. None of these representations considers the participating mass of the soil-abutment system, thus no mass was assigned to the deck-abutment contact. The corresponding relative abutment-pier displacements u_{rel} are illustrated in Figure 7.15. It is evident that all these representations lead to an important underestimation of the relative displacements caused by a too stiff behaviour of the deck-abutment contact. The nonlinear response of the macro-element of abutment produces the greatest attenuation of the amplitudes of u_{rel} without being able however to produce appreciable permanent displacements because of the very limited plastic response at those amplitudes of the internal force. Moreover, it is apparent that the response of the full soil-bridge model is characterised by much longer periods compared to the response of the sub-system of the structure, that is instead characterised by very high frequencies in the all cases examined.

When the masses of the macro-element are activated, however, the response changes drastically. Figure 7.16 shows the response of the macro-element of abutment provided with the two masses $m_1 = m_2$ identified in Section 5.14.2, limiting

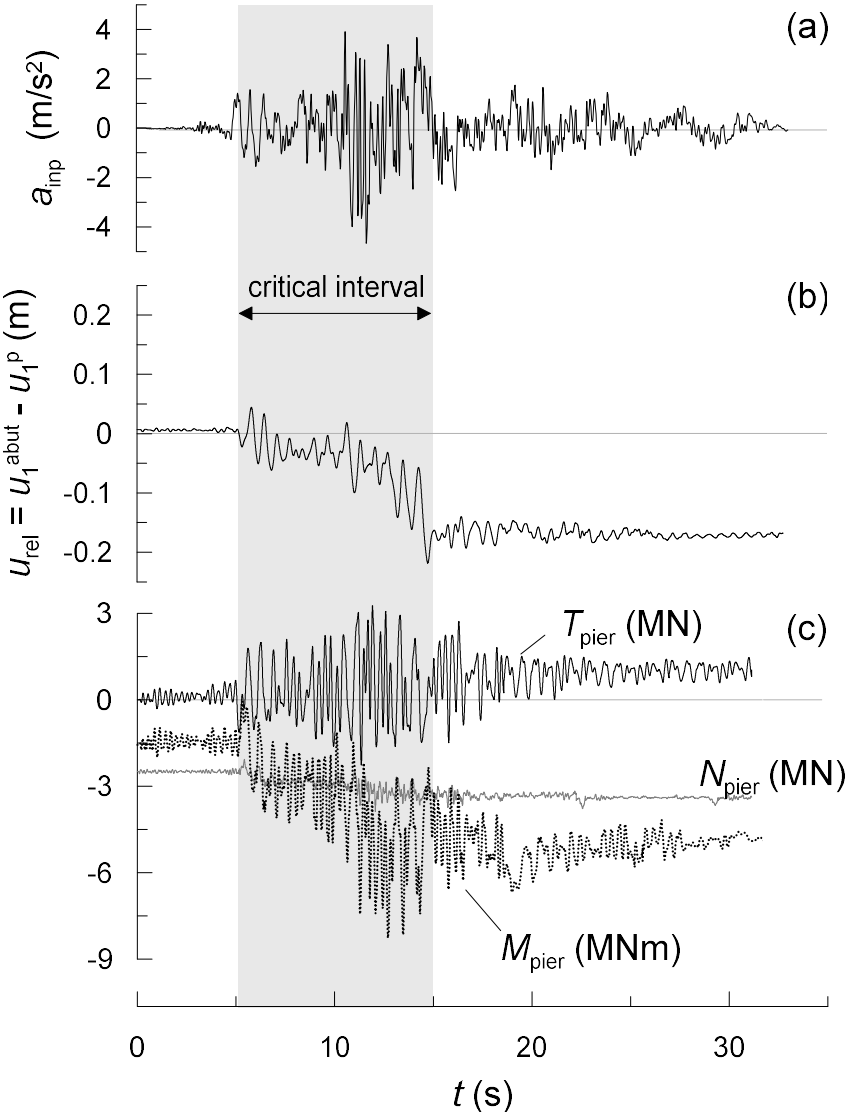

Figure 7.14: Full soil-bridge model: (a) acceleration time history of the input motion, time histories of the relative displacement between the strong abutment and the strong pier (b) and of the internal forces at the base of the strong pier (c) .

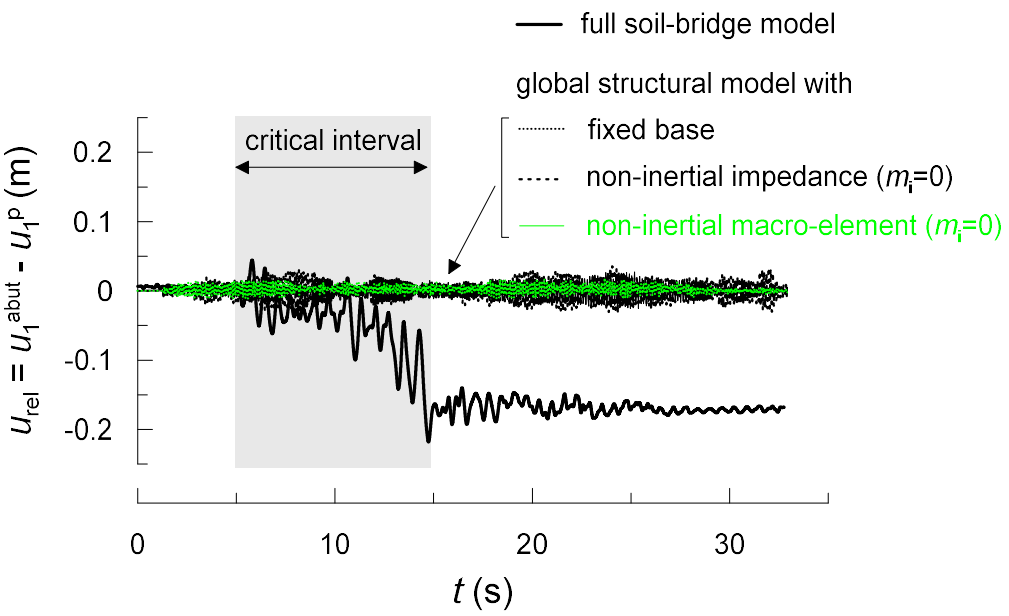

Figure 7.15: Time evolution of the relative displacement between the strong abutment and the strong pier evaluated through different representation strategies of soil-abutment interaction: structure with fixed-base, structure with non-inertial impedance function ($m_i = 0$) and structure with non-inertial macro-element ($m_i = 0$) at the abutment location.

the representation to 20 s in order to focus on the critical time interval. The amplitudes of the relative displacement increase considerably, becoming comparable with the response exhibited by the full soil-bridge model. The oscillations of the relative displacement are a bit too slow in the first part of the signal, for then following quite well the response of the full model when the amplitudes increase. In the critical time interval, permanent effects develop gradually in time, giving a final offset of about 0.146 m, that is equal to 67 % the final relative displacement computed on the soil-bridge model. This discrepancy could be in part overcome through a more accurate calibration of the mass of the macro-element, especially the second mass retrieved by trial and error, but it can be also due to the coupled behaviour between the strong abutment and the strong pier. For the latter, the soil-foundation interaction has been completely neglected, with direct application of the input motion to the base node of the pier, that could limit the permanent effects in the structural system due

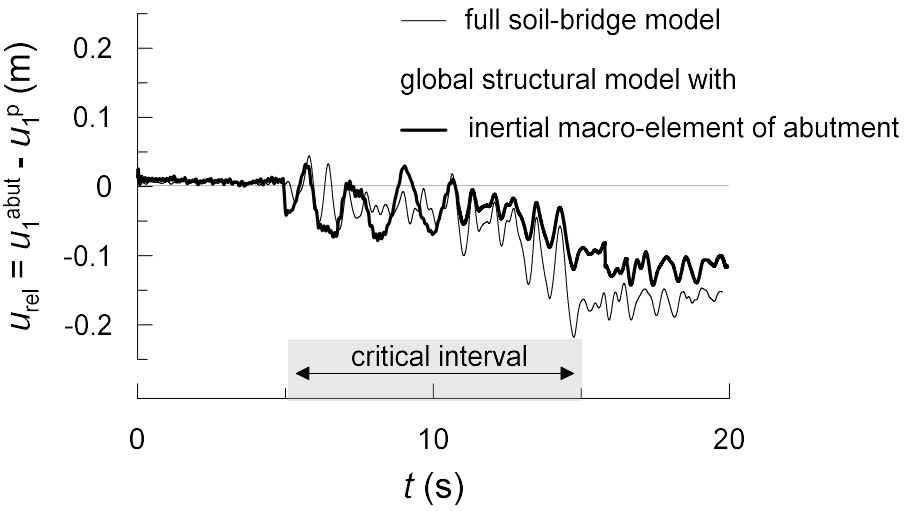

Figure 7.16: Effect of the inertial response of the macro-element of bridge abutment on the relative displacements between the strong abutment and the strong pier.

to the soil behaviour. Some insight into this aspect will be given later, including the macro-element of shallow foundation in the structural model. Anyway, the introduction of the masses into the macro-element have noticeably improved the global response of the structural model, confirming again the important role of the inertial effects coming from the embankment. A much minor effect was instead observed including the mass to the dynamic impedance function placed at the deck-abutment contact (see Section 7.2.1), not shown herein for brevity.

The internal shear force and moment at the base of the pier obtained by applying the inertial macro-element of abutment are shown in Figures 7.17 and 7.18, respectively. It can be seen quite a good agreement with the results of the full model, though the macro-element leads to a moderate overestimation of the internal forces in the pier when permanent effects start arising, that could be a consequence of neglecting the soil-foundation interaction. As noted for the relative displacements, the oscillations of the internal forces associated with the use of the macro-element are slightly longer than the actual ones and this could indicate that the mass introduced into the macro-element is somewhat too large.

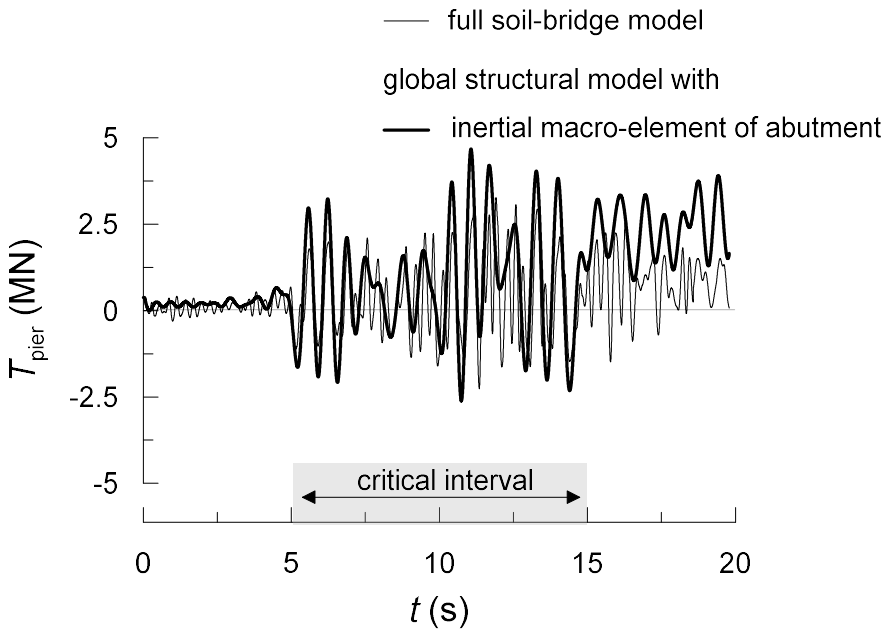

Figure 7.17: Effect of the inertial response of the macro-element of bridge abutment on the internal shear force at the base of the strong pier.

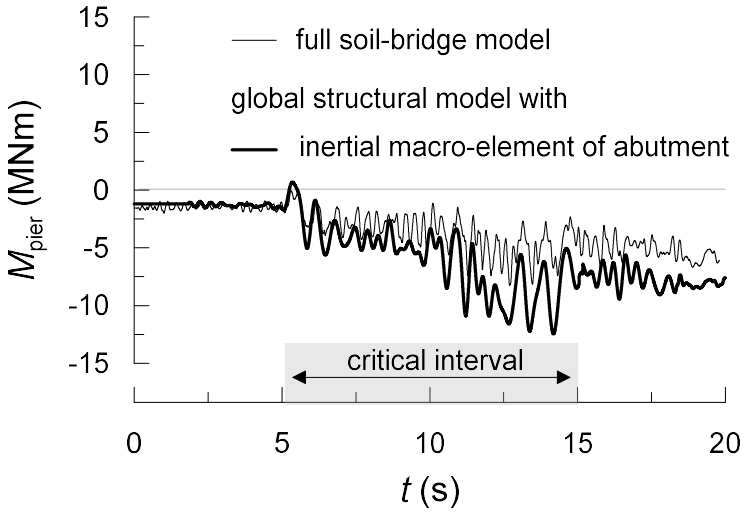

Figure 7.18: Effect of the inertial response of the macro-element of bridge abutment on the internal moment at the base of the strong pier.

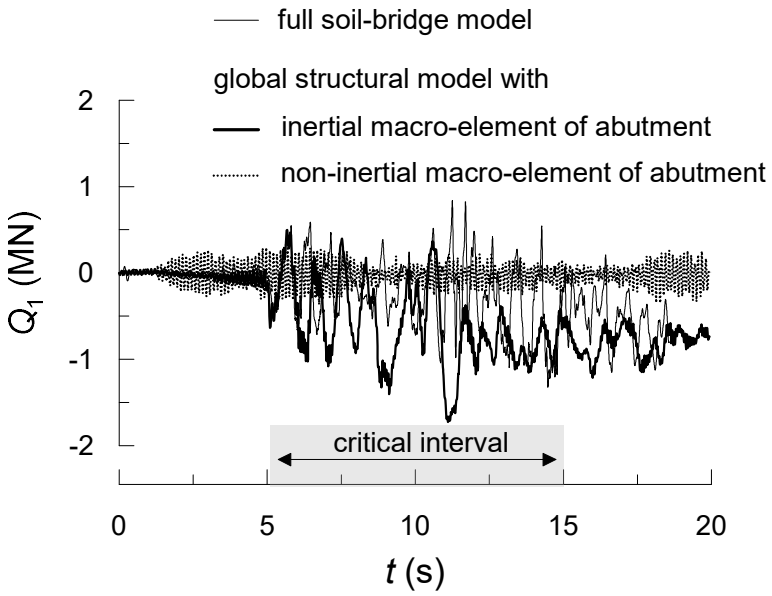

Figure 7.19: Internal force in the macro-element with and without inertial effects.

In light of the above results, the structural response is strongly influenced by the force-displacement response of the deck-abutment contact. The relative displacements of the deck, in fact, are profoundly affected by the interaction forces exchanged between the soil-abutment system and the superstructure. The abutment-deck interaction force, representing the internal force of the macro-element, is shown in Figure 7.19. The comparison between the macro-element and the interaction force evaluated on the full model reflects the considerations made above regarding the alteration of the seismic performance of the structure, with a completely inappropriate response of the macro-element when the relative mass is set equal to zero. The response of the inertial macro-element, instead, is magnified by its mass, leading to a much more pronounced plastic response with development of irreversible forces and displacements at the deck-abutment contact.

A more complete view of the soil-abutment-superstructure interaction effects can be inferred looking at the results in Figure 7.20. The maximum values of the three output quantities of the structure were computed for all the methods employed to

simulate the soil-abutment interaction, that are:

- model A: full soil-bridge model (reference model);
- model B: global structural model with fixed-base;
- model C: global structural model with inertial impedance functions for the strong abutment and the strong pier foundation;
- model D: global structural model with non-inertial macro-element of the strong abutment;
- model E: global structural model with inertial macro-element of the strong abutment;
- model F: global structural model with inertial macro-elements of strong abutment and of the strong pier foundation.

The use of linear models (model B and C) for the soil-abutment interaction leads to a substantial overestimation of the flexural internal forces in the strong pier and, at the same time, to an important underestimation of the axial force in the deck, proportional to the relative abutment-pier displacement u_{rel}, because of the very low longitudinal forces transferred by the equivalent soil-abutment model. The nonlinear behaviour of the non-inertial macro-element of the soil-abutment system (model D) on the one hand reduces further the axial forces in the deck, proportional to u_{rel}, leading to an erroneous evaluation of the final configuration of the bridge, but on the other hand returns a significant attenuation of the internal forces in the strong pier. The inertial macro-element of the soil-abutment system (model E) gives a much better comparison with the response of the full model (model A) with a net increase of the relative displacements between abutment and pier, due to the inertial effects that magnify the soil-abutment interaction. The internal forces in the

strong pier are still moderately overestimated, in part caused by having neglected the soil-foundation interaction for the pier. In fact, model F, relative to a fully nonlinear representation of soil-structure interaction in the global structural model, shows a further decrement of the maximum forces in the pier and a moderate increase of the relative abutment-pier maximum displacements.

The macro-element of the soil-abutment system was tested in the other three seismic scenarios selected as representative of the No-Collapse Earthquake for the Pantano viaduct (see Section 3.4 and 3.5). The results are shortly shown in Figures 7.21 and 7.22, as the comparison between the full soil-bridge model and the global structural model with inertial macro-element of the strong abutment, in terms of maximum values of the reference output quantities plotted as a function of the mean square period T_m (Rathje et al. 1998) associated with the four seismic records. In all cases, the structural performance is moderately emphasised by the macro-element response, in a manner that does not seem to depend on the frequency content of the input motion. The dynamic response of the bridge shows instead evident frequency-dependent effects. As expected, the Tabas record is the most severe seismic scenario for the bridge, because of its extremely high intensity and wide frequency content. Moreover, the Tabas record leads to a higher dynamic coupling with the superstructure (first mode in the longitudinal direction at 0.16 s), but especially with the soil-abutment system since the relative dominant responses occur between 0.6 s and 0.8 s, that can constitute another factor of amplification of the structural response.

To sum up, the macro-element of the soil-abutment system has shown good capabilities to incorporate the dynamic response of the soil-abutment system in the global dynamic behaviour of the structure, especially compared to existing methods. The inertial effects developing into the embankment and the nonlinear behaviour of the soil interacting with the abutment represent a central factor in the response of the latter, with a consequent relevant impact on the seismic performance of the su-

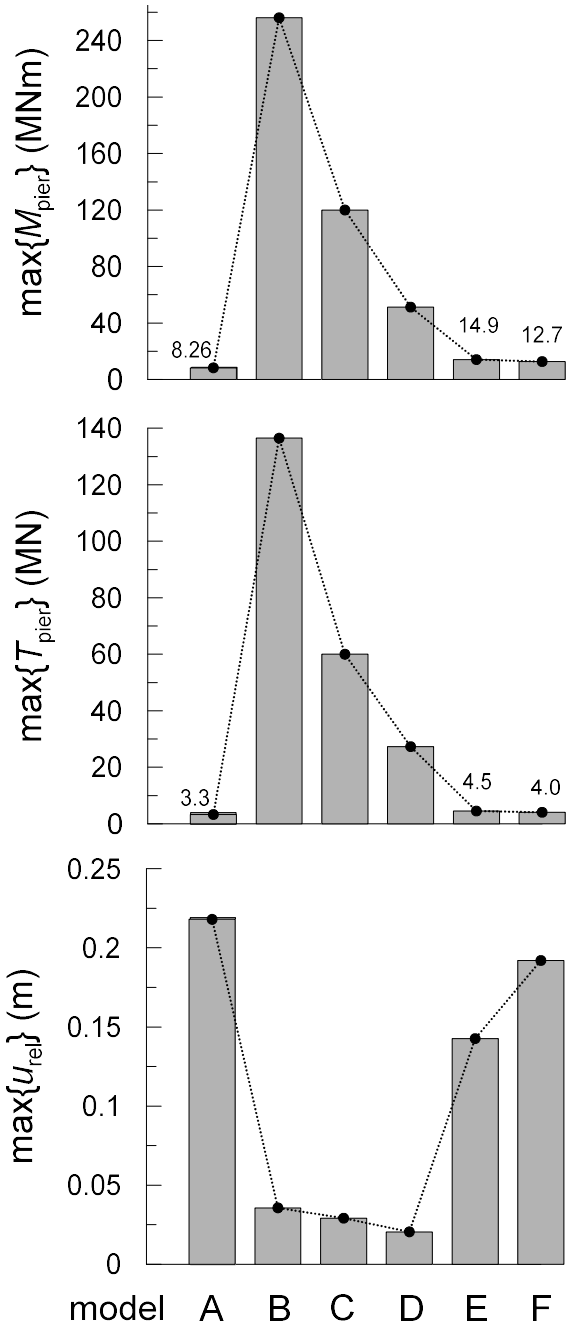

Figure 7.20: Histogram of the maximum relative displacements of the deck and the maximum internal shear force and moment in the strong pier, using different approaches for soil-structure interaction.

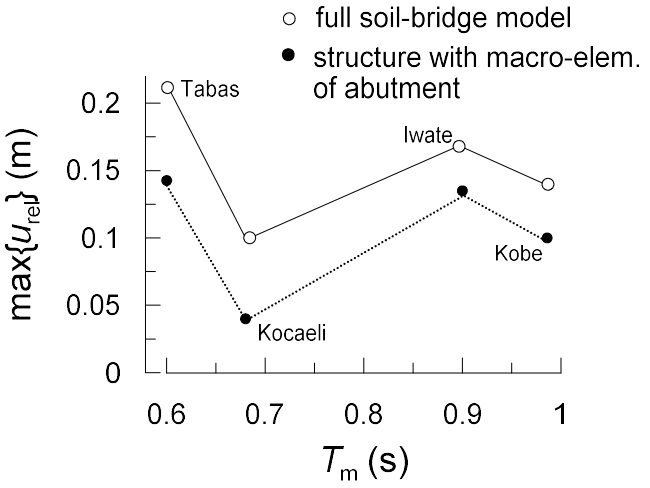

Figure 7.21: Maximum relative displacements of the deck, between the strong abutment and the strong pier, obtained for different seismic scenarios.

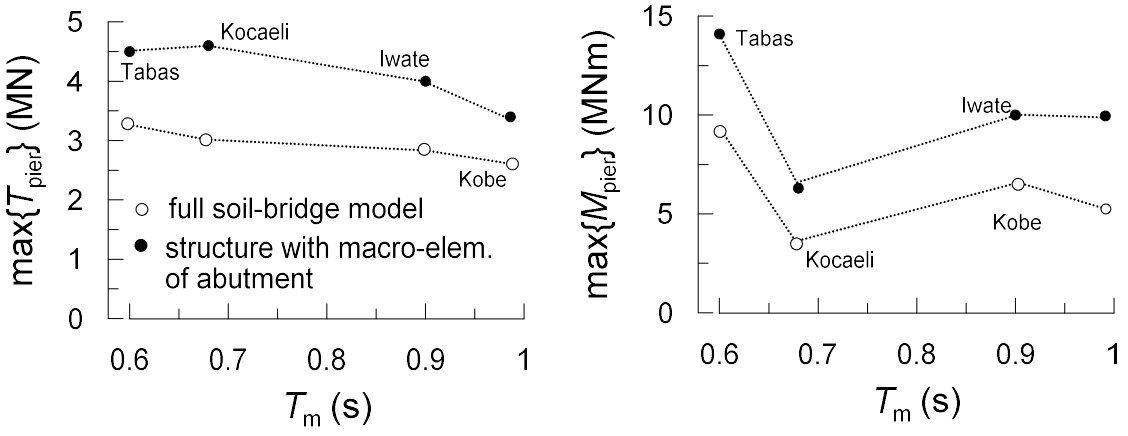

Figure 7.22: Maximum internal forces at the base of the strong pier obtained for different seismic scenarios.

perstructure. It has been pointed out that a more accurate calibration of the mass of the macro-element associated with higher order plastic flows might lead to more accurate results and this will constitute a forthcoming development of the present research.

7.3.3 Local performance of the abutment

The local performance of the strong abutment was evaluated by including the macro-element of the bridge structure (see Section 6.9) in the local model of the soil-abutment system. This paragraph focuses on the relationship existing between the two complementary representations of the soil-structure interaction. The two macro-elements of bridge abutment and of bridge structure represent two sides of the same coin, connecting the response of the two sub-systems identified by sub-structuring, i. e. the superstructure and the soil-abutment system. The connecting element is right the internal response of the two macro-elements that reproduce the behaviour of the missing part of the domain.

Considering the soil-structure models perturbed by the longitudinal component of the Tabas record, Figure 7.23(a) shows the time evolution of the longitudinal internal force in the two macro-elements, obtained by the global structural model and by the local soil-abutment model. The macro-element of the bridge structure (thick continuous line) reproduces quite well the interaction force at the deck-abutment contact, in terms of maximum amplitudes and frequency content, but, differently from the macro-element of the soil-abutment system (dotted line), it cannot account for the progressive development of the permanent interaction forces at the deck-abutment contact (offset with respect to the axis $Q_1 = 0$). This limitation of the macro-element of the bridge structure has already been pointed out in Section 6.5, showing that this effect can be relevant for very stiff structures such as that one under examination. This effect arises from the permanent differential displacements

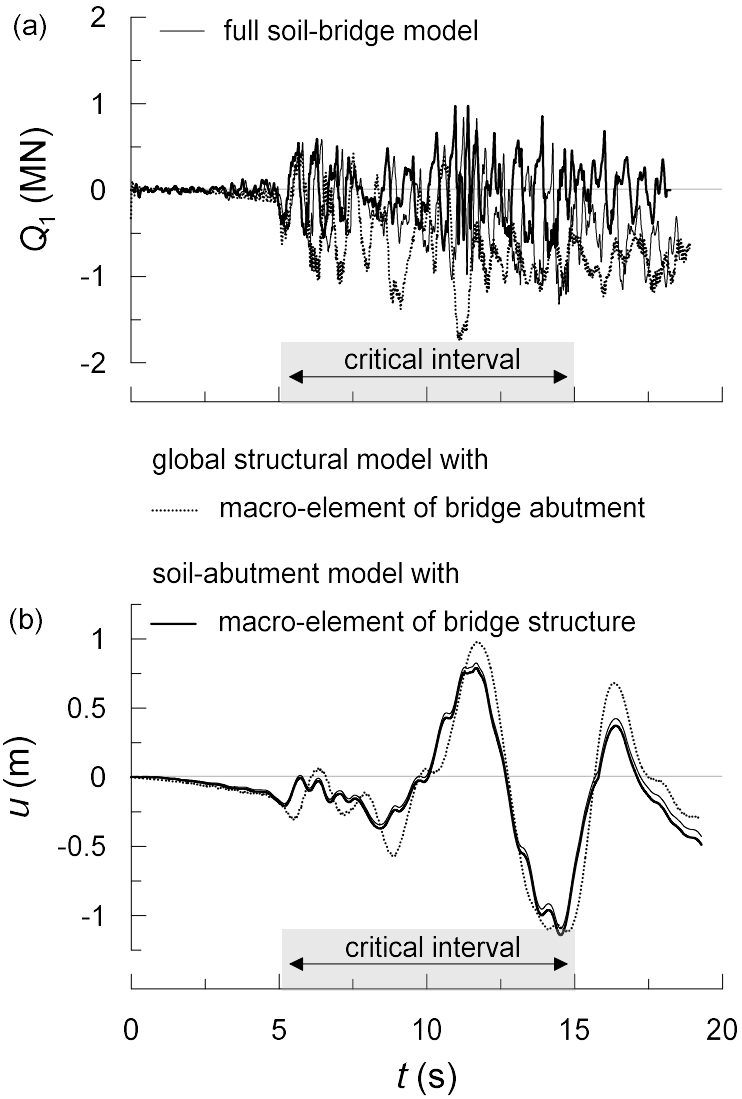

Figure 7.23: Comparison between the response of the top of the abutment in the global structural model with macro-element of the bridge abutment and in the local model of abutment with macro-element of the bridge structure: (a) time evolution of the internal force in the two macro-elements and (b) of the longitudinal displacement.

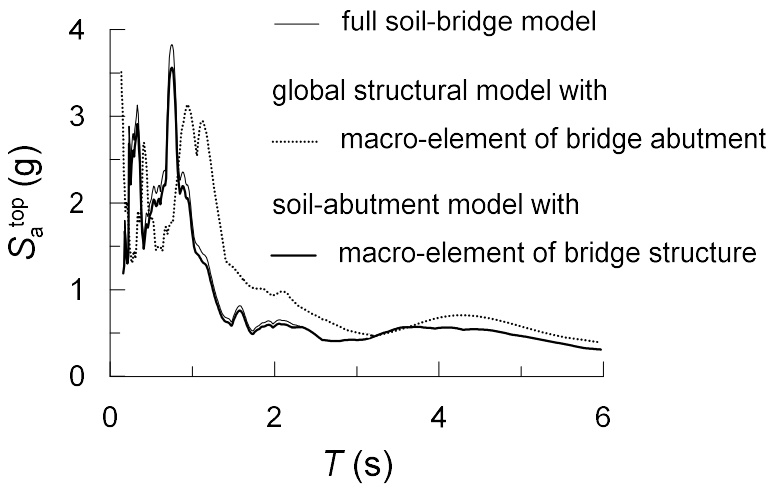

Figure 7.24: 5%-damped elastic response spectra at the deck-abutment contact, evaluated through the full soil-bridge model, the structural model with macro-element of the soil-abutment system and the local soil-abutment model with macro-element of the bridge structure.

developing between the abutment and pier foundations, caused by the nonlinear behaviour of soil, resulting in a deformed configuration of the structure after the earthquake. This effect on the interaction force Q_1 can be estimated, in first approximation, through the soil plasticity curve of the transfer tensor (see Section 6.5.1).

The displacement field of the abutment in the local model is well reproduced by the macro-element of the bridge structure, concisely represented in Figure 7.23(b) looking at the longitudinal displacement of the abutment top in the critical time interval of the Tabas record. In the global structural model, the macro-element of the soil-abutment system gives a modest amplification of the maximum displacements, probably associated with a slightly excessive mass introduced into the macro-element. This amplification of the displacement field leads to a longer spectral response at the deck-abutment contact compared to the spectra obtained from the full soil-bridge model and the local model with macro-element of the bridge structure, depicted in Figure 7.24. As already observed before, this alteration of the significant frequency content could be improved through an appropriate reduction of the second

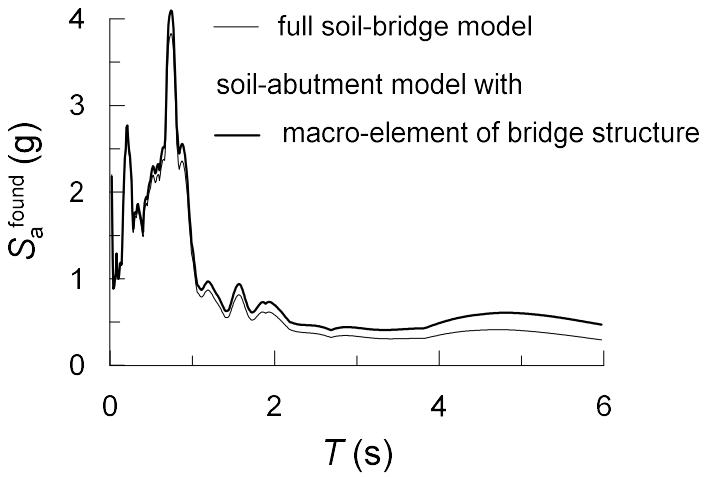

Figure 7.25: Foundation input motion at the base of the abutment, evaluated through the full soil-bridge model and in the local model of the abutment with macro-element of the bridge structure.

mass m_2 of the macro-element of abutment.

As a final result, Figure 7.25 compares the foundation input motion for the strong abutment obtained through the local soil-abutment model and that of the full soil-bridge model, in terms of elastic response spectra. In both models, the response spectra at the abutment foundation takes explicitly into account in the computation the propagation of seismic waves through the foundation soils and the soil-structure interaction. The spectral accelerations of the abutment in the local model follows very well the spectral shape deriving from the fully coupled analysis. Only at large periods, greater than about 4 s, the local model of the abutment presents a moderate amplification of the spectral ordinates, that might be due to a limited overestimation of the inertial forces in the macro-element of the structure in this range of periods, that is completely decoupled with respect to the dominant peaks of the respective transfer function.

Conclusions

The seismic design of a bridge requires a check of the performance of the superstructure and of the structural elements directly in contact with the soil, in terms of internal forces and displacements. Focusing on the soil-abutment-superstructure interaction, a semi-direct method of analysis has been developed to this end, which consists in the introduction of two complementary macro-elements in the two structural and geotechnical sub-systems that, through their internal response, define a link between the superstructure and the abutment. The macro-elements are aimed to reproduce the main features of this interaction, that are: the inertial effects, associated with a strongly frequency-dependent response, and the marked nonlinear behaviour of the system. The procedure developed in this work leads to a drastic reduction of the computational demand of the numerical soil-structure interaction models.

More specifically, the two models consist of a macro-element of the soil-abutment system, for a global analysis of the bridge structure, and a macro-element of the bridge structure used in a local numerical model of the soil-abutment system. The former has been developed according to a rigorous thermodynamic formulation in which the plastic response of the model is regarded as a transition phase towards the ultimate capacity of the system, plastic response that is modelled by the inertial effects reflecting the dynamic characteristics of the interaction between the abutment and the soil from small to large strain levels. Conversely, the macro-element of

the bridge structure is developed using a phenomenological approach for a prompt implementation in numerical simulations. The methodology has been implemented in the analysis framework OpenSees. In particular, the macro-element of bridge abutment can be used in the OpenSees framework as a new uni-axial material for the one-dimensional problem, and as a new zero-length finite element for the general multi-axial response.

A fully coupled soil-bridge system was used as a reference for validating the proposed methodology. It showed that the soil-abutment-superstructure interaction alters remarkably the global response of the reference bridge. The abutment, including the soil interacting dynamically with it, generates significant inertial effects that are transferred to the superstructure, leading to a considerably amplified response of the latter. These large inertial forces mobilise the nonlinear behaviour of the soil interacting with the abutment developing irreversible displacements and, consequently, significant internal forces in the crucial components of the superstructure after severe ground shaking. On the other hand, the inertial forces transferred by the structure to the abutment alter the stress-strain state in the soil, especially in the backfill, favouring further the attainment of the soil strength.

At the same time, the nonlinear dynamic analyses on the entire system have highlighted the complications associated with the use of the direct approach, that requires very large computation times and a non-trivial control of the model implementation and interpretation of the results. In this light, the macro-elements have represented not only an efficient analysis tool but also a method to clearly identify the factors that affect the reciprocal interaction between the superstructure and the abutments, leading to the definition of a calibration procedure of the two models based on a limited number of parameters.

The amplitude and the frequency content of the inertial effects have been introduced in the formulations of the two macro-elements as additional masses related

to the significant vibration periods of the sub-system considered. The study of the dominant responses of the soil-abutment system have shown that the dynamic response of the abutment is mainly controlled by the behaviour of the large volume of soil interacting with it. It has been demonstrated that the closed-form analytical solutions for the modal characteristics of the soil-abutment system allows to identify the first mass of the macro-element, associated with the surface of first yield, that is the most crucial component to reproduce the dominant response of the system. Through the numerical study on the effect of the nonlinear behaviour of soil, it has been found that the dominant periods, starting from the reversible behaviour at small strains, increase with the intensity of the perturbation, reaching a steady dynamic response corresponding to the activation of a global plastic mechanism. As a result, in addition to the first mass, it has been found that a very limited number of masses associated with the other plastic flows can be sufficient to improve the dynamic response of the macro-element at medium and large strain levels. For the reference case study, a sole mass has been associated with the second yield surface, resulting of the same order of magnitude of the first mass. On the other hand, the transfer functions of the macro-element of bridge structure can be easily calibrated with reference to the modal analysis on a global structural model. It has been shown, at least for the specific structural configurations examined, that the longitudinal interaction forces transmitted to the abutment top are mainly controlled by the axial dynamic response of the deck triggered by the activation of the higher modes of the abutments and of the piers, with maximum interaction forces localised at high frequencies. The vertical transfer function is instead characterised by several dominant peaks because of the significant contribution of the flexural modes of the deck in the vertical plane.

The nonlinear response of the macro-elements is confined by the conditions of first yield and ultimate capacity. The latter is represented in the macro-element of the

soil-abutment system by an ellipsoidal surface in the space of the forces exchanged at the deck-abutment contact. The ellipsoid is highly decentralised and rotated in the space of forces, reflecting the highly asymmetric response of the abutment. It has been shown, through the aid of elastoplastic analyses, that the shape of the ultimate surface can be also used to describe the first yield of the soil-abutment system under multi-axial loading conditions. Accordingly, the entire plastic domain of the macro-element has been conceived as a series of homothetic yield surfaces that evolve in the space of the generalised forces according to a prescribed kinematic hardening law. Looking at the structural response, in the case of a pronounced nonlinear behaviour of the superstructure, the nonlinear behaviour of the macro-element has been introduced in the formulation through the capacity curves of the structure, which modify the frequency-dependent inertial forces transmitted by the superstructure as a function of the intensity of the seismic motion. A simplified bi-linear trend for the shape functions can be adopted for a prompt use in numerical simulations, by simply introducing an upper bound to the internal forces developing in the elastic macro-element. This expedient can be particularly efficient in those cases in which the structure is provided with anti-seismic devices that limit the maximum seismic actions in the superstructure, such as fuses and isolators.

In light of the results obtained in this work, bridge abutments seem to be less rigid than expected. The amplified behaviour of the abutment associated with its dominant responses and its interaction with the superstructure indicates a marked effect of the plastic behaviour of soil on the overall response. This concept is leading to explore the intrinsic dissipative capabilities of the soil-abutment system, regardless the adoption of specific anti-seismic devices. In this view, the abutment would be guided towards the activation of some favourable dissipative mechanisms that can represent an efficient solution to limit the seismic actions in the superstructure, at cost of a certain amount of irreversible displacements. The integrated macro-

element approach proposed appears as an efficient means for testing new solutions for bridge abutments, allowing a clear definition and interpretation of the numerical models. The clear identification of the plastic domain of an abutment and of its nonlinear response points to an extension of the current principles of capacity design of bridges, in which the dissipative behaviour of the soil-abutment system could play a key role in controlling the seismic performance of the bridge.

Bibliography

Arya, L., and Paris, J. (1981). "A physicoempirical model to predict the soil moisture characteristic from particle-size distribution and bulk density data." *Soil Sci. Soc. Am. J.*, 45, 1023-1030.

Baldi, G., Bellotti, R., Ghionna, V., Jamiolkovski, M., and Pasqualini, E. (1985). "Penetration Resistance and Liquefaction of Sands." *Proc. XI ICSMFE*, San Francisco, 4, 1891-1896.

Been, K., and Jefferies, M. G. (1985). "A state parameter for sands." *Geotechnique*, 35(2), 99-112.

Bienen, B., Byrne, B. W., Houlsby, G. T., and Cassidy, M. J. (2006). "Investigating six-degree-of-freedom loading of shallow foundations on sand." *Geotechnique*, 56(6), 367-379.

Bolton M.D. (1986). "The strength and Dilatancy of Sands." *Géotechnique*, 36(1), 65-78.

Bommer, J. J., and Martinez-Pereira, A. (1999). "The effective duration of earthquake strong motion." *Journal of Earthquake Engineering*, 3(2), 127-172.

Brancaleoni, F., Diana, G., Faccioli, E., Fiammenghi, G., Firth, I. P. T., Gimsing, N. J., Jamiolkowski, M., Sluszka, P., Solari, G., Valensise, G., Vullo, E. (2010). *The Messina Strait Bridge. A challenge and a dream.* CRC Press.

Buscarnera, G., Nova, R., Vecchiotti, M., Tamagnini, C., and Salciarini, D. (2010). "Settlement analysis of wind turbines." In R. P. Orense, N. Chouw, & M. J. Pender (Eds.), *Proc. Int. Workshop on Soil–Foundation–Structure Interaction (SFSI 09)*, Auckland, New Zealand.

Butterfield, R., and Gottardi, G. (1994). "A complete three-dimensional failure envelope for shallow footings on sand." *Geotechnique*, 44(1), 181-184.

Callisto, L., and Gorini D. N.. "Evaluating the seismic response of a suspension bridge with dissipative foundations." *Submitted to Rivista Italiana Geotecnica*, 2019.

Callisto, L., Rampello, S., and Viggiani, G. M. B. (2013). "Soil–structure interaction for the seismic design of the Messina Strait Bridge." *Soil Dynamics and Earthquake Engineering*, 52, 103-115.

Callisto, L., Rampello, S. (2013). "Capacity design of retaining structures and bridge abutments with deep foundations." *J. Geotech. Geoenviron. Eng.*, 139(7), 1085-1095.

Caltrans SDC (2010). *Caltrans Seismic Design Criteria version 1.6*. California Department of Transportation, Division of Engineering Services, Office of Structure Design, Sacramento, CA.

Cassidy, M. J., Martin, C. M., and Houlsby, G. T. (2004). "Development and application of force resultant models describing jacking-up foundation behavior." *Mar. Struct.*, 173(4), 165-193.

Chatzigogos, C. T., Pecker, A., and Salencon, J. (2009). "Macroelement modelling of shallow foundations." *Soil Dynamics and Earthquake Engrg.* 29,765-781.

Chatzigogos, C. T., Figini, R., Pecker, A., and Salencon, J. (2011). "A macroelement formulation for shallow foundations on cohesive and frictional soils." *Int. J. Numer. Anal. Methods Geomech.*, 35(8), 902-931.

Collins, I. F., and Houlsby, G. T. (1997). "Application of thermomechanical principles to the modeling of geotechnical materials." *Proc., R. Soc.*, The Royal Society, London, A, 453, 1975-2001.

Correia, A. A. (2011). *A Pile-Head Macro-Element Approach to Seismic Design of Monoshaft-Supported Bridges*. PhD thesis: ROSE School Università degli Studi di Pavia & Istituto Universitario di Studi Superiori, Pavia, Italy.

Correia, A. A., Pecker, A., Kramer, S. L., and Pinho, R. (2012). "Nonlinear pile-head macro-element model: SSI effects on the seismic response of a monoshaft-supported bridge." *Proc. 15th World Conference on Earthquake Engineering*, Lisbon, Portugal.

Cremer, C., Pecker, A., and Davenne, L. (2001). "Cyclic macro-element for soil-structure interaction: material and geometrical non-linearities." *Int. J. Numer. Anal. Methods Geomech.*, 25(13), 1257-1284.

Cremer, C., Pecker, A., and Davenne, L. (2002). "Modelling of nonlinear dynamic behaviour of a shallow strip foundation with macro-element." *J. Earthquake Eng.*, 6(2), 175-211.

Crova, R., Jamiolkowski, M., Lancellotta, R., and Lo Presti, D. C. F. (1993). "Geotechnical characterization of gravelly soils at Messina site." *Predictive Soil Mechanics (Proc., Wroth Memorial Symp.), Thomas Telford*, London, 199-218.

Cubrinovski, M., and Ishihara, K. (1999). "Empirical correlation between SPT N-value and relative density for sandy soils." *Soils Found.*, 39(5), 61-71.

Dafalias, Y. F. (1986). "Bounding surface plasticity. I: Mathematical foundation and hypoplasticity." *J. Eng. Mech.*, 112(9), 966-987.

Dafalias, Y. F., and Manzari, M. T. (2004). "Simple plasticity sand model accounting for fabric change effects." *J. Eng. Mech.*, 130(6), 622- 634.

Diaz, N. D., and Amat, P. S. (1999). GID the personal pre/postprocessor user's manual, version 5.0. CIMNE, Barcelona, Spain, http://gid.cimne.upc.es.

Di Laora, R., de Sanctis, L., and Aversa, S. (2018). "Bearing capacity of pile groups under vertical eccentric load." *Acta Geotechnica*, Published online 31 March 2018.

Di Prisco, C., Nova, R., Sibilia A. (2003). "Shallow footing under cyclic loading: experimental behaviour and constitutive modelling." In *Geotechnical analysis of the seismic vulnerability of historical monuments*, Maugeri M. & Nova R. (Eds.), Pàtron, Bologna, 99-122.

Di Prisco, C., Massimino, M. R., Maugeri, M., Nicolosi, M., and Nova, R. (2006). "Cyclic numerical analyses of Noto Cathedral: soil-structure interaction modelling." *Italian Geotechnical Journal*, 2, 49- 63.

Dvorkin, E. N., and Bathe, K.J. (1984). "A continuum mechanics based four node shell element for general nonlinear analysis." *Eng. Comput.*, 1, 77-88.

Fang, Y. S., Chen, T. J., and Wu, B. F. (1994). "Passive earth pressures with various

wall movements." *J. Geotech. Eng.*, 1208, 1307-1323.

Fioravante, V., Giretti, D., Jamiolkowski, M., and Rocchi, G.F. (2012). "Triaxial tests on undisturbed samples of gravelly soils from the Sicilian shore of Messina strait". *Bulletin of Earthquake Engineering*, 10, 1717-1744.

Gadre, A. D., and Dobry, R. (1998). "Centrifuge modeling of cyclic lateral response of pilecap systems and seat-type abutments in dry sand." *Rep. MCEER-98-0010*, Rensselaer Institute, Civil Engineering Dept., Troy, N.Y.

Gazetas. G. (1987). "Seismic response of earth dams: some recent developments." *Soil Dynamics and Earthquake Engrg.* 6(1),1-47.

Gazetas, G. (1991). *Chapter 15: foundation vibrations*, Foundation engineering handbook, Hsai-Yang Fang, ed., Van Nostrand Reinhold, New York, 553-593.

Gerolymos, N., and Gazetas, G. (2005). "Phenomenological model applied to inelastic response of soil-pile interaction systems." *Soils Found.*, 45(4), 119-132.

Gerolymos, N., Papakyriakopoulos, O., and Brinkgreve, R. B. J. (2015). "Macroelement modeling of piles in cohesive soil subjected to combined lateral and axial loading." *Proc. 8th Eur. Conf. on Numerical Methods in Geotechnical Engineering*, Delft, Balkema, Rotterdam.

Gorini D. N., and Callisto, L. (2015). "Dynamic soil-structure interaction for a long-span suspension 9 bridge with dissipative foundations." *In: Proc. of the 4th International Workshop on 10 Dynamic Interaction of Soil and Structure (DISS_15)*, ISBN: 978-88-940114-2-5: 11 289-297.

Gorini D. N., and Callisto, L. (2016). "Predicting the dynamic response of friction dissipative 17 foundations using a modified Newmark model." *Procedia Engineering*, 158, 170-75.

Gorini D. N., and Callisto, L. (2017). "Study of the dynamic soil-abutment-superstructure interaction for a bridge abutment." *Proc. 1st European Conference on OpenSees (OpenSees Days Europe 2017)*, 57-60.

Gorini D. N., and Callisto, L.. "Seismic performance and design approach of friction dissipative foundations." *Submitted to Soil Dynamics and Earthquake Engineering*, 2018.

Gottardi, G., and Butterfield, R. (1995). "The displacement of a model rigid surface footing on dense sand under general planar loading." *Soils Found.*, 35(3), 71-82.

Gottardi, G., Houlsby, G. T., and Butterfield, R. (1999). "Plastic response of circular footings on sand under general planar loading." *Geotechnique*, 49(4), 453-469.

Hansen, J. B. (1970). "A revised and extended formula for hearing capacity." *Geoteknisk Inst.*, *Bull.*, 28, 5-11.

Houlsby, G. T., and Martin, C. M. (1993). "Modelling on the behaviour of jack-up units on clay." *Predictive soil mechanics*. Thomas Telford, London, 339-358.

Houlsby, G. T., and Cassidy, M. J. (2002). "A plasticity model for the behaviour of footings on sand under combined loading." *Geotechnique*, 52(2), 117-129.

Houlsby, G. T., and Puzrin, A. M. (2006). *Principles of hyperplasticity*, Springer, Berlin.

Houlsby, G. T., Abadie, C. , Beuckelaers, W. , and Byrne, B. (2017). "A model for nonlinear hysteretic and ratcheting behaviour." *International Journal of Solids and Structures*, 120, 67-80.

Ishihara, K., Tatsuoka, F., and Yasuda, S. (1975). "Undrained deformation and liquefaction of sand under cyclic stresses." *Soils Found.*, 15(1), 29-44.

Italian Building Code (IBC). (2008). "Norme Tecniche per le Costruzioni." D.M. 14.01.2008, Italian Ministry of Infrastructures and Transportation, Rome (in Italian).

Iwan, W. D. (1967). "On a class of models for the yielding behavior of continuous and composite systems." *J. Appl. Mech.*, 34, 612-617.

Jaky J. (1948). "Pressure in Soils." *II ICSMFE*, London, 1, 103-107.

Jamiolkowski, M., and Lo Presti, D. C. F. (2002). "Geotechnical characterization of Holocene and Pleistocene Messina sand and gravel deposits." *Charact. and Engng. Properties of Natural Soils*, Singapore, Balkema Publishers, 2, 1087-11120.

Joyner, W. B., Chen, A. T. F. (1975). "Calculation of nonlinear ground response in earthquakes." *Bull Seismol Soc Am*, 65(5), 1315-1336.

Kotsoglou, A., and Pantazopoulou, S. (2007). "Bridge–embankment interaction under transverse ground excitation." *Earthq Eng Struct Dyn*, 36(12), 1719–1740.

Kramer, S. L. (1996). *Geotechnical earthquake engineering*, Prentice- Hall, Upper Saddle River, N.J.

Lacy, S. (1986). "Numerical procedures for nonlinear transient analysis of two-phase soil system." *PhD dissertation*, Princeton Univ., Princeton, N.J.

Le Pape, Y., and Sieffert, J. P. (2001). "Application of thermodynamics to the global modelling of shallow foundations on frictional material." *Int. J. Numer. Anal. Methods Geomech.*, 25(14), 1377-1408.

Li, X. S., and Wang, Y. (1998). "Linear representation of steady-state line for sand." *J. Geotech. Geoenviron. Eng.*, 124(12), 1215-1217.

Li, X. S., and Dafalias, Y. F. (2000). "Dilatancy for cohesionless soils." *Geotechnique*, 50(4), 449-460.

Ling, H. I., Liu, H., and Mohri, Y. (2005). "Parametric studies on the behavior of reinforced soil retaining walls under earthquake loading." *J. Eng. Mech.*, 13110, 1056-1065.

Ling, H. I., Mohri, Y., Leshchinsky, D., Burke, C., Matsushima, K., and Liu, H. (2005). "Large-scale shaking table tests on modular-block reinforced soil retaining walls." *J. Geotech. Geoenviron. Eng.*, 1314, 465–476

Loukidis, D., and Salgado, R. (2009). "Modeling sand response using two-surface plasticity." *Computers and Geotechnics*, 36, 166-186.

Luco, J. E., and Westman, R. A. (1971). "Dynamic response of circular footings." *J. Eng. Mech. Div. Am. Soc. Civil Engrs*, 97(5), 1381-1395.

Maroney, B., Romstad, K., and Chajes, M. (1990). "Interpretation of Rio Del Freeway response during six recorded earthquake events." *Proc., 4th U.S. National Conference on Earthquake Engineering*, 1, 1007-1016.

Martin, C. M. (1994). "Physical and numerical modeling of offshore foundations under combined loads." *PhD thesis*, University of Oxford.

Martin, G. R., Lam, I. P., Yan, L.-P., Kapuskar, M., and Law, H. (1996). "Bridge

abutments-Modeling for seismic response analysis." *Proc., 4th CALTRANS Seismic Research Workshop*.

Martin, C. M., and Houlsby, G. T. (2000). "Combined loading of spudcan foundations on clay: Laboratory tests." *Geotechnique*, 50(4), 325- 338.

Martin, C. M., and Houlsby, G. T. (2001). "Combined loading of spudcan foundations on clay: Numerical modelling." *Geotechnique*, 51(8), 687-700.

McKenna, F. (1997). *Object-oriented finite element analysis: Frameworks for analysis, algorithms and parallel computing*. Ph.D. dissertation, Univ. of California, Berkeley, CA.

McKenna, F., Fenves, G. L., Scott, M. H., and Jeremić, B. (2000). Open system for earthquake engineering simulation. http:// opensees.berkeley.edu.

McKenna, F., and Fenves, G. L. (2008). "Using the OpenSees interpreter on parallel computers, Network for Earthquake Engrg. Simulations." Berkeley, CA.

Mesri, G., and Castro, A. (1989). "Reduction of inertial seismic forces in bridges by using the abutment backwall as a "yielding" stopper"." *Journal of Geotechnical Engineering*, 3(3).

Mitoulis, S.A., and Tegos, I.A. (2005). "Reduction of inertial seismic forces in bridges by using the abutment backwall as a "yielding" stopper"." *Proc., Earthquake Resistant Engineering Structures* (ERES), Skiathos, Greece, Chapter V, 1, 507-520.

Mitoulis, S.A., and Tegos, I.A. (2010). "Restrain of a seismically isolated bridge by external stoppers." *Bulletin of Earthquake Engineering*, 8(4),973-993.

Mroz, Z. (1967). "On the description of anisotropic work hardening." *J. Mech. Phys. Solids*, 15, 163-175.

Mylonakis, G., Nikolau S., and Gazetas, G. (2006). "Footings under seismic loading: Analysis and design issues with emphasis on bridge foundations." *Soil Dynamics and Earthquake Eng.*, 26(9), 824-853.

Nojoumi, S. (2016). *Modeling the coupled cyclic translational and rotational responses of skew bridge abutment backfill*. Ph.D. dissertation, Univ. of California, Los Angeles, CA.

Nova, R., and Montrasio, L. (1991). "Settlements of shallow foundations on sand." *Geotechnique*, 41(2), 243-256.

Odong, J. (2007). "Evaluation of empirical formulae for determination of hydraulic conductivity based on grain-size analysis." *J. Am. Sci.*, 3(3), 54-60.

OptumCE (2016). "OptumG2 v. 2016". Manual. https://optumce.com/products/brochure-and-datasheet/.

Pais, A., and Kausel, E. (1988). "Approximate formulas for dynamic stiffness of rigid foundations." *Soil Dynamics and Earthquake Eng.*, 7, 213-227.

Paolucci, R. (1997). "Simplified evaluation of earthquake induced permanent displacements of shallow foundations." *J. Earthquake Eng.*, 1(3), 563-579.

Papadimitriou, A. G., Bouckovalas, G. D., and Dafalias, Y. F. (2001). "Plasticity model for sand under small and large cyclic strains." *J. Geotech. Geoenviron. Eng.*, 127(11), 973-983.

Parra, E. (1996). "Numerical modeling of liquefaction and lateral ground deformation including cyclic mobility and dilation response in soil systems." *PhD thesis*, Dept. of Civil Engineering, Rensselaer Polytechnic Inst., Troy, N.Y.

Patra, C. R., Sivakugan, N., Das, B. M., and Rout, S. K. (2013). "Correlations for relative density of clean sand with median grain size and compaction energy." *Int. J. Geotech. Eng.*, 4(2), 195-203.

Pecker, A. (2003). "Aseismic foundation design process, lessons learned from two major projects: 18 the Vasco de Gama and the Rion Antirion bridges." *In: ACI Int. Conf. Seismic Bridge 19 Design & Retrofit*, La Jolla, California.

Prager, W. (1949). "Recent developments in the mathematical theory of plasticity." *J. Appl. Phys.*, 20, 235-241.

Prevost, J. H. (1985). "A simple plasticity theory for frictional cohesionless soils." *Soil Dyn. Earthquake Eng.*, 4(1), 9-17.

Price, T. E., and Eberhard, M. O. (2005). "Factors contributing to bridge– embankment interaction." *J. Struct. Eng.*, 7, 1319, 1345–1354.

Pujol, S., Hanai, N., Ichinose, T., and Sozen M. A. (2016). "Using Mohr-Coulomb

criterion to estimate shear strength of reinforced concrete columns." *ACI Structural Journal*, 113, 459-468.

Rampello, S., Callisto, L., and Viggiani, G. (2014). "Predicting the seismic behaviour of the foundations of the Messina Strait Bridge." *Bullettin of Earthquake Engineering*, 12(3), 1201-1219.

Rathje, E. M., Abrahamson, N. A., and Bray, J. D. (1998). "Simplified Frequency Content Estimates Of Earthquake Ground Motions." *Journal of Geotechnical and Geoenviromental Engineering*, 124(2), 150-159.

Rha, C., and Taciroglu, E. (2007). "Coupled Macroelement Model of Soil-Structure Interaction in Deep Foundations." *Journal of Engineering Mechanics*, 133(12).

Richart, F. E., Brandtzaeg, A., and Brown, R. L. (1929). "The failure of plain and spirally reinforced concrete in compression." *Bulletin 190*, Univ. of Illinois Engineering Experimental Station, Champaign, 111.

Richart, F. E., Jr., Hall, J. R., and Woods, R. D. (1970). "Vibration of soils and foundations." *International series in theoretical and applied mechanics*, Prentice-Hall, Englewood Cliffs, N.J.

Romstad, K., Kutter, B., Maroney, B., Vanderbilt, E., Griggs, M., and Chai, Y. H. (1995). "Experimental measurements of bridge abutment behavior." *Rep. No. UCD-STR-95-1*, Dept. of Civil and Environmental Eng., Univ. of California, Davis, Calif.

Roscoe, K. H., and Schofield, A. N. (1956). "The stability of short pier foundations on sand, discussion." *British Welding Jour.*

Roscoe, K.H., and Schofield, A.N. (1957). "The stability of short pier foundations on sand, discussion." *British Welding Jour.*, 12-18.

Salciarini, D, and Tamagnini, C. (2009). "A hypoplastic macroelement model for shallow foundations under monotonic and cyclic loads." *Acta Geotechnica*, 4(3),163,176.

Schanz, T., Vermeer, P. A., and Bonnier, P. G. (1999). "The hardening soil model-Formulation and verification." *Proc., Plaxis Symp.: Beyond 2000 in Computational Geotechnics*, Balkema, Rotterdam, The Netherlands, 281-296.

Seed, H. B., and Idriss, I. M. (1970). "Soil moduli and damping factors for dynamic analysis". *Report No. EERC 70-10*, University of California, Berkeley.

Shamsabadi, A., Ashour, M., and Norris, G. (2005). "Bridge abutment nonlinear force-deflection-capacity prediction for seismic design." *J. Geotech. Geoenviron. Eng.*, 1312, 151–161.

Shamsabadi, A., Rollins, K. M., and Kapuskar, M. (2007). "Nonlinear soil-abutment-bridge structure interaction for seismic performance based design." *J. Geotech. Geoenviron. Eng.*, 1336, 707–720.

Shamsabadi, A., Khalili-Tehrani, P., Stewart, J. P., and Taciroglu, E. (2010). "Validated simulation models for lateral response of bridge abutments with typical backfills." *J. Bridge Eng.*, 10.1061/(ASCE)BE.1943-5592 .0000058, 302–311.

Skempton, A. K. (1986). "Standard penetration test procedures and the effects in sands of overburden pressure, relative density, particle size, aging, and overconsolidation." *Geotechnique, London*, 36(3), 425-447.

Siddharthan, R., El-Gamal, M., and Maragakis, E. A. (1997). "Stiffnesses of abutments on spread footings with cohesionless backfill." *Can. Geotech. J.*, 345, 686-697.

Sloan, S.W. (1988). "Lower bound limit analysis using finite elements and linear programming." *Int. J. Numer. Anal. Methods Geomech.*, 12, 61-67.

Sloan, S.W. (1989). "Lower bound limit analysis using finite elements and linear programming." *Int. J. Numer. Anal. Methods Geomech.*, 13, 263-282.

Stefanidou, S. P., Sextos, A. G., Kotsoglou, A. N., and Lesgidis, N. (2017). "Soil-structure interaction effects in analysis of seismic fragility of bridges using an intensity-based ground motion selection procedure." *Eng. Str*, 151, 366-380.

Stewart, J. P., Taciroglu, E., Wallace, J. W., Ahlberg, E. R., Lemnitzer, A., Rha, C., and Tehrani, P. K., (2007). "Full scale cyclic testing of foundation support systems for highway bridges. Part II: Abutment backwalls." *Rep. No. UCLA-SGEL-2007/02*, Structural and Geotechnical Engineering Laboratory, Univ. of Calif., Los Angeles.

Taiebat, M., Jeremi´c, B., Dafalias, Y. F., Kaynia, A. M., and Cheng, Z. (2010). "Propagation of seismic waves through liquefied soils." Soil Dyn. Earthquake Eng.,

30(4), 236-257.

Tanaka Y., Kudo Y., Yoshida Y., and Ikemi M. (1987). "A study on the mechanical properties of sandy gravel dynamic properties of reconstituted samples." Central Research Institute of Electric Power Industry, Report 1987;U87019.

Tehrani, F. S., Prezzi, M., and Salgado, R. (2016). "A multidirectional semi-analytical method for analysis of laterally loaded pile groups in multi-layered elastic strata." *International Journal for Numerical and Analytical Methods in Geomechanics*, 40(12), 1730-1757.

Terzaghi, K. (1934). "Seismic response of short and medium span bridges equipped with energy dissipating shear keys." *Engineering News Record*, 112(5), 136-140.

Terzaghi, K., and Peck, R.B. (1964). *Soil Mechanics in Engineering Practice*. Wiley, New York.

Vasseghi, A. (2008). "Lateral and rocking vibration of footings." *Proc., IV World Conference on Earthquake Engineering*, Beijing, China.

Veletsos, A. S., and Wei, Y. T. (1971). "Lateral and rocking vibration of footings." *J. Soil Mech. Found. Div.*, 97, 1227-1248.

Venanzi, I., Salciarini, D., and Tamagnini, C. (2014). "The effect of soil-foundation-structure interaction on the wind-induced response of tall buildings." *Engineering Structures*, 79, 117-130.

Vermeer, P. A., and Brinkgreve, R. B. J. (1998). *PLAXIS: Finite-element code for soil and rock analyses (version 7.1)*, Balkema, Rotterdam, The Netherlands.

Wang, K., and Brennan, A. J. (2015). "Centrifuge modelling of fibre-reinforcement using as a liquefaction countermeasure of quay wall backfill." *Proc., VI International Conference on Earthquake Geotechnical Engineering*, Christchurch, New Zealand.

Yang, Z., Elgamal, A., and Parra, E. (2003). "A computational model for liquefaction and associated shear deformation." *J. Geotech. Geoenviron. Eng.*, 129(12), 1119-1127.

Zhang, Y., Yao, S., and Christie, S. R. (2013). "Non-linear and equivalent linear site response analysis for 15 the Izmit Bay bridge." *In: Proc. 3rd International FLAC*

/DEM Symposium, Hangzhou, paper 05/2.

Ziegler, H. (1977) *An introduction to thermomechanics*, North Holland, Amsterdam.

Zienkiewicz, O. C , and Shiomi, T. (1984). "Dynamic behavior of saturated porous media: The generalized Biot formulation and its numerical solution." *Int. J. Numer. Anal. Meth. Geomech.*, 8, 71-96.

Chapter 8

Appendix 1: dissipative abutments

Dissipative abutments can constitute an important source of energy dissipation for a bridge. In Chapter 2 it has been seen that local and global mechanisms have been analysed in recent years, in order to mitigate the displacement field induced by a seismic event or to dissipate energy. Focusing on the latter purpose, the anti-seismic expedients usually aim to localise dissipation in the backfill or in the abutment structure. Friction geogrids have been vastly studied as fiber-reinforcements for the backfill while an *ad hoc* design of the backwall, with a limited yielding compared to the other structural elements of the abutment and the soil, and the adoption of dissipative shear keys can be regarded as a fuse that activates under large seismic forces transmitted by the deck. All these design solutions are conceived to emphasise the effects associated with a sole plastic mechanism occurring in a specific direction of loading, typically that induced by the longitudinal force coming from the deck and pushing the abutment against the backfill. In Section 5.9.1 it was demonstrated, however, that the three-dimensionality of the deck load can involve a much higher capacity of the soil-abutment system with a possible loss of efficiency of the anti-seismic technology adopted. Without the use of specific anti-seismic design solutions, in the following the intrinsic dissipative features of the soil-abutment

system are investigated, interpreting them in the light of the framework established for the capacity of bridge abutments under multi-axial loading conditions.

In some cases a controlled yielding of the abutment structure may produce favourable effects, dissipating seismic energy and limiting the seismic actions into the superstructure. In fact, the abutment could be designed by taking expressly into account its dissipative features, guiding the yielding towards ductile plastic mechanisms, at the cost of accepting a certain amount of irreversible displacements compatibly with the performance levels prescribed for the bridge. In this view, the entire soil-abutment system would be conceived as a dissipative part of a bridge, with a potential relevant impact on the seismic performance of the structure since the strong interaction of the abutment with both the soil and the superstructure.

Combined soil-abutment failure

The preliminary results of a study on the dissipative capabilities of bridge abutments and their influence on the structural performance are presented, focusing on the potential combined soil-structure mechanisms obtained through limit analysis solutions using the software Optum G2 and Optum G3. The combined mechanisms are initially investigated for abutments with shallow foundations for then analysing the effect of the plastic behaviour of deep foundations. Afterwards, a topology optimisation of the plastic volume of soil is presented, intended as a global isolation technique for the soil-abutment system.

Abutments with shallow foundations

In order to explore the possibility to have a combined soil-structure failure, a rigid-perfectly plastic behaviour was assumed for the abutment. Each structural member was designed by application of limit state design, allowing the structure to yield un-

Group	Config. 5 C32/40	Config. 6 C45/55	Config. 7 C20/25
c_{abut} (MPa)	8.0	11.0	5.0
μ_{abut}	1.428	1.428	1.428

Tabella 8.1: Constitutive parameters of the equivalent Mohr-Coulomb failure criterion associated with the abutment.

der severe ground shaking. The Mohr-Coulomb failure criterion was assigned to all the elements of the abutment and the piles, as a linear approximation of the failure criterion due to shearing for reinforced concrete members proposed by Pujol et al. (2016). This is a further development of the classical linear criterion used to estimate the shear strength of concrete cylinders proposed by Richart et al. (1929). In the Pujol's method, the effects of the longitudinal and transverse reinforcement are estimated through a simplified formulation based on the interpretation of Mohr circles at failure due to shearing. The resulting nonlinear criterion was approximated by a linear relationship in the significant range of stress for the problem at hand in order to get the equivalent properties to be assigned in Optum. Three different mechanical properties of the abutment section were taken into consideration, reported in Table 8.1, referred to different classes of concrete, expressed in European standards. The strength parameters of soil are $\mu_{soil} = 0.577$ and $c_{soil} = 0$ kPa for all the cases above. In Optum, the walls and the foundation were modelled as solid elements in order to account for the effective geometry of the abutment and, therefore, for the local attainment of strength in the structure. The contact surfaces between soil and abutment were modelled as shear joints in Optum G2 and through thin layers of solid elements in Optum G3, with appropriate strength parameters.

Referring to two-dimensional modelling, Figure 8.1 compares the surface of ultimate loads of the rigid abutment taken as reference in Section 5.9.1.1 ($\mu_{soil} = 0.577$) with that computed for the plastic abutment of Config. 5 (Table 8.1), for a bi-axial load coming from the deck. It can be observed that the failure surface corresponding

to a plastic behaviour of the abutment follows the ellipse relative to a rigid abutment on the left side of the graph (Q_1<0) while it shows lower values on the right side (Q_1>0), where the capacity becomes maximum. This reduction is due to the mobilization of the abutment strength according to two different mechanisms, whose activation in turn depends on the ratio of the external load Q_3/Q_1, as highlighted by the deformed shapes in Figure 8.1. When the external force is nearly vertical, for ratios Q_3/Q_1 greater than 3, the structural strength is attained in the footing close to the joint with the stem. Starting from this point, the sliding surface divides into two branches, directed downstream and upstream, for a global mechanism representing a combined failure of bearing capacity of the footing and mobilization of the passive resistance in the embankment, conceptually similar to that shown for a rigid abutment (Figure 5.8). When the longitudinal component of the external force is dominant compared to the vertical force, instead, a plastic hinge forms at the base of the abutment wall, with rotation of the stem and mobilization of the passive resistance in the backfill. The sliding surface starts in correspondence of the plastic hinge for then extending into the embankment, without involving the response of the soil underneath the foundation. Hence, the plastic response of the abutment seems to play a relevant role on the capacity for high external forces directed downwards and towards the backfill, leading to a significant contraction of the ultimate surface.

This result is valid also for different strength properties of the abutment, as illustrated in Figure 8.2(a). The failure points can be still described by an ellipse whose maximum capacity increases with the abutment strength, the latter occurring for the same ratio of the bi-axial load ($Q_3/Q_1 = 3$). As done for the case of a rigid abutment, a convenient strategy to calibrate the ellipse is to represent the loci in a normalised plane, shown in Figure 8.2(b). In this plane, a unique locus describes the combined soil-structure failure and the two constitutive parameters, the maximum capacity Q_{max} and the orientation of the ellipse δ, can be calibrated as follows. The

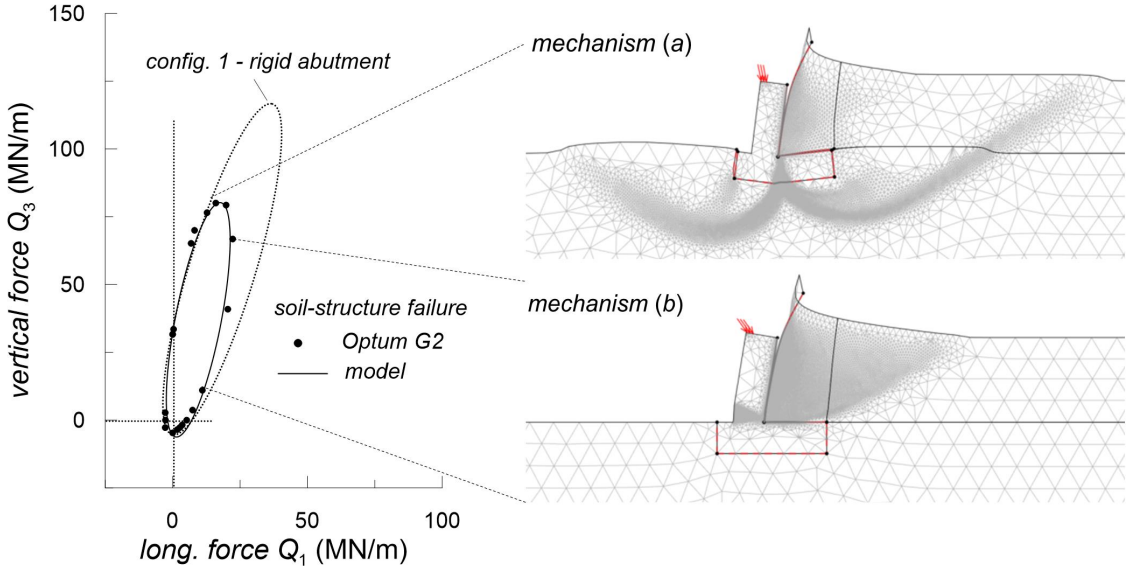

Figure 8.1: Combined soil-abutment failure: ultimate locus in the $Q_1 - Q_3$ plane considering a rigid-perfectly plastic abutment ($\mu_{soil} = \mu_{int} = 0.577$; $c_{abut} = 8000$ kPa; $\mu_{abut} = 1.428$).

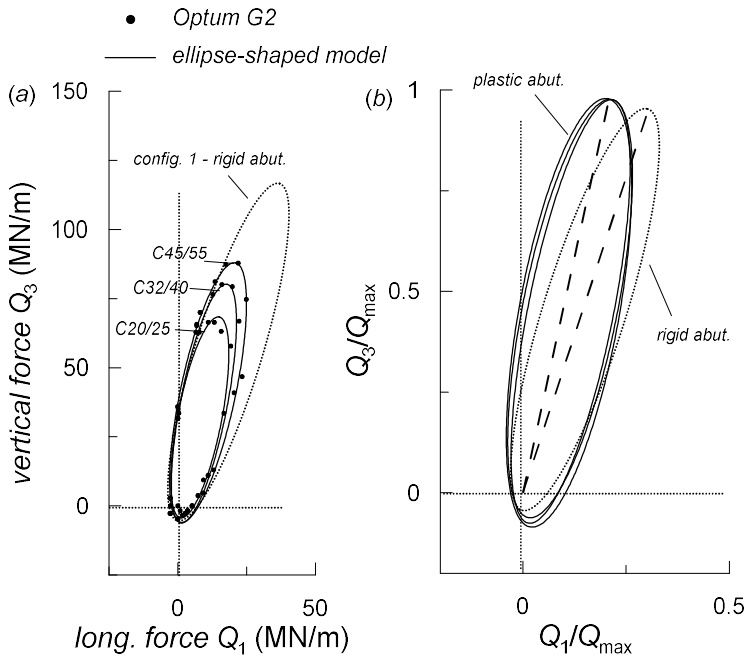

Figure 8.2: (a) Coupled soil-structure failure for different values of the abutment strength and (b) normalised representation of the failure loci.

change in orientation $\Delta\delta$ with respect to the locus for rigid abutment can be taken equal to 4°, at least for the systems under examination, while Q_{max} is a function of the abutment strength. More specifically, a combined failure occurs when the bending moment acting in the section at the base of the abutment wall M_E is at least equal to the moment of resistance M_R. The former can be simply evaluated through the following expression

$$M_E = Q_{1,max} \cdot H - S_p \cdot h_p \tag{8.1}$$

in which $Q_{1,max}$ is the longitudinal component of Q_{max} when the abutment is considered as a rigid body and S_p is the longitudinal force produced by the earth pressure, considering the passive resistance in the backfill fully mobilised and applied at a distance $h_p = 0.3 \cdot H$ from the base of the wall. In the range of the ratio M_R/M_E explored in this study, from 1 down to a value of 0.3, the results showed that the maximum capacity Q_{max}/Q_{max}^{rigid}, normalised to the value Q_{max}^{rigid} obtained for rigid abutment, varies with the ratio M_R/M_E according to the following expression

$$Q_{max}/Q_{max}^{rigid} = 0.7906 \cdot M_R/M_E + 0.2, \ 0.3 \leq M_R/M_E \leq 1.0 \tag{8.2}$$

that defines the size reduction of the admissible domain.

The effective three-dimensional geometry of the abutment however mitigates the reduction of the capacity observed above, as shown by the ultimate surface related to three-dimensional conditions in Figure 8.3. The structural failure is attained in the same region identified for the 2D case but the compact shape of the abutment, transverse aspect ratio H/L_{tr} equal to 0.77, confers a higher strength to the whole structure. This consideration is confirmed by the mechanism shown in Figure 8.4 in correspondence of the maximum capacity: conversely to the 2D failure with formation of a plastic hinge at the base of the stem, the 3D failure happens for formation

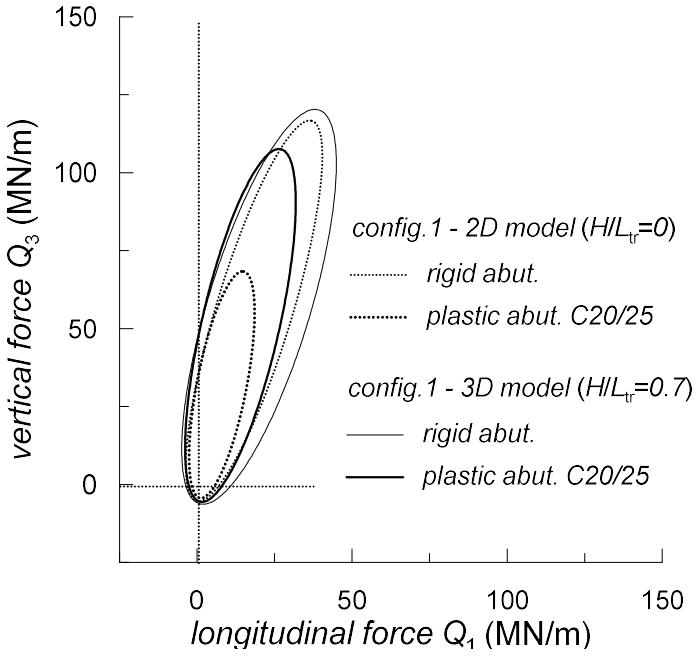

Figure 8.3: Comparison between the soil-abutment failure surface obtained through two-dimensional models (dashed lines) and the surface relative to three-dimensional models (continuous lines).

of two cylindrical plastic hinges along the central wall, that are lateral hinges curved by the presence of the wing walls. The abutment under examination is however a very compact structure and the transition from this case to plain strain conditions, obtained for a high value of the transverse aspect ratio, would lead to a gradual decrease of the capacity.

Abutments with deep foundations

As done for the abutment structure, the plastic behaviour of piles was described by means of an equivalent Mohr-Coulomb criterion (Pujol et al. 2016). The piles are made up of reinforced concrete and were modelled as solid elements in Optum G3, in order to reproduce the effective plastic flow of the soil between the piles and to detect the local mobilisation of the structural strength along the shaft. The class of the conglomerate is C20/25, as typically adopted for deep foundations, and the

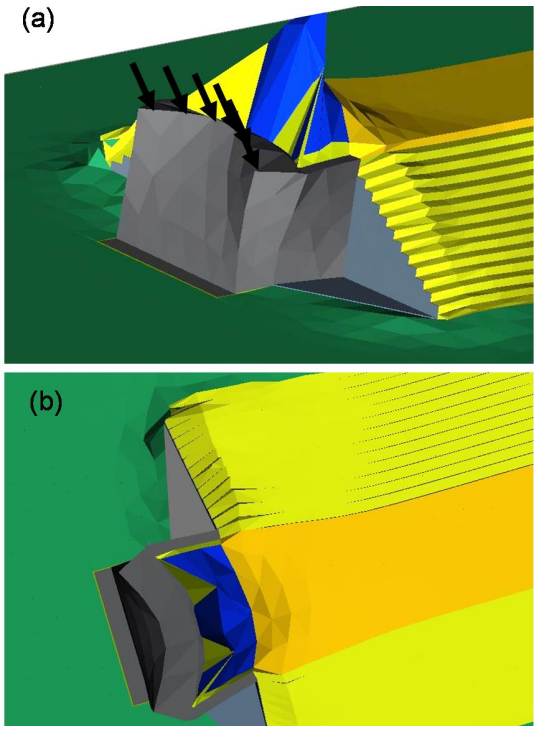

Figure 8.4: Three-dimensional soil-abutment mechanism in correspondence of the maximum capacity: three-dimensional (a) and plan (b) view of the deformed shape.

reinforcement is designed by application of standardised procedures. The equivalent cohesion and angle of shearing resistance are equal to 5000 kPa and 55°, respectively. The soil-pile interface was modelled through thin layers interposed between soil and structure: the piles were surrounded by interface layers whose thickness was set equal to 5 times the median diameter D_{50} of soil (Tehrani et al. 2016).

Figure 8.5 shows how the ultimate surface of an abutment with deep foundation can be still determined through the model proposed: the capacity of the reference rigid abutment with shallow foundation (Section 5.9.1.1) is compared with that relative to the same abutment but with the presence of a pile group, for two different slenderness ratios L_p/D_p of the pile, equal to 18.5 and 5.0. The normalised interaxes of the pile group in the longitudinal and transverse direction are $i_{long}/D_p = 3.5$ and $i_{tr}/D_p = 3.3$, respectively. It is evident that the piles do not change the shape of the ultimate surface but they confer a higher capacity to the abutment. The capacity

increases with the slenderness ratio, especially in the region where the abutment exhibits the maximum capacity, and also a slight rotation of the ellipse occurs with respect to the case of shallow foundation. Looking at the plastic mechanisms in correspondence of the maximum capacity (Figure 8.5), for the long pile mechanism the strength of the piles is completely attained in proximity of the joint with the raft, while the depth of the second plastic hinge depends on the row considered, because the yielding moment of the pile is a function of the axial load acting in it. The higher the axial load in the pile, the deeper the plastic hinge, which is in accordance with the results obtained by Callisto and Rampello (2013). For stubby piles ($L_p/D_p = 5$) instead, an intermediate mechanism occurs in which the raft and the piles behave as a more massive shallow foundation: the sliding surface passes through the first two rows for then extending into the soil. Because of its ductility, flexural yielding in the piles can be regarded as a favourable dissipative mechanism with respect to the shear mechanism observed for an abutment with shallow foundation subjected to high load ratios $Q_3/Q_1 > 3$.

The presence of the transverse force Q_2, in addition to the other two components of the deck load, leads to a contraction of the ultimate locus in the plane $Q_1 - Q_3$, as illustrated in Figure 8.6. Although the reduction of capacity is more pronounced in the case of long piles, the percentage reduction is nearly identical between the two cases. This behaviour is conceptually identical to that observed for an abutment with shallow foundation, that confirms the validity of the formulation proposed to describe stability of bridge abutments.

The results shown in this paragraph are aimed at taking into consideration the possibility to admit a plastic response of the structural members, as an additional source of energy dissipation under earthquake loading. In fact, an appropriate calibration of the abutment resistance, compared to that of the soil, can lead to a favourable contraction of the ultimate surface in order to control the maximum

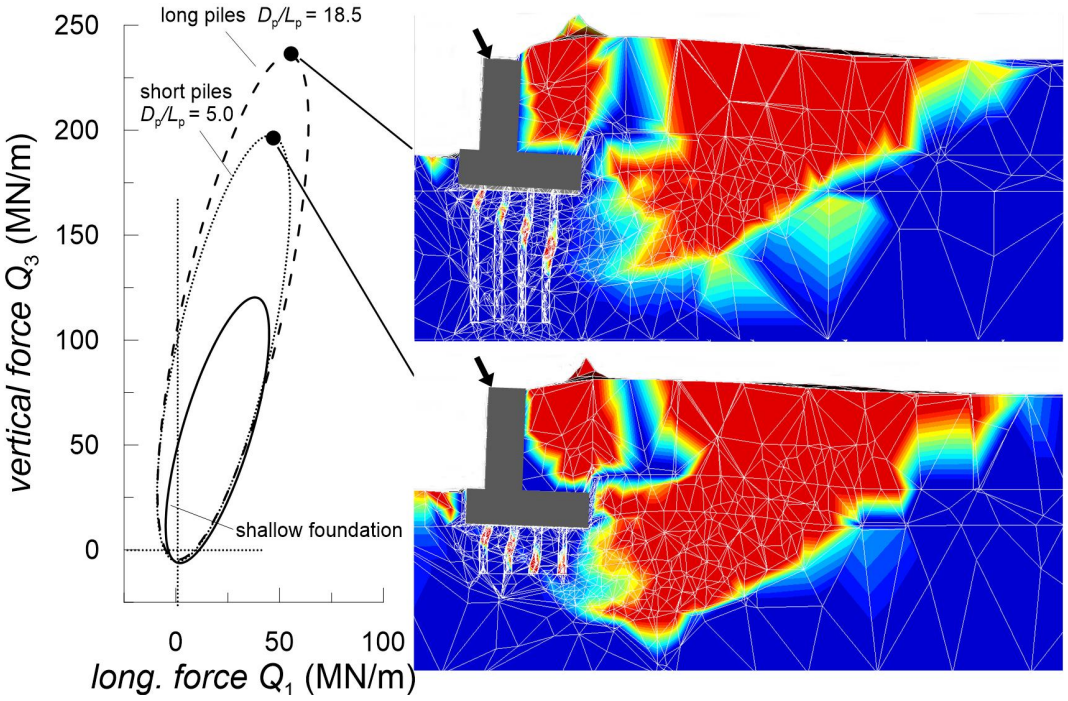

Figure 8.5: Three-dimensional failure of an abutment with deep foundation: surface of ultimate loads for a rigid abutment founded on a shallow raft (continuous line), a group of short piles with $L_{pile}/D_{pile} = 6.0$, $L_{pile}/H = 1.4$ (dotted line) and a group of long piles with $L_{pile}/D_{pile} = 18.5$ and $L_{pile}/H = 3.4$ (dashed line).

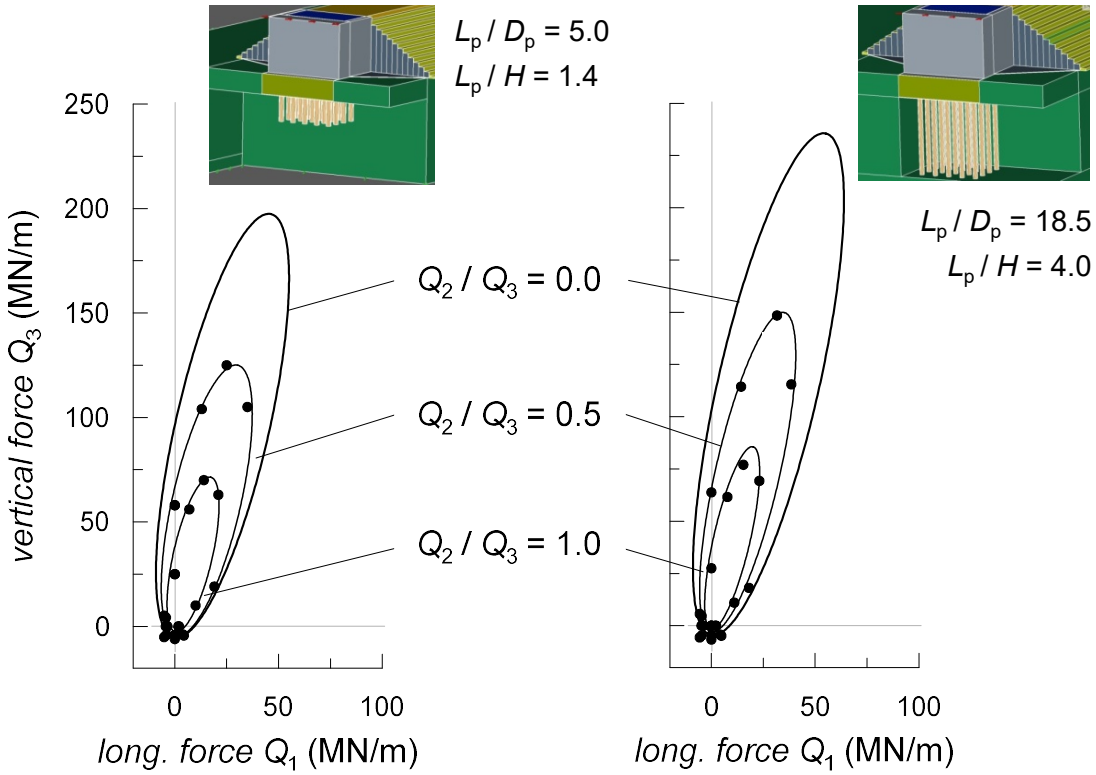

Figure 8.6: Comparison between the abutment founded on short piles and on long piles: traces of the surface of ultimate loads in the $Q_1 - Q_3$ plane, for different levels of the transverse force applied to the abutment top.

seismic actions transmitted to the deck. The mobilization of a global mechanism under dynamic conditions is temporary and therefore it does not necessarily lead the abutment to failure but it implies a progressive accumulation of displacements that have to be compatible with the performance levels prescribed for the bridge. It has been demonstrated that all the mechanisms examined so far can be described by the ellipsoidal ultimate surface defined for a rigid abutment, in which in this case the dimension of the ultimate locus depends also on the structural strength. Accordingly, the macro-element of bridge abutment can represent a useful tool for a prompt evaluation of these dissipative effects on the global performance of the bridge, that will constitute one of the next steps of the present research.

Piles detached from the raft

In the case of abutments with deep foundations, the seismic actions transmitted to the superstructure can be limited by inserting a frictional device into a piled foundation, at the contact of the piles with the connecting cap. This allows a controlled sliding when the seismic forces reach a given critical value, that should be chosen to provide a desired seismic performance of the structure. This type of dissipative foundation has recently been adopted for the towers of two long-span bridges, namely the Rion Antirion cable stayed bridge in Greece (Pecker 2003) and the Izmit Bay suspension bridge in Turkey (Zhang et al. 2013). For the specific case of the Izmit Bay suspension bridge, the dynamic behaviour of the frictional foundations were evaluated with a series of coupled dynamic analyses of a three-dimensional soil-structure numerical model carried out by Gorini and Callisto (2015) and Callisto and Gorini (2017). Afterwards, a more general conceptual framework was found by Gorini and Callisto (2016, 2018) for the seismic performance of this type of friction dissipative foundation. It was shown that the adoption of a frictional contact between the foundation and the underlying soil can lead to an efficient seismic control of the

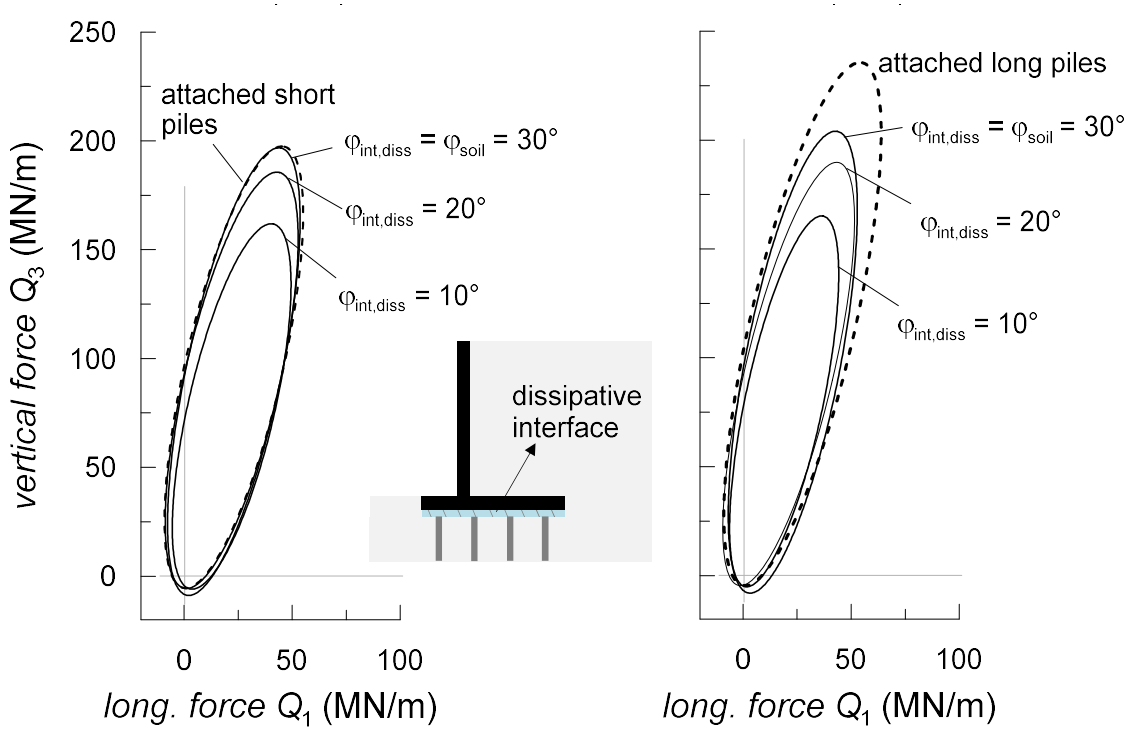

Figure 8.7: Influence of the friction angle $\varphi_{int,diss}$ of the dissipative soil-pile interface on the capacity of the soil-abutment system, for two values of the slenderness ratio of the piles L_p/D_p equal to 5.0 (short piles) and 18.5 (long piles).

structure, limiting the maximum accelerations transmitted to the superstructure, provided that the properties of the frictional contact are appropriately calibrated considering the dynamic characteristics of the entire soil-structure system.

This solution might be conceptually employed also in the case of a bridge abutment as a base isolation system for the foundation. In this view, consider a frictional interface interposed between the piles and the raft, characterised by a friction angle $\varphi_{int,diss}$. Figure 8.7 shows the envelopes of the ultimate surfaces of the abutment, evaluated by the limit analysis solutions in Optum G2, for the two reference slenderness ratios of the piles of 5.0 (short piles) and 18.5 (long piles) and considering different values of the friction angle of the dissipative interface $\varphi_{int,diss} = 30°, 20°, 10°$. The most evident result is that, for a given friction angle of the dissipative interface, the corresponding limit surface does not depend significantly on the slenderness ratio

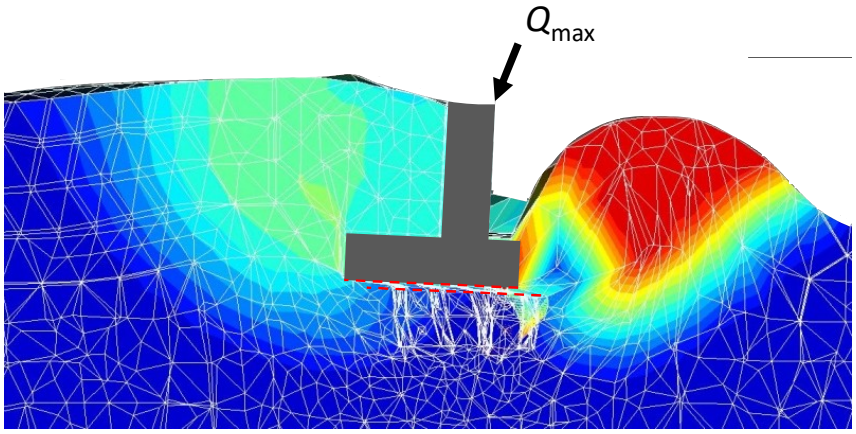

Figure 8.8: Deformed shape of the central section of the soil-abutment model obtained for a friction angle along the soil-pile interface of 10° and in correspondence of the maximum capacity $Q_3/Q_1 = 3$.

of the piles. This can be explained looking at the deformed shape, in correspondence of the maximum capacity Q_{max} and for a friction angle $\varphi_{int,diss} = 10°$, represented in Figure 8.8: the strength is mobilised along the frictional interface and the piled foundation is not involved in the plastic mechanism. When the friction angle of the soil-pile interface is equal to that of the soil, $\varphi_{int,diss} = \varphi_{soil} = 30°$, the ultimate surface in the case of long piles is essentially identical to that obtained for the short piles, which in turn exhibits the same capacity as the abutment with fully connected piles. In this case, for the short piles, the angle of friction at the pile-base contact is too large to modify substantially the global plastic mechanisms. Hence, if the use of a dissipative interface is aimed to reduce the seismic forces transmitted to the structure, it appears more effective in the case of long piles. Moreover, the effect of the friction interface is confined to values of the load ratio Q_3/Q_1 close to the maximum capacity and, even for very low friction angles, the gain in terms of reduction of the capacity is however limited, as shown in Figure 8.9. This happens because, differently from a foundation, the global mechanisms of a bridge abutment, such as that in Figure 8.8, involve a large volume of soil upstream and downstream the abutment. It follows that the capacity associated with the attainment of a global plastic

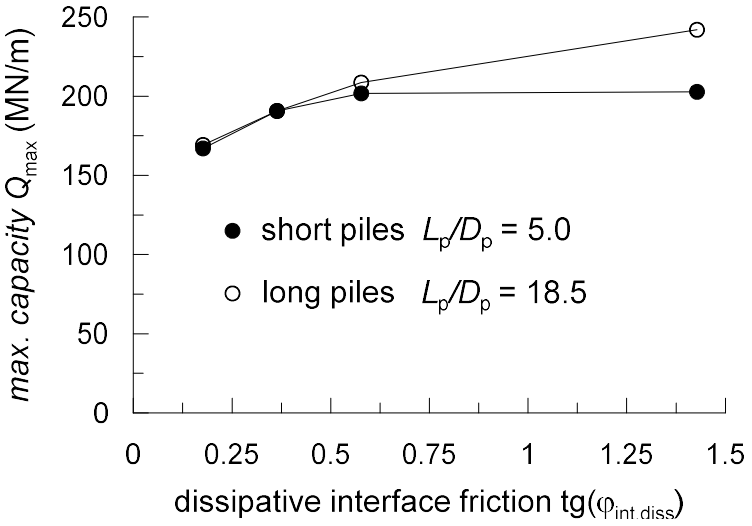

Figure 8.9: Maximum capacity of the soil-abutment system plotted as a function of the friction coefficient of the soil-pile interface.

mechanism is only to a lesser extent influenced by the soil-foundation contact.

On the basis the above results, a new technique was developed for a better seismic isolation of the abutment system, as recounted in the following paragraph.

Technique of the isolated volume of soil

The previous experience have given evidence that a sole dissipative interface placed underneath the foundation has an appreciable, although not relevant, effect only for load ratios close to the maximum capacity. As noted before, this is due to the participation of a large volume of soil upstream and downstream the abutment in a global plastic mechanism whose contribution on the overall resistance is much higher than that associated with the weak interface between soil and foundation. This result constituted the starting point for a new anti-seismic solution based on the concept of base isolation. The idea is to limit the seismic actions transferred to the superstructure through the isolation of the significant volume of soil that interacts with the abutment under multi-axial loading conditions. The isolation is accomplished

by a series of weak interfaces introduced opportunely into the soil, characterised by a sufficient low angle of shearing resistance, that activate the desired plastic mechanisms under seismic conditions. The full attainment of the strength in the soil can be deemed as a favourable dissipating energy mechanism for a structure for its high ductility and because it prevents damage in the structural members. The preliminary results of this development, obtained with the aid of numerically-evaluated limit analysis solutions, are presented focusing on the capability of the solution to control the capacity of the soil-abutment system.

Consider the reference two-dimensional soil-abutment system in Section 5.9.1.3. The global plastic mechanisms of this system are shown in Figure 8.10, for different load ratios Q_3/Q_1 belonging to the zone of the ultimate surface of major interest for this study. Two regions of the ultimate surface can be identified as characterised by a different mobilisation of the whole resistance. The demarcation point is represented by the maximum capacity Q_{max}, obtained for a load ratio equal to 3, at which a combined mechanism occurs with the concomitant attainment of the bearing capacity of the foundation soil and the passive resistance in the embankment. For lower load ratios the capacity of the soil-abutment system is essentially controlled by the passive resistance in the embankment, whereas for greater load ratios the embankment is marginally involved in the mechanism, because the relevant contribution to the whole resistance is given by the passive resistance of the soil downstream due to the attainment of the bearing capacity of the foundation.

As a result of a study of topology optimisation of the isolated volume of soil, here omitted for the sake of conciseness, the best solution is represented by the configuration illustrated in Figure 8.11. The goodness of the solution was judged in terms of reduction of the capacity of the system in a wide range of load ratios, preserving at the same time a reasonable implementation in real structures. The geometry of the isolated volume is composed of two shear interfaces placed behind

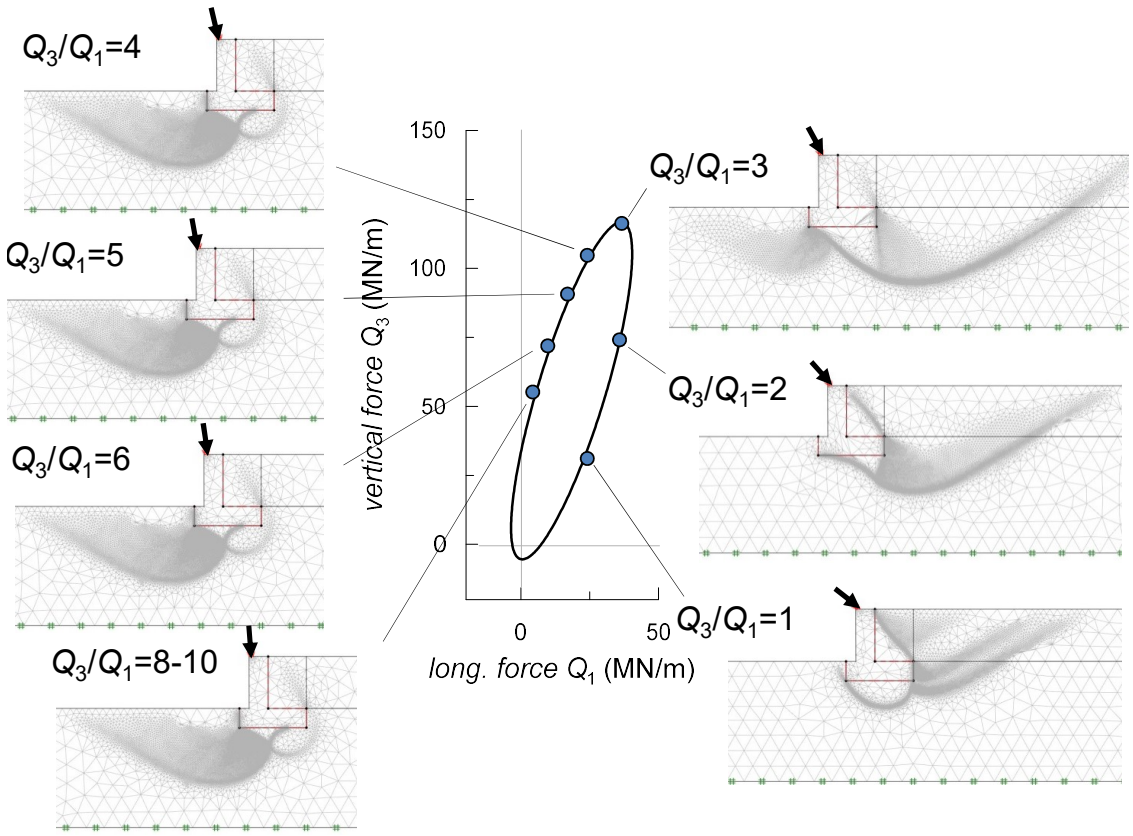

Figure 8.10: Global plastic mechanisms for the reference rigid abutment varying the load ratio Q_3/Q_1.

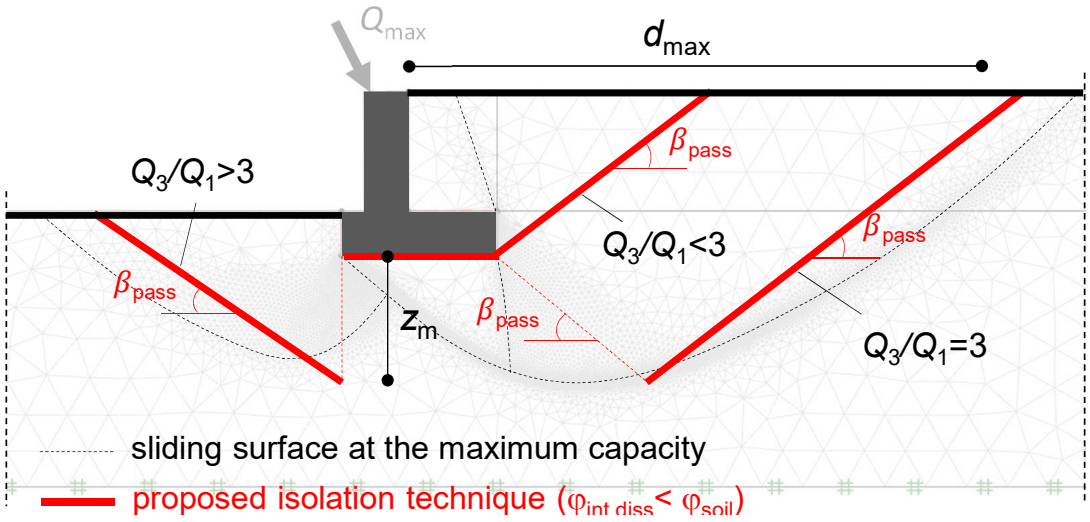

Figure 8.11: Geometry of the optimised isolation-based solution proposed for the soil-abutment system.

the abutment wall and a shear interface downstream. These weak interfaces act as sliding surfaces, characterised by a friction angle lower than that of the soil. Their inclination is equal to the inclination of the sliding surfaces of the soil in passive limit conditions. This is due to control the activation of the plastic mechanisms occurring in all the range of the load ratio where the abutment capacity shows the maximum values. More specifically, the outermost weak interface behind the wall is aimed to control the mechanisms in close proximity of the maximum capacity, while the second weak interface placed on the soil-foundation contact and extending behind the wall should activate for lower load ratios $Q_3/Q_1 < 3$ in which the plastic mechanism is closer to the abutment structure. The weak interface placed downstream the footing serves instead to limit the capacity for high vertical forces compared to the longitudinal one.

For an angle of shearing resistance equal to $\varphi_{int,diss} = 0.5 \cdot \varphi_{soil} = 15°$, the resulting envelope of the ultimate surface is shown in Figure 8.12. It can be noticed a relevant reduction of the capacity in a very wide range of the load ratio, as demonstrated by the variability of the capacity with the angle ψ of the resultant external force depicted

in Figure 8.13. The maximum reduction of the capacity is more than 60 %, kept in the interval of ψ between 70° and 225°. As expected, the corresponding plastic mechanisms (Figure 8.12) consist in a combined sliding between the three weak surfaces, depending on the load ratio. In correspondence of the maximum capacity, the two outermost weak interfaces activate, while the strength of internal one is mobilised for lower values of the load ratio. For $Q_3/Q_1 > 3$, only the downstream shear interface is needed to control the capacity. The isolated volume preserves however a moderate safety factor associated with the abutment stability under static conditions since, in the $Q_1 - Q_3$ plane, the origin of the axes is well contained in the ultimate surface.

To sum up, this is just a preliminary result of an ongoing research, showing the capability of the proposed global isolation technique to reduce the capacity of the soil-abutment system and, accordingly, the seismic actions that can be transmitted to the superstructure of the bridge. Moreover, the isolated volume preserves the abutment itself from structural damage, at cost of greater permanent displacements developing along the weak interfaces that require the adoption of a performance-based design for the abutment. Therefore, the forthcoming developments of this study will consider the three-dimensional geometry of the abutment system and the definition of a calibration procedure of the strength parameters of the weak interfaces, as a function of the soil strength. It has been demonstrated that the ultimate conditions of the abutment with isolated volume of soil can be still predicted by the general formulation defined in Section 5.9.1.6, and therefore further investigations will be performed to examine the response of the system far from failure. In this view, the macro-element of bridge abutments would represent the fundamental method to test this technique in the global structural behaviour, for a proper quantification of its effects on the seismic performance of the whole structure.

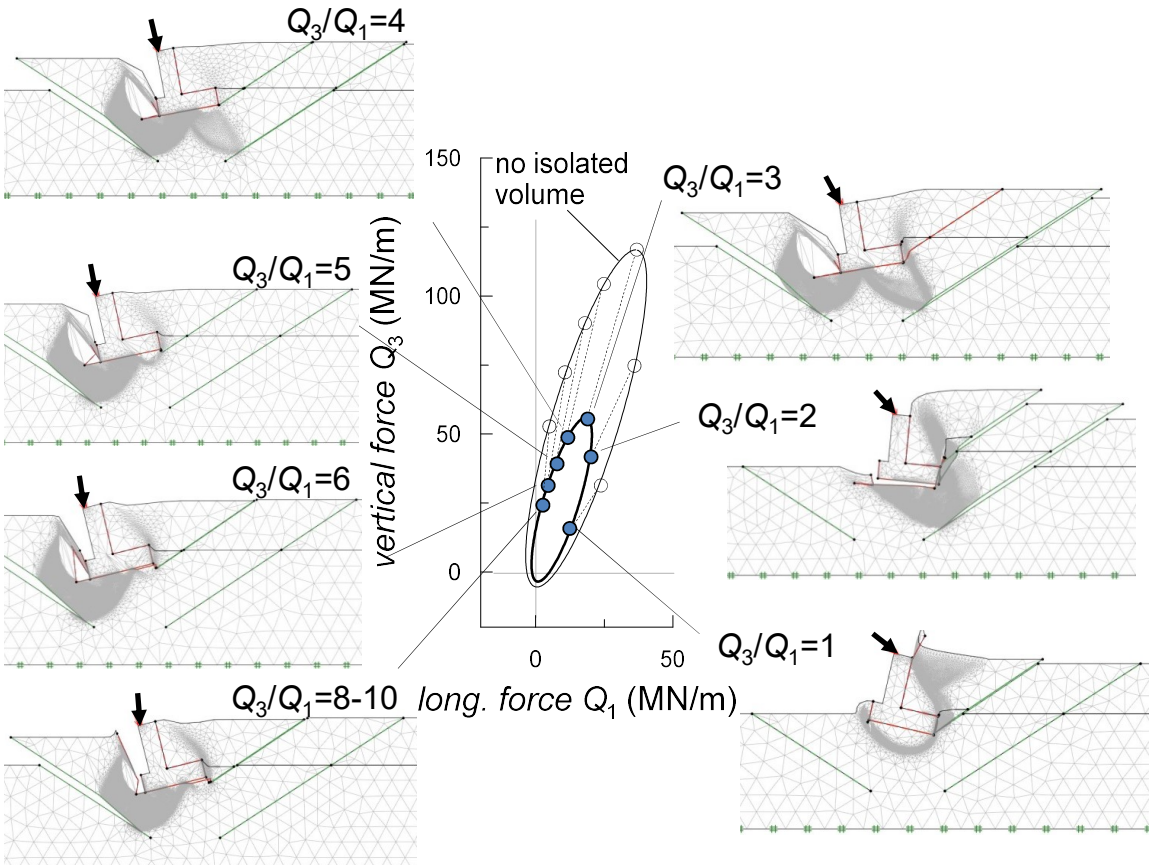

Figure 8.12: Global plastic mechanisms for the base isolated soil-abutment system varying the load ratio Q_3/Q_1.

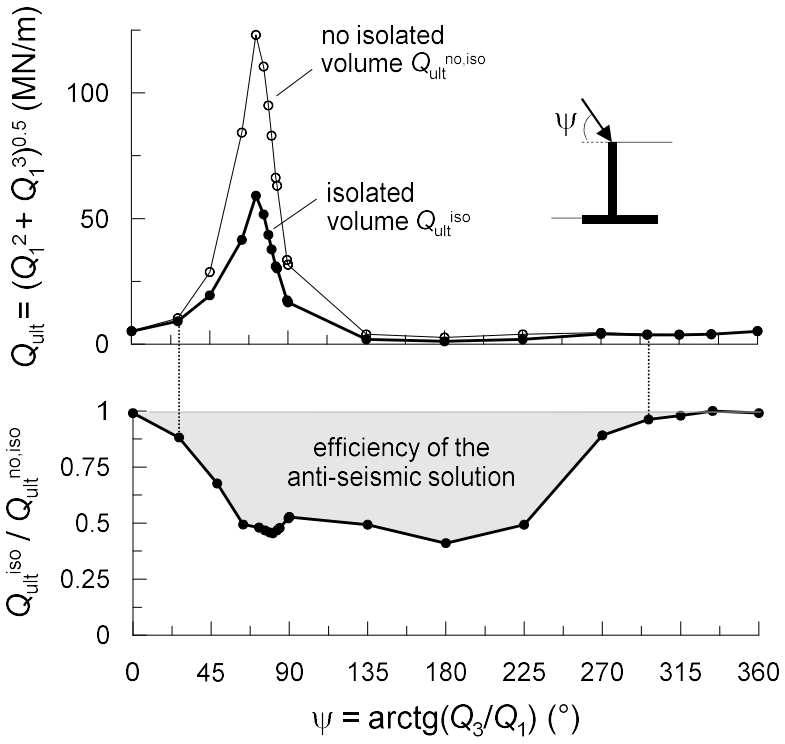

Figure 8.13: Comparison between the capacity of the reference soil-abutment system and that of the base isolated soil-abutment system: capacity of the abutment (a) and capacity reduction factor (b) plotted as a function of the angle $\psi = arctg(Q_3/Q_1)$ of the resultant external force on top.

Chapter 9

Appendix 2: incremental response of the macro-element for bridge abutments

As mentioned before, the macro-element can be modelled in a numerical model of the bridge structure as an intrinsically inertial finite element, considering the inertial effects of the masses in its incremental response, or as a non-inertial finite element with masses modelled explicitly in the global model of the bridge. Following the latter option, the incremental response of the 3 degrees of freedom macro-element would read

$$\dot{Q}_i^{(ext)} = H_{ij}^{(0)} \cdot \left[\dot{q}_j - \sum_{n=1}^{N} \lambda_n \cdot \frac{\partial y_n^g}{\partial \chi_i^{(n)}} - S\left(Q_i^{(ext)}\right) \cdot \sum_{n=1}^{N} R^{(n)} \cdot \lambda_n \cdot \frac{\partial y_n^g}{\partial \chi_i^{(n)}} \right]. \qquad (9.1)$$

Neglecting the contribution of ratcheting ($R^{(n)} = 0$) and substituting Eqs. 5.183, 5.184, 5.185, 5.186, 5.187 and 5.188 into Eq. 9.1, the latter becomes

$$\dot{Q}_i^{(ext)} = H_{ij}^{(0)} \cdot \left[\dot{q}_j - \sum_{n=1}^{N} \lambda_n \cdot \frac{\partial y_n^g}{\partial \chi_i^{(n)}} \right] =$$

$$= H_{ij}^{(0)} \cdot \dot{q}_j - H_{ij}^{(0)} \cdot \sum_{n=1}^{N} \frac{\{[N_1] + [N_2] + [N_3]\}}{\{[D_1] + [D_2] + [D_3]\}} \cdot \frac{\partial y_n^g}{\partial \chi_i^{(n)}} \tag{9.2}$$

in which the general expression of the n-th plastic multiplier is developed as follows

$$\lambda_n = \Bigg\{ \Bigg[\dot{Q}_1{}^{(n)} \cdot \frac{2 \cdot sin\,(\delta) \cdot S(\chi_1^{(n)})}{a_M^{(n)2}} \cdot \left(\chi_3^{(n)} - c_3^{(n)} \right) \cdot cos\,(\delta) +$$

$$+ \dot{Q}_1{}^{(n)} \cdot \frac{2 \cdot sin\,(\delta) \cdot S(\chi_1^{(n)})}{a_M^{(n)2}} \cdot \left(\chi_1^{(n)} - c_1^{(n)} \right) \cdot sin\,(\delta) -$$

$$- \dot{Q}_1{}^{(n)} \cdot \frac{2 \cdot cos\,(\delta) \cdot S(\chi_1^{(n)})}{a_m^{(n)2}} \cdot \left(\chi_3^{(n)} - c_3^{(n)} \right) \cdot sin\,(\delta) +$$

$$+ \dot{Q}_1{}^{(n)} \cdot \frac{2 \cdot cos\,(\delta) \cdot S(\chi_1^{(n)})}{a_m^{(n)2}} \cdot \left(\chi_1^{(n)} - c_1^{(n)} \right) \cdot cos\,(\delta) \Bigg] +$$

$$+ \left[\frac{1}{a_i^{(n)2}} \cdot 2 \cdot \chi_2^{(n)} \cdot S(\chi_2^{(n)}) \cdot \dot{Q}_2{}^{(n)} \right] +$$

$$+ \Bigg[\dot{Q}_3{}^{(n)} \cdot \frac{2 \cdot cos\,(\delta) \cdot S(\chi_3^{(n)})}{a_M^{(n)2}} \cdot \left(\chi_3^{(n)} - c_3^{(n)} \right) \cdot cos\,(\delta) +$$

$$+ \dot{Q}_3{}^{(n)} \cdot \frac{2 \cdot cos\,(\delta) \cdot S(\chi_3^{(n)})}{a_M^{(n)2}} \cdot \left(\chi_1^{(n)} - c_1^{(n)} \right) \cdot sin\,(\delta) +$$

$$+ \dot{Q}_3{}^{(n)} \cdot \frac{2 \cdot sin\,(\delta) \cdot S(\chi_3^{(n)})}{a_m^{(n)2}} \cdot \left(\chi_3^{(n)} - c_3^{(n)} \right) \cdot sin\,(\delta) -$$

$$-\dot{Q}_3{}^{(n)} \cdot \frac{2 \cdot sin\,(\delta) \cdot S(\chi_3^{(n)})}{a_m^{(n)2}} \cdot \left(\chi_1^{(n)} - c_1^{(n)}\right) \cdot cos\,(\delta)\Bigg]\Bigg\} /$$

$$/ \left\{ H_{11}^{(n)} \cdot \left[\frac{4}{a_M^{(n)4}} \cdot \left(\chi_3^{(n)} - c_3^{(n)}\right)^2 \cdot cos^2\,(\delta) \cdot sen^2\,(\delta) + \right.\right.$$

$$+ \frac{4}{a_M^{(n)4}} \cdot \left(\chi_1^{(n)} - c_1^{(n)}\right)^2 \cdot sen^4\,(\delta) +$$

$$+ \frac{8}{a_M^{(n)4}} \cdot \left(\chi_3^{(n)} - c_3^{(n)}\right) \cdot \left(\chi_1^{(n)} - c_1^{(n)}\right) \cdot cos\,(\delta) \cdot sen^3\,(\delta) +$$

$$+ \frac{4}{a_m^{(n)4}} \cdot \left(\chi_3^{(n)} - c_3^{(n)}\right)^2 \cdot cos^2\,(\delta) \cdot sen^2\,(\delta) +$$

$$+ \frac{4}{a_m^{(n)4}} \cdot \left(\chi_1^{(n)} - c_1^{(n)}\right)^2 \cdot cos^4\,(\delta) -$$

$$- \frac{8}{a_m^{(n)4}} \cdot \left(\chi_3^{(n)} - c_3^{(n)}\right) \cdot \left(\chi_1^{(n)} - c_1^{(n)}\right) \cdot cos^3\,(\delta) \cdot sen\,(\delta) -$$

$$- \frac{8}{a_m^{(n)2} \cdot a_M^{(n)2}} \cdot \left(\chi_3^{(n)} - c_3^{(n)}\right)^2 \cdot cos^2\,(\delta) \cdot sen^2\,(\delta) +$$

$$+ \frac{8}{a_m^{(n)2} \cdot a_M^{(n)2}} \cdot \left(\chi_3^{(n)} - c_3^{(n)}\right) \cdot \left(\chi_1^{(n)} - c_1^{(n)}\right) \cdot cos^3\,(\delta) \cdot sen\,(\delta) -$$

$$- \frac{8}{a_m^{(n)2} \cdot a_M^{(n)2}} \cdot \left(\chi_3^{(n)} - c_3^{(n)}\right) \cdot \left(\chi_1^{(n)} - c_1^{(n)}\right) \cdot cos\,(\delta) \cdot sen^3\,(\delta) +$$

$$+ \frac{8}{a_m^{(n)2} \cdot a_M^{(n)2}} \cdot \left(\chi_1^{(n)} - c_1^{(n)}\right)^2 \cdot cos^2\,(\delta) \cdot sen^2\,(\delta) \Bigg] +$$

$$+H_{22}^{(n)} \cdot \left[\frac{4}{a_i^{(n)4}} \cdot \chi_2^{(n)2} \right] +$$

$$+H_{33}^{(n)} \cdot \left[\frac{4}{a_M^{(n)4}} \cdot \left(\chi_3^{(n)} - c_3^{(n)} \right)^2 \cdot cos^4(\delta) + \right.$$

$$+ \frac{4}{a_M^{(n)4}} \cdot \left(\chi_1^{(n)} - c_1^{(n)} \right)^2 \cdot cos^2(\delta) \cdot sen^2(\delta) +$$

$$+ \frac{8}{a_M^{(n)4}} \cdot \left(\chi_3^{(n)} - c_3^{(n)} \right) \cdot \left(\chi_1^{(n)} - c_1^{(n)} \right) \cdot cos^3(\delta) \cdot sen(\delta) +$$

$$+ \frac{4}{a_m^{(n)4}} \cdot \left(\chi_3^{(n)} - c_3^{(n)} \right)^2 \cdot sen^4(\delta) +$$

$$+ \frac{4}{a_m^{(n)4}} \cdot \left(\chi_1^{(n)} - c_1^{(n)} \right)^2 \cdot cos^2(\delta) \cdot sen^2(\delta) -$$

$$- \frac{8}{a_m^{(n)4}} \cdot \left(\chi_3^{(n)} - c_3^{(n)} \right) \cdot \left(\chi_1^{(n)} - c_1^{(n)} \right) \cdot cos(\delta) \cdot sen^3(\delta) +$$

$$+ \frac{8}{a_m^{(n)2} \cdot a_M^{(n)2}} \cdot \left(\chi_3^{(n)} - c_3^{(n)} \right)^2 \cdot cos^2(\delta) \cdot sen^2(\delta) -$$

$$- \frac{8}{a_m^{(n)2} \cdot a_M^{(n)2}} \cdot \left(\chi_3^{(n)} - c_3^{(n)} \right) \cdot \left(\chi_1^{(n)} - c_1^{(n)} \right) \cdot cos^3(\delta) \cdot sen(\delta) +$$

$$+ \frac{8}{a_m^{(n)2} \cdot a_M^{(n)2}} \cdot \left(\chi_3^{(n)} - c_3^{(n)} \right) \cdot \left(\chi_1^{(n)} - c_1^{(n)} \right) \cdot cos(\delta) \cdot sen^3(\delta) -$$

$$\left. - \frac{8}{a_m^{(n)2} \cdot a_M^{(n)2}} \cdot \left(\chi_1^{(n)} - c_1^{(n)} \right)^2 \cdot cos^2(\delta) \cdot sen^2(\delta) \right] \Bigg\} =$$

$$= \left\{ \dot{Q_1}^{(n)} \cdot 2 \cdot S(\chi_1^{(n)}) \cdot \left(\chi_3^{(n)} - c_3^{(n)}\right) \cdot \left(\frac{1}{a_M^{(n)2}} - \frac{1}{a_m^{(n)2}}\right) \cdot sin\,(\delta) \cdot cos\,(\delta) + \right.$$

$$+\dot{Q_1}^{(n)} \cdot \frac{2 \cdot S(\chi_1^{(n)})}{a_M^{(n)2}} \cdot \left(\chi_1^{(n)} - c_1^{(n)}\right) \cdot sin^2\,(\delta) +$$

$$+\dot{Q_1}^{(n)} \cdot \frac{2 \cdot S(\chi_1^{(n)})}{a_m^{(n)2}} \cdot \left(\chi_1^{(n)} - c_1^{(n)}\right) \cdot cos^2\,(\delta) +$$

$$+\dot{Q_2}^{(n)} \cdot \frac{2 \cdot S(\chi_2^{(n)})}{a_i^{(n)2}} \cdot \chi_2^{(n)} +$$

$$+\dot{Q_3}^{(n)} \cdot \frac{2 \cdot S(\chi_3^{(n)})}{a_M^{(n)2}} \cdot \left(\chi_3^{(n)} - c_3^{(n)}\right) \cdot cos^2\,(\delta) +$$

$$+\dot{Q_3}^{(n)} \cdot \frac{2 \cdot S(\chi_3^{(n)})}{a_m^{(n)2}} \cdot \left(\chi_3^{(n)} - c_3^{(n)}\right) \cdot sen^2\,(\delta) +$$

$$\left. +\dot{Q_3}^{(n)} \cdot 2 \cdot S(\chi_3^{(n)}) \cdot \left(\chi_1^{(n)} - c_1^{(n)}\right) \cdot \left(\frac{1}{a_M^{(n)2}} - \frac{1}{a_m^{(n)2}}\right) \cdot cos\,(\delta) \cdot sin\,(\delta) \right\} /$$

$$/ \left\{ H_{11}^{(n)} \cdot 4 \cdot \left(\chi_3^{(n)} - c_3^{(n)}\right)^2 \cdot \left(\frac{1}{a_M^{(n)4}} + \frac{1}{a_m^{(n)4}} - \frac{2}{a_m^{(n)2} \cdot a_M^{(n)2}}\right) \cdot cos^2\,(\delta) \cdot sen^2\,(\delta) + \right.$$

$$\left. +H_{11}^{(n)} \cdot 4 \cdot \left(\chi_1^{(n)} - c_1^{(n)}\right)^2 \cdot \left[\frac{sen^2\,(\delta)}{a_M^{(n)2}} + \frac{cos^2\,(\delta)}{a_m^{(n)2}}\right]^2 + \right.$$

$$+H_{11}^{(n)} \cdot \frac{8}{a_M^{(n)4}} \cdot \left(\chi_3^{(n)} - c_3^{(n)}\right) \cdot \left(\chi_1^{(n)} - c_1^{(n)}\right) \cdot cos\left(\delta\right) \cdot sen^3\left(\delta\right) -$$

$$-H_{11}^{(n)} \cdot \frac{8}{a_m^{(n)4}} \cdot \left(\chi_3^{(n)} - c_3^{(n)}\right) \cdot \left(\chi_1^{(n)} - c_1^{(n)}\right) \cdot cos^3\left(\delta\right) \cdot sen\left(\delta\right) +$$

$$+H_{11}^{(n)} \cdot \frac{8}{a_m^{(n)2} \cdot a_M^{(n)2}} \cdot \left(\chi_3^{(n)} - c_3^{(n)}\right) \cdot \left(\chi_1^{(n)} - c_1^{(n)}\right) \cdot cos^3\left(\delta\right) \cdot sen\left(\delta\right) -$$

$$-H_{11}^{(n)} \cdot \frac{8}{a_m^{(n)2} \cdot a_M^{(n)2}} \cdot \left(\chi_3^{(n)} - c_3^{(n)}\right) \cdot \left(\chi_1^{(n)} - c_1^{(n)}\right) \cdot cos\left(\delta\right) \cdot sen^3\left(\delta\right) +$$

$$+H_{22}^{(n)} \cdot \frac{4}{a_i^{(n)4}} \cdot \chi_2^{(n)2} +$$

$$+H_{33}^{(n)} \cdot 4 \cdot \left(\chi_1^{(n)} - c_1^{(n)}\right)^2 \cdot \left(\frac{1}{a_M^{(n)4}} + \frac{1}{a_m^{(n)4}} - \frac{2}{a_m^{(n)2} \cdot a_M^{(n)2}}\right) \cdot cos^2\left(\delta\right) \cdot sen^2\left(\delta\right) +$$

$$+H_{33}^{(n)} \cdot 4 \cdot \left(\chi_3^{(n)} - c_3^{(n)}\right)^2 \cdot \left[\frac{cos^2\left(\delta\right)}{a_M^{(n)2}} + \frac{sen^2\left(\delta\right)}{a_m^{(n)2}}\right]^2 +$$

$$+H_{33}^{(n)} \cdot \frac{8}{a_M^{(n)4}} \cdot \left(\chi_3^{(n)} - c_3^{(n)}\right) \cdot \left(\chi_1^{(n)} - c_1^{(n)}\right) \cdot cos^3\left(\delta\right) \cdot sen\left(\delta\right) -$$

$$-H_{33}^{(n)} \cdot \frac{8}{a_m^{(n)4}} \cdot \left(\chi_3^{(n)} - c_3^{(n)}\right) \cdot \left(\chi_1^{(n)} - c_1^{(n)}\right) \cdot cos\left(\delta\right) \cdot sen^3\left(\delta\right) -$$

$$-H_{33}^{(n)} \cdot \frac{8}{a_m^{(n)2} \cdot a_M^{(n)2}} \cdot \left(\chi_3^{(n)} - c_3^{(n)}\right) \cdot \left(\chi_1^{(n)} - c_1^{(n)}\right) \cdot cos^3\left(\delta\right) \cdot sen\left(\delta\right) +$$

$$+H_{33}^{(n)} \cdot \frac{8}{a_m^{(n)2} \cdot a_M^{(n)2}} \cdot \left(\chi_3^{(n)} - c_3^{(n)}\right) \cdot \left(\chi_1^{(n)} - c_1^{(n)}\right) \cdot \cdot cos\left(\delta\right) \cdot sen^3\left(\delta\right) \Bigg\} =$$

$$= \Bigg\{ \dot{Q_1}^{(n)} \cdot \left[2 \cdot S(\chi_1^{(n)}) \cdot \left(\chi_3^{(n)} - c_3^{(n)}\right) \cdot \left(\frac{1}{a_M^{(n)2}} - \frac{1}{a_m^{(n)2}} \right) \cdot cos\left(\delta\right) \cdot sin\left(\delta\right) + \right.$$

$$\left. +2 \cdot S(\chi_1^{(n)}) \cdot \left(\chi_1^{(n)} - c_1^{(n)}\right) \cdot \left(\frac{sin^2\left(\delta\right)}{a_M^{(n)2}} + \frac{cos^2\left(\delta\right)}{a_m^{(n)2}} \right) \right] +$$

$$+\dot{Q_2}^{(n)} \cdot \frac{2 \cdot S(\chi_2^{(n)})}{a_i^{(n)2}} \cdot \chi_2^{(n)} +$$

$$+\dot{Q_3}^{(n)} \cdot \left[2 \cdot S(\chi_3^{(n)}) \cdot \left(\chi_1^{(n)} - c_1^{(n)}\right) \cdot \left(\frac{1}{a_M^{(n)2}} - \frac{1}{a_m^{(n)2}} \right) \cdot cos\left(\delta\right) \cdot sin\left(\delta\right) + \right.$$

$$\left. +2 \cdot S(\chi_3^{(n)}) \cdot \left(\chi_3^{(n)} - c_3^{(n)}\right) \cdot \left(\frac{cos^2\left(\delta\right)}{a_M^{(n)2}} + \frac{sen^2\left(\delta\right)}{a_m^{(n)2}} \right) \right] \Bigg\} /$$

$$/ \left\{ 4 \cdot \left(\frac{1}{a_M^{(n)4}} + \frac{1}{a_m^{(n)4}} - \frac{2}{a_m^{(n)2} \cdot a_M^{(n)2}} \right) \cdot cos^2\left(\delta\right) \cdot sen^2\left(\delta\right) \cdot \right.$$

$$\left. \cdot \left[H_{11}^{(n)} \cdot \left(\chi_3^{(n)} - c_3^{(n)}\right)^2 + H_{33}^{(n)} \cdot \left(\chi_1^{(n)} - c_1^{(n)}\right)^2 \right] +$$

$$+8 \cdot \left(\chi_3^{(n)} - c_3^{(n)}\right) \cdot \left(\chi_1^{(n)} - c_1^{(n)}\right) \cdot cos\left(\delta\right) \cdot sen^3\left(\delta\right) \cdot \left(\frac{H_{11}^{(n)}}{a_M^{(n)4}} - \frac{H_{33}^{(n)}}{a_m^{(n)4}} \right) +$$

$$+8\cdot\left(\chi_3^{(n)}-c_3^{(n)}\right)\cdot\left(\chi_1^{(n)}-c_1^{(n)}\right)\cdot cos^3\left(\delta\right)\cdot sen\left(\delta\right)\cdot\left(-\frac{H_{11}^{(n)}}{a_m^{(n)4}}+\frac{H_{33}^{(n)}}{a_M^{(n)4}}\right)+$$

$$+\frac{8}{a_m^{(n)2}\cdot a_M^{(n)2}}\cdot\left(\chi_3^{(n)}-c_3^{(n)}\right)\cdot\left(\chi_1^{(n)}-c_1^{(n)}\right)\cdot\left(H_{11}^{(n)}-H_{33}^{(n)}\right)\cdot cos^3\left(\delta\right)\cdot sen\left(\delta\right)+$$

$$+\frac{8}{a_m^{(n)2}\cdot a_M^{(n)2}}\cdot\left(\chi_3^{(n)}-c_3^{(n)}\right)\cdot\left(\chi_1^{(n)}-c_1^{(n)}\right)\cdot\left(-H_{11}^{(n)}+H_{33}^{(n)}\right)\cdot cos\left(\delta\right)\cdot sen^3\left(\delta\right)+$$

$$+H_{22}^{(n)}\cdot\frac{4}{a_i^{(n)4}}\cdot\chi_2^{(n)2}+$$

$$+H_{11}^{(n)}\cdot 4\cdot\left(\chi_1^{(n)}-c_1^{(n)}\right)^2\cdot\left[\frac{sen^2\left(\delta\right)}{a_M^{(n)2}}+\frac{cos^2\left(\delta\right)}{a_m^{(n)2}}\right]^2+$$

$$+H_{33}^{(n)}\cdot 4\cdot\left(\chi_3^{(n)}-c_3^{(n)}\right)^2\cdot\left[\frac{cos^2\left(\delta\right)}{a_M^{(n)2}}+\frac{sen^2\left(\delta\right)}{a_m^{(n)2}}\right]^2\Bigg\}=$$

$$=\Bigg\{\dot{Q_1}^{(n)}\cdot\Bigg[S(\chi_1^{(n)})\cdot\left(\chi_3^{(n)}-c_3^{(n)}\right)\cdot\left(\frac{1}{a_M^{(n)2}}-\frac{1}{a_m^{(n)2}}\right)\cdot cos\left(\delta\right)\cdot sin\left(\delta\right)+$$

$$+S(\chi_1^{(n)})\cdot\left(\chi_1^{(n)}-c_1^{(n)}\right)\cdot\left(\frac{sin^2\left(\delta\right)}{a_M^{(n)2}}+\frac{cos^2\left(\delta\right)}{a_m^{(n)2}}\right)\Bigg]+$$

$$+\dot{Q_2}^{(n)}\cdot\frac{S(\chi_2^{(n)})}{a_i^{(n)2}}\cdot\chi_2^{(n)}+$$

$$+\dot{Q}_3{}^{(n)} \cdot \left[S(\chi_3^{(n)}) \cdot \left(\chi_1^{(n)} - c_1^{(n)} \right) \cdot \left(\frac{1}{a_M^{(n)2}} - \frac{1}{a_m^{(n)2}} \right) \cdot cos\left(\delta\right) \cdot sin\left(\delta\right) + \right.$$

$$\left. + S(\chi_3^{(n)}) \cdot \left(\chi_3^{(n)} - c_3^{(n)} \right) \cdot \left(\frac{cos^2\left(\delta\right)}{a_M^{(n)2}} + \frac{sen^2\left(\delta\right)}{a_m^{(n)2}} \right) \right] \Bigg\} /$$

$$/ \left\{ 2 \cdot \left(\frac{1}{a_M^{(n)4}} + \frac{1}{a_m^{(n)4}} - \frac{2}{a_m^{(n)2} \cdot a_M^{(n)2}} \right) \cdot cos^2\left(\delta\right) \cdot sen^2\left(\delta\right) \cdot \right.$$

$$\left. \cdot \left[H_{11}^{(n)} \cdot \left(\chi_3^{(n)} - c_3^{(n)} \right)^2 + H_{33}^{(n)} \cdot \left(\chi_1^{(n)} - c_1^{(n)} \right)^2 \right] + \right.$$

$$+4 \cdot \left(\chi_3^{(n)} - c_3^{(n)} \right) \cdot \left(\chi_1^{(n)} - c_1^{(n)} \right) \cdot cos\left(\delta\right) \cdot sen^3\left(\delta\right) \cdot \left(\frac{H_{11}^{(n)}}{a_M^{(n)4}} - \frac{H_{33}^{(n)}}{a_m^{(n)4}} \right) +$$

$$+4 \cdot \left(\chi_3^{(n)} - c_3^{(n)} \right) \cdot \left(\chi_1^{(n)} - c_1^{(n)} \right) \cdot cos^3\left(\delta\right) \cdot sen\left(\delta\right) \cdot \left(-\frac{H_{11}^{(n)}}{a_m^{(n)4}} + \frac{H_{33}^{(n)}}{a_M^{(n)4}} \right) +$$

$$+\frac{4}{a_m^{(n)2} \cdot a_M^{(n)2}} \cdot \left(\chi_3^{(n)} - c_3^{(n)} \right) \cdot \left(\chi_1^{(n)} - c_1^{(n)} \right) \cdot \left(H_{11}^{(n)} - H_{33}^{(n)} \right) \cdot cos^3\left(\delta\right) \cdot sen\left(\delta\right) +$$

$$+\frac{4}{a_m^{(n)2} \cdot a_M^{(n)2}} \cdot \left(\chi_3^{(n)} - c_3^{(n)} \right) \cdot \left(\chi_1^{(n)} - c_1^{(n)} \right) \cdot \left(-H_{11}^{(n)} + H_{33}^{(n)} \right) \cdot cos\left(\delta\right) \cdot sen^3\left(\delta\right) +$$

$$+2 \cdot \frac{H_{22}^{(n)}}{a_i^{(n)4}} \cdot \chi_2^{(n)2} +$$

$$+2\cdot H_{11}^{(n)}\cdot\left(\chi_1^{(n)}-c_1^{(n)}\right)^2\cdot\left[\frac{sen^2\left(\delta\right)}{a_M^{(n)2}}+\frac{cos^2\left(\delta\right)}{a_m^{(n)2}}\right]^2+$$

$$+2\cdot H_{33}^{(n)}\cdot\left(\chi_3^{(n)}-c_3^{(n)}\right)^2\cdot\left[\frac{cos^2\left(\delta\right)}{a_M^{(n)2}}+\frac{sen^2\left(\delta\right)}{a_m^{(n)2}}\right]^2\Bigg\}. \tag{9.3}$$

The expressions of the plastic multiplier (Eq. 9.3) and of the gradient associated with the n-th yield surface give the incremental response of the 3 degrees of freedom macro-element. The gradient of the n-th yield surface is recalled here below

$$\frac{\partial y^{(n)}\left(\chi_i^{(n)}\right)}{\partial\chi_1^{(n)}}=\frac{2}{a_M^{(n)2}}\cdot\left[\left(\chi_3^{(n)}-c_3^{(n)}\right)\cdot cos\left(\delta\right)+\left(\chi_1^{(n)}-c_1^{(n)}\right)\cdot sin\left(\delta\right)\right]\cdot$$

$$\cdot sin\left(\delta\right)\cdot S(\chi_1^{(n)})+\frac{2}{a_m^{(n)2}}\cdot\left[-\left(\chi_3^{(n)}-c_3^{(n)}\right)\cdot sin\left(\delta\right)+\left(\chi_1^{(n)}-c_1^{(n)}\right)\cdot cos\left(\delta\right)\right]\cdot$$

$$\cdot cos\left(\delta\right)\cdot S(\chi_1^{(n)}); \tag{9.4}$$

$$\frac{\partial y^{(n)}\left(\chi_i^{(n)}\right)}{\partial\chi_2^{(n)}}=\frac{2}{a_i^{(n)2}}\cdot\chi_2^{(n)}\cdot S(\chi_2^{(n)}); \tag{9.5}$$

$$\frac{\partial y^{(n)}\left(\chi_i^{(n)}\right)}{\partial\chi_3^{(n)}}=\frac{2}{a_M^{(n)2}}\cdot\left[\left(\chi_3^{(n)}-c_3^{(n)}\right)\cdot cos\left(\delta\right)+\left(\chi_1^{(n)}-c_1^{(n)}\right)\cdot sin\left(\delta\right)\right]\cdot$$

$$\cdot cos\left(\delta\right)\cdot S(\chi_3^{(n)})-\frac{2}{a_m^{(n)2}}\cdot\left[-\left(\chi_3^{(n)}-c_3^{(n)}\right)\cdot sin\left(\delta\right)+\left(\chi_1^{(n)}-c_1^{(n)}\right)\cdot cos\left(\delta\right)\right]\cdot$$

$$\cdot sin\,(\delta)\cdot S(\chi_3^{(n)}). \tag{9.6}$$

From Eq. 5.114 (global balance equation), it derives that the external forces $\dot{Q}_i$ are exactly equal to the internal forces $\dot{Q}_i^{(n)}$ when the masses are set equal to zero. Accordingly, the rate of the three interaction forces $\dot{Q}_i$ at the deck-abutment contact read

- rate of the longitudinal force $\dot{Q}_1$

$$\dot{Q}_1 = function(\dot{q}_j) = H_{11}^{(0)}\cdot\dot{q}_1 - H_{11}^{(0)}\cdot\sum_{n=1}^{N}\lambda_n\cdot\frac{\partial y_n^g}{\partial\chi_1^{(n)}} = H_{11}^{(0)}\cdot\dot{q}_1 -$$

$$-H_{11}^{(0)}\cdot\sum_{n=1}^{N}\left\{\dot{Q}_1\cdot\left[S(\chi_1^{(n)})\cdot\left(\chi_3^{(n)}-c_3^{(n)}\right)\cdot\left(\frac{1}{a_M^{(n)2}}-\frac{1}{a_m^{(n)2}}\right)\cdot cos\,(\delta)\cdot sin\,(\delta)+\right.\right.$$

$$\left.+S(\chi_1^{(n)})\cdot\left(\chi_1^{(n)}-c_1^{(n)}\right)\cdot\left(\frac{sin^2\,(\delta)}{a_M^{(n)2}}+\frac{cos^2\,(\delta)}{a_m^{(n)2}}\right)\right]+$$

$$+\dot{Q}_2\cdot\frac{S(\chi_2^{(n)})}{a_i^{(n)2}}\cdot\chi_2^{(n)}+$$

$$+\dot{Q}_3\cdot\left[S(\chi_3^{(n)})\cdot\left(\chi_1^{(n)}-c_1^{(n)}\right)\cdot\left(\frac{1}{a_M^{(n)2}}-\frac{1}{a_m^{(n)2}}\right)\cdot cos\,(\delta)\cdot sin\,(\delta)+\right.$$

$$\left.\left.+S(\chi_3^{(n)})\cdot\left(\chi_3^{(n)}-c_3^{(n)}\right)\cdot\left(\frac{cos^2\,(\delta)}{a_M^{(n)2}}+\frac{sen^2\,(\delta)}{a_m^{(n)2}}\right)\right]\right\}/$$

$$/\left\{2\cdot\left(\frac{1}{a_M^{(n)4}}+\frac{1}{a_m^{(n)4}}-\frac{2}{a_m^{(n)2}\cdot a_M^{(n)2}}\right)\cdot cos^2\,(\delta)\cdot sen^2\,(\delta)\cdot\right.$$

$$\cdot \left[H_{11}^{(n)} \cdot \left(\chi_3^{(n)} - c_3^{(n)} \right)^2 + H_{33}^{(n)} \cdot \left(\chi_1^{(n)} - c_1^{(n)} \right)^2 \right] +$$

$$+4 \cdot \left(\chi_3^{(n)} - c_3^{(n)} \right) \cdot \left(\chi_1^{(n)} - c_1^{(n)} \right) \cdot cos\left(\delta\right) \cdot sen^3\left(\delta\right) \cdot \left(\frac{H_{11}^{(n)}}{a_M^{(n)4}} - \frac{H_{33}^{(n)}}{a_m^{(n)4}} \right) +$$

$$+4 \cdot \left(\chi_3^{(n)} - c_3^{(n)} \right) \cdot \left(\chi_1^{(n)} - c_1^{(n)} \right) \cdot cos^3\left(\delta\right) \cdot sen\left(\delta\right) \cdot \left(-\frac{H_{11}^{(n)}}{a_m^{(n)4}} + \frac{H_{33}^{(n)}}{a_M^{(n)4}} \right) +$$

$$+\frac{4}{a_m^{(n)2} \cdot a_M^{(n)2}} \cdot \left(\chi_3^{(n)} - c_3^{(n)} \right) \cdot \left(\chi_1^{(n)} - c_1^{(n)} \right) \cdot \left(H_{11}^{(n)} - H_{33}^{(n)} \right) \cdot cos^3\left(\delta\right) \cdot sen\left(\delta\right) +$$

$$+\frac{4}{a_m^{(n)2} \cdot a_M^{(n)2}} \cdot \left(\chi_3^{(n)} - c_3^{(n)} \right) \cdot \left(\chi_1^{(n)} - c_1^{(n)} \right) \cdot \left(-H_{11}^{(n)} + H_{33}^{(n)} \right) \cdot cos\left(\delta\right) \cdot sen^3\left(\delta\right) +$$

$$+2 \cdot \frac{H_{22}^{(n)}}{a_i^{(n)4}} \cdot \chi_2^{(n)2} +$$

$$+2 \cdot H_{11}^{(n)} \cdot \left(\chi_1^{(n)} - c_1^{(n)} \right)^2 \cdot \left[\frac{sen^2\left(\delta\right)}{a_M^{(n)2}} + \frac{cos^2\left(\delta\right)}{a_m^{(n)2}} \right]^2 +$$

$$+2 \cdot H_{33}^{(n)} \cdot \left(\chi_3^{(n)} - c_3^{(n)} \right)^2 \cdot \left[\frac{cos^2\left(\delta\right)}{a_M^{(n)2}} + \frac{sen^2\left(\delta\right)}{a_m^{(n)2}} \right]^2 \Bigg\} \cdot$$

$$\cdot \Bigg\{ \left[\left(\chi_3^{(n)} - c_3^{(n)} \right) \cdot cos\left(\delta\right) + \left(\chi_1^{(n)} - c_1^{(n)} \right) \cdot sin\left(\delta\right) \right] \cdot \frac{2}{a_M^{(n)2}} \cdot sin\left(\delta\right) \cdot$$

$$\cdot S(\chi_1^{(n)}) + \left[- \left(\chi_3^{(n)} - c_3^{(n)} \right) \cdot sin\,(\delta) + \left(\chi_1^{(n)} - c_1^{(n)} \right) \cdot cos\,(\delta) \right] \cdot$$

$$\cdot \frac{2}{a_m^{(n)2}} \cdot cos\,(\delta) \cdot S(\chi_1^{(n)}) \Bigg\} \tag{9.7}$$

- rate of the transverse force $\dot{Q}_2$

$$\dot{Q}_2 = function(\dot{q}_j) = H_{22}^{(0)} \cdot \dot{q}_2 - H_{22}^{(0)} \cdot \sum_{n=1}^{N} \lambda_n \cdot \frac{\partial y_n^g}{\partial \chi_2^{(n)}} = H_{22}^{(0)} \cdot \dot{q}_2 -$$

$$- H_{22}^{(0)} \cdot \sum_{n=1}^{N} \Bigg\{ \dot{Q}_1 \cdot \Bigg[S(\chi_1^{(n)}) \cdot \left(\chi_3^{(n)} - c_3^{(n)} \right) \cdot \left(\frac{1}{a_M^{(n)2}} - \frac{1}{a_m^{(n)2}} \right) \cdot cos\,(\delta) \cdot sin\,(\delta) +$$

$$+ S(\chi_1^{(n)}) \cdot \left(\chi_1^{(n)} - c_1^{(n)} \right) \cdot \left(\frac{sin^2\,(\delta)}{a_M^{(n)2}} + \frac{cos^2\,(\delta)}{a_m^{(n)2}} \right) \Bigg] +$$

$$+ \dot{Q}_2 \cdot \frac{S(\chi_2^{(n)})}{a_i^{(n)2}} \cdot \chi_2^{(n)} +$$

$$+ \dot{Q}_3 \cdot \Bigg[S(\chi_3^{(n)}) \cdot \left(\chi_1^{(n)} - c_1^{(n)} \right) \cdot \left(\frac{1}{a_M^{(n)2}} - \frac{1}{a_m^{(n)2}} \right) \cdot cos\,(\delta) \cdot sin\,(\delta) +$$

$$+ S(\chi_3^{(n)}) \cdot \left(\chi_3^{(n)} - c_3^{(n)} \right) \cdot \left(\frac{cos^2\,(\delta)}{a_M^{(n)2}} + \frac{sen^2\,(\delta)}{a_m^{(n)2}} \right) \Bigg] \Bigg\} /$$

$$/ \left\{ 2 \cdot \left(\frac{1}{a_M^{(n)4}} + \frac{1}{a_m^{(n)4}} - \frac{2}{a_m^{(n)2} \cdot a_M^{(n)2}} \right) \cdot cos^2\,(\delta) \cdot sen^2\,(\delta) \cdot \right.$$

$$\left. \cdot \left[H_{11}^{(n)} \cdot \left(\chi_3^{(n)} - c_3^{(n)} \right)^2 + H_{33}^{(n)} \cdot \left(\chi_1^{(n)} - c_1^{(n)} \right)^2 \right] +$$

$$+4\cdot\left(\chi_3^{(n)}-c_3^{(n)}\right)\cdot\left(\chi_1^{(n)}-c_1^{(n)}\right)\cdot cos\left(\delta\right)\cdot sen^3\left(\delta\right)\cdot\left(\frac{H_{11}^{(n)}}{a_M^{(n)4}}-\frac{H_{33}^{(n)}}{a_m^{(n)4}}\right)+$$

$$+4\cdot\left(\chi_3^{(n)}-c_3^{(n)}\right)\cdot\left(\chi_1^{(n)}-c_1^{(n)}\right)\cdot cos^3\left(\delta\right)\cdot sen\left(\delta\right)\cdot\left(-\frac{H_{11}^{(n)}}{a_m^{(n)4}}+\frac{H_{33}^{(n)}}{a_M^{(n)4}}\right)+$$

$$+\frac{4}{a_m^{(n)2}\cdot a_M^{(n)2}}\cdot\left(\chi_3^{(n)}-c_3^{(n)}\right)\cdot\left(\chi_1^{(n)}-c_1^{(n)}\right)\cdot\left(H_{11}^{(n)}-H_{33}^{(n)}\right)\cdot cos^3\left(\delta\right)\cdot sen\left(\delta\right)+$$

$$+\frac{4}{a_m^{(n)2}\cdot a_M^{(n)2}}\cdot\left(\chi_3^{(n)}-c_3^{(n)}\right)\cdot\left(\chi_1^{(n)}-c_1^{(n)}\right)\cdot\left(-H_{11}^{(n)}+H_{33}^{(n)}\right)\cdot cos\left(\delta\right)\cdot sen^3\left(\delta\right)+$$

$$+2\cdot\frac{H_{22}^{(n)}}{a_i^{(n)4}}\cdot\chi_2^{(n)2}+$$

$$+2\cdot H_{11}^{(n)}\cdot\left(\chi_1^{(n)}-c_1^{(n)}\right)^2\cdot\left[\frac{sen^2\left(\delta\right)}{a_M^{(n)2}}+\frac{cos^2\left(\delta\right)}{a_m^{(n)2}}\right]^2+$$

$$+2\cdot H_{33}^{(n)}\cdot\left(\chi_3^{(n)}-c_3^{(n)}\right)^2\cdot\left[\frac{cos^2\left(\delta\right)}{a_M^{(n)2}}+\frac{sen^2\left(\delta\right)}{a_m^{(n)2}}\right]^2\Bigg\}\cdot$$

$$\cdot\frac{2}{a_i^{(n)2}}\cdot\chi_2^{(n)}\cdot S(\chi_2^{(n)}) \tag{9.8}$$

- rate of the longitudinal force $\dot{Q}_3$

$$\dot{Q}_3=function(\dot{q}_j)=H_{33}^{(0)}\cdot\dot{q}_3-H_{33}^{(0)}\cdot\sum_{n=1}^{N}\lambda_n\cdot\frac{\partial y_n^g}{\partial\chi_3^{(n)}}=H_{33}^{(0)}\cdot\dot{q}_3-$$

$$-H_{33}^{(0)} \cdot \sum_{n=1}^{N} \left\{ \dot{Q}_1 \cdot \left[S(\chi_1^{(n)}) \cdot \left(\chi_3^{(n)} - c_3^{(n)} \right) \cdot \left(\frac{1}{a_M^{(n)2}} - \frac{1}{a_m^{(n)2}} \right) \cdot cos\left(\delta\right) \cdot sin\left(\delta\right) + \right. \right.$$

$$\left. + S(\chi_1^{(n)}) \cdot \left(\chi_1^{(n)} - c_1^{(n)} \right) \cdot \left(\frac{sin^2\left(\delta\right)}{a_M^{(n)2}} + \frac{cos^2\left(\delta\right)}{a_m^{(n)2}} \right) \right] +$$

$$+ \dot{Q}_2 \cdot \frac{S(\chi_2^{(n)})}{a_i^{(n)2}} \cdot \chi_2^{(n)} +$$

$$+ \dot{Q}_3 \cdot \left[S(\chi_3^{(n)}) \cdot \left(\chi_1^{(n)} - c_1^{(n)} \right) \cdot \left(\frac{1}{a_M^{(n)2}} - \frac{1}{a_m^{(n)2}} \right) \cdot cos\left(\delta\right) \cdot sin\left(\delta\right) + \right.$$

$$\left. \left. + S(\chi_3^{(n)}) \cdot \left(\chi_3^{(n)} - c_3^{(n)} \right) \cdot \left(\frac{cos^2\left(\delta\right)}{a_M^{(n)2}} + \frac{sen^2\left(\delta\right)}{a_m^{(n)2}} \right) \right] \right\} /$$

$$/ \left\{ 2 \cdot \left(\frac{1}{a_M^{(n)4}} + \frac{1}{a_m^{(n)4}} - \frac{2}{a_m^{(n)2} \cdot a_M^{(n)2}} \right) \cdot cos^2\left(\delta\right) \cdot sen^2\left(\delta\right) \cdot \right.$$

$$\left. \cdot \left[H_{11}^{(n)} \cdot \left(\chi_3^{(n)} - c_3^{(n)} \right)^2 + H_{33}^{(n)} \cdot \left(\chi_1^{(n)} - c_1^{(n)} \right)^2 \right] +$$

$$+ 4 \cdot \left(\chi_3^{(n)} - c_3^{(n)} \right) \cdot \left(\chi_1^{(n)} - c_1^{(n)} \right) \cdot cos\left(\delta\right) \cdot sen^3\left(\delta\right) \cdot \left(\frac{H_{11}^{(n)}}{a_M^{(n)4}} - \frac{H_{33}^{(n)}}{a_m^{(n)4}} \right) +$$

$$+ 4 \cdot \left(\chi_3^{(n)} - c_3^{(n)} \right) \cdot \left(\chi_1^{(n)} - c_1^{(n)} \right) \cdot cos^3\left(\delta\right) \cdot sen\left(\delta\right) \cdot \left(-\frac{H_{11}^{(n)}}{a_m^{(n)4}} + \frac{H_{33}^{(n)}}{a_M^{(n)4}} \right) +$$

$$+\frac{4}{a_m^{(n)2}\cdot a_M^{(n)2}}\cdot\left(\chi_3^{(n)}-c_3^{(n)}\right)\cdot\left(\chi_1^{(n)}-c_1^{(n)}\right)\cdot\left(H_{11}^{(n)}-H_{33}^{(n)}\right)\cdot cos^3(\delta)\cdot sen(\delta)+$$

$$+\frac{4}{a_m^{(n)2}\cdot a_M^{(n)2}}\cdot\left(\chi_3^{(n)}-c_3^{(n)}\right)\cdot\left(\chi_1^{(n)}-c_1^{(n)}\right)\cdot\left(-H_{11}^{(n)}+H_{33}^{(n)}\right)\cdot cos(\delta)\cdot sen^3(\delta)+$$

$$+2\cdot\frac{H_{22}^{(n)}}{a_i^{(n)4}}\cdot\chi_2^{(n)2}+$$

$$+2\cdot H_{11}^{(n)}\cdot\left(\chi_1^{(n)}-c_1^{(n)}\right)^2\cdot\left[\frac{sen^2(\delta)}{a_M^{(n)2}}+\frac{cos^2(\delta)}{a_m^{(n)2}}\right]^2+$$

$$+2\cdot H_{33}^{(n)}\cdot\left(\chi_3^{(n)}-c_3^{(n)}\right)^2\cdot\left[\frac{cos^2(\delta)}{a_M^{(n)2}}+\frac{sen^2(\delta)}{a_m^{(n)2}}\right]^2\Bigg\}\cdot$$

$$\cdot\left\{\frac{2}{a_M^{(n)2}}\cdot\left[\left(\chi_3^{(n)}-c_3^{(n)}\right)\cdot cos(\delta)+\left(\chi_1^{(n)}-c_1^{(n)}\right)\cdot sin(\delta)\right]\cdot cos(\delta)\cdot\right.$$

$$\cdot S(\chi_3^{(n)})-\frac{2}{a_m^{(n)2}}\cdot\left[-\left(\chi_3^{(n)}-c_3^{(n)}\right)\cdot sin(\delta)+\left(\chi_1^{(n)}-c_1^{(n)}\right)\cdot cos(\delta)\right]\cdot$$

$$\left.\cdot sin(\delta)\cdot S(\chi_3^{(n)})\right\}. \tag{9.9}$$

In the equations above, the "incremental" variables are the rates of the displacements $\dot{q}_i$ and of the resulting interaction forces $\dot{Q}_i$ at the deck-abutment contact, while the other quantities refer to the current time step. In fact, the generic dissipative force $\chi_i^{(n)} = -\partial g_2(\alpha_i)/\partial\alpha_i + Q_i$ represents the distance of the generic point in the force space (internal forces in the macro-element) from the center $c_i^{(n)}$ of the n-th

yield surface. The latter evolves during plastic loading according to the kinematic hardening rule defined in Section 5.9.3. Since there is no isotropic hardening, the distances $\chi_i^{(n)} - c_i$ do not not vary during loading. It follows that $\chi_i^{(n)} - c_i$ is a constant value in the incremental response. The parameters $a_M^{(n)}$, $a_i^{(n)}$, $a_m^{(n)}$ and δ characterise completely the yield functions and can be evaluated through Eqs. 5.135 to 5.143. The stiffness matrices $H_{ii}^{(0)}$ and $H_{ii}^{(n)}$ are constant in time. Accordingly, despite their apparently complex form, Eqs. 9.7, 9.8 and 9.9 can be written in a much more compact form

$$\dot{Q}_1 = H_{11}^{(0)} \cdot \dot{q_1} - H_{11}^{(0)} \cdot \sum_{n=1}^{N} \Big\{ \dot{Q}_1 \cdot S(\chi_1^{(n)}) \cdot (F_{N1} + F_{N2}) +$$

$$+ \dot{Q}_2 \cdot \frac{S(\chi_2^{(n)})}{a_i^{(n)2}} \cdot \chi_2^{(n)} + \dot{Q}_3 \cdot S(\chi_3^{(n)}) \cdot (F_{N3} + F_{N4}) \Big\} / F_D \cdot$$

$$\cdot S(\chi_1^{(n)}) \cdot (F_{Y1} + F_{Y2}) \tag{9.10}$$

$$\dot{Q}_2 = H_{22}^{(0)} \cdot \dot{q_2} - H_{22}^{(0)} \cdot \sum_{n=1}^{N} \Big\{ \dot{Q}_1 \cdot S(\chi_1^{(n)}) \cdot (F_{N1} + F_{N2}) +$$

$$+ \dot{Q}_2 \cdot \frac{S(\chi_2^{(n)})}{a_i^{(n)2}} \cdot \chi_2^{(n)} + \dot{Q}_3 \cdot S(\chi_3^{(n)}) \cdot (F_{N3} + F_{N4}) \Big\} / F_D \cdot$$

$$\cdot \frac{2}{a_i^{(n)2}} \cdot \chi_2^{(n)} \cdot S(\chi_2^{(n)}) \tag{9.11}$$

$$\dot{Q}_3 = H_{33}^{(0)} \cdot \dot{q_3} - H_{33}^{(0)} \cdot \sum_{n=1}^{N} \Big\{ \dot{Q}_1 \cdot S(\chi_1^{(n)}) \cdot (F_{N1} + F_{N2}) +$$

$$+\dot{Q}_2 \cdot \frac{S(\chi_2^{(n)})}{a_i^{(n)2}} \cdot \chi_2^{(n)} + \dot{Q}_3 \cdot S(\chi_3^{(n)}) \cdot (F_{N3} + F_{N4}) \Bigg\} / F_D \cdot$$

$$\cdot S(\chi_3^{(n)}) \cdot (F_{Y3} - F_{Y4}) \tag{9.12}$$

in which the factors F_{N1}, F_{N2}, F_{N3}, F_{N4} and F_D are constant variable in the incremental response and are defined as follows

$$F_{N1} = \left(\chi_3^{(n)} - c_3^{(n)}\right) \cdot \left(\frac{1}{a_M^{(n)2}} - \frac{1}{a_m^{(n)2}}\right) \cdot cos\,(\delta) \cdot sin\,(\delta) \tag{9.13}$$

$$F_{N2} = \left(\chi_1^{(n)} - c_1^{(n)}\right) \cdot \left(\frac{sin^2\,(\delta)}{a_M^{(n)2}} + \frac{cos^2\,(\delta)}{a_m^{(n)2}}\right) \tag{9.14}$$

$$F_{N3} = \left(\chi_1^{(n)} - c_1^{(n)}\right) \cdot \left(\frac{1}{a_M^{(n)2}} - \frac{1}{a_m^{(n)2}}\right) \cdot cos\,(\delta) \cdot sin\,(\delta) \tag{9.15}$$

$$F_{N4} = \left(\chi_3^{(n)} - c_3^{(n)}\right) \cdot \left(\frac{cos^2\,(\delta)}{a_M^{(n)2}} + \frac{sen^2\,(\delta)}{a_m^{(n)2}}\right) \tag{9.16}$$

$$F_D = 2 \cdot \left(\frac{1}{a_M^{(n)4}} + \frac{1}{a_m^{(n)4}} - \frac{2}{a_m^{(n)2} \cdot a_M^{(n)2}}\right) \cdot cos^2\,(\delta) \cdot sen^2\,(\delta) \cdot$$

$$\cdot \left[H_{11}^{(n)} \cdot \left(\chi_3^{(n)} - c_3^{(n)}\right)^2 + H_{33}^{(n)} \cdot \left(\chi_1^{(n)} - c_1^{(n)}\right)^2\right] +$$

$$+4 \cdot \left(\chi_3^{(n)} - c_3^{(n)}\right) \cdot \left(\chi_1^{(n)} - c_1^{(n)}\right) \cdot cos\,(\delta) \cdot sen^3\,(\delta) \cdot \left(\frac{H_{11}^{(n)}}{a_M^{(n)4}} - \frac{H_{33}^{(n)}}{a_m^{(n)4}}\right) +$$

$$+4 \cdot \left(\chi_3^{(n)} - c_3^{(n)}\right) \cdot \left(\chi_1^{(n)} - c_1^{(n)}\right) \cdot cos^3\,(\delta) \cdot sen\,(\delta) \cdot \left(-\frac{H_{11}^{(n)}}{a_m^{(n)4}} + \frac{H_{33}^{(n)}}{a_M^{(n)4}}\right) +$$

$$+\frac{4}{a_m^{(n)2}\cdot a_M^{(n)2}}\cdot\left(\chi_3^{(n)}-c_3^{(n)}\right)\cdot\left(\chi_1^{(n)}-c_1^{(n)}\right)\cdot\left(H_{11}^{(n)}-H_{33}^{(n)}\right)\cdot cos^3\left(\delta\right)\cdot sen\left(\delta\right)+$$

$$+\frac{4}{a_m^{(n)2}\cdot a_M^{(n)2}}\cdot\left(\chi_3^{(n)}-c_3^{(n)}\right)\cdot\left(\chi_1^{(n)}-c_1^{(n)}\right)\cdot\left(-H_{11}^{(n)}+H_{33}^{(n)}\right)\cdot cos\left(\delta\right)\cdot sen^3\left(\delta\right)+$$

$$+2\cdot\frac{H_{22}^{(n)}}{a_i^{(n)4}}\cdot\chi_2^{(n)2}+$$

$$+2\cdot H_{11}^{(n)}\cdot\left(\chi_1^{(n)}-c_1^{(n)}\right)^2\cdot\left[\frac{sen^2\left(\delta\right)}{a_M^{(n)2}}+\frac{cos^2\left(\delta\right)}{a_m^{(n)2}}\right]^2+$$

$$+2\cdot H_{33}^{(n)}\cdot\left(\chi_3^{(n)}-c_3^{(n)}\right)^2\cdot\left[\frac{cos^2\left(\delta\right)}{a_M^{(n)2}}+\frac{sen^2\left(\delta\right)}{a_m^{(n)2}}\right]^2 \tag{9.17}$$

$$F_{Y1}=\left[\left(\chi_3^{(n)}-c_3^{(n)}\right)\cdot cos\left(\delta\right)+\left(\chi_1^{(n)}-c_1^{(n)}\right)\cdot sin\left(\delta\right)\right]\cdot\frac{2}{a_M^{(n)2}}\cdot sin\left(\delta\right) \tag{9.18}$$

$$F_{Y2}=\left[-\left(\chi_3^{(n)}-c_3^{(n)}\right)\cdot sin\left(\delta\right)+\left(\chi_1^{(n)}-c_1^{(n)}\right)\cdot cos\left(\delta\right)\right]\cdot\frac{2}{a_m^{(n)2}}\cdot cos\left(\delta\right) \tag{9.19}$$

$$F_{Y3}=\left[\left(\chi_3^{(n)}-c_3^{(n)}\right)\cdot cos\left(\delta\right)+\left(\chi_1^{(n)}-c_1^{(n)}\right)\cdot sin\left(\delta\right)\right]\cdot\frac{2}{a_M^{(n)2}}\cdot cos\left(\delta\right) \tag{9.20}$$

$$F_{Y4} = \left[- \left(\chi_3^{(n)} - c_3^{(n)} \right) \cdot sin\left(\delta\right) + \left(\chi_1^{(n)} - c_1^{(n)} \right) \cdot cos\left(\delta\right) \right] \cdot \frac{2}{a_m^{(n)2}} \cdot sin\left(\delta\right). \quad (9.21)$$

Eqs. 9.10, 9.11 and 9.12 can be also expressed taking the forces $Q_i^{(n)}$ as the input variable and the displacements $q_i^{(n)}$ the output variable as follows

$$\dot{q}_1 = H_{11}^{(0)-1} \cdot \dot{Q}_1 +$$

$$+ \sum_{n=1}^{N} \frac{(F_{N1} + F_{N2}) \cdot (F_{Y1} + F_{Y2})}{F_D} \cdot \dot{Q}_1 +$$

$$+ \sum_{n=1}^{N} S(\chi_2^{(n)}) \cdot S(\chi_1^{(n)}) \cdot \frac{\chi_2^{(n)} \cdot (F_{Y1} + F_{Y2})}{a_i^{(n)2} \cdot F_D} \cdot \dot{Q}_2 +$$

$$+ \sum_{n=1}^{N} S(\chi_3^{(n)}) \cdot S(\chi_1^{(n)}) \cdot \frac{(F_{N3} + F_{N4}) \cdot (F_{Y1} + F_{Y2})}{F_D} \cdot \dot{Q}_3 \quad (9.22)$$

$$\dot{q}_2 = H_{22}^{(0)-1} \cdot \dot{Q}_2 +$$

$$+ \sum_{n=1}^{N} S(\chi_2^{(n)}) \cdot S(\chi_1^{(n)}) \cdot \frac{(F_{N1} + F_{N2}) \cdot 2 \cdot \chi_2^{(n)}}{F_D \cdot a_i^{(n)2}} \cdot \dot{Q}_1 +$$

$$+ \sum_{n=1}^{N} \frac{\chi_2^{(n)2} \cdot 2}{a_i^{(n)4} \cdot F_D} \cdot \dot{Q}_2 +$$

$$+ \sum_{n=1}^{N} S(\chi_3^{(n)}) \cdot S(\chi_2^{(n)}) \cdot \frac{(F_{N3} + F_{N4}) \cdot 2 \cdot \chi_2^{(n)}}{F_D \cdot a_i^{(n)2}} \cdot \dot{Q}_3 \quad (9.23)$$

$$\dot{q}_3 = H_{33}^{(0)-1} \cdot \dot{Q}_3 +$$

$$+\sum_{n=1}^{N} S(\chi_3^{(n)}) \cdot S(\chi_1^{(n)}) \cdot \frac{(F_{N1}+F_{N2}) \cdot (F_{Y3}-F_{Y4})}{F_D} \cdot \dot{Q}_1 +$$

$$+\sum_{n=1}^{N} S(\chi_3^{(n)}) \cdot S(\chi_2^{(n)}) \cdot \frac{\chi_2^{(n)} \cdot (F_{Y3}-F_{Y4})}{a_i^{(n)2} \cdot F_D} \cdot \dot{Q}_2 +$$

$$+\sum_{n=1}^{N} \frac{(F_{N3}+F_{N4}) \cdot (F_{Y3}-F_{Y4})}{F_D} \cdot \dot{Q}_3 \tag{9.24}$$

In the equations above, some further constant factors can be identified in the response at the time step $j+1$

$$F_{q11} = \frac{(F_{N1}+F_{N2}) \cdot (F_{Y1}+F_{Y2})}{F_D} \tag{9.25}$$

$$F_{q12} = S(\chi_2^{(n)}) \cdot S(\chi_1^{(n)}) \cdot \frac{\chi_2^{(n)} \cdot (F_{Y1}+F_{Y2})}{a_i^{(n)2} \cdot F_D} \tag{9.26}$$

$$F_{q13} = S(\chi_3^{(n)}) \cdot S(\chi_1^{(n)}) \cdot \frac{(F_{N3}+F_{N4}) \cdot (F_{Y1}+F_{Y2})}{F_D} \tag{9.27}$$

$$F_{q21} = S(\chi_2^{(n)}) \cdot S(\chi_1^{(n)}) \cdot \frac{(F_{N1}+F_{N2}) \cdot 2 \cdot \chi_2^{(n)}}{F_D \cdot a_i^{(n)2}} \tag{9.28}$$

$$F_{q22} = \frac{\chi_2^{(n)2} \cdot 2}{a_i^{(n)4} \cdot F_D} \tag{9.29}$$

$$F_{q23} = S(\chi_3^{(n)}) \cdot S(\chi_2^{(n)}) \cdot \frac{(F_{N3}+F_{N4}) \cdot 2 \cdot \chi_2^{(n)}}{F_D \cdot a_i^{(n)2}} \tag{9.30}$$

$$F_{q31} = S(\chi_3^{(n)}) \cdot S(\chi_1^{(n)}) \cdot \frac{(F_{N1}+F_{N2}) \cdot (F_{Y3}-F_{Y4})}{F_D} \tag{9.31}$$

$$F_{q32} = S(\chi_3^{(n)}) \cdot S(\chi_2^{(n)}) \cdot \frac{\chi_2^{(n)} \cdot (F_{Y3} - F_{Y4})}{a_i^{(n)2} \cdot F_D} \tag{9.32}$$

$$F_{q33} = \frac{(F_{N3} + F_{N4}) \cdot (F_{Y3} - F_{Y4})}{F_D} \tag{9.33}$$

and finally a more compact form of the incremental equations can be given below

$$\dot{q}_1 = \left(H_{11}^{(0)-1} + \sum_{n=1}^{N} F_{q11} \right) \cdot \dot{Q}_1 + \sum_{n=1}^{N} F_{q12} \cdot \dot{Q}_2 + \sum_{n=1}^{N} F_{q13} \cdot \dot{Q}_3 \tag{9.34}$$

$$\dot{q}_2 = \sum_{n=1}^{N} F_{q21} \cdot \dot{Q}_1 + \left(H_{22}^{(0)-1} + \sum_{n=1}^{N} F_{q22} \right) \cdot \dot{Q}_2 + \sum_{n=1}^{N} F_{q23} \cdot \dot{Q}_3 \tag{9.35}$$

$$\dot{q}_3 = \sum_{n=1}^{N} F_{q31} \cdot \dot{Q}_1 + \sum_{n=1}^{N} F_{q32} \cdot \dot{Q}_2 + \left(H_{33}^{(0)-1} + \sum_{n=1}^{N} F_{q33} \right) \cdot \dot{Q}_3 \tag{9.36}$$

in which it appears evident the contribution of the plastic response of the macro-element in the terms $\sum_{n=1}^{N} F_{qij}$. A matrix notation can be used for Eqs. 9.34, 9.35 and 9.36, where the vector of the displacement rate $\dot{q}_j^{(n)}$ is related to the vector of the force rate $\dot{Q}_i^{(n)}$ by a tangent compliant matrix C_{ji}

$$\dot{q}_j^{(n)} = C_{ji} \cdot \dot{Q}_i = \left(H_{ij}^{(0)-1} \cdot \delta_{ji} + \sum_{n=1}^{N} F_{qji} \right) \cdot \dot{Q}_i \tag{9.37}$$

with the compliant matrix composed as follows

$$\begin{bmatrix} C_{11} & C_{12} & C_{13} \\ C_{21} & C_{22} & C_{23} \\ C_{31} & C_{23} & C_{33} \end{bmatrix} = \begin{bmatrix} H_{11}^{(0)-1} + \sum_{n=1}^{N} F_{q11} & \sum_{n=1}^{N} F_{q12} & \sum_{n=1}^{N} F_{q13} \\ \sum_{n=1}^{N} F_{q21} & H_{22}^{(0)-1} + \sum_{n=1}^{N} F_{q22} & \sum_{n=1}^{N} F_{q23} \\ \sum_{n=1}^{N} F_{q31} & \sum_{n=1}^{N} F_{q32} & H_{33}^{(0)-1} + \sum_{n=1}^{N} F_{q33} \end{bmatrix}. \tag{9.38}$$

that is non-symmetric. The tangent stiffness matrix $K_{ij} = C_{ji}^{-1}$ is therefore

computed as follows

- term K_{11}

$$K_{11} = \left[H_{11}^{(0)} \cdot \left(\sum_{n=1}^{N} F_{q22} \cdot H_{22}^{(0)} + \sum_{n=1}^{N} F_{q33} \cdot H_{33}^{(0)} + \right.\right.$$

$$\left.\left. + \sum_{n=1}^{N} F_{q22} \cdot \sum_{n=1}^{N} F_{q33} \cdot H_{22}^{(0)} \cdot H_{33}^{(0)} - \sum_{n=1}^{N} F_{q23} \cdot \sum_{n=1}^{N} F_{q32} \cdot H_{22}^{(0)} \cdot H_{33}^{(0)} + 1 \right) \right] /$$

$$/ \left(\sum_{n=1}^{N} F_{q11} \cdot H_{11}^{(0)} + \sum_{n=1}^{N} F_{q22} \cdot H_{22}^{(0)} + \sum_{n=1}^{N} F_{q33} \cdot H_{33}^{(0)} - \right.$$

$$- \sum_{n=1}^{N} F_{q21}^{2} \cdot H_{11}^{(0)} \cdot H_{22}^{(0)} - \sum_{n=1}^{N} F_{q31}^{2} \cdot H_{11}^{(0)} \cdot H_{33}^{(0)} + \sum_{n=1}^{N} F_{q11} \cdot \sum_{n=1}^{N} F_{q22} \cdot H_{11}^{(0)} \cdot H_{22}^{(0)} +$$

$$+ \sum_{n=1}^{N} F_{q11} \cdot \sum_{n=1}^{N} F_{q33} \cdot H_{11}^{(0)} \cdot H_{33}^{(0)} + \sum_{n=1}^{N} F_{q22} \cdot \sum_{n=1}^{N} F_{q33} \cdot H_{22}^{(0)} \cdot H_{33}^{(0)} - \sum_{n=1}^{N} F_{q23} \cdot \sum_{n=1}^{N} F_{q32} \cdot H_{22}^{(0)} \cdot H_{33}^{(0)} -$$

$$- \sum_{n=1}^{N} F_{q22} \cdot \sum_{n=1}^{N} F_{q31}^{2} \cdot H_{11}^{(0)} \cdot H_{22}^{(0)} \cdot H_{33}^{(0)} - \sum_{n=1}^{N} F_{q21}^{2} \cdot \sum_{n=1}^{N} F_{q33} H_{11}^{(0)} \cdot H_{22}^{(0)} \cdot H_{33}^{(0)} +$$

$$+ \sum_{n=1}^{N} F_{q11} \cdot \sum_{n=1}^{N} F_{q22} \cdot \sum_{n=1}^{N} F_{q33} \cdot H_{11}^{(0)} \cdot H_{22}^{(0)} \cdot H_{33}^{(0)} - \sum_{n=1}^{N} F_{q11} \cdot \sum_{n=1}^{N} F_{q23} \cdot \sum_{n=1}^{N} F_{q32} \cdot H_{11}^{(0)} \cdot H_{22}^{(0)} \cdot H_{33}^{(0)} +$$

$$+ \sum_{n=1}^{N} F_{q21} \cdot \sum_{n=1}^{N} F_{q23} \cdot \sum_{n=1}^{N} F_{q31} \cdot H_{11}^{(0)} \cdot H_{22}^{(0)} \cdot H_{33}^{(0)} +$$

$$+\sum_{n=1}^{N} F_{q21} \cdot \sum_{n=1}^{N} F_{q31} \cdot \sum_{n=1}^{N} F_{q32} \cdot H_{11}^{(0)} \cdot H_{22}^{(0)} \cdot H_{33}^{(0)} + 1\Bigg) \tag{9.39}$$

- term K_{12}

$$K_{12} = -\Bigg[H_{11}^{(0)} \cdot H_{22}^{(0)} \cdot \Bigg(\sum_{n=1}^{N} F_{q21} + \sum_{n=1}^{N} F_{q21} \cdot \sum_{n=1}^{N} F_{q33} \cdot H_{33}^{(0)} -$$

$$-\sum_{n=1}^{N} F_{q31} \cdot \sum_{n=1}^{N} F_{q32} \cdot H_{33}^{(0)}\Bigg)\Bigg] / \Bigg(\sum_{n=1}^{N} F_{q11} \cdot H_{11}^{(0)} + \sum_{n=1}^{N} F_{q22} \cdot H_{22}^{(0)} + \sum_{n=1}^{N} F_{q33} \cdot H_{33}^{(0)} -$$

$$-\sum_{n=1}^{N} F_{q21}^2 \cdot H_{11}^{(0)} \cdot H_{22}^{(0)} - \sum_{n=1}^{N} F_{q31}^2 \cdot H_{11}^{(0)} \cdot H_{33}^{(0)} + \sum_{n=1}^{N} F_{q11} \cdot \sum_{n=1}^{N} F_{q22} \cdot H_{11}^{(0)} \cdot H_{22}^{(0)} +$$

$$+\sum_{n=1}^{N} F_{q11} \cdot \sum_{n=1}^{N} F_{q33} \cdot H_{11}^{(0)} \cdot H_{33}^{(0)} + \sum_{n=1}^{N} F_{q22} \cdot \sum_{n=1}^{N} F_{q33} \cdot H_{22}^{(0)} \cdot H_{33}^{(0)} - \sum_{n=1}^{N} F_{q23} \cdot \sum_{n=1}^{N} F_{q32} \cdot H_{22}^{(0)} \cdot H_{33}^{(0)} -$$

$$-\sum_{n=1}^{N} F_{q22} \cdot \sum_{n=1}^{N} F_{q31}^2 \cdot H_{11}^{(0)} \cdot H_{22}^{(0)} \cdot H_{33}^{(0)} - \sum_{n=1}^{N} F_{q21}^2 \cdot \sum_{n=1}^{N} F_{q33} \cdot H_{11}^{(0)} \cdot H_{22}^{(0)} \cdot H_{33}^{(0)} +$$

$$+\sum_{n=1}^{N} F_{q11} \cdot \sum_{n=1}^{N} F_{q22} \cdot \sum_{n=1}^{N} F_{q33} \cdot H_{11}^{(0)} \cdot H_{22}^{(0)} \cdot H_{33}^{(0)} - \sum_{n=1}^{N} F_{q11} \cdot \sum_{n=1}^{N} F_{q23} \cdot \sum_{n=1}^{N} F_{q32} \cdot H_{11}^{(0)} \cdot H_{22}^{(0)} \cdot H_{33}^{(0)} +$$

$$+\sum_{n=1}^{N} F_{q21} \cdot \sum_{n=1}^{N} F_{q23} \cdot \sum_{n=1}^{N} F_{q31} \cdot H_{11}^{(0)} \cdot H_{22}^{(0)} \cdot H_{33}^{(0)} +$$

$$+\sum_{n=1}^{N} F_{q21} \cdot \sum_{n=1}^{N} F_{q31} \cdot \sum_{n=1}^{N} F_{q32} \cdot H_{11}^{(0)} \cdot H_{22}^{(0)} \cdot H_{33}^{(0)} + 1\Bigg) \tag{9.40}$$

- term K_{13}

$$K_{13} = -\Bigg[H_{11}^{(0)} \cdot H_{33}^{(0)} \cdot \Bigg(\sum_{n=1}^{N} F_{q31} - \sum_{n=1}^{N} F_{q21} \cdot \sum_{n=1}^{N} F_{q23} \cdot H_{22}^{(0)} +$$

$$+\sum_{n=1}^{N} F_{q22} \cdot \sum_{n=1}^{N} F_{q31} \cdot H_{22}^{(0)}\Bigg)\Bigg] / \Bigg(\sum_{n=1}^{N} F_{q11} \cdot H_{11}^{(0)} + \sum_{n=1}^{N} F_{q22} \cdot H_{22}^{(0)} + \sum_{n=1}^{N} F_{q33} \cdot H_{33}^{(0)} -$$

$$-\sum_{n=1}^{N} F_{q21}^{2}\cdot H_{11}^{(0)}\cdot H_{22}^{(0)}-\sum_{n=1}^{N} F_{q31}^{2}\cdot H_{11}^{(0)}\cdot H_{33}^{(0)}+\sum_{n=1}^{N} F_{q11}\cdot\sum_{n=1}^{N} F_{q22}\cdot H_{11}^{(0)}\cdot H_{22}^{(0)}+$$

$$+\sum_{n=1}^{N} F_{q11}\cdot\sum_{n=1}^{N} F_{q33}\cdot H_{11}^{(0)}\cdot H_{33}^{(0)}+\sum_{n=1}^{N} F_{q22}\cdot\sum_{n=1}^{N} F_{q33}\cdot H_{22}^{(0)}\cdot H_{33}^{(0)}-\sum_{n=1}^{N} F_{q23}\cdot\sum_{n=1}^{N} F_{q32}\cdot H_{22}^{(0)}\cdot H_{33}^{(0)}-$$

$$-\sum_{n=1}^{N} F_{q22}\cdot\sum_{n=1}^{N} F_{q31}^{2}\cdot H_{11}^{(0)}\cdot H_{22}^{(0)}\cdot H_{33}^{(0)}-\sum_{n=1}^{N} F_{q21}^{2}\cdot\sum_{n=1}^{N} F_{q33}\cdot H_{11}^{(0)}\cdot H_{22}^{(0)}\cdot H_{33}^{(0)}+$$

$$+\sum_{n=1}^{N} F_{q11}\cdot\sum_{n=1}^{N} F_{q22}\cdot\sum_{n=1}^{N} F_{q33}\cdot H_{11}^{(0)}\cdot H_{22}^{(0)}\cdot H_{33}^{(0)}-\sum_{n=1}^{N} F_{q11}\cdot\sum_{n=1}^{N} F_{q23}\cdot\sum_{n=1}^{N} F_{q32}\cdot H_{11}^{(0)}\cdot H_{22}^{(0)}\cdot H_{33}^{(0)}+$$

$$+\sum_{n=1}^{N} F_{q21}\cdot\sum_{n=1}^{N} F_{q23}\cdot\sum_{n=1}^{N} F_{q31}\cdot H_{11}^{(0)}\cdot H_{22}^{(0)}\cdot H_{33}^{(0)}+$$

$$+\sum_{n=1}^{N} F_{q21}\cdot\sum_{n=1}^{N} F_{q31}\cdot\sum_{n=1}^{N} F_{q32}\cdot H_{11}^{(0)}\cdot H_{22}^{(0)}\cdot H_{33}^{(0)}+1\Bigg) \tag{9.41}$$

- term K_{21}

$$K_{21}=-\Bigg[H_{11}^{(0)}\cdot H_{22}^{(0)}\cdot\Bigg(\sum_{n=1}^{N} F_{q21}+\sum_{n=1}^{N} F_{q21}\cdot\sum_{n=1}^{N} F_{q33}\cdot H_{33}^{(0)}-$$

$$-\sum_{n=1}^{N} F_{q23}\cdot\sum_{n=1}^{N} F_{q31}\cdot H_{33}^{(0)}\Bigg)\Bigg]\Big/\Bigg(\sum_{n=1}^{N} F_{q11}\cdot H_{11}^{(0)}+\sum_{n=1}^{N} F_{q22}\cdot H_{22}^{(0)}+\sum_{n=1}^{N} F_{q33}\cdot H_{33}^{(0)}-$$

$$-\sum_{n=1}^{N} F_{q21}^{2}\cdot H_{11}^{(0)}\cdot H_{22}^{(0)}-\sum_{n=1}^{N} F_{q31}^{2}\cdot H_{11}^{(0)}\cdot H_{33}^{(0)}+\sum_{n=1}^{N} F_{q11}\cdot\sum_{n=1}^{N} F_{q22}\cdot H_{11}^{(0)}\cdot H_{22}^{(0)}+$$

$$+\sum_{n=1}^{N} F_{q11}\cdot\sum_{n=1}^{N} F_{q33}\cdot H_{11}^{(0)}\cdot H_{33}^{(0)}+\sum_{n=1}^{N} F_{q22}\cdot\sum_{n=1}^{N} F_{q33}\cdot H_{22}^{(0)}\cdot H_{33}^{(0)}-\sum_{n=1}^{N} F_{q23}\cdot\sum_{n=1}^{N} F_{q32}\cdot H_{22}^{(0)}\cdot H_{33}^{(0)}-$$

$$-\sum_{n=1}^{N} F_{q22}\cdot\sum_{n=1}^{N} F_{q31}^{2}\cdot H_{11}^{(0)}\cdot H_{22}^{(0)}\cdot H_{33}^{(0)}-\sum_{n=1}^{N} F_{q21}^{2}\cdot\sum_{n=1}^{N} F_{q33}\cdot H_{11}^{(0)}\cdot H_{22}^{(0)}\cdot H_{33}^{(0)}+$$

$$+\sum_{n=1}^{N} F_{q11}\cdot\sum_{n=1}^{N} F_{q22}\cdot\sum_{n=1}^{N} F_{q33}\cdot H_{11}^{(0)}\cdot H_{22}^{(0)}\cdot H_{33}^{(0)}-\sum_{n=1}^{N} F_{q11}\cdot\sum_{n=1}^{N} F_{q23}\cdot\sum_{n=1}^{N} F_{q32}\cdot H_{11}^{(0)}\cdot H_{22}^{(0)}\cdot H_{33}^{(0)}+$$

$$+\sum_{n=1}^{N} F_{q21} \cdot \sum_{n=1}^{N} F_{q23} \cdot \sum_{n=1}^{N} F_{q31} \cdot H_{11}^{(0)} \cdot H_{22}^{(0)} \cdot H_{33}^{(0)} +$$

$$+\sum_{n=1}^{N} F_{q21} \cdot \sum_{n=1}^{N} F_{q31} \cdot \sum_{n=1}^{N} F_{q32} \cdot H_{11}^{(0)} \cdot H_{22}^{(0)} \cdot H_{33}^{(0)} + 1\Bigg) \tag{9.42}$$

- term K_{22}

$$K_{22} = \Bigg[H_{22}^{(0)} \cdot \Bigg(\sum_{n=1}^{N} F_{q11} \cdot H_{11}^{(0)} + \sum_{n=1}^{N} F_{q33} \cdot H_{33}^{(0)} +$$

$$+\sum_{n=1}^{N} F_{q11} \cdot \sum_{n=1}^{N} F_{q33} \cdot H_{11}^{(0)} \cdot H_{33}^{(0)} - \sum_{n=1}^{N} F_{q31}^{2} \cdot H_{11}^{(0)} \cdot H_{33}^{(0)} + 1\Bigg)\Bigg] /$$

$$/ \Bigg(\sum_{n=1}^{N} F_{q11} \cdot H_{11}^{(0)} + \sum_{n=1}^{N} F_{q22} \cdot H_{22}^{(0)} + \sum_{n=1}^{N} F_{q33} \cdot H_{33}^{(0)} -$$

$$-\sum_{n=1}^{N} F_{q21}^{2} \cdot H_{11}^{(0)} \cdot H_{22}^{(0)} - \sum_{n=1}^{N} F_{q31}^{2} \cdot H_{11}^{(0)} \cdot H_{33}^{(0)} + \sum_{n=1}^{N} F_{q11} \cdot \sum_{n=1}^{N} F_{q22} \cdot H_{11}^{(0)} \cdot H_{22}^{(0)} +$$

$$+\sum_{n=1}^{N} F_{q11} \cdot \sum_{n=1}^{N} F_{q33} \cdot H_{11}^{(0)} \cdot H_{33}^{(0)} + \sum_{n=1}^{N} F_{q22} \cdot \sum_{n=1}^{N} F_{q33} \cdot H_{22}^{(0)} \cdot H_{33}^{(0)} - \sum_{n=1}^{N} F_{q23} \cdot \sum_{n=1}^{N} F_{q32} \cdot H_{22}^{(0)} \cdot H_{33}^{(0)} -$$

$$-\sum_{n=1}^{N} F_{q22} \cdot \sum_{n=1}^{N} F_{q31}^{2} \cdot H_{11}^{(0)} \cdot H_{22}^{(0)} \cdot H_{33}^{(0)} - \sum_{n=1}^{N} F_{q21}^{2} \cdot \sum_{n=1}^{N} F_{q33} H_{11}^{(0)} \cdot H_{22}^{(0)} \cdot H_{33}^{(0)} +$$

$$+\sum_{n=1}^{N} F_{q11} \cdot \sum_{n=1}^{N} F_{q22} \cdot \sum_{n=1}^{N} F_{q33} \cdot H_{11}^{(0)} \cdot H_{22}^{(0)} \cdot H_{33}^{(0)} - \sum_{n=1}^{N} F_{q11} \cdot \sum_{n=1}^{N} F_{q23} \cdot \sum_{n=1}^{N} F_{q32} \cdot H_{11}^{(0)} \cdot H_{22}^{(0)} \cdot H_{33}^{(0)} +$$

$$+\sum_{n=1}^{N} F_{q21} \cdot \sum_{n=1}^{N} F_{q23} \cdot \sum_{n=1}^{N} F_{q31} \cdot H_{11}^{(0)} \cdot H_{22}^{(0)} \cdot H_{33}^{(0)} +$$

$$+\sum_{n=1}^{N} F_{q21} \cdot \sum_{n=1}^{N} F_{q31} \cdot \sum_{n=1}^{N} F_{q32} \cdot H_{11}^{(0)} \cdot H_{22}^{(0)} \cdot H_{33}^{(0)} + 1\Bigg) \tag{9.43}$$

- term K_{23}

$$K_{23} = -\Bigg[H_{22}^{(0)} \cdot H_{33}^{(0)} \cdot \Bigg(\sum_{n=1}^{N} F_{q23} + \sum_{n=1}^{N} F_{q11} \cdot \sum_{n=1}^{N} F_{q23} \cdot H_{11}^{(0)} -$$

$$-\sum_{n=1}^{N} F_{q21} \cdot \sum_{n=1}^{N} F_{q31} \cdot H_{11}^{(0)}\Bigg)\Bigg] \Big/ \Bigg(\sum_{n=1}^{N} F_{q11} \cdot H_{11}^{(0)} + \sum_{n=1}^{N} F_{q22} \cdot H_{22}^{(0)} + \sum_{n=1}^{N} F_{q33} \cdot H_{33}^{(0)} -$$

$$-\sum_{n=1}^{N} F_{q21}^2 \cdot H_{11}^{(0)} \cdot H_{22}^{(0)} - \sum_{n=1}^{N} F_{q31}^2 \cdot H_{11}^{(0)} \cdot H_{33}^{(0)} + \sum_{n=1}^{N} F_{q11} \cdot \sum_{n=1}^{N} F_{q22} \cdot H_{11}^{(0)} \cdot H_{22}^{(0)} +$$

$$+\sum_{n=1}^{N} F_{q11} \cdot \sum_{n=1}^{N} F_{q33} \cdot H_{11}^{(0)} \cdot H_{33}^{(0)} + \sum_{n=1}^{N} F_{q22} \cdot \sum_{n=1}^{N} F_{q33} \cdot H_{22}^{(0)} \cdot H_{33}^{(0)} - \sum_{n=1}^{N} F_{q23} \cdot \sum_{n=1}^{N} F_{q32} \cdot H_{22}^{(0)} \cdot H_{33}^{(0)} -$$

$$-\sum_{n=1}^{N} F_{q22} \cdot \sum_{n=1}^{N} F_{q31}^2 \cdot H_{11}^{(0)} \cdot H_{22}^{(0)} \cdot H_{33}^{(0)} - \sum_{n=1}^{N} F_{q21}^2 \cdot \sum_{n=1}^{N} F_{q33} \cdot H_{11}^{(0)} \cdot H_{22}^{(0)} \cdot H_{33}^{(0)} +$$

$$+\sum_{n=1}^{N} F_{q11} \cdot \sum_{n=1}^{N} F_{q22} \cdot \sum_{n=1}^{N} F_{q33} \cdot H_{11}^{(0)} \cdot H_{22}^{(0)} \cdot H_{33}^{(0)} - \sum_{n=1}^{N} F_{q11} \cdot \sum_{n=1}^{N} F_{q23} \cdot \sum_{n=1}^{N} F_{q32} \cdot H_{11}^{(0)} \cdot H_{22}^{(0)} \cdot H_{33}^{(0)} +$$

$$+\sum_{n=1}^{N} F_{q21} \cdot \sum_{n=1}^{N} F_{q23} \cdot \sum_{n=1}^{N} F_{q31} \cdot H_{11}^{(0)} \cdot H_{22}^{(0)} \cdot H_{33}^{(0)} +$$

$$+\sum_{n=1}^{N} F_{q21} \cdot \sum_{n=1}^{N} F_{q31} \cdot \sum_{n=1}^{N} F_{q32} \cdot H_{11}^{(0)} \cdot H_{22}^{(0)} \cdot H_{33}^{(0)} + 1\Bigg) \tag{9.44}$$

- term K_{31}

$$K_{31} = -\Bigg[H_{11}^{(0)} \cdot H_{33}^{(0)} \cdot \Bigg(\sum_{n=1}^{N} F_{q31} - \sum_{n=1}^{N} F_{q21} \cdot \sum_{n=1}^{N} F_{q32} \cdot H_{22}^{(0)} +$$

$$+\sum_{n=1}^{N} F_{q22} \cdot \sum_{n=1}^{N} F_{q31} \cdot H_{22}^{(0)}\Bigg)\Bigg] \Big/ \Bigg(\sum_{n=1}^{N} F_{q11} \cdot H_{11}^{(0)} + \sum_{n=1}^{N} F_{q22} \cdot H_{22}^{(0)} + \sum_{n=1}^{N} F_{q33} \cdot H_{33}^{(0)} -$$

$$-\sum_{n=1}^{N} F_{q21}^2 \cdot H_{11}^{(0)} \cdot H_{22}^{(0)} - \sum_{n=1}^{N} F_{q31}^2 \cdot H_{11}^{(0)} \cdot H_{33}^{(0)} + \sum_{n=1}^{N} F_{q11} \cdot \sum_{n=1}^{N} F_{q22} \cdot H_{11}^{(0)} \cdot H_{22}^{(0)} +$$

$$+\sum_{n=1}^{N} F_{q11} \cdot \sum_{n=1}^{N} F_{q33} \cdot H_{11}^{(0)} \cdot H_{33}^{(0)} + \sum_{n=1}^{N} F_{q22} \cdot \sum_{n=1}^{N} F_{q33} \cdot H_{22}^{(0)} \cdot H_{33}^{(0)} - \sum_{n=1}^{N} F_{q23} \cdot \sum_{n=1}^{N} F_{q32} \cdot H_{22}^{(0)} \cdot H_{33}^{(0)} -$$

$$-\sum_{n=1}^{N} F_{q22} \cdot \sum_{n=1}^{N} F_{q31}^2 \cdot H_{11}^{(0)} \cdot H_{22}^{(0)} \cdot H_{33}^{(0)} - \sum_{n=1}^{N} F_{q21}^2 \cdot \sum_{n=1}^{N} F_{q33} \cdot H_{11}^{(0)} \cdot H_{22}^{(0)} \cdot H_{33}^{(0)} +$$

$$+\sum_{n=1}^{N} F_{q11} \cdot \sum_{n=1}^{N} F_{q22} \cdot \sum_{n=1}^{N} F_{q33} \cdot H_{11}^{(0)} \cdot H_{22}^{(0)} \cdot H_{33}^{(0)} - \sum_{n=1}^{N} F_{q11} \cdot \sum_{n=1}^{N} F_{q23} \cdot \sum_{n=1}^{N} F_{q32} \cdot H_{11}^{(0)} \cdot H_{22}^{(0)} \cdot H_{33}^{(0)} +$$

$$+\sum_{n=1}^{N} F_{q21} \cdot \sum_{n=1}^{N} F_{q23} \cdot \sum_{n=1}^{N} F_{q31} \cdot H_{11}^{(0)} \cdot H_{22}^{(0)} \cdot H_{33}^{(0)} +$$

$$+\sum_{n=1}^{N} F_{q21} \cdot \sum_{n=1}^{N} F_{q31} \cdot \sum_{n=1}^{N} F_{q32} \cdot H_{11}^{(0)} \cdot H_{22}^{(0)} \cdot H_{33}^{(0)} + 1\Bigg) \tag{9.45}$$

- term K_{32}

$$K_{32} = -\Bigg[H_{22}^{(0)} \cdot H_{33}^{(0)} \cdot \Bigg(\sum_{n=1}^{N} F_{q32} + \sum_{n=1}^{N} F_{q11} \cdot \sum_{n=1}^{N} F_{q32} \cdot H_{11}^{(0)} -$$

$$-\sum_{n=1}^{N} F_{q21} \cdot \sum_{n=1}^{N} F_{q31} \cdot H_{11}^{(0)}\Bigg)\Bigg] \Bigg/ \Bigg(\sum_{n=1}^{N} F_{q11} \cdot H_{11}^{(0)} + \sum_{n=1}^{N} F_{q22} \cdot H_{22}^{(0)} + \sum_{n=1}^{N} F_{q33} \cdot H_{33}^{(0)} -$$

$$-\sum_{n=1}^{N} F_{q21}^2 \cdot H_{11}^{(0)} \cdot H_{22}^{(0)} - \sum_{n=1}^{N} F_{q31}^2 \cdot H_{11}^{(0)} \cdot H_{33}^{(0)} + \sum_{n=1}^{N} F_{q11} \cdot \sum_{n=1}^{N} F_{q22} \cdot H_{11}^{(0)} \cdot H_{22}^{(0)} +$$

$$+\sum_{n=1}^{N} F_{q11} \cdot \sum_{n=1}^{N} F_{q33} \cdot H_{11}^{(0)} \cdot H_{33}^{(0)} + \sum_{n=1}^{N} F_{q22} \cdot \sum_{n=1}^{N} F_{q33} \cdot H_{22}^{(0)} \cdot H_{33}^{(0)} - \sum_{n=1}^{N} F_{q23} \cdot \sum_{n=1}^{N} F_{q32} \cdot H_{22}^{(0)} \cdot H_{33}^{(0)} -$$

$$-\sum_{n=1}^{N} F_{q22} \cdot \sum_{n=1}^{N} F_{q31}^2 \cdot H_{11}^{(0)} \cdot H_{22}^{(0)} \cdot H_{33}^{(0)} - \sum_{n=1}^{N} F_{q21}^2 \cdot \sum_{n=1}^{N} F_{q33} \cdot H_{11}^{(0)} \cdot H_{22}^{(0)} \cdot H_{33}^{(0)} +$$

$$+\sum_{n=1}^{N} F_{q11} \cdot \sum_{n=1}^{N} F_{q22} \cdot \sum_{n=1}^{N} F_{q33} \cdot H_{11}^{(0)} \cdot H_{22}^{(0)} \cdot H_{33}^{(0)} - \sum_{n=1}^{N} F_{q11} \cdot \sum_{n=1}^{N} F_{q23} \cdot \sum_{n=1}^{N} F_{q32} \cdot H_{11}^{(0)} \cdot H_{22}^{(0)} \cdot H_{33}^{(0)} +$$

$$+\sum_{n=1}^{N} F_{q21} \cdot \sum_{n=1}^{N} F_{q23} \cdot \sum_{n=1}^{N} F_{q31} \cdot H_{11}^{(0)} \cdot H_{22}^{(0)} \cdot H_{33}^{(0)} +$$

$$+\sum_{n=1}^{N} F_{q21} \cdot \sum_{n=1}^{N} F_{q31} \cdot \sum_{n=1}^{N} F_{q32} \cdot H_{11}^{(0)} \cdot H_{22}^{(0)} \cdot H_{33}^{(0)} + 1\Bigg) \tag{9.46}$$

- term K_{33}

$$K_{33} = \Bigg[H_{33}^{(0)} \cdot \Bigg(\sum_{n=1}^{N} F_{q11} \cdot H_{11}^{(0)} + \sum_{n=1}^{N} F_{q22} \cdot H_{22}^{(0)} +$$

$$+\sum_{n=1}^{N} F_{q11} \cdot \sum_{n=1}^{N} F_{q22} \cdot H_{11}^{(0)} \cdot H_{22}^{(0)} - \sum_{n=1}^{N} F_{q21}^{2} \cdot H_{11}^{(0)} \cdot H_{22}^{(0)} + 1\Bigg)\Bigg] /$$

$$/ \Bigg(\sum_{n=1}^{N} F_{q11} \cdot H_{11}^{(0)} + \sum_{n=1}^{N} F_{q22} \cdot H_{22}^{(0)} + \sum_{n=1}^{N} F_{q33} \cdot H_{33}^{(0)} -$$

$$-\sum_{n=1}^{N} F_{q21}^{2} \cdot H_{11}^{(0)} \cdot H_{22}^{(0)} - \sum_{n=1}^{N} F_{q31}^{2} \cdot H_{11}^{(0)} \cdot H_{33}^{(0)} + \sum_{n=1}^{N} F_{q11} \cdot \sum_{n=1}^{N} F_{q22} \cdot H_{11}^{(0)} \cdot H_{22}^{(0)} +$$

$$+\sum_{n=1}^{N} F_{q11} \cdot \sum_{n=1}^{N} F_{q33} \cdot H_{11}^{(0)} \cdot H_{33}^{(0)} + \sum_{n=1}^{N} F_{q22} \cdot \sum_{n=1}^{N} F_{q33} \cdot H_{22}^{(0)} \cdot H_{33}^{(0)} - \sum_{n=1}^{N} F_{q23} \cdot \sum_{n=1}^{N} F_{q32} \cdot H_{22}^{(0)} \cdot H_{33}^{(0)} -$$

$$-\sum_{n=1}^{N} F_{q22} \cdot \sum_{n=1}^{N} F_{q31}^{2} \cdot H_{11}^{(0)} \cdot H_{22}^{(0)} \cdot H_{33}^{(0)} - \sum_{n=1}^{N} F_{q21}^{2} \cdot \sum_{n=1}^{N} F_{q33} H_{11}^{(0)} \cdot H_{22}^{(0)} \cdot H_{33}^{(0)} +$$

$$+\sum_{n=1}^{N} F_{q11} \cdot \sum_{n=1}^{N} F_{q22} \cdot \sum_{n=1}^{N} F_{q33} \cdot H_{11}^{(0)} \cdot H_{22}^{(0)} \cdot H_{33}^{(0)} - \sum_{n=1}^{N} F_{q11} \cdot \sum_{n=1}^{N} F_{q23} \cdot \sum_{n=1}^{N} F_{q32} \cdot H_{11}^{(0)} \cdot H_{22}^{(0)} \cdot H_{33}^{(0)} +$$

$$+\sum_{n=1}^{N} F_{q21} \cdot \sum_{n=1}^{N} F_{q23} \cdot \sum_{n=1}^{N} F_{q31} \cdot H_{11}^{(0)} \cdot H_{22}^{(0)} \cdot H_{33}^{(0)} +$$

$$+\sum_{n=1}^{N} F_{q21} \cdot \sum_{n=1}^{N} F_{q31} \cdot \sum_{n=1}^{N} F_{q32} \cdot H_{11}^{(0)} \cdot H_{22}^{(0)} \cdot H_{33}^{(0)} + 1\Bigg). \tag{9.47}$$

The terms K_{ij} have a common denominator, termed D_K, and they can be therefore written in a more compact form

- term K_{11}

$$K_{11} = \Bigg[H_{11}^{(0)} \cdot \Bigg(\sum_{n=1}^{N} F_{q22} \cdot H_{22}^{(0)} + \sum_{n=1}^{N} F_{q33} \cdot H_{33}^{(0)} +$$

$$+\sum_{n=1}^{N} F_{q22} \cdot \sum_{n=1}^{N} F_{q33} \cdot H_{22}^{(0)} \cdot H_{33}^{(0)} -$$

$$-\sum_{n=1}^{N} F_{q23} \cdot \sum_{n=1}^{N} F_{q32} \cdot H_{22}^{(0)} \cdot H_{33}^{(0)} + 1\Bigg)\Bigg] / D_K \tag{9.48}$$

- term K_{12}

$$K_{12} = -\Bigg[H_{11}^{(0)} \cdot H_{22}^{(0)} \cdot \Bigg(\sum_{n=1}^{N} F_{q21} + \sum_{n=1}^{N} F_{q21} \cdot \sum_{n=1}^{N} F_{q33} \cdot H_{33}^{(0)} -$$

$$-\sum_{n=1}^{N} F_{q31} \cdot \sum_{n=1}^{N} F_{q32} \cdot H_{33}^{(0)}\Bigg)\Bigg] / D_K \tag{9.49}$$

- term K_{13}

$$K_{13} = -\Bigg[H_{11}^{(0)} \cdot H_{33}^{(0)} \cdot \Bigg(\sum_{n=1}^{N} F_{q31} - \sum_{n=1}^{N} F_{q21} \cdot \sum_{n=1}^{N} F_{q23} \cdot H_{22}^{(0)} +$$

$$+\sum_{n=1}^{N} F_{q22} \cdot \sum_{n=1}^{N} F_{q31} \cdot H_{22}^{(0)}\Bigg)\Bigg] / D_K \tag{9.50}$$

- term K_{21}

$$K_{21} = -\left[H_{11}^{(0)} \cdot H_{22}^{(0)} \cdot \left(\sum_{n=1}^{N} F_{q21} + \sum_{n=1}^{N} F_{q21} \cdot \sum_{n=1}^{N} F_{q33} \cdot H_{33}^{(0)} - \right.\right.$$

$$\left.\left. - \sum_{n=1}^{N} F_{q23} \cdot \sum_{n=1}^{N} F_{q31} \cdot H_{33}^{(0)}\right)\right] / D_K \tag{9.51}$$

- term K_{22}

$$K_{22} = \left[H_{22}^{(0)} \cdot \left(\sum_{n=1}^{N} F_{q11} \cdot H_{11}^{(0)} + \sum_{n=1}^{N} F_{q33} \cdot H_{33}^{(0)} + \right.\right.$$

$$\left.\left. + \sum_{n=1}^{N} F_{q11} \cdot \sum_{n=1}^{N} F_{q33} \cdot H_{11}^{(0)} \cdot H_{33}^{(0)} - \sum_{n=1}^{N} F_{q31}^{2} \cdot H_{11}^{(0)} \cdot H_{33}^{(0)} + 1\right)\right] / D_K \tag{9.52}$$

- term K_{23}

$$K_{23} = -\left[H_{22}^{(0)} \cdot H_{33}^{(0)} \cdot \left(\sum_{n=1}^{N} F_{q23} + \sum_{n=1}^{N} F_{q11} \cdot \sum_{n=1}^{N} F_{q23} \cdot H_{11}^{(0)} - \right.\right.$$

$$\left.\left. - \sum_{n=1}^{N} F_{q21} \cdot \sum_{n=1}^{N} F_{q31} \cdot H_{11}^{(0)}\right)\right] / D_K \tag{9.53}$$

- term K_{31}

$$K_{31} = -\left[H_{11}^{(0)} \cdot H_{33}^{(0)} \cdot \left(\sum_{n=1}^{N} F_{q31} - \sum_{n=1}^{N} F_{q21} \cdot \sum_{n=1}^{N} F_{q32} \cdot H_{22}^{(0)} + \right.\right.$$

$$\left.\left. + \sum_{n=1}^{N} F_{q22} \cdot \sum_{n=1}^{N} F_{q31} \cdot H_{22}^{(0)}\right)\right] / D_K \tag{9.54}$$

- term K_{32}

$$K_{32} = -\left[H_{22}^{(0)} \cdot H_{33}^{(0)} \cdot \left(\sum_{n=1}^{N} F_{q32} + \sum_{n=1}^{N} F_{q11} \cdot \sum_{n=1}^{N} F_{q32} \cdot H_{11}^{(0)} - \right.\right.$$

$$\left.\left. - \sum_{n=1}^{N} F_{q21} \cdot \sum_{n=1}^{N} F_{q31} \cdot H_{11}^{(0)}\right)\right] / D_K \tag{9.55}$$

- term K_{33}

$$K_{33} = \left[H_{33}^{(0)} \cdot \left(\sum_{n=1}^{N} F_{q11} \cdot H_{11}^{(0)} + \sum_{n=1}^{N} F_{q22} \cdot H_{22}^{(0)} + \right. \right.$$

$$\left. \left. + \sum_{n=1}^{N} F_{q11} \cdot \sum_{n=1}^{N} F_{q22} \cdot H_{11}^{(0)} \cdot H_{22}^{(0)} - \sum_{n=1}^{N} F_{q21}^{2} \cdot H_{11}^{(0)} \cdot H_{22}^{(0)} + 1 \right) \right] / D_K \qquad (9.56)$$

The tangent stiffness matrix above was coded in the finite element representing the response of the 3 degrees of freedom macro-element included in the OpenSees library.

Chapter 10

Appendix 3: three-dimensional site response analysis

The SANISAND and the PDMY models used for soil are tested in three-dimensional site response analyses of the soil column representing the Pantano subsoil (see Section 7.1.1), considering the full three-component seismic record of Tabas.

Considering the response of the soil column with the SANISAND model, a plan view of the two components of the horizontal displacement induced by a three-dimensional seismic motion is shown in Figure 10.1. It can be seen that relevant displacements occur at the foundation level, in terms of maximum (u_{max}) and final (u_{perm}) values, and they are essentially constant over the ground water table, indicating that the soil strength is attained at greater depths. The displacements associated with the fault normal component of the seismic motion (FN), aligned to the longitudinal direction of the bridge, are approximately twice those produced by the transverse motion (FP), because the former is sharply more severe than the latter. This leads to a response in the horizontal plane ($FN - FP$) strongly oriented towards the longitudinal direction, as confirmed by the deformed shape of the soil column in the post-earthquake condition depicted in Figure 10.2. As ob-

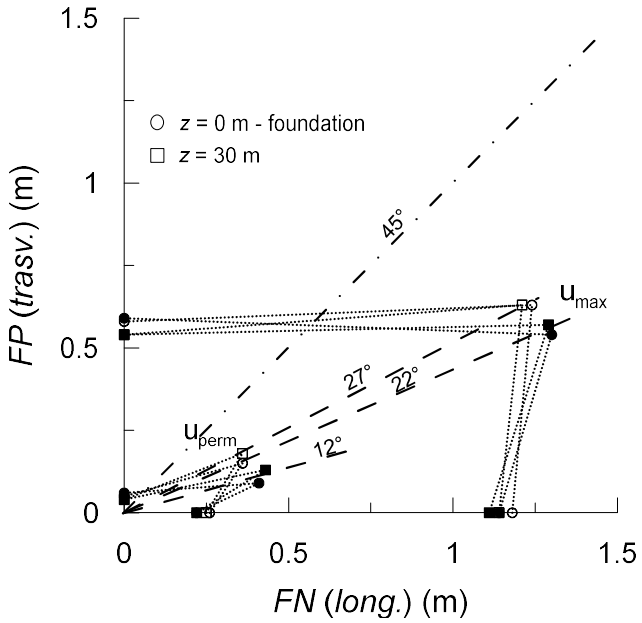

Figure 10.1: Effect of the multi-directionality of the seismic motion on the horizontal displacements evaluated at the foundation level (circles) and a depth of 30 m (squares), either in absence (void symbols) or in presence (filled symbols) of the vertical motion.

served in the one-dimensional site response, the maximum shear strains develop in depth, in between the strata $MG1$ and $MG2$, for the progressive development of important excess pore water pressures at those depths. This represents the main difference between the behaviour of the Pantano subsoil and the simplified version of the soil domain used in the reference soil-bridge system, leading to an amplified displacement field due to the lower effective strength of the saturated soil and, as a result, to reduced seismic actions transferred to the superstructure. The co-presence of the two components of the horizontal motion has an ever-amplifying effect of the displacement field with respect to the mono-dimensional propagation, whereas the effect of the vertical motion on the horizontal displacements is definitely more limited.

The above effects of multi-directionality of the ground motion on the displacement field can be read in a dual manner in the spectral shapes evaluated at the foundation level of the abutment, represented in Figure 10.3. Also in this case, in

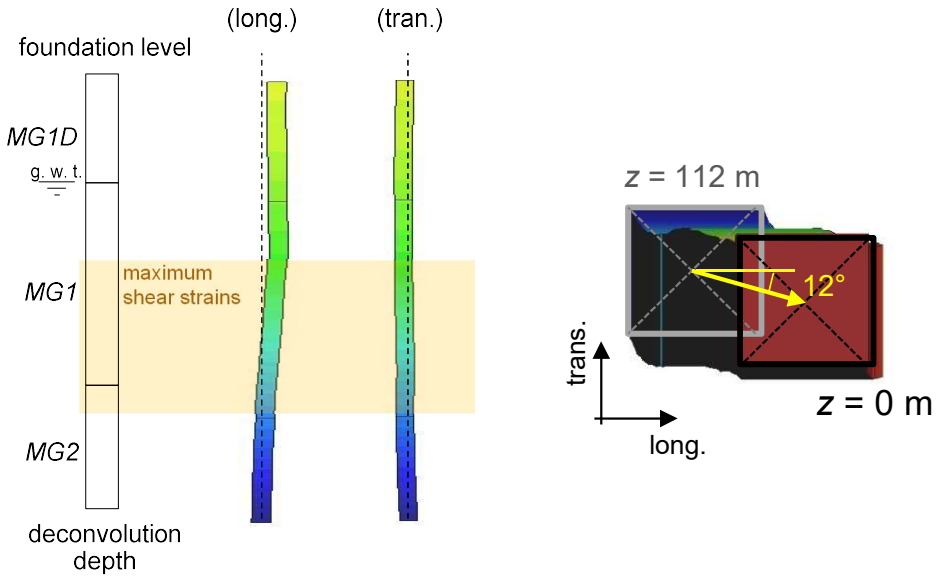

Figure 10.2: Post-earthquake deformed shape of the soil column.

fact, the bi-directionality of the seismic motion in the horizontal plane leads to a soil response essentially overlapped to that associated with a three-component seismic motion. This happens because the combined shear stress state in the horizontal plane is the main reason for the development of plastic mechanisms in the soil. In addition to this, compared to the input motion, the spectral shapes at the foundation level show a noticeable amplification for periods greater than about 1 s, due to the deformability of the foundation soils, while for lower periods the spectral accelerations are practically unchanged.

Focusing on the response at the ground level, Figure 10.4 shows the time evolution of the displacements computed through the two constitutive models. The discrepancy on the longitudinal displacements follows the same logic exposed for the mono-dimensional propagation of the ground motion, with greater maximum displacements in the critical interval between 12 s and 17.5 s and a consequent more displaced permanent configuration of the soil domain associated with the use of the SANISAND model. This result is accompanied by the comparison between

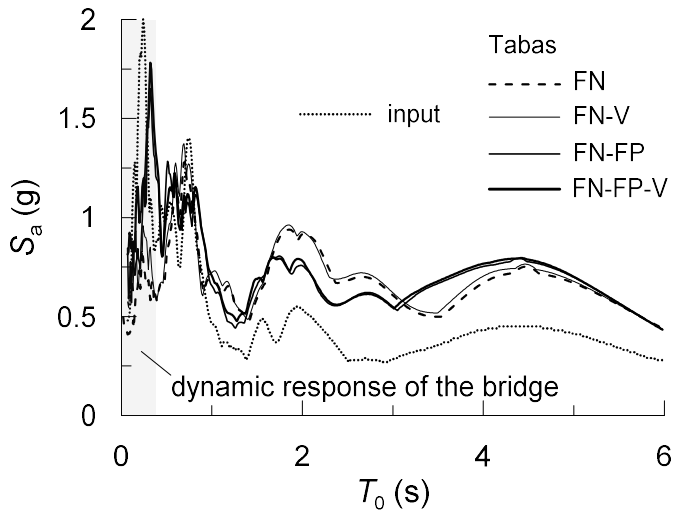

Figure 10.3: 5%-damped elastic response spectra at the foundation level in the longitudinal direction.

the response spectra in Figure 10.5, in which the moderately stiffer behaviour of the PDMY model leads to higher amplitudes between $T = 1.4 \div 2.3$ s and a more attenuated response at larger periods.

The vertical displacements, instead, are the result of a combined deformation mechanism. In addition to the vertical oscillations caused by the vertical seismic motion, the top of the column undergoes a progressive settlement induced by the combined volumetric-deviatoric behaviour of the soil models. When the soil exhibits an elastic-plastic response, in fact, the development of plastic shear strains implies the arise of plastic volumetric strains as well, according to Eqs. 3.4 and 3.5 for the SANISAND model and to Eqs. 3.21 and 3.23 for the PDMY model. More in detail, the rate of volumetric strain is controlled by the dilatancy parameters A_0, for the SANISAND model, and by the parameters d_1 and d_2, for the PDMY model. Based on the optimised constitutive parameters adopted, the response of the PDMY model presents a higher rate of contraction induced by the plastic shear behaviour. The resulting vertical response spectra at the ground level show a pronounced amplification compared to the spectra shapes in correspondence of the ground water table,

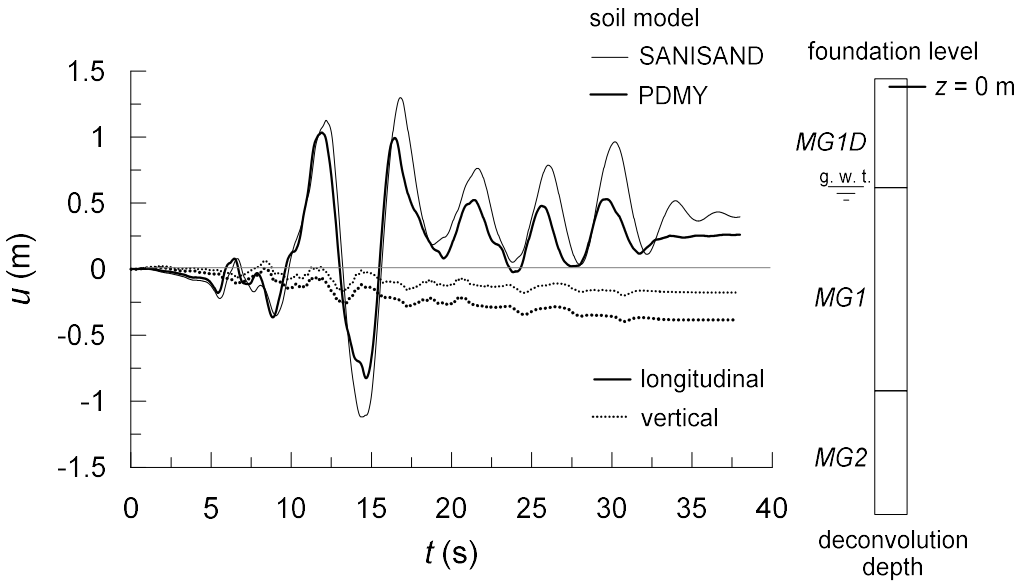

Figure 10.4: Comparison between the response of the SANISAND model and of the PDMY model: time histories of the displacements at $z = 0$ m (foundation level) in the longitudinal and vertical directions.

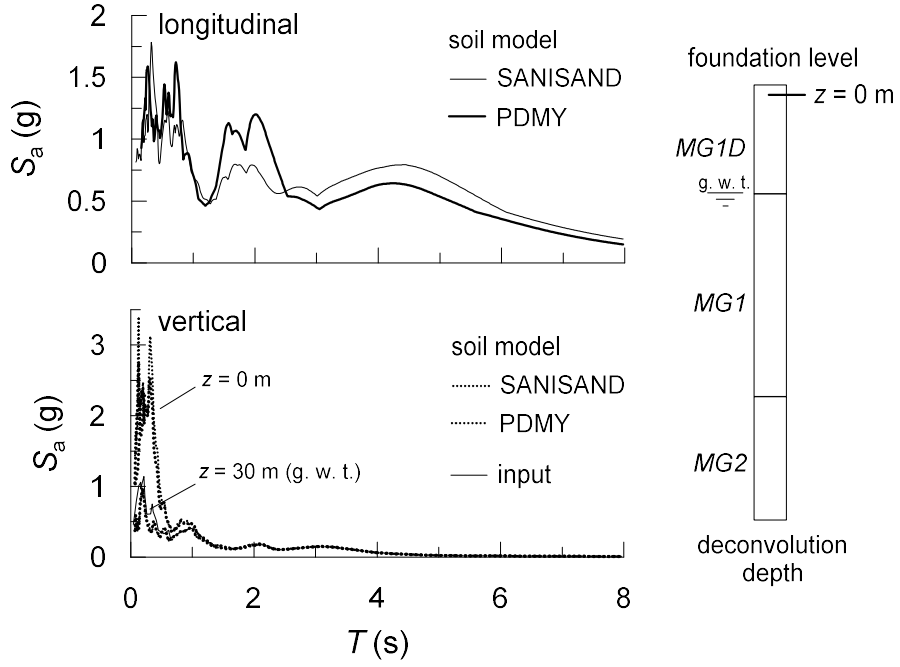

Figure 10.5: Comparison between the response of the SANISAND model and of the PDMY model: 5 %-damped elastic response spectra at (a) $z = 0$ m (foundation level) in the longitudinal and vertical directions.

which instead are nearly identical to the spectrum of the vertical input motion. This happens because the propagation of the vertical motion is controlled by the bulk modulus of water in the saturated zone, while it is amplified by the volumetric behaviour of soil above the ground water table, with amplification well confined at high frequencies for the high bulk modulus of the Messina Gravels.